Published in Journals: Solar, Energies,
Batteries, Electronics, Sustainability and Applied Sciences

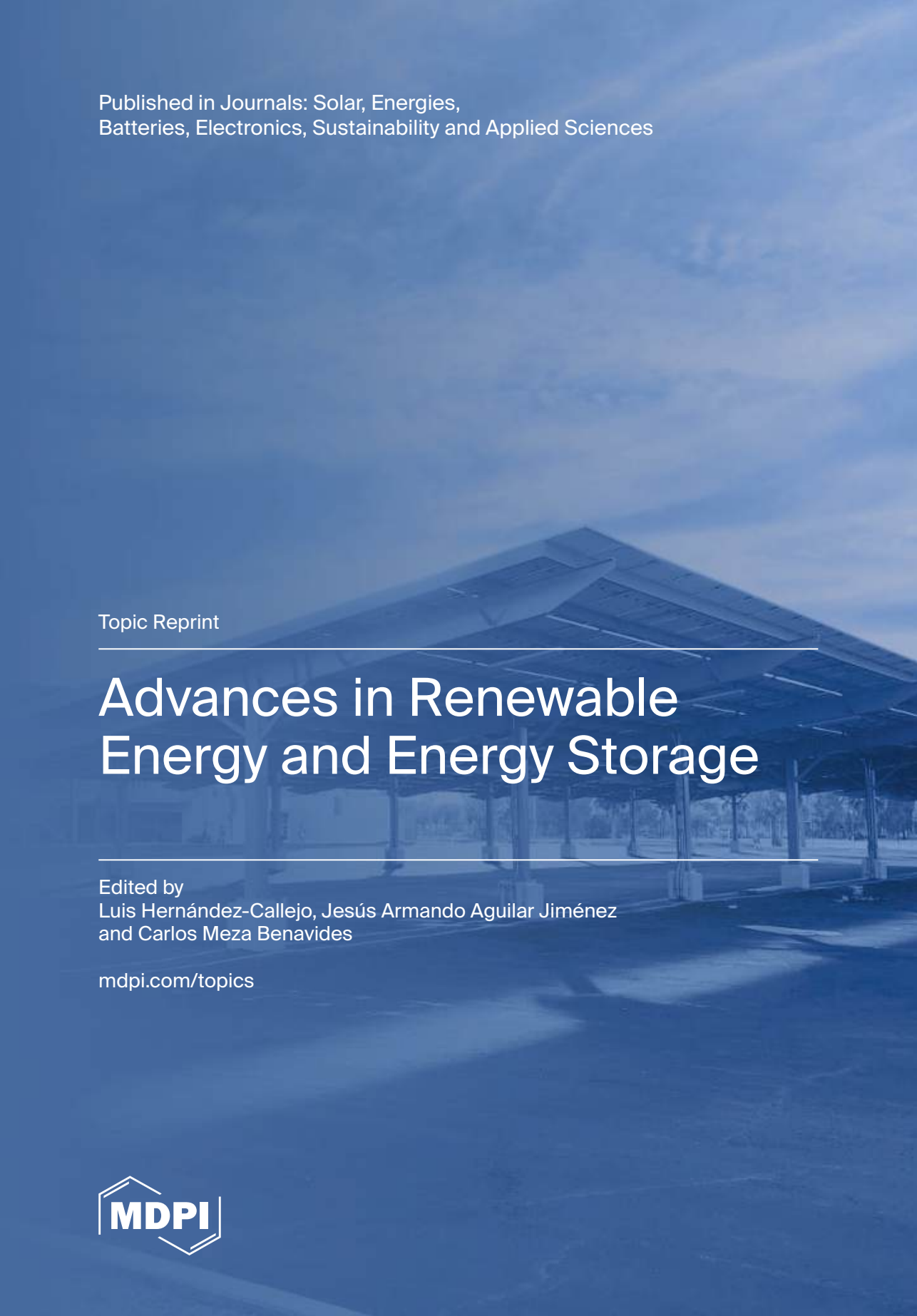

Topic Reprint

Advances in Renewable Energy and Energy Storage

Edited by
Luis Hernández-Callejo, Jesús Armando Aguilar Jiménez
and Carlos Meza Benavides

mdpi.com/topics

MDPI

Advances in Renewable Energy and Energy Storage

Advances in Renewable Energy and Energy Storage

Editors

Luis Hernández-Callejo
Jesús Armando Aguilar Jiménez
Carlos Meza Benavides

MDPI

Basel • Beijing • Wuhan • Barcelona • Belgrade • Novi Sad • Cluj • Manchester

Editors

Luis Hernández-Callejo
Department of Agricultural and Forestry Engineering, University of Valladolid, Campus Duques de Soria
Soria, Spain

Jesús Armando Aguilar Jiménez
Facultad de Ingeniería, Universidad Autónoma de Baja California
Mexicali, Mexico

Carlos Meza Benavides
Department of Electrical, Mechanical and Industrial Engineering, Anhalt University of Applied Sciences
Köthen, Germany

Editorial Office
MDPI
St. Alban-Anlage 66
4052 Basel, Switzerland

This is a reprint of articles from the Topic published online in the open access journals *Solar* (ISSN 2673-9941), *Energies* (ISSN 1996-1073), *Batteries* (ISSN 2313-0105), *Electronics* (ISSN 2079-9292), *Sustainability* (ISSN 2071-1050), and *Applied Sciences* (ISSN 2076-3417) (available at: https://www.mdpi.com/topics/Energy_Storage).

For citation purposes, cite each article independently as indicated on the article page online and as indicated below:

Lastname, A.A.; Lastname, B.B. Article Title. *Journal Name* **Year**, *Volume Number*, Page Range.

ISBN 978-3-0365-9552-8 (Hbk)
ISBN 978-3-0365-9553-5 (PDF)
doi.org/10.3390/books978-3-0365-9553-5

Cover image courtesy of Luis González Uribe and Jesús Armando Aguilar Jiménez
Solar Photovoltaic Parking Lot of the Engineering Faculty of the Autonomous University of Baja California.

Contents

About the Editors

Luis Hernández-Callejo

Prof. Dr. Luis Hernández-Callejo holds degrees as an Electrical Engineer at Universidad Nacional de Educación a Distancia (UNED, Spain), a Computer Engineer at UNED, and a PhD at Universidad de Valladolid (Spain). A professor and researcher at the Universidad de Valladolid, his areas of interest are renewable energy, microgrids, photovoltaic energy, wind energy, smart cities, artificial intelligence.

Prof. Dr. Hernandez Callejo is an editor in numerous scientific journals, and is a guest editor in many Special Issues. He has directed four doctoral theses, and at the moment, he is directing six doctoral theses. He is a professor in wind energy, solar energy, and microgrids, and he collaborates with many universities in Spain and in the rest of the world.

Jesús Armando Aguilar Jiménez

Dr. Jesús Armando Aguilar Jiménez holds a PhD in Engineering from the Institute of Engineering at the Autonomous University of Baja California (UABC). He is a faculty member at the Faculty of Engineering, Mexicali Campus, UABC, and is recognized as a Level 1 member of the National System of Researchers. His research interests encompass renewable energies, energy simulation, energy conservation, and efficient energy use, as well as energy innovation. Currently engaged in energy projects for both the public and private sectors, he actively participates in academic committees for the evaluation of scientific research. Dr. Aguilar-Jiménez also contributes to the development of human capital through teaching at both undergraduate and postgraduate levels, including the supervision of postgraduate theses.

Carlos Meza Benavides

Dr. Carlos Meza Benavides is an electronics engineer with a Master's degree in Embedded System Design from the Università della Svizzera italiana (USI), Lugano, Switzerland; an Advanced Studies Diploma in Dynamic Systems; and a PhD in Advanced Automation and Robotics from the Universitat Politècnica de Catalunya—BarcelonaTech (UPC), Spain. He has held various research positions, including as a visiting researcher at the University of Groningen, Netherlands; a postdoctoral researcher at the Institute of Applied Sustainability for the Built Environment in Cannobio, Switzerland; and a senior postdoctoral researcher at UNESCO's International Centre for Theoretical Physics in Trieste, Italy. Dr. Meza has served as a consultant on energy issues in Latin America for European projects and the Organization of American States. He was the founder and first president of the Costa Rican Solar Energy Association (Acesolar). Currently, he is a professor in the Master's program in Photovoltaic Engineering at Anhalt University of Applied Sciences in Germany and teaches and advises students at the Costa Rica Institute of Technology (TEC) and the Valencia International University. His research interests include photovoltaic system analysis, embedded system design for energy systems, and power electronics for renewable energy and storage systems ....

Preface

"Advances in Renewable Energy and Energy Storage" constitutes a thorough examination of the crucial transition towards a global energy matrix based on renewable sources. This reprint focuses on cutting-edge technologies, highlighting enhanced efficiency, superior energy integration, and cost-effectiveness to foster the widespread adoption of renewable energies. The objectives encompass guiding collective efforts towards sustainable development, mitigating environmental pollution, and addressing the challenges of climate change.

Motivated by the urgent need for sustainable energy solutions, this reprint aims to inform and inspire diverse stakeholders, including academics, industry professionals, and policymakers. The authors, distinguished experts in the field, have collaborated to distill innovative research, providing a comprehensive resource for decision makers in both the public and private sectors. We extend our sincere gratitude to those who contributed to this effort, recognizing the collective commitment needed to steer our world towards a resilient and environmentally conscious energy future.

Luis Hernández-Callejo, Jesús Armando Aguilar Jiménez, and Carlos Meza Benavides
Editors

solar

MDPI

Article

Assessing the Potential of Qatari House Roofs for Solar Panel Installations: A Feasibility Survey

Ayed Banibaqash, Ziad Hunaiti and Maysam Abbod *

Department of Electronic and Electrical Engineering, College of Engineering, Design and Physical Sciences, Brunel University London, Uxbridge, London UB8 3PH, UK
* Correspondence: maysam.abbod@brunel.ac.uk

Abstract: Qatar's ambitious Vision 2030 includes a major shift towards clean energy, and residential solar PV installation can be an obvious option, given its abundant sunlight and high power for residential cooling. Despite significant solar panel farm investment, there has been limited progress in deploying solar panels on home roofs, and further research is needed to identify the potential for such an initiative and its impact on the country's move towards clean energy. This field survey assesses the potential for residential rooftop solar panel installation across Qatar, considering space availability, currently utilized space, remaining space, shading, and roof type. It also provided indications of potential obstacles and shading that might affect panel sunlight exposure. The results showed that there is significant potential for installing solar panels on Qatari homes, which could contribute to a considerable portion of the energy consumed by households during peak usage periods, particularly in the summer months. Moreover, excess energy generated could be exported to other countries with high demand during periods of low demand in Qatar. The study's findings complement previous research efforts and provide insights for policymakers and stakeholders to develop strategies that endorse the vision for 2030 and promote the transition towards clean energy in Qatar.

Keywords: renewable energy; solar panels; Qatar; roof solar panels; roof survey; installation feasibility; solar panel installation drivers

Citation: Banibaqash, A.; Hunaiti, Z.; Abbod, M. Assessing the Potential of Qatari House Roofs for Solar Panel Installations: A Feasibility Survey. *Solar* **2023**, *3*, 650–662. https://doi.org/10.3390/solar3040035

Academic Editor: Jürgen Heinz Werner

Received: 22 July 2023
Revised: 25 September 2023
Accepted: 26 October 2023
Published: 10 November 2023

1. Introduction

Qatar is committed to achieving its Vision 2030, which aims to create a sustainable and diversified economy as well as a healthy and secure society. One of the key strategies to achieve this vision is through a major shift towards clean energy [1]. Given the country's geographic location, Qatar is well-suited to harnessing the power of the sun to achieve its sustainable electricity goals. The country has abundant sunlight throughout the year, making it an ideal location for the installation of solar PV arrays [2]. Qatar has already taken significant steps towards achieving its vision of clean energy and has invested heavily in solar panel farms, such as the 800 MW Al-Kharsaah Solar Power Plant, which is expected to power around 10% of the country's energy needs [3]. These farms are a critical component of Qatar's clean energy strategy, but more can be undertaken. The majority of Qatar's energy load is domestic use, especially for cooling during the summer months, as noted by the Annual Statistics Report 2021 of Qatar General Electricity & Water Corporation (KAHRAMAA), accounting for 38,284,270 MWh out of the total amount of electricity generated nationally per year (Figure 1) [4]. It is clear from the figure that domestic users account for nearly four times the number of industrial consumers. This fact supports the objective of this study, indicating that residential buildings have the potential to play a significant role in the transition toward clean energy and achieve milestones toward the national net-zero target. At the time of this study, there is still limited progress in deploying solar panels on home roofs, despite the country's high levels of sunshine and the potential benefits that such installations can bring [2].

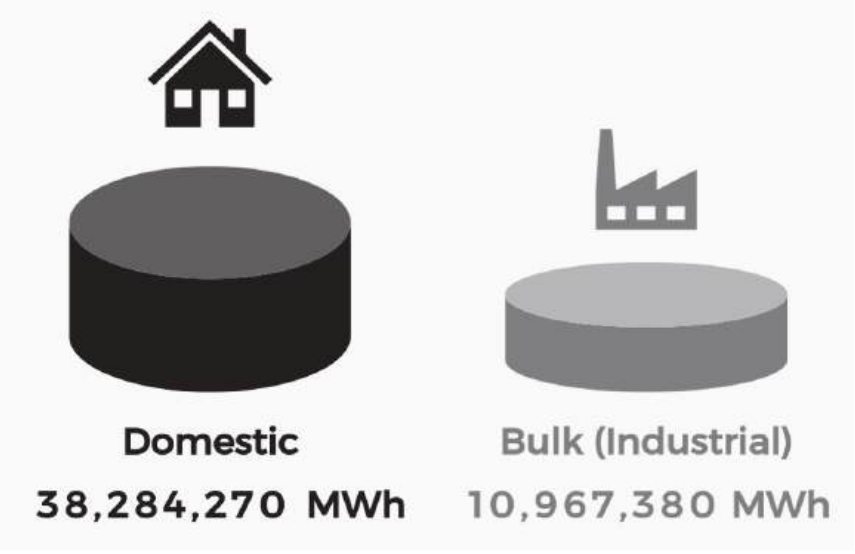

Figure 1. Domestic energy consumption [4].

Deploying solar panels on home roofs can contribute to the country's clean energy goals by creating a distributed network of clean energy production. This can help reduce the country's dependence on fossil fuels (as well as the cannibalization of its primary national exports), lower carbon emissions, and create a more resilient energy system. Given that the country is one of the main energy exporters and experiences a high number of sunny days, it can enable significant clean energy generation that can be exported [2]. However, further research is needed to identify the potential for this initiative and its impact on the country's move towards clean energy. This includes examining factors such as the availability of suitable roof space, the orientation of the roofs, and the presence of any shading or obstructions that might limit the effectiveness of the solar panels. By conducting such research, stakeholders can better understand the potential of solar panels on residential roofs and develop strategies to accelerate and optimize their deployment.

2. Drivers for Roof Solar Panels in Qatar

Qatar has made progress in large-scale solar farm investments, but residential solar panel deployment is still needed to achieve the nation's clean energy vision by 2030 [1]. Previous research has identified key challenges, as summarized in Figure 2, that must be addressed before scaling up solar panel deployment in Qatar [5]. These challenges include a lack of interest in renewable energy, competition from other energy sources, uncompetitive pricing due to subsidized conventional electricity, limited awareness of renewable energy, insufficient government initiatives, and a lack of environmental concern. Similar challenges exist in other Gulf Cooperation Council (GCC) countries. Thus, addressing these issues is necessary before considering residential and commercial solar panel deployment in Qatar. A national roadmap for sustainable energy is crucial for achieving this long-term goal.

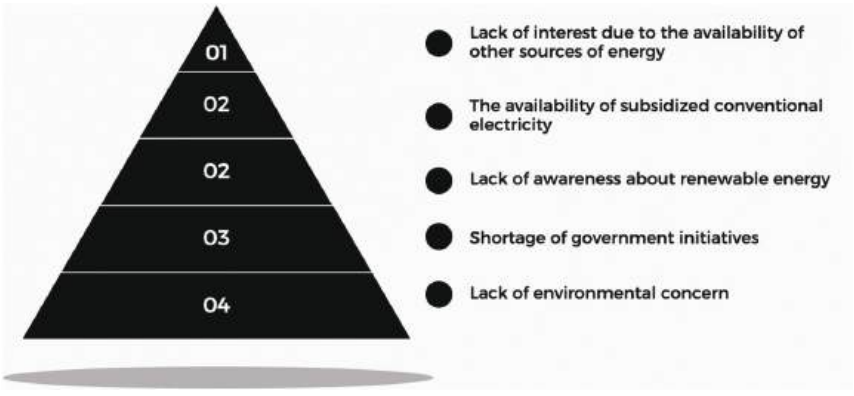

Figure 2. Five key challenges to residential solar PV adoption [5].

By considering the six drivers for promoting solar panel adoption, namely potential, awareness, the net-zero pathway, energy efficiency, lowering subsidies, and sustainability, stakeholders can develop effective strategies to encourage the installation of solar panels and achieve the vision of a sustainable future (Figure 3).

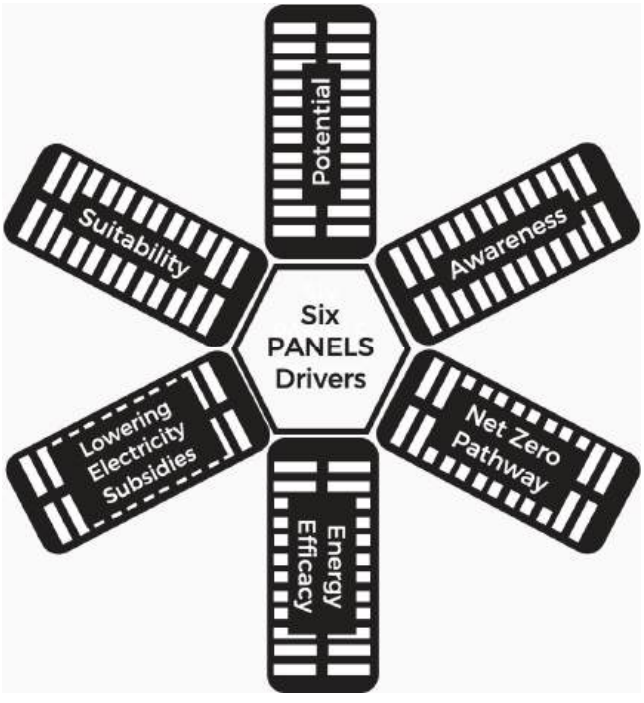

Figure 3. Six PANELS drivers [authors].

2.1. Potential

Qatar has vast potential for solar energy investment, positioning itself as a leader in clean energy exports. Factors such as high sun hours, market experience, and financial capacity make Qatar an ideal location for solar energy ventures [6]. Qatar is well-suited for solar energy investments, with an average of 3600 h of direct solar radiation annually [7].

The country is committed to reducing its carbon footprint and aims to generate 20% of its energy from renewables by 2030, with solar energy playing a significant role [8].

A recent feasibility study explored various scenarios of solar panel deployment in Qatar's residential and commercial buildings, considering panel sizes, efficiency, and daily sun exposure. Results indicated substantial potential for rooftop solar panels, generating significant energy during peak usage, particularly in hot summer months. Surplus energy could be exported to countries with high energy demands, positioning Qatar as a major contributor to solving global energy crises [2].

Qatar's extensive experience in the energy market, particularly in the oil and gas industry, can be leveraged to develop the solar energy sector and gain a competitive advantage in the global clean energy market [9]. The country's financial capacity and resources enable large-scale solar energy investments [10]. Notably, Qatar has already invested in significant solar energy projects, including the Al-Kharsaah Solar Power Plant, one of the world's largest [11]. With its potential for solar energy investment and clean energy exports, Qatar can contribute to its own energy needs, reduce carbon emissions, and address global energy demands [12]. Its high sun hours, market experience, and financial capacity make it an ideal destination for solar energy investment [2].

2.2. Awareness

Awareness plays a vital role in promoting the adoption of renewable energy resources. In Qatar, a lack of awareness has been identified as a significant challenge hindering the deployment of renewable energy [13]. To address this challenge, the government should implement projects that allow households to actively participate and experience the benefits of installing solar panels. This can effectively raise awareness throughout the nation [14]. Given Qatar's socially connected society, visible solar panels on homes would initiate conversations and spark interest in renewable energy, leading to a snowball effect of adoption [15]. The installation of solar panels serves as a strategic tool to raise awareness and drive the transition toward clean energy use [16]. Not only does it offer tangible benefits like reduced energy bills, but it also visually demonstrates individuals', businesses', and nations' commitment to reducing carbon emissions and contributing to global climate change mitigation efforts [17]. This visual representation can generate public interest and awareness of renewable energy, inspiring more individuals and businesses to embrace clean energy sources [18].

Moreover, increasing public awareness about renewable energy can garner support for policies and initiatives promoting clean energy adoption [17]. This creates a favorable environment for renewable energy investment and deployment in Qatar, encouraging businesses to invest in renewable energy projects. Therefore, enhancing public understanding of the nature and significance of clean and renewable energy sources is a crucial step in establishing them as a normative and primary component of the national energy mix. In Qatar, the installation of solar panels on homes acts as a catalyst for raising awareness and driving the transition to clean energy. By generating public interest and support for renewable energy, Qatar can contribute to global climate change mitigation efforts and foster a more sustainable future for all.

2.3. Net-Zero Building Pathway

To achieve more sustainable and energy-efficient buildings, implementing a net-zero strategy is crucial. Net-zero buildings have the capability to generate as much energy as they consume, resulting in a neutral or net-zero energy balance [19]. Currently, homes in Qatar heavily rely on external energy sources, but the installation of solar panels on rooftops can pave the way towards net-zero buildings [20]. By incorporating solar panels, homes in Qatar can reduce their dependence on conventional energy sources and promote the use of renewable energy. The region's abundant sunshine makes solar energy an ideal solution for meeting residential energy needs [13]. Local energy production allows homes

to decrease their reliance on grid-supplied electricity, which is often costly and contributes to carbon emissions [2].

Apart from the environmental advantages, transitioning to net-zero buildings can lead to significant cost savings for homeowners. By generating their own energy, homeowners can reduce their electricity bills and even potentially sell surplus energy back to the grid [19]. This introduces a new revenue stream and helps offset the upfront costs of solar panel installation [2]. Additionally, adopting a net-zero strategy improves overall energy efficiency in buildings, resulting in reduced energy consumption and lower carbon emissions. These efforts align with global initiatives to combat climate change [21]. Therefore, installing solar panels on homes in Qatar serves as a strategic step towards achieving net-zero buildings. Through localized energy production, homeowners can decrease their reliance on conventional energy sources, lower energy expenses, and contribute to global climate change mitigation [20]. Thus, implementing a net-zero strategy is essential for creating a more sustainable and energy-efficient built environment in Qatar.

2.4. Energy Efficiency

Energy efficiency is crucial for a sustainable energy strategy in Qatar, where all homes currently rely on fossil fuel-generated energy. Promoting energy efficiency is vital to reduce consumption, lower carbon emissions, and create a sustainable built environment [22]. By installing solar panels and implementing a net-zero strategy, homeowners are expected to shift towards using energy-efficient appliances and monitoring their energy usage [23]. Solar panel installation on Qatar's homes can transform the way homeowners consume energy. Producing their own energy raises awareness about consumption and environmental impact, fostering a greater appreciation for energy efficiency and a willingness to invest in low-energy appliances [23].

Furthermore, a net-zero strategy incentivizes energy efficiency through a feedback loop between production and consumption [23]. As homeowners become adept at generating their own energy, they become conscious of consumption patterns and take steps to reduce energy usage. This includes adopting energy-efficient habits, investing in efficient appliances, and monitoring consumption for potential savings. Therefore, promoting energy efficiency is vital for a sustainable energy strategy, especially in Qatar, where homes solely rely on fossil fuel-generated energy. Through solar panel installation and a net-zero approach, homeowners can enhance awareness, invest in efficient technologies, and contribute to a sustainable built environment [24]. Energy efficiency is essential for achieving a sustainable and energy-efficient future in Qatar.

2.5. Lowering Electricity Subsidies

Qatar can transition to a sustainable energy future by deploying solar panels on homes. Energy subsidies pose a challenge as the government provides free energy to citizens, hindering solar panel installation. However, the government can support panel installation to reduce non-clean energy use and subsidies [10,13]. This empowers homeowners to generate their own energy, reducing their reliance on non-clean sources [25]. It shifts the energy production burden from the government to individuals, lowering subsidies [10]. Homeowners can contribute to the grid and export excess energy, generating revenue [2]. Government support for solar panels demonstrates a commitment to sustainability and emission reduction, fosters environmental consciousness, and encourages investment in sustainable energy [25,26].

2.6. Suitability

The deployment of solar panels in Qatar can contribute significantly to achieving sustainability across the three main pillars: the economy, society, and the environment. Solar energy is a clean and renewable source of energy that can support the economy by providing a new source of energy and sustaining the other available sources for future generations [10]. By investing in solar energy, the country can reduce its reliance on non-clean

sources of energy, which can reduce the costs associated with importing and transporting non-renewable fuels. This can, in turn, support economic growth and development [27]. Moreover, solar energy can benefit society by minimizing pollution, particularly carbon emissions. The use of solar panels can help reduce the amount of carbon particles in the air, which can lead to a healthier and more sustainable society. This can contribute to the overall well-being of the population, as reducing pollution can lead to a reduction in respiratory illnesses and other health issues [28]. By reducing the generation of CO_2 from clean sources of energy, solar panels can contribute to a more sustainable environment that can be kept for future generations. This can also help reduce the negative impact of climate change on the environment and support the preservation of natural resources [29].

In order to effectively facilitate the implementation of the six drivers for solar panel deployment in Qatar, it is essential to carry out a field survey aimed at evaluating the viability of installing solar panels on different types of residential buildings. This survey will provide valuable insights to homeowners and decision-makers, enabling them to develop suitable scenarios for the installation and effective utilization of solar panels on domestic roofs in Qatar [30].

3. Materials and Methods

To evaluate the feasibility of installing solar panels on homes in Qatar, a survey was conducted using a manual approach with a structured interview sheet with closed-ended questions as the data collection method, based on the previous literature (as explained in Table 1). The reason for opting for manual surveying instead of remote sensing methods, such as the use of satellite images [31], is primarily due to cost, accessibility, and issues related to legal and ethical approvals. Additionally, the use of drones has been considered; however, as of now, drone surveying is not yet allowed in Qatar [32].

The survey aimed to gather data on the availability of space for solar panel installation, currently utilized space, remaining space, shading, and roof type. The use of a structured interview sheet with closed-ended questions provided a standardized approach to data collection and made the process more efficient. Closed-ended questions were used to collect quantitative data, which could be easily analyzed statistically to identify patterns and relationships in the data [33]. As shown in Figure 4, the research design consisted of four stages to complete the research project. The first stage was designing and testing the data collection instrument, which was the most important part of the research design. It involved identifying the main aspects to be included within the data collection instruments, and an interview sheet was established. Each item included had a justification, as shown in Table 1.

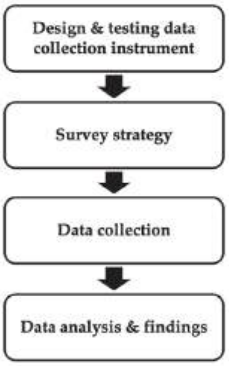

Figure 4. Research design [authors].

Table 1. Collected data and justification.

Interview Question	Rationale
House location	The location of a house in the field survey is essential to obtaining accurate geographical representation [3,34].
Number of similar houses in the street or compound	Knowing the number of similar houses in the same area is essential for a wider and more representative study. It helps with solar panel installation planning, as a community solar setup can be considered [34].
Number of bedrooms in the house	The number of bedrooms in a house is crucial for solar panel installation. It helps estimate energy consumption and the correct number of panels needed. Also, analyzing energy usage patterns identifies areas for conservation measures, reducing consumption, and enhancing solar panel effectiveness [35].
Items on the roof	Before installing solar panels, it is essential to identify existing objects that may hinder the process or limit available space. These can include AC units, chimneys, skylights, and other structures. Assessing their current use and placement on the roof helps determine the best solar panel installation approach [3].
Approximate total roof size in square meters	Determining the approximate size of a roof (in square meters) is essential when considering the installation of solar panels. This information can be used to calculate the amount of viable free space available for solar panel installation [3].
Average remaining empty space on the roof	To install solar panels on a roof effectively, assess the available space for optimal energy generation. Utilize the average remaining empty space, avoiding obstructions like vents or chimneys, to maximize panels and energy output. Plan and design carefully for an aesthetically pleasing integration with the roof's architecture [3].
Recreational use of the roof	Before installing solar panels on a recreational roof, assess their potential impact on leisure activities. The size and orientation of the panels might obstruct or limit recreational use [3]. However, with careful planning, solar panels can serve a dual purpose by providing shade and protection for leisure activities while generating renewable energy for the home [34].
Roof type	To install solar panels on a house, assess the roof type, condition, orientation, and angle for sufficient sunlight. Evaluating the roof's suitability ensures the maximum benefits of renewable energy for the home [3].
House height	When assessing the feasibility of solar panels for a house, consider the building height compared to surrounding structures. If taller neighboring buildings block direct sunlight from the east or west, optimal sun exposure may be challenging [3]. Also, evaluate the roof angle and orientation. Proper assessment ensures efficient solar panel installation, maximizing the benefits of solar energy for the home [34].
Solar shading	Solar shading is the process of identifying potential obstructions, like nearby buildings or tall trees, that may block sunlight from reaching a rooftop or solar panel installation. By understanding shading risks, effective measures can be taken to optimize sunlight exposure, maximize energy generation, and reduce the need for additional energy sources [3].

The second stage of the research design was the survey strategy. Since the majority of the country's population is based in Doha, the study selected areas to be included in the survey. Moreover, due to the fact that homes in similar neighborhoods typically have many similarities, the interview included asking the homeowners if nearby homes are similar to their own. This enabled achieving geographical representation as well as statistical representation to represent the whole number of homes in Qatar, which is expected to be around 365,000 domestic customers, according to KAHRAMAA's Annual Statistics Report 2021 [4].

The third stage of the research design involved data collection. To facilitate this process, the interview questions were digitized into an electronic form that allowed for convenient and efficient data collection on the spot [36]. This eliminated the need for further processing and streamlined the data collection process. Additionally, using an electronic form allowed for anonymous data storage, thereby ensuring the confidentiality of the participants [37]. Electronic data collection methods have become increasingly popular in recent years as they offer a range of advantages over traditional paper-based methods. For example,

electronic forms can reduce the risk of errors and inconsistencies as well as improve the speed and efficiency of data collection. Furthermore, electronic forms can be easily stored and accessed, making it easier to analyze and interpret the data.

The final stage of the research design involved data analysis and the presentation of the findings. To achieve this task, Excel was used to plot graphs and perform the necessary statistical analyses to convert the collected data into meaningful information. Excel is a widely used spreadsheet software that can be used for data analysis and has many built-in statistical functions that can aid in the analysis process [38]. The use of Excel in data analysis has several advantages, such as the ability to handle large amounts of data, perform calculations efficiently, and present data in an easily understood way using graphs and charts [39]. Furthermore, the use of objective data in presenting research findings helps draw meaningful conclusions.

4. Results

Given the homogeneity of homes in Qatar [40], the use of a cluster sampling plan [41] enabled the surveying of 10 different areas in Doha, with a total of 50 homes physically surveyed from these areas, resulting in a total sample of 1068 similar homes in the same street or compound, as shown in Table 2. This sample size is considered larger than the typically required sample of 384 from the total population of 365,000, ensuring a statistically representative sample [42].

Table 2. Areas and number of houses surveyed.

Surveyed House Area	Number	Similar Houses in the Street or Compound
Al-Kheesa	20	700
Al Waab	10	240
The Pearl-Qatar	4	25
Al Waab	3	20
Musheireb	3	20
Al Sadd	3	20
Abu Hamour	2	13
Ain Khaled	2	12
Lusail	1	8
Al-Hilal	2	10
Total	50	1068

Table 3 summarizes the survey results.

Table 3. Survey results.

Survey Item	Outcome				
Average number of bedrooms per house	4				
Average total roof area [m^2]	244				
Average remaining total roof area [m^2]	144				
Average house height [m]	9				
Use of roof for recreational purposes	Yes 10%		No 90%		
Possibility for shading	Yes 30%		No 70%		
Type of house roof	Flat roof 100%	Gable roof 0%		Bonnet roof 0%	
Items on the roof	External AC units 80%	Satellite dishes 80%	Water tank 100%	Storage shed (box) 10%	Solar panel for water heating 20%

The survey findings indicate that the majority of homes in the area are relatively spacious, with 40% being five-bedroom homes and 20% being four-bedroom homes. The

remaining 40% comprise three- and two-bedroom homes. The average total size of the homes is 244 square meters, which is quite substantial.

Regarding the features on the roofs of these homes, all houses have water tanks, and a significant majority (80%) have external AC units and satellite dishes installed. However, storage sheds are less common, present on only 10% of houses, and solar panels for water heating are found on 20% of homes.

Approximately 59% of the roof space remains empty after accounting for the mentioned items, suggesting that over 50% of houses have enough available space to potentially accommodate solar panel installations.

Furthermore, it appears that roofs are rarely used for recreational purposes, with 90% of respondents confirming that their roofs are not utilized for any other activities, likely due to the hot climate and modern indoor lifestyles. This means that if solar panels were installed on the roofs, they would not interfere with daily activities in the homes.

An important consideration for solar panel installation is the roof orientation. Fortunately, all the roofs in the area are flat, making them suitable for solar panel placement to maximize energy generation.

Moreover, the majority of houses have a height ranging from 7 to 10 m, with an average height of 9 m. This height distribution indicates that there is a low likelihood of shading or obstruction of sunlight, which is favorable for solar energy generation.

Finally, the survey revealed that 70% of surveyed houses do not have nearby buildings, trees, or other objects that may cause shading, while 30% reported potential shading issues. Overall, these results demonstrate a high potential for solar PV installation in the area to generate an optimal amount of clean energy.

5. Discussion

The presented results indicate that Qatari homes are highly germane to the installation of solar panels due to their relatively large area and spaciousness. The study found that 50% or more of the roof space is available for solar panel installation without interfering with the daily activities of the homeowners. This is in line with a previous study, which reported that most Qatari homes have spacious rooftops with significant potential for solar panel installation [43]. Moreover, the study found that there are limited problems caused by shading from trees or tall neighboring structures. This is because most Qatari homes are of similar height in wholly residential neighborhoods; thus, they are not typically in proximity to obstructions that could otherwise block sunlight, as reported by the homeowners. However, if there is latent shading, solar panels can be installed in locations that provide a minimum degree of shading and the best sun view. This is consistent with the findings of a study [43], which indicated that shading can be minimized by choosing the best location for solar panel installation. Additionally, solar PV arrays can themselves be used as shading devices, thus reducing direct solar heat gain by homes (while having unimpeded exposure to sunlight for power generation) and thus reducing the latent energy demand required for cooling [44].

The study also discovered that the prevalence of flat roofs on Qatari homes offers several benefits for solar panel installation, as depicted in Figure 5. These flat roofs offer easy access for technicians during installation and allow for the adjustment of panel orientation to maximize energy generation, a crucial factor impacting performance. Moreover, flat roofs support the use of automatic platforms for sun tracking, significantly enhancing energy generation—unlike angled roofs, which have limitations in this regard. Tracking systems can boost energy production by up to 25%, a valuable advantage, particularly in regions with high solar irradiance like Qatar [45,46].

Furthermore, the high similarities between homes in Qatar [40], as shown in Figure 6, enable the establishment of an easy strategy for technical teams to replicate the installation design in similar homes, which can reduce time costs and achieve the intended deployments within a realistic timescale. The similarities between homes can make it easier for homeowners to make the decision to install solar panels, as they can see examples

of installations on homes similar to theirs, and installers will become highly proficient in installing required arrays and equipment in similar types of structures. This is in line with previous research on the benefits of standardization in building design for renewable energy adoption. For example, a study [47] found that standardizing building design can facilitate the integration of renewable energy systems, particularly in residential buildings. Another study [47] found that standardizing building design can reduce the cost of renewable energy systems by streamlining the installation process.

Figure 5. Example of a surveyed home roof.

Figure 6. Example of structural homogeneity of Qatari homes.

The outcomes from this study complement previous research conducted by the authors, aimed at establishing the analytical feasibility of deploying solar panels on Qatar's houses [2]. The primary objective was to calculate various solar panel deployment scenarios using analytical methods, considering different panel sizes, efficiency, and daily sun exposure. These scenarios were then compared to estimate the generated energy and its comparison with actual consumption over a twelve month period. The findings revealed the most viable scenarios that enable homes in Qatar to sufficiently generate solar energy to cover their consumption. Moreover, there is a high possibility that surplus energy generated during the low season can be exported to areas experiencing high energy demands, such as the Western world. This potential not only benefits Qatar but also supports global efforts towards transitioning to clean energy, providing a valuable solution for energy crises [48].

Hence, the findings of this study support the potential for solar panel installation on Qatari homes. With their spaciousness, limited shading, and flat roofs, Qatari homes are ideally suited for solar panel installation. This aligns with the Qatari government's ambitious goal of generating 200 MW of solar energy by 2022 [49]. By encouraging and facilitating the installation of solar panels on homes, Qatar can move towards a more sustainable future. This should begin with pilot projects involving the installation of solar panels on real homes to gather actual information on their performance, taking into account factors such as solar radiation, temperature, and dust that might reduce generation potential. This is essential to ensure optimal and sustainable performance [50].

6. Conclusions

The study has successfully achieved its primary objective of assessing the suitability of Qatari homes for solar panel installation. The obtained results are highly promising and offer significant value to various stakeholders involved in decision-making regarding the deployment of solar panels in residential areas. Furthermore, these findings hold invaluable importance for the parties responsible for the deployment, as they can utilize them to develop a comprehensive national strategy for replicating the deployment plan in different regions, considering the high similarities observed among homes in Qatar. These findings also complement and align with past research efforts conducted using analytical means.

However, to draw a definitive conclusion, it is recommended to conduct real pilot projects involving the installation of solar panels on actual homes and gather additional information on their performance in situ. This should include aspects like solar radiation, temperature, air quality (as dust can reduce generation potential), connectivity with the main grid, storage, and all relevant variables. Such an approach will yield crucial insights into potential challenges that may arise during installation and usage, thereby enabling the formulation of practical solutions based on user experiences and operational evidence.

Despite the potential difficulties that may arise, the positive outcomes of this study indicate a promising future for solar panel installation on Qatari homes. By implementing such initiatives, Qatari households can effectively reduce their carbon footprint and contribute to the creation of a greener and more sustainable environment for future generations. This will undoubtedly play a significant role in Qatar's commitment to clean energy and global efforts towards combating climate change.

Author Contributions: Conceptualization, A.B. and Z.H.; methodology, A.B. and Z.H.; investigation, A.B.; writing—original draft preparation, A.B.; writing—review and editing, Z.H.; supervision, M.A. All authors have read and agreed to the published version of the manuscript.

Funding: This research received no external funding.

Institutional Review Board Statement: Not applicable.

Informed Consent Statement: Not applicable.

Data Availability Statement: The data can be shared upon request.

Acknowledgments: The authors would like to thank all homeowners who participated in this study.

Conflicts of Interest: The authors declare no conflict of interest.

References

1. Al-Hababi, R. The evolvement of Qatar's environmental sustainability policy: The strategies, regulations, and institutions. In *Sustainable Qatar: Social, Political and Environmental Perspectives*; Cochrane, L., Al-Hababi, R., Eds.; Springer Nature: Singapore, 2023; pp. 17–35. [CrossRef]
2. Banibaqash, A.; Hunaiti, Z.; Abbod, M. An analytical feasibility study for solar panel installation in Qatar based on generated to consumed electrical energy indicator. *Energies* **2022**, *15*, 9270. [CrossRef]
3. Torcellini, P.A.; Crawley, D.B. Understanding zero-energy buildings. *ASHRAE J.* **2006**, *48*, 62–69.
4. Qatar General Electricity & Water Corporation "KAHRAMAA". *Annual Statistics Report 2021*; KAHRAMAA: Doha, Qatar, 2022; pp. 26–46.
5. Scharfenort, N. Urban development and social change in Qatar: The Qatar National Vision 2030 and the 2022 FIFA World Cup. *J. Arab. Stud.* **2012**, *2*, 209–230. [CrossRef]
6. Omer, A.M. Energy, environment and sustainable development. *Renew. Sustain. Energy Rev.* **2008**, *12*, 2265–2300. [CrossRef]
7. Darwish, S.; Abdo, H.; Alshuwaiee, W.M. Opportunities, challenges and risks of transition into renewable energy: The case of the Arab Gulf Cooperation Council. *Int. Energy J.* **2018**, *18*, 391–400.
8. World Data: Sunrise and Sunset in Qatar. Available online: https://www.worlddata.info/asia/qatar/sunset.php (accessed on 13 March 2023).
9. Bayram, I.S.; Saffouri, F.; Koc, M. Generation, analysis, and applications of high resolution electricity load profiles in Qatar. *J. Clean. Prod.* **2018**, *183*, 527–543. [CrossRef]
10. Bohra, M.; Shah, N. Optimising Qatar's energy transition through model-based analysis. *Energy Transit* **2020**, *4*, 11–29. [CrossRef]
11. Oxford Analytica. Qatar's Green Strategy Will Focus on Greening of LNG. *Emerald Expert Briefings*, 26 October 2022. [CrossRef]
12. Global Investors Move into Renewable Infrastructure: Reviewing the World's Top Renewable Energy Financiers. Available online: https://ieefa.org/sites/default/files/resources/Global-Investors-Move-Into-Renewable-Infrastructure_July-2021.pdf (accessed on 13 March 2023).
13. Obaideen, K.; AlMallahi, M.N.; Alami, A.H.; Ramadan, M.; Abdelkareem, M.A.; Shehata, N.; Olabi, A.G. On the contribution of solar energy to sustainable developments goals: Case study on Mohammed bin Rashid Al Maktoum Solar Park. *Int. J. Thermofluids* **2021**, *12*, 100123. [CrossRef]
14. Bergman, N.; Eyre, N. What role for microgeneration in a shift to a low carbon domestic energy sector in the UK? *Energy Effic.* **2011**, *4*, 335–353. [CrossRef]
15. Al-Ammari, B.; Romanowski, M.H. The impact of globalisation on society and culture in Qatar. *Pertanika J. Soc. Sci. Humanit.* **2016**, *24*, 1535–1556.
16. International Renewable Energy Agency. *Community Renewable Energy Deployment: The Role of Community Energy in Accelerating Renewable Energy Deployment*, IRENA: Masdar City, United Arab Emirates, *in press*.
17. Seyfang, G.; Haxeltine, A. Growing grassroots innovations: Exploring the role of community-based initiatives in governing sustainable energy transitions. *Environ. Plan. C Gov. Policy* **2012**, *30*, 381–400. [CrossRef]
18. Almulhim, A.I. Understanding public awareness and attitudes toward renewable energy resources in Saudi Arabia. *Renew. Energy* **2022**, *192*, 572–582. [CrossRef]
19. Voss, K.; Musall, E. *Net Zero Energy Buildings: International Projects of Carbon Neutrality in Buildings*; Walter de Gruyter: Berlin, Germany, 2012.
20. Tsalikis, G.; Martinopoulos, G. Solar energy systems potential for nearly net zero energy residential buildings. *Sol. Energy* **2015**, *115*, 743–756. [CrossRef]
21. Cao, X.; Dai, X.; Liu, J. Building energy-consumption status worldwide and the state-of-the-art technologies for zero-energy buildings during the past decade. *Energy Build.* **2016**, *128*, 198–213. [CrossRef]
22. Jaber, S.; Saidur, R. The role of energy efficiency in the sustainable development of Qatar: A review. *Renew. Sustain. Energy Rev.* **2020**, *120*, 109675.
23. Torres, A.R.; Herold, M. Energy consumption behavior in households with photovoltaic panels. *Energy Build.* **2019**, *195*, 68–79.
24. Saidur, R.; Jaber, S.; Mohamed, E.A. Opportunities and challenges for renewable energy in the State of Qatar. *Renew. Energy* **2021**, *177*, 583–599.
25. Residential Solar Panels and Their Impact on the Reduction of Carbon Emissions. Available online: https://nature.berkeley.edu/classes/es196/projects/2013final/ArifM_2013.pdf (accessed on 13 March 2023).
26. Karakaya, E.; Hidalgo, A.; Nuur, C. Motivators for adoption of photovoltaic systems at grid parity: A case study from Southern Germany. *Renew. Sustain. Energy Rev.* **2015**, *43*, 1090–1098. [CrossRef]
27. Bryan, H.; Rallapalli, H.; Ho, J.J. Designing a solar ready roof: Establishing the conditions for a high-performing solar installation. In Proceedings of the 39th ASES National Solar Conference, Phoenix, AZ, USA, 17–22 May 2010; Volume 5, pp. 4081–4110.
28. Shahsavari, A.; Akbari, M. Potential of solar energy in developing countries for reducing energy-related emissions. *Renew. Sustain. Energy Rev.* **2018**, *90*, 275–291. [CrossRef]

29. Monna, S.; Abdallah, R.; Juaidi, A.; Albatayneh, A.; Zapata-Sierra, A.J.; Manzano-Agugliaro, F. Potential Electricity Production by Installing Photovoltaic Systems on the Rooftops of Residential Buildings in Jordan: An Approach to Climate Change Mitigation. *Energies* **2022**, *15*, 496. [CrossRef]
30. Hussain, H.M.; Rahi, K.; Al Tarawneh, M.; Preece, C. Developing applicable scenarios to install and utilize solar panels in the houses of Abu Dhabi city. *Sustainability* **2022**, *14*, 15361. [CrossRef]
31. Starková, L. Toward a High-Definition Remote Sensing Approach to the Study of Deserted Medieval Cities in the Near East. *Geosciences* **2020**, *10*, 369. [CrossRef]
32. AL-Dosari, K.; Hunaiti, Z.; Balachandran, W. Civilian UAV Deployment Framework in Qatar. *Drones* **2023**, *7*, 46. [CrossRef]
33. Fink, A. *How to Conduct Surveys: A Step-by-Step Guide*; Sage Publications Ltd.: London, UK, 2019.
34. Khan, M.M.A.; Asif, M.; Stach, E. Rooftop PV Potential in the Residential Sector of the Kingdom of Saudi Arabia. *Buildings* **2017**, *7*, 46. [CrossRef]
35. Bekele, M.T.; Atakara, C. Residential Building Energy Conservation in Mediterranean Climate Zone by Integrating Passive Solar and Energy Efficiency Design Strategies. *Buildings* **2023**, *13*, 1073. [CrossRef]
36. Salgado, C.D.; Segura, O.R.; León, I.G. Electronic data collection methods in research. *Rev. Med. Inst. Mex. Seguro Soc.* **2017**, *55*, 236–242.
37. Creswell, J.W.; Creswell, J.D. *Research Design: Qualitative, Quantitative, and Mixed Methods Approaches*; Sage Publications Ltd.: London, UK, 2018.
38. Khan, J. Data analysis using Excel. *J. Appl. Res. High. Educ.* **2017**, *9*, 307–315.
39. Hulland, J. Use of partial least squares (PLS) in strategic management research: A review of four recent studies. *Strateg. Manag. J.* **1999**, *20*, 195–204. [CrossRef]
40. Scheller, F.; Doser, I.; Schulte, E.; Johanning, S.; McKenna, R.; Bruckner, T. Stakeholder dynamics in residential solar energy adoption: Findings from focus group discussions in Germany. *Energy Res. Soc. Sci.* **2021**, *76*, 102065. [CrossRef]
41. Thompson, S.K. Adaptive Cluster Sampling: Designs with Primary and Secondary Units. *Biometrics* **1991**, *47*, 1103–1115. [CrossRef]
42. Bujang, M.A. An Elaboration on Sample Size Planning for Performing a One-Sample Sensitivity and Specificity Analysis by Basing on Calculations on a Specified 95% Confidence Interval Width. *Diagnostics* **2023**, *13*, 1390. [CrossRef] [PubMed]
43. Morphology of Urban Qatari Homes. Available online: https://sites.northwestern.edu/buildingdoha/morphology-of-urba (accessed on 25 October 2023).
44. Mohammed, A.; Tariq, M.A.U.R.; Ng, A.W.M.; Zaheer, Z.; Sadeq, S.; Mohammed, M.; Mehdizadeh-Rad, H. Reducing the Cooling Loads of Buildings Using Shading Devices: A Case Study in Darwin. *Sustainability* **2022**, *14*, 3775. [CrossRef]
45. Ayoub, J.; Al-Jibouri, S. Analysis of the impact of solar panel orientation on the electricity generation using solar energy. *Int. J. Energy Environ. Eng.* **2021**, *12*, 63–73.
46. Gupta, R.; Nayak, J.K. Solar tracking systems: Technologies and trackers. In *Handbook of Research on Energy Systems and Sustainable Energy*; Sharma, D.K., Reddy, K.S., Eds.; IGI Global: Hershey, PA, USA, 2019; pp. 379–411. [CrossRef]
47. Murshed, S.; Shafie, S.; Saidur, R. Review on solar energy storage and thermal energy storage for sustainable energy houses. *Renew. Sustain. Energy Rev.* **2018**, *82*, 1518–1542.
48. Environmental Sustainability Initiatives in Qatar. Available online: https://www.qf.org.qa/research/environmental-sustainability (accessed on 25 October 2023).
49. Al-Sulaiman, F.A.; Zubair, S.M. Solar energy potential and policies in Qatar: Opportunities and challenges. *Renew. Sustain. Energy Rev.* **2019**, *103*, 325–333. [CrossRef]
50. Olorunfemi, B.O.; Ogbolumani, O.A.; Nwulu, N. Solar Panels Dirt Monitoring and Cleaning for Performance Improvement: A Systematic Review on Smart Systems. *Sustainability* **2022**, *14*, 10920. [CrossRef]

energies

MDPI

Article

Optimal Design and Analysis of a Hybrid Hydrogen Energy Storage System for an Island-Based Renewable Energy Community

Robert Garner and Zahir Dehouche *

College of Engineering, Design and Physical Sciences, Brunel University London, London UB8 3PH, UK; robert.garner2@brunel.ac.uk
* Correspondence: zahir.dehouche@brunel.ac.uk

Abstract: Installations of decentralised renewable energy systems (RES) are becoming increasing popular as governments introduce ambitious energy policies to curb emissions and slow surging energy costs. This work presents a novel model for optimal sizing for a decentralised renewable generation and hybrid storage system to create a renewable energy community (REC), developed in Python. The model implements photovoltaic (PV) solar and wind turbines combined with a hybrid battery and regenerative hydrogen fuel cell (RHFC). The electrical service demand was derived using real usage data from a rural island case study location. Cost remuneration was managed with an REC virtual trading layer, ensuring fair distribution among actors in accordance with the European RED(III) policy. A multi-objective genetic algorithm (GA) stochastically determines the system capacities such that the inherent trade-off relationship between project cost and decarbonisation can be observed. The optimal design resulted in a levelized cost of electricity (LCOE) of 0.15 EUR/kWh, reducing costs by over 50% compared with typical EU grid power, with a project internal rate of return (IRR) of 10.8%, simple return of 9.6%/year, and return on investment (ROI) of 9 years. The emissions output from grid-only use was reduced by 72% to 69 gCO_2e/kWh. Further research of lifetime economics and additional revenue streams in combination with this work could provide a useful tool for users to quickly design and prototype future decentralised REC systems.

Keywords: decentralised energy systems; renewable energy community; hydrogen energy storage system; decarbonisation; techno-economic assessment; multi-objective optimisation

Citation: Garner, R.; Dehouche, Z. Optimal Design and Analysis of a Hybrid Hydrogen Energy Storage System for an Island-Based Renewable Energy Community. *Energies* **2023**, *16*, 7363. https://doi.org/10.3390/en16217363

Academic Editors: Luis Hernández-Callejo, Jesús Armando Aguilar Jiménez and Carlos Meza Benavides

Received: 2 August 2023
Revised: 26 October 2023
Accepted: 27 October 2023
Published: 31 October 2023

1. Introduction

The current state of the energy generation landscape is undergoing a significant change as concerns are raised over climate change, energy cost, and energy security. The aim as stipulated in the Paris Agreement [1] of keeping the average surface temperature increase below 2 °C by 2050 is unlikely given global trends [2], and will be impossible without an ambitious sustainable energy development and technological innovation [3]. Recent events on the global stage have also caused nations in Europe and around the world to reconsider their energy security strategies [4,5]. The adoption of renewable energy at scale should include measures to increase the effectiveness whilst providing cost reductions [6].

The introduction of renewable energy systems (RES), including photovoltaic (PV) solar panels and wind turbines, have been the key driving force in removing global dependence on fossil fuels from the energy sector [7]. These types of generation assets are known as non-dispatchable as they are completely dependent on weather conditions [8] and so cannot be precisely controlled. This is a problem for transmission service operators (TSOs) as ensuring the voltage and frequency are balanced at a grid level becomes challenging [9]. The increasing volume of decentralised RES installed at the demand side is also problem for grid operators [10], as they can induce bidirectional grid flows and put additional strain on the network.

One solution to this problem is the use of energy storage systems (ESS) to store excess energy and increase the share of the total RES production directly through self-consumption [11,12]. Electro-chemical storage such as batteries have been deployed in many cases for use as grid-level storage [13–15], as they have the advantage of fast response to demand and can be installed in most global climates. A number of battery technologies including high-performance solid state chemistries are a promising solution due to their long-term stability and high capacity retention [16,17]. Most grid storage applications deploy LiFePO4 variants as they are widely available and have a relatively low cost [18]. Crucially for the research methods used in this work, the retrieval of reliable cost and environmental data is vital for an accurate result, which for LiFePO4 is widely available within the literature. Hydrogen has often been considered for long-term seasonal storage [19], due in part to the mentioned capacity retention challenges of battery storage. Hydrogen is also a flexible energy vector for many other uses, such as heating and industrial processes [20]. A hybrid battery and hydrogen ESS has a great potential to increase the share of renewables within the energy mix [21], thus decreasing the reliance on traditional power stations. The advent of widely available ESS has meant that it is now possible to emphasise the self-consumption of energy at a local level to reduce the problems of grid stress and planning. A 'prosumer' (an end user that is able to both consume and produce energy [22]) or group of prosumers could install decentralised RES coupled with storage technology, and self-consume the power generated at a local level.

To address these challenges, this work presents and evaluates the application of decentralised renewable energy communities (RECs). RECs in practice have many advantages and solve the most common issues associated with increased decentralised generation, while also promoting the further self-consumption of electricity. In a REC configuration, consumers and prosumers are no longer restricted to buying and selling energy from their utility company and can virtually 'share' the excess energy between actors within the energy community itself. This is mutually beneficial for both the network operator, as they no longer need to manage unpredictable grid flows, and for the REC participants as they receive direct renumeration and a reduction in carbon emissions.

The REC considered in this work was based on the policy recommendations recently implemented by a number of EU countries outlined in the Renewable Energy Directive (RED-II) (EU) 2018/2001 [23]. The directive defines a REC as "a legal entity that is based on open and voluntary participation, it is autonomous and controlled by shareholders or members located in the proximity of renewable energy plants belonging to the community itself. The members may be physical persons, companies or local authorities…". While the directive has been transposed into several other national laws and decrees, including Austria [24], France [25], Germany [26], and the Netherlands [27], the REC modelled in this work most closely resembles the framework practiced in Italy as discussed by Trevisan et al. [28]. Although the study was in Spanish territory, it was chosen to follow the Italian implementation as there are more example cases available and, as of 2021, further improvements to the 2019 Spanish REC policy are currently in progress [29].

As laid out in decree-law 199/2021 [30], a group of self-consuming members within the REC must be located within the same low-voltage (LV) network downstream of the same LV/MV substation. Energy is shared in the existing physical network using a virtual network model. The difference between the energy consumed and energy produced by the REC is resolved over each one-hour period to determine the capacity available to be shared [31]. The model created in this work uses the principles of the relevant regulation to design the virtual REC.

A number of studies including operational renewable energy communities have investigated the use of ESS within a REC to further improve the economic performance of centralised renewables. Trevisan et al. presented an optimised energy model considering PV solar and ESS to provide renewable power to a port REC, showing a decrease in energy bills of 28% compared with the business-as-usual case [32]. Bartolini et al. investigated how to size a mixed RES to fully self-consume all generation at a community level, as

well as meeting the heat energy needs, and showed that using hydrogen generation and storage is an economically viable alternative to battery systems [33]. Although less explored in the literature, there have also been studies focused on the environmental and emissions reductions possible with such a community-based system. Wang et al. proposed a community-based virtual power plant solution in Japan with PV and battery ESS with the ability to reduce carbon emissions by 16.26% [34].

Several different modelling and optimisation software tools have also emerged to assist in model-based design and assessment. An in-depth review by Cuesta et al. presented popular renewable energy modelling tools, including the ability to model different renewable assets and output different technical, economic, environmental, and social key performance indicators [35]. Software such as HOMER (version 3.16), TRNSYS (version 18), and MATLAB/Simulink (2022b) are most often used due to their ease of use and available documentation. However, they can be restrictive for some REC cases due to their proprietary nature. Creating the model in Python will provide the flexibility of an open-source platform and a scalable product suitable for deployment as a lightweight software or web applications.

A number of optimisation procedures have been addressed and utilised in the literature to determine the optimal design of hybrid RES and ESS. Most cases vary the design capacities to achieve one or more competing criteria such as economics, grid independence, and environmental impact. Niveditha and Rajan Singaravel consider a multi-objective design criteria for achieving near zero energy buildings (NZEB), using the functions of cost, loss of load probability (LLP), and total energy transfer (TET) to determine the best sizing arrangement for the PV-wind-battery storage system [36]. Zhang et al. presents a capacity configuration for both an on-grid and off-grid mixed renewable system with hydrogen and batteries [37]. The NSGA-II algorithm was used to determine the trade-off relationship between system cost, renewable curtailment, and loss of load probability (LLP), which can be considered analogous to grid independence for grid-connected configurations. Xu et al. considers the design of an off-grid PV-wind-hydrogen storage system using the multi-objective criteria of LCOE, LLP, and power abandonment rate (PAR). The pareto optimal solution produces an LCOE of 0.226 USD/kWh at acceptable LLP and PAR values [38]. Studying the emissions associated with the grid independence would more accurately determine the positive environmental impact, which was of particular focus in this work. Results from the literature also do not consider the implementation of such an optimization procedure for RECs, and the impact of trading arrangements between members. Other algorithms including multi-objective particle swarm optimisation (MOPSO) [39] and multi-objective evolutionary algorithm with decision-making (MOEA-DM) [40] have also been applied to ESS design; however, NSGA-II remains very popular and has proven robustness in energy flow optimisation problems [41].

2. Contribution

In this study, a techno-economic and carbon emissions assessment was conducted for a decentralised REC. The case study location was chosen as Formentera; a largely rural Balearic Island located in the Mediterranean Sea as illustrated in Figure 1. Emphasis is put on the isolated nature of the energy grid, which naturally increases the energy cost and embedded carbon of electricity usage, making it an ideal location for the study. A comparison of the base case scenario was used to compare the improvements made with the implementation of the REC.

The community has shared usage of PV solar and wind power to produce energy, and a hybrid battery and regenerative hydrogen fuel cell to store excess production. The combination of battery and hydrogen minimises the potential shortcomings of decentralised storage. A virtual trading scheme based on the EU decree-law 199/2021 for REC implementation was used to evaluate the energy shared between community members, without considering incentives or feed in tariffs. Through the implementation of key economic and

environmental parameters, the multi-objective optimisation determines the best design topology within the defined REC boundary conditions.

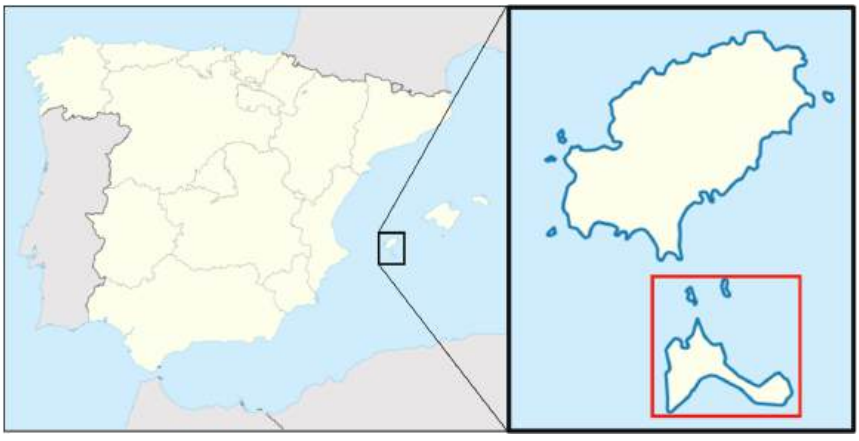

Figure 1. Formentera Island, highlighted in red, is located east of the Spanish mainland in the Mediterranean [42].

The multi-objective results reveal an inherent trade-off relationship between low-cost energy and the ability to decarbonise supply, and that this approaches a critical limit at both extremes of the pareto front. This work shows that across the pareto optimal sets, the hybridisation of energy storage provides a better overall performance than a battery-only or hydrogen-only case. Additional constraints can be applied to the objective domain to assist in design decision-making.

The implementation of the model in Python allows for the creation of a scalable product, which following digitisation trends in model-based design could provide a vital tool for communities and policymakers to determine the best method for assisting communities to reach net-zero emissions. To summarise, the novelty of this work is summarised as follows:

- The modelling of a hybridised battery and RHFC system for a remote renewable energy community application using real-world power consumption data from a rural island location;
- the use of multi-objective optimisation to evaluate the system pareto front based on economic and environmental performance;
- the inclusion of a virtual trading layer based on the latest RED(III) REC policies;
- the formulation of a scalable and modular renewable energy community modelling and simulation platform.

3. Materials and Methods

For the purposes of simplification, the simulation model was discretised into one hour time steps using kWh as the function unit for all energy flows within the system. The case study input assumptions including building load and meteorological datasets are defined first. The meteorological data at the chosen coordinate location were obtained from the National Aeronautics and Space Administration (NASA) Langley Research Center (LaRC) Prediction of Worldwide Energy Resource Project funded through the NASA Earth Science/Applied Science Program [43]. A combination of hourly and monthly energy consumption collected from the case study location was used to recreate typical annual load profiles for each of the seven buildings within the virtual REC. A selection of 24 industrial, commercial, and residential load profiles produced by Farhad et al. (2020) were used to augment the profiles where required [44].

3.1. Renewable Energy Community Implementation

It was assumed that the community members will have a shared capital investment in the generation and storage assets. PV solar and wind assets can either be installed in the low-voltage energy grid within the same secondary substation of the REC, or spread out between the members, installing in open areas such as rooftops. The stationary ESS consisting of both a lithium-ion battery and a RHFC was installed with the REC boundary conditions in accordance with the EU decree-law 199/2021, with the capacity to accept but also release energy to the physical energy grid. A simple diagram of the system architecture is shown in Figure 2.

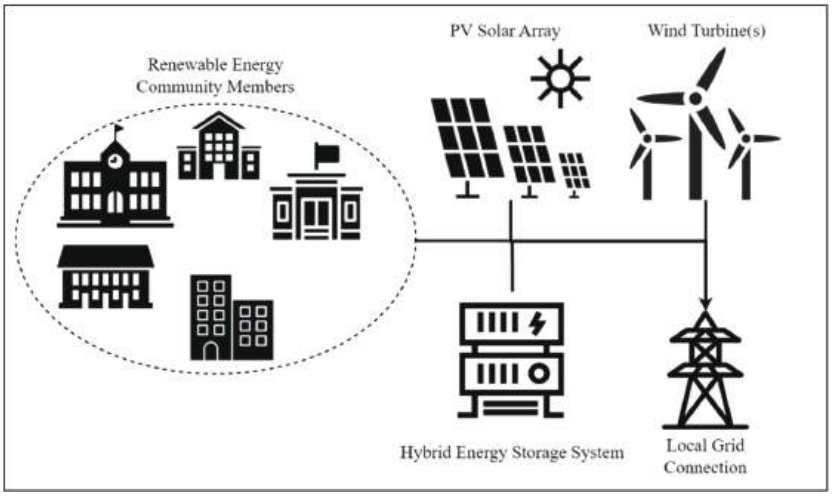

Figure 2. Renewable energy community system architecture. The community buildings grouped on the left are connected virtually to the distributed generation and storage assets, which are also able to export to the local power grid.

The control strategy consists of a load-following authority, but with additional considerations for the hybrid ESS. Since batteries have an improved performance as short-term storage, these are allowed to discharge first to cover the load of the REC. Once the battery depth-of-discharge (DOD) limit is reached, the hydrogen system is then activated to cover the remaining demand. During the charging phase, this control scheme occurs in reverse. By evaluating the excess energy available between the total REC consumption and production over each one-hour increment in line with decree-law 162/19 for community implementation in Italy, the total virtual energy flows between community members were derived. This case does not consider incentives to reduce financial strain and instead evaluates through a techno-economic assessment over a 20-year project period whether the hybrid system was able to provide net-positive economic and environmental performance over the business-as-usual case.

The electrical load profiles form the foundation of the assessment of economic and environmental improvements to the REC. The community consists of seven member buildings; a community centre, a small school, a large school, local government offices, and three typical residential units. For the community centre, two schools, and offices, sample daily load profiles, as well as the monthly average energy consumption, were collected directly from the test site. For the residential units, a combination of the annual heating, cooling, and appliances usage of 80.7 kWh/m^2 was used to evaluation the typical characteristics of a residence in Spain [45], where the buildings were assumed to be 50 m^2 in area. The monthly and yearly consumption was used to create a spline, over which the daily load profile was interpolated and repeated to create the one-year load profiles for each building. The total yearly consumption for each member is included in Table 1, with the monthly

and daily load profiles shown in Figure 3. The three mixed homes have been combined to represent a mixed family building and to improve visibility within the analysis.

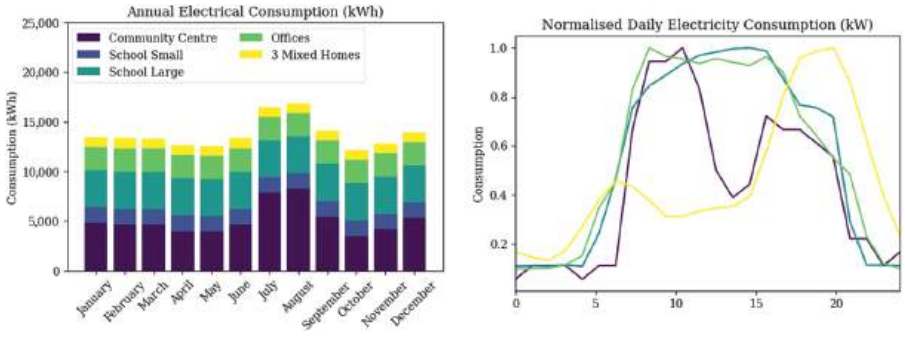

(**a**) Monthly electricity demand (**b**) Normalised daily electricity demand

Figure 3. Building electrical energy service demand model based on the requirements of the renewable energy community. Figure 3b displays the average daily power demand curves of the different building types within the model.

Table 1. Total annual electrical consumption for each member of the renewable energy community.

	Annual Consumption
Community centre	66,500
Elementary school	19,200
High school	46,200
Government offices	28,900
3× Residential units	12,000

3.2. Weather and Environment Data

The weather data were collected for the year 2022 at the coordinate location of the chosen REC case study site. The model requires accurate measurements of ambient temperature, wind speed, and global horizontal irradiance (GHI) solar conditions to evaluate the hour-by-hour power output of the renewable generation technologies. Figure 4 shows the hourly mean temperature and GHI for each month over one year. A higher GHI is observed in the summer period as expected in the northern hemisphere.

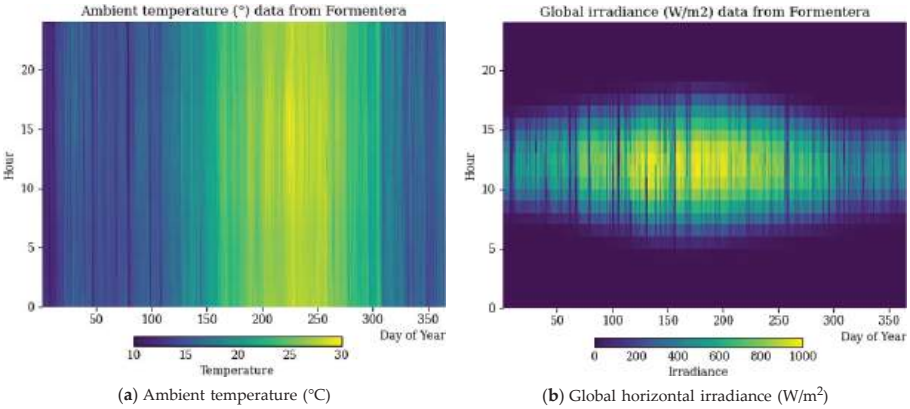

(**a**) Ambient temperature (°C) (**b**) Global horizontal irradiance (W/m^2)

Figure 4. Temperature and solar conditions over a one-year period at the island location. The weather conditions are assumed to remain constant year-on-year through the lifetime of the system.

3.3. System Design and Characteristics

3.3.1. PV Solar Array Model

The Mediterranean region's warm and dry climate promotes the use of PV solar systems to generate clean energy. For the purposes of the study, the solar array was assumed to be installed at 180° directly to the south, and at an optimal tilt angle of 38.7°. The power output of the solar panels P_{PV} was modelled using the following governing equation [46]:

$$P_{PV} = C_{PV} d_f \left(\frac{G(t)_{module}}{G_{STC}}\right)[1 + \alpha_P (T_c - T_{c,STC})] \quad (1)$$

where C_{PV} is the generation capacity (kW) of the solar installation under standard conditions, d_f is the derate factor, $G(t)_{module}$ is the direct solar irradiance in W/m^2, G_{STC} is the direct solar irradiance under standard test conditions (1000 W/m^2), α_P is the thermal power coefficient (%/°C), and $T_{c,STC}$ is the PV cell temperature under standard test conditions (25 °C). T_c is the PV cell temperature and is calculated by considering the measured nominal operating cell temperature (NOCT). NOCT is the cell measured temperature at a solar irradiance G_{NOCT} of 800 W/m^2, an ambient temperature $T_{a,NOCT}$ of 20 °C, and a wind speed of 1 m/s [44]. This known thermal characteristic can then be used to adjust the cell temperature and find the corrected power output using the following equation [47]:

$$T_c = T(t)_a + (T_{c,NOCT} - T_{a,NOCT})\left(\frac{G(t)_{module}}{G_{NOCT}}\right)\left(\frac{1 - \eta_{mp}}{\tau\alpha}\right) \quad (2)$$

where $T(t)_a$ is the ambient temperature at timestep t and η_{mp} is the cell efficiency. The constants $\tau\alpha$ can be assumed to be 0.9 for most cases. Since η_{mp} is not known, the efficiency under standard conditions $\eta_{mp,STC}$ is substituted into the cell temperature equation above and the result yields the following:

$$T_c = \frac{T(t)_a + (T_{c,NOCT} - T_{a,NOCT})(G(t)_{module}/G_{NOCT})[1 - (\eta_{mp,STC}(1 - \alpha_P T_{c,STC}))/\tau\alpha])}{(1 + (T_{c,NOCT} - T_{a,NOCT})(G(t)_{module}/G_{NOCT})[(\alpha_P \eta_{mp,STC})/\tau\alpha]} \quad (3)$$

The GHI input data need to be adjusted based on the local latitude φ and module tilt β to find the module irradiance $G(t, module)$ for the time of day and year. This is found with the following equations [48]:

$$G(t)_{module} = \frac{G(t)_{horizontal} \sin(\alpha + \beta)}{\sin \alpha} \quad (4)$$

$$\alpha = 90^\circ - \varphi + \delta \quad (5)$$

$$\delta = 23.45^\circ \cdot \sin[360/365(284 + d)] \quad (6)$$

where $G(t)_{module}$ is the module irradiance, $G(t)_{horizontal}$ is the GHI data, α is the elevation angle, and δ is the declination angle which deviates from the earth's tilt of 23.45° depending on the day of the year d.

3.3.2. Wind Turbine Model

A generic dynamic wind turbine model was used to calculate the expected power output in the selected location using the following [49]:

$$P(t) = \frac{1}{2} C_p \rho(t) A V^3(t)(\eta_m \cdot \eta_e) \quad (7)$$

where C_p is the power coefficient, $\rho(t)$ is the air density at the hub height, A is the selected swept area in m^2, $V(t)$ is the wind speed in m/s at the time step t, and η_m and η_e are the mechanical and electrical efficiencies. The wind speed is usually measured at a different

height compared to the hub height, Z_{hub}. Therefore, the model uses the logarithmic law to derive the hourly wind speed at the hub height as follows [49]:

$$V_{hub} = V_{anem}\left(\frac{\ln(Z_{hub}/Z_0)}{\ln(Z_{anem}/Z_0)}\right) \quad (8)$$

where Z_0 is the surface roughness length (m), Z_{anem} is the anemometer height (m), V_{hub} is the wind speed at the required hub height (m/s), and the V_{anem} is the measured wind speed at the anemometer height (10 m for the dataset used). For simplicity, C_p is evaluated by way of a 2D-look up table based on the four classes of wind turbines described in IEC 61400 standard [50]. The average wind speed and distribution was evaluated and the most appropriate characteristic was chosen from the four available classes ranked from low to high wind speeds [51]. The normalised power range for each class of "Offshore", "IEC-1", "IEC-2", and "IEC-3" are shown in Figure 5a. The energy output over the course of one year can also be determined analytically by assessing the wind speed distribution. The Rayleigh distribution, shown in Figure 5b, has been overlaid to show that the wind speed distribution data follow this statistical law, which indicates that the normalised power curves will operate effectively for the model.

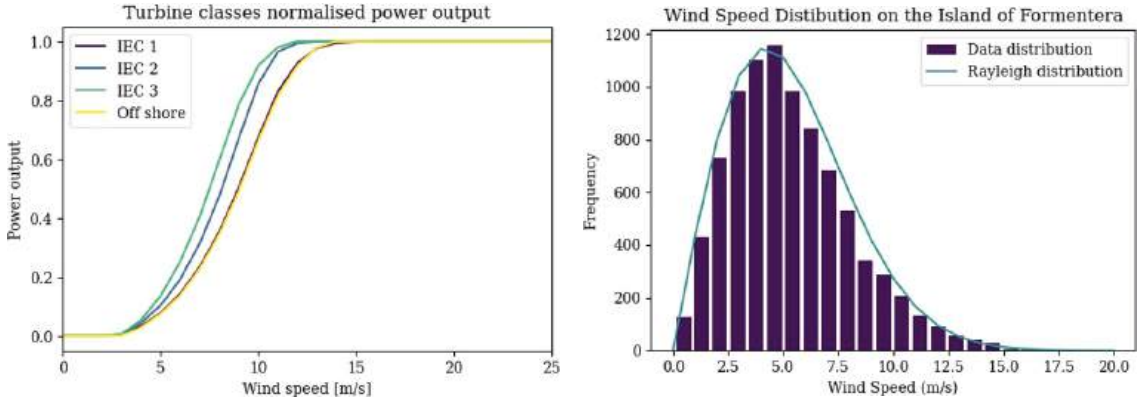

(**a**) Turbine normalised power output curve

(**b**) Wind speed distribution at Formentera

Figure 5. Wind model input assumptions are primarily a combination of standardised wind turbine power coefficients and the load wind speed data measured at 10 m above sea level.

3.3.3. Lithium Ion Battery Model

The battery model utilises a simplified version of the Shepard battery model [52], replacing internal and other resistive losses with a total charge $\eta charge$ discharge $\eta discharge$ efficiency for the hourly discharge case. The simplification allows for less information to be known about the chemistry and dynamics of the specific battery to perform calculations for the current capacity and state of charge (SOC). The battery system contains two parts: a charge model and a discharge model. The models take the power requirement from the battery and output the resulting SOC for the end of the timestep. These parts are defined as follows:

$$\begin{cases} \mathrm{SOC}(t+1)_{batt} = \dfrac{Q(t)_{batt} + \int P(t)_{batt}\eta_{charge}, dt)}{Q(t_0)_{batt}} \cdot 100 & \text{charging} \\ \mathrm{SOC}(t+1)_{batt} = \dfrac{Q(t)_{batt} - \int P(t)_{batt}\eta_{discharge}, dt)}{Q(t_0)_{batt}} \cdot 100 & \text{discharging} \end{cases} \quad (9)$$

where $\mathrm{SOC}_{t+1,batt}$ is the next timestep battery SOC, $Q_{t,batt}$ is the battery state of charge at timestep t, $Q_{t0,batt}$ is the initial SOC, $P_{t,charge}$ is the average charge power draw, and $P_{t,discharge}$ is the discharge power draw. These outputs are subject to the minimum and

maximum SOC limits SOC_{min} and SOC_{max}. The model includes degradation in the battery capacity linearly as a function of charge cycles, as shown below:

$$Q(l,t)_{batt} = Q(t_0)_{batt} - \alpha l \tag{10}$$

where $Q(l, t)_{batt}$ is the dynamic capacity in kWh as a function of cycles the cycles l, and α is the ageing factor (kWh/cycle).

3.3.4. Regenerative Hydrogen Fuel Cell

The RHFC model provides an alternative energy storage facility to the electrochemical battery. The model consists of a PEM fuel cell and PEM electrolyser capable of consuming and producing hydrogen, respectively. The system also considers a hydrogen storage module with its own rated capacity and efficiency. The overall equations are like that of the simplified battery model in that the electrolyser and fuel cell analogously represent the charge and discharge elements. The system can therefore be shown as the following:

$$\begin{cases} Q(t+1)_{H2} = Q(t)_{H2} - \int P(t)_{fc}\eta_{fc}, dt & \text{Fuel cell} \\ Q(t+1)_{H2} = Q(t)_{H2} + \int P(t)_{el}\eta_{el}, dt & \text{Electrolyser} \end{cases} \tag{11}$$

where $Q(t + 1)_{H2}$ is the next timestep hydrogen energy stored (kWh), $Q(t)_{H2}$ is the current timestep hydrogen energy stored (kWh) $P(t)_{fc}$ is the average fuel cell power production [kW] in the current one-hour timestep t, and $P(t)_{el}$ is the average electrolyser power consumption [kW]. ηfc and ηel are the average lifetime fuel cell and electrolyser efficiencies [%], respectively. Like the battery, these energy values are also subject to $Q_{H2,min}$ and $Q_{H2,max}$ limits.

3.3.5. Model Input Assumptions

Table 2 contains the necessary input assumptions for the energy models, including efficiencies and other system dynamics that determine the output power generated or stored. The PV panel characteristics are based on the Sunpower Maxeon panel series, while the wind turbine is an approximation of common small-scale turbine systems on the market. The roughness length assumption of 0.05 is defined as rural, farmland area with low crops and without many trees [53]. The hydrogen system efficiency values are based on industry knowledge gathered from leading European fuel cell and electrolyser manufacturers.

Table 2. Hybrid renewable energy system design input assumptions across the different included technologies.

PV Solar	
Panel Power (W)	400
Panel Area (m^2)	2
Thermal Coefficient (%/°C)	−0.3
NOCT (°C)	42
Lifetime (years)	20
Wind turbine	
Hub Height (m)	20
Roughness Height (m)	0.05
Lifetime (years)	20
Lithium battery	
Total Efficiency (%)	95
Maximum Cycles	8000
Maximum Age (years)	10
Regenerative hydrogen fuel cell	
Fuel Cell Efficiency (%)	46
Electrolyser Efficiency (%)	68
Lifetime (years)	20

3.4. Energy Management Strategy

The energy management strategy for the hybrid storage system is shown in Figure 6. When generation supply is available in excess of demand, the battery charges first, followed by the larger capacity hydrogen storage via the electrolyser. When the demand outgrows the supply, the battery discharges first, followed by the activation of the fuel cell. In practical terms, the battery is actually being charged by the fuel cell while active, as the fuel cell cannot module its output without incurring performance losses. The charge and discharge states are is shown in Figure 6.

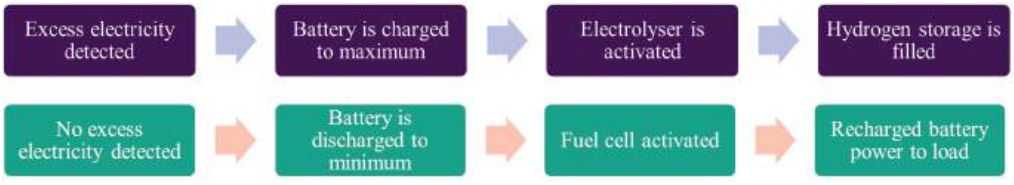

Figure 6. Energy management strategy of the hybrid storage system.

Virtual trading was used to fairly satisfy the community members based on the shared energy available. The excess energy available is shared equally, satisfying each load in ascending order of magnitude. This means that it is more likely that a member's electricity demand will be fully satisfied if smaller. It should be noted that this algorithm can be modified to suit any location-specific REC policy.

3.5. Economic and Environmental Indicators

A selection of three different system configurations: the best economic outcome, best environmental outcome, and a midpoint configuration between the two would be assessed in the model. It is important from a financial perspective to understand the investment requirements and expected returns for prospective REC members. The net present value (NPV) is commonly employed to determine economic feasibility, as well as the internal rate of return (IRR), simple return [%], payback period [years], and levelized cost of electricity (LCOE) for energy specific cases. Generally, if the NPV is positive compared to the base scenario, the investment is worthwhile [54].

$$\mathrm{NPV} = \sum_{n=1}^{N} \frac{C_{O\&M,n} + C_{f,n}}{(1+R)^n} - C_0 \tag{12}$$

where $C_{O\&M,t}$ is the operation and maintenance cashflow for year t, $C_{f,t}$ is the fuel input cashflow, R is the discount rate, and C_0 is the initial capital investment. It was assumed that any grid consumption is included in $C_{f,t}$ in units of EUR/year. The capital requirement and operating cashflows are summed for each generation and storage asset to solve for the system NPV. The IRR evaluates the rate of return if the NPV is set to zero, at which point the project breaks even.

$$\mathrm{NPV} = \sum_{n=1}^{N} \frac{C_n}{(1+IRRR)^n} \tag{13}$$

Calculating the LCOE is beneficial when assessing the economic feasibility of different technologies. The LCOE was evaluated against the grid cost to assess the cost savings per unit of electricity which could be expected by the community members. LCOE is defined as the total cost or lifetime cost of the asset divided by the total electricity delivered to the consumer [55].

$$\mathrm{LCOE}(/\mathrm{kWh}) = \frac{\sum_{n=1}^{N} C_{0,n} + C_{O\&M,n} + C_{f,n}}{\sum_{n=1}^{N} E_n} \tag{14}$$

where $C_{0,n}$ is the capital cost of the asset, and E_n is the lifetime energy delivered. A range of different assessments exist for the economics of renewable assets, as it is highly dependent on the capital requirement, location, delivery and installation cost, and available labour among other factors. The resulting CAPEX, OPEX, and lifetime parameters are shown in Table 2. The costs include the balance of plant (BOP), such as DC-AC inverters and IoT control equipment. The project has an assumed discount rate R of 5% and an estimated inflation rate of 2% per year, as well as a year-one electricity grid unit cost of 0.30 EUR/kWh for each building. Where the asset lifetime is less than 20 years, the asset is retired and the cost of a new equivalent system was included in the NPV assessment in that given replacement year. This method assumes the BOP cost is relatively low.

The environmental impact was estimated through the global warming potential (GWP) of the assets, which when summed together and divided by the total energy delivered over the system lifetime derives the emissions intensity, measured in $extgCO_2eext/kWh$. The values are then compared with the grid emissions intensity for the island, for which the total decarbonisation potential was evaluated. The grid emissions were found using generation data gathered from the national TSO (Red Electrica de Espana) for the year 2021 and found to have an average of 325 gCO_2e/kWh.

$$EI_{total} = \frac{\sum_{j=1}^{m} (EI_j \cdot E_j)}{\sum_{j=1}^{m} (E_j)} \tag{15}$$

EI_j is the emissions intensity and E_j is the energy output for m number of generators and energy storage systems. This calculation was performed for each timestep of the simulation to find the dynamic emissions value depending on the instantaneous energy mix of the REC. The emissions intensity found within the literature can vary due to the range of manufacturing techniques and factors considered when performing the life cycle assessment (LCA). For this reason, some values such as those used for the hydrogen system are taken as an educated estimation of the emissions impact based on a variety of sources. The GWP embedded during manufacturing and installation for the assets and technology costs are shown in Table 3.

Table 3. Hybrid renewable energy system economic and climate impact assumptions for the different modelled technologies.

Technology	CAPEX	OPEX	Lifetime	Emissions
				Embedded
PV Solar Array [55–57]	2500 EUR/kW	30 EUR/kW/year	20 years	1826 kgCO2e/kW
Wind Turbine [58,59]	2850 EUR/kW	32 EUR/kW/year	20 years	520 kgCO2e/kW
Lithium-Ion LFP [18,60]	328 EUR/kWh	5 EUR/kWh/year	10 years or 8000 cycles	254 kgCO2e/kWh
PEM Fuel Cell [18,61]	1200 EUR/kW	13 EUR/kW/year	20 years	73.3 kgCO2e/kWh
AEM Electrolyser [18,62,63]	1500 EUR/kW	14 EUR/kW/year	20 years or 35,000 h	239 kgCO2e/kWh
Hydrogen Storage Vessel [64–66]	30 EUR/kWh	-	20+ years	5.1 kgCO2e/kWh

3.6. Multi-Objective Optimisation Procedure

Designing and configuring the optimal system sizing for a hybrid decentralized energy system is a complex process. There are a number of non-linear phenomena being simulated, as well as many potential design objectives and constraints. The chosen objective functions considering both cost and carbon reduction are the NPV and the equivalent GWP. The objective functions rely on varying the capacities of the PV solar, wind, battery, and RHFC installations at the site.

The NSGA-II uses a heuristic evolutionary learning algorithm with a population of potential design solutions within the defined constraints. It then ranks the population based on a non-dominated sorting, producing a pareto front of optimal solutions by minimizing both objective functions [36]. Each individual in the population was determined based on the simulation of the model of a one-year period and evaluating the two objectives. The best-performing individuals are passed to the next generation, whereas a combination of mutations and created offspring (crossover) determines the remaining individuals. NSGA-II provides several advantages including the use of elitism and reduced computational complexity [67]. The solving process for NSGA-II implementation is shown in Figure 7. The algorithm also requires inputs, including the population size, number of offspring, stopping conditions, and variable constraints, as shown in Table 4. The lower limit for all system assets was set to zero, while the upper limit was set to 200 kW in line with the adopted REC regulation for this study. The *pymoo* module created and maintained by Blank et al. [68] was used to implement the NSGA-II algorithm in Python.

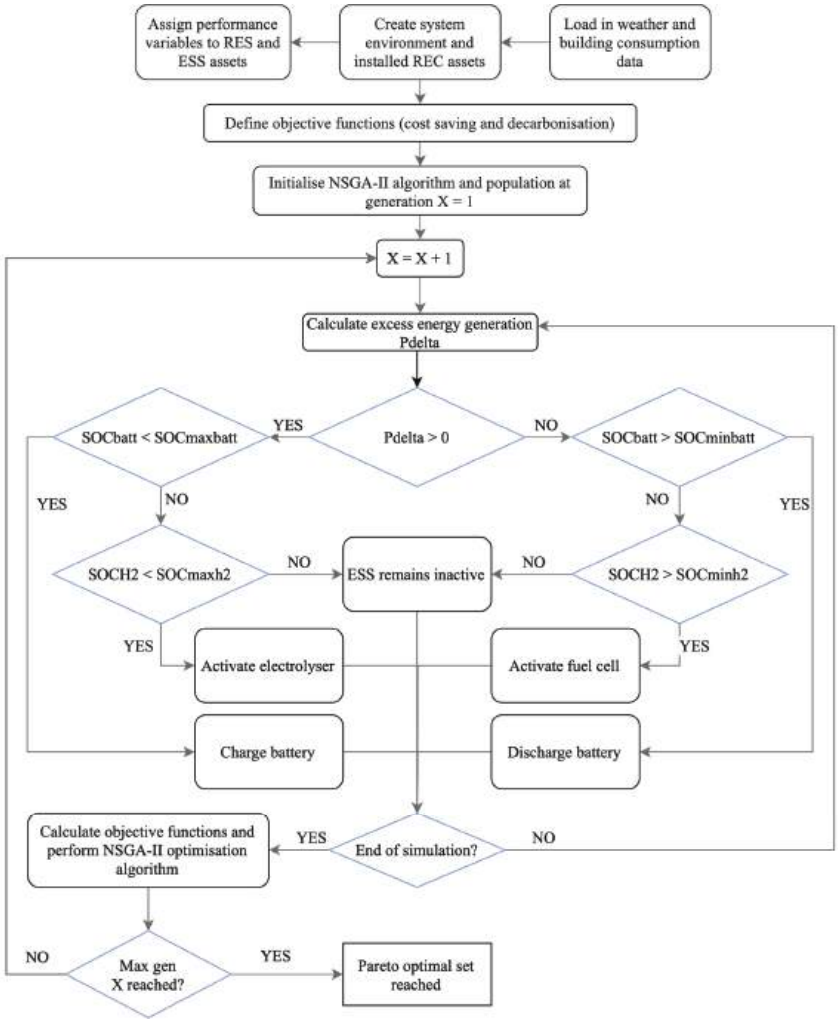

Figure 7. Hybrid energy system model approach with multi-objective optimisation algorithm NSGA-II solving process.

Table 4. Initialisation parameters and constraints of the NSGA-II optimisation algorithm.

Parameter	Value
Population Size	72
No. of Offspring	24
Max No. of Generations	400
Lower Bounds (all assets)	0 kW/kWh
Upper Bounds (all assets)	200 kW/kWh

The input parameters were set into the simulation model with the selected objective functions and run within the NSGA-II algorithm. The optimisation ran to the maximum allowed generations before terminating. Due to the bound nature of the problem, the component capacity variables start as a random distribution, from which the non-dominated solutions on the pareto front are derived. Well-performing individuals are moved forward to the next generation, as well as a selection of offspring and individuals that have experienced random mutation. As the generations progress, the population steadily converges on a large set of non-dominated solutions that align with the pareto front between the best system economics and decarbonisation performance, denoted by the objective functions of cost savings and emissions intensity. The graph in Figure 8 shows the convergence of the objective function products during the progression through the first 200 generations of the hybrid system optimisation, which will converge towards a single value.

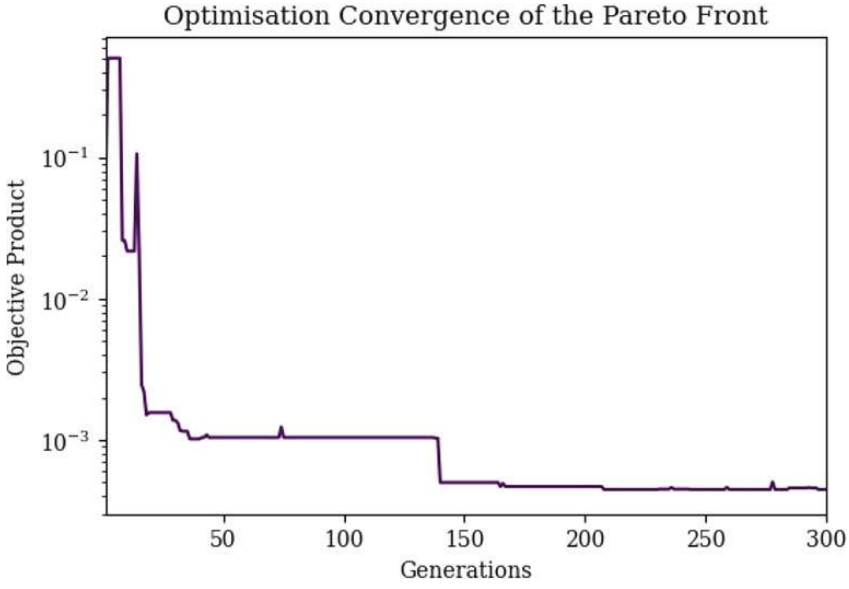

Figure 8. Convergence of the optimisation pareto front as shown by an aggregated scalar objective function minimising towards a single value.

4. Results and Discussion

4.1. Optimisation Results of the Hybrid Energy Generation and Storage Renewable Energy Community

The primary case studied was the hybrid architecture consisting of both a lithium battery and an RHFC. Within the resulting pareto front in Figure 9a, each point on the graph represents a different combination of design capacities ranging from the configuration able to achieve the highest economic returns to the system able to deliver the lowest net carbon output. The lifetime cost savings potential ranges from approximately EUR 130k to EUR 186k, while the emission intensity ranges from 82 to 140 gCO_2e/kWh. It is interesting to note that the savings do not start at zero, implying that below EUR 130k returns, the

configuration was able to increase in economic performance as well as decarbonisation before reaching an inflection point. At this point, it is clear that the net savings were able to continue increasing, while the net emissions reached its minimum and began to climb again. At the other end of the front, the gradient began to increase as both the returns increase but also the emissions intensity. This continued up to the point where the system can no longer provide additional savings without an exponential increase in embedded emissions and therefore environmental impact.

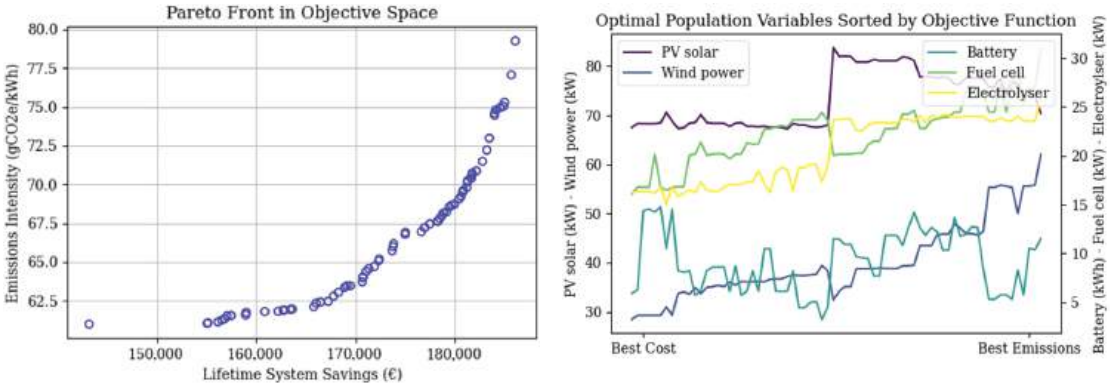

(**a**) Pareto front in objective space

(**b**) Optimal variables sorted by objective

Figure 9. Key outputs from the multi-objective optimisation process, indicating relationship between cost reduction and climate impact of the system design.

The resulting pareto front presents several crucial outcomes and challenges for providing a low cost and net-zero energy system. Firstly, an inherent trade-off relationship was observed between the ability to decarbonise and ensure net profitability. Secondly, the REC architecture, within the context and constraints of the study, can reduce carbon emissions by over 75% compared to local grid usage. However, this is a hard limit due to the capacity factors of the components and the embedded carbon within the system during manufacturing. Additionally, trying to decrease the carbon emissions further only incurs a financial penalty, which would be hard to incentivise to the REC members.

The graph in Figure 9b displays the capacities of PV solar, wind power, battery, fuel cell, and electrolyser systems with the final population arranged by the two objective functions. The best economic outcome is on the left, while the best environmental outcome is on the right. It can be observed that all systems generally tend towards an increase in capacity as the emissions improve. This is most likely because a larger total off-grid capacity has a higher self-consumption rate, and therefore is relying less on the grid which has a high emissions intensity of 325 gCO_2e/kWh. The REC was consequently able to reduce emissions to a greater extent. This, of course, negatively impacts the economics of the REC as more capital has to be invested into a more substantial design. It appears from the graph that the wind power, as well as the fuel cell and electrolyser which make up the RHFC are most sensitive to changes in the objective functions. The following section explores the chosen optimal design, and details why the capacities affect the objective functions in this way.

4.2. Best Hybrid System Design for the Renewable Energy Community

The pareto front provides a range of potential non-dominated solutions in which neither objective function is favoured over the other. There are several methods that can be used to choose a nominally 'best' system from the population to perform further analysis. Based on the research conducted by Wang and Rangaiah [69], it was chosen to use simple additive weighting (SAW). SAW normalises both objective function values, where zero is

the worst possible result and one is the most improved. The values are then summed for each member of the population to find the best overall solution.

$$\begin{cases} F_{ij} = \frac{f_{ij}}{f_j^+} & \text{for a maximisation criterion, where } f_{i^+} = \underset{i \in m}{max} f_{ij} \\ F_{ij} = \frac{f_{ij}}{f_j^-} & \text{for a maximisation criterion, where } f_{i^-} = \underset{i \in m}{min} f_{ij} \end{cases} \tag{16}$$

$$A_i = \sum_{j=1}^{n} F_{ij} \tag{17}$$

F_{ij} is the normalised set of objective functions j for the pareto population i and f_{ij} is the initial set. f_{i^+} and f_{i^-} are the maximum and minimum criteria of the set, respectively. A_i then provides the best set of design variables to use in the hybrid REC, given in Table 5. The system was then simulated to perform analysis of all performance indicators.

Table 5. Optimal installed capacities of the energy system assets.

REC Asset	Optimal Values
PV Solar	71 kW
Wind Turbine(s)	32 kW
Lithium Battery	14 kWh
PEM Fuel Cell	20 kW
AEM Electrolyser	18 kW

Figure 10 contains two one-week sample periods obtained from the simulation, displaying the balance of each asset and their contribution to balancing the total REC load. Typical summer and winter periods are used to observe the seasonal variation in the system response. The REC load was higher on average during the summer period, leading to increased reliance and leading the energy grid to fill gaps in the consumption requirement when the ESS was unavailable. The winter period, by contrast, was able to satisfy the load requirement with the exception of some short periods. This shows that although the REC can operate largely off-grid, it is still beneficial from both an economic and emissions perspective to remain grid-connected from the short period when the REC generation and hybrid storage cannot fully balance the consumption. The hydrogen system requires a maximum storage of 1835k, which was evaluated from the simulation as the storage required to avoid any state-of-charge limits. The value therefore is a worst-case scenario for the system, as it is likely that a smaller storage would be chosen in accordance with the installation space available within the REC. Given the lower heating value (LHV) of hydrogen and the average fuel cell efficiency of 46%, the system would require approximately 14 Nm^2 of hydrogen stored at 35bar to supply the required quantity of a one-year period.

Table 6 below shows a full breakdown of the economic and environmental performance of each grouped asset. The solar array was able to deliver the most energy to the REC due to the high capacity of 71 kW, but also the higher solar potential on the island of Formentera of 4.7 kWh/m^2, compared to London, UK, of 2.9 kWh/m^2. Energy generated from wind provides the next greatest portion of over 24%, the benefit of which is that energy is generated during the night period as well as the day to charge the battery and a steady quantity of hydrogen. The battery itself was relatively small compared to the other components at 14 kWh and responds only when the energy generated is no longer available in excess of supply. The fuel cell and electrolyser were sized at 20 kW and 18 kW, respectively. It is interesting to note that the electrolyser was smaller in power input capacity than the fuel cell, even though the efficiencies would dictate the fuel cell would need approximately half the rated power of the electrolyser to achieve the same capacity factor. The increased generation from wind power over more of the simulation may allow the electrolyser to run for longer periods and make up the fuel cell's lower efficiency.

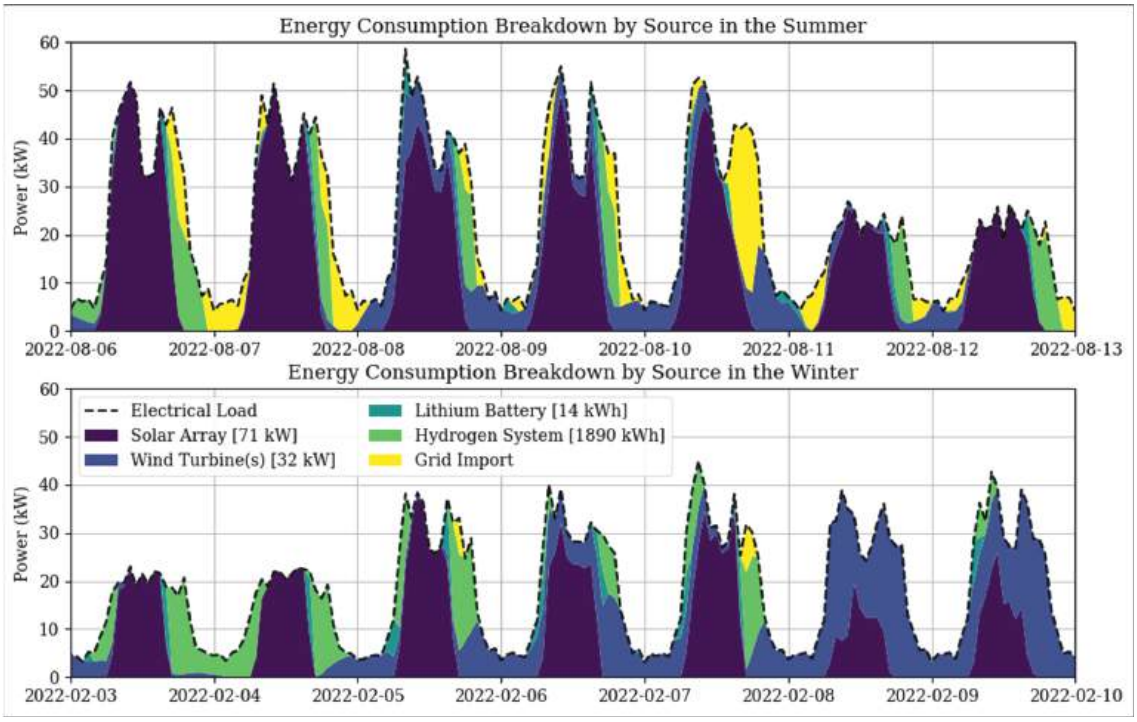

Figure 10. Energy generation hour-by-hour breakdown by source. Example shown includes typical summer and winter weeks.

Table 6. The economic and environmental performance of the different REC assets in the optimal design configuration.

Technology Asset	Energy-Delivered (kWh)	Capacity-Factor (%)	CAPEX (EUR)	OPEX (EUR/year)	LCOE (EUR/kWh)	Emissions (gCO_2e/kWh)
PV Solar [71 kW]	141,184	19	177,500	2130	0.07	40.7
Wind Turbine(s) [32 kW]	60,517	22	91,200	1024	0.09	15.9
Lithium Battery [14 kWh]	4910	8	5446	308	0.08	72.4
Hydrogen System [1836 kWh]	26,360	15	106,000	570	0.17	18.6

4.2.1. Techno-Economic Assessment

It is important to analyse each component on an individual basis to fully understand their contribution to the economic and emissions performance within the system. This would not only help to confirm the results seen in the pareto optimality, but also from a practical perspective assist a potential system designer to identify the most important assets, any particularly sensitive parameters, and assess the risks associated with each.

The solar array has the largest capital and operational costs compared with the wind power alternative due to the higher unit costs per kW. Despite this, the PV solar was able to achieve a greater capacity factor, which is the measure of energy output as a ratio of the total potential output of the same period. PV solar is naturally limited by the hours of solar available, while wind power is limited by the average wind speed and distribution.

The higher capacity is the main mechanism which produced a lower LCOE for the PV solar of 0.07 compared with wind power's 0.09 EUR/kWh, despite the higher CAPEX and OPEX costs. This result also implies that although wind power is possible on with the REC, it may be beneficial from a to study a PV solar generation only option due to the potential impracticalities of local wind turbines. The inverse was then observed for the environmental impact, in that the PV solar has considerably higher embedded emissions of 40.7 gCO_2e/kWh compared with the 15.9 gCO_2e/kWh expected from equivalent wind energy. These results show a good agreement with the reported embedded emissions from the IPCC AR5 report [70] of 45 gCO_2e/kWh and 13 gCO_2e/kWh for solar and wind, respectively.

At EUR 106k, the RHFC CAPEX was a factor of twenty higher than the battery. This trend carries over into the LCOE results, where an approximate doubling of the levelized cost was observed for the hydrogen system compared with lithium batteries. These outcomes are in line with similar hydrogen system results found in the literature [55,71]. It is widely known that hydrogen technology is a less financially viable alternative for many applications, so this result was somewhat expected. This could change in the near future as the costs of hydrogen technology reduce.

The emissions output from the battery per kWh delivery was far higher than the hydrogen solution at 72.4 and 18.6 gCO_2e/kWh, respectively. The trend is also supported by the population variables in Figure 9b, in which it is noted that as the hydrogen assets increased in capacity, the emissions result improved, while the net savings deteriorated.

Figure 11 contains the present value curve of the grid-only case, that is when electricity cost is paid to the utility company over the project period. The curve starts at zero as there is no capital cost associated with grid usage, but the operational cost per year is high. By contrast, the modelled REC requires an initial investment of EUR 380k. However, the lower year-on-year cost means that the system can pay off the investment cost, described as the payback term, in 9 years. The project ends with a final total savings of EUR 178k when the inflation and discounts rates of 2% and 5%, respectively, are considered. The result produces an IRR of 10.9%, year's returns of 9.6%, and an average system LCOE of 0.16 EUR/kWh. This assessment was based on the cost of equipment and installation since 2020.

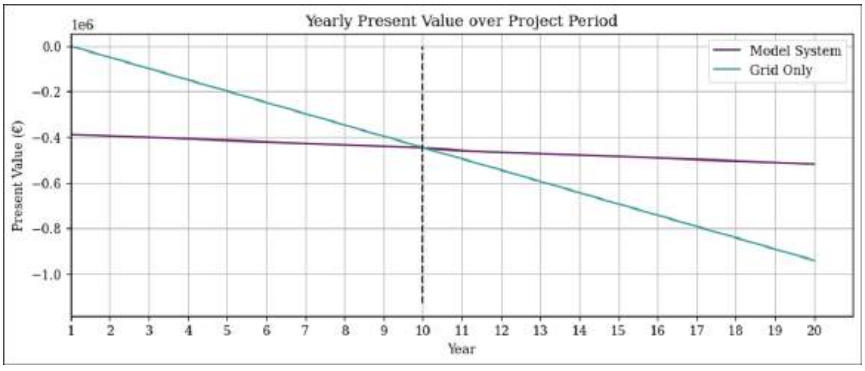

Figure 11. The present value over the project period. The system was primarily compared with a 'business-as-usage' grid-only scenario.

Considering the historical and currently observed trends in renewable generation and storage equipment cost, it is projected that by 2030 and beyond there will continue to be a substantial decrease in the financial requirements for this type of system. The results shown here are therefore towards the upper bounds in terms of uncertainty about the future cost of an REC implementation.

4.2.2. REC Members' Net Savings and Environmental Impacts

The model not only provides a global view of the potential impact of an REC configuration but is also able to analyse the reduction in cost and emissions on a per load basis. There were seven discretised loads within the model, with each being able to mutually accept and trade energy with the decentralised assets. Table 7 below shows the average LCOE and emissions intensity for each building and the percentage decrease in emissions. The REC provided a considerable degree of self-consumption, ranging from 91.1% for the largest load to over 98% for the smallest. In terms of the impact on the energy cost, the new LCOE ranged between 0.16 and 0.17 EUR/kWh compared to 0.30 EUR/kWh for grid-only. The decarbonisation of energy usage was also seen to be in the range of 75–77% in the first year of installation.

Table 7. Quantity of energy delivered to the REC compared with the quantity of energy delivered from the grid.

REC Member	REC Delivered (kWh)	Grid Delivered (kWh)
Community centre	61,078	5461
Elementary school	18,807	348
High school	44,743	1437
Council offices	28,244	683
Residential units	11,975	514

4.3. Best Case and Extremes Comparison

During the study, it was vital to understand not only the characteristics of the system at the 'best' pareto result, but also the performance at the extremes of the multi-objective optimisation. The result gives an indication as to how sensitive the result was to changing parameters. Table 8 contains the results of the three chosen REC configurations in terms of hybrid generation and storage capacities.

Table 8. Comparison REC configurations for extreme cases for net savings and decarbonisation potential compared with the chosen nominal case.

	Best Net Savings	Nominal	Best Emissions Savings
REC Delivered (kWh)	151,493	156,536	158,823
Self-Consumption (%)	91.0	94.5	96.2
LCOE (EUR/kWh)	0.15	0.16	0.19
Net Savings (EUR)	187,080	178,229	139,647
Savings (%)	51	47	36
IRR (%)	12.6	10.9	7.1
Simple Payback (%)	10.1	9.6	8.0
Payback Term (years)	8.3	9.0	11.5
Emissions (gCO2*e*/kwh)	79	69	61
Decarbonisation (%)	75.6	78.8	81.2

4.4. Pareto Front Comparison of Energy Storage System Technologies

The hybrid ESS comprised of a lithium battery and RHFC system produces differing performance outcomes based on the relative capacities of the technologies. Therefore, a comparison of the multi-objective optimisation for the same REC set-up with an additional battery-only ESS and RHFC-only ESS are required to ensure that the hybrid design was able to provide the best performance in terms of environmental impact and cost savings for the REC members. Figure 12 compares these pareto fronts, from which the combination of the technologies was able to produce a significant improvement over the technologies working independently. This was likely due to the fact that the battery is better at providing a short-term response but suffers from increased degradation if used frequently for charge and

discharge, and similarly the hydrogen system requires a high capital cost and is best suited to the long-term storage of grid energy. The battery alone also has increased embedded carbon, which limited its ability to decarbonise. The hydrogen-only system suffered from the limitation that the electrolyser only runs at rated power, limiting flexibility.

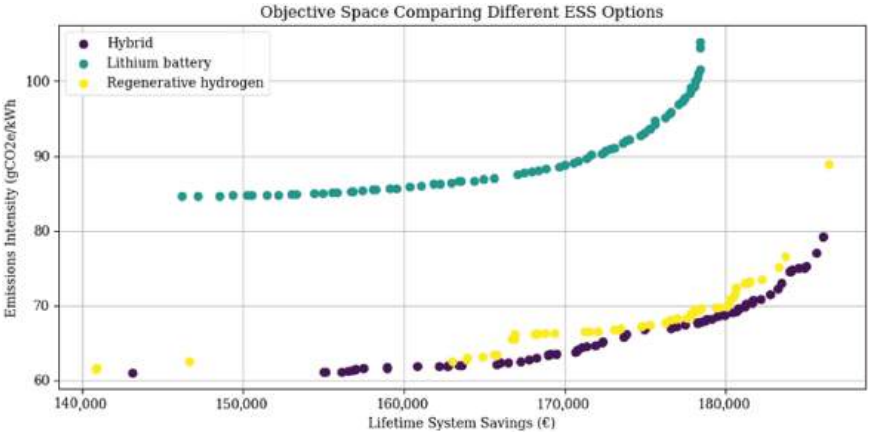

Figure 12. The present value over project period compared with the 'business-as-usual' grid-only scenario.

Table 9 below summarises a range of LCOE results from the literature with similar smart grid and renewable energy architectures, incorporating hydrogen storage where available. It should be noted that specific parameters such as renewable resource availability, local technology costs, and system sizing may induce uncertainty in the resulting total system LCOE. For example, locations with a higher solar potential are naturally able to achieve a lower PV solar LCOE, and conversely, remote areas with high delivery and installation costs would experience higher project costs. The resulting average is 0.13 EUR/kWh, which is in good agreement with the central economic and environmental trade-off case produced in this work.

Table 9. Comparison of the levelized cost of electricity results of similar hybrid hydrogen smart grid systems within the literature.

Reference	Smart Grid Architecture	Assets	Location	Scale	LCOE (EUR/kWh)
This work	Energy community	Solar, wind, battery/RHFC	Formentera, Spain	<100 kW	0.15
[55]	DC microgrid	Solar, battery/RHFC	Sub-Saharan	<100 kW	0.16
[72]	AC microgrid	Solar/wind, genset/RHFC	Morocco	<1 MW	0.07
[73]	AC microgrid	Solar/wind, hydrogen	India	<1 MW	0.08
[74]	Energy community	Solar/wind, battery/RHFC	Ghana	<100 kW	0.26
[75]	Energy community	Solar/wind, hydrogen	Canada	>1 MW	0.08

5. Conclusions

This work presents a novel decentralised hybrid generation and ESS implementing both battery and hydrogen technology for use in a geographically isolated rural renewable energy community. A review of the existing state of the art was presented and highlighted the gaps in knowledge for such a system, particularly when considering both economic

feasibility and a dynamic calculation of the environmental impact. This discussion comes at an interesting time for Europe and around the world as policymakers work to facilitate the potential benefits of aggregating decentralised renewables, one such method being the REC. The steady cost reduction in PV solar and wind power as seen over the past years has also accelerated growth in the decentralised energy sector. The rise of cost-effective hydrogen technology is set to make a considerable impact on how energy is stored and transported as a vector.

The results from this study show that there is an inherent trade-off relationship between cost reduction and the ability to decarbonise the energy system. By using a model built in Python, several different economic and environmental scenarios can be assessed. The implementation of a multi-objective algorithm gives potential system designers and policymakers a range of possible solutions. In this case, the optimal design results in an LCOE of 0.15W EUR/kWh, a project IRR of 10.8%, and an ROI of 9 years. Greenhouse gas emissions were reduced by 72% in the first year of installation to 69 gCO_2e/kWh.

In further studies, emphasis should be placed on performing a sensitivity analysis and understanding where uncertainty may arise in the energy model. In particular, varying the component input assumptions such as capital cost and embedded emissions in line with reported ranges from the literature would further account for future uncertainty in performance. Additionally, further improvements to the system sizing optimisation method, including additional objective functions such as the loss of load probability from the literature, quantifying social impacts, and applying local space constraints would capture other potential strengths and weaknesses of the hybrid storage technology. Finally, research into the implementation of REC architectures in other locations around the world beyond the case study in this work would not only provide additional validation but also give a global perspective of how effective an REC could be in keeping energy costs stable and curbing the impacts of climate change.

Author Contributions: R.G.: Conceptualization, methodology, software, validation, formal analysis, investigation, resources, data curation, writing—original draft preparation, writing—review and editing, visualization. Z.D.: Supervision, project administration, funding acquisition, writing—review and editing. All authors have read and agreed to the published version of the manuscript.

Funding: This research is sponsored by the EU Horizon 2020 research and innovation program under the grant agreement No 957852: Virtual Power Plant for Interoperable and Smart isLANDS—VPP4ISLANDS. More information is available at https://cordis.europa.eu/project/id/957852 (accessed on 30 August 2023).

Data Availability Statement: Data will be made available on request.

Acknowledgments: Special thanks are extended to the Consel de Formentera for allowing access to energy consumption data, from which the energy community model was built.

Conflicts of Interest: The authors declare no conflict of interest.

Abbreviations

The following abbreviations are used in this manuscript:

CAPEX	Capital Expenditure
DOD	Depth of Discharge
ESS	Energy Storage System
GA	Genetic Algorithm
GHI	Global Horizontal Irradiance
GWP	Global Warming Potential
IEC	International Electrotechnical Commission
IRR	Internal Rate of Return
LCOE	Levelised Cost of Electricity
NPV	Net Present Value
NSGA	Non-dominated Sorting Genetic Algorithm
OPEX	Operational Expenditure

PEM	Proton Exchange Membrane
PV	Photovoltaic
REC	Renewable Energy Community
RED	Renewable Energy Directive
RES	Renewable Energy System
RHFC	Regenerative Hydrogen Fuel Cell
ROI	Return on Investment
SOC	State of Charge
TSO	Transmissions System Operator

References

1. United Nations. *The Paris Agreement*; United Nations: Paris, France, 2015.
2. Intergovernmental Panel on Climate Change. *Synthesis Report of the IPCC Sixth Assessment Report (AR6)*; IPCC Secretariat: Geneva, Switzerland, 2022.
3. Wang, R.; Usman, M.; Radulescu, M.; Cifuentes Faura, J.; Lorente, D. Achieving ecological sustainability through technological, innovations, financial development, FDI and energy consumption in developing European countries. *Gondwana Res.* **2023**, *119*, 138–152. [CrossRef]
4. Department for Business, Energy & Industrial Strategy. *British Energy Security Strategy*; HM Goverment UK: London, UK, 2022.
5. Boie, I.; Fernandes, C.; Frías, P.; Klobasa, M. Efficient strategies for the integration of renewable energy into future energy, infrastructures in Europe—An analysis based on transnational modeling and case studies for nine European regions. *Energy Policy* **2014**, *67*, 170–185. [CrossRef]
6. Kabeyi, M.J.B.; Olanrewaju, O.A. Sustainable Energy Transition for Renewable and Low Carbon Grid Electricity Generation and Supply. *Front. Energy Res.* **2022**, *9*, 743114. [CrossRef]
7. Gielen, D.; Boshell, F.; Saygin, D.; Bazilian, M.D.; Wagner, N.; Gorini, R. The role of renewable energy in the global energy transformation. *Energy Strategy Rev.* **2019**, *24*, 38–50. [CrossRef]
8. Saboori, H.; Mohammadi, M.; Taghe, R. Virtual Power Plant (VPP), Definition, Concept, Components and Types. In Proceedings of the 2011 Asia-Pacific Power and Energy Engineering Conference, Washington, DC, USA, 25–28 March 2011; pp. 1–4. [CrossRef]
9. Hirth, L.; Ziegenhagen, I. Balancing power and variable renewables: Three links. *Renew. Sustain. Energy Rev.* **2015**, *50*, 1035–1051. [CrossRef]
10. Mohd Azmi, K.H.; Mohamed Radzi, N.A.; Azhar, N.A.; Samidi, F.S.; Thaqifah Zulkifli, I.; Zainal, A.M. Active Electric Distribution Network: Applications, Challenges, and Opportunities. *IEEE Access* **2022**, *10*, 134655–134689. [CrossRef]
11. Rezaeimozafar, M.; Monaghan, R.F.; Barrett, E.; Duffy, M. A review of behind-the-meter energy storage systems in smart grids. *Renew. Sustain. Energy Rev.* **2022**, *164*, 112573. [CrossRef]
12. Aneke, M.; Wang, M. Energy storage technologies and real life applications—A state of the art review. *Appl. Energy* **2016**, *179*, 350–377. [CrossRef]
13. Hesse, H.C.; Schimpe, M.; Kucevic, D.; Jossen, A. Lithium-Ion Battery Storage for the Grid—A Review of Stationary Battery Storage System Design Tailored for Applications in Modern Power Grids. *Energies* **2017**, *10*, 2107. [CrossRef]
14. Wali, S.; Hannan, M.; Ker, P.J.; Rahman, M.A.; Mansor, M.; Muttaqi, K.; Mahlia, T.; Begum, R. Grid-connected lithium-ion battery energy storage system: A bibliometric analysis for emerging future directions. *J. Clean. Prod.* **2022**, *334*, 130272. [CrossRef]
15. Vykhodtsev, A.V.; Jang, D.; Wang, Q.; Rosehart, W.; Zareipour, H. A review of modelling approaches to characterize lithium-ion battery energy storage systems in techno-economic analyses of power systems. *Renew. Sustain. Energy Rev.* **2022**, *166*, 112584. [CrossRef]
16. Jamal, H.; Khan, F.; Si, H.R.; Kim, J.H. Enhanced compatibility of a polymer-based electrolyte with Li-metal for stable and dendrite-free all-solid-state Li-metal batteries. *J. Mater. Chem. A* **2021**, *9*, 27304–27319. [CrossRef]
17. Jamal, H.; Khan, F.; Si, H.R.; Kim, J.H. Enhancement of the ionic conductivity of a composite polymer electrolyte via surface functionalization of SSZ-13 zeolite for all-solid-state Li-metal batteries. *J. Mater. Chem. A* **2021**, *9*, 4126–4137. [CrossRef]
18. Mongird, K. *2020 Grid Energy Storage Performance Assessment*; US Department of Energy: Richland, WA, USA, 2020.
19. Zhang, W.; Maleki, A.; Rosen, M.A.; Liu, J. Optimization with a simulated annealing algorithm of a hybrid system for renewable energy including battery and hydrogen storage. *Energy* **2018**, *163*, 191–207. [CrossRef]
20. French, S. The Role of Zero and Low Carbon Hydrogen in Enabling the Energy Transition and the Path to Net Zero Greenhouse Gas Emissions: With global policies and demonstration projects hydrogen can play a role in a net zero future. *Johns. Matthey Technol. Rev.* **2020**, *64*, 357–370.
21. Coppitters, D.; De Paepe, W.; Contino, F. Robust design optimization and stochastic performance analysis of a grid-connected photovoltaic system with battery storage and hydrogen storage. *Energy* **2020**, *213*, 118798. [CrossRef]
22. Haji Bashi, M.; De Tommasi, L.; Le Cam, A.; Relaño, L.S.; Lyons, P.; Mundó, J.; Pandelieva-Dimova, I.; Schapp, H.; Loth-Babut, K.; Egger, C.; et al. A review and mapping exercise of energy community regulatory challenges in European member states based on a survey of collective energy actors. *Renew. Sustain. Energy Rev.* **2023**, *172*, 113055. [CrossRef]
23. European Parliament. *Directive (EU) 2018/2001 of the European Parliament and of the Council of 11 December 2018 on the Promotion of the Use of Energy from Renewable Sources*; European Parliament: Brussels, Belgium, 2018.

24. Fina, B.; Monsberger, C. Legislation for renewable energy communities and citizen energy communities in Austria: Changes from the legislative draft to the finally enacted law. *J. World Energy Law Bus.* **2022**, *15*, 237–244. [CrossRef]
25. Sebi, C.; Vernay, A.L. Community renewable energy in France: The state of development and the way forward. *Energy Policy* **2020**, *147*, 111874. [CrossRef]
26. Broska, L.H.; Vögele, S.; Shamon, H.; Wittenberg, I. On the Future(s) of Energy Communities in the German Energy Transition: A Derivation of Transformation Pathways. *Sustainability* **2022**, *14*, 3169. [CrossRef]
27. Swens, J.; Diestelmeier, L. 4—Developing a legal framework for energy communities beyond energy law. In *Energy Communities*; Löbbe, S., Sioshansi, F., Robinson, D., Eds.; Academic Press: Cambridge, MA, USA, 2022; pp. 59–71. [CrossRef]
28. Trevisan, R.; Ghiani, E.; Pilo, F. Renewable Energy Communities in Positive Energy Districts: A Governance and Realisation Framework in Compliance with the Italian Regulation. *Smart Cities* **2023**, *6*, 563–585. [CrossRef]
29. Gallego-Castillo, C.; Heleno, M.; Victoria, M. Self-consumption for energy communities in Spain: A regional analysis under the new legal framework. *Energy Policy* **2021**, *150*, 112144. [CrossRef]
30. Official Gazette. *Legislative Decree no. 192/2021*; Official Gazette: Rome, Italy, 2021.
31. Di Silvestre, M.L.; Ippolito, M.G.; Sanseverino, E.R.; Sciumè, G.; Vasile, A. Energy self-consumers and renewable energy communities in Italy: New actors of the electric power systems. *Renew. Sustain. Energy Rev.* **2021**, *151*, 111565. [CrossRef]
32. Trevisan, R.; Ghiani, E.; Ruggeri, S.; Mocci, S.; Pisano, G.; Pilo, F. Optimal sizing of PV and Storage for a Port Renewable Energy Community. In Proceedings of the 2022 2nd International Conference on Energy Transition in the Mediterranean Area (SyNERGY MED), Thessaloniki, Greece, 17–19 October 2022; pp. 1–5. [CrossRef]
33. Bartolini, A.; Carducci, F.; Muñoz, C.B.; Comodi, G. Energy storage and multi energy systems in local energy communities with high renewable energy penetration. *Renew. Energy* **2020**, *159*, 595–609. [CrossRef]
34. Wang, Y.; Gao, W.; Li, Y.; Qian, F.; Yao, W. Techno-economic analysis of the transition toward the energy self-sufficiency community based on virtual power plant. *Front. Energy Res.* **2023**, *11*, 1010846. [CrossRef]
35. Cuesta, M.; Castillo-Calzadilla, T.; Borges, C. A critical analysis on hybrid renewable energy modeling tools: An emerging opportunity to include social indicators to optimise systems in small communities. *Renew. Sustain. Energy Rev.* **2020**, *122*, 109691. [CrossRef]
36. Niveditha, N.; Rajan Singaravel, M. Optimal sizing of hybrid PV–Wind–Battery storage system for Net Zero Energy Buildings to reduce grid burden. *Appl. Energy* **2022**, *324*, 119713. [CrossRef]
37. Zhang, Y.; Sun, H.; Tan, J.; Li, Z.; Hou, W.; Guo, Y. Capacity configuration optimization of multi-energy system integrating wind turbine/photovoltaic/hydrogen/battery. *Energy* **2022**, *252*, 124046. [CrossRef]
38. Xu, C.; Ke, Y.; Li, Y.; Chu, H.; Wu, Y. Data-driven configuration optimization of an off-grid wind/PV/hydrogen system based on modified NSGA-II and CRITIC-TOPSIS. *Energy Convers. Manag.* **2020**, *215*, 112892. [CrossRef]
39. Xuan, J.; Chen, Z.; Zheng, J.; Zhang, Z.; Shi, Y. Optimal planning of hybrid electric-hydrogen energy storage systems via multi-objective particle swarm optimization. *Front. Energy Res.* **2023**, *10*, 1034985. [CrossRef]
40. He, Y.; Guo, S.; Zhou, J.; Ye, J.; Huang, J.; Zheng, K.; Du, X. Multi-objective planning-operation co-optimization of renewable energy system with hybrid energy storages. *Renew. Energy* **2022**, *184*, 776–790. [CrossRef]
41. Wang, H.; Xie, Z.; Pu, L.; Ren, Z.; Zhang, Y.; Tan, Z. Energy management strategy of hybrid energy storage based on Pareto optimality. *Appl. Energy* **2022**, *327*, 120095. [CrossRef]
42. ©NordNordWest. CC-BY-SA-3.0. Spain Location Map. 2008. Available online: https://en.wikipedia.org/wiki/File:Spain_location_map.svg (accessed on 30 August 2023).
43. NASA. *LARC Power Data Access Viewer*; NASA: Houston, TX, USA, 2023.
44. Farhad, A.; Ali, G.; Mohsen, J. *Dataset on Hourly Load Profiles for a Set of 24 Facilities from Industrial, Commercial, and Residential Enduse Sectors*; Mendeley Data; Rutgers The State University of New Jersey: New Brunswick, NJ, USA, 2020; p. 1.
45. Pinto, E.S.; Serra, L.M.; Lázaro, A. Energy communities approach applied to optimize polygeneration systems in residential buildings: Case study in Zaragoza, Spain. *Sustain. Cities Soc.* **2022**, *82*, 103885. [CrossRef]
46. Chung, M.; Shin, K.Y.; Jeoune, D.S.; Park, S.Y.; Lee, W.J.; Im, Y.H. Economic Evaluation of Renewable Energy Systems for the Optimal Planning and Design in Korea—A Case Study. *J. Sustain. Dev. Energy Water Environ. Syst.* **2018**, *6*, 725–741. [CrossRef]
47. Duffie, J.; Beckman, W. *Solar Engineering of Thermal Processes*; Wiley: Hoboken, NJ, USA, 1991.
48. Reda, I.; Andreas, A. *Solar Position Algorithm for Solar Radiation Applications*; National Renewable Energy Laboratory: Golden, CO, USA, 2008.
49. Corke, T.; Nelson, R. *Wind Energy Design*; Taylor and Francis Group: Miami, FL, USA, 2018.
50. Wood, D. *Improvements to the Simplified Loads Methodology in IEC 61400-2*; National Renewable Energy Laboratory: Golden, CO, USA, 2021.
51. Draxl, C.; Clifton, A.; Hodge, B.M.; McCaa, J. The Wind Integration National Dataset (WIND) Toolkit. *Appl. Energy* **2015**, *151*, 355–366. [CrossRef]
52. Shepherd, C.M. Design of Primary and Secondary Cells: II. An Equation Describing Battery Discharge. *J. Electrochem. Soc.* **1965**, *112*, 657. [CrossRef]
53. Burton, T.; Sharp, D.; Jenkins, N.; Bossanyi, E. *Wind Energy Handbook*; John Wiley and Sons: Chichester, UK, 2001.
54. Warner, S.; Hussain, S. *The Finance Book*; Pearson Education Ltd.: Harlow, UK, 2017.

55. Jansen, G.; Dehouche, Z.; Corrigan, H. Cost-effective sizing of a hybrid Regenerative Hydrogen Fuel Cell energy storage system for remote and off-grid telecom towers. *Int. J. Hydrog. Energy* **2021**, *46*, 18153–18166. [CrossRef]
56. Feldman, D.; Dummit, K.; Zuboy, J.; Margolis, R. *Fall 2022 Solar Industry Update*; National Renewable Energy Laboratory: Golden, CO, USA, 2022.
57. Carvalho, M.; Menezes, V.L.; Gomes, K.C.; Pinheiro, R. Carbon footprint associated with a mono-Si cell photovoltaic ceramic roof tile system. *Environ. Prog. Sustain. Energy* **2019**, *38*, 13120. [CrossRef]
58. Stehly, T.; Beiter, P.; Duffy, P. *2019 Cost of Wind Energy Review*; National Renewable Energy Laboratory: Golden, CO, USA, 2019.
59. Intergovernmental Panel on Climate Change. *Climate Change 2021: The Physical Science Basis Contribution of Working Group I to the Sixth Assessment Report of the Intergovernmental Panel on Climate Change*; Cambridge University Press: Cambridge, UK, 2021.
60. Romare, M.; Dahllöf, L. *The Life Cycle Energy Consumption and Greenhouse Gas Emissions from Lithium-Ion Batteries*; IVL Swedish Environmental Research Institute: Stockholm, Sweden, 2017.
61. Ballard. *Fuel Cell Life Cycle Assessment, Burnaby*; Ballard: Burnaby, BC, Canada, 2018.
62. Department for Business, E.; Strategy, I. *Hydrogen Production Costs*; HM Government UK: London, UK, 2021.
63. Enapter. *A Small Carbon Footprint for Big Climate Impact*; Enapter: Saerbeck, Germany, 2022.
64. Reddi, K.; Elgowainy, A.; Rustagi, N.; Gupta, E. Techno-economic analysis of conventional and advanced high-pressure tube trailer configurations for compressed hydrogen gas transportation and refueling. *Int. J. Hydrog. Energy* **2018**, *43*, 4428–4438. [CrossRef]
65. Agostini, A.; Belmonte, N.; Masala, A.; Hu, J.; Rizzi, P.; Fichtner, M.; Moretto, P.; Luetto, C.; Sgroi, M.; Baricco, M. Role of hydrogen tanks in the life cycle assessment of fuel cell-based auxiliary power units. *Appl. Energy* **2018**, *215*, 1–12. [CrossRef]
66. Salameh, T.; Al-Othman, A.; Olabi, A.G.; Issa, S.; Tawalbeh, M.; Alami, A.H. Comparative life cycle assessment for PEMFC stack including fuel storage materials in UAE. In Proceedings of the 2020 Advances in Science and Engineering Technology International Conferences (ASET), Dubai, United Arab Emirates, 4 February–9 April 2020; pp. 1–5. [CrossRef]
67. Deb, K.; Pratap, A.; Agarwal, S.; Meyarivan, T. A fast and elitist multiobjective genetic algorithm: NSGA-II. *IEEE Trans. Evol. Comput.* **2002**, *6*, 182–197. [CrossRef]
68. Blank, J.; Deb, K. Pymoo: Multi-Objective Optimization in Python. *IEEE Access* **2020**, *8*, 89497–89509. [CrossRef]
69. Wang, Z.; Rangaiah, G.P. Application and Analysis of Methods for Selecting an Optimal Solution from the Pareto-Optimal Front obtained by Multiobjective Optimization. *Ind. Eng. Chem. Res.* **2017**, *56*, 560–574. [CrossRef]
70. Intergovernmental Panel on Climate Change. *Climate Change 2014: Synthesis Report*; IPCC Secretariat: Geneva, Switzerland, 2014.
71. Hasan, T.; Emami, K.; Shah, R.; Hassan, N.; Belokoskov, V.; Ly, M. Techno-economic Assessment of a Hydrogen-based Islanded Microgrid in North-east. *Energy Rep.* **2023**, *9*, 3380–3396. [CrossRef]
72. El Hassani, S.; Oueslati, F.; Horma, O.; Santana, D.; Moussaoui, M.A.; Mezrhab, A. Techno-economic feasibility and performance analysis of an islanded hybrid renewable energy system with hydrogen storage in Morocco. *J. Energy Storage* **2023**, *68*, 107853. [CrossRef]
73. Alluraiah, N.C.; Vijayapriya, P. Optimization, Design, and Feasibility Analysis of a Grid-Integrated Hybrid AC/DC Microgrid System for Rural Electrification. *IEEE Access* **2023**, *11*, 67013–67029. [CrossRef]
74. Pai, P.F.; Acakpovi, A.; Adjei, P.; Nwulu, N.; Asabere, N.Y. Optimal Hybrid Renewable Energy System: A Comparative Study of Wind/Hydrogen/Fuel-Cell and Wind/Battery Storage. *J. Electr. Comput. Eng.* **2020**, *2020*, 1756503. [CrossRef]
75. Temiz, M.; Dincer, I. Development of solar and wind based hydrogen energy systems for sustainable communities. *Energy Convers. Manag.* **2022**, *269*, 116090. [CrossRef]

batteries

MDPI

Article

Battery Degradation Impact on Long-Term Benefits for Hybrid Farms in Overlapping Markets

Pedro Luis Camuñas García-Miguel [1,*], Jaime Alonso-Martinez [1], Santiago Arnaltes Gómez [1,*], Manuel García Plaza [2] and Andrés Peña Asensio [2]

[1] Electrical Engineering Department, Carlos III University of Madrid, Avda. Universidad, 30, 28911 Leganés, Madrid, Spain
[2] Siemens Gamesa Renewable Energy, C. de Ramírez de Arellano, 37, 28043 Madrid, Spain; manuel.garcia.p@siemensgamesa.com (M.G.P.); andres.pena@siemensgamesa.com (A.P.A.)
* Correspondence: pcamunas@pa.uc3m.es (P.L.C.G.-M.); arnalte@ing.uc3m.es (S.A.G.)

Abstract: Participation in the electricity market requires making commitments without knowing the real generation or electricity prices. This is problematic for renewable generators due to their fluctuating output. Battery energy storage systems (BESSs) integrated with renewable sources in a hybrid farm (HF) can alleviate imbalances and increase power system flexibility. However, the impact of battery degradation on long-term profitability must be taken into account when choosing the correct market participation strategy. This study evaluates the state-of-the-art on energy management systems (EMS) for HFs participating in day-ahead and intraday markets, incorporating both BESSs' calendar and cycling degradation. Results suggest that efforts to attain additional profits in intraday markets can be detrimental, especially when the degradation effect is considered in the analysis. A new market participation strategy is proposed that aims to address the limitations of market overlapping and forecasting errors. The results demonstrate that the proposed method can enhance long-term benefits while also reducing battery degradation.

Keywords: BESS; optimization; degradation; markets

Citation: Camuñas García-Miguel, P.L.; Alonso-Martínez, J.; Arnaltes Gómez, S.; García Plaza, M.; Peña Asensio, A. Battery Degradation Impact on Long-Term Benefits for Hybrid Farms in Overlapping Markets. *Batteries* **2023**, *9*, 483. https://doi.org/10.3390/batteries9100483

Academic Editors: Pascal Venet, Luis Hernández-Callejo, Jesús Armando Aguilar Jiménez and Carlos Meza Benavides

Received: 27 July 2023
Revised: 13 September 2023
Accepted: 20 September 2023
Published: 22 September 2023

1. Introduction

Renewable energy systems face uncertainty in resource availability, which can create challenges in participating in electricity markets that require prior commitments. Energy storage systems (ESS) can mitigate this uncertainty by storing energy for later use [1].

The energy commitment for the day-ahead market is made by submitting offers to the market operator the day before delivery. Forecasting techniques are applied to predict electricity prices and resource availability [2], using techniques such as the SARIMA model, which can capture seasonal correlations in historical data. The authors in [3] demonstrate how a SARIMA model can outperform deep-learning techniques. In this work, SARIMA models are used to forecast both electricity prices and wind speeds, and have been shown to outperform deep-learning techniques in previous studies.

An offering strategy for energy commitment is typically formulated as a constrained optimization problem [4]. The decision vector includes offers for each hour of the market, and the objective is to maximize revenue during the session. Constraints include physical parameters of the plant and market rules, which heavily influence the feasible solution space.

Multi-market participation, which includes day-ahead and intraday market sessions, cannot be formulated as a single optimization problem due to the different timeframes of each market. A progressive optimization approach, as proposed by the authors in [5], is used in this work.

Intraday markets can be utilized to increase profits through revenue stacking, which typically involves combining energy and power services. Studies such as [6] demonstrate

that combining frequency response and arbitrage can increase revenue by up to 25%. Similar results are found in studies such as [7], which consider multiple spot market participation. This is also proposed by the authors in [7]. These approaches are compared in this work.

The aforementioned studies do not model the forecast generation and market offering processes. Generated forecasts at different times of the day can contradict each other and lead to issues when various markets overlap. This work addresses this issue.

Balancing mechanisms in electricity markets, such as penalties for deviations, can be used to address deviations caused by forecasting errors. Intraday markets can be used to correct errors [8], but require prior commitments. An alternative solution is to use energy storage systems for real-time corrections through a service called capacity firming (CF) [9].

Capacity firming has received increasing attention in recent literature as a service provided in real-time as opposed to arbitrage. Studies such as [10] propose energy conservation methods for control schemes of BESSs integrated with a PV system. Other works, such as [11], show how a simple control algorithm can achieve capacity firming in a BESS combined with a wind farm, although the storage system is only used for this service.

The Iberian electricity markets are used as an example in this work since, like many other systems, they have day-ahead and intraday spot markets. Market operator rules are incorporated into the optimization algorithm and the calculation of net benefits. Participation in intraday markets and the use of the CF service are compared, and the revenue stacking of different services is evaluated. This work also considers the effect of degradation on long-term profits, an approach that has not been considered in the previous literature.

A HF model consisting of a Gamesa G128 Wind Turbine Generator (WTG) and a BESS is presented. Unlike a virtual power plant (VPP), the system components are not distributed; thus, they share a point of common coupling (PCC). The SARIMA forecasting model uses wind historical data from the Sotavento experimental wind farm [12] and electricity prices from the Iberian market as inputs for the EMS.

The results show that participating in all markets may be counter-productive due to market overlap. The best results in terms of profits per degradation are obtained by allowing the BESS to participate only in the day-ahead market and performing capacity firming in real time.

The work proposes a new service called SOC Emptying (SE), which involves dividing the BESS into two virtual energy storage systems (VESS). One VESS provides regular services, while the other is used to empty the BESS whenever the combined state of charge (SOC) exceeds a specific threshold. This service aims to reduce upward deviations and give the BESS more maneuverability. The inclusion of this service further improves the results, resulting in increased profits per percentage of capacity loss and higher net present values when extrapolating the results for the entire project.

The contributions of this work are outlined as follows:

- A formulation for a progressive optimization algorithm for hybrid farm multi-market participation that takes into account degradation effects caused by operation.
- The implementation of a real-time BESS degradation model that assesses capacity and power losses in a simulation framework to evaluate different market participation strategies.
- Evidence shows that using the BESS in all markets does not necessarily result in a better income after comparing different simulation scenarios.
- A proposed service that enhances the BESS utilization efficiency and increases the project's net present value (NPV).

The paper is structured as follows: Section 2 provides an overview of the Iberian electricity market rules. Section 3 describes the HF model used in the study. The day-ahead and intraday market offering optimization models are analyzed in Section 4. Section 5 presents the simulation use cases and results. Conclusions and future research directions are discussed in Section 6.

2. Iberian Market's Rules

Before each market session opening time, the EMS must have forecasted data of prices and wind power generation. It is therefore necessary to know when each market session takes place and which hourly delivery periods are negotiated, both for forecasting and optimization problem definition. To obtain real benefits, this study follows the regulations of the Iberian markets, which take into account deviation costs.

This section introduces the rules of the Iberian markets, starting with the day-ahead market, followed by the intraday markets, and finally, the deviation rules are described, which consider four different deviation costs.

2.1. Day-Ahead Market

The majority of energy traded in the Iberian wholesale markets is conducted through the day-ahead market. In 2020, it accounted for 74% of the total energy traded [13]. Therefore, it is the most important market for arbitrage operations. The Iberian day-ahead market session takes place every day of the year at 12:00 CET.

The price and volume of energy is determined for each hour of the following day by the intersection of demand and supply. Market agents submit their offers through the market operator OMIE [14]. As a result, the EMS has to submit 24-hourly offers for the following day, using price and generation forecasts generated 12 to 36 hours prior to delivery time.

2.2. Intraday Markets

After the day-ahead market, intraday markets accounted for 14% of the energy traded in 2020 [13]. Since intraday spot markets had six times more energy than continuous intraday markets, this work only considers the former. In Table 1, the closing times and delivery hours of the market sessions are shown.

Table 1. Intraday market sessions in 2018.

Session	1	2	3	4	5	6
Closing time	18:50	21:50	1:50	4:50	8:50	12:50
Delivery hours	22(D-1)–23	0–23	4–23	7–23	11–23	15–23

The closing times in Table 1 are the deadlines for submitting offers to the market operator. Decisions must be made before this time. The delivery hours in the table are the hours during which the energy negotiated in each intraday market session will be delivered on day D.

Since Sessions 1 and 2 cover the same hours, Session 1 is neglected as Session 2 has a closer opening time to the delivery. Intraday markets allow agents to correct their schedules in the day-ahead market. This can be performed by purchasing energy during hours when a deviation from the day-ahead program is expected. Arbitrage can also be performed to gain additional liquidity. Both options are considered in the simulation cases.

2.3. Adjustment Mechanism

Four different deviation costs need to be considered in the Iberian market:

- Positive deviation costs for upward deviations that have a negative impact on the system;
- Positive deviation costs for upward deviations that have a positive impact on the system;
- Negative deviation costs for downward deviations that have a negative impact on the system;
- Negative deviation costs for downward deviations that have a positive impact on the system.

A deviation during an hourly period h is calculated as follows:

$$\lambda(h) = |E_d(h) - E_c(h)|, \quad (1)$$

where the following apply:

- $\lambda(h)$: Deviation during hour h (MWh).
- $E_d(h)$: Delivery during hour h (MWh).
- $E_c(h)$: Commitment during hour h (MWh).

If the deviation is upwards and in favor of the system, the additional energy is remunerated at the day-ahead price during hour h; therefore, the bonus is calculated as:

$$\beta(h) = \lambda(h) * \Pi_{dM}(h), \tag{2}$$

where the following apply:

- $\beta(h)$: Bonus obtained during hour h (EUR).
- $\Pi_{dM}(h)$: Day-ahead price during hour h (EUR/MWh).

If the deviation is upwards and against the system, the energy excess is remunerated at less than the day-ahead price during hour h. This bonus is calculated as:

$$\beta(h) = \lambda(h) * \Pi_{dM}(h) * (1 - \lambda_{coef}(h)), \tag{3}$$

where the following applies:

- $\lambda_{coef}(h)$: Coefficient for deviations against the system during hour h.

If the deviation is downwards and in favor of the system, the energy deficit is charged at the same price as the day-ahead price during hour h; therefore, the penalty is calculated as:

$$\rho(h) = \lambda(h) * \Pi_{dM}(h), \tag{4}$$

where the following applies:

- $\rho(h)$: Penalty during hour h (EUR).

If the deviation is downwards and against the system, the energy deficit is charged at a rate surpassing the day-ahead price during hour h; therefore, the penalty is calculated as:

$$\rho(h) = \lambda(h) * \Pi_{dM}(h) * (1 + \lambda_{coef}(h)). \tag{5}$$

The total deviation cost is formulated as follows. As can be seen, it can be negative when more energy is available than committed:

$$\lambda_{cost}(h) = \rho(h) - \beta(h) \tag{6}$$

where the following applies:

- $\lambda_{cost}(h)$: Deviation costs during hour h (EUR).

The coefficient $\lambda_{coef}(h)$ represents the system's vulnerability to deviations against it. A higher coefficient means that a higher penalty will be paid. As seen in (3), if the coefficient is greater than 1, the bonus for upward deviations can be negative, which implies a penalty. During the same hourly period, if downward deviations are against the system, upward deviations are in favor of the system, and vice versa. The deviation coefficient is determined by the system operator and is the same for both types of deviations.

3. Hybrid Plant Model Overview

The model consists of the physical systems and their control architecture. In this section, the model inputs' generation is described for both wind speed and market prices. Afterwards, the plant model and its control architecture are introduced. Lastly, the daily earning calculation is formulated.

3.1. Model Inputs

3.1.1. Wind Power

Wind power is obtained through a two-stage approach, as in [15]. First, hourly wind speed is forecasted using a SARIMA; then, forecasted data are fed into a function that expresses a Gamesa G128 wind turbine power curve. The optimization and energy

management system (EMS) models directly receive the forecasted and real wind power hourly values.

Wind speed historical data are obtained from Sotavento experimental park in Galicia, Spain [12]. This source was chosen due to its publicly available data and its location within the Iberian market region. The data have a resolution of one hour, and the measured wind speed for the year 2018 is presented in Figure 1.

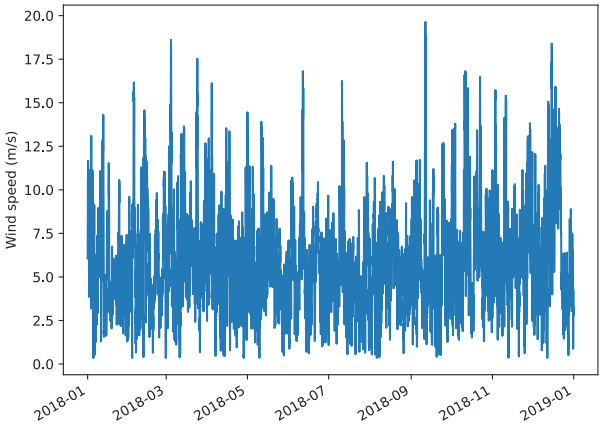

Figure 1. Hourly wind speed historical data for the year 2018.

Hourly wind speed forecasts are required during the opening hours of market sessions. The first forecast is at 12:00 h, when the day-ahead market commences, and subsequent forecasts are generated during the opening hours of intraday market sessions. For real-time operations, actual measured wind speed data are utilized. The SARIMA model utilized in this work has an order of $(2,0,3)(2,1,3)_{12}$, obtained from [16]. The configuration process for the model is not covered in this work. Figure 2 illustrates the 2018 average mean absolute percentage error (MAPE) of the wind speed forecasts generated during different market sessions. It is observed that the prediction error tends to decrease.

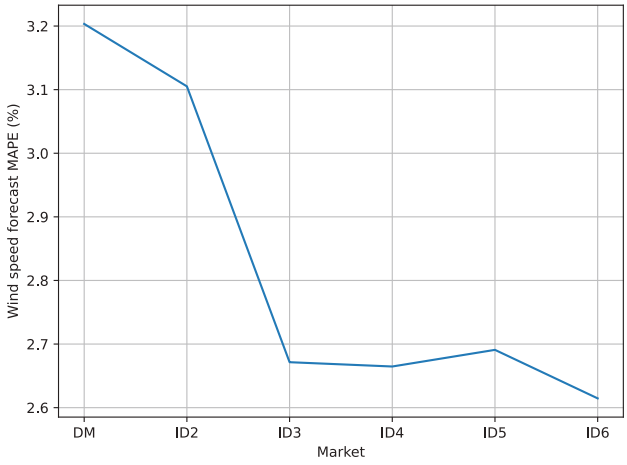

Figure 2. Average MAPE of each wind speed forecast for 2018.

3.1.2. Electricity Price Forecasts

The 24-hourly prices for the next day are predicted at 12:00 h on the previous day. A SARIMA model of order $(2,1,3)(1,0,1)_{24}$ was obtained from [16]. In Figure 3, the predicted and real day-ahead prices for April the 16th are shown. Intraday prices are considered as known beforehand for simplicity.

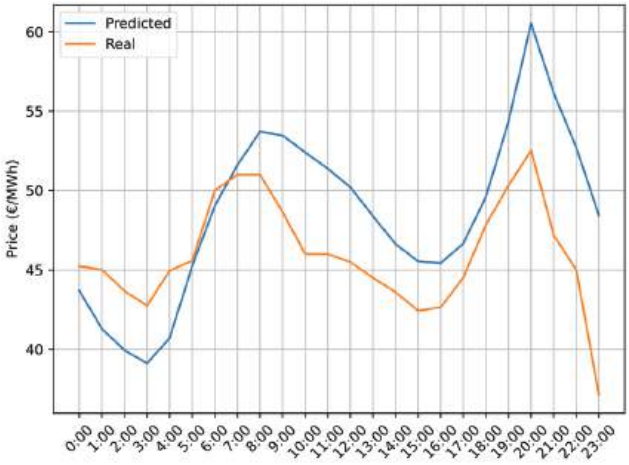

Figure 3. Day-ahead market price forecast for April the 16th.

3.1.3. Deviation Prices

The hourly deviation coefficients derived from 2018 historical data are used to calculate the final deviation costs. However, a deviation coefficient is required for the optimization model of intraday market offerings. Since deviation coefficients are only known after the delivery period has ended, a forecasting technique for predicting the direction (favorable or unfavorable) of deviation is required, but it is outside the scope of this paper. Therefore, a deviation coefficient of 21%, the average of 2017, is considered when participating in the intraday market.

3.2. Plant Model Components

The HF model consists of a wind turbine generator and a BESS.

3.2.1. Wind Turbine Generator

The generation system is a single Gamesa G128 WTG with a nominal power of 4.5 MW. The power curve is taken from [17]. Only a WTG is considered for convenience. Generator converter efficiency is considered part of the power curve characteristic.

3.2.2. Battery Energy Storage System

The storage system is composed of a 10 MWh/2.5 MW lithium iron phosphate (LFP) battery, whose round-trip efficiency is assumed to be constant at 90%, as in [18]. A cycling degradation model, based on depth of discharge (DOD) is implemented, sourced from a finalization of the degradation curve presented in [19]. The model calculates degradation by using rainflow counting of the cycles performed during the day and determines the State of Health (SOH) lost based on the DOD of these cycles, in accordance with the curve shown in Figure 4.

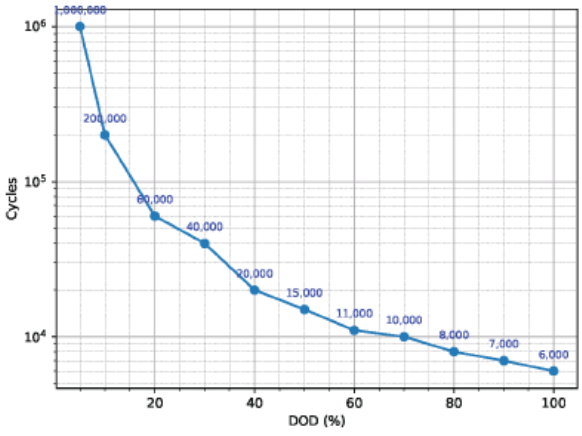

Figure 4. Cycling degradation model.

A calendar degradation model, sourced from [20], is incorporated into the plant model. This model is based on tests conducted on different LFP batteries over 899 days, where they were maintained at various SOCs and temperatures. The test results for 25 °C were selected and are presented in Table 2.

Table 2. Calendar degradation results at 25 °C [20].

SOC (%)	Capacity Lost (%)
0	0.002
50	0.0055
100	0.012

As depicted in Table 2, daily calendar degradation can be represented as a linear function of SOC. Since it is also considered linear with respect to time, the following expression has been obtained from the table:

$$Deg_{cal}(h) = SOC(h) \times \frac{1.2 \times 10^{-4}}{24} \tag{7}$$

where the following apply:

- $Deg_{cal}(h)$: Calendar degradation during hour h (%).
- SOC(h): SOC at the end of hour h (%)

3.3. Control Architecture

The EMS operates on three levels. The tertiary level operates in advance, and is responsible for formulating strategies for offerings in various energy markets. It receives as inputs the predicted prices, generation, and the real-time SOC for the intraday market and SE optimization models, which are executed at this control level. It then sends market commitments to the secondary level.

The secondary control level operates in real-time and generates the setpoints for the BESS based on the difference between generation and commitments generated on the third level. The BESS setpoints are calculated as follows:

$$P_{ESS}(h) = P_{Com}(h) - P_{Gen}(h), \tag{8}$$

where the following apply:

- $P_{ESS}(h)$: BESS setpoint during hour h (MW).
- $P_{Gen}(h)$: Generation during hour h (MW).

- $P_{Com}(h)$: Commitment during hour h (MW).

As shown, when an upward deviation is anticipated, the BESS will receive a setpoint to charge the excess. Conversely, when a downward deviation is expected, a discharging setpoint is generated.

The primary control level manages the energy storage system; it receives charge–discharge setpoints from the secondary level and adjusts them based on the real-time SOC. If the BESS does not have enough energy to cover the missing energy, a downward deviation will occur during that hour. If the BESS is unable to store the excess energy, then an upward deviation will occur.

A sketch of the EMS control architecture is illustrated in Figure 5.

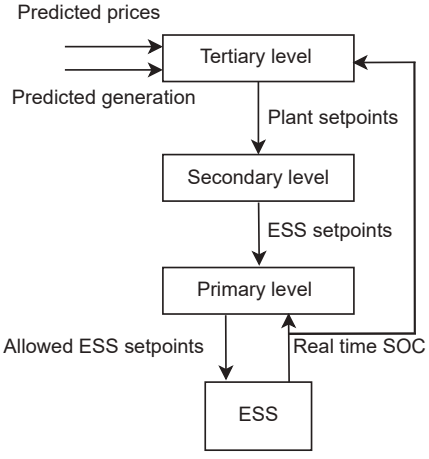

Figure 5. EMS control levels.

3.4. Daily Profits Calculation

The daily profits are calculated as the sum of the hourly profits. In Equation (9), the calculation of daily earnings is depicted. The daily losses are formulated as in Equation (10).

$$Earnings = \sum_{h=1}^{24} \left(E_{DM,C}(h) \cdot \Pi_{DM}(h) + E_{ID,C}(h) \cdot \Pi_{ID}(h) \right). \quad (9)$$

$$Losses = \sum_{h=1}^{24} \left(P_{\varphi}(h) \cdot \Pi_{ID}(h) + \lambda_{cost}(h) \right). \quad (10)$$

where the following apply:

- *Earnings*: Daily earnings (EUR).
- $E_{DM,C}(h)$: Energy commitment in day-ahead market during hour h (MWh).
- $\Pi_{DM}(h)$: Day ahead market real price during hour h (EUR/MWh).
- $E_{ID,C}(h)$: Energy commitment in intraday markets during hour h (MWh).
- $\Pi_{ID}(h)$: Intraday market real price during hour h (EUR/MWh).
- *Losses*: Daily losses (EUR).
- $P_{\varphi}(h)$: Power purchased in intraday market during hour h (MW).

Downward deviations can be corrected in intraday markets in two ways:

- By purchasing the expected energy deficit in the intraday market ($P_{\varphi}(h)$).
- By using stored energy to cover the imbalance.

The optimization algorithm chooses how to correct expected deviations depending on the intraday market prices and deviation costs at each hour.

4. Optimization Problems for Market Participation

In this work, market scheduling strategies are formulated as mathematical optimization problems. The progressive optimization approach, similar to the one described in [5], is employed. The day-ahead market scheduling problem is first solved to generate an hourly power schedule vector P_{Sch}. This vector is updated and sent to the secondary control level in real-time throughout the day. The process is illustrated in Figure 6.

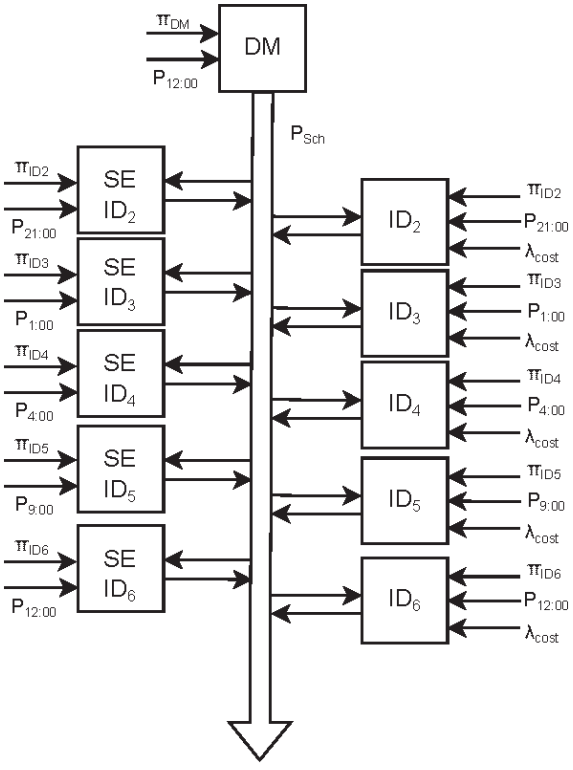

Figure 6. Daily optimization process.

This section presents the formulation of the optimization problems. The day-ahead market offering is explained first, followed by the intraday market offering, and finally the proposed SE service optimization is described as a separate problem.

4.1. Day-Ahead Market Offering

The inputs for the day-ahead market offering include the price and power generation forecasts for the next day generated at 12:00 PM and the plant assets' parameters. The optimization problem is subject to the following constraints:

1. The charge power cannot be higher than the nominal value:

$$P_{ch}(h) \leq P_{nom,BESS} \cdot \phi_d(h), \tag{11}$$

where the following apply:

- $P_{ch}(h)$: Charging power during hour h (MW).
- P_{nom}: Nominal power (MW).
- $\phi_d(h)$: A binary variable that equals 1 when the battery is not discharging during hour h.

2. The discharge power cannot be higher than the nominal value:

$$P_{dis}(h) \leq P_{nom,ESS} \cdot \phi_c(h), \tag{12}$$

where the following apply:

- $P_{dis}(h)$: Discharging power during hour h (MW).
- P_{nom}: Nominal power (MW)
- $\phi_c(h)$: A binary variable that equals 1 when the battery is not charging during hour h.

3. The charging power is always positive:

$$P_{ch}(h) \geq 0. \tag{13}$$

4. For optimization algorithm simplicity, the discharge power is also always positive:

$$P_{dis}(h) \geq 0. \tag{14}$$

5. The simultaneous charge and discharge is not possible:

$$\phi_c(h) + \phi_d(h) \leq 1. \tag{15}$$

6. The energy stored at the end of each period is calculated as follows:

$$E(h) = E(h-1) + \left(P_{ch}(h) \cdot \xi - \frac{P_{dis}(h)}{\xi}\right), \tag{16}$$

where the following apply:

- E(h): Energy stored in the battery at the end of hour h (MWh).
- ξ: Efficiency (%)
- E(h − 1): Energy stored on the battery at the beginning of hour h, which is considered to be 0 at the first hour.

7. The stored energy cannot have a negative value:

$$E(h) \geq 0. \tag{17}$$

8. The BESS cannot discharge if its participation in the day-ahead market is disabled; this constraint is activated depending on the case of study:

$$P_{dis}(h) = 0. \tag{18}$$

9. The power flow of the plant is defined as follows:

$$P_{gen}(h) = P_s(h) + P_{ch}(h), \tag{19}$$

where the following apply:

- $P_{gen}(h)$: Total generation power during hour h (MW).
- $P_s(h)$: Generation power sent directly to the grid during hour h (MW).
- $P_{ch}(h)$: Generation power sent to the storage system during hour h (MW).

The following objective function seeks to maximize the income:

$$Max\left\{\sum_{h=1}^{24} \Pi_{DM}(h) \cdot \left(P_s(h) + P_{dis}(h)\right)\right\}. \tag{20}$$

The objective of this function is to maximize profits through the generation of the optimal schedule based on forecasted energy and prices. Deviations are not accounted for in this optimization problem and are addressed in the intraday market optimization. The output of this offering strategy is the hourly schedules for the following day, which serve as input for the next optimization problems.

As it can be seen, the BESS does not purchase energy from the market. As per the regulations of the Renewable Energy Economic Regime [21], a BESS is not allowed to purchase energy from electricity markets when operating in hybrid plants.

4.2. Intraday Market Participation

The intraday market participation aims to adjust the hourly schedule in the case of expected deviations. It does so through two means: selling expected excess energy if enabled and purchasing energy in case of expected downward deviation. The optimization function takes the following inputs: committed hourly schedules, generated power prediction, deviation costs, intraday market prices, and the expected state of charge at the beginning of delivery.

Each intraday market session occurs three hours before delivery, as shown in Table 1. The expected SOC at the start of delivery is communicated by the tertiary control level. The constraints for this optimization are the same as those for the day-ahead market scheduling problem, with the addition of the following constraints:

1. The upward deviations are

$$\lambda_{\uparrow}(h) = P_{PCC}(h) - P_{sch}(h), \tag{21}$$

where the following apply:

- $\lambda_{\uparrow}(h)$: Upward deviation during hour h (MW).
- $P_{PCC}(h)$: PCC power during hour h (MW).
- $P_{sch}(h)$: Scheduled power during hour h (MW).

2. The downward deviations are

$$\lambda_{\downarrow}(h) = P_{sch}(h) - P_{PCC}(h), \tag{22}$$

where the following applies:

- $\lambda_{\downarrow}(h)$: Downward deviation during hour h (MW).

3. The downward deviations are considered always positive, for simplicity purposes:

$$\lambda_{\downarrow}(h) \geq 0. \tag{23}$$

4. The same happens with upward deviations:

$$\lambda_{\uparrow}(h) \geq 0. \tag{24}$$

As can be seen, when one type of deviation takes place, the other is equal to zero.

5. The hourly deviation costs are

$$\lambda_{cost}(h) = \lambda_{\downarrow}(h) \cdot \rho(h) - \lambda_{\uparrow}(h) \cdot \beta(h), \tag{25}$$

The deviation penalty and bonuses are calculated from expressions (3) to (5). The intraday optimization uses real day-ahead market prices, available at the time of the intraday market. The deviation coefficient is set at 21% and the average is from 2017, and it is used only as an assumption at this stage, while historical deviation coefficients are used later to calculate real benefits.

6. The internal power flow constraint depicted in (19) is modified:

$$P_{gen}(h) = P_s(h) + P_{ch}(h) + P_{del}(h) + P_{curt}(h), \tag{26}$$

where the following apply:

- $P_{del}(h)$: Generated power used to cover deviations during hour h (MW).
- $P_{cur}(h)$: Generation power curtailed during hour h (MW).

The generated power is allocated to either cover expected deviations or to maximize profits in the intraday market.

7. The constraint regulating stored energy is a modification of (16) as follows:

$$E(h) = E(t-1) + \left(P_{ch}(h) \cdot \xi - \frac{P_{dis}(h) + P_{dis,s}(h)}{\xi}\right), \tag{27}$$

where the following applies:

- $P_{dis,s}(h)$: BESS power sold during hour h (MW).

This division of discharged power into two parts—one used to cover deviations and one used for arbitrage—is similar to the division of generated power.

8. If arbitrage in the intraday market is disabled, the following constraints are applied:

$$P_{dis,s}(h) = 0. \tag{28}$$

$$P_s(h) = 0. \tag{29}$$

9. The PCC output power is computed as follows:

$$P_{PCC}(h) = P_{del}(h) + P_{dis}(h) + P_{\varphi}(h), \tag{30}$$

The intraday market purchased power is not physically received by the plant and serves to fulfill commitments in the day-ahead market in case of deviations. It is therefore not included in the PCC output power constraint, which measures expected deviations. The exchanged power is part of the scheduled power vector input for the subsequent intraday market optimization, as shown in the constraints represented by expressions (21) and (22).

The objective function is defined in (31) with two goals: minimizing expected deviations and maximizing profits through energy trading.

$$Max\left\{\sum_{h=1}^{ID_{len}} \Pi_{ID}(h) \cdot \left(P_s(h) + P_{dis,s}(h) - P_{\varphi}(h)\right) - \lambda_{cost}(h)\right\}, \tag{31}$$

where the following applies:

- ID_{len}: Intraday market length.

The hourly commitment vector is updated using the outputs of the intraday market optimization problem:

$$P_{Sch,new}(h) = P_{Sch,prev}(h) - P_{\varphi}(h) + (P_s(h) + P_{dis,s}(h)) \tag{32}$$

where the following apply:

- $P_{Sch,new}(h)$: New hourly schedule (MW).
- $P_{Sch,prev}(h)$: Previous hourly schedule (MW).

4.3. State of Charge Emptying

As previously discussed, the secondary control level sends generated energy to the grid when the BESS is full and hourly commitments are fulfilled, leading to an upward deviation. The market operator only pays for excess energy at the day-ahead market price when the deviation is in favor of the system, as described in Equations (2) and (3). This can result in a missed opportunity to sell energy at higher prices when the deviation is against the system.

Moreover, the highest calendar degradation occurs when the BESS is full, as shown in Table 2. A new operating mode is proposed that involves selling part of the stored energy on the nearest intraday market when the BESS SOC exceeds a set threshold. This service differs from intraday market arbitrage in the following ways:

- It operates simultaneously with the intraday market optimization process.
- It only manages energy above a certain threshold, not the entire BESS.
- It is limited to offering energy only in the first hours of each intraday market, to prevent overlap with the next one.

In Figure 7, the operating hours of the proposed service are shown, marked in blue, over the delivery hours of the intraday market, which are represented as white bars.

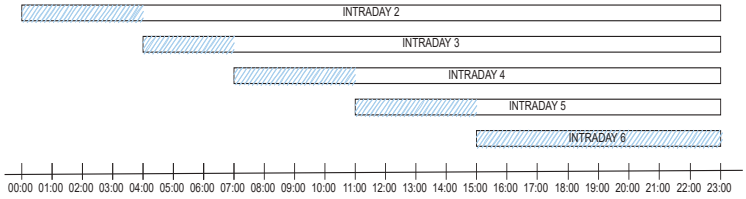

Figure 7. SE service operating hours.

This service splits the BESS into two virtual energy storage systems (VESS), one for profit generation and the other for deviation reduction. The stored energy is divided with a threshold of 75% set for the SE service. This value was determined through testing various values in the study and was found to be the optimal balance between profits and deviation reduction.

$$SOC_i = SOC_{SE} - SOC_{thr}, \tag{33}$$

where the following apply:

- SOC_{SE}: SOC used for SE service (%).
- SOC_{thr}: SOC threshold (%).

The SE service is managed as an optimization problem identical to the one for intraday market participation but limited to the first hours of the next intraday market. The variables used for deviation coverage are disabled as the objective of this service is solely profit generation. The objective function is as follows:

$$Max\left\{\sum_{h=1}^{SE_{len}} \Pi_{ID} \cdot P_{SE}(h)\right)\right\}, \tag{34}$$

where the following apply:

- SE_{len}: SE length for the next intraday market .
- $P_{SE}(h)$: Power sold during hour h (MW).

The goal is to sell available energy at the most expensive hours. The scheduled power vector is updated as in (32).

$$P_{Sch,new}(h) = P_{Sch,prev}(h) + P_{SE}(h) \tag{35}$$

5. Simulations and Results

In this section, the simulation scenarios are presented, each showcasing a different approach to using the BESS on the HF. Each scenario involves simulating the HF with the respective approach operating during 2018 in the Iberian electricity markets. The aim is to compare and assess whether revenue-stacking is more efficient than focusing on individual services, and the performance of the proposed service.

At the end of each day, the accumulated degradation and SOC serve as initial values for the following day's operation. The average daily profits and degradation under each scenario are used in a full project extrapolation for a comprehensive view of the different cases.

5.1. Simulation Cases

The simulation cases used are the following:

- Ideal: Perfect foresight of prices and power generation, which operates only in the day-ahead market.
- DM: Energy sales in the day-ahead and intraday markets to cover deviations.
- DM + SE: Same as DM, but with additional SOC emptying service.

- DM + ID: Energy sales in day-ahead market and intraday markets to sell excess and cover deviations.
- ID: Only participates in intraday markets for energy sales and covering deviations.
- SE: Only participates in intraday markets to cover deviations and performs SE service.
- CF: No market participation; covers deviations through capacity firming services (already provided in previous cases).

5.2. Simulation Results

The simulation was conducted using the same input data in each case. Expected profits were calculated by summing the earnings from day-ahead and intraday market commitments and real prices. Real profits were calculated as the difference between daily earnings (Equation (9)) and daily losses (Equation (10)) using historical data of electricity prices and deviation coefficients. Figure 8 displays the accumulated profits and costs for each scenario, and Table 3 shows the numerical results.

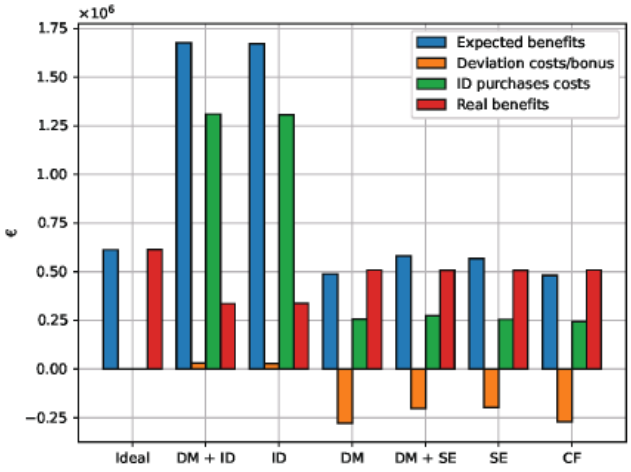

Figure 8. Simulations results.

Table 3. Numerical results.

Case	Expected Profits (EUR M)	Deviation Costs (EUR M)	Purchases Costs (EUR M)	Real Profits (EUR M)
Ideal	0.614	0	0	0.614
DM + ID	1.677	0.031	1.309	0.336
ID	1.671	0.029	1.305	0.338
DM	0.488	−0.277	0.256	0.509
DM + SE	0.581	−0.201	0.276	0.507
SE	0.568	−0.195	0.255	0.508
CF	0.482	−0.27	0.244	0.509

The results indicate that expected profits increase with intraday market arbitrage, as anticipated. These profits are calculated based on the delivery of all committed energy to the market, resulting in higher profits in scenarios with intraday market participation as all expected energy excess can be sold. The worst expected outcomes occur in scenarios without intraday market participation, and similar results are observed when the BESS performs capacity firming.

The deviation costs are negative in almost all scenarios, indicating when upward deviations are more frequent. Purchasing energy in the intraday market effectively avoids

downward deviations. The fewer services the BESS provides, the greater the negative deviation costs, suggesting that the BESS tends to be fully charged most of the time, leading to upward deviations.

Purchases in the intraday market are the primary cause of profitability losses. These costs are significantly higher with intraday market participation. The fact that intraday market purchases occur when the BESS cannot cover expected deviations highlights that increased BESS involvement in markets can have negative effects.

Committing more energy to various markets increases the risk of having to make corrections by purchasing energy in the intraday market. The best results seem to be achieved by letting the BESS operate solely in the day-ahead market or providing capacity firming services. As shown in Figure 9, intraday market participation has resulted in the need to cover up to 40% of committed energy through intraday market purchases.

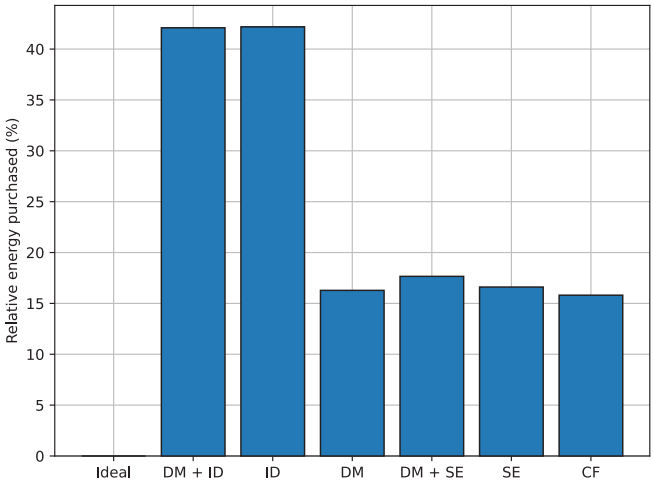

Figure 9. Committed energy covered with purchases in intraday markets.

Figure 10 displays the accumulated degradation. In scenarios where the BESS provides the most services, it tends to be emptier, which reduces calendar degradation and results in lower overall aging of the BESS.

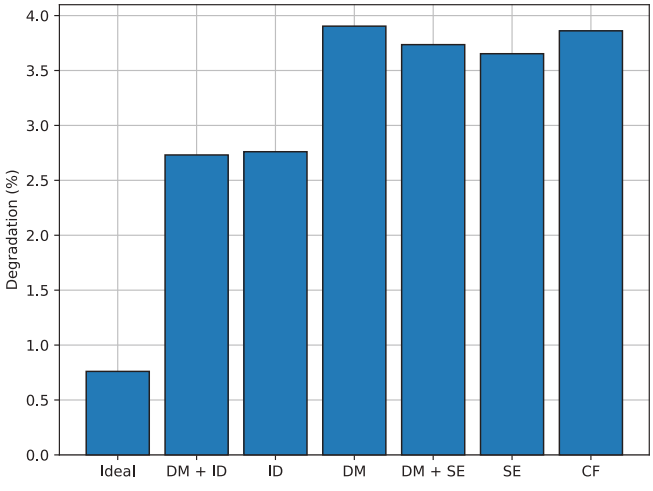

Figure 10. Degradation in each case.

Figure 11 shows the comparison between real profits and degradation. It reveals that reserving the BESS for SOC emptying and capacity firming yields the best outcome when profits are compared to capacity loss, which indicates a more efficient usage of the BESS.

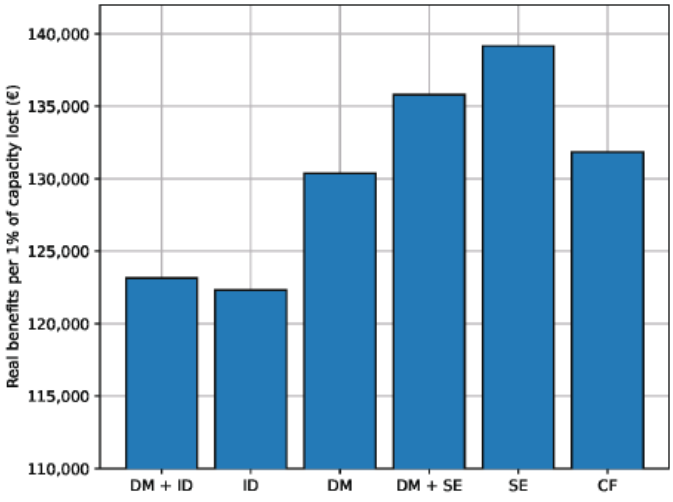

Figure 11. Real profits per 1% of capacity lost.

5.3. Full Project Extrapolation Results

The trade-off between maximizing short-term profits and stretching the life of the energy storage system is a crucial factor to consider. The NPV is a useful metric that takes into account future cash flows and discount rates to determine a project's overall profitability.

In the table, the NPV of each case is calculated, discounting the daily cash flow and the purchase cost of the BESS. The results show that the best NPV is achieved when the BESS is reserved for SE and capacity firming. When only participating in the day-ahead market, the NPV is not very different, but participating in the intraday market significantly lowers the NPV, indicating lower project profitability.

The results of each simulation scenario are extrapolated for the entire project life. The average daily cash flow is determined from the average daily results of 2018, and daily degradation is similarly calculated to estimate project completion. The project ends when the accumulated degradation of the BESS reaches 20%, a commonly used value in the relevant literature (e.g., [22,23]). The average values and estimated project lifetimes for each case are presented in Table 4.

Table 4. Project extrapolation under each case.

Case	Average Daily Capacity Loss (%)	Average Daily Profits (EUR)	Lifetime (Years)
Ideal	2.08×10^{-3}	1682.28	26.31
DM + ID	7.48×10^{-3}	921.44	7.32
ID	7.56×10^{-3}	925.11	7.25
DM	1.06×10^{-2}	1394.37	5.12
DM + SE	1.02×10^{-2}	1389.89	5.36
SE	1×10^{-2}	1392.7	5.48
CF	1.05×10^{-2}	1394.74	5.18

It is worth noting that the BESS is not operated in the ideal scenario. In this case, the BESS is only utilized for allocating generated energy when prices are the highest. However, due to the degradation costs and the BESS efficiency, this operation is not profitable.

The SE has lower daily profits but a higher NPV compared to the case with CF. The NPV of each project is calculated using a 7.5% discount rate and is presented in Table 5. The results show that using the BESS for the SE service and capacity firming provides the highest NPV.

Table 5. NPV under each case.

Case	NPV (EUR M)
Ideal	7.226
DM + intraday market	1.912
Intraday market	1.905
DM	2.179
DM + SE	2.253
SE	2.299
CF	2.2

6. Conclusions

A three-level EMS for a HF to participate in the Iberian electricity market has been presented. The day-ahead and intraday market offering strategies are formulated as linear programming problems, with generation and price forecasts at the start of each market session as inputs. The model has incorporated adjustments based on Iberian market regulations to account for committed power correction impacts. It also includes a real-time degradation model of the BESS to assess capacity and power losses.

A simulation framework has been proposed to assess various BESS market participation strategies. The results indicate that participating in both day-ahead and intraday wholesale markets generates the highest expected profits, but actual profits are lower compared to other strategies. The proposed optimization algorithm and results of the study can be applied to any electrical system that operates with concurrent day-ahead and intraday spot markets, which is a common practice in many countries. This can be used as a guide for agents trying to optimize their plants.

The results show that using the BESS in all markets does not necessarily result in a higher income, challenging the common belief that utilizing the BESS in all markets leads to the best outcome. The proposed SE service enables participation in intraday markets without the drawback of market overlap, enhancing the BESS utilization efficiency and increasing the NPV of the project. Moreover, it highlights the crucial role of adjustment mechanisms on actual income and the importance of modeling them thoroughly. Lastly, it is worth remarking that the plant proposed in this work is considered a price-taker; the effect of a plant or a number of plants large enough to impact electricity market prices is proposed as a future work.

Author Contributions: The authors contributed equally to this work. All authors have read and agreed to the published version of the manuscript.

Funding: This research received no external funding.

Data Availability Statement: Data is available by request.

Conflicts of Interest: The authors declare no conflict of interest.

Abbreviations

The following abbreviations are used in this manuscript:

BESS	Battery energy storage system
HyF	Hybrid farm
EMS	Energy management system
DOD	Depth of discharge
SOC	State of charge
SOH	State of Health
NPV	Net present value
EOL	End of life
MILP	Mixed-integer linear program

References

1. Günter, N.; Marinopoulos, A. Energy storage for grid services and applications: Classification, market review, metrics, and methodology for evaluation of deployment cases. *J. Energy Storage* **2016**, *8*, 226–234. [CrossRef]
2. Sweeney, C.; Bessa, R.J.; Browell, J.; Pinson, P. The future of forecasting for renewable energy. *WIREs Energy Environ.* **2020**, *9*, e365. [CrossRef]
3. Liu, X.; Lin, Z.; Feng, Z. Short-term offshore wind speed forecast by seasonal ARIMA—A comparison against GRU and LSTM. *Energy* **2021**, *227*, 120492. [CrossRef]
4. Legrand, M.; Labajo-Hurtado, R.; Rodríguez-Antón, L.M.; Doce, Y. Price arbitrage optimization of a photovoltaic power plant with Liquid Air Energy Storage. implementation to the Spanish case. *Energy* **2022**, *239*, 121957. [CrossRef]
5. Wang, Y.; Zhao, H.; Li, P. Optimal offering and operating strategies for wind-storage system participating in spot electricity markets with progressive stochastic-robust hybrid optimization Model Series. *Math. Probl. Eng.* **2019**, *2019*, 2142050. [CrossRef]
6. Pusceddu, E.; Zakeri, B.; Castagneto Gissey, G. Synergies between energy arbitrage and fast frequency response for battery energy storage systems. *Appl. Energy* **2021**, *283*, 116274. [CrossRef]
7. Englberger, S.; Jossen, A.; Hesse, H. Unlocking the Potential of Battery Storage with the Dynamic Stacking of Multiple Applications. *Cell Rep. Phys. Sci.* **2020**, *1*, 100238. [CrossRef]
8. Shinde, P.; Amelin, M. A Literature Review of Intraday Electricity Markets and Prices. In Proceedings of the 2019 IEEE Milan PowerTech, Milan, Italy, 23–27 June 2019; pp. 1–6. [CrossRef]
9. Pantos, M.; Riaz, S.; Chapman, A.C.; Verbič, G. Capacity firming of intermittent generation by dispersed energy storage. In Proceedings of the 2017 Australasian Universities Power Engineering Conference (AUPEC), Melbourne, VIC, Australia, 19–22 November 2017; pp. 1–6. [CrossRef]
10. Abdelrazek, S.A.; Kamalasadan, S. Integrated PV Capacity Firming and Energy Time Shift Battery Energy Storage Management Using Energy-Oriented Optimization. *IEEE Trans. Ind. Appl.* **2016**, *52*, 2607–2617. [CrossRef]
11. Robles, M.; Kim, J.S.; Song, H. Capacity firming for wind generation using one-step model predictive control and battery energy storage system. *J. Electr. Eng. Technol.* **2017**, *12*, 2043–2050. [CrossRef]
12. Sotavento Experimental Wind Park. Available online: https://www.sotaventogalicia.com/area-tecnica/datos-tiempo-real/instantaneos-parque/ (accessed on 30 May 2022).
13. CNMC . *Informe de Supervisión del Mercado Peninsular Mayorista al Contado de Electricidad*; CNMC: Madrid, Spain, 2020 .
14. Day-Ahead-Market-Operation. Available online: https://www.omie.es/sites/default/files/inline-files/day_ahead_market.pdf. (accessed on 30 May 2022).
15. Zheng, D.; Shi, M.; Wang, Y.; Eseye, A.T.; Zhang, J. Day-Ahead Wind Power Forecasting Using a Two-Stage Hybrid Modeling Approach Based on SCADA and Meteorological Information, and Evaluating the Impact of Input-Data Dependency on Forecasting Accuracy. *Energies* **2017**, *10*, 1988 . [CrossRef]
16. McHugh, C.; Coleman, S.; Kerr, D.; McGlynn, D. Forecasting Day-ahead Electricity Prices with A SARIMAX Model. In Proceedings of the 2019 IEEE Symposium Series on Computational Intelligence (SSCI), Xiamen, China, 6–9 December 2019; pp. 1523–1529. [CrossRef]
17. The Wind Power. Available online: https://www.thewindpower.net/turbines_manufacturers_es.php. (accessed on 30 May 2022).
18. Kim, R.K.; Glick, M.; Olson, K.; Kim, Y.S. MILP-PSO Combined Optimization Algorithm for an Islanded Microgrid Scheduling with Detailed Battery ESS Efficiency Model and Policy Considerations. *Energies* **2020**, *13*, 1898. . [CrossRef]
19. Cheng, S.; Liu, Y.H.; Hesse, H.; Naumann, M.; Truong, C.; Jossen, A. A PSO-Optimized Fuzzy Logic Control-Based Charging Method for Individual Household Battery Storage Systems within a Community. *Energies* **2018**, *11*, 469. [CrossRef]
20. Naumann, M.; Schimpe, M.; Keil, P.; Hesse, H.C.; Jossen, A. Analysis and modeling of calendar aging of a commercial LiFePO4/graphite cell. *J. Energy Storage* **2018**, *17*, 153–169. [CrossRef]
21. BOE-A-2020-13591, 2020. Available online: https://www.boe.es/buscar/doc.php?lang=en&id=BOE-A-2020-13591 (accessed on 14 April 2023).

22. Smith, K.; Saxon, A.; Keyser, M.; Lundstrom, B.; Ziwei Cao.; Roc, A. Life prediction model for grid-connected Li-ion battery energy storage system. In Proceedings of the 2017 American Control Conference (ACC), Seattle, WA, USA, 24–26 May 2017; pp. 4062–4068. [CrossRef]
23. Maheshwari, A.; Paterakis, N.G.; Santarelli, M.; Gibescu, M. Optimizing the operation of energy storage using a non-linear lithium-ion battery degradation model. *Appl. Energy* **2020**, *261*, 114360. [CrossRef]

electronics

MDPI

Article

Research on a High-Precision State-of-Charge Estimation Method Based on Forgetting Factor Recursive Least Squares and Adaptive Extended Kalman Filter Applied to LiFePO4 Battery

Yihui Xia, Zhihao Ye *, Liming Huang, Lucheng Sun and Yunxiang Jiang

School of Electrical Engineering, Naval University of Engineering, Wuhan 430033, China; xiayihui2005@163.com (Y.X.); huangliming1998@163.com (L.H.); d23380807@nue.edu.cn (L.S.); jiangyunxaing@163.com (Y.J.)
* Correspondence: yxyx928@126.com

Abstract: The state-of-charge (SOC) estimation accuracy is closely associated with the estimation method and the battery parameter identification performance. The battery parameter identification method based on forgetting factor recursive least squares (FFRLS) has the advantages of high parameter identification accuracy and fast dynamic response speed. On this basis, the performance of two SOC estimation methods, the extended Kalman filter (EKF) and adaptive extended Kalman filter (AEKF) are compared and studied. The results show that AEKF has better steady-state and dynamic SOC estimation performance, but the estimation accuracy and dynamic response performance are still not objective. To further improve the performance of SOC estimation, a joint SOC estimation method based on FFRLS-AEKF is proposed, and the SOC estimation experimental results with FFRLS-AEKF and AEKF are conducted. The experimental results show that the proposed joint SOC estimation method based on FFRLS-AEKF has a better steady-state and dynamic performance of SOC estimation. The maximum absolute error of the proposed algorithm is 4.97%. As the battery working time increases, the SOC estimation accuracy continues to converge to the true value, and the average absolute error is reduced to 2.5%. The proposed method and theoretical analysis are proven to be correct and feasible.

Keywords: LiFePO4 battery; high precision; FFRLS; AEKF; SOC estimation

Citation: Xia, Y.; Ye, Z.; Huang, L.; Sun, L.; Jiang, Y. Research on a High-Precision State-of-Charge Estimation Method Based on Forgetting Factor Recursive Least Squares and Adaptive Extended Kalman Filter Applied to LiFePO4 Battery. *Electronics* **2023**, *12*, 3670. https://doi.org/10.3390/electronics12173670

Academic Editors: Luis Hernández-Callejo, Jesús Armando Aguilar Jiménez and Carlos Meza Benavides

Received: 2 July 2023
Revised: 3 August 2023
Accepted: 4 August 2023
Published: 31 August 2023

1. Introduction

The LiFePO4 battery has advantages such as good safety, long service life, and high power density, and so on [1,2], which is widely used in electric vehicles and energy storage systems. To prevent battery failures such as overcharging and over-discharging, it is necessary to monitor the battery operating status in real time, especially its state of charge (SOC).

The methods of accurate SOC estimation can generally be categorized into the following types: open-circuit voltage, ampere-hour integral-based estimation method, data-driven-based estimation method, and filtering algorithms based on equivalent circuit models [3–5]. There is a monotonic one-to-one correspondence between the open-circuit voltage and the SOC value of the battery. The corresponding table of open-circuit voltage and SOC can be established, and the SOC value can be determined by looking up the table [6]. However, this method requires a long time after the battery is charged and discharged before measuring the open-circuit voltage. Reference [7] proposed a fast open-circuit voltage prediction method. The battery only needs to be placed within 15 min to accurately predict the open-circuit voltage. However, the calculation process is complex, and the requirements for the processor are high. The ampere-hour integral method tracks the SOC by the change in the current integral value. The measurement error will accumulate in the integral, resulting in a large error of SOC. Reference [8] analyzed the error sources

of the ampere-hour analysis method and proposed a method to reduce the cumulative error of time and the proportional error of the SOC. However, it is more dependent on the current accuracy, and the accuracy of the current sensor is higher.

If the data-driven algorithm is trained properly, it can predict the SOC of any type of battery without knowing its inherent characteristics in advance. Reference [9] proposed a method of predicting SOC via artificial neural network machine learning. The root-mean-squared error (RMSE) of the LiFePO4 battery used in this paper is 0.33% during the test cycle. The author of Reference [10] proposed a recurrent neural network (RNN) with long short-term memory (LSTM) to accurately estimate the SOC of lithium-ion batteries, and it can achieve high accuracy at temperatures from 10 °C to 25 °C. Reference [11] used the support vector machine (SVM) method to estimate the SOC of the battery from the experimental data set, which has high accuracy. In the method of machine learning or deep learning, a data-driven algorithm collects terminal voltage, working current, temperature, and other data in the work of the battery, and it uses neural network and machine learning to train a large amount of data to obtain the current SOC value. This method needs to collect a large amount of data for calculation, which requires a powerful processor and is sensitive to the type of battery. If the internal parameters of the battery change, the data-driven model cannot follow the internal changes well, resulting in a larger SOC estimation error.

The filtering algorithms based on equivalent circuit models mainly use derivative algorithms of Kalman filtering (KF) and particle filtering algorithms for SOC estimation [12–17]. As the most popular model-based method, the KF-based algorithm has enhanced robustness to measurement and process noise and has a high estimation accuracy [18]. Based on the extended Kalman filter (EKF) algorithm, an adaptive dual EKF algorithm is proposed in Ref. [12]; the EKF algorithm is used to improve the nonlinear battery model for SOC estimation in Refs. [17,19] for the LiFePO4 battery. A strong tracking volume EKF algorithm (STEKF) is proposed in Ref. [20] to provide accurate SOC prediction and a faster computing time. A multi-rate strong tracking EKF algorithm (MRSTEKF) is proposed by introducing multi-rate control strategy and enhancement technology in Ref. [21], and the SOC tracking stability and estimation accuracy is improved from 55.34% and 49.51% with STEKF to 52.66% and 33.88% with MRSTEKF, respectively. An online adaptive EKF algorithm based on the Davidson model is used to estimate SOC [22], and the SOC estimation error can be reduced to 2%. The sigma points Kalman filter (SPKF) is another nonlinear system filtering algorithm that can be used to estimate SOC, which uses numerical approximations instead of analytical approximations of EKF. A joint battery model and SOC estimation algorithm based on SPKF is proposed in Ref. [23], which has the same computational complexity as EKF but has higher accuracy. In Ref. [24], a combination of the volumetric Kalman filtering algorithm and the forgetting factor recursive least squares (FFRLS) algorithm is used to estimate SOC, and the maximum estimation error of SOC under high-rate pulses is reduced to be less than 1%. On the other hand, the method of approximating a probability density function based on a particle filter is used to estimate the SOC. In Ref. [25], a volumetric particle filter for accurate SOC estimation is proposed. In Ref. [26], dual-scale, dual-particle, and dual-scale adaptive particle filters for SOC estimation are proposed. However, compared with SOC estimation algorithms based on the Kalman filter, the SOC estimation algorithms based on the particle filter have a larger computational burden [27]. In Ref. [28], an analytical mathematical formulation of storage and its SOC is presented. In Ref. [29], a power allocation strategy based on cluster switching to relieve the stated problem in two levels is proposed, which is used to eliminate the imbalanced SOC and decrease battery energy loss. To address the power allocation challenges, a novel optimized state-of-charge (SOC) feedback-based energy management strategy in Ref. [30] is proposed for HESS in IPS to restrain the DC bus voltage fluctuation in this paper.

In this paper, a FFRLS-AEKF joint estimation algorithm based on time-varying parameter model is proposed, which considers the characteristics that the FFRLS algorithm can update the battery parameters in real time and the AEKF algorithm can correct the initial value error of SOC and follows the parameters of the battery. Firstly, the working principle

of FFRLS for battery parameter identification is analyzed. Secondly, the second-order equivalent circuit state discretization equation based on the AEKF algorithm is established, and the steps of the battery SOC estimation method based on AEKF are discussed. Thirdly, a joint SOC estimation method based on FFRLS-AEKF is proposed. Fourthly, the SOC estimation performance of three methods as EKF, AEKF, and FFRLS-AEKF is compared by experiments. The experimental results show that the FFRLS-AEKF algorithm can have a higher SOC estimation and faster accuracy convergence speed. Finally, the thesis is summarized.

2. The Basic Principle of Parameter Identification Based on the FFRLS

2.1. Mathematical Modeling of a Second-Order RC Circuit

The second-order RC equivalent circuit model of the LiFePO4 battery is shown in Figure 1. The two RC circuits, respectively, describe the electrochemical polarization process with a small time constant and the concentration polarization process with a large time constant. Among them, U_{OC} is the open-circuit voltage of the battery, R_0 is the internal resistance, and R_{p1} and C_{p1} are the electrochemical polarization internal resistance and electrochemical polarization capacitance, respectively. R_{p2} and C_{p2} are the concentration difference polarization internal resistance and concentration difference polarization capacitance, respectively. U_{L} and I_{L} are load voltage and load current, respectively.

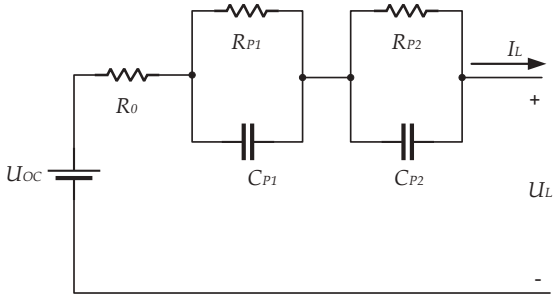

Figure 1. Second-order RC model.

According to Figure 1, the state space equation expression of the second-order RC model circuit can be listed as follows:

$$\begin{gathered}\begin{pmatrix} \frac{dU_{p1}}{dt} \\ \frac{dU_{p2}}{dt} \end{pmatrix} = \begin{pmatrix} -\frac{1}{R_{p1}C_{p1}} & 0 \\ 0 & -\frac{1}{R_{p2}C_{p2}} \end{pmatrix} \begin{pmatrix} U_{p1} \\ U_{p2} \end{pmatrix} + \begin{pmatrix} \frac{1}{C_{p1}} \\ \frac{1}{C_{p2}} \end{pmatrix} I_L \\ U_{OC} = U_{p1} + U_{p2} + R_0 I_L + U_L \end{gathered} \tag{1}$$

where $\frac{dU_{p1}}{dt}$ and $\frac{dU_{p2}}{dt}$ represent the electrochemical polarization voltage and the concentration difference polarization voltage, respectively.

2.2. The Basic Principle of the FFRLS

The traditional recursive least squares (RLS) method is widely used in the field of system identification. For linear systems, its mathematical description can be expressed as follows:

$$\begin{gathered} Y(k) = \varphi(k)\theta(k)^T + e(k) \\ \varphi(k) = [-Y(k-1) \cdots - Y(k-n)\ u(k) \cdots u(k-n)] \end{gathered} \tag{2}$$

where $Y(k)$ is the output signal of the system at k time, $u(k)$ is the input signal of the system at k time, $\theta(k)$ represents the parameter vector to be estimated, $\varphi(k)$ is the input matrix of

the system at time k, n is the parameter to be estimated, and $e(k)$ is the noise of the system. The recursive formula of the FFRLS method is as follows:

$$\begin{array}{l}\hat{\theta}(k+1)=\hat{\theta}(k)+K(k+1)[Y(k+1)-\varphi^T(k+1)\theta(k)]\\ K(k+1)=P(k+1)\varphi(k+1)\\ P(k+1)=P(k)-\frac{P(k)\varphi(k+1)\varphi^T(k+1)}{1+\varphi^T(k+1)P(k)\varphi(k+1)}\end{array} \quad (3)$$

In Equation (3), $P(k)$ is the covariance matrix, and $K(k)$ is the gain matrix. During the recursive process, RLS uses the difference between the estimated value and the measured value of the system output, as well as the gain matrix $K(k)$, to make adjustments to the parameter vector $\hat{\theta}(k)$. During initialization, the initial value of $\hat{\theta}(k)$ and $K(k)$ can be any value, $P(0) = \alpha I$, α is as large as possible a constant, and I is the identity matrix.

To reduce the influence of past data and give greater weight to new data, a forgetting factor is introduced by setting it to $\lambda(0 < \lambda < 1)$, leading to the development of FFRLS [31,32]. Equation (3) is modified as follows:

$$\begin{array}{l}\hat{\theta}(k+1)=\hat{\theta}(k)+K(k+1)[y(k+1)-\varphi^T(k+1)\hat{\theta}(k)]\\ K(k+1)=\frac{P(k)\varphi(k+1)}{\lambda+\varphi^T(k+1)P(k)\varphi(k+1)}\\ P(k+1)=\frac{1}{\lambda}[1-K(k+1)\varphi^T(k+1)]P(k)\end{array} \quad (4)$$

Equation (4) is a recursive formula based on the forgetting factor recursive least squares method, where the forgetting factor λ is generally taken between 0.95 and 1. The larger the value of λ, the smaller the weight of new data. When $\lambda = 1$, it degenerates into the ordinary RLS method.

2.3. Online Identification of Parameters for a Second-Order RC Circuit

From Figure 1, the KVL (Kirchhoff's voltage law) equation of the circuit can be obtained:

$$U_{OC} = U_{p1} + U_{p2} + R_0 I_L + U_L \quad (5)$$

According to Equation (1), taking the Laplace transform on both sides:

$$U_{OC}(s) = (\frac{R_{p1}}{R_{p1}C_{p1}s+1} + \frac{R_{p2}}{R_{p2}C_{p2}s+1} + R_0)I(s) + U_L(s) \quad (6)$$

Let the time constants be $\tau_{p1} = R_{p1}C_{p1}$ and $\tau_{p2} = R_{p2}C_{p2}$, and let $a = \tau_{p1}\tau_{p2}$, $b = \tau_{p1} + \tau_{p2}$, $c = R_{p1} + R_{p2} + R_0$; then, Equation (6) can be simplified as:

$$aU_{OC}s^2 + bU_{OC}s + U_{OC} = aR_0I_s^2 + dI_s + cI + aU_s^2 + U_L \quad (7)$$

Equation (8) can be obtained via discretion using Equation (7) as follows:

$$U(k) = \frac{-bT-2a}{T^2+bT+a}U(k-1) + \frac{a}{T^2+bT+a}U(k-2) + \frac{cT^2+dT+aR_0}{T^2+bT+a}I(k) + \frac{-dT-2aR_0}{T^2+bT+a}I(k-1) + \frac{aR_0}{T^2+bT+a}I \quad (8)$$

After simplification, the expression (8) becomes:

$$U(k) = k_1U(k-1) + k_2U(k-2) + k_3I(k) + k_4I(k-1) + k_5I(k-2) \quad (9)$$

Substituting Equation (9) into FFRLS, the value of parameter $\theta(k) = (k_1, k_2, k_3, k_4, k_5)$ can be calculated, and then the circuit model parameter R_0, R_{p1}, R_{p2}, C_{p1}, C_{p2} from the identification results can be deduced as follows:

$$\begin{array}{l}\tau_{p1}=\frac{T}{2(k_1+k_2+1)}[\sqrt{k_1^2-4k_2}-k_1-2k_2]\\ \tau_{p2}=-\frac{T}{2(k_1+k_2+1)}[\sqrt{k_1^2-4k_2}+k_1+2k_2]\end{array} \quad (10)$$

Combining Equations (4), (8) and (10), Equation (11) can be obtained as follows:

$$\begin{array}{l} R_0 = \frac{k_5}{k_2} \\ R_{p1} = \frac{\tau_{p1}\frac{k_3+k_4+k_5}{k_1+k_2+1}+\tau_{p2}R_0+\frac{T(k_4+2k_5)}{k_1+k_2+1}}{\tau_{p1}-\tau_{p2}} \\ R_{p2} = \frac{k_3+k_4+k_5}{k_1+k_2+1} - R_{p1} - R_0 \\ C_{p1} = \frac{\tau_{p1}}{R_{p1}} \\ C_{p2} = \frac{\tau_{p2}}{R_{p2}} \end{array} \tag{11}$$

3. SOC Estimation Method Based on AEKF

3.1. Adaptive Extended Kalman Filter State Equation

The Kalman filter algorithm applies to linear systems. If it is used in a nonlinear system, the Taylor expansion formula needs to be used to locally approximate the nonlinear state equation as a linear equation. The method used for nonlinear systems is called the extended Kalman filter algorithm. Nonlinear systems can be represented by Formula (12):

$$\begin{cases} x_{k+1} = f(x_k, u_k) + w_k \\ y_k = g(x_k, u_k) + v_k \end{cases} \tag{12}$$

where x_k is the state variable, y_k is the observation variable, $f(x_k, u_k)$ is the nonlinear state function, $g(x_k, u_k)$ is the nonlinear observation function, and w_k and v_k are gaussian white noise with zero means and covariances of Q_k and R_k, respectively. The EKF algorithm takes advantage of the local linearity property of nonlinear functions by locally linearizing both nonlinear functions. As described in the previous section, $\hat{x}_{k/k}$ this is the optimal estimated value of the state variable at k time. By performing a first-order Taylor expansion of the nonlinear state function $f(x_k, u_k)$ around $\hat{x}_{k/k}$, Equation (13) can be obtained as follows:

$$f(x_k, u_k) = f(\hat{x}_{k/k}, u_k) + \frac{\partial f}{\partial x_k}\Big|_{x_k=\hat{x}_{k/k}} (x_k - \hat{x}_{k/k}) + o(x_k - \hat{x}_{k/k}) \tag{13}$$

In Equation (13), ignoring the high-order term $o(x_k - \hat{x}_{k/k})$ and letting $\frac{\partial f}{\partial x_k}\Big|_{x_k=\hat{x}_{k/k}} = F_k$, Equation (2) can be simplified as follows:

$$x_{k+1} = f(\hat{x}_{k/k}, u_k) + F_k(x_k - \hat{x}_{k/k}) + w_k \tag{14}$$

Expanding the nonlinear observation function $g(x_k, u_k)$ around the prior state estimate $\hat{x}_{k/k-1}$ at k time by a first-order Taylor series, Equation (15) can be obtained as follows:

$$g(x_k, u_k) = g(\hat{x}_{k/k-1}, u_k) + \frac{\partial g}{\partial x_k}\Big|_{x_k=\hat{x}_{k/k-1}} (x_k - \hat{x}_{k/k-1}) + o(x_k - \hat{x}_{k/k-1}) \tag{15}$$

Ignoring higher-order terms in $o(x_k - \hat{x}_{k/k-1})$ and setting $\frac{\partial g}{\partial x_k}\Big|_{x_k=\hat{x}_{k/k-1}} = G_k$, Equation (14) can be simplified as follows:

$$y_k = g(\hat{x}_{k/k-1}, u_k) + G_k(x_k - \hat{x}_{k/k-1}) + v_k \tag{16}$$

If both the nonlinear state equation and the observation equation are linear, then Equation (11) can be rewritten as follows:

$$\begin{cases} x_{k+1} = F_k x_k + f(\hat{x}_{k/k}, u_k) - F_k \hat{x}_{k/k} + w_k \\ y_k = G_k x_k + g(\hat{x}_{k/k-1}, u_k) - G_k \hat{x}_{k/k-1} + v_k \end{cases} \tag{17}$$

Here, matrices F_k and G_k can be obtained by calculating the Jacobian matrices of f and g. If the state variable x is n-dimensional, i.e., $x = [x_1, x_2, \ldots, x_n]^T$, then the solution for matrices F_k and G_k is as follows.

$$F_k = \frac{\partial f}{\partial x} = \begin{bmatrix} \frac{\partial f_1}{\partial x_1} & \frac{\partial f_1}{\partial x_2} & \cdots & \frac{\partial f_1}{\partial x_n} \\ \frac{\partial f_2}{\partial x_1} & \frac{\partial f_2}{\partial x_2} & \cdots & \frac{\partial f_2}{\partial x_n} \\ \vdots & \vdots & \cdots & \vdots \\ \frac{\partial f_n}{\partial x_1} & \frac{\partial f_n}{\partial x_2} & \cdots & \frac{\partial f_n}{\partial x_n} \end{bmatrix} \tag{18}$$

$$G_k = \frac{\partial g}{\partial x} = \begin{bmatrix} \frac{\partial g_1}{\partial x_1} & \frac{\partial g_1}{\partial x_2} & \cdots & \frac{\partial g_1}{\partial x_n} \\ \frac{\partial g_2}{\partial x_1} & \frac{\partial g_2}{\partial x_2} & \cdots & \frac{\partial g_2}{\partial x_n} \\ \vdots & \vdots & \cdots & \vdots \\ \frac{\partial g_n}{\partial x_1} & \frac{\partial g_n}{\partial x_2} & \cdots & \frac{\partial g_n}{\partial x_n} \end{bmatrix} \tag{19}$$

The EKF algorithm requires advanced calibration of the covariance matrices for observation noise and process noise, which is often calculated by experience, and the covariance matrices Q_k and R_k are fixed values. However, in high-rate conditions of lithium iron phosphate batteries, the noise often changes due to the internal chemical reaction and resulting temperature variation and is no longer a fixed value. To improve the accuracy of SOC estimation, the AEKF algorithm is introduced. Based on the EKF algorithm, the AEKF adds the Sage–Husa adaptive filtering algorithm, enabling the observation noise covariance matrix and the process noise covariance matrix in the EKF algorithm to be adaptively updated, thus improving the accuracy of the SOC estimation. The steps of the AEKF algorithm are listed as follows:

Step 1. Initialization

Set $\hat{x}_0 = x_0$, y_0, P_0, Q_0, R_0 when $k = 0$, where $\hat{x}_0$ is the initial estimate of the state variables, y_0 is the initial observation value, P_0 is the initial value of the error covariance matrix, and Q_0 and R_0 are the initial values of the process covariance matrix and observation noise covariance matrix, respectively.

Step 2. State prediction

$$\hat{x}_{k/k-1} = f\left(\hat{x}_{k-1/k-1}, u_{k-1}\right) \tag{20}$$

Step 3. Prediction of error covariance

$$P_{k/k-1} = F_{k-1} P_{k-1/k-1} {F_{k-1}}^T + Q_{k-1} \tag{21}$$

Step 4. Calculate the Kalman gain

$$K_k = P_{k/k-1} G_k^T \left[G_k P_{k/k-1} G_k^T + R_{k-1} \right]^{-1} \tag{22}$$

Step 5. State estimation

$$\hat{x}_{k/k} = \hat{x}_{k/k-1} + K_k [y_k - g(\hat{x}_{k/k-1}, u_k)] \tag{23}$$

Step 6. Update the noise covariance matrix

$$e_k = y_k - g(\hat{x}_{k/k-1}, u_k) \tag{24}$$

$$\begin{cases} E_k = E\left(e_k e_k^T\right) \\ d = e_k^T E_k^{-1} e_k \end{cases} \tag{25}$$

In Equations (24) and (25), e_k is called the innovation matrix, and d is the estimated residual value expressed using the adaptive window factor in the windowing function, which is used to calculate the observation dimension M. According to the principle of the windowing function, if M is small, the computational burden of the adaptive algorithm is reduced, but the accuracy of the algorithm is lower. Conversely, if M is large, the accuracy of the algorithm is significantly improved, but the computational burden is too high, which is not suitable for recursive estimation algorithms. Therefore, M needs to be adjusted according to the convergence time, as shown in Equation (26).

$$\begin{cases} M = 1, d = 1 \\ M = k, d = 0 \\ M = k \times \eta^d, 0 < d < 1 \end{cases} \tag{26}$$

In Equation (26), η is the window convergence rate, which has a range of $0 < \eta < 1$. After calculating M, the noise covariance matrix can be updated as shown in Equations (27) and (28):

$$H_k = \frac{1}{M} \sum_{i=k-M+1}^{i=k} e_k e_k^T \tag{27}$$

$$\begin{cases} R_k = H_k - G_k P_{k/k-1} G_k^T \\ Q_k = K_k H_k K_k^T \end{cases} \tag{28}$$

Step 7. Estimation of error covariance.

$$P_{k/k} = (I - K_k G_k) P_{k/k-1} \tag{29}$$

Subsequently, repeat step 2~step 7 for recursive estimation to obtain the optimal estimate of the state variables.

3.2. Discretization of State Space Equation

Taking the operating current I_L as the input variable, battery SOC, battery electrochemical polarization voltage U_{p1}, and concentration difference polarization voltage U_{p2} as state variables, and U_{OC} as the observation variable, Equation (30) can be obtained by combining Equations (8) and (9):

$$\begin{pmatrix} SOC(t) \\ \frac{dU_{p1}(t)}{dt} \\ \frac{dU_{p2}(t)}{dt} \end{pmatrix} = \begin{pmatrix} 1 & 0 & 0 \\ 0 & -\frac{1}{R_{p1}(t)C_{p1}(t)} & 0 \\ 0 & 0 & -\frac{1}{R_{p2}(t)C_{p2}(t)} \end{pmatrix} \begin{pmatrix} SOC_{t0} \\ U_{p1}(t) \\ U_{p2}(t) \end{pmatrix} + \begin{pmatrix} -\frac{\int_{t_0}^{t} \eta dt}{Q_0} \\ \frac{1}{C_{p1}(t)} \\ \frac{1}{C_{p2}(t)} \end{pmatrix} I(t) \tag{30}$$

$$U_L(t) = U_{OC}[SOC(t)] - I(t)R_0(t) - U_{p1}(t) - U_{p2}(t) \tag{31}$$

Equations (30) and (31) are the continuous state equation and continuous observation equation, respectively. Here, $U_{OC}[SOC(t)]$ is the open-circuit voltage at time t obtained using the OCV-SOC relation function.

Setting the Coulomb efficiency η to be 1 and defining the sampling period as T, Equations (30) and (31) are discretized as follows:

$$\begin{pmatrix} SOC(k+1) \\ U_{p1}(k+1) \\ U_{p2}(k+1) \end{pmatrix} = \begin{pmatrix} 1 & 0 & 0 \\ 0 & e^{\frac{-T}{\tau_{p1}(k)}} & 0 \\ 0 & 0 & e^{\frac{-T}{\tau_{p2}(k)}} \end{pmatrix} \begin{pmatrix} SOC(k) \\ U_{p1}(k) \\ U_{p2}(k) \end{pmatrix} + \begin{pmatrix} -\frac{T}{Q_0} \\ R_{p1}(k)(1 - e^{\frac{-T}{\tau_{p1}(k)}}) \\ R_{p2}(k)(1 - e^{\frac{-T}{\tau_{p2}(k)}}) \end{pmatrix} I(k) \tag{32}$$

$$U_L(k) = U_{OC}[SOC(k)] - U_{p1}(k) - U_{p2}(k) - I(k)R_0(k) \tag{33}$$

The vector composed of $SOC(k)$, $U_{p1}(k)$, and $U_{p2}(k)$ in the above equation is the state vector x_k of the system at k time in Equation (11), while $U_L(k)$ is the observation vector y_k of the system at k time. Equation (32) is a linear equation, while the nonlinearity of the battery system state space equation is reflected in the $U_{OC}[SOC(k)]$ part of Equation (33). Therefore, the Kalman filtering algorithm for SOC estimation is carried out using both EKF and AEKF, and the results are compared with the coulomb counting method for SOC estimation.

3.3. SOC Estimation Process for LiFePO4 Battery

Step 1. Data input. Input the test data of the LiFePO4 battery, including the working current sampling data $I_L(k)$, terminal voltage $U_L(k)$, battery capacity of 13 Ah, parameter model identification results, and sampling period T = 0.1 s.

Step 2. Algorithm initialization. Initialize the battery state vector $x_0 = [SOC(0), 0, 0]$, estimation error covariance matrix $P_0 = \begin{bmatrix} 10^{-6} & 0 & 0 \\ 0 & 10^{-6} & 0 \\ 0 & 0 & 10^{-6} \end{bmatrix}$, process noise covariance matrix $Q_0 = \begin{bmatrix} 10^{-6} & 0 & 0 \\ 0 & 10^{-6} & 0 \\ 0 & 0 & 10^{-6} \end{bmatrix}$, and observation noise covariance matrix R_0 = 0.05.

Step 3. Calculate the prior estimate of the state variable and the predicted covariance matrix. Firstly, according to Equation (10), calculate the state transition matrix $A_k = diag[1, e^{\frac{-T}{\tau_{p1}(k)}}, e^{\frac{-T}{\tau_{p2}(k)}}]$ and the system input matrix $B_k = [-\frac{T}{Q_0}, R_{p1}(1 - e^{\frac{-T}{\tau_{p1}(k)}}), R_{p2}(1 - e^{\frac{-T}{\tau_{p2}(k)}})]^T$ using the model parameters at time k. Secondly, substitute the state vector $x_k = [SOC(k), U_{p1}(k), U_{p2}(k)]$ and the operating current $I(k)$ at k time into Equation (20) to calculate the prior estimate value $\hat{x}_{k+1/k}$ of the state variable. Finally, calculate the predicted error covariance matrix $P_{k+1/k}$ according to Equation (21).

Step 4. Calculating the Kalman gain matrix. Firstly, the nonlinear observation equation is linearized based on Equation (8), and the Jacobian matrix G_k of the observation equation is calculated, as given in equation (33). Secondly, the Jacobian matrix G_k, the predicted error covariance matrix $P_{k+1/k}$, and the observation noise matrix R_k are substituted into Equation (22) to calculate the Kalman gain matrix K_k.

$$G_k = [\frac{\partial U_{OC}[SOC] - IR_0}{\partial SOC}|_k, \frac{\partial - U_{p1}}{U_{p1}}|_k, \frac{\partial - U_{p2}}{U_{p2}}|_k] = [\frac{\partial U_{OC}[SOC]}{\partial SOC}|_k, -1, -1] \quad (34)$$

Step 5. Calculating the optimal estimated value of the state vector and updating the error covariance matrix. Based on Equation (34), the observation value, i.e., the estimated value $U_L(k)$ of the battery terminal voltage at k time, is calculated. Then, Equation (23) is used to calculate the optimal estimated value $\hat{x}_{k+1/k+1} = [SOC(k+1), U_{p1}(k+1), U_{p2}(k+1)]^T$ of the state vector, where $SOC(k+1)$ is the SOC value estimated by AEKF at $(k+1)$ time. Finally, Equation (13) is used to update the error covariance matrix $P_{k+1/k}$.

Step 6. Updating the noise covariance matrix. The process noise covariance matrix Q_k and the observation noise covariance matrix $R(k)$ are calculated based on Equations (24) and (25). Steps 2 to 6 are repeated recursively to estimate the SOC value at each moment.

3.4. Comparison and Analysis of SOC Estimation Results between EKF and AEKF Algorithms

To compare and analyze the performance of EKF and AEKF algorithms for SOC estimation of lithium iron phosphate batteries, a comparative study is conducted on SOC estimation based on the second-order equivalent circuit parameter model. Through battery charge–discharge testing, the corresponding relationship between battery OCV and SOC can be obtained through fitting. A 13 Ah-rated capacity and 3.2 V-rated voltage LiFePO4 battery is selected for HPPC testing to obtain its SOC and OCV data. The testing procedure involved discharging at 1 C for 10 s, resting for 40 s, and then charging at 0.75 C for 10 s. After resting for 45 min for every 10% drop in SOC, the OCV is measured, followed by another cycle of testing until the SOC of the battery reached 0.06, which is considered as

the end of the discharge. Under the global discharge, the battery terminal voltage U_L, the output current $I_{L,}$ and the real values of SOC are shown in Figures 2 and 3, respectively.

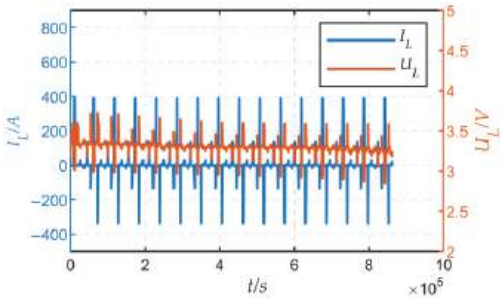

Figure 2. The waveform of terminal voltage U_L and the output current I_L.

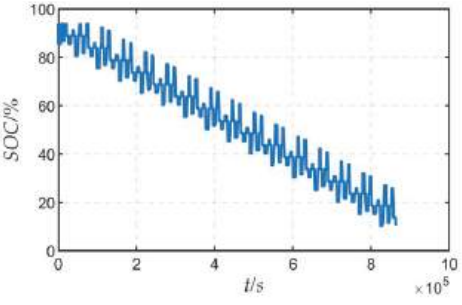

Figure 3. The waveform of real values of SOC.

Figures 4 and 5, respectively, show the SOC estimation results and estimation errors under the EKF and AEKF algorithms. From Figures 4 and 5, it can be seen that compared with the EKF algorithm, the AEKF algorithm can converge to the vicinity of the true value more quickly. The convergence time of the EKF algorithm and the AEKF algorithm is 532.8 s and 124.5 s, respectively. The SOC estimation accuracy of the AEKF algorithm is higher than that of the EKF algorithm. Experimental results show that the AEKF algorithm has a better SOC estimation convergence speed and accuracy.

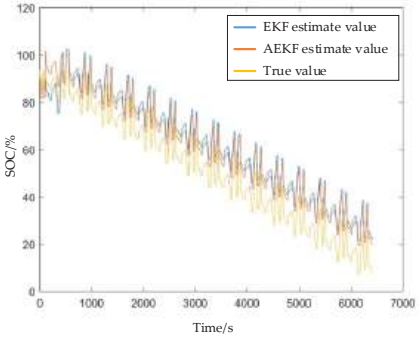

Figure 4. The SOC estimating results with EKF and AEKF.

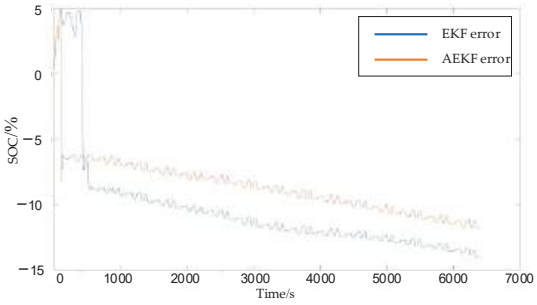

Figure 5. The SOC estimating errors with EKF and AEKF.

The specific statistical characteristics of SOC estimation errors under EKF and AEKF algorithms are shown in Table 1 (absolute error, AE; relative error, RE; mean absolute error, MAE; mean relative error, MRE), and the relevant features are calculated based on the converged results. From Table 1, it can be seen that the SOC estimation accuracy of the AEKF algorithm is better than that of the EKF algorithm, with a maximum absolute error (MaxAE) of 11.9% and a maximum relative error (MaxRE) of 152.6%, which occurs at the end of discharge. And the MAE of the SOC estimation is 8.8%, and the MRE of the SOC estimation is 25.4% with the AEKF algorithm, which is lower than that with the EKF. It can also be seen from Table 1 that the errors of both EKF and AEKF algorithms gradually increase. Therefore, the adaptive noise covariance matrix updating method of the AEKF algorithm can reduce SOC estimation errors. However, the SOC estimation precision is still large, which cannot meet the actual use needs of the battery energy management system. And, further optimization of the SOC estimation algorithm is needed.

Table 1. SOC estimation error under the EKF algorithm and AEKF algorithm.

Estimation Algorithm	MaxAE	MaxRE	MAE	MRE
EKF	14.1%	180.3%	10.9%	31.2%
AEKF	11.9%	152.6%	8.8%	25.4%

4. SOC Estimation Method Based on FFRLS-AFKF

The FFRLS-AEKF joint estimation algorithm uses the SOC value estimated using the AEKF algorithm to replace the estimated value of the ampere-hour integration method in the FFRLS algorithm to improve the battery equivalent circuit parameters identification accuracy. The identified model parameters are substituted into the AEKF algorithm to recursively estimate the SOC and improve the accuracy of the AEKF algorithm. Then, the estimated SOC value is fed back to FFRLS, and through positive feedback, the SOC estimation accuracy is finally improved. The specific calculation process is shown in Figure 6.

Step 1. Initialize the FFRLS algorithm and the AEKF algorithm, where SOC(0) is obtained by the open-circuit voltage method.

Step 2. Obtain the model parameters at k time through the FFRLS algorithm, substitute them into the AEKF algorithm, construct the corresponding transfer matrix and input matrix, and obtain the SOC at $(k + 1)$ time.

Step 3. Substitute the SOC at $(k + 1)$ time into the OCV-SOC relationship formula, and then use the FFRLS algorithm to obtain the model parameters at $(k + 1)$ time.

Step 4. Update the transfer matrix and input matrix in the AEKF algorithm to obtain the SOC of the next time step; repeat steps 2 to step 4 and recursively obtain the SOC at each time step. The specific calculation process is shown in the diagram.

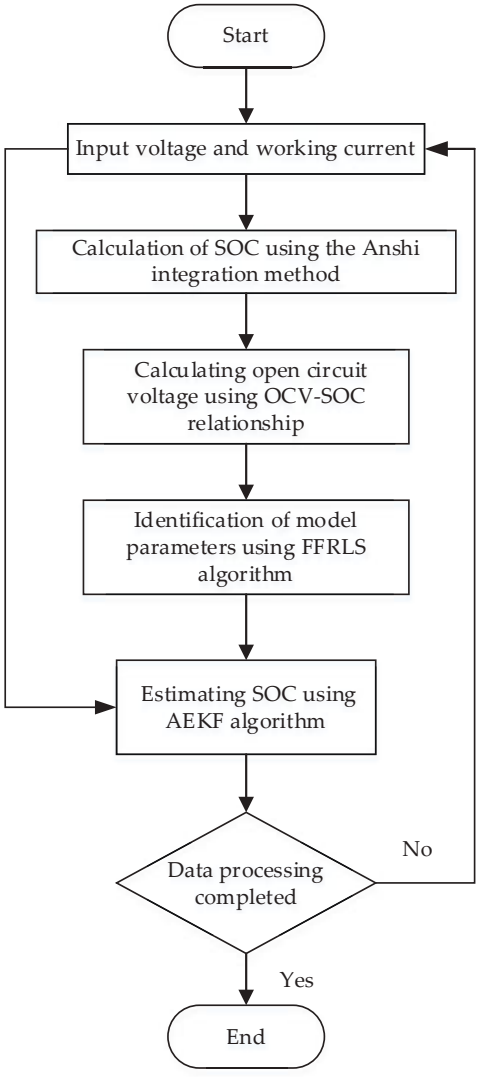

Figure 6. FFRLS + AEKF processes.

5. Experimental Results

The experimental parameters setting is the same as in Section 3.2. The structure of the battery pack used in the experiment is first parallel and then series. The batteries used are all new, and the working temperature is 25 °C. According to the method in Section 2.3, the battery parameters R_0, R_{p1}, C_{p1}, R_{p2}, and C_{p2} can be identified at 25 °C, and the identification results are in Table 2. Four single cells form a parallel unit, and ten parallel units, a total of forty battery cells form a series battery pack. The parallel unit is composed of ten parallel units, and a total of forty battery cells are composed of series battery packs. The model of the battery is IFP9380, the rated capacity is 15 Ah, the nominal voltage is 3.2 V, the operating voltage range is 2.0–3.65 V, and the maximum discharge current is 2.00 A. The main control chip of the switching circuit selects STM32F103VB8T6 battery voltage measurement using the battery management chip LTC6811. The measurement error is less than 1 mV, and the sampling frequency is greater than 3 kHz. The sampling of the circuit

current uses a shunt, and the sampling error is less than 0.1%. The experimental platform is shown in Figure 7.

Table 2. The identification results.

R_0/Ω	R_{p1}/Ω	C_{p1}/F	R_{p2}/Ω	C_{p2}/F
0.0005206917	0.0001007158	1256.806552	0.0024315296	26355.45136

(**a**)

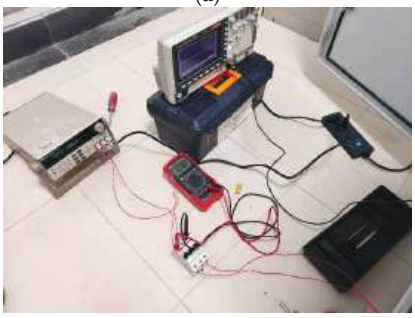

(**b**)

(**c**)

Figure 7. Experimental platform of battery charge and discharge. (**a**) Control board physical diagram. (**b**) DC power supply charging. (**c**) Battery pack interface diagram.

Figures 8 and 9 show the SOC estimation results and errors using the AEKF and FFRLS-AEKF algorithms, respectively. From Figures 6 and 7, it can be seen that the estimation results with the FFRLS-AEKF algorithm are closer to the true values, and the SOC estimation

errors with the FFRLS-AEKF algorithm are smaller than with the AEKF algorithm. The estimation errors of the AEKF and FFRLS-AEKF algorithms are shown in Table 3. It can be seen from Table 3 that the maximum absolute error of the joint estimation algorithm is 4.97%, and the error is controlled within 5%. As the battery operating time increases, the SOC estimation accuracy continuously converges to the vicinity of the true value, with the average absolute error decreasing to 2.5%. The experimental results show that the FFRLS-AEKF joint estimation algorithm has good convergence performance and high estimation accuracy, verifying that the proposed method is correct and feasible. Therefore, the SOC estimation performances with EKF, AEKF, and FFRLS-AEKF are shown in Table 4.

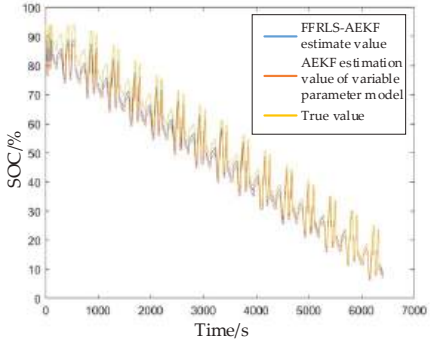

Figure 8. The SOC estimating results of the FFRLS-AEKF and AEKF.

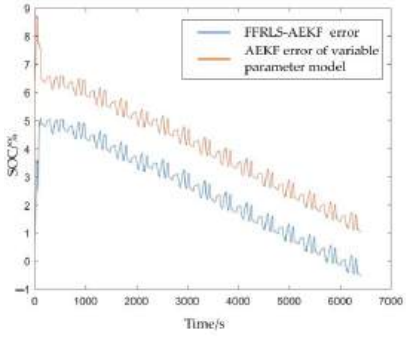

Figure 9. The SOC estimating errors of the FFRLS-AEKF and AEKF.

Table 3. Compared FFRLS-AEKF and AEKF algorithm of SOC errors.

Estimation Algorithm	MaxAE	MaxRE	MAE	MRE
AEKF	6.6%	15.7%	4.0%	8.1%
FFRLS-AEKF	4.97%	6.8%	2.5%	4.3%

Table 4. The SOC estimation performances with EKF, AEKF, and FFRLS-AEKF.

Estimation Algorithm	EKF	AEKF	FFRLS-AEKF
Steady-precision	low	lower	lowest
Convergence speed	fast	faster	fastest

6. Conclusions

The working principle of FFRLS for battery parameter identification is analyzed. The second-order equivalent circuit state discretization equation based on the AEKF algorithm

is established, and the steps of the battery SOC estimation method based on AEKF are discussed and simulated. The simulation results show that it has the disadvantages of low steady-state accuracy and slow convergence rate. To improve SOC estimation precision, combining the advantages of high precision and adaptability of FFRLS and AEKF, a joint SOC estimation method based on FFRLS-AEKF is proposed and experimented with. The experimental results show that the FFRLS-AEKF algorithm can have higher SOC estimation and faster accuracy convergence speed, verifying that the proposed method is correct and feasible.

In the actual use of the battery pack, it is often necessary to combine the battery cells in series and parallel to provide sufficient capacity and voltage level. However, in the process of series and parallel grouping of the battery pack, there will be problems such as more complex model parameters and difficult data sampling. Therefore, the next step in this research field needs to consider the influence of physical parameters such as the small number of sampling points, incomplete sampling data, and contact resistance on the accuracy of the battery model. The establishment of a perfect equivalent model of the battery pack is the focus of the next step in this research.

Author Contributions: Conceptualization, Y.X.; methodology, Z.Y.; software, L.H.; validation, Y.X., Z.Y. and L.S.; formal analysis, L.H.; investigation, L.H.; resources, Z.Y.; data curation, Y.X.; writing—original draft preparation, L.H.; writing—review and editing, Y.X.; visualization, Z.Y.; supervision, L.H.; project administration, L.S.; funding acquisition, Y.J. All authors have read and agreed to the published version of the manuscript.

Funding: This research was funded by the National Natural Science Foundation of China (Grant No. 51507183 and 51877212).

Data Availability Statement: The data that support the findings of this study are available from the corresponding author upon reasonable request.

Conflicts of Interest: The authors declare no conflict of interest.

References

1. Marc, D.; Thomas, F.F.; John, N. Modeling of Galvanostatic Charge and Discharge of the Lithium/Polymer/Insertion Cell. *J. Electrochem. Soc.* **2019**, *140*, 13–21.
2. Hu, X.S.; Tang, X.L. Review of modeling techniques for lithium-ion traction batteries in electric vehicles. *J. Mech. Eng.* **2017**, *16*, 20–31. [CrossRef]
3. Qays, M.O.; Buswig, Y.; Hossain, M.L.; Abu-Siada, A. Recent progress and future trends on the state of charge estimation methods to improve battery-storage efficiency: A review. *CSEE J. Power Energy Syst.* **2022**, *8*, 105–114.
4. Xiong, R.; Cao, J.; Yu, Q.; He, H.; Sun, F. Critical Review on the Battery State of Charge Estimation Methods for Electric Vehicles. *IEEE Access* **2017**, *6*, 1832–1843. [CrossRef]
5. Naguib, M.; Kollmeyer, P.; Emadi, A. Lithium-Ion Battery Pack Robust State of Charge Estimation, Cell Inconsistency, and Balancing: Review. *IEEE Access* **2021**, *9*, 50570–50582. [CrossRef]
6. He, H.; Zhang, X.; Xiong, R.; Xu, Y.; Guo, H. Online model-based estimation of state-of-charge and open-circuit voltage of lithium-ion batteries in electric vehicles. *Energy* **2012**, *39*, 310–318. [CrossRef]
7. Meng, J.; Stroe, D.-I.; Ricco, M.; Luo, G.; Swierczynski, M.; Teodorescu, R. A Novel Multiple Correction Approach for Fast Open Circuit Voltage Prediction of Lithium-Ion Battery. *IEEE Trans. Energy Convers.* **2018**, *34*, 1115–1123. [CrossRef]
8. Movassagh, K.; Raihan, A.; Balasingam, B.; Pattipati, K. A Critical Look at Coulomb Counting Approach for State of Charge Estimation in Batteries. *Energies* **2021**, *14*, 4074. [CrossRef]
9. Vidal, C.; Hausmann, M.; Barroso, D.; Shamsabadi, P.M.; Biswas, A.; Chemali, E.; Ahmed, R.; Emadi, A. Hybrid Energy Storage System State-Of-Charge Estimation Using Artificial Neural Network for Micro-Hybrid Applications. In Proceedings of the 2018 IEEE Transportation Electrification Conference and Expo (ITEC), Long Beach, CA, USA, 13–15 June 2018.
10. Chemali, E.; Kollmeyer, P.J.; Preindl, M.; Ahmed, R.; Emadi, A.; Kollmeyer, P. Long Short-Term Memory Networks for Accurate State-of-Charge Estimation of Li-ion Batteries. *IEEE Trans. Ind. Electron.* **2018**, *65*, 6730–6739. [CrossRef]
11. Antón, J.C.; Nieto, P.J.G.; Viejo, C.B.; Vilán, J.A.V. Support Vector Machines Used to Estimate the Battery State of Charge. *IEEE Trans. Power Electron.* **2013**, *28*, 5919–5926. [CrossRef]
12. Hou, J.; Yang, Y.; He, H.; Gao, T. Adaptive Dual Extended Kalman Filter Based on Variational Bayesian Approximation for Joint Estimation of Lithium-Ion Battery State of Charge and Model Parameters. *Appl. Sci.* **2019**, *9*, 1726. [CrossRef]
13. Hu, X.; Li, S.; Peng, H. A comparative study of equivalent circuit models for Li-ion batteries. *J. Power Sources* **2012**, *198*, 359–367. [CrossRef]

14. Wan, E.A.; Van Der Merwe, R. The unscented Kalman filter for nonlinear estimation. In Proceedings of the IEEE 2000 Adaptive Systems for Signal Processing, Communications, and Control Symposium (Cat. No.00EX373), Lake Louise, AB, Canada, 4 October 2000.
15. Plett, G.L. Extended Kalman filtering for battery management systems of LiPB-based HEV battery packs—Part 3. State and parameter estimation. *Power Sources* **2004**, *134*, 277–292. [CrossRef]
16. Bhangu, B.; Bentley, P.; Stone, D.; Bingham, C. Nonlinear Observers for Predicting State-of-Charge and State-of-Health of Lead-Acid Batteries for Hybrid-Electric Vehicles. *IEEE Trans. Veh. Technol.* **2005**, *54*, 783–794. [CrossRef]
17. Pavkovic, D.; Smetko, V.; Hrgetic, M.; Komljenovic, A. Dual Kalman filter-based SOC/SoH estimator for an ultracapacitor module. In Proceedings of the 2014 IEEE Conference on Control Applications (CCA), Juan Les Antibes, France, 8–10 October 2014.
18. Lai, X.; Zheng, Y.; Sun, T. A comparative study of different equivalent circuit models for estimating state-of-charge of lithium-ion batteries. *Electrochim. Acta* **2018**, *259*, 566–577. [CrossRef]
19. Zhou, D.; Yin, H.; Xie, W.; Fu, P.; Lu, W. Research on Online Capacity Estimation of Power Battery Based on EKF-GPR Model. *J. Chem.* **2019**, *2019*, 1–9. [CrossRef]
20. Gao, Z.C.; Chin, C.S.; Toh, W.D.; Chiew, J.; Jia, J. State-of-Charge Estimation and Active Cell Pack Balancing Design of Lithium Battery Power System for Smart Electric Vehicle. *J. Adv. Transp.* **2017**, *2017*, 1–14. [CrossRef]
21. Jia, J.; Lin, P.; Chin, C.S.; Toh, W.D.; Gao, Z.; Lyu, H.; Cham, Y.T.; Mesbahi, E. Multirate strong tracking extended Kalman filter and its implementation on lithium iron phosphate (LiFePO4) battery system. In Proceedings of the 11th IEEE International Conference on Power Electronics and Drive Systems, Sydney, NSW, Australia, 9–12 June 2015.
22. Ali, M.U.; Khan, H.F.; Masood, H.; Kallu, K.D.; Ibrahim, M.M.; Zafar, A.; Oh, S.; Kim, S. An adaptive state of charge estimator for lithium-ion batteries. *Energy Sci. Eng.* **2022**, *10*, 2333–2347. [CrossRef]
23. Ge, D.; Zhang, Z.; Kong, X.; Wan, Z. Online SoC Estimation of Lithium-Ion Batteries Using a New Sigma Points Kalman Filter. *Appl. Sci.* **2021**, *11*, 11797. [CrossRef]
24. Zhang, Z.Y.; Wang, G.S.; Nie, S.X.; Xing, P.X. State of Charge Estimation of LiFePO4 battery under Pulse High Rate Discharge. *J. Electr. Eng. Technol.* **2019**, *8*, 1769–1779.
25. Xia, B.; Sun, Z.; Zhang, R.; Lao, Z. A Cubature Particle Filter Algorithm to Estimate the State of the Charge of Lithium-Ion Batteries Based on a Second-Order Equivalent Circuit Model. *Energies* **2017**, *10*, 457. [CrossRef]
26. Ye, M.; Guo, H.; Xiong, R.; Yu, Q. A double-scale and adaptive particle filter-based online parameter and state of charge estimation method for lithium-ion batteries. *Energy* **2017**, *144*, 789–799. [CrossRef]
27. Schwunk, S.; Armbruster, N.; Straub, S.; Kehl, J.; Vetter, M. Particle filter for state of charge and state of health estimation for lithium–iron phosphate batteries. *J. Power Sources* **2013**, *239*, 705–710. [CrossRef]
28. Giannelos, S.; Borozan, S.; Aunedi, M.; Zhang, X.; Ameli, H.; Pudjianto, D.; Konstantelos, I.; Strbac, G. Modelling Smart Grid Technologies in Optimisation Problems for Electricity Grids. *Energies* **2023**, *16*, 5088. [CrossRef]
29. Li, X.; Lyu, L.; Geng, G.; Jiang, Q.; Zhao, Y.; Ma, F.; Jin, M. Power Allocation Strategy for Battery Energy Storage System Based on Cluster Switching. *IEEE Trans. Ind. Electron.* **2021**, *69*, 3700–3710. [CrossRef]
30. Gao, X.; Fu, L. SOC Optimization Based Energy Management Strategy for Hybrid Energy Storage System in Vessel Integrated Power System. *IEEE Access* **2020**, *8*, 54611–54619. [CrossRef]
31. Song, Q.; Mi, Y.; Lai, W. A Novel Variable Forgetting Factor Recursive Least Square Algorithm to Improve the Anti-Interference Ability of Battery Model Parameters Identification. *IEEE Access* **2019**, *7*, 61548–61557. [CrossRef]
32. Badoni, M.; Singh, A.; Singh, B. Variable Forgetting Factor Recursive Least Square Control Algorithm for DSTATCOM. *IEEE Trans. Power Deliv.* **2015**, *30*, 2353–2361. [CrossRef]

batteries

MDPI

Article

Optimal Capacity Configuration of Wind–Solar Hydrogen Storage Microgrid Based on IDW-PSO

Ge He [1], Zhijie Wang [1,*], Hengke Ma [1] and Xianli Zhou [2]

[1] Department of Electricity, Shanghai Dianji University, Shanghai 201306, China
[2] Department of Electricity, Shanghai University of Electric Power, Shanghai 201306, China
* Correspondence: wzjsdstu@163.com; Tel.: +86-18964586826

Abstract: Because the new energy is intermittent and uncertain, it has an influence on the system's output power stability. A hydrogen energy storage system is added to the system to create a wind, light, and hydrogen integrated energy system, which increases the utilization rate of renewable energy while encouraging the consumption of renewable energy and lowering the rate of abandoning wind and light. Considering the system's comprehensive operation cost economy, power fluctuation, and power shortage as the goal, considering the relationship between power generation and load, assigning charging and discharging commands to storage batteries and hydrogen energy storage, and constructing a model for optimal capacity allocation of wind–hydrogen microgrid system. The optimal configuration model of the wind, solar, and hydrogen microgrid system capacity is constructed. A particle swarm optimization with dynamic adjustment of inertial weight (IDW-PSO) is proposed to solve the optimal allocation scheme of the model in order to achieve the optimal allocation of energy storage capacity in a wind–hydrogen storage microgrid. Finally, a microgrid system in Beijing is taken as an example for simulation and solution, and the results demonstrate that the proposed approach has the characteristics to optimize the economy and improve the capacity of renewable energy consumption, realize the inhibition of the fluctuations of power, reduce system power shortage, and accelerate the convergence speed.

Keywords: independent microgrid system; wind and solar complementary power generation; hydrogen energy storage; IDW-PSO; capacity configuration

Citation: He, G.; Wang, Z.; Ma, H.; Zhou, X. Optimal Capacity Configuration of Wind–Solar Hydrogen Storage Microgrid Based on IDW-PSO. *Batteries* **2023**, *9*, 410. https://doi.org/10.3390/batteries9080410

Academic Editors: Luis Hernández-Callejo, Jesús Armando Aguilar Jiménez and Carlos Meza Benavides

Received: 24 May 2023
Revised: 21 July 2023
Accepted: 26 July 2023
Published: 6 August 2023

1. Introduction

In recent years, wind and photovoltaic power generation have been essential for new power systems mainly based on new energy sources. With the promotion of carbon neutrality and the increasingly prominent problem of energy shortage, the large-scale application of new energy generation has become the trend of power system development. Because wind and sunlight are the primary energy sources of new energy generation, they are randomly influenced by the environment, temperature, geographical location, and other aspects, quickly leading to the imbalance of power conversion and the instability of power generation time, affecting the system's stability. Given the intermittent and uncertain influence of new energy, with the popularization of new energy, the proportion is increasing, which will significantly impact the stability, safety, and system operating rate for new energy sources [1]. The application of energy storage technology in new energy systems helps to improve the utilization rate of power generation in new energy power systems, keep the system stable in power supply during peak power generation and low power generation due to external influence, and improve the utilization efficiency of power generation systems [2]. Aiming at the intermittency and instability nature of new energy power generation, the energy storage is utilized in order to store and release the electric energy, and power supplementation is carried out so as to improve the energy utilization rate and the stability of the power supply of the power system.

Because of the uncertainty and fluctuation of scenery, large-scale access to clean energy will also contain more uncertain factors, which will cause the phenomenon of abandoning wind and light and affect power stability [3]. The incorporation of hydrogen energy storage in the system has the advantages of being pollution-free, sustainable, and energy-saving, and is a green and clean energy storage system. The use of a hydrogen energy storage system allows for the storage of excess electricity from wind and solar energy abandonment, realizing the use of clean energy in the form of integrated energy of electricity–hydrogen–electricity, and improving the efficiency of the available renewable energy sources. Hydrogen energy storage has high energy density, a low cost of running and sustaining compared with other energy storage, long-term storage and non-pollution, applicable to both instantaneous power supply and long time power supply, applicable to different situations. Compared with the traditional battery, the fuel cell in hydrogen energy storage can be between the hydrogen chemical energy converted to electrical energy without the mutual conversion of other energy forms, which significantly reduces the loss and increases the power generation efficiency, and has the advantage of high energy conversion, environmental protection and the like.

With the gradual increase in the occupation of new energy sources, the percentage of wind and solar farms has been increasing, and consequently the research on power fluctuation problems has been gradually deepened. There have been many studies at home and abroad on the problem of optimal allocation of integrated energy system capacity. Literature [4] uses variational mode decomposition (VMD) to analyze the unbalanced power in a wind–solar hybrid microgrid. It establishes a model for the optimal allocation of hybrid energy capacity for the storage of batteries and supercapacitors. Literature [5] established a capacity optimization allocation method to reduce grid-connected photovoltaic power for photovoltaic power plants as well as hybrid energy storage systems. According to [6], the megawatt isolated microgrid consisting of photovoltaic/wind turbines, energy storage, diesel, and gas turbines is optimized in capacity allocation to solve electricity supply problems for powerless remote locations. Literature [7] proposes a quantitative optimal configuration method for a wind and solar complementary power supply system. Literature [8] puts forward an optimization strategy of double-layer hybrid energy storage capacity for a distribution grid by accounting for the distribution network loss and the total cost of the stored capacity system. In literature [9], a configuration model of a multi-source microgrid is constructed considering three aspects: installation location, unit arrangement and combination, extraordinary load of electric vehicles, and the dynamic matching problem between power generation and power consumption is analyzed. In reference [10], a multi-objective optimal allocation method of energy storage systems is proposed to deal with the issue of energy storage allocation under one-party investment and multiple benefits. These studies all show that the adoption with hybrid energy storage is crucial in rational distribution of microgrids, both consider the issues of reducing power loss and system investment cost or maximum economy, but do not consider the utilization of clean energy. In literature [11], the coupling of renewable energy power generation and hydrogen energy storage is shown to be a powerful means of achieving clean and carbon-neutral energy consumption, which has excellent potential for development. Literature [12] explains the application value system of hydrogen energy storage in the "source-network load" of the new power system. Hydrogen energy storage has the advantages of cross-season, cross-regional and large-scale storage. It has a specific rapid response ability, which has substantial application value in all aspects of the "source-network load" of new power systems. Literature [13] mainly considers how to construct a multi-energy combined storage and supply model in the integrated energy system with hydrogen storage as the conversion hub of multiple energy forms in low carbon parks, so as to achieve the optimized allocation method with low carbon emission and low cost; literature [14] uses the hydrogen produced by the hydrogen storage system to work together with a heat storage system and air source heat pump to reduce the use cost of electricity, heat and cold energy in the park, and establishes a capacity optimal allocation model taking integrated

energy cost minimization as the optimization target. The research on hydrogen energy storage systems mainly focuses on using hydrogen without considering the conversion of hydrogen energy storage as electric energy. Literature [15] builds a typical wind and solar hydrogen storage capacity configuration model based on wind energy, solar photovoltaic, electric energy storage, and hydrogen production equipment, Then establishes a demand response model of day-ahead segmented electricity price load to reduce the total cost of running the system. The application of hydrogen energy storage focuses on the recycling of hydrogen. Increasing hydrogen energy conversion into electric energy is conducive to improving the rate of abandoning wind and light and transforming into a green and low-carbon environment [16].

Based on the issues described above, a wind–solar hydrogen storage microgrid system with a wind turbine, photovoltaic generator, hydrogen storage system, and battery system as subsystems is constructed in the paper, and the particle swarm algorithm for improving the dynamic adjustment of inertia weights is applied to the system's capacity configuration, and the optimal configuration proposal on system capacity is obtained, which makes the highest system economy, achieves power stabilization, reduces the rate of abandoning wind and solar power, as well as the reduction of the system's shortage of power.

2. Wind–Solar Hydrogen Microgrid System

The distributed new energy system has wind power, photovoltaic, geothermal, tidal, and other subsystems with random output. The integrated development of a comprehensive energy system enhances the combined application of energy [17]. This paper's wind, light, and hydrogen microgrid system consists of wind turbines, photovoltaic generators, hydrogen production units, hydrogen storage units, fuel cells, and other auxiliary equipment. Hydrogen energy storage is used to realize the interconnection of electricity–hydrogen–electricity, to suppress the power fluctuation of distributed new power sources, which can contribute to the sustainability of energy [18]. The electricity–hydrogen system architecture of the park is schematically displayed in Figure 1. By matching and coupling various forms of energy storage, the energy utilization rate can be improved, achieving peak shaving and valley filling, stabilizing power fluctuation, and leading to certain economic benefits.

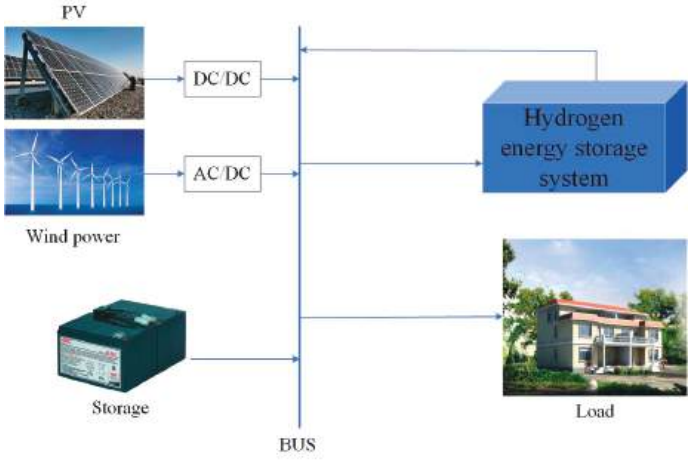

Figure 1. Schematic diagram of electric–hydrogen integrated energy structure.

Figure 1 is a schematic structural diagram of an electric–hydrogen system, mainly consisting of a generation unit, a capacity storage unit and load. The electricity generation unit comprises of wind power generation and photovoltaic power generation, which takes renewable energy as the main energy source of the system, while the energy storage unit

comprises a storage battery and hydrogen storage system, which has a role of balancing the load of the system, and absorbs excess energy through the energy storage system when there is sufficient wind and light energy; and supplements it through the energy storage system when there is insufficient wind and light energy.

2.1. Modeling of Generator Set

2.1.1. Photovoltaic Generation System

Physical photovoltaic (PV) power generation is the direct transformation of solar energy through PV panels into electrical energy. Photovoltaic power generation is affected by solar radiation, the radiation angle, sunshine hours, and environmental temperature. The specific photovoltaic power generation output model is shown in Formula (1) [19]:

$$P_{\mathrm{pv}}(t) = P_{\mathrm{pvN}} f_{\mathrm{pv}} \frac{G(t)}{G_{\mathrm{ref}}} [1 + \alpha (T_c(t) - T_{\mathrm{ref}})] \tag{1}$$

where: $P_{\mathrm{pv}}(t)$ represents the actual electricity generation power of the photovoltaic panel; P_{pvN} is the nominal capacity of the photovoltaic panel to generate electricity; f_{pv} is the operation efficiency of photovoltaic system; $G(t)$ is the actual light intensity at time t; G_{ref} is the reference standard light intensity; α is the temperature coefficient; $T_c(t)$ is the operating temperature of the photovoltaic panel at time t; T_{ref} is the reference standard ambient temperature.

Photovoltaic panel operation temperature transformation is caused by the ambient temperature, and solar light intensity is caused by many aspects of the influence of the relationship shown in Formula (2):

$$T_C(t) = T(t) + \frac{T_{\mathrm{rated}}}{800} G(t) \tag{2}$$

where: $T(t)$ is the actual ambient temperature; and T_{rated} is the standard reference temperature of a photovoltaic panel.

2.1.2. Wind Power Generation Model

Wind turbine power output is affected by various aspects such as the speed of wind, blades, ambient temperature, air pressure, etc. [20]. Wind power generation means to convert the kinetic energy to mechanical energy and utilize a turbine to convert the mechanical energy into electrical power. The wind speed changes randomly due to external factors, leading to intermittent and fluctuating wind power generation. The power delivery by wind turbine is most affected by the wind speed, and approximated relationship with the wind speed is shown in Formula (3):

$$P_{wt}(t) = \begin{cases} 0, \ \ v(t) < v_{\mathrm{in}} \ \ v(t) > v_{\mathrm{o}} \\ P_{\mathrm{r}} \frac{v(t) - v_{\mathrm{in}}}{v_{\mathrm{r}} - v_{\mathrm{in}}}, v_{\mathrm{in}} \le v(t) \le v_{\mathrm{r}} \\ P_{\mathrm{r}}, \ \ v_{\mathrm{r}} < v(t) \le v_{\mathrm{o}} \end{cases} \tag{3}$$

where: $P_{\mathrm{wt}}(t)$ is the active output power of the wind farm in time t, P_{r} is the rated output power of the wind turbine, $v(t)$ is the actual wind speed of the wind turbine in time t, v_{r} is the rated wind speed, v_{in} is the cut-in wind speed, and v_{o} is the cut-out wind speed.

2.2. Modeling of Hydrogen Energy Storage System

The hydrogen energy storage system is an integral part for the energy storage system in an independent microgrid system. The hydrogen energy storage system mainly comprises electrolytic cells, fuel cells, and hydrogen storage equipment. Its structural schematic diagram is shown in Figure 2.

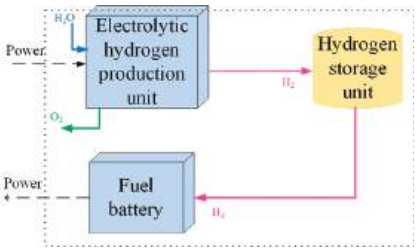

Figure 2. Structure diagram of hydrogen energy storage system.

2.2.1. Mathematical Modeling of Electrolytic Cell

Electrolyzed water is a widely used primary hydrogen production method in industrial hydrogen production [21]. The electrolyzer electrolyzes water into hydrogen and oxygen. There are alkaline electrolyzers, proton exchange membrane electrolyzers, and solid oxide electrolyzers. Compared with other electrolyzers, alkaline electrolyzers have higher efficiency and the best hydrogen production capacity. The system life is twice as long as that of proton exchange membrane electrolyzers, and the cold start-up time is shorter than that of solid oxide electrolyzers. An alkaline electrolyzer is the safest, most mature, and most widely used. The hydrogen production rate of an alkaline electrolyzer is [22]

$$\begin{cases} V_{\mathrm{H}_2} = \eta_F \frac{N_C}{2F} I \\ \eta_F = 96.5\mathrm{e}^{\left(\frac{0.09}{I} - \frac{75.5}{I^2}\right)} \end{cases} \tag{4}$$

where: V_{H2} is the hydrogen production rate; η_F is Faraday efficiency; N_C is the number of electrolyzers; F is Faraday constant (C/mol); I is the current in the electrolytic cell.

In practice, the electrolytic cell cannot be electrolyzed entirely, and its conversion efficiency is represented by

$$P_{\mathrm{H}_2}(t) = \eta_{\mathrm{EL}} P_{\mathrm{e}}(t) \tag{5}$$

where: $P_{\mathrm{H2}}(t)$ is the power generated by hydrogen production in the electrolytic cell; $P_{\mathrm{e}}(t)$ is the electricity consumption of the electrolytic cell; and η_{EL} is the conversion efficiency of electricity and hydrogen in the electrolyzer.

2.2.2. Mathematical Modeling of Fuel Cell

A mathematical example is provided for the fuel cell:

$$Q_{\mathrm{H}_2\mathrm{fc}} = \frac{N_{\mathrm{S}} P_{\mathrm{fc}}}{U_{\mathrm{fc}}(2F)} \tag{6}$$

where: Q_{H2fc} is the hydrogen consumption of the fuel cell; N_{S} is the number of batteries connected in series; P_{fc} is the output power of the fuel cell; U_{fc} is the battery voltage; and F is the Faraday constant (C/mol).

2.2.3. Mathematical Modeling of Hydrogen Storage Device

Most hydrogen storage devices use hydrogen storage tanks, which can store the hydrogen produced by electrolytic cells and provide hydrogen for fuel cells. The hydrogen storage tank device has the characteristics of low cost, high safety, and fast charging and discharging speed. A hydrogen storage tank is characterized by a mathematical model:

$$Pa_{\mathrm{H}_2} = \frac{RT_a}{V} \int_{t_1}^{t_2} \left(V_{\mathrm{H}_2} - Q_{\mathrm{H}_2\mathrm{fc}}\right) dt \tag{7}$$

where: Pa_{H2} is the pressure of the hydrogen storage tank; R is a gas constant; T_{a} is the thermodynamic temperature of the gas; V is the total capacity of the hydrogen storage tank;

t_1 and t_2 are the start time for starting hydrogen production and the end time for stopping hydrogen production, respectively.

2.3. Battery Modeling

A storage battery is a kind of galvanic energy storage, while chemical energy storage is a relatively stable and high-grade energy storage method. This article selected a lithium battery as a storage battery, and the running state of the storage system is marked by the state of charge (*SOC*) of the lithium battery. When *SOC* = 1, the battery capacity reaches a maximum value [23]. The battery output model is

Charging status:

$$SOC(t) = SOC(t-1)(1-\sigma) + P_c(t)\eta_c \frac{\Delta t}{E_{\max}} \tag{8}$$

Discharge state:

$$SOC(t) = SOC(t-1)(1-\sigma) - P_f(t)\frac{\Delta t}{\eta_f E_{\max}} \tag{9}$$

where: σ is the charge and discharge rate of the storage battery; P_c and P_f are the charging and discharging power of the battery in t time; η_c and η_f are charge and discharge efficiency; and $E_{\max}$ is the maximum capacity of the battery.

3. Capacity Optimal Allocation Model

Based on the microgrid system of wind–solar hydrogen storage, this paper not only considers the economy of the independent microgrid of wind–solar hydrogen storage; but also to consider the power fluctuations on the wind generated by the wind and light abandonment, so as to make the wind utilization rate to reach the highest, and put forward the corresponding optimization scheme.

3.1. Objective Function

In this paper, the most economical price is used as the objective function in the independent wind, solar, and hydrogen storage microgrid.

Objective function 1 includes: In the hydrogen-containing composite energy storage system, investment and recovery costs are considered to achieve the best economic benefits. In this paper, the objective function of minimizing the integrated operating cost of the system can be expressed as:

C_T is the system's total operation cost, composed of each piece of equipment's investment and operation cost. Each piece of equipment is comprised of wind turbines, photovoltaics, batteries, and hydrogen storage, and their installation cost, replacement cost, in addition to operation and maintenance cost together constitute the operating cost of the investment [24].

$$C_T = \min\{C_{IN} + C_{RE} + C_{OM}\} \tag{10}$$

where: C_T is the total operating cost of the system; C_{IN} is the installed cost of the equipment; C_{RE} is the replacement cost of the equipment; and C_{OM} is the operation and maintenance cost of the equipment.

C_{IN} represents the installed cost for the equipment, which can be expressed as

$$C_{IN} = QP_{IN}\frac{r(1+r)^m}{(1+r)^m - 1} \tag{11}$$

where: C_{IN} is the installed cost of the equipment; Q is the rated capacity of the equipment; P_{IN} is the unit installed cost of the equipment; r is the discount rate of equipment; and m is the service life of the equipment.

C_{RE} as replacement cost for devices, which can be expressed as

$$C_{RE} = QP_{RE}\frac{r(1+r)^m}{(1+r)^m - 1} \tag{12}$$

where: C_{RE} is the replacement cost of the equipment; Q is the rated capacity of the equipment; P_{RE} is the unit replacement cost of equipment; r is the discount rate of equipment; and m is the service life of the equipment.

C_{OM} is the operation and maintenance cost for equipment, which can be expressed as

$$C_{OM} = \lambda QP \tag{13}$$

where: C_{OM} is the operation and maintenance cost of the equipment; Q is the rated capacity of the equipment; P is the unit cost of equipment; and λ is the ratio of the operation and maintenance cost of each equipment to the total cost of each equipment.

Objective function 2 can restrain the power fluctuation and build an optimal configuration model of a microgrid, including the wind–hydrogen storage as well as the energy storage system formed by the battery, which can be expressed as follows:

$$E_A = E_{\mathrm{PV}} + E_{\mathrm{W}} + E_{\mathrm{Li}} \tag{14}$$

where: E_{A} is the sum capacity for energy storage of wind and solar batteries. Because the battery has the function of charging and discharging, E_{A} has a maximum and minimum value.

$$\min E_A \le E_A \le \max E_A \tag{15}$$

Hydrogen storage system discharge:

$$E_A + E_{\mathrm{H_2}} = E_{\mathrm{L}} \tag{16}$$

Charging (hydrogen storage) of hydrogen energy storage system:

$$E_A = E_{\mathrm{H_2}} + E_{\mathrm{L}} \tag{17}$$

where: E_{H2} is the energy storage capacity of the hydrogen energy storage system; and E_{L} is the total capacity of the load.

Objective function 3 for the wind–solar hydrogen storage-independent microgrid, due to many external influences, after increasing the energy storage system, cannot completely guarantee the reliability of the system power supply [25]. The critical index of load shortage can refer to the power fluctuation problem. When the load is short of electricity, the system is more stable and reliable, and vice versa. Figure 3 shows the load power shortage operation flow in the wind–solar hydrogen storage microgrid system. E_{lps} shows a power shortage of the load, which can be expressed as

$$f_{\mathrm{L}} = \sum_{k=1}^{n} E_{lps}(k) / \sum_{k=1}^{n} E_L(k) \tag{18}$$

When power generation from wind and solar meets the load requirements, when $\Delta E > 0$, power shortage $E_{lps} = 0$, and the ΔE is judged, and different charging combination devices are selected. When ΔE is greater than or equal to the max range between the battery and hydrogen storage capacity, the maximum value of the battery and hydrogen storage is used for charging; When ΔE is greater than the maximum range of the battery capacity, the maximum value of the battery is used to charge, and the remaining electricity is used to charge the hydrogen storage. When ΔE exceeds the upper range of the hydrogen storage capacity, the maximum amount in hydrogen storage is used for charging. When ΔE becomes less than the maximum range of capacity of hydrogen storage, hydrogen storage is used for charging.

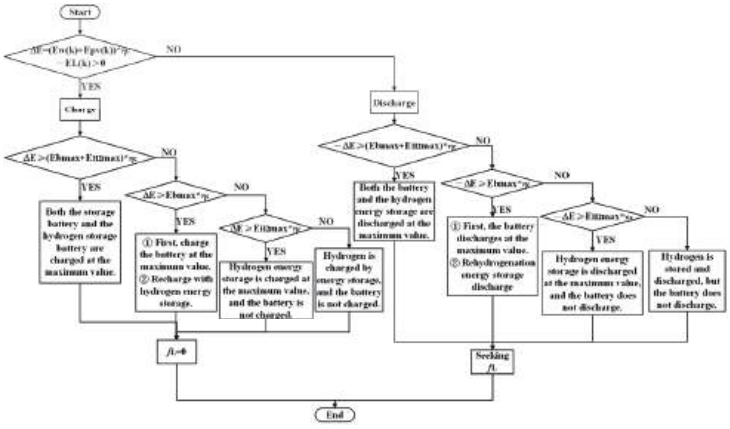

Figure 3. Operation flow chart of load power shortage.

When the amount of wind–solar power generation satisfies the load requirement, that is, $\Delta E < 0$, the wind–solar power generation is insufficient, so it is necessary to discharge the stored power to supplement the shortage of the system, judge ΔE, and choose different discharge combination distribution methods. When $-\Delta E$ is greater than or equal to the maximum range of the storage battery and hydrogen storage capacity, the maximum value of storage battery and hydrogen storage capacity is used for discharge. When $-\Delta E$ is greater than the maximum range of the battery capacity, the maximum value of the battery is employed for discharge, and the balance of the power is used to discharge on hydrogen energy storage. When $-\Delta E$ is greater than the maximum range of the hydrogen storage capacity, the maximum value of hydrogen storage is used for discharge. When $-\Delta E$ is less than the maximum range of hydrogen storage capacity, hydrogen storage is used for discharge.

3.2. Constraints

(1) Capacity constraints of hydrogen storage equipment:

$$V_{\min} \leq V \leq V_{\max} \tag{19}$$

where: $V_{\min}$ and $V_{\max}$ are the minimum and maximum capacities of the hydrogen storage tank.

(2) Capacity constraints of hydrogen storage equipment:

$$SOC \in [0, 1] \tag{20}$$

where: SOC is the operating state of charge in the energy storage system.

(3) Power load constraint:

$$P_{\mathrm{L}} = P_{\mathrm{W}} + P_{\mathrm{PV}} + P_{\mathrm{H_2}} + P_{\mathrm{Li}} \tag{21}$$

where: P_L is the power load of the system, kW.

(4) Energy waste rate constraint:

Excess power is generated in the system when the power generated in the system is greater than the load demand in the system and the maximum energy stored in the system, resulting in wasted energy. This is because the capacity allocation is unreasonable, and the power generation unit is configured with excessive output. When the system energy waste rate is less, the system capacity allocation is more reasonable, which can significantly reduce the waste of resources.

$$f_{\mathrm{L}} < f_{set} \tag{22}$$

where: f_{set} is the control range of the energy waste efficiency of the system for a setting of 0.5.

To solve the multi-objective function problem, fuzzy mathematics is used in this paper. In most cases, the objective functions may affect each other, so it is not easy to achieve simultaneous optimization. The sub-objective optimization and multi-objective are solved by fuzzy mathematics. Under the condition of satisfying all constraints, each objective function is fuzzified, and the objective function is solved based on fuzzy statistics by taking the maximum value according to the affiliation function, and the optimal solution is obtained.

In this paper, the membership function of the distributed function of half Γ decline is

$$u_k(t) = \begin{cases} 1, & F_k(t) \le F_{k\min}(t) \\ \exp(\frac{F_{k\min}(t) - F_k(t)}{F_{k\min}(t)}), & F_k(t) > F_{k\min}(t) \end{cases} \tag{23}$$

where: $F_{kmin}(t)$ is the minimum value of the single objective function $F_k(t)$ under the constraint conditions.

Under the principle of maximum affiliation, the fuzzy multi-objective optimization problem is converted into a nonlinear but targeted optimization issue, and the multi-objective function solving model becomes

$$\max u(t) = \begin{cases} u(t) \le u_1(t) \\ u(t) \le u_2(t) \\ u(t) \le u_3(t) \end{cases} \tag{24}$$

where: $u(t)$, $u_1(t)$, $u_2(t)$, and $u_3(t)$ are, respectively, the satisfaction of fuzzy optimization, the satisfaction of system total operation cost, the satisfaction of power fluctuation, and the satisfaction of load power shortage.

4. Improved Particle Swarm Optimization Algorithm

4.1. Particle Swarm Optimization

The particle swarm optimization (PSO) algorithm was inspired by the study of artificial life and was proposed as a global stochastic search algorithm in the simulation of bird flock foraging [26]. The particle swarm optimization algorithm has strong anti-interference ability, good results, fast speed, and memory function, and is also a multi-agent optimization system. Each particle can dynamically adjust according to the surrounding state to find its optimal and overall solution [27].

In the optimization process, after initializing the target population in N-dimensional space, the particles constantly update their positions and velocities, generating a new position each time and solving the next time to attain the optimal result. The iterative expression for the update rate as well as the position in the process of particle solution is

$$\begin{cases} v_i^{k+1} = \omega v_i^k + c_1 r_1 (P_M - x_i^k) + c_2 r_2 (G_M - x_i^k) \\ x_i^{k+1} = v_i^{k+1} + x_i^k \end{cases} \tag{25}$$

where: k is the number of iterations; ω is the inertia weight coefficient; ${v_i}^k$ and ${x_i}^k$ are the velocity and position of particles; c_1 and c_2 are acceleration factors; r_1 and r_2 are random numbers between [0,1]; P_M is the particle individual extreme value; and G_M is the extreme value of the population.

4.2. Improved Particle Swarm Optimization

For the particle swarm optimization algorithm, it is susceptible to problems such as falling into the local extremum and poor local search ability. To solve these problems, the particle swarm optimization algorithm is improved. A particle swarm optimization with dynamic adjustment of intrinsic weight is used, and exponential function and random

function of beta distribution [28] are used to improve it, achieve the algorithm's global search ability, and reduce the possibility of falling into local extremum.

The inertia weight ω is an essential variable among the particle swarm, determining influence degree of particle velocity on the velocity in the next iteration. The capability of global search is strong when ω is large, the capability of local search is weak, and it can easily fall into the local optimization state. With the increase in iteration times, the exponential function $e^{\frac{-k}{k_{\max}}}$ is adopted to increase the global search ability and the later search accuracy.

The improved expression for the inertia weights is

$$\omega = \omega_{\min} + (\omega_{\max} - \omega_{\min}) e^{\frac{-k}{k_{\max}}} + \sigma \times \text{betarnd}(p, q) \tag{26}$$

where: $k_{\max}$ is the maximum number of iterations; σ is the inertia adjustment factor; $\omega_{\max}$ is the initial inertia weight; $\omega_{\min}$ is the inertia weight of the maximum number of iterations.

In particle swarm optimization, the acceleration factor determines the influence of individual particle experience information and other particle experience information on the optimization trajectory. For the acceleration factor, c_1 is the global acceleration factor and c_2 is the local acceleration factor [29]. To converge faster, the acceleration factor is improved so that c_1 gradually increases and c_2 gradually decreases, thus strengthening the convergence ability of particles to the global optimum.

$$\begin{aligned} c_1 &= c_0 \sin^2\left[\frac{\pi}{2}\left(1 - \frac{k}{k_{\max}}\right)\right] \\ c_2 &= c_0 \sin^2\left(\frac{\pi}{2}\frac{k}{k_{\max}}\right) \end{aligned} \tag{27}$$

where: c_0 is the initial value.

4.3. Solution Steps

In solving the problem of optimal system capacity configuration, the paper applies the improved IDW-PSO problem solving and the flow is shown in Figure 4.

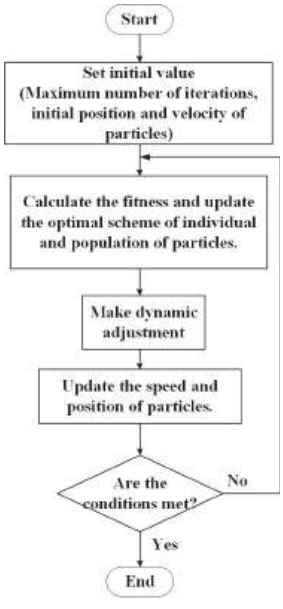

Figure 4. Solution flow.

5. Model Solving

This paper uses the improved particle swarm optimization algorithm with dynamically adjusted inertia weight to optimize the configuration of each device's hydrogen-containing hybrid energy storage microgrid capacity. Firstly, the fundamental parameter models of each device unit, including illumination intensity and load parameters, are determined—secondly, input parameters, including capacity range, conversion rate, etc. Then, the system's capacity is optimized according to the system's total operating cost. The core of the system optimal analysis method based on IDW-PSO is to determine the optimal capacity allocation under the condition of minimum total system cost, to reduce the loss of power supply probability, reduce the fluctuation of power, preventing instability of the microgrid. A flow diagram of the operation strategy is illustrated in Figure 5:

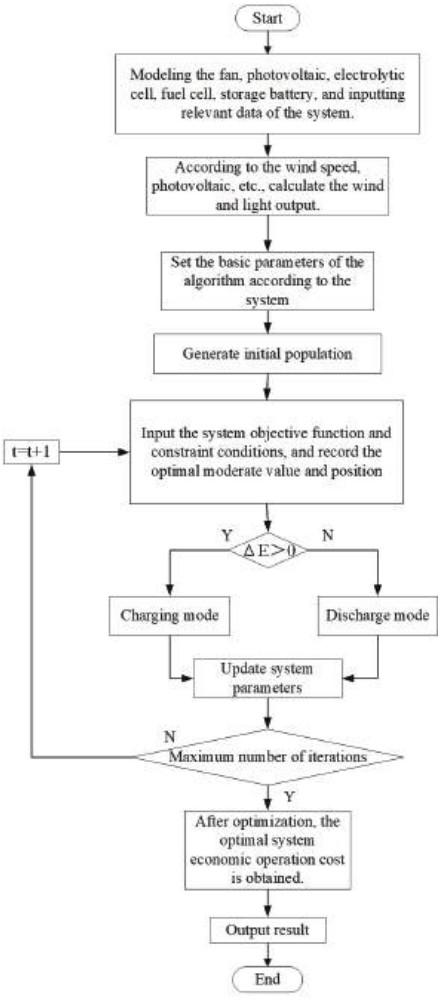

Figure 5. Operation strategy flow chart.

Step (1): Modeling each unit of the microgrid, inputting data such as wind speed and load, and inputting relevant parameters;
Step (2): Initialize the calculated output of photovoltaic and wind power generation;
Step (3): Input system constraints and objective functions;

Step (4): Calculate whether the wind and solar power generation meet the load demand ΔE, execute an objective function, and select different operation processes;
Step (5): After executing the objective function, check whether the microgrid is within the constraint range and update the relevant parameters of the system;
Step (6): Whether the maximum number of iterations has been reached. Without satisfying the condition, the program will continue to run;
Step (7): Obtain optimal economic operating cost and related data.

6. Example Analysis

Taking a wind, solar, and hydrogen microgrid system in Beijing as an example, the capacity of centralized photovoltaic units is 200 KW, and that of centralized wind turbines is 350 KW. Figure 6 shows the data on wind power, photovoltaic power generation, and load consumption on a specific day in this area. Relevant parameters of battery and hydrogen storage of the system are presented in Table 1. The optimization model of the capacity optimization of wind and hydrogen storage system constructed in this paper is solved by MATLAB.

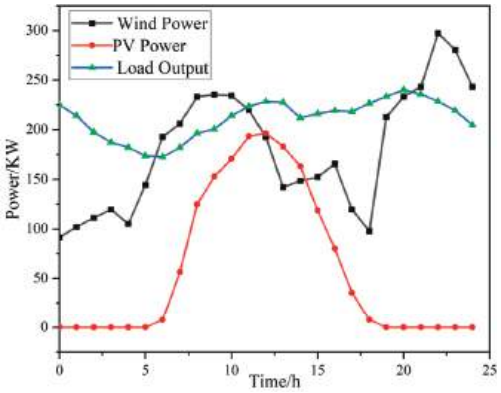

Figure 6. Wind–solar load curve.

Table 1. Example parameters.

Parameter	Value
The daily investment cost of storage battery is RMB/set	397
Battery charging efficiency/%	0.75
Battery discharge efficiency/%	0.85
The daily investment cost of hydrogen energy storage is RMB/set	534
Hydrogen storage charging efficiency/%	0.75
Hydrogen energy storage discharge efficiency/%	0.6
Efficiency of inverter/%	0.95
Type	**Service life/year**
Wind generator [30]	20
PV	25
Storage battery	15
Electrolytic bath	15
Hydrogen storage tank	25
Fuel battery	10
Inverter	20

In the whole microgrid system, the equipment at the power generation end includes a wind turbine, photovoltaic equipment, storage battery, and hydrogen energy storage system. According to a defined objective value function and various parameters, wind

turbine, photovoltaic unit, and hydrogen energy storage jointly bear the load consumption of the system and keep the power balance in real time. At 5~18 h, due to the sun's rising, the light amplitude appeared and reached the maximum peak at 12 h at noon, when the light incident angle reached the maximum. Because wind turbines are built in places with abundant wind resources, they can generate electricity 24 h a day.

Simulation Results Analysis

To comprehensively analyze the economic advantages of the energy storage operation of the system according to the improved IDW-PSO algorithm, the effects of system load shortage and power balance on the configuration results are considered, this paper sets the following four schemes for comparative analysis. Scheme 1: Choose the energy storage configuration scheme that is currently widely used. Scheme 2: The battery and hydrogen energy storage is selected as the energy storage schemes of the system for optimal configuration, and the compression factor particle swarm optimization algorithm is used. Scheme 3: Select battery and hydrogen energy storage as the system energy storage scheme for optimal configuration, and use the IDW-PSO algorithm. Scheme 4: Select battery and hydrogen energy storage as the system energy storage scheme to optimize the structure and use the improved IDW-PSO algorithm. The simulation establishes the population scale of 200, and iteration number of 200, acceleration factor initial value is set to 1.65, the battery SOC lower limit is 0.1, the SOC upper limit is 0.9, while a battery SOC initial value is set to 0.5, and a simulation results are as follows:

Upon calculation, the results of the optimized configuration under each scenario are obtained as shown in Figure 7 and Table 2. Scheme 2, Scheme 3, and Scheme 4, respectively, show the differences in iteration times, average time, and total cost caused by different operation results. The above three schemes can all be applied to the capacity optimization arrangement of hydrogen-containing composite power storage system. From a comparative analysis of Figure 7, the improved IDW-PSO algorithm can reduce the number of iterations, speed up the calculation time, and calculate the optimal system operating cost more effectively. The convergence speed and accuracy of the improved IDW-PSO are different from those of IDW-PSO and compressed factor particle swarm optimization, which reduces the local optimal solution, slow divergence speed and efficiency. The algorithms in the present paper have fewer iteration times and operation times. Compared with other algorithms, this algorithm is superior to different algorithms with the capacity optimization configuration scheme, which improves the system economy.

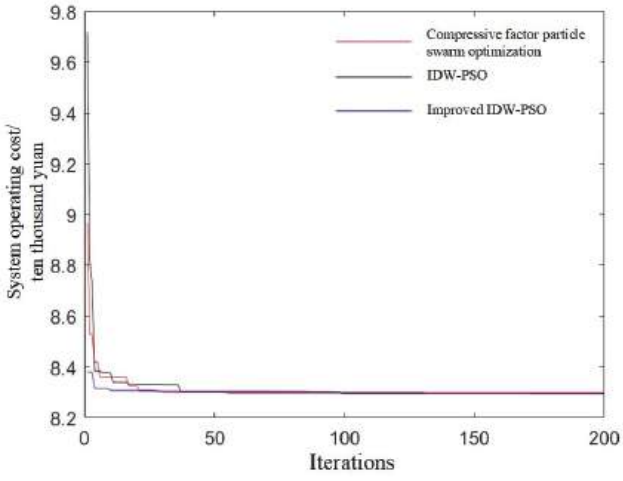

Figure 7. Comparison of convergence curves of various algorithms.

Table 2. Comparison of economic results of each algorithm.

Algorithm Name	Minimum Operating Cost/Ten Thousand Yuan	Average Number of Iterations	Average Time/s
Compressive factor particle swarm optimization [31]	8.359	150	16.12
IDW-PSO	8.328	144	15.15
Improved IDW-PSO	8.326	124	15.05

At this time, see Table 3 for the system capacity optimization configuration scheme through Scheme 1, Scheme 3, and Scheme 4.

Table 3. Optimization result.

Application Scheme	Storage Battery/Unit	Supercapacitor/Unit	Hydrogen Energy Storage/Unit	LPSP	Minimum Cost/Ten Thousand Yuan
Scheme 1	2034	28,956	—	0.0321	8.321
Scheme 3 (Before improvement)	1975	—	127	0.0297	8.359
Scheme 4 (After improvement)	1989	—	106	0.014	8.323

Table 3 shows that the optimal configuration for the microgrid system in the hybrid energy storage of supercapacitors and storage batteries in Scheme 1 is 2034 storage batteries and 28,956 supercapacitors. In this case, the system loss of power supply probability is 0.0321, and the system's total operating cost is 83,210 yuan. The optimal configuration of the Scheme 3 microgrid system before improvement is 1975 batteries and 127 hydrogen storage batteries; now the system loss of power supply probability is 0.0297, and the comprehensive operating of the system costs 83,590 yuan. The optimal configuration of the improved Scheme 4 microgrid system is 1989 batteries and 106 hydrogen storage batteries. Currently, the system loss of power supply probability is 0.014, and the system's total operating cost is 83,230 yuan. From the comparative analysis of Table 3, in the hybrid energy storage of battery and supercapacitor, the minimum price for Scheme 3 is higher than that of Scheme 1 because the cost of hydrogen energy storage is much higher than that of the supercapacitor, and the operating cost of Scheme 4 is unchanged. The scheme proposed in this paper (Scheme 4) reduces the power shortage by 56.4% in Scheme 1 and 52.9% in Scheme 3 while maintaining the running cost unchanged. Therefore, the scheme used in this paper is superior to other projects, which improves the power shortage problem caused by the system's unbalanced configuration.

From the perspective of solving the problem of the power shortage rate, the scheme in this paper has increased by 1.81% and 1.57%, respectively, compared with Scheme 1 and 3. In this paper, Beijing's average daily electricity consumption in 2022 is 210 degrees. According to this ratio, the scheme in this paper can solve the power shortage of about 3.5 degrees by storing energy. Thermal power plants need about 320 g standard coal for the first generation of electricity, saving 1 kg of typical coal = reducing emissions by 2.493 kg "carbon dioxide" = reducing emission by 0.68 kg "carbon." Then, this scheme can reduce carbon dioxide and carbon emissions by about 1019.13 kg a year in this area. Therefore, the scheme proposed in this paper has great practical significance for promoting carbon neutrality.

For wind–solar hybrid electricity generation, both wind turbines and photovoltaic units have limited capacities, and the adjustment range is relatively small. Hydrogen storage has excellent advantages for power generation because hydrogen storage can perform charging and discharging functions and has a wide range of power adjustments. As can be seen from Figure 8, from 0:00 to 6:00, since the load output is higher than the wind and light energy export power, batteries and hydrogen energy storage are discharged; At 6:00–16:00, because the load output is less than the wind and light output power, the

battery and hydrogen energy storage are charged. From 16:00 to 22:00, the battery and hydrogen energy storage discharge because the load output is greater than the wind and light output power. From 22:00 to 24:00, the battery and hydrogen energy storage charge because the load output is less than the wind and light output power.

Based on the economic and system loss of power supply probability, the system optimizes the capacity allocation scheme for wind, light, and hydrogen storage systems, thus achieving the purpose of shaving peaks and filling valleys and restraining power fluctuation. When the generating power of wind and light is greater than the load output, the hydrogen storage is optimized by the algorithm to realize "peak clipping". When the generating power of wind and light is less than the load output, the hydrogen storage system is discharged through algorithm optimization to realize "valley filling" of the system power.

Figure 8 is a power comparison chart before and after system optimization, which is, respectively, the power comparison in the whole system before and after the optimization of the hydrogen energy storage system. Before the optimal configuration of the hydrogen energy storage system, a variance of the output power of the whole system was 9171.78 kW^2. After the optimal configuration, the variance of the whole system's output power is 6582.22 kW^2, with an obvious decrease in the fluctuation of the output power. The 0-A region represents the supplementary power region where the fuel cell of the hydrogen energy storage system discharges to supplement wind power and photovoltaic power, thus achieving the function of "valley filling" for the system power. The area A-B region represents the electrolyze in the hydrogen storage system for hydrogen storage, to absorb the force of wind power and photovoltaic, and thus achieve the "peak clipping" effect on the system power. The B—C region is the same as the 0—A region, and the C—D region is the same as the A—B region. Meanwhile, the waste power of the hydrogen energy storage system before configuration is 3.7435 kW, while after configuration, it is 1.8263 kW, which significantly reduces the waste air volume.

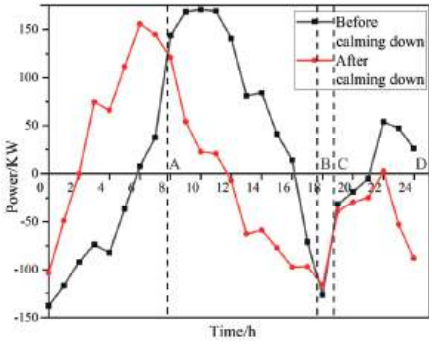

Figure 8. Power comparison diagram before and after optimization.

7. Conclusions

In this paper, the influence of wind turbines, photovoltaic systems, hydrogen storage systems, and battery output ratios on the operation of independent microgrid systems is considered, which is experimentally verified to improve the degree of renewable energy consumption.

In this paper, a particle swarm algorithm is proposed to improve the particle swarm algorithm for dynamically adjusting the inertia weights, establish a capacity optimization model, and obtain a capacity optimization scheme with the optimal system operating cost, system loss of power supply probability and system power. The integrated operation cost of the wind–solar hydrogen storage microgrid system is reduced by 0.431%, and the variance of the whole system after hydrogen storage configuration is 28.23% of that

before configuration. The power fluctuation and the rate of abandoning wind and light are reduced.

The improved IDW-PSO algorithm will improve the optimization accuracy, reduce the risk of falling into the optimal local solution, and accelerate the iteration speed so that the system can get the optimal solution faster and better. The improved algorithm is improved from 142 to 124 iterations, and the accuracy of the results is improved by 0.024%.

This scheme can reduce carbon dioxide and carbon emissions by about 1019.13 km annually in this area. When building the optimal configuration of wind and solar hydrogen storage systems, considering the economic indicators and power shortage load, the complementary relationship between hydrogen energy storage and storage battery is used to combine them and realize the suppression of power fluctuations, to achieve the purpose of peak shaving peaks and filling in valleys, to eliminate the wind and light rejection rate better, increase system economic efficiency, to reduce the amount of power shortage in the system, and strive to make the system more environmentally friendly by realizing carbon neutrality.

This paper in the microgrid capacity optimization configuration model allows for a wind-optical-hydrogen-storage microgrid system to provide some support. Starting from the energy demand side, this model can not only configure the capacity of wind, light, storage battery, and hydrogen storage, but also add more forms of energy—for example, flywheel energy storage, biological energy storage, pumped storage, and so on. The system is more environmentally friendly for the application of hydrogen energy storage, and the interconnection of electricity and hydrogen is used to realize carbon emission reduction. With the development of time and the application of hydrogen energy, the cost of hydrogen production is reduced, the difficulty of hydrogen production is reduced, and the efficiency of hydrogen production is improved. Hydrogen energy storage can optimize power and energy simultaneously in electricity storage and power generation and will be further studied. High-density, pollution-free, and sustainable utilization of hydrogen is a significant trend and the significance of efficient production. In future research, the load-side model or the model of demand-side response and load-side interaction will be further considered when optimizing the system to be closer to the actual demand.

Author Contributions: Conceptualization, G.H. and Z.W.; methodology, G.H.; software, G.H.; H.M.; validation, G.H.; formal analysis, G.H.; investigation, G.H.; H.M.; X.Z.; resources, G.H.; H.M.; data curation, G.H.; Z.W.; writing—original draft preparation, G.H.; writing—review and editing, G.H.; Z.W.; visualization, G.H.; Z.W.; supervision, Z.W.; project administration, G.H.; Z.W.; funding acquisition, none. All authors have read and agreed to the published version of the manuscript.

Funding: This research received no external funding.

Institutional Review Board Statement: Not applicable.

Informed Consent Statement: Not applicable.

Data Availability Statement: Data sharing not applicable.

Conflicts of Interest: The authors declare no conflict of interest.

References

1. Xia, D. Overview of new energy power system stability. *Sci. Technol. Innov. Appl.* **2021**, *331*, 69–72.
2. Lian, Z. Research on Capacity Allocation Optimization of Hybrid Energy Storage System of Wind Power Heat Pump Based on Particle Swarm Optimization. Master's Thesis, Shenyang University of Technology, Shenyang, China, 2021.
3. Xiong, Y.; Chen, L.; Zheng, T.; Si, Y.; Mei, S. Optimal configuration of hydrogen energy storage in low-carbon park integrated energy system considering electricity-heat-gas coupling characteristics. *Electr. Power Autom. Equip.* **2021**, *41*, 31–38.
4. Lei, S.; He, Y.; Zhang, J.; Deng, K. Optimal Configuration of Hybrid Energy Storage Capacity in a Microgrid Based on Variational Mode Decomposition. *Energies* **2023**, *16*, 4307. [CrossRef]
5. Li, W.; Jin, R.; Ma, X.; Zhang, G. Capacity Optimal Allocation Method and Frequency Division Energy Management for Hybrid Energy Storage System Considering Grid-Connected Requirements in Photovoltaic System. *Energies* **2023**, *16*, 4154. [CrossRef]
6. Xie, H.; Zheng, S.; Ni, M. Microgrid Development in China: A method for renewable energy and energy storage capacity configuration in a megawatt-level isolated microgrid. *IEEE Electrif. Mag.* **2017**, *5*, 28–35. [CrossRef]

7. Xiu, X. Research on Optimal Allocation of Energy Storage System Capacity and Life Cycle Economic Evaluation Method. Master's Thesis, China Agricultural University, Beijing, China, 2018.
8. Sun, H.; Jie, C.; Liang, S.; Hu, J.; Zang, J.; Li, Y. Optimization of double-layer energy storage capacity of wind, solar and electricity grid-connected based on improved slime mold algorithm. *Power Grid Clean Energy* **2023**, *39*, 128–136.
9. Sun, S. Study on Optimal Allocation and Economic Operation Model of Multi-Energy Microgrid. Master's Thesis, Hefei University of Technology, Hefei, China, 2012.
10. Ye, C.; Huang, M.; Wang, Y.; Sun, F.; Zhong, Y. Optimal configuration of wind-solar hybrid power supply system based on discrete probability model. *Power Syst. Autom.* **2013**, *37*, 48–54.
11. Zhou, J.L.; Wu, Y.N.; Zhong, Z.M. Modeling and configuration optimization of the natural gas-wind-photovoltaic-hydrogen integrated energy system: A novel deviation satisfaction strategy. *Energy Convers. Manag.* **2021**, *243*, 114340. [CrossRef]
12. Xu, C.; Liu, J. Application value, challenge and prospect of hydrogen energy storage in China's new power system. *China Eng. Sci.* **2022**, *24*, 89–99. [CrossRef]
13. Zhang, J.; Cheng, H.; Hu, Z.; Ma, Z.; Zhang, J.; Yao, L. Power System Probabilistic Production Simulation Including Wind Farms. *Proc. CSEE* **2009**, *29*, 34–39.
14. Yu, X. Study on Optimal Allocation and Operation of Comprehensive Energy System in the Park with Hydrogen Storage and Heat Storage. Master's Thesis, North China Electric Power University, Beijing, China, 2020.
15. Hong, F.; Xu, F.; Liu, G. Optimal capacity allocation of photovoltaic hydrogen storage system considering load demand response. *Power Supply* **2023**, *40*, 45–51. [CrossRef]
16. Zhao, B.; Zhao, P.; Hu, J.; Niu, M.; Xiao, Y.; Liu, F. Overview of Hydrogen Energy Storage Technology in Large Scale Intermittent Renewable Energy Integration Application. *Dianqi Yu Nengxiao Guanli Jishu* **2018**, *16*, 1–7.
17. Peng, S.; Zhu, L.; Dou, Z.; Liu, D.; Yang, R.; Pecht, M. Method of Site Selection and Capacity Setting for Battery Energy Storage System in Distribution Networks with Renewable Energy Sources. *Energies* **2023**, *16*, 3899. [CrossRef]
18. Liu, H.; Wang, S.; Liu, G.; Zhang, J.; Wen, S. SARAP Algorithm of Multi-Objective Optimal Capacity Configuration for WT-PV-DE-BES Stand-Alone Microgrid. *IEEE Access* **2020**, *8*, 126825–126838. [CrossRef]
19. Zhu, Z.; Guo, J.; Yu, G.; Xu, M.; Hu, Z. Bi-Layer Optimization Model for Energy Storage Systems Under Wind and PV Access. *Acta Energiae Solaris Sin.* **2022**, *43*, 443–451.
20. Du, G.; Zhao, D.; Liu, X. Research review on optimal scheduling considering wind power uncertainty. *Proc. CSEE* **2022**, *10*, 1–21.
21. Xie, X.; Wang, H.; Tian, S.; Liu, Y. Optimal capacity configuration of hybrid energy storage for an isolated microgrid based on QPSO algorithm. In Proceedings of the International Conference on Electric Utility Deregulation & Restructuring & Power Technologies, Changsha, China, 26–29 November 2015. [CrossRef]
22. Li, Q.; Zhao, S.; Pu, Y.; Chen, W.; Yu, J. Capacity Optimization of Hybrid Energy Storage Microgrid Considering Electricity-Hydrogen Coupling. *Trans. China Electrotech. Soc.* **2021**, *36*, 486–495.
23. Wang, C.; Meng, J.; Wang, Y.; Li, C. Multi-source Coordinated Control Strategy Considering Battery's SOC for Islanded DC Microgrid. *High Volt. Eng.* **2018**, *44*, 160–168.
24. Pan, X.; Liu, K.; Wang, J.; Hu, Y.; Zhao, J. Capacity Allocation Method Based on Historical Data-Driven Search Algorithm for Integrated PV and Energy Storage Charging Station. *Sustainability* **2023**, *15*, 5480. [CrossRef]
25. Xu, L.; Ruan, X.; Zhang, B.; Mao, C. Improved optimal allocation method of wind-solar hybrid power generation system capacity. *J. China Electr. Eng.* **2012**, *32*, 11.
26. Dang, X.; He, B.; Sun, J.; Kong, L.; Meng, F. Photovoltaic maximum power point tracking based on improved particle swarm optimization. *Shandong Electr. Power Technol.* **2022**, *49*, 36–43.
27. Shi, Y.H.; Eberhart, R.C. Empirical study of particle swarm optimization. In Proceedings of the Congress on Evolutionary Computation, Washington, DC, USA, 6–9 July 1999. [CrossRef]
28. Dong, H.; Li, D.; Zhang, X. A Particle Swarm Optimization Algorithm with Dynamic Adjustment of Inertia Weight. *Comput. Sci.* **2018**, *45*, 98–102+139.
29. Mao, K.F.; Bao, G.Q.; Xu, C. Particle Swarm Optimization Algorithm Based on Non-symmetric Learning Factor Adjusting. *Comput. Eng.* **2010**, *36*, 182–184.
30. Li, Y.; Guo, X.; Dong, H.; Gao, Z. Optimal Capacity Configuration of Wind/PV/Storage Hybrid EnergyStorage System in Microgrid. *Power Syst. Its Acta Autom. Sin.* **2020**, *32*, 6. [CrossRef]
31. Kennedy, J.; Eberhart, R.C. A discrete binary version of the particle swarm algorithm. In Proceedings of the 1997 IEEE International Conference on Systems, Man, and Cybernetics. Computational Cybernetics and Simulation, Orlando, FL, USA, 12–15 October 1997. [CrossRef]

electronics

MDPI

Article

Optimal Configuration of Battery Energy Storage for AC/DC Hybrid System Based on Improved Power Flow Exceeding Risk Index

Yanming Tu [1], Libo Jiang [2], Bo Zhou [1], Xinwei Sun [1], Tianwen Zheng [2,*], Yunyang Xu [1] and Shengwei Mei [2]

[1] State Grid Sichuan Electric Power Research Institute, Chengdu 610041, China; zbv_s@126.com (B.Z.); sunxiw09@126.com (X.S.)
[2] Sichuan Energy Internet Research Institute, Tsinghua University, Chengdu 610200, China; jliboc3@163.com (L.J.); Msw9821@126.com (S.M.)
* Correspondence: tianwenscu@163.com

Abstract: After the fault disturbance (DC bi-polar blocking) in the AC/DC hybrid system, when the battery energy storage system (BESS) near the fault location is used to eliminate the power transfer, some sensitive and vulnerable transmission lines still have the problem of power flow exceeding the limit value. Therefore, an optimal configuration of BESS for AC/DC hybrid systems based on power flow exceeding risk index is proposed, which is used to eliminate the impact of power transfer on transmission lines. Firstly, considering the line outage distribution factor, the power flow exceeding risk index is established, which is used to judge the sensitive and vulnerable transmission lines on the shortest path power flow after the fault in the AC/DC hybrid system. The shortest path power flow is found by using the Dijkstra algorithm; the transmission lines nodes of the shortest path power flow are selected as candidate nodes for BESS configuration. Secondly, considering the safe and stable operation capability of the transmission lines, a multi-objective optimal mathematical model of BESS configuration for the AC/DC hybrid system is established, which minimizes the annual investment cost of BESS and maximizes the sum of the power flow exceeding risk index. Finally, the CEPRI36V7 power grid model in Power System Analysis Software Package (PSASP) is used for simulation analysis to verify the effectiveness of the proposed method.

Keywords: AC/DC hybrid system; battery energy storage system (BESS); improved power flow exceeding risk index; fault disturbance; optimal configuration; line outage distribution factor

Citation: Tu, Y.; Jiang, L.; Zhou, B.; Sun, X.; Zheng, T.; Xu, Y.; Mei, S. Optimal Configuration of Battery Energy Storage for AC/DC Hybrid System Based on Improved Power Flow Exceeding Risk Index. *Electronics* **2023**, *12*, 3169. https://doi.org/10.3390/electronics12143169

Academic Editors: Luis Hernández-Callejo, Jesús Armando Aguilar Jiménez and Carlos Meza Benavides

Received: 20 June 2023
Revised: 15 July 2023
Accepted: 18 July 2023
Published: 21 July 2023

1. Introduction

With the emergence of new phenomena, such as the widespread interconnection of power grids and the high penetration of renewable energy, in the past decades, cascading failures of power systems have caused several large-scale power outages worldwide, such as the power outages in California [1], and the disconnection accident in the power grid of Europe [2], which have caused huge economic losses and threatened the stable operation of power grids.

Due to its good technical and economic benefits in large capacity, long-distance, and flexible transmission, DC transmission technology has been widely used in long-distance power transmission, power grid interconnection, and other aspects. DC transmission technology has improved the ability of friendly large-scale renewable energy and effectively solved the imbalance between regional supply and demand of electricity [3]. With the continuous development of HVDC transmission technology and the application of many DC projects, China has built a large-scale complex AC/DC hybrid power grid [4,5]. However, the DC blocking fault in the DC transmission converter station will inevitably transfer the power from the DC transmission line to the AC transmission line, which will cause the power flow of the AC transmission line to exceed the thermal stability limit power and the

cascading failure. And then blackout accidents of power systems will happen, which seriously influence the local society and economy [6,7]. Therefore, to ensure the safe and stable operation of the AC/DC hybrid system, it is of great practical significance to eliminate the out-of-limit power flow caused by DC power transfer in AC transmission lines.

The energy storage has good dynamic active and reactive power regulation capabilities, and it can adapt to operational control requirements of different time scales. To reduce the load shedding after the system failure, improve the system operation flexibility and stability, and ensures the safe, reliable, and efficient operation of the AC/DC hybrid system, the DC power transfer of the AC/DC hybrid system is eliminated by using the energy storage [8]. However, due to the different impact of DC power transfer on other lines, the energy storage near the fault location is used to eliminate the power transfer after the fault disturbance (DC bi-polar blocking) in the AC/DC hybrid system, some sensitive and vulnerable transmission lines still have the problem of power flow exceeding the limit value. It is necessary to quickly identify the sensitive line set that has a great impact on the transmission power, and configure the energy storage in this node line, which can quickly eliminate the power limit, improve the system stability, and prevent the occurrence of major accidents.

At this stage, the method of identifying the vulnerability of the power system based on the dynamic characteristics of the power grid has been widely used [9]. In [10], the risk theory assessment method is used to identify key lines by simulating the hidden fault model in the chain fault, but it requires many simulation results to determine the probability of line disconnection through tests, which increases the workload and is difficult to achieve online application and reduces the practicality of the project. In [11], a vulnerability assessment method of power grid cascading fault propagation elements based on power flow entropy is proposed, which can distinguish the vulnerability of branches from impact and consequence. This method accurately models the physical characteristics of the power grid and can improve the simulation speed by reducing the fault search space. However, there is still a contradiction between sampling times and simulation accuracy, which is difficult to achieve online application. In [12], a comprehensive index is proposed to identify the vulnerable lines, which applies the impact vulnerability to represent its impact-resistance ability and the transfer vulnerability to represent the damage caused by its removal from the system. However, this method does not consider the margin of power flow out-of-limit capacity of other lines after the disconnected transmission line. The method of identifying the sensitive and vulnerable transmission lines based on power flow exceeding risk index is proposed in [13]. The method would not have to repeatedly calculate the impedance matrix of the line disconnection and connection. But it is difficult to apply to AC/DC hybrid systems, weak power grids, and other power systems. The scope of the application is limited. The improved power flow exceeding risk index is used for AC/DC hybrid systems and other various power systems. And this method preserved the advantages of traditional methods.

The optimal configuration of BESS is mainly to determine its optimal access location and capacity, to better play its performance, and to improve the absorption rate of renewable energy. In [14,15], the proposed coordinated operational planning for wind farms with BESS is that it can reduce the impacts of wind power forecast errors. Considering the uncertainty and curtailment rate constraint of wind power, reference [16] focuses on the BESS configuration method in wind farms. In [17], the capacity allocation of BESS is used to smooth wind power fluctuations, and the BESS capacity size at different confidence levels is studied. In [18], this paper proposes a bi-level optimal energy storage system (ESS) siting and sizing algorithm to mitigate the voltage deviation in distribution networks. A capacity allocation method of BESS in secondary frequency regulation with the goal of maximum net benefit is proposed in [19]. The literature [14–19] focuses on a single application scenario, such as reducing prediction error, improving new energy consumption, and ensuring power grid stability to achieve BESS configuration, which has significant limitations. They do not fully explore their advantages in coordinated operation or multiple application

scenarios. Large BESS capacity needs to be configured, and the utilization rate of BESS is low.

References [20–22] propose an optimized configuration method for the coordinated operation of BESS and renewable energy. Collaborative configuration of distributed generation and BESS in microgrids considering the state of health is studied in [23]. In [24], considering the uncertainty of the net load, this study provides an approach to analyzing the BESS demand capacity for peak shaving and frequency regulation. In reference [25], the feasibility and compatibility of using such idle capacity and power of BESS to participate in the electricity energy market and reserve ancillary service market are explored, and a coordinated operation strategy for the three application scenarios of BESS is proposed to improve its utilization. When the power system is in a steady state, to achieve economic efficiency, ensure grid stability, and improve the utilization rate of BESS, the optimization configuration of BESS for the collaborative operation of BESS and renewable energy and multiple application scenarios of BESS services is studied by domestic and foreign scholars. But the frequent occurrence of extreme weather would seriously affect the safe and stable operation ability of the power grid. It is necessary to study the optimal configuration of BESS considering the influence of extreme weather on the power grid. This can enhance the safe and stable operation capacity of the power grid.

To cope with the impact of extreme weather, such as typhoons and freezing rain, on the power grid, BESS has been configured to improve the reliability and flexibility of the power grid in recent years. Literature [26] takes the load-shedding cost of the system under extreme events as the toughness index and studies the optimal allocation of BESS considering the toughness of the distribution network. In [27], a distributed energy storage planning model for the distribution network considering the influence of typhoon weather is established, and a decomposition collaborative solution method based on the Benders decomposition is proposed. In [28], a new quantitative index of toughness and formulates of a method of BESS planning were proposed to enhance the seismic capacity of the distribution network. Literature [29] proposed a distribution network BESS planning method considering toughness and established a two-stage robust optimization model, which can effectively ensure the uninterrupted power supply of important loads. The above literature configures BESS to improve the flexibility or toughness of the power grid by ensuring a continuous power supply of important loads in extreme weather. However, with the increase in the penetration rate of new energy, the probability of power grid failures has increased, such as exceeding the power limit of transmission lines and cascading faults in the power grid. It is very necessary to allocate BESS reasonably after a power grid failure, such as to quickly eliminate the over-limit of AC line power and improve the stability of the system; how to reasonably configure BESS after the DC locking fault occurs in the AC/DC hybrid system.

And then, a large amount of research has been conducted domestically and internationally on solution methods for BESS optimization configuration. Intelligent optimization algorithms, such as genetic algorithm [30] and particle swarm optimization (PSO) [31], have been widely applied. The optimization configuration method proposed provides a good reference for the solution in this article.

Aiming at the advantages and disadvantages of the existing research, considering the millisecond level active dynamic response capability of the BESS system, an optimized configuration of BESS in the AC/DC hybrid system based on the improved power flow exceeding risk index is proposed. Firstly, the improved power flow exceeding risk index is established to evaluate the sensitivity and vulnerability of other lines to the transferred power flow after the branch is disconnected. Secondly, the Dijkstra algorithm is used to find out the shortest path of the closed loop formed by the breaking line, and the key nodes are selected as the candidate sites for BESS by calculating the improved power flow exceeding risk index of the shortest path. Finally, a multi-objective function with the maximum sum of improved power flow exceeding risk index and the minimum annual investment cost of BESS is established, and particle swarm optimization (PSO) is used to obtain the optimal

configuration scheme of BESS in the AC/DC hybrid system. Meanwhile, the BESS system adopted the active power control strategy, including plant-level control and local control, which quickly eliminates the power exceeding the limit of the AC line and suppresses the power fluctuation of the power grid.

This paper is organized as follows: The identification of sensitive and vulnerable lines is talked about in Section 2. The mathematical model for the optimal allocation of BESS is proposed in Section 3. The Model-solving method is given in Section 4. In Section 5, the effectiveness and feasibility performance of the proposed method are examined on the CEPRI36V7 grid model. Section 6 is the conclusion.

2. Identification of Sensitive and Vulnerable Lines

2.1. Line Outage Distribution Factor

If line A of the AC/DC hybrid system is faulty, and it causes the line disconnection (DC line causes blocking fault, etc.), which causes the transfer of active power flow in the system, that is, the active power flow of other lines is changed. The relationship between the change of normal line power flow and the original power flow of the disconnected line can be expressed by the Line Outage Distribution Factor (LODF) [32]:

$$D_{R-A} = \frac{\Delta P_{R-A}}{P_A} \tag{1}$$

where ΔP_{R-A} is the change of line R's active power flow after line A is disconnected; D_{R-A} is the LODF that causes the change of line R's active power flow after line A is disconnected; P_A is the steady-state initial active power of line A.

Assuming that the nodes at both ends of line A are i and j, and the injected active power remains unchanged before and after disconnection, the change of node active power flow caused by line A disconnection is

$$\Delta P = [0 \cdots 1 \cdots -1 \cdots 0]^T P_A = M_A P_A \tag{2}$$

where M_A is the node-branch associated $n \times 1$ order column vector of branch A, and the row corresponds to the node number.

The $n \times 1$ order change $\Delta\theta$ of node voltage phase angle caused by line A disconnection. $\Delta\theta$ can be expressed as

$$\Delta\theta = \left(B - M_A x_A^{-1} M_A^T\right)^{-1} M_A P_A \tag{3}$$

where B is the $n \times n$ order admittance matrix; the admittance matrix is sparse type; x_A is the reactance of line A.

Then, the change of active power flow of branch R ($R \neq A$) caused by line A disconnection is

$$\Delta P_{R-A} = \frac{M_R^T \Delta\theta}{x_R} = D_{R-A} P_A = \frac{M_R^T \left(B - M_A x_A^{-1} M_A^T\right)^{-1} M_A P_A}{x_R} \tag{4}$$

where M_R is the node-branch associated $n \times 1$ order column vector of branch R; x_R is the 1 order reactance of line R.

Let $B^{-1} = X$, after simplification, the expression of D_{R-A} is:

$$D_{R-A} = \frac{X_{R-A}/x_R}{1 - X_{A-A}/x_R} \tag{5}$$

Among them,

$$X_{R-A} = M_R^T X M_A \tag{6}$$

$$X_{A-A} = M_A^T X M_A \tag{7}$$

where X is the $n \times n$ order impedance matrix; X_{A-A}, X_{R-A} is the 1 order self-impedance and mutual impedance between nodes of port R and port A, respectively.

After the DC blocking fault occurs in the AC/DC hybrid system, the influence of DC power transfer on the AC line can be measured by calculating the LODF of the AC line.

2.2. The Improved Power Flow Exceeding Risk Index

The improved power flow exceeding risk index takes into account the impact of power transfer on other lines and the margin of the out-of-limit capacity of line power flow. After considering the margin of the out-of-limit capacity of line power flow, it is not necessary to consider the problem of reverse power flow of other lines caused by power flow transfer separately, which reduces unnecessary calculations, and can better reflect the sensitivity and vulnerability of other lines, and identify the sensitive and vulnerable lines in the system. Under the change of power flow of line R caused by the disconnection of line A, the margin of the out-of-limit capacity of the power flow of line R can be expressed as follows:

When $D_{R-A} < 0$, this is true, the expression of line power flow out-of-limit capacity margin is as follows:

$$\Delta P' = \begin{cases} |P_{R,\max} + P_R| & P_R \geq 0 \\ |-P_{R,\max} - P_R| & P_R < 0 \end{cases} \tag{8}$$

When $D_{R-A} > 0$, this is true, the expression of line power flow out-of-limit capacity margin is as follows:

$$\Delta P' = \begin{cases} |-P_{R,\max} + P_R| & P_R \geq 0 \\ |P_{R,\max} - P_R| & P_R < 0 \end{cases} \tag{9}$$

Combined with the LODF, the improved power flow exceeding risk index is given to evaluate the sensitivity and vulnerability of other lines to the transferred power flow after the branch break, as follows:

$$\Phi_{R-A} = \frac{\Delta P'}{D_{R-A} \cdot P_{\mathrm{A,max}}} \tag{10}$$

where $P_{\mathrm{A,max}}$ is the thermal stability limit value of the breaking line.

After a DC blocking fault occurs in the AC/DC hybrid system, the sensitivity and vulnerability of each AC line can be effectively evaluated by calculating the improved power flow exceeding risk index of each AC line. The smallest the improved power flow exceeding risk index of each AC line, the lower its ability to receive the transferred power flow, and the higher the improved power flow exceeding risk index. This paper selects the sensitive vulnerability line when the absolute value of the improved power flow exceeding risk index is less than 0.5. Secondly, after the DC blocking fault occurs in the AC/DC hybrid system, the DC power flow is mainly transferred to the shortest path that forms a closed loop with the DC line, so the shortest path set of DC power transfer needs to be searched.

2.3. The Shortest Path Search Based on the Dijkstra Algorithm

Using the knowledge of graph theory, the AC/DC hybrid system is simplified and abstracted into a graph G (V, E), where V represents the bus set in the grid, E represents the line set between buses, and the line side weight value is the line reactance. Then, the shortest path algorithm related to graph theory is adopted.

The shortest path search algorithms in graph theory include the Dijkstra algorithm, Floyd algorithm, etc. The Dijkstra algorithm has small time complexity and is easy to expand; the Floyd algorithm has high time complexity and space complexity, which increases the calculation amount. Its advantage is that it can be used to search the shortest path of the line with negative weight. Because of the scalability of the Dijkstra algorithm and the fact that there are no branches with negative weights in the graph, and to meet the requirements of fast calculation, the shortest path search based on the Dijkstra algorithm is adopted.

After the DC blocking fault occurs in the AC/DC hybrid system, the shortest path forming a closed loop with the DC line can be searched by using the Dijkstra algorithm, and then the sensitive AC line can be identified by combining the improved power flow exceeding risk index, and the power input node of the sensitive, vulnerable line is used as the candidate location for configuring BESS.

3. The Mathematical Model for Optimal Allocation of BESS

3.1. Objective Function

After the DC locking fault occurs in the AC/DC hybrid system, when the system optimizes the configuration of BESS, it should also have a certain economy while eliminating the power flow over-limit on the sensitive and vulnerable lines. Therefore, the multi-objective function of the optimal configuration of BESS in the AC/DC hybrid system is as follows:

$$\max\Gamma = \sum_{k=1}^{K} \left| \frac{\Delta P'}{D_{k-A} \cdot P_{\mathrm{dc-max}}} \right| \tag{11}$$

$$\min G_{inv} = \frac{r(1+r)^y}{(1+r)^y - 1} \cdot (c_1 \cdot P_e + c_2 \cdot E_e) \tag{12}$$

where Γ is the sum of the improved power flow exceeding risk index of sensitive vulnerable lines after DC blocking fault; D_{k-A} is the LODF; $P_{\mathrm{dc-max}}$ is the thermal stability limit value of DC line; G_{inv} is the annual investment cost of BESS; c_1, c_2 are the unit power cost and capacity cost of BESS; P_e, E_e are the rated power and rated capacity of the BESS, respectively; r is the annual interest rate of the fund; Y is the life cycle of BESS; K is the sensitive vulnerability line.

3.2. Constraint

(1) Power balance constraints

$$\sum_{m=1}^{M} P_{G,m} + \sum_{n=1}^{N} P_{L,n} + \sum_{s=1}^{S} P_{B,s} = 0 \tag{13}$$

where $P_{G,m}$, $P_{L,n}$, $P_{B,s}$ are, respectively, the output of generator m, the required power of load n, and the charging and discharging power of BESS s; S is the quantity of configured BESS in the system; M and N are the number of generators and the number of loads in the system.

(2) Line loss constraint

$$P'_R U_R^2 \geq R_R \cdot (P_R'^2 + Q_R'^2) \tag{14}$$

where P'_R, Q'_R are the active power and reactive power transmitted by the receiving end of the R line, respectively; R_R is the resistance of the R line; U_R is the voltage amplitude of the receiving terminal node of the Rth line.

(3) Generator power constraint

$$\overline{P}_{G,m} \leq P_{G,m} \leq \underline{P}_{G,m} \tag{15}$$

where $\overline{P}_{G,m}$, $\underline{P}_{G,m}$ are the upper and lower limits of generator output, respectively.

(4) Line power constraint

$$\overline{P}_{L,m} \leq P_{L,m} \leq \underline{P}_{L,m} \tag{16}$$

where $\overline{P}_{L,m}$, $\underline{P}_{L,m}$ are the upper and lower limits of the active power of the transmission line.

(5) Capacity constraints of BESS

$$S_{\min} \leq S_r \leq S_{\max} \tag{17}$$

where $S_{\min}$, $S_{\max}$ are the minimum and maximum capacities of BESS, respectively.

(6) Power constraint of BESS charge and discharge

$$\begin{array}{c} -P_{r,\max} \le P_r^c \le 0 \\ 0 \le P_r^d \le P_{r,\max} \end{array} \tag{18}$$

where $P_{r,\max}$ is the maximum value of BESS discharge power; P_r^c, P_r^d are the charge power and discharge power of the BESS system, respectively.

4. Model-Solving Method

The sharing of information among the entire population is beneficial for the population towards a better position in genetic algorithms. Only the best individual's information is shared in PSO, and the entire search process is tracking the optimal solution. So, the PSO algorithm has faster convergence than the genetic algorithm. And due to its advantages of high accuracy and fast convergence, the PSO algorithm is widely used in BESS capacity configuration [33,34]. Therefore, this article chooses the PSO algorithm for solving BESS capacity configuration.

To reasonably obtain the location of BESS, the PSO algorithm is used to solve for the optimal capacity of BESS, and the optimal location of BESS is selected from candidate nodes. Meanwhile, BESS adopts the active power control strategy, including plant-level control and local control, which quickly eliminates the power exceeding the limit of the AC line, suppresses the power fluctuation of the power grid, and ensures the safe and stable operation ability of the power grid.

The specific process is shown in Figure 1, and the solution steps are as follows:

(1) The graph obtained by abstracting the power grid is G0, and the reactance value of each line in the power system is taken as the weight value of each side;

(2) After DC blocking occurs in the converter station at the sending end, the Dijkstra algorithm is used to find the shortest path between the converter station and the designated node;

(3) The branch set contained in the target source point and destination point are combined to obtain the branch set of power flow transfer;

(4) Calculate the improved power flow exceeding risk index of all branches in the power flow transfer branch set, and select the branches whose absolute value of the improved power flow exceeding risk index is less than 0.5 to form the main branch set;

(5) For the lines in the main branch set, if there is a reverse flow and the branch flow meets $|P'_R| \le |P_R|$, it will be removed from the main branch set (P'_R is the branch flow after the line is disconnected);

(6) Input parameters. Input PSO controlling variables of the original parameters. Set PSO algorithm parameters: the maximum iteration number is 300, and the population size is 200;

(7) Initialize the population. According to Equation (19), the N solutions are generated, such as the energy storage power and capacity, and they also are guaranteed to satisfy the condition. The objective function value is calculated for all the scenes using Equations (11) and (12).

$$x_{ij} = x_j^{\min} + rand() \cdot (x_j^{\max} - x_j^{\min}) \tag{19}$$

where i = 1, 2, ... , N is a D-dimension vector; j = 1, 2, ... , d; $rand()$ represents random numbers between 1 and 0; $x_j^{\max}$, $x_j^{\min}$ are the maximum and minimum values of particles, respectively;

(8) Calculate the fitness value for particles by using (20). It is updated local optimal position and global optimal position by using Equations (21) and (22).

$$p_i = \frac{F_i}{\sum_{k=1}^{N} F_k} \tag{20}$$

$$v_{ij}(t+1) = w \times v_{ij}(t) + c_1 \times rand() \times \left(p_{ij}(t) - x_{ij}(t)\right) + c_2 \times rand() \times \left(p_{gj}(t) - x_{ij}(t)\right) \tag{21}$$

$$x_{ij}(t+1) = x_{ij}(t) + v_{ij}(t+1) \tag{22}$$

where F_i is the corresponding fitness value for particles I; $v_{ij}(t+1)$, $v_{ij}(t)$ are the velocity of the ith particle at $t+1$, t times, respectively; w is the inertia factor; $w = 0.8$, c_1 and c_2 are the learning rate; $c_1 = 0.9, c_2 = 0.9$. $p_{ij}(t)$, $p_{gj}(t)$ respectively represent the individual optimal value and the global optimal value of particles;

(9) Output optimal solution. If the iteration number is greater than the set value, then output the Parote optimal. Otherwise, return to step (7).

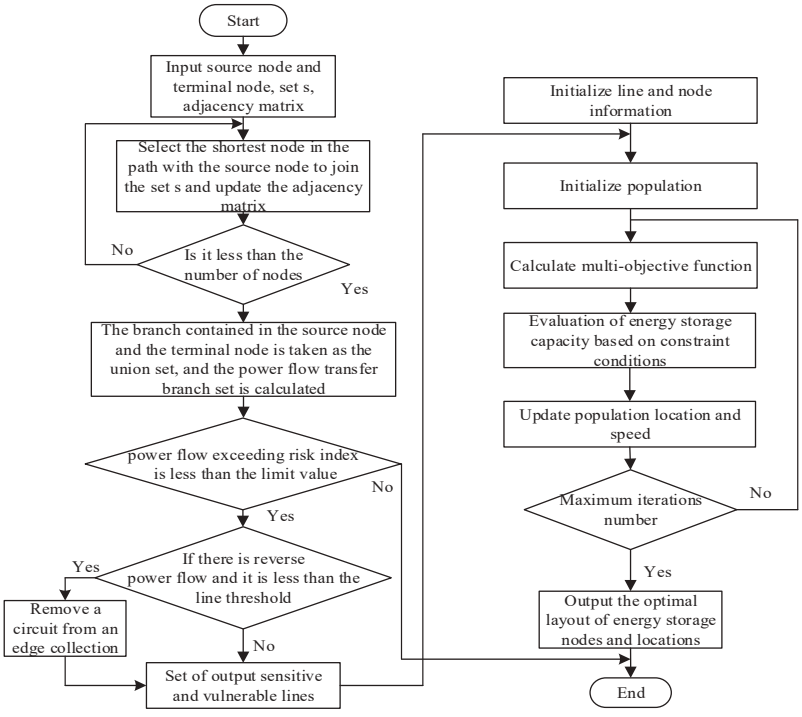

Figure 1. Solution flow of BESS optimization configuration.

5. Simulation Analysis

5.1. Parameter Design

The CEPRI36V7 power grid model in the power system analysis comprehensive program (PSASP) was used for simulation analysis to verify the effectiveness of the proposed BESS configuration strategy. The parameters of the CEPRI36V7 model are referred to in reference [35]. The topology of the CEPRI36V7 model is shown in Figure 2. The parameters of the CEPRI36V7 model are referred to in reference [35]. The node parameters, generator parameters, and branch parameters of the CEPRI36V7 model are shown in Tables 1–3, respectively.

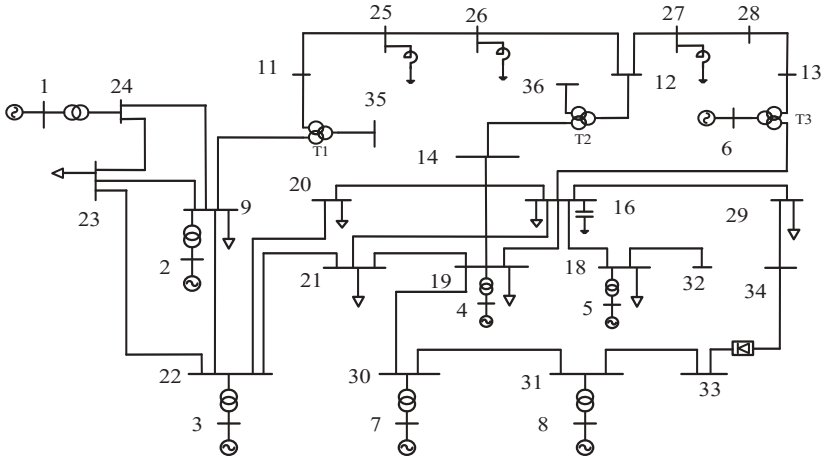

Figure 2. The power grid structure of CEPRI36V7.

Table 1. The node parameters of the CEPRI36V7 model.

Bus_i	Type	P_d/MW	Q_d/Mvar	Base/kV	Bus_i	Type	P_d/MW	Q_d/Mvar	Base/kV
1	3	0	0	10.5	19	1	86.4	66.2	220
2	1	0	0	20	20	1	71.9	47.4	220
3	2	0	0	10.5	21	1	70	50	220
4	1	0	0	15.7	22	1	226.5	169	220
5	1	0	0	10.5	23	1	287	144	220
6	2	0	0	10.5	24	1	0	0	220
7	2	0	0	10.5	25	1	0	0	500
8	2	0	0	10.5	26	1	0	0	500
9	1	376	221	220	27	1	0	0	500
10	1	0	0	20	28	1	0	0	500
11	1	0	0	500	29	1	520	10	220
12	1	0	0	500	30	1	0	0	220
13	1	0	0	500	31	1	0	0	220
14	1	0	0	220	32	1	0	0	220
15	1	0	0	20	33	1	0	0	220
16	1	500	230	220	34	1	0	0	220
17	1	0	0	20	35	1	0	0	0
18	1	430	220	220	36	1	0	0	0

Table 2. The generator parameters of the CEPRI36V7 model.

Bus	P_g/MW	Q_g/Mvar	V_g/p.u.
1	0	0	1
2	600	360	1
3	310	0	1
4	160	70	1
5	430	334	1
6	−1	0	1
7	225	0	1
8	306	0	1

Table 3. The branch parameters of the CEPRI36V7 model.

Fbus	Tbus	r	x	b	Ratio	Fbus	Tbus	r	x	b
11	25	0	0.0001	0	0	31	32	0	0.0001	0
12	26	0	0.0001	0	0	9	22	0.0559	0.218	0.3908
12	27	0	0.0001	0	0	9	23	0.0034	0.0131	0
13	28	0	0.0001	0	0	9	24	0.0147	0.104	0
14	19	0.0034	0.02	0	0	24	1	0	0.015	0
16	18	0.0033	0.0333	0	0	9	2	0	0.0217	0
16	19	0.0578	0.218	0.3774	0	22	3	0	0.0124	0
16	20	0.0165	0.0662	0.4706	0	19	4	0	0.064	0
16	21	0.0374	0.178	0.328	0	18	5	0	0.0375	0
16	29	0	0.0001	0	0	30	7	0	0.0438	0
18	34	0	0.001	0	0	31	8	0	0.0328	0
19	21	0.0114	0.037	0	0	12	15	0	0.018	0
19	30	0.0196	0.0854	0.162	0	6	17	0	0.0337	0
20	22	0.0214	0.0859	0.6016	0	9	10	0	−0.002	0
21	22	0.015	0.0607	0.4396	0	14	15	0	−0.002	0
22	23	0.0537	0.19	0.3306	0	13	17	0	0.01	0
23	24	0.0106	0.074	0	0	11	10	0	0.018	0
25	26	0.0033	0.0343	3.7594	0	36	15	0	0.0001	0
27	28	0.00245	0.0255	2.79	0	16	17	0	0.001	0
29	33	0	0.0001	0	0	35	10	0	0.001	0
30	31	0	0.0001	0	0					

The capacity of the CEPRI36V7 power grid is 2600 MW, and nodes 33 to 34 are DC transmission lines, with a DC transmission capacity of 2 × 200 MW; DC power flows from 33 nodes to 34 nodes, and nodes 10, 15, and 17 in the system are the central nodes of three-winding transformers T1, T2, and T3.

This article uses lithium BESS. The maximum rated power and capacity of the total installed BESS are 800 MW and 1600 MW. h respectively, and the cost coefficients are 1500 yuan/kW and 2000 yuan/kWh. The charge and discharge rate of BESS is 0.5 C.

5.2. Sensitive Line Identification

The simplified structure of the power grid is shown in Figure 3. The red line represents the DC bipolar locking fault line. The blue line and black line represent the non-shortest path AC line. The green line represents the shortest path AC line. The converter station of node 33 has a DC bipolar locking fault, and the Dijkstra algorithm is used to obtain the shortest path composed of node 33 and node 34, namely: 33, 31, 30, 19, 14, 15, 12, 27, 28, 13, 17, 16, 29, and 34, a total of 13 AC lines. The power change curve of the AC line is shown in Figures 4 and 5 after the converter station of node 33 has a dual-machine locking fault at 5 s.

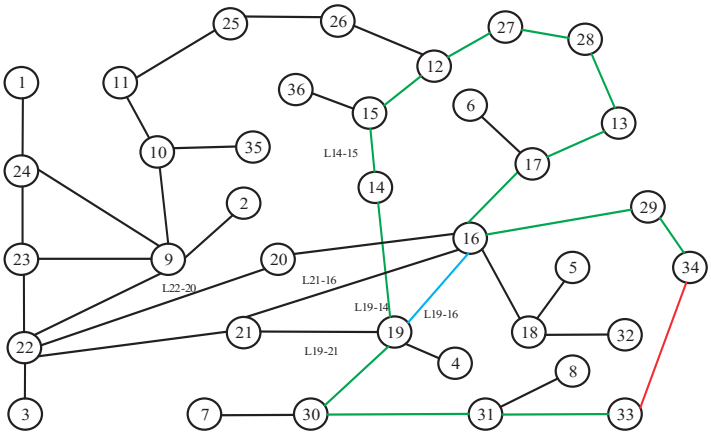

Figure 3. The simplified grid structure of CEPRI36V7.

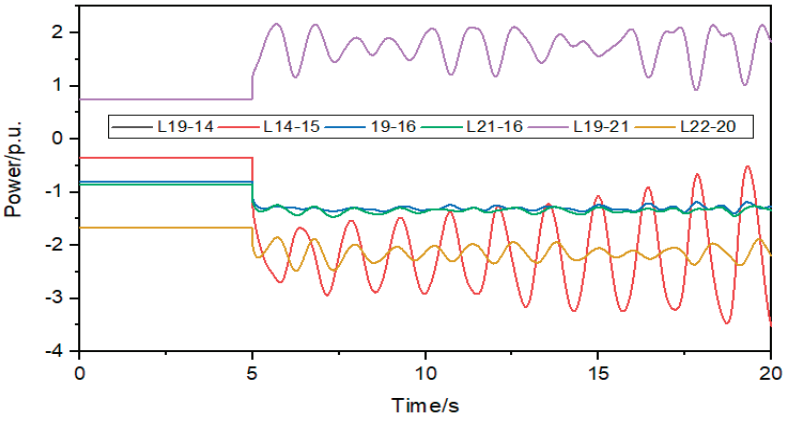

Figure 4. Change curve of AC line after DC blocking.

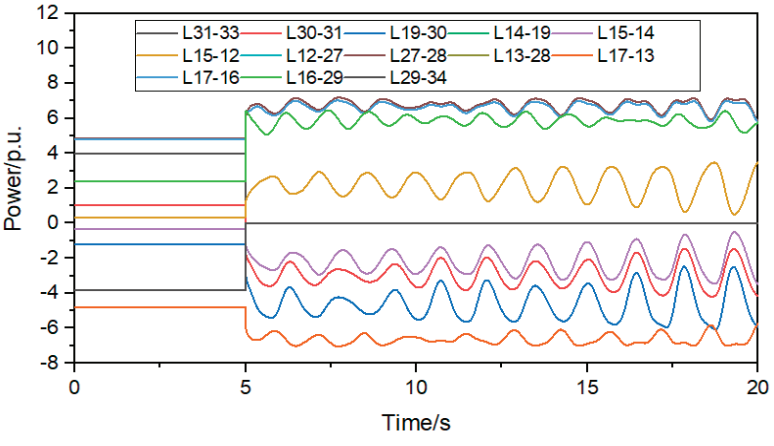

Figure 5. Power change curve of the shortest path line after DC blocking.

It can be seen from Figure 4 that the power variation of lines L19-14 and L14-15 is the largest, with a power variation greater than 2 p.u., and the power variation of other lines is less than 1.3 p.u. It can be seen from Figure 5 that the power variation of the AC line on the shortest path is greater than 1.5 p.u. It can be seen that after the DC bipolar locking fault, the power flow is mainly in the shortest path composed of node 33 and node 34.

The improved power flow exceeding risk index of each line on the shortest path is shown in Table 4 after the bipolar locking fault occurs at the converter station of node 33 at 5 s. From Table 4, it can be seen that the absolute value of the improved power flow exceeding risk index of lines L30-31, L19-30, L14-19, L15-14, L15-12, L17-13, L17-16, and L16-29 is less than 0.5, so the above AC lines are sensitive and vulnerable. Since node 15 and node 17 are the central nodes of the three-winding transformer, and BESS is configured at the sending end of the AC line, the candidate nodes for BESS are 31, 19, 14, and 16.

Table 4. The improved power flow exceeding risk index of the shortest path.

AC Line	Initial Power/p.u.	Power after Fault/p.u.	LODF	The Improved Power Flow Exceeding Risk Index
L31-33	4.00	0.00	−1.00	1.67
L30-31	1.02	−2.98	−1.00	0.41
L19-L30	−1.20	−5.17	−1.00	0.70
L14-19	−0.34	−2.94	−0.82	0.42
L15-14	−0.34	−2.94	−0.65	0.32
L15-12	0.34	2.94	0.65	0.14
L12-27	4.86	7.18	0.58	1.29
L27-28	4.86	7.18	0.58	1.29
L13-28	−4.61	−7.04	−0.61	3.70
L17-13	−4.80	−7.04	−0.56	3.22
L17-16	4.79	7.01	0.56	0.36
L16-29	2.38	6.20	1.02	0.32
L29-L34	−3.82	0.00	−0.96	2.15

5.3. Optimization Configuration Results of Single BESS

To verify that the BESS is configured in the sensitive and vulnerable line, the BESS to improve the improved power flow exceeding risk index is the best. Firstly, the PSO algorithm is used to obtain a set of Pareto solutions of the BESS configuration capacity and location, as shown in Table 5.

Table 5. The single BESS configuration capacity and location.

ESS Power/MW	ESS Capacity/MW·h	ESS Location	Annual Investment Cost/Million Yuan	the Sum of the Improved Power Flow Exceeding Risk Index
541.15	541.15 × 2	31	443.47	24.18
276.31	276.31 × 2	16	226.44	18.29
391.88	391.88 × 2	16	321.15	19.47

From Table 5, there are two sets for the BESS configuration at node 16. There are two sets for the BESS configuration at node 16. The annual investment cost of BESS is 226.44 million yuan and 321.15 million yuan. Similarly, the BESS configuration also obtains the optimal solution at 31 nodes; the annual investment cost of BESS is 226.44 million yuan

and 443.47 million yuan. Therefore, we obtained the lowest annual investment costs in Pareto solutions in Table 2.

To verify that the PSO algorithm has obtained the optimal solution, the iterative convergence curve comparison between PSO and GA (Genetic algorithm) is shown in Figure 6. According to the iterative convergence curve of Figure 6, it can conclude that the PSO has fewer convergence times, more effectively avoid local convergence, and has better stability than the GA. We know that the PSO algorithm can obtain the optimal solution.

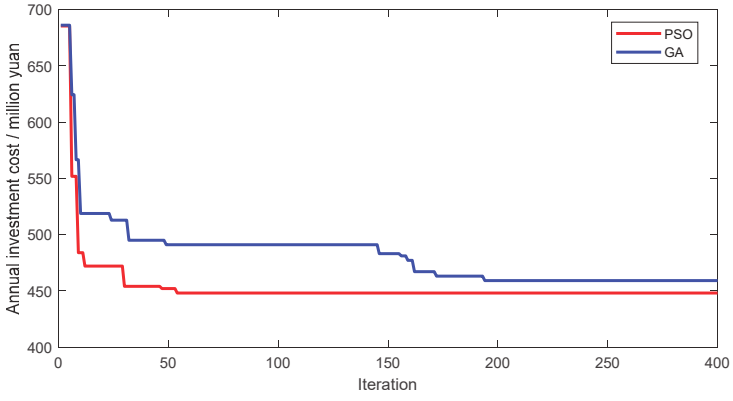

(**a**)

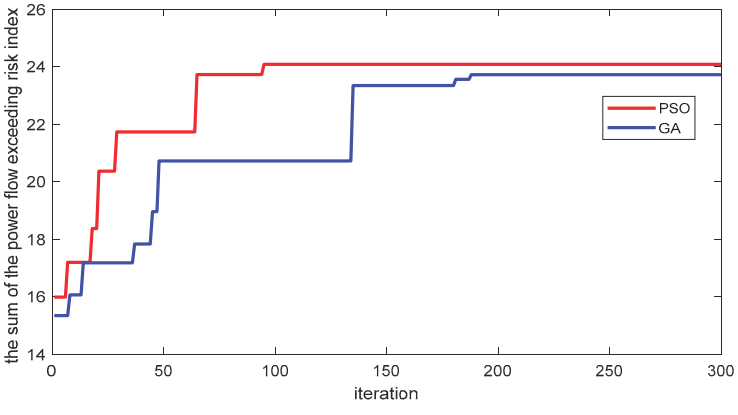

(**b**)

Figure 6. The iterative convergence curve. (**a**) Iterative convergence curve of energy storage annual investment cost. (**b**) Iterative convergence curve of the sum of improved power flow exceeding the risk index.

Then, the following three scenarios are compared and analyzed: (1) the BESS is configured in a node in the sensitive and vulnerable line, and 31 nodes are selected in this paper; (2) the BESS is configured in the nodes in the shortest path except for the sensitive and vulnerable lines. This paper selects 27 nodes; (3) 21 nodes are selected for other nodes with BESS configured outside the shortest path. Under the three conditions, each node is connected to 541.15 MW of BESS, and the improved power flow exceeding risk index of sensitive and vulnerable AC lines is shown in Tables 6–8.

Table 6. The improved power flow exceeding risk index of the AC line with vulnerability after node 31 is connected to BESS.

AC Line	Initial Power/p.u.	Power after Fault/p.u.	LODF	The Improved Power Flow Exceeding Risk Index
L30-31	1.02	−1.68	−0.68	−0.71
L14-19	−0.34	−1.3	−0.41	−0.83
L15-14	−0.34	−1.3	−0.24	−0.87
L15-12	0.34	1.3	0.24	0.39
L17-16	4.79	6.37	0.39	0.51
L16-29	2.38	6.79	1.1	0.29

Table 7. The improved power flow exceeding risk index of the AC line with vulnerability after node 27 is connected to BESS.

AC Line	Initial Power/p.u.	Power after Fault/p.u.	LODF	The Improved Power Flow Exceeding Risk Index
L30-31	1.02	−2.98	−1	−0.48
L14-19	−0.34	−4.17	−1.13	−0.3
L15-14	−0.34	−4.17	−0.96	−0.22
L15-12	0.34	4.17	0.96	0.1
L17-16	4.79	6.36	0.39	0.51
L16-29	2.38	6.69	1.08	0.3

Table 8. The improved power flow exceeding risk index of the AC line with vulnerability after node 21 is connected to BESS.

AC Line	Initial Power/p.u.	Power after Fault/p.u.	LODF	The Improved Power Flow Exceeding Risk Index
L30-31	1.02	−2.98	−1	−0.48
L14-19	−0.34	−1.69	−0.51	−0.67
L15-14	−0.34	−1.69	−0.34	−0.61
L15-12	0.34	1.69	0.34	0.27
L17-16	4.79	6.9	0.53	0.38
L16-29	2.38	7.03	1.16	0.28

It can be seen from Tables 6–8 that after the BESS is arranged at the 31 nodes of the sensitive and vulnerable line, the risk index of tidal current out-of-limit of lines L31-30, 19-14, L14-15 and L17-16 exceeds 0.5, and only the risk index of tidal current out-of-limit of lines L15-12 and L16-29 is lower than 0.5; After the BESS is arranged at 27 nodes, only the improve power flow exceeding risk index of line L17-16 exceeds 0.5, and the improve power flow exceeding risk index of other lines does not exceed 0.5; After the BESS is configured at node 21, the improve power flow exceeding risk index of lines 19-14 and L14-15 exceeds 0.5, and the improve power flow exceeding risk index of other lines does not exceed 0.5; It can be seen that the BESS configuration on the sensitive and vulnerable lines has greatly improved the safe operation ability of AC lines.

It can be seen from Figures 7–9 that after the BESS is incorporated into 31 nodes, it is helpful to suppress the oscillation of line power, and the change of line power is lower than 1.5 p.u; after the BESS is incorporated into 27 nodes, the oscillation of line power is increased, and the power variation of some lines is greater than 1.5 p.u; after the BESS is

connected to 21 nodes, the power of AC lines on the shortest path changes irregularly, and the power of some lines increases gradually after 17 s, greatly reducing the system stability. It can be seen that only when the BESS is connected to the sensitive and vulnerable lines that the safe and stable operation capacity of the AC lines can be effectively improved.

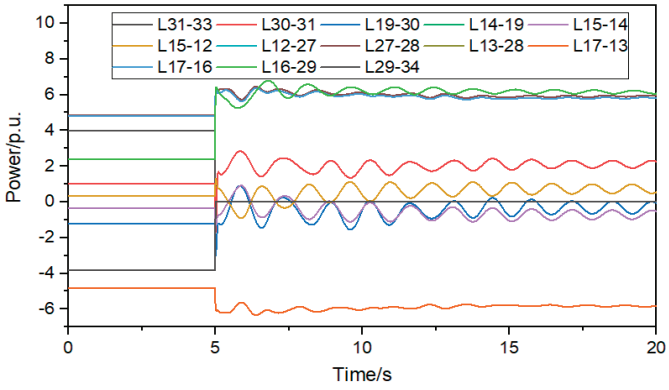

Figure 7. The shortest path power change curve after BESS is connected to node 31.

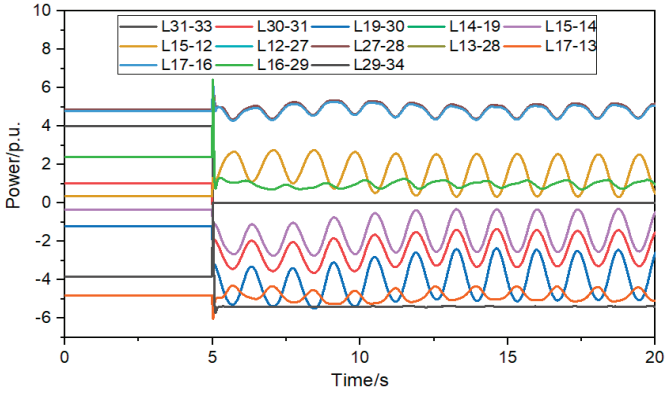

Figure 8. Shortest path power change curve after BESS access node 27.

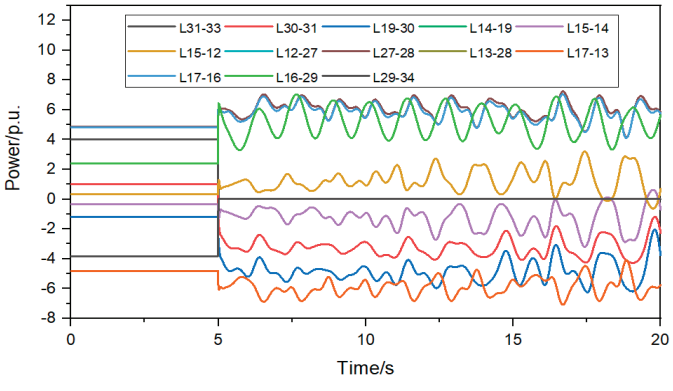

Figure 9. The shortest path power change curve after BESS is connected to node 21.

5.4. Optimization Configuration Results of Multi-BESS

When the system configures two and three BESS, a set of Pareto solutions is shown in Table 9. The improved power flow exceeding risk index of sensitive and vulnerable AC lines after configurations two and three BESS is shown in Tables 10 and 11. The shortest path power change curve after BESS is shown in Figures 10 and 11.

Table 9. The multi-BESS configuration capacity and location.

Nodes	BESS Power/MW	ESS Capacity/MW·h	BESS Location	Investment and Construction Costs/Million Yuan	the Sum of the Improved Power Flow Exceeding Risk Index
2 nodes	88.09	88.09 × 2	29	248.89	17.78
	299.25	299.25 × 2	31		
3 nodes	88.09	88.09 × 2	29	248.89	17.78
	11.87	11.87 × 2	19		
	287.38	287.38 × 2	31		

Table 10. The improved power flow exceeding risk index of sensitive and vulnerable AC lines after the configuration of two BESS.

AC Line	Initial Power/p.u.	Power after Fault/p.u.	LODF	The Improved Power Flow Exceeding Risk Index
L30-31	1.02	−2.98	−1	−1.38
L14-19	−0.34	−4.17	−1.13	−1.48
L15-14	−0.34	−4.17	−0.96	−0.5
L15-12	0.34	4.17	0.96	0.5
L17-16	4.79	6.36	0.39	0.58
L16-29	2.38	6.69	1.08	0.5

Table 11. The improved power flow exceeding risk index of sensitive and vulnerable AC lines after configuration three BESS.

AC Line	Initial Power/p.u.	Power after Fault/p.u.	LODF	The Improved Power Flow Exceeding Risk Index
L30-31	1.02	−2.98	−1	−1.24
L14-19	−0.34	−1.69	−0.51	−1.48
L15-14	−0.34	−1.69	−0.34	−0.5
L15-12	0.34	1.69	0.34	0.5
L17-16	4.79	6.9	0.53	0.58
L16-29	2.38	7.03	1.16	0.5

It can be seen from Table 6 that when two and three BESS are configured on sensitive lines, the total power of the BESS is the same, and the annual investment cost and the sum of improved power flow exceeding risk index are also the same. Moreover, the sum of the power of 19 nodes and 31 nodes, when three BESS are configured on sensitive lines, is equal to the sum power of configured two BESS. It can be seen from Tables 7 and 8 that the improved power flow exceeding risk index for sensitive and vulnerable AC lines is greater than 0.5, and when three BESS are configured, the impact on the improved power flow exceeding risk index is relatively small. It can be seen from Figures 9 and 10 that when two and three BESS are configured for sensitive lines, the power variation of the line is much

lower than configuring one BESS for sensitive lines. And suppressing power oscillation is greatly improved. We know that configuring BESS for multiple nodes eliminating the impact of DC power transfer on AC lines is better than the BESS configured for a single node. Configuring BESS for multiple nodes to improve the safe and stable operation ability of AC lines is better than the BESS configured for a single node. Secondly, when the configured BESS quantity is greater than 2, it has a small impact on the sum of improved power flow exceeding risk index and annual investment cost.

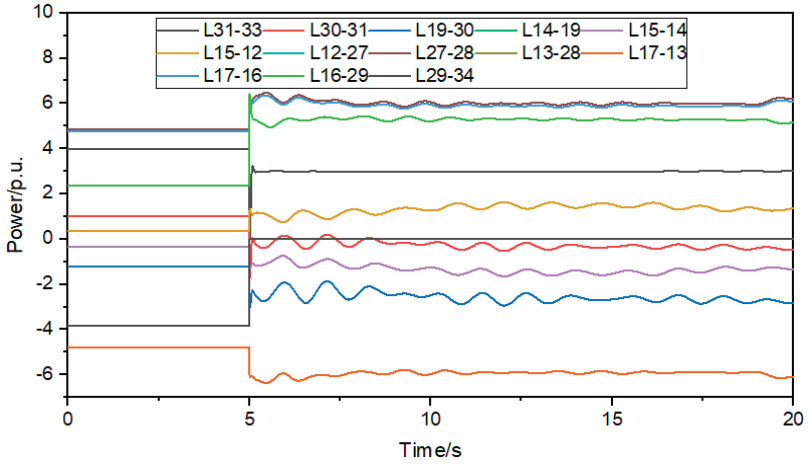

Figure 10. Shortest path power change curve after configuring 2 BESS.

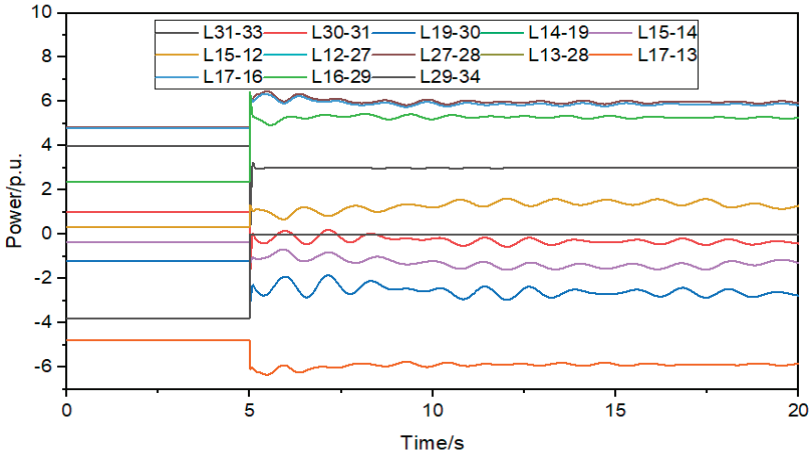

Figure 11. Shortest path power change curve after configuring 3 BESS.

6. Conclusions

The method of identifying the sensitive and vulnerable transmission lines based on improved power flow exceeding risk index is proposed, and it can apply to AC/DC hybrid systems, weak power grids, and other power systems. And the proposed method can quickly identify the sensitive and vulnerable transmission lines in the shortest path and simplify the method of calculating the branch disconnection coefficient. The method would not have to repeatedly calculate the impedance matrix of the line disconnection and connection.

The optimal energy storage configuration can be obtained by the multi-objective optimal mathematical model, including minimizing the annual investment cost of BESS and maximizing the sum of the improved power flow exceeding the risk index of the sensitive and vulnerable transmission lines. The BESS for sensitive and fragile lines can quickly eliminate the impact of DC power transfer on AC lines, and the BESS can also suppress power fluctuations and greatly improve the transient stability operation ability of the power grid.

The proposed energy storage configuration method does not only improve the transient stability of the power grid. Simultaneously, during the stability power grid, the configured energy storage can actively supports voltage, frequency, etc. The configuration method proposed in this article enriches the application scenarios of energy storage. The safe and stable operation ability of the system is greatly improved.

In the future, we will study the HIL implementation of the proposed system along with the proposed optimal allocation method. After this, the fault disturbance, power system planning BESS resources will be explored through the robust optimization-based model.

Author Contributions: Conceptualization, L.J. and T.Z.; investigation, Y.T., L.J., B.Z., X.S. and Y.X.; resources, B.Z., X.S. and Y.X.; data curation, L.J. and T.Z.; writing—original draft preparation, L.J. and T.Z.; writing—review and editing, L.J., T.Z. and S.M.; supervision, T.Z. and S.M.; project administration, Y.T.; funding acquisition, Y.T. All authors have read and agreed to the published version of the manuscript.

Funding: This research was funded by the Technology Project of State Grid Sichuan Electric Power Company (No. B1199721009N).

Data Availability Statement: The data presented in this study are available on request from the corresponding author.

Conflicts of Interest: The authors declare no conflict of interest.

References

1. ENTSO-E. *System Separation in the Continental Europe Synchronous Area on 8 January 2021—Interim Report[R/OL]*; ENTSO-E: Geneva, Switzerland, 26 February 2021. Available online: https://www.entsoe.eu/news/2021/02/26/system-separation-in-the-contnetal-europe-synchronous-area-on-8-january-2021-interim-report/ (accessed on 14 June 2023).
2. California ISO. *AWE Grid History Report[R/OL]*; California ISO: Folsom, CA, USA, 9 September 2020. Available online: http://www.caiso.com/Documents/AWE-Grid-History-Report-1998-Present.pdf (accessed on 14 June 2023).
3. Wang, S.; Zhou, L.; Wang, T.; Chen, T.; Wang, Y. Fast protection strategy for DC transmission lines of MMC-based MT-HVDC grid. *Chin. J. Electr. Eng.* **2021**, *7*, 83–92. [CrossRef]
4. Liu, Y.; Shen, C. Review and research on construction methods of the energy function for hybrid AC-DC power system. *Proc. CSEE* **2022**, *42*, 2842–2853.
5. Xin, B.; Guo, M.; Wang, S.; Li, X. Friendly HVDC transmission technologies for large-scale renewable energy and their engineering practice. *Autom. Electr. Power Syst.* **2022**, *45*, 1–8.
6. Zheng, C.; Ma, S.; Shen, X.; Liu, D. Definition, connotation and form of strong HVDC and weak AC and countermeasures for stable operation of the hybrid power grid. *Power Syst. Technol.* **2017**, *14*, 2491–2498.
7. Hines, P.; Balasubramaniam, C.; Sanchez, C. Cascading failures in power grids. *IEEE Potentials* **2009**, *28*, 24–30. [CrossRef]
8. Li, J.; Wang, J.; Ge, L.; Meng, G.J.; Yuan, X.D.; Zhou, J.H. Review on application technology of electrochemical energy storage power station group in ultrahigh voltage AC/DC hybrid receiver power grid. *Proc. CSEE* **2020**, *46*, 51–61.
9. Ma, Z.; Liu, F.; Shen, C.; Zhang, S.; Tian, B. Rapid identification of vulnerable lines in power grid using modified PageRank algorithm—Part I: Theoretical foundation. *Proc. CSEE* **2016**, *36*, 6363–6370+6601.
10. Lijie, D.; Meijun, L.; Yijia, C. Power system key-lines identification based on hidden failure model risk theory. *Autom. Electr. Power Syst.* **2007**, *31*, 1–6.
11. Li, Y.; Liu, J.; Liu, X.; Jiang, L.; Wei, Z.; Xu, W. Vulnerability assessment in power grid cascading failures based on the entropy of power flow. *Autom. Electr. Power Syst.* **2012**, *36*, 11–16.
12. Ren, J.; Wei, J. Vulnerableline identification and its transmission section search for power system. *Electr. Power Autom. Equip.* **2015**, *35*, 37–42.
13. Ruo-fa, C.; Xin, F. Fast search of transmission section in power flow transferring resulting from simultaneous multi-branch removal. *Adv. Technol. Electr. Eng. Energy* **2020**, *39*, 62–71.
14. Naziri Moghaddam, I.; Chowdhury, B.; Mohajeryami, S. Predictive operation and optimal sizing of battery energy storage with high wind energy penetration. *IEEE Trans. Ind. Electron.* **2017**, *65*, 6686–6695.

15. Luo, F.; Meng, K.; Dong, Z.Y.; Zheng, Y.; Chen, Y.; Wong, K.P. Coordinated operational planning for wind farm with battery energy storage system. *IEEE Trans. Sustain. Energy* **2015**, *6*, 253–262. [CrossRef]
16. Xiaowei, D.; Guiping, Z.; Liangzhong, Y. Two-Stage optimization of battery energy storage capacity to decrease wind power curtailment in grid-connected wind farms. *IEEE Trans. Power Syst.* **2018**, *33*, 3296–3305.
17. Sun, Y.S.; Tang, X.S.; Sun, X.Z.; Jia, D.Q.; Zhang, G.W.; Wang, P. Research on energy storage capacity allocation method for smoothing wind power fluctuations. *Proc. CSEE* **2017**, *37*, 88–97.
18. Jiang, T.; Li, X.; Chen, H.; Zhang, R.; Li, G.; Kou, X.; Wang, M.; Li, F. Optimal energy storage siting and sizing to mitigate voltage deviation in distribution networks. In Proceedings of the 2019 IEEE Power & Energy Society General Meeting (PESGM), Atlanta, GA, USA, 4–8 August 2019; IEEE: Piscateville, NJ, USA, 2020; pp. 1–5.
19. Tang, J.; Li, X.R.; Huang, J.Y.; Xu, P.; He, C. Capacity allocation of BESS in secondary frequency regulation with the goal of maximum net benefit. *Trans. China Electrotech. Soc.* **2019**, *34*, 963–972.
20. Zheng, L.; Hu, W.; Lu, Q.; Min, Y. Optimal energy storage system allocation and operation for improving wind power penetration. *IET Gener. Transm. Distrib.* **2015**, *9*, 2672–2678. [CrossRef]
21. Hou, L.; Chen, Y.; Su, K.; Wang, Y.; Zhang, Z. Research on bi-level planning method of active distribution network considering flexible interconnection of source network load and storage. In Proceedings of the 2019 IEEE Sustainable Power and Energy Conference, Beijing, China, 21–23 November 2019; IEEE: Piscateville, NJ, USA, 2020.
22. Zhang, Y.; Dong, Z.; Luo, F.; Zheng, Y.; Meng, K.; Wong, K.P. Optimal allocation of battery energy storage systems in distribution networks with high wind power penetration. *IET Renew. Power Gener.* **2016**, *10*, 1105–1113. [CrossRef]
23. Xiu, X.; Tang, W.; Li, J.; Tian, C. Collaborative Configuration of distributed generation, energy storage and load in microgrid considering state of health. *High Volt. Eng.* **2017**, *43*, 3118–3126.
24. Wang, S.; Li, F.; Zhang, G.; Yin, C. Analysis of energy storage demand for peak shaving and frequency regulation of power systems with high penetration of renewable energy. *Energy* **2023**, *267*, 126586.
25. Song, T.; Li, T.H.X. Coordinated operation strategy of energy storage system participating in multiple application scenarios. *Autom. Electr. Power Syst.* **2021**, *45*, 43–51.
26. Yuan, W.; Wang, J.; Qiu, F.; Chen, C.; Kang, C.; Zeng, B. Robust optimization-based resilient distribution network planning against natural disasters. *IEEE Trans. Smart Grid* **2016**, *7*, 2817–2826. [CrossRef]
27. Shen, Z.; Sun, F.; Dan, Y.; Dai, P.; Song, K.; Wang, L. Optimal Planning of Distributed Energy Storage in Distribution Network Considering the Influence of Typhoon-like Extreme Weather. In Proceedings of the 2021 3rd International Academic Exchange Conference on Science and Technology Innovation (IAECST), Guangzhou, China, 10–12 December 2021; IEEE: Piscateville, NJ, USA, 2021; pp. 1882–1886.
28. Nazemi, M.; Moeini-Aghtaie, M.; Fotuhi-Firuzabad, M.; Dehghanian, P. Energy storage planning for enhanced resilience of power distribution networks against earthquakes. *IEEE Trans. Sustain. Energy* **2020**, *11*, 795–806. [CrossRef]
29. Haibo, Z.; Shentong, M.; Xin, C. Energy storage planning method of distribution network to ensure uninterrupted power supply of important loads. *Power Syst. Technol.* **2021**, *45*, 259–268.
30. Liu, Z.; Tan, Q.; Zhou, Y.; Xu, H. Syncretic application of IBAS-BP algorithm for monitoring equipment online in power system. *IEEE Access* **2021**, *9*, 2169–3536. [CrossRef]
31. Al Ahmad, A.K.; Sirjani, R. Optimal allocation of energy storage system in transmission system considering wind power. In Proceedings of the 2020 7th International Conference on Electrical and Electronics Engineering, Antalya, Turkey, 14–16 April 2020; IEEE: Piscateville, NJ, USA, 2020; pp. 181–187.
32. Shu, H.; Shen, X.; Xu, L.; Guo, Q.; Sun, H. A validity test method for transmission betweens and transmission sections based on chain attack analysis and line outage distribution factors. In Proceedings of the 2018 2nd IEEE Conference on Energy Internet and Energy System Integration (EI2), Beijing, China, 20–22 October 2018; pp. 1–6.
33. Clerc, M.; Kennedy, J. The particle swarm-explosion, stability, and convergence in a multidimensional complex space. *IEEE Trans Evol. Comput.* **2002**, *6*, 58–73. [CrossRef]
34. Ozcan, E.; Mohan, C. Particle swarm optimization: Surfing the waves. In Proceedings of the Congress on Evolutionary Computation, Piscataway, NJ, USA, 6–9 July 1999; Volume 1, pp. 1939–1944.
35. Li, Y.; Shuai, Z.; Liu, X.; Hong, Y.; Wu, X.; Shen, Z.J. Study on damping low frequency oscillation of an AC/DC power grid based on UPFC & DC-SDC. *Power Syst. Prot. Control* **2020**, *48*, 73–79.

sustainability

MDPI

Article

A Causal Relationship between the New-Type Urbanization and Energy Consumption in China: A Panel VAR Approach

Cheng Chen [1,*], Yajie Gao [1] and Yidong Qin [2]

[1] School of Business, Hunan University of Science and Technology, Xiangtan 411201, China; 21301503001@mail.hnust.edu.cn
[2] School of Economics, Wuhan University of Technology, Wuhan 430070, China; qyd@whut.edu.cn
* Correspondence: 20301503001@mail.hnust.edu.cn

Abstract: The accelerated urbanization process has been considered to be the root cause of increasingly severe energy consumption growth in China. However, energy is still an essential factor for the urbanization process, so arbitrarily mitigating energy use currently will unquestionably slow down the urbanization process. The principal contribution of this paper is to comprehensively analyze the dynamic interaction mechanism between the new-type urbanization and energy consumption, and further put forward a new idea of comparing the benefit of an increase in the level of new-type urbanization resulting from energy consumption and the negative externality of environmental damage related with energy consumption. This paper conducts an empirical study on the causal relationship between new-type urbanization and energy consumption using Chinese provincial administrative units from 1999 to 2020. And we find that new-type urbanization leads to energy consumption negatively and energy consumption leads to new-type urbanization positively for provinces in the eastern region. There is only a one-way effect of energy consumption on new-type urbanization for provinces in the central and northeastern regions, and there is negative feedback causality for provinces in the western region. Additionally, the benefit of an increase in the level of new-type urbanization resulting from energy consumption is larger than the negative externality of environmental damage related to energy consumption for provinces in the eastern, central, and northeastern regions, yet it is totally opposite for provinces in the western region. Finally, we propose some fruitful policy recommendations to construct new-type urbanization under the background of clear reduction targets for energy consumption in China.

Keywords: new-type urbanization; energy consumption; environmental Kuznets curve; PVAR approach

Citation: Chen, C.; Gao, Y.; Qin, Y. A Causal Relationship between the New-Type Urbanization and Energy Consumption in China: A Panel VAR Approach. *Sustainability* **2023**, *15*, 11117. https://doi.org/10.3390/su151411117

Academic Editors: Luis Hernández-Callejo, Jesús Armando Aguilar Jiménez, Carlos Meza Benavides and Sergio Nardini

Received: 9 May 2023
Revised: 4 July 2023
Accepted: 10 July 2023
Published: 17 July 2023

1. Introduction

When the "Reform and Opening-up" policy was put into practice in the year of 1978, China's urbanization experienced a steady upward trend [1,2]. According to the statistics from the National Bureau of Statistics (NBS), China's urbanization rate increased from 17.9% in 1978 to 65.2% in 2022. Nevertheless, much of China remains to be urbanized, especially the inland regions. As China has a larger population, millions of rural residents will move into urban areas every year during to-be urbanization process. Although China's urbanization greatly raises people's living standards, it has also been deemed to be the root cause of increasingly severe energy consumption growth; for example, the heavy use of fossil energy, which undoubtedly brings about a series of environmental pollution [3]. The total energy consumption in China even made up 23.6% of the global total in the year 2018 [4]. Specifically, urban areas solely account for 75.15% of total energy consumption in China [5]. As a responsible country, China has been determined to set clear reduction targets for energy consumption. Because the urbanization process in China is still accelerating at present, energy is still an essential factor for the urbanization process. Arbitrarily mitigating

energy use currently will unquestionably slow down the urbanization process. Therefore, there are two kinds of opposite effects simultaneously, which are the benefit of an increase in the level of urbanization resulting from energy consumption and the negative externality of environmental damage related to energy consumption respectively. Could the advantages sufficiently offset the disadvantages? Investigating these two kinds of opposite effects has vital theoretical and practical significance for promoting the urbanization process under the background of clear reduction targets for energy consumption in China. If the advantages of energy consumption outweigh its disadvantages, it pays to promote the urbanization process by increasing energy consumption. However, if energy consumption does not promote or even adversely affect the urbanization process, an energy conservation policy should be adopted to offset the negative externality of environmental damage related to energy consumption.

Previous studies have extensively investigated this subject, yet the majority emphasized the one-way effect of urbanization on energy consumption in the beginning. Many scholars found that the urbanization process leads to energy consumption growth [6–9]. In contrast, some scholars argued that urbanization may lead to energy consumption negatively [10–16]. Based on Northam [17], the third strand of research further examined the nonlinear relationship between the two due to the mixed findings. Most scholars confirmed that the nexus of the two is indeed nonlinear [2,18–20]. Another branch of the literature used city size as a proxy variable for urbanization rate, which indicated that there also was a nonlinear relationship between city size and energy consumption [21,22]. There are two kinds of explanations for the nonlinear relationship between the two. On the one hand, the essence of urbanization can be ascribed to the agglomeration effect, scale effect, and spatial spillover effect, which are conducive to reducing the energy consumption of residents or increasing energy efficiency [5,14,23–25]. On the other hand, the urbanization process reduces energy consumption through industrial structure upgrading and technical innovation [19,26–28].

The level of urbanization is mainly measured by the single index method in the above studies. These simple indicators can only mirror the level of population-oriented urbanization rather than the improvement of production and lifestyle. Especially after China issued the "National New-type Urbanization Plan" in 2014, human-centered urbanization has been put into practice. Therefore, investigating the relationship between new-type urbanization and energy consumption has much more practical significance currently. Recently, a few scholars used the comprehensive index method to measure its connotation and further examine its effect on energy consumption. Liu et al. [14] used a spatial econometric model for China's regions on this subject and found that new-type urbanization leads energy consumption negatively, yet its effect on adjacent areas or the spatial spillover effect is positive. Lin and Zhu [4] examined the effect of new-type urbanization on energy saving and its transmission channels based on Chinese cities and found that it can bring about an energy-saving effect. Yu [29] examined the ecological effect of new-type urbanization and found that China's new-type urbanization can improve energy efficiency. Feng et al. [30] examined the effect of new-type urbanization on energy efficiency based on Chinese cities and found that it has a double-threshold effect. Shao and Wang [31] examined the effect of new-type urbanization on green total factor energy efficiency and found that it has a heterogeneous effect for different cities. Not surprisingly, the relationship between the two is much more complicated compared to traditional urbanization.

Apart from that, as an essential factor of economic development, energy consumption is also conducive to promoting the level of urbanization. Ghosh and Kanjilal [32] investigated the cointegration relationship between the two for India and found that there is causality running from energy consumption to urbanization. Wu et al. [2] estimated the direct effects of various energy consumption patterns in China and found that energy consumption leads to urbanization positively, and the positive effect is dependent on energy consumption intensity, energy consumption scale, and energy consumption structure. Xu and Wang [33] examined the threshold effect of energy consumption on new-type

urbanization in China and found that there was a significant threshold effect. Some scholars further explored how energy consumption affected the urbanization process. These studies found that the carbon emission reduction effect [34], agglomeration economy effect and economies of scale [32,35,36], and the industrial structure effect [36–38] are primary transmission channels through which energy consumption affects urbanization.

The above studies in this field indicate that there should be a bi-directional causality between the two. So far, a wealth of studies primarily investigated uni-directional causality on this subject, yet the bi-directional causality between the two is still scarce. Comparatively, a large body of studies proved that economic growth and energy consumption present a bi-directional causal relationship [39–44]. As urbanization is widely considered a symbol of economic development [37–39], an abundance of support can be indirectly found for the bi-directional causality relationship on our subject. To the best of our knowledge, only Tang et al. [45] explored the two-way correlation mechanism between new-type urbanization and clean energy consumption based on Chinese provincial data and found that there is a significant two-way promoting effect between the two. To sum up, the extant literature in this field actually denotes that energy consumption probably affects urbanization by means of its effects on economic development.

Despite the existing studies in this field having explored extensively the relationship between the two, there are still a few drawbacks on this subject. Firstly, the bulk of empirical studies simply examined how urbanization affects energy consumption, or whether energy consumption promoted the level of urbanization, and these empirical results did not compare the benefit of an increase in the level of urbanization resulting from energy consumption and the negative externality of environmental damage related to energy consumption, so they cannot provide corresponding policy implications for promoting the urbanization process. Secondly, there should be a bi-directional causality between the two, and the existing studies mainly examined the one-way effect of urbanization on energy consumption. Thirdly, the empirical studies on this subject are generally conducted based on the linear relationship hypothesis, and the estimated results are always inconsistent. The nonlinear relationship hypothesis may be more realistic, especially for the effect of new-type urbanization, which remains to be further examined empirically. In this regard, our study makes the following contributions. Firstly, this paper comprehensively analyzes the dynamic interaction mechanism between new-type urbanization and energy consumption, aiming to reveal the bi-directional causality between the two and extend the depth and breadth of this subject. Secondly, this paper put forward a new idea of comparing the benefit of an increase in the level of new-type urbanization resulting from energy consumption and the negative externality of environmental damage related to energy consumption, which can provide targeted policy recommendations. Thirdly, this paper creatively explains the estimated results with the concept of the well-known Environmental Kuznets Curve (EKC) hypothesis based on some energy-related data, which not only adds new empirical evidence for the EKC relation but also provides a robustness test for our regression results given that new-type urbanization and energy consumption factually present the two-way causal relationship.

The remainder of this article is arranged as follows. The following section introduces the measurement methods and analysis of the measurement results; Section 3 outlines the econometric specification and presents empirical results; and Section 4 concludes.

2. Measurement Methods and Analysis of Measurement Results

2.1. Measurement Methods

The most critical things are methods for calculating the level of new-type urbanization and energy consumption in this paper. According to Ma et al. [46], the amount of energy consumption per capital is applied to measure the level of energy consumption. Similar to the existing studies [4,47], the composite index method is used to fully measure the level of new-type urbanization. The index system is made up of two levels, which include a total of 19 computable indices, as is shown in Table 1. To overcome some shortcomings

of the subjective weighting method, the entropy method is employed to calculate the constructed comprehensive urbanization index. The "+" and "−" of Index Attributes in Table 1 signify the influence of 19 computable indices on the comprehensive index, and "+" indicates an increase in the metric of indices would promote the comprehensive index, and "−" indicates an increase in the metric of indices would decrease the comprehensive index.

Table 1. China's comprehensive urbanization index system. Reprinted from [48]. Copyright 5584080645167 (2023) with permission from Elsevier.

Index I	Index II	Index Attribute
Population	Urban population density	+
	Full-time equivalent of R&D personnel	+
	Urban population ratio	+
	Number of college degrees or above per ten thousand people	+
	Proportion of employed persons in the tertiary industry	+
Economy	Gross domestic products per capita	+
	Consumption proportion of urban to rural residents	−
	Disposable income of urban household per capita	+
	Tertiary industry as a percentage of regional GDP	+
Living environment	Urban wastewater treatment ability per day	−
	Green covered area as a percentage of completed area	+
	Greenery area of per capital park	+
	Area under a cleaning program per square kilometer of built-up area	+
Living conditions	Urban gas access rate	+
	Urban water access rate	+
	Number of public toilets per ten thousand people	+
	Number of public transportation vehicles per ten thousand people	+
	Urban per capita area of paved roads	+
	Number of patent grants per ten thousand people	+

The sample data of our empirical research spans 22 years, from 1999 to 2020, and includes all provincial administrative units in China. The original data for energy consumption are obtained from the China Energy Statistical Yearbook and the China Statistical Yearbook. All relevant data for calculating the comprehensive urbanization index are obtained from the China Statistical Yearbook, China Energy Statistical Yearbook, China City Statistical Yearbook, China Statistical Yearbook on Science and Technology, each provincial statistical yearbook, and so on. Considering the data unavailability, Tibet, Hong Kong, Macao, and Taiwan are deleted from the sample in our empirical study. Consequently, the research sample finally consists of 30 provincial administrative units. And these 30 provincial administrative units can be classified into four categories according to the National Bureau of Statistics: east, northeast, central, and west. So as to cancel the impact of the price level in different years, all data related to nominal GDP are revised to a constant price based on the 1999 price index in the process of computation.

2.2. Analysis of Measurement Results

According to the specific calculation method introduced above, the provincial level of energy consumption in China from 1999 to 2020 is calculated firstly. To visually describe the characteristics of the temporal–spatial evolution in the provincial level of energy consumption, the measurement results are reported in the form of topographic maps. Figure 1 shows the concrete results. Due to space constraints, the results from 1999, 2007, 2013, and 2020 are only displayed. It can be clearly seen in Figure 1 that the dark blue areas represent the highest level of energy consumption in 30 provincial administrative units. Obviously, the

number of dark blue regions increased from zero in 1999 to ten in 2020. For the convenience of discussions, all provincial administrative units are called "province". Therefore, we can conclude from these results that the provincial level of energy consumption in China is on the rise over the study period [43,49]. And in 2020, the provincial level of energy consumption demonstrated visible spatial differentiation. Among the provinces with the highest level of energy consumption, four provinces lie in the western region: Xinjiang, Qinghai, Gansu, and Inner Mongolia. Four provinces, Beijing, Shanghai, Hebei, and Jiangsu, are in the eastern region. Only one province, Shaanxi, lies in the central region, and only one province, Liaoning, lies in the northeastern region. Generally, the western region has the highest level of energy consumption among the four types of regions, followed by the eastern region. And the rest of the two regions have comparatively lower levels of energy consumption. The provincial level of energy consumption from the eastern to the central, northeastern, and western regions is similar to the U-shaped curve [49]. The spatial characteristics of the provincial level of energy consumption imply preliminarily that it is necessary to give thought to regional heterogeneity on this subject.

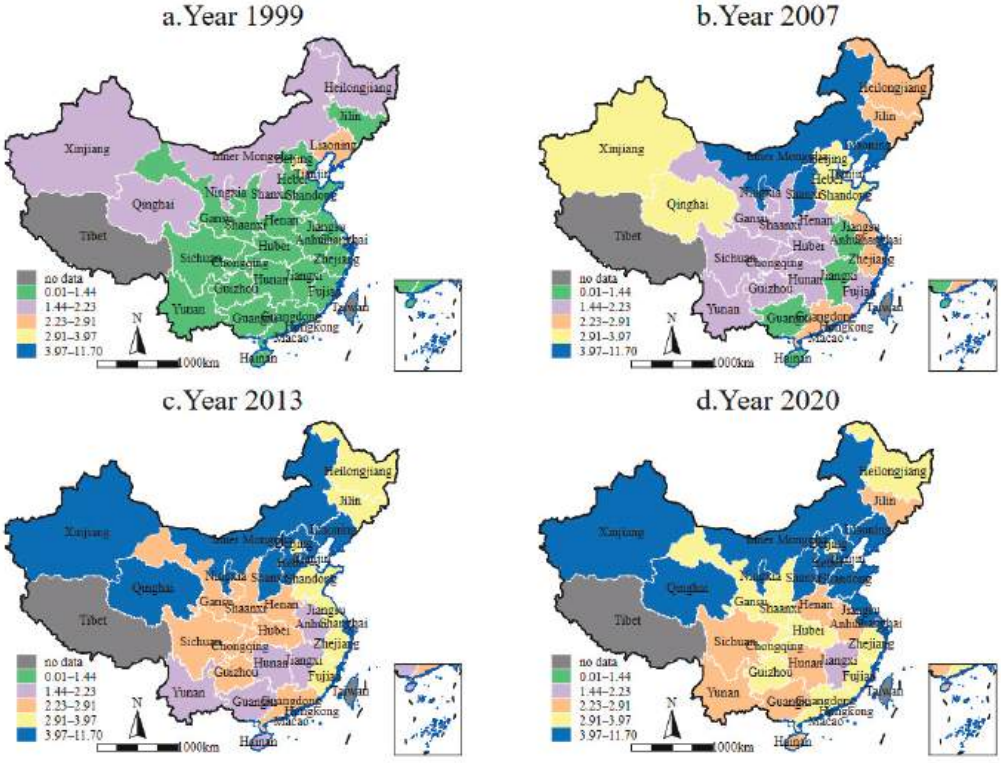

Figure 1. Chinese provincial level of energy consumption for some years (million tons).

Then, the comprehensive urbanization index is calculated by the widely used entropy method. To visually describe the characteristics of the temporal–spatial evolution of this index, the measurement results are reported similarly in the same way. Figure 2 shows the concrete results. Due to space constraints, the results from 1999, 2007, 2013, and 2020 are only displayed. It can be clearly seen in Figure 2 that the dark blue areas represent the highest level of new-type urbanization in 30 provincial administrative units. Obviously, the number of dark blue regions is zero in 1999, yet nearly all provinces in the eastern and central regions belonged to the highest group in 2020. Therefore, we can conclude from these results that the provincial level of new-type urbanization has also

increased greatly over the study period, especially after the year 2013 [2,4,49]. On the one hand, the main reason for these time series characteristics can be probably ascribed to the "National New-type Urbanization Plan", which makes the economy, society, and ecology balanced in the process of urbanization. On the other hand, the increase in the level of energy consumption may also be conducive to speeding up the process of urbanization. And in 2020, the provincial level of new-type urbanization has also displayed significant spatial differentiation. Specifically, the majority of provinces have achieved the highest status in 2020. And only a few provinces have not reached the highest level, these are Xinjiang, Jilin, Shanxi, Gansu, Guizhou, Qinghai, Yunnan, and Guangxi. Additionally, these provinces mainly lie in the western and central regions. The average comprehensive urbanization index of the provinces in the eastern, central, northeastern, and western regions is calculated to be 0.299, 0.169, 0.188, and 0.159, respectively, which verifies that the provincial level of new-type urbanization looks like the inverted S-shaped curve, which is slightly different with the provincial level of energy consumption [46,47]. Therefore, the spatial characteristics of the provincial level of new-type urbanization further imply that it is necessary to give thought to regional heterogeneity on this subject.

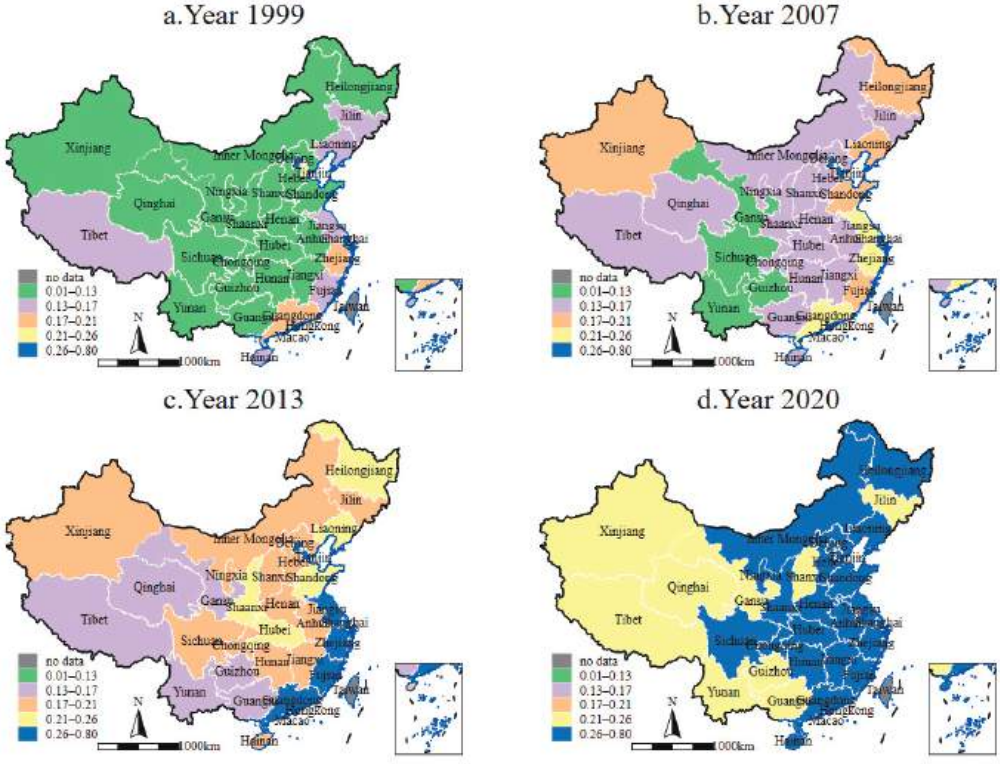

Figure 2. Chinese provincial level of new-type urbanization for some years.

To display the tendency intuitively, the growth rate of the above measured variables is depicted with a scatter diagram in Figure 3 for the four groups, eastern (Figure 3a), central (Figure 3b), northeastern (Figure 3c), and western regions (Figure 3d), respectively. In Figure 3, the relationship between comprehensive urbanization index growth and energy consumption growth is significantly different in the four groups. Specifically, there seems to be a strong relationship between the northeast and western regions, yet no such relationship emerges in the eastern and central regions. These results further prove that we cannot neglect the "one size for all" homogeneity issue among provinces when investigating

the causal relationship between the two, and it is reasonable to classify the data into four groups: east, northeast, central, and west. Secondly, the weak relationship between the two in the eastern and central regions denotes there may be a nonlinear relationship between comprehensive urbanization index growth and energy consumption growth, and the traditional linear model is not suitable for this subject. Nevertheless, it should be noted that these kinds of scatter charts roughly reflect the possible correlation relationship between the two, and the exact relationship between the two remains to be confirmed rigorously by employing reasonable econometric models.

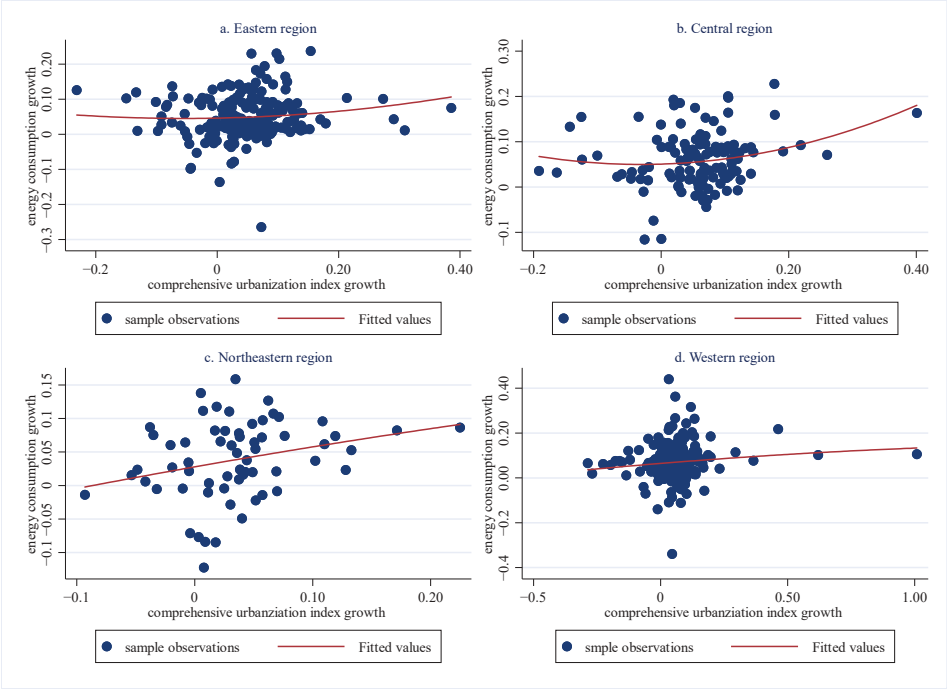

Figure 3. Comprehensive urbanization index growth vs. energy consumption growth.

3. PVAR Model Regression Results and Analysis

3.1. Model Specification

So as to fully reveal the causal on this subject, the panel vector autoregression (PVAR) model is employed to conduct empirical research. Compared with the widely used vector autoregression (VAR) model, the PVAR model has the advantage of dealing with long-term panel data and endogenous causality in the traditional linear regression model. The corresponding PVAR model is constructed as follows:

$$Y_{it} = \Gamma_0 + \sum_{p=1}^{n} \Gamma_p Y_{it\text{-}p} + \delta_i + f_t + \varepsilon_{it}$$

where the subscripts i and t denote province and year, respectively; Y_{it} is a multi-dimensional variable, which is *NU* and *EC*, representing the level of new-type urbanization and energy consumption, respectively, measured by the methods introduced hereinabove; $Y_{it\text{-}p}$ is a p-period lag term of Y_{it}; and δ_i and f_t indicate individual province fixed effects and year fixed effects, respectively. ε_{it} is termed the random disturbance.

As the PVAR model includes the lag term of dependent variables and individual province fixed effects, it can be considered a typical dynamic panel data model. Thus, the

OLS estimation will be biased and inconsistent. Therefore, the system GMM proposed by Blundell and Bond [49] is used to estimate the PVAR model. The PVAR model is commonly conducted by the following steps [50,51]. Firstly, the stationarity of the panel data and the causal relationship between *NU* and *EC* have to be tested. Secondly, the optimal lag order needs to be selected, and the PVAR model can be estimated logically. Thirdly, the impulse response graph will be displayed based on the PVAR model regression. The last step is the variance decomposition.

3.2. PVAR Model Regression Analysis

3.2.1. Stationarity Tests

First of all, it is necessary to inspect the stationarity of time series variables. The IPS, Fisher-ADF, and Fisher-PP are comprehensively used to implement unit root tests, and the results are reported in Table 2. In Table 2, the *p*-values of all tests for the first-difference series of *NU* and *EC* are all 0.000, which rejects the null hypothesis at the 1% significance level. Hence, we can conclude that the first-difference series of *NU* and *EC* are stationary. In other words, these original data are integrated processes of order one.

Table 2. Unit root test results.

Variables	IPS		Fisher-ADF		Fisher-PP	
	Statistics	***p*-Value**	**Statistics**	***p*-Value**	**Statistics**	***p*-Value**
NU	−3.272	0.001	107.964	0.000	39.533	0.988
NU_{-1}	−13.091	0.000	290.177	0.000	615.121	0.000
EC	−1.569	0.363	141.268	0.000	45.468	0.943
EC_{-1}	−10.008	0.000	219.605	0.000	290.094	0.000

Notes: The null hypothesis is that the time series variables have a unit root process.

3.2.2. Benchmark Regression Results

Before estimating the PVAR model, an optimal lag *p*-period of time series variables remains to be explored. Based on the standard procedure in empirical studies, the AIC, BIC, and HQIC are used to select the optimal lag order. The selection of two lag periods is reasonable. Therefore, 2 is the optimal lag order in this paper. The estimation results of the PVAR model are reported in Table 3. The *EC* equation reflects the effects of *EC* and *UN* on *EC*, and the *UN* equation reflects the effects of *UN* and *EC* on *UN*. The estimated results for all provinces as a whole are reported in the top line of Table 3. As shown in Table 3, in the *EC* equation, the first-period lag of *EC* has a significant positive effect on *EC*, and the second-period lag of *EC* has a significant negative effect on *EC*, which indicates that energy consumption presents the characteristics of path-dependent inertia in the short run, yet it tends to converge in the long run [4,47]. The first-period lag of *NU* has a significant negative effect on *EC* and the second-period lag of *NU* has a significant positive effect on *EC*, which indicates that new-type urbanization leads to energy consumption negatively in the short run [10–16], yet the new-type urbanization leads to energy consumption positively in the long run [6–9]. In the *NU* equation, the first-period lag of *NU* has a significant positive effect on *NU*, and the second-period lag of *NU* does not have any significant effect on *NU*, which indicates that new-type urbanization also presents the characteristics of path-dependent inertia in the short run. The first-period lag of *EC* has a significant positive effect on *NU* [33], and the second-period lag of *EC* has a significant negative effect on *NU* [45], which indicates that an increase in energy consumption brings about a further increase in the level of new-type urbanization in the short run, yet it is detrimental to new-type urbanization in the long run.

Table 3. Estimation results of the PVAR model.

Sample	Type	Variable	Coefficient	Variable	Coefficient
Countrywide	*EC* equation	EC_{-1}	1.553 *** (14.04)	NU_{-1}	−1.279 ** (2.00)
		EC_{-2}	−0.513 *** (−8.32)	NU_{-2}	1.138 * (1.81)
	NU equation	NU_{-1}	1.342 *** (4.84)	EC_{-1}	0.021 ** (2.37)
		NU_{-2}	−0.257 (−0.84)	EC_{-2}	−0.022 *** (−2.58)
Eastern	*EC* equation	EC_{-1}	1.492 *** (15.46)	NU_{-1}	−0.879 * (−1.80)
		EC_{-2}	−0.465 *** (−5.45)	NU_{-2}	0.638 (1.18)
	NU equation	NU_{-1}	1.083 *** (5.09)	EC_{-1}	0.042 *** (4.42)
		NU_{-2}	0.008 (0.04)	EC_{-2}	−0.035 *** (−4.80)
Central	*EC* equation	EC_{-1}	1.451 *** (11.31)	NU_{-1}	−1.188 (−1.40)
		EC_{-2}	−0.495 *** (−4.21)	NU_{-2}	1.321 * (1.69)
	NU equation	NU_{-1}	1.507 *** (7.37)	EC_{-1}	0.031 ** (2.35)
		NU_{-2}	−0.448 ** (−2.02)	EC_{-2}	−0.027 ** (−2.02)
Northeastern	*EC* equation	EC_{-1}	1.689 *** (10.52)	NU_{-1}	−10.142 (−1.35)
		EC_{-2}	−0.408 *** (−3.43)	NU_{-2}	5.158 * (1.87)
	NU equation	NU_{-1}	0.891 *** (3.59)	EC_{-1}	0.029 *** (2.81)
		NU_{-2}	0.189 (0.94)	EC_{-2}	−0.026 *** (−2.93)
Western	*EC* equation	EC_{-1}	1.508 *** (18.47)	NU_{-1}	−3.508 *** (−3.05)
		EC_{-2}	−0.415 *** (−5.21)	NU_{-2}	1.462 * (1.95)
	NU equation	NU_{-1}	1.339 *** (4.57)	EC_{-1}	0.010 (2.37)
		NU_{-2}	−0.284 (−0.97)	EC_{-2}	−0.008 * (−1.66)

Notes: ***, **, and * show significant levels at 1%, 5%, and 10%, respectively. The value given in parentheses is *t* statistics. The subscripts $_{-1}$ and $_{-2}$ represent the first-period lag and the second-period lag, respectively.

The estimated results for all provinces as a whole neglect regional heterogeneity. To explore this issue, groups of provinces are classified into four types of regions according to NBS. The estimated results for provinces in the eastern region are reported in the top second line of Table 3. As shown in Table 3, in the *EC* equation, the first-period lag of *EC* and the second-period lag of *EC* have a similar effect on *EC* compared to the whole country. The first-period lag of *NU* has a significant negative effect on *EC*, and the second-period lag of *NU* does not have any effect on *EC*, which indicates that new-type urbanization leads to energy consumption negatively in the short run [4,30], yet this inhibitory effect gradually disappears over time. In the *NU* equation, both *NU* and *EC* have a similar effect on *UN* compared to the whole country.

The estimated results for provinces in the central region are reported in the top third line of Table 3. As shown in Table 3, in the *EC* equation, the first-period lag of *EC* and the

second-period lag of *EC* have a similar effect on *EC* compared to the whole country. Both the first-period lag of *NU* and the second-period lag of *NU* do not have any significant effect on *EC*, which indicates that an increase in the level of new-type urbanization does not bring about energy consumption [52]. In the *NU* equation, the first-period lag of *NU* has a significant positive effect on *NU*, and the second-period lag of *NU* has a significant negative effect on *NU*. The first-period lag of *EC* and the second-period lag of *EC* have a similar effect on *UN* compared to the whole country.

The estimated results for provinces in the northeastern region are reported in the fourth line of Table 3. As shown in Table 3, in the *EC* equation, the first-period lag of *EC* and the second-period lag of *EC* have a similar effect on *EC* compared to the whole country. Both the first-period lag of *NU* and the second-period lag of *NU* do not have any significant effect on *EC*, which also indicates that an increase in the level of new-type urbanization does not bring about energy consumption [52]. In the *NU* equation, both *NU* and *EC* have a similar effect on *UN* compared to the whole country.

The estimated results for provinces in the western region are reported in the fifth line of Table 3. As shown in Table 3, in the *EC* equation, the first-period lag of *EC* and the second-period lag of *EC* have a similar effect on *EC* compared to the whole country. The first-period lag of *NU* and the second-period lag of *NU* have a similar effect on *EC* as the eastern region, which indicates that new-type urbanization leads to energy consumption negatively in the short run [4,30], yet this inhibitory effect gradually disappears over time. In the *NU* equation, the first-period lag of *NU* and the second-period lag of *NU* have a similar effect on *NU* compared to the whole country. The first-period lag of *EC* does not have any effect on *UN*, and the second-period lag of *EC* has a significantly negative effect on *UN*, which indicates that an increase in energy consumption is detrimental to new-type urbanization.

3.2.3. Discussions with Concept of EKC

According to existing studies, energy consumption may lead to economic development and environmental pollution simultaneously [53–55]. Since new-type urbanization is widely considered a symbol of economic development [38], the critical issue is whether energy consumption can bring about larger benefits with respect to its cost. This basic benefit–cost tradeoff can be inferred from the causal relationship between the two. When energy consumption is conducive to promoting the level of new-type urbanization, it may indicate that the benefit of an increase in the level of new-type urbanization resulting from energy consumption is larger than the negative externality of environmental damage related to energy consumption. On the contrary, if the new-type urbanization leads to energy consumption positively, it may indicate that the advantage of energy consumption exceeds its disadvantage. From the estimated results for all provinces as a whole, we can conclude that the advantage of energy consumption is larger than its disadvantage in the short run, yet the relationship is opposite over time. From the estimated results for provinces in the eastern region, we can conclude that the advantage of energy consumption is always larger than its disadvantage over time. This again proves that those provinces in the eastern region may have started to cope with the possible environmental damage related to energy consumption. From the estimated results for provinces in the central, northeastern, and western regions, the advantages of energy consumption and its disadvantages are similar to the whole country, where the negative externality of environmental damage exceeds its benefit over time.

The PVAR model regression results can also be interpreted with the concept of the EKC, which assumes that economic growth and environmental pollution present an "inverted U" relationship [56]. Initially, as the level of new-type urbanization is relatively low, there are not too many industrial activities that lead to environmental pollution. Therefore, an increase in the level of new-type urbanization is conducive to reducing energy consumption for all samples in the short run. As the pace of new-type urbanization accelerates, there will be more and more high-pollution industries, and environmental pollution

may gradually increase. As the estimation results indicated, an increase in the level of new-type urbanization may enhance energy consumption in the long run for the central, northeast, and western regions. Even so, for provinces in the eastern region, new-type urbanization is not conducive to increasing energy consumption over time. As the economy improves, these provinces may start to focus on the possible environmental damage related to energy consumption and attempt to take some remedial actions [57]. Generally speaking, as long as new-type urbanization reaches a high level as the eastern region, more resources may be dedicated to environmental protection. Consequently, an increase in the level of new-type urbanization will be conducive to reducing environmental pollution. Our main target is not to explore the EKC, yet the implications of the estimated results are compatible with the EKC prediction. To sum up, as the pace of new-type urbanization accelerates, a negative externality, such as environmental pollution related to energy consumption, gradually increases. Once a province reaches a high level of new-type urbanization, it may conversely reduce the negative externality related to energy consumption, as indicated by the EKC assumption.

3.3. Impulse Response Analysis

So as to further investigate the dynamic relationship between the variables in the PVAR model, the impulse response function is computed. Specifically, we set up Monte Carlo simulations for four types of subsamples and finally obtained a 4 × 4 impulse response graph, and the corresponding results are displayed in Figure 4 for the different groups: eastern (Figure 4a), central (Figure 4b), northeastern (Figure 4c), and western regions (Figure 4d), respectively.

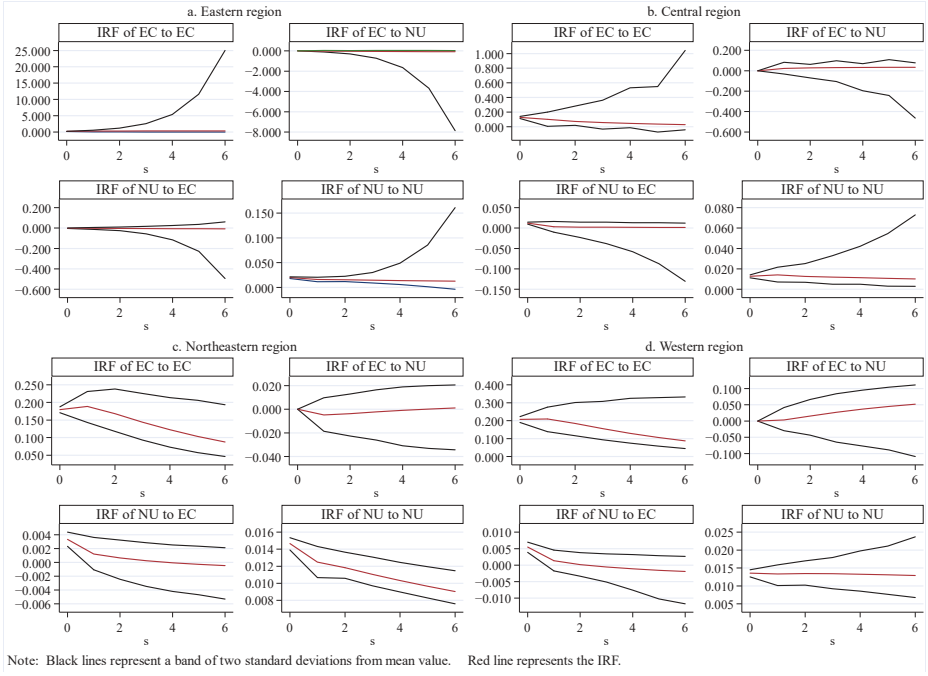

Figure 4. Variable impulse responses.

For provinces in the eastern regions, only *NU* shows a positive response to a standard deviation in its own unit. These results further verify that provinces in the eastern region may have been committed to environmental protection, hence there is no dynamic relationship. For provinces in the central region, the impulse response of *EC* to *NU* is positive,

which is consistent with the PVAR model regression analysis. The implication is that these provinces should pay much attention to the high-pollution industries while the pace of new-type urbanization accelerates. The impulse response of *NU* to *EC* is positive in the current period, and then it decreases in the first period and tends to be weak after the second period, which is also consistent with the PVAR model regression analysis. The implication is that the negative externality of environmental damage related to energy consumption may offset the benefit of an increase in the level of new-type urbanization from energy consumption over time. While energy consumption is not conducive to promoting the level of new-type urbanization, these provinces should adopt some conservation policies. For provinces in the northeastern region, the impulse response of *EC* to *NU* is negative, which quickly reaches the highest value and then converges to zero. The implication is that the negative externality of environmental damage related to energy consumption may gradually increase over time. The impulse response of *NU* to *EC* is positive in the current period, and then it decreases in the first period and tends to be weak after the fourth period, which is the same as the provinces in the central region. For the provinces in the western region, the impulse response of *EC* to *NU* and the impulse response of *NU* to *EC* are virtually the same as the provinces in the central region, hence it is not necessary to interpret these results. In contrast to other regions, it is noteworthy that the impulse response of EC to NU does not diminish over time. This further denotes that the urbanization process in the western region relies predominantly on high energy consumption and highly pollutant-intensive inputs, and the legacy of conventional economic development approaches remains an arduous obstacle to overcome.

3.4. Variance Decomposition

In order to compare the relative contribution degree of unit standard deviation in *EC* and *NU*, we further adopt the variance decomposition. The variance decomposition results of period 5, period 10, and period 20 are displayed in Table 3 for different groups: (a) eastern, (b) central, (c) northeastern, and (d) western regions. As shown in Table 4, for provinces in the eastern, central, and western regions, the variance decomposition of *EC* is dominated by its own shock, and *NU* has a small effect. However, for provinces in the northeastern region, the variance decomposition of *EC* is dominated by the effect of *NU*, and its own shock has a small effect. For provinces in the eastern region, the variance decomposition of *NU* to its own shock is almost equal to the effect of *EC*. However, for provinces in central, northeastern, and western regions, the variance decomposition of *NU* is dominated by its own shock, and *EC* has a small effect. Combined with the variance decomposition of both variables, the effect of *EC* on *NU* is much larger than the effect of *NU* on *EC* for provinces in the eastern region, yet it is the opposite for provinces in central, northeastern, and western regions. These variance decomposition results also further confirm that energy consumption may bring about greater advantages relative to its disadvantage for provinces in the eastern region, yet it is imperative to cope with the possible cost of environmental pollution related to energy consumption for the provinces in central, northeastern, and western regions.

Table 4. Variance decomposition.

Response Variable	s	Eastern		Central		Northeastern		Western	
		EC	*NU*	*EC*	*NU*	*EC*	*NU*	*EC*	*NU*
EC	5	0.979	0.021	0.916	0.084	0.443	0.557	0.986	0.014
NU	5	0.057	0.943	0.177	0.823	0.233	0.767	0.036	0.964
EC	10	0.950	0.050	0.818	0.182	0.255	0.745	0.913	0.087
NU	10	0.194	0.806	0.124	0.876	0.118	0.882	0.032	0.968
EC	15	0.924	0.076	0.756	0.244	0.160	0.840	0.820	0.180
NU	15	0.360	0.640	0.106	0.894	0.069	0.931	0.040	0.960
EC	20	0.903	0.097	0.724	0.276	0.103	0.897	0.744	0.256
NU	20	0.507	0.493	0.099	0.901	0.043	0.957	0.047	0.953

So as to visually display the relative contribution degree of unit standard deviation in *EC* and *NU*, we further draw the variance decomposition results of *EC* and *NU* in the form of a coordinate axis. Figure 5 shows the variance decomposition of *EC* to *NU* for different groups: variance decomposition of *EC* to *NU* (Figure 5a) and variance decomposition of *NU* to *EC* (Figure 5b), respectively. As shown in Figure 5a, *NU* has a remarkable influence on *EC* for the provinces in the northeastern region, and the contribution rate is the largest among the four groups. Additionally, *NU* has an increasing contribution rate to unit standard deviation in *EC* for all groups. As explained above, these results imply that it is imperative to cope with the possible cost of environmental pollution related to energy consumption. As shown in Figure 5b, *EC* has decreasing contribution rate to unit standard deviation in *NU* for provinces in the central, northeastern, and western regions, yet *EC* has an increasing contribution rate to unit standard deviation in *NU* for provinces in the eastern region, which became the largest after the tenth forecast period. These results also imply that environmental pollution related to energy consumption may gradually increase as the pace of new-type urbanization accelerates for provinces in the central, northeastern, and western regions, which are consistent with the estimation results of the PVAR model.

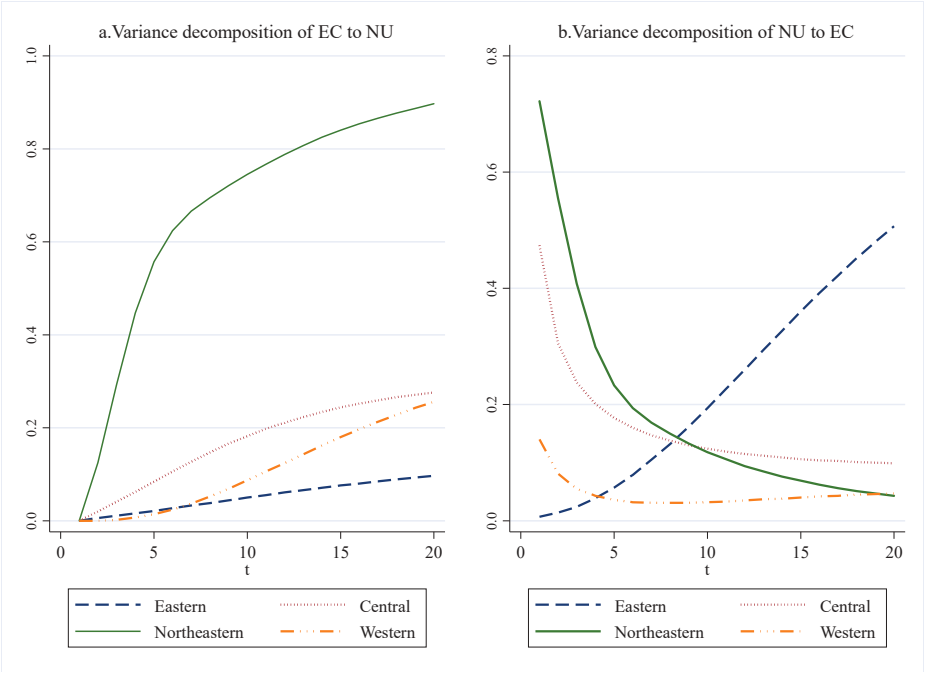

Figure 5. Variance decomposition of *EC* and *NU*.

4. In-Depth Analysis of Energy-Related Data

Finally, the pollution-related calculations are included for an in-depth analysis. We collect supplementary data, such as carbon emissions per real CNY 10,000, energy used per real CNY 10,000 (energy consumption intensity), the ratio of output value in the tertiary industry to real GDP, and the average per capita real GDP. All the relevant data are from each year's China Statistical Yearbooks, China Energy Statistical Yearbooks, each provincial statistical yearbook, and so on. As original data for the carbon emissions can be obtained from 2003 to 2019, the sample data span from 2003 to 2019. Figure 6 shows these calculations for different groups: carbon emissions (Figure 6a), energy consumption intensity (Figure 6b), industrial structure (Figure 6c), and per capita real GDP (Figure 6d), respectively.

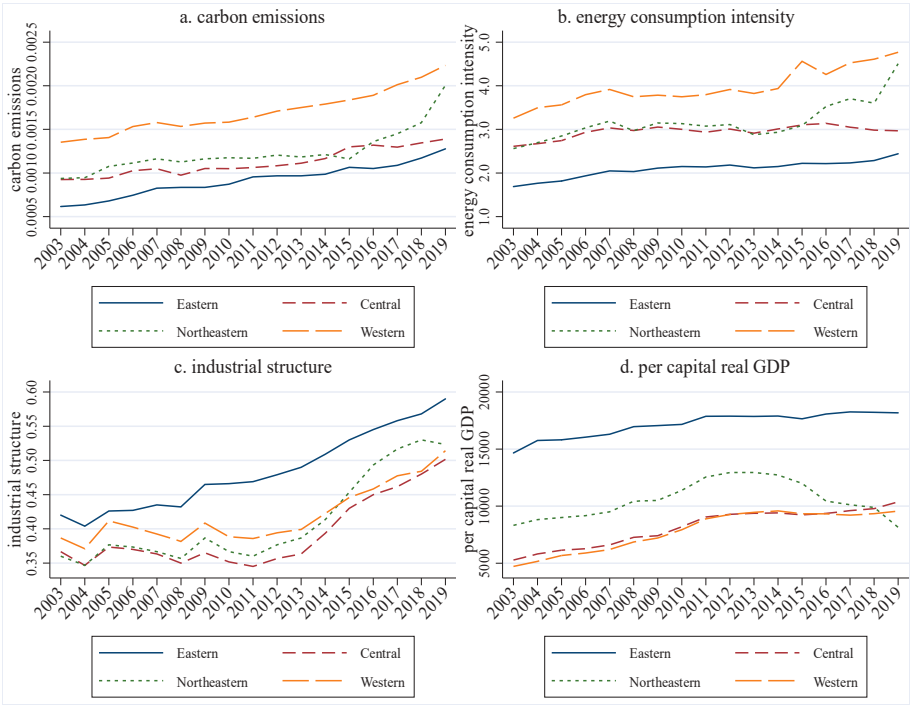

Figure 6. Some energy-related data.

As shown in Figure 6a, the largest carbon emitter appears in the western region, followed by the northeastern and central regions, and the least carbon emitter happens to be in the eastern region. As the pace of the new-type urbanization accelerates, provinces in the eastern region may make great strides to reduce the pollution of carbon emissions related to energy consumption. These results undoubtedly denote that there is an EKC relation. As shown in Figure 6b, the western region has the highest energy consumption intensity, followed by the northeastern and central regions, and finally the eastern region. As energy consumption intensity represents the efficiency of energy use, the characteristics of this variable in the four different groups denote that the energy is the most efficiently used in the eastern regions, followed by central and northeastern regions, and finally the western region. As the pace of new-type urbanization accelerates, provinces in the eastern region may successfully change their energy mix, and a decrease in carbon emissions is also can be anticipated. For example, pollution-free electrical energy can be massively put to use. To sum up, these two variables both confirm the causal relationship that new-type urbanization leads to energy consumption negatively for provinces in the eastern region, and new-type urbanization leads to energy consumption positively for provinces in the central, northeastern, and western regions over time, which seems to be in agreement with the estimation results of the PVAR model.

Figure 6c,d further provides the economic reality for the EKC relation and the causal relationship between the two. As shown in Figure 6c, the ratio of output value in the tertiary industry to real GDP in the eastern region is the highest among the four groups, followed by the northeastern region, the western region, and the central region. As shown in Figure 6d, per capita real GDP in the four groups is the same as Figure 6c. As the economy develops in the eastern region, there may be a trend toward the tertiary industry, which produces low-pollution products. Therefore, new-type urbanization leads to negative energy consumption. Provinces in the central, northeastern, and western regions are

generally eager to raise the per capita real GDP level, so standards are lax concerning relevant environmental regulations. Even some high-pollution industries are encouraged in these regions, and spontaneously their ratio of output value in the tertiary industry to real GDP is behind the eastern region. Hence, the economic reality is consistent with the EKC relation and the causal relationship between the two.

5. Concluding Remarks

The panel data of Chinese provincial administrative units are classified into four categories according to the widely adopted standard in this paper. In order to explore the causal relationship between new-type urbanization and energy consumption, we employ the PVAR model to investigate this issue and obtain the following conclusions. (1) For provinces in the eastern region, new-type urbanization leads to energy consumption negatively, and energy consumption leads to new-type urbanization positively, which becomes negative over time. For the provinces in the central and northeastern regions, an increase in the level of new-type urbanization does not bring about energy consumption, while the uni-directional causal relationship running from energy consumption to new-type urbanization is similar to provinces in the eastern region. For provinces in the western region, there is negative feedback causality between the two. (2) For provinces in the eastern region, the advantage of energy consumption is larger than its disadvantage in the short run, yet the relationship is the opposite in the long run. For provinces in the central and northeastern regions, the advantages of energy consumption and its disadvantages are similar to provinces in the eastern region. However, for provinces in the western region, the disadvantage of energy consumption may exceed its advantage. These findings are also consistent with the EKC relation. Once a province reaches a high level of new-type urbanization, it may conversely reduce the negative externality of environmental damage related to energy consumption. (3) The impulse response analysis further presents the dynamic relationship between the two. The variance decomposition demonstrates that the effect of energy consumption on new-type is much larger than the effect of new-type urbanization on energy consumption for the provinces in the eastern region, while it is totally the opposite for provinces in the central, northeastern, and western regions. (4) The largest carbon emitter appears in the western region, followed by the northeastern and central regions, and the smallest carbon emitter happens to be in the eastern region. The western region has the highest energy consumption intensity, followed by the northeastern and central regions, and finally the eastern region. The ratio of output value in tertiary industry to real GDP in the eastern region is the highest among the four groups, followed by the northeastern region, the western region, and the central region, and the per capita real GDP in the four groups is the same as the ratio of output value in the tertiary industry to real GDP.

On the basis of our conclusions above, several straightforward policy implications can be put forward. As the causal relationship presents regional heterogeneity, a one-size-for-all energy policy will not work effectively. Our government should take into consideration the different levels of new-type urbanization while implementing an energy consumption policy. Specifically, for provinces in the eastern region, they should spare no effort to promote the level of new-type urbanization and mitigate energy use in the construction of new-type urbanization. For provinces in the central region, energy consumption is not conducive to promoting the level of new-type urbanization, hence they should adopt some conservation policies to avoid the negative externality of environmental damage related to energy consumption. For provinces in the northeastern and western regions, the negative externality of environmental damage related to energy consumption may gradually increase, and they should especially pay attention to cope with the possible environmental damage and take remedial actions. Finally, according to the in-depth analysis of energy-related data, for the provinces in the northeastern and western regions, they should try to raise the efficiency of energy use, so as to reduce carbon emissions. For example, our Chinese government can encourage enterprises to carry out energy-

saving technologies in the production of goods and services. Additionally, for provinces in the northeastern and western regions, some high-pollution industries may have been encouraged, hence standards have to be strict concerning environmental protection and relevant environmental regulations.

The used methodology in this paper has some shortcomings, which calls for further research. Firstly, the constructed comprehensive urbanization index does not take into consideration the aspect of income inequality due to data availability. A comprehensive urbanization index should be constructed to reflect more about social welfare. Secondly, the empirical study in this paper does not consider the spatial spillover effect when exploring the causal relationship between energy consumption and urbanization. As we all know, both the level of energy consumption and urbanization probably present a spatial autocorrelation relationship, so future studies should employ spatial econometric techniques in this topic to deal with the possible estimation bias of the non-spatial econometric models. Thirdly, the empirical study in this paper is still based on Chinese provincial-level data. As the urban areas are the primary body to promote the urbanization process currently, it is of great value to conduct in-depth investigations at the city level.

Author Contributions: Conceptualization, Y.Q.; methodology, Y.Q.; formal analysis, C.C. and Y.G.; data curation, Y.G.; writing—original draft preparation, C.C.; writing—review and editing, C.C. All authors have read and agreed to the published version of the manuscript.

Funding: This research received no external funding.

Institutional Review Board Statement: Not applicable.

Informed Consent Statement: Not applicable.

Data Availability Statement: The data presented in this study are available on request from the corresponding author.

Conflicts of Interest: The authors declare no conflict of interest.

References

1. He, S.; Li, S.M.; Chan, K.W. Migration, communities, and segregation in Chinese cities: Introducing the special issue. *Eurasia. Geogr. Econ.* **2015**, *56*, 223–230. [CrossRef]
2. Wu, H.T.; Hao, Y.; Weng, J.H. How does energy consumption affect China's urbanization? New evidence from dynamic threshold panel models. *Energy Policy* **2019**, *127*, 24–38. [CrossRef]
3. Lv, Y.L.; Chen, W.; Cheng, J.Q. Effects of urbanization on energy efficiency in China: New evidence from short run and long run efficiency models. *Energy Policy* **2020**, *147*, 111858. [CrossRef]
4. Lin, B.Q.; Zhu, J.P. Impact of China's new-type urbanization on energy intensity: A city-level analysis. *Energy Econ.* **2021**, *99*, 105292. [CrossRef]
5. Xu, J.J.; Wang, J.C.; Li, R.; Yang, X.J. Spatio-temporal effects of urbanization on CO_2 emissions: Evidences from 268 Chinese cities. *Energy Policy* **2023**, *177*, 113569. [CrossRef]
6. Ma, B. Does urbanization affect energy intensities across provinces in China? Long-run elasticities estimation using dynamic panels with heterogeneous slopes. *Energy Econ.* **2015**, *49*, 390–401. [CrossRef]
7. Han, F.; Xie, R.; Lu, Y.; Fang, J.; Liu, Y. The effects of urban agglomeration economies on carbon emissions: Evidence from Chinese cities. *J. Clean. Prod.* **2018**, *172*, 1096–1110. [CrossRef]
8. Zhou, N.; Khanna, N.; Feng, W.; Ke, J.; Levine, M. Scenarios of energy efficiency and CO_2 emissions reduction potential in the buildings sector in China to year 2050. *Nat. Energy* **2018**, *3*, 978–984. [CrossRef]
9. Nathaniel, S.P. Modelling urbanization, trade flow, economic growth and energy consumption with regards to the environment in Nigeria. *GeoJournal* **2020**, *85*, 1499–1513. [CrossRef]
10. Chen, H.; Jia, B.; Lau, S.S.Y. Sustainable urban form for Chinese compact cities: Challenges of a rapid urbanized economy. *Habitat Int.* **2008**, *32*, 28–40. [CrossRef]
11. Mishra, V.; Sharma, S.; Smyth, R. Are fluctuations in energy consumption per capital transitory? Evidence from a panel of Pacific Island countries. *Energy Policy* **2009**, *37*, 2318–2326. [CrossRef]
12. Sun, C.; Ouyang, X.; Cai, H.; Luo, Z.; Li, A. Household pathway selection of energy consumption during urbanization process in China. *Energy Convers. Manag.* **2014**, *84*, 295–304. [CrossRef]
13. Wang, Q. Effects of urbanization on energy consumption in China. *Energy Policy* **2014**, *65*, 332–339. [CrossRef]
14. Liu, Y.; Xiao, H.; Lv, Y.; Zhang, N. The effect of new-type urbanization on energy consumption in China: A spatial econometric analysis. *J. Clean. Prod.* **2017**, *163*, s299–s305. [CrossRef]

15. Fang, J.C.; Gozgor, G.; Mahalik, M.K.; Mallick, H.; Padhan, H. Does urbanization induce renewable energy consumption in emerging economies? The role of education in energy switching policies. *Energy Econ.* **2022**, *111*, 106081. [CrossRef]
16. Ding, R.; Zhou, T.; Yin, J.; Zhang, Y.L.; Shen, S.W.; Fu, J.; Du, L.Y.; Du, Y.M.; Chen, S.H. Does the urban agglomeration policy reduce energy intensity? Evidence from China. *Int. J. Environ. Res. Public Health* **2022**, *19*, 14764. [CrossRef]
17. Northam, R.M. Vacant urban land in the American city. *Lan Econ.* **1971**, *47*, 345–355. [CrossRef]
18. Lin, B.Q.; Zhu, J.P. Energy and carbon intensity in China during the urbanization and industrialization process: A panel VAR approach. *J. Clean. Prod.* **2017**, *168*, 780–790. [CrossRef]
19. Wang, Q.; Yang, X. Urbanization impact on residential energy consumption in China: The roles of income, urbanization level, and urban density. *Environ. Sci. Pollut. Res.* **2019**, *26*, 3542–3555. [CrossRef]
20. Chen, Z.; Zhou, M. Urbanization and energy intensity: Evidence from the institutional threshold effect. *Environ. Sci. Pollut. Res.* **2021**, *28*, 11142–11157. [CrossRef]
21. Hu, W.; Fan, Y. City size and energy conservation: Do large cities in China consume more energy. *Energy Econ.* **2020**, *92*, 104943. [CrossRef]
22. Zarco-Soto, I.M.; Zarco-Periñán, P.J.; Sánchez-Durán, R. Influence of cities population size on their energy consumption and CO_2 emissions: The case of Spain. *Enviro. Sci. Pollut. Res.* **2021**, *28*, 28146–28167. [CrossRef]
23. Parikh, J.; Shukla, V. Urbanization, energy use and greenhouse effects in economic development: Results from a cross-national study of developing countries. *Glob. Environ. Chang.* **1995**, *5*, 87–103. [CrossRef]
24. Lenze, M.; Wier, M.; Cohen, C.; Hayami, H.; Pachauri, S.; Schaeffer, R. A comparative multivariate analysis of household energy requirement in Australia, Brazil, Denmark, India and Japan. *Energy* **2006**, *31*, 181–207. [CrossRef]
25. Ostuka, A. Population Agglomeration and Residential Energy Consumption: Evidence from Japan. *Sustainability* **2018**, *10*, 469.
26. Shen, L.; Cheng, S.; Gunson, A.J.; Wan, H. Urbanization, sustainability and the utilization of energy and mineral resources in China. *Cities* **2005**, *22*, 287–302. [CrossRef]
27. Sadorsky, P. Do urbanization and industrialization affect energy intensity in developing countries. *Energy Econ.* **2013**, *37*, 52–59. [CrossRef]
28. Cheng, Z.H.; Wang, L. Can new urbanization improve urban total-factor energy efficiency in China. *Energy* **2023**, *266*, 126494. [CrossRef]
29. Yu, B.B. Ecological effects of new-type urbanization in China. *Renew. Sustain. Energy Rev.* **2021**, *135*, 110239. [CrossRef]
30. Feng, Y.D.; Yuan, H.X.; Liu, Y.B. The energy-saving effect in the new transformation of urbanization. *Econ. Anal. Policy* **2023**, *78*, 41–59. [CrossRef]
31. Shao, J.; Wang, L.H. Can new-type urbanization improve the green total factor energy efficiency? Evidence from China. *Energy* **2023**, *262*, 125499. [CrossRef]
32. Ghosh, S.; Kanjilal, K. Long-term Relationship between urbanization, energy consumption and economic activity: Empirical evidence from India. *Energy* **2014**, *66*, 324–331. [CrossRef]
33. Xu, Y.Z.; Wang, Q.T. The impact of energy consumption on new urbanization—An analysis based on threshold effect. *East China Econ. Manag.* **2018**, *32*, 5–13.
34. Shafiei, S.; Salim, R. Non-renewable and renewable energy consumption and CO emissions in OECD countries: A comparative analysis. *Energy Policy* **2014**, *66*, 547–556. [CrossRef]
35. Bakirtas, T.; Akpolat, A.G. The relationship between energy consumption, urbanization, and economic growth in new emerging-market countries. *Energy* **2018**, *147*, 110–121. [CrossRef]
36. Moomaw, R.L.; Shatter, A.M. Urbanization and economic development: A bias toward large cities. *J. Urban Econ.* **1996**, *40*, 13–37. [CrossRef]
37. Davis, J.C.; Henderson, J.V. Evidence on the political economy of the urbanization process. *J. Urban Econ.* **2003**, *53*, 98–125. [CrossRef]
38. Zhao, J.; Tang, J. Industrial structure change and economic growth: A China-Russia comparison. *China Econ. Rev.* **2018**, *47*, 219–233. [CrossRef]
39. Lee, C.C.; Chang, C.P. Energy consumption and GDP revisited: A panel analysis of developed and developing countries. *Energy Econ.* **2007**, *29*, 1206–1223. [CrossRef]
40. Huang, B.N.; Hwang, M.J.; Yang, C.W. Causal relationship between energy consumption and GDP growth revisited: A dynamic panel data approach. *Ecol. Econ.* **2008**, *67*, 41–54. [CrossRef]
41. Shahbaz, M.; Lean, H.H. The dynamics of electricity consumption and economic growth: A revisit study of their causality in Pakistan. *Energy* **2012**, *39*, 146–153. [CrossRef]
42. Ben-Salha, M.; Sebri, O. On the causal dynamics between economic growth, renewable energy consumption, CO_2 emissions and trade openness: Fresh evidence from BRICS countries. *Renew. Sustain. Energy Rev.* **2014**, *39*, 14–23.
43. Zheng, W.; Walsh, P.P. Economic growth, urbanization and energy consumption-A provincial level analysis of China. *Energy Econ.* **2019**, *80*, 153–162. [CrossRef]
44. Ha, N.M.; Ngoc, B.H. Revisiting the relationship between energy consumption and economic growth nexus in Vietnam: New evidence by asymmetric ARDL cointegration. *Appl. Econ. Lett.* **2021**, *28*, 978–984. [CrossRef]
45. Tang, L.Z.; Shi, J.X.; Li, Y.J. Two-way correlation mechanism and measurement between new urbanization and clean energy consumption. *Soc. Sci. Nanjing* **2022**, *18*, 27–36.

46. Ma, M.Y.; Zheng, J.W.; Ma, T. Spatiotemporal characteristics of the impact of new urbanization on China's carbon dioxide emissions from a multi-dimensional perspective. *Acta Sci. Circumstantiae* **2021**, *41*, 2474–2486.
47. Hao, Y.; Peng, H. On the convergence in China's provincial per capital energy consumption: New evidence from a spatial econometric analysis. *Energy Econ.* **2017**, *68*, 31–43. [CrossRef]
48. Chen, C.; Qin, Y.; Gao, Y. Does new urbanization affect CO_2 emissions in China: A spatial econometric analysis. *Sustain. Cities Soc.* **2023**, *96*, 104687. [CrossRef]
49. Blundell, R.; Bond, S. Initial conditions and moment restrictions in dynamic panel data models. *J. Econ.* **1998**, *87*, 115–143. [CrossRef]
50. Jawadi, F.; Mallick, S.K.; Sousa, R.M. Fiscal and monetary policies in the BRICS: A panel VAR approach. *Econ. Model.* **2016**, *58*, 535–542. [CrossRef]
51. Hou, J.; Lu, X.; Wu, S.M.; Ke, S.G.; Li, J.; Fu, J. Analysis of the dynamic relationship between green economy efficiency and urban land development intensity in China. *Int. J. Environ. Res. Public Health* **2022**, *19*, 7960. [CrossRef]
52. Feng, Y.D.; Liu, Y.B.; Yuan, H.X. The spatial threshold effect and its regional boundary of new-type urbanization on energy efficiency. *Energy Policy* **2022**, *164*, 112866. [CrossRef]
53. Omri, A. CO_2 emissions, energy consumption and economic growth nexus in MENA countries: Evidence from simultaneous equations models. *Energy Econ.* **2013**, *40*, 657–664. [CrossRef]
54. Ozcan, B.; Tzeremes, P.; Tzeremes, N. Energy consumption, economic growth and environmental degradation in OECD countries. *Econ. Model.* **2020**, *84*, 203–213. [CrossRef]
55. Xiong, J.H.; Xu, D.Y. Relationship between energy consumption, economic growth and environmental pollution in China. *Environ. Res.* **2021**, *194*, 110718. [CrossRef] [PubMed]
56. Grossman, G.M.; Krueger, A.B. Economic growth and the environment. *Q. J. Econ.* **1995**, *110*, 353–377. [CrossRef]
57. Sun, Y.P.; Li, H.N.; Andlib, Z.; Genie, M.G. How do renewable energy and urbanization cause carbon emission? Evidence from advanced panel estimation techniques. *Renew. Energy* **2022**, *185*, 996–1005. [CrossRef]

energies

MDPI

Article

A Health-Aware Energy Storage Sharing Mechanism for a Renewable Energy Base

Chong Shao [1], Bolin Zhang [1], Bo Wei [1], Wenfei Liu [2], Yong Yang [2] and Zhaoyuan Wu [3,*]

[1] State Grid Gansu Electric Power Company, Lanzhou 730030, China; shaoch_dkzx@gs.sgcc.com.cn (C.S.); zhangblgsepc@163.com (B.Z.); edisonjoke@163.com (B.W.)
[2] State Grid Gansu Electric Power Research Institute, Lanzhou 730070, China; liuwenfeitgh@163.com (W.L.); yy8801@163.com (Y.Y.)
[3] School of Electrical and Electronic Engineering, North China Electric Power University, Beijing 102206, China
* Correspondence: wuzy@ncepu.edu.cn

Abstract: With the increasing global demand for renewable energy (RE), the growing share of new energy sources has become an inevitable trend. However, due to the uncertainty and fluctuation of renewable energy generation, this poses challenges to the stability of the power system. To mitigate the volatility of wind power output, ensure reliable power supply, and improve energy storage utilization, shared energy storage (SES) can be deployed in renewable energy bases (REBs) to alleviate the pressure on the power supply. However, electrochemical energy storage (EES) faces issues such as lifespan degradation and maintenance cost allocation. In this regard, this paper establishes an EES characterization model considering the dynamic degradation characteristics of batteries and analyzes the coupled relationship between lifespan degradation laws and key parameters in SES operation. Additionally, to assess the impact of electrochemical energy storage's dynamic degradation characteristics on energy capacity allocation and operational strategies, an optimization model for SES in REBs is developed. Building upon this, a cost allocation mechanism is designed based on the marginal contribution in both the day-ahead and the real-time markets to address the differing demands for SES among different units within the REBs. Case studies are conducted to validate the rationality of the proposed optimization model for SES in REBs and the adaptability of the cost allocation mechanism. The results provide valuable insights for practical applications.

Keywords: shared energy storage; renewable energy base; dynamic degradation characteristics; two-stage market optimization; cost allocation mechanism

Citation: Shao, C.; Zhang, B.; Wei, B.; Liu, W.; Yang, Y.; Wu, Z. A Health-Aware Energy Storage Sharing Mechanism for a Renewable Energy Base. *Energies* **2023**, *16*, 5356. https://doi.org/10.3390/en16145356

Academic Editors: Luis Hernández-Callejo, Jesús Armando Aguilar Jiménez and Carlos Meza Benavides

Received: 14 June 2023
Revised: 8 July 2023
Accepted: 11 July 2023
Published: 13 July 2023

1. Introduction

With the implementation of the dual-carbon target, it has become clear that large-scale renewable energy generation, specifically through wind and photovoltaic power, is the direction and necessary choice for new power systems in the future [1–3]. To achieve the strategic goals of building a new power system, China has proposed to further build REBs to facilitate the high-quality and rapid development of RE. The "14th Five-Year Plan for China's Economic and Social Development and the Long-Range Objectives through the Year 2035" released in March 2021 proposes to focus on developing nine clean energy bases and four offshore wind power bases during the duration of the 14th Five-Year Plan. In June 2022, the National Development and Reform Commission and nine other departments issued the "14th Five-Year Plan for the Development of RE", which explicitly proposes active steps to promote the development of wind and solar power generation facilities, and expedite the construction of large-scale REB projects, with a particular emphasis on desert, Gobi, and other barren regions [4–6]. However, the "anti-peak" characteristic of wind power and the weather impact on photovoltaic power generation have increased volatility of the net load curve, which imposes higher requirements on flexible resources for the new power system. Several provinces have implemented policies mandating that RE plants

install a specific percentage of ES to reduce the influence of RE integration on the safety and stability of the power grid. The integration of energy storage systems with renewable energy sources addresses the mismatch between renewable energy generation and load demand and reduces the uncertainty of renewable energy output, thereby enhancing the overall operational efficiency of the grid, lowering power supply costs, improving system stability, and enhancing power quality [7–9].

Due to the instability of RE, ES is needed to improve the total efficiency and stability of the power grid, reduce electricity supply costs, and enhance the utilization rate of RE. Currently, EES is the main ES technology, and its application has become increasingly widespread as its technology continues to develop and costs continue to decline [10]. Nevertheless, when ES is solely coupled with REBs, its usage rate is comparably low, making it challenging to recoup the expenses of ES, particularly in the present scenario where raw material costs are surging while RE project prices continue to fall [11,12]. The utilization rate of ES will further decrease when coupled solely with REBs, thereby hindering the promotion of the development of RE. To address the low utilization rate and poor economics of ES paired only with REBs, SES can provide an effective solution. By using SES, ES expenses can be reduced and utilization rates can be increased, thereby better supporting the development of RE [13–15].

A large-scale REB is composed of multiple wind and photovoltaic units, as well as their collection and transmission networks. Essentially, configuring SES for REBs means meeting the ES needs of various RE units within the base. Therefore, we need to consider the differences in ES needs of different RE units within the base to achieve fair distribution of ES costs. The core of the SES mechanism for REBs is how to quantify the contribution of SES to the ES capacity requirements of various RE units and then share the cost of SES accordingly [7]. Several studies have been conducted on the modes of operation for SES and cost allocation among RE units. Some researchers have investigated the impact of performance quality and prediction errors of renewable energy units on the demand for energy storage capacity and the allocation of energy storage costs [16]. Ref. [17] proposed a wind power cluster and SES coordination optimization mechanism, and allocated the benefits of each member of the alliance to demonstrate that the coordination optimization mechanism is conducive to reducing operating costs of each member and ensuring fairness of benefit distribution. In [18], a novel non-cooperative game mechanism is proposed, which optimally regulates the operation of distributed generation and flexibility resources by considering economic factors and electric power quality. Ref. [19] introduced a new two-stage credit-based model for SES which, considering time accumulation effects, developed an SES pricing strategy and a capacity planning scheme, and demonstrated the advantages of the proposed novel shared model in the field of economic efficiency and the utilization rate of ES. The research results indicate that SES has enormous potential value, not only for configuring SES in REBs but also for applying SES to various links in the power supply chain. Ref. [20] aimed to examine the real advantages of implementing SES in residential neighborhoods, established optimization operation models for independent and SES, compared and analyzed the optimal energy operations of the two, and developed an efficient control strategy suitable for the use of SES to demonstrate the advantages of SES in saving electricity costs and improving the ES utilization rate. Some studies have also proposed transactional operation mechanisms for energy storage systems based on non-cooperative game theory [21,22]. In [22], an interactive energy management scheme is defined for multiple SES systems and users to achieve information sharing. These studies have provided certain theoretical support and a decision-making basis for the formulation of SES modes among a considerable quantity of RE units within a large REB. Existing research has primarily focused on optimal capacity allocation and economic benefits of SES among renewable energy units while neglecting the impact of cost allocation mechanisms on the sustainable operation of SES. Therefore, this paper formulates a fair cost allocation mechanism considering the differential ES demands of each renewable energy unit within the base, aiming to achieve equitable distribution of ES costs.

EES, mainly consisting of energy storage batteries, is one of the most economically advantageous ES technologies among existing RE storage technologies. However, it should be noted that EES has the characteristic of dynamic degradation of its lifespan. Although SES operation modes can improve ES utilization rate, they can accelerate the degradation of the lifespan of EES. However, in the research on SES for renewable energy integration currently, the influence of shared operation on energy storage battery lifespan degradation is often overlooked or simplified. For instance, some studies consider the working efficiency of energy storage batteries as a constant value, disregarding the dynamic changes in charging and discharging efficiencies [23,24]. However, in actual operation, energy storage batteries experience dynamic changes in charging and discharging efficiencies due to power losses generated during operation to meet load demand [25,26]. Additionally, to simplify the complex degradation variations in practical operation, certain studies assume the same degree of lifespan degradation under different operating conditions, without accounting for the nuanced degradation of ES capacity under different operational scenarios [27]. However, it is clear that the lifespan of EES will gradually shorten with changes in the state of charge (SOC) and the number of charging-and-discharging cycles. To more accurately estimate the degradation of the lifespan of energy storage batteries, equivalent circuit models, empirical models, and aging mechanism models are currently mainly used [28]. Ref. [29] proposed a method to detect the decay of the available capacity of energy storage batteries using the discharge curve and capacity data based on a first-order Thevenin equivalent circuit model. Ref. [30] established a calendar aging model of energy storage batteries based on experimental data and quantified the impact of SOC, temperature, and battery operating time on the degree of battery life decay. Ref. [31] studied the dynamic performance changes of energy storage batteries under different environmental conditions in a residential photovoltaic energy storage battery system, and analyzed the impact of charging-and-discharging curves on battery aging. Moreover, existing research tends to focus on the lifespan degradation characteristics of distributed independent energy storage systems, lacking investigations on the impact of dynamic degradation characteristics of SES on system operation. This paper, however, conducts a refined analysis of the dynamic degradation characteristics in the actual operation of EES.

Moreover, due to the diverse output characteristics of different renewable energy units, there are variations in the capacity requirements for SES. Existing research has primarily focused on optimal capacity allocation and economic benefits of SES among renewable energy units while neglecting the impact of cost allocation mechanisms on the sustainable operation of SES. To analyze the influence of dynamic degradation characteristics on the operational strategies and capacity allocation of electrochemical shared energy storage in REBs, and to address the issue of uneven cost allocation resulting from differences in ES capacity requirements, this paper presents a refined modeling of SES lifespan degradation. Building upon the health status of EES, known as the state of health (SoH), this research investigates the optimization of operational strategies and cost allocation mechanisms for SES in REBs by considering dynamic degradation characteristics. The main innovations can be summarized in the following three aspects:

- This paper refines the coupling relationship between the degradation laws and key parameters in the operation process of shared energy storage, and establishes a refined degradation model for the operation of electrochemical energy storage sharing. This model can better reflect the changes in performance parameters such as shared energy storage charging and discharging efficiencies and state of health (SoH), thus quantifying the degree of degradation in the lifespan of shared energy storage. It also provides important theoretical support for the practical application of shared energy storage.
- A renewable energy base–shared energy storage operation framework that considers dynamic lifespan degradation is designed. This framework fully utilizes the advantages of shared energy storage and enhances the profitability of various units within high renewable energy bases in the day-ahead market through "peak shaving and valley filling". At the same time, it mitigates the uncertainty of wind power output

and reduces the assessment cost of real-time balancing markets. The design of this framework can better promote the sustainable development of renewable energy generation.

- A shared energy storage cost allocation mechanism is proposed for renewable energy bases based on the marginal contribution in both the day-ahead and the real-time market. This mechanism can meet the energy storage demands of different renewable energy generators and incentivize compatibility. The numerical results demonstrate a positive correlation between the shared energy storage costs allocated to different renewable energy generators and their corresponding energy storage demands. The implementation of this mechanism can better promote the coordinated optimization of renewable energy and shared energy storage operations, achieving a win-win situation.

The rest of this paper is structured in the following manner. The SES operation framework for a REB is proposed in Section 2. The refined model of dynamic life decay of EES is introduced in Section 3. In Section 4, an optimized operational approach for SES in a REB is presented, taking into account the dynamic degradation characteristics of EES. The SES cost allocation mechanism based on the marginal contribution in both the day-ahead and real-time markets is introduced in Section 5. Section 6 contains the conclusions and future prospects of this study.

2. Framework of Energy Storage Sharing

A two-stage optimal collaborative operation strategy for a REB and SES is proposed by combining day-ahead optimization and real-time optimization. This strategy includes two stages: during the first stage, the optimization of day-ahead scheduling is carried out, and each unit in the REB optimizes its day-ahead operation strategy based on the day-ahead output prediction data. In the second stage, the charging and discharging operation statuses of SES vary according to real-time electricity prices and the uncertainty of wind power output, then embedded it into the day-ahead optimization model of the first stage. Meanwhile, the dynamic degradation characteristics of the SES's lifespan are taken into account, and the influence of battery health status changes on ES capacity allocation is considered. Considering the differential SES capacity demands of different units within the REB, this paper measures the contribution of each member to the overall alliance and allocates the investment and operational costs of SES among various renewable energy units within the base. This allocation is performed in a manner that reflects the varying needs of different units and ensures a fair distribution of the investment and operational costs associated with SES. This strategy aims to optimize the overall operation of the system, fully consider the uncertainty and fluctuations of wind power output in actual operation, and improve the efficiency and economic viability of RE generation. The Operation framework for energy storage sharing in a renewable energy base is shown in Figure 1.

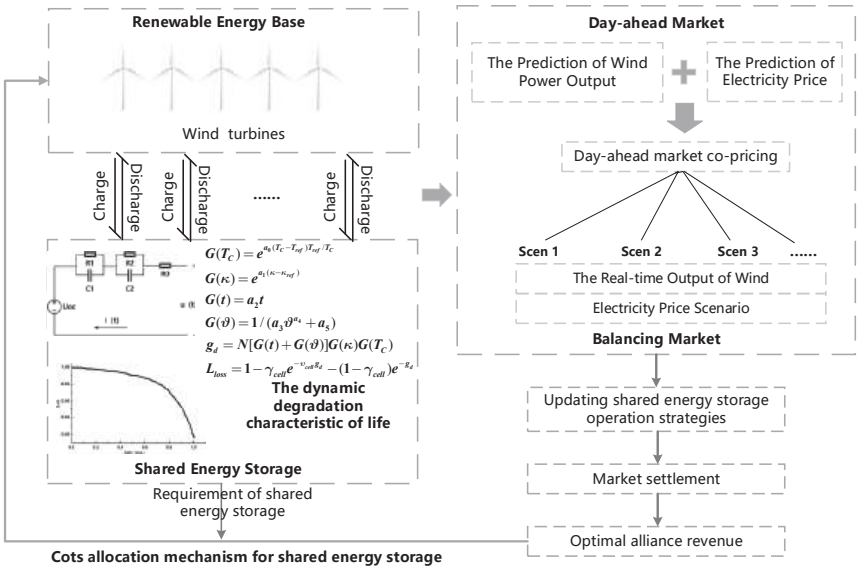

Figure 1. Operation framework for energy storage sharing in a renewable energy base.

3. Dynamic Degradation Model in Battery Energy Storage Sharing

To alleviate the impact of large-scale RE, such as wind and solar power, it may be necessary to frequently adjust the charge and discharge states of RE batteries and the power flow in and out of the grid. Therefore, the capacity degradation caused by the changes in charge and discharge behavior of RE batteries in a brief span of time cannot be ignored. It is necessary to consider the influence of changes in charge and discharge power on the performance and lifespan of ES devices. Therefore, the fine-grained dynamic degradation characteristics of EES are of great significance. In this section, the dynamic degradation characteristics of EES will be finely modeled to provide more theoretical support for the subsequent research on operation and cost allocation mechanisms of SES in REB.

3.1. Health-Aware Perception Model

The previous literature has used the SoH of an electrochemical battery to characterize its degree of life degradation. Within this segment, a health-aware perception model utilizing the battery's equivalent circuit is established. Since the dual-polarization (DP) equivalent circuit model is superior to the Thevenin model in the field of balance estimation precision and calculative speed, the DP model has been chosen to characterize the SOH of the battery. The DP model is essentially a series circuit, consisting of a power source, internal resistance, and a second-order RC parallel circuit, shown in Figure 2 [32].

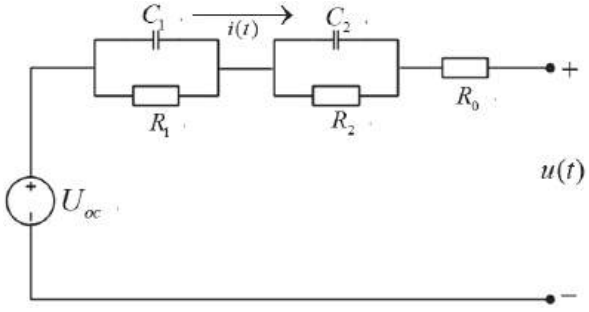

Figure 2. DP equivalent circuit.

The spatial state equations for the DP equivalent circuit can be derived as follows:

$$\begin{cases} u_t = U_{oc} - u_{c1,t} - u_{c2,t} - i_t R_0 \\ i_t = \frac{u_{c1,t}}{R_1} + C_1 \frac{du_{c1,t}}{dt} = \frac{u_{c2,t}}{R_2} + C_2 \frac{du_{c2,t}}{dt} \end{cases} \tag{1}$$

where U_{oc} is the open circuit voltage, R_0 is the internal resistance of the battery, $i(t)$ is the internal current of the battery, and $u_{c1,t}$ and $u_{c2,t}$ represent voltage across the two RC circuits. By measuring the open circuit voltage and voltage across each RC circuit, the circuit current can be calculated using the spatial state equations. Battery capacity can then be calculated using Equation (2).

$$E_{SES,t} = E_{SES,t_0} - \eta_{SES} \int_{t_0}^{t} i_t dt \tag{2}$$

where η_{SES} is the Coulombic efficiency of the battery, E_{SES,t_0} represents the rated capacity of the battery at initial state, $E_{SES,t}$ represents the capacity of the battery at time t, and t_0 represents the initial operating time of the battery. Based on the stored energy capacity, the SoH of the ES battery can be calculated.

The SoH of the ES battery at time t SOH_t is expressed as the present available capacity divided by the rated capacity at initial state, as follows:

$$SOH_t = \frac{E_{SES,t}}{E_{SES,t_0}} \times 100\% \tag{3}$$

As energy storage batteries undergo continuous charging-and-discharging cycles, internal aging occurs, resulting in increased internal resistance and decayed capacity. For a brand-new RE storage battery, its initial SoH is 1. When SoH_t is lower than a certain value δ or the internal resistance of the battery increases to more than twice the initial resistance, the energy storage battery should be dismantled and recycled. Therefore, the final state of health for the battery is δ, which is set to 0.8 in this paper [33–35]. Thus, the SoH_t and internal resistance of energy storage batteries are subject to the following constraints:

$$\begin{cases} SOH_t \geq \delta \\ Z_t \geq 2Z_{start} \end{cases} \tag{4}$$

where Z_t is the internal resistance of the battery at time t. The relationship between SoH and battery internal resistance can be further established using DP equivalent circuits, which facilitates the determination of whether the battery is still suitable for ES based on its internal resistance, as shown below:

$$Z_t = Z_{start} + \frac{SOH_{t_0} - SOH_t}{SOH_{t_0} - SOH_{t_N}} (Z_{end} - Z_{start}) \tag{5}$$

where SOH_{t_0} and SOH_{t_N}, respectively, represent the initial and final health status of the battery during its lifespan, Z_{start} and Z_{end} are the battery's resistance at the beginning and end of the entire lifespan, respectively, and t_N is the end time of the battery's lifespan.

In addition, the relationship between the maximum power output P_t of a battery at a certain moment and its SoH can be derived from DP equivalent circuits, as shown in Equation (6):

$$P_t = \frac{Z_{start}}{Z_t} P_0 \tag{6}$$

where P_0 refers to the maximum power output that the battery can produce at the initial state.

3.2. Energy Storage Battery Life Degradation Model

The life degradation of ES batteries is influenced by various external stress factors, such as temperature and operating time, and is also affected by the battery's life status. Therefore, its degradation can be considered as a nonlinear process that is the result of the combined effect of external stress and time by establishing a nonlinear life degradation model that can be decomposed into multiple stress factor models.

The life degradation caused by calendar aging L_{cal}, can be considered as a function of the average state of charge $Soc(\overline{\kappa})$, battery average temperature $\overline{T_c}$, and time t.

$$L_{cal} = g_t(\overline{\kappa}, t, \overline{T_C}) \tag{7}$$

Each charge and discharge cycle of the battery results in life degradation. The cumulative life degradation is obtained by adding up life degradation of each cycle.

$$L_{cyc} = \sum_{t=1}^{N} \omega_t g_c(\kappa_t, \vartheta_t, T_c) \tag{8}$$

where $L_{cyc,loss}$ refers to the life degradation caused by cycle aging; ϑ_t represents the depth of discharge of the battery in the t-th cycle; and ω_t is a 0–1 variable that characterizes the operating state of the battery in the cycle t, with a value of 1 indicating that the battery is in a cyclic charging-and-discharging state and 0 indicating that the battery is not undergoing charging and discharging, during which the life degradation of the battery only includes the life degradation caused by calendar aging. The life degradation of the entire lifetime of the battery can be represented as the function g_d of $\kappa, t, T_c, \vartheta$:

$$g_d(\kappa, t, T_C, \vartheta) = g_t(\overline{\kappa}, t, \overline{T_C}) + \sum_{t=1}^{N} \omega_t g_c(\kappa_t, \vartheta_t, T_c) \tag{9}$$

If cycles are identical, in a single cycle, the average temperature and SOC equals the overall averages of the battery lifetime, thus $\overline{T_c} = T_c, \overline{\kappa} = \kappa$. Equation (8) can be simplified as shown below:

$$g_d(\kappa, t, T_C, \vartheta, N) = N g_d(\kappa, t, T_C, \vartheta, 1) = N g_{d,1} \tag{10}$$

where $g_d(\kappa, t, T_c, \vartheta, 1)$ is denoted as $g_{d,1}$, which represents the life degradation during a single cycle, and N is the number of charge and discharge cycles.

The life degradation caused by calendar aging and cycle aging can be expressed in a product form of multiple linear stress factor models as follows:

$$g_{d,1} = [G(t) + G(\vartheta)]G(\kappa)G(T_C) \tag{11}$$

(1) The temperature stress model:

$$G(T_C) = e^{a_0(T_C - T_{ref})\frac{T_{ref}}{T_C}} \tag{12}$$

(2) The state-of-charge stress model:

$$G(\kappa) = e^{a_1(\kappa - \kappa_{ref})} \tag{13}$$

(3) The time stress model:

$$G(t) = a_2 t \tag{14}$$

(4) The depth-of-discharge stress model:

$$\begin{aligned} G(\vartheta) &= \frac{1}{a_3 \vartheta^{a_4} + a_5} \\ \vartheta_t &= \frac{P_t^{ch} + P_t^{dis}}{2E_{c,t}} \end{aligned} \tag{15}$$

where a_0 represents the temperature stress coefficient; T_{ref} refers the reference temperature in Kelvin (K); a_1 is the SOC stress coefficient; κ_{ref} is the reference SOC, which can be generally taken as 0.4–0.5; a_2 is the time stress coefficient, indicating that after excluding factors such as temperature and life dependence, the degradation rate has a linear relationship with time; $P^{ch}(t)$ and $P^{dis}(t)$ represent the charging and discharging powers of the battery during the t-th cycle, respectively; and a_3, a_4, and a_5 are stress coefficients about DOD.

According to the empirical formula [30], the life degradation of an energy storage battery can be calculated as follows:

$$L_{loss} = 1 - \gamma_{cell} e^{-v_{cell} g_d} - (1 - \gamma_{cell}) e^{-g_d} \tag{16}$$

where L_{loss} represents the life degradation of the battery over its entire life cycle (pu), and γ_{cell} and v_{cell} are parameters related to the formation process of SEI film.

3.3. Dynamic Efficiency Model for Energy Storage Batteries

3.3.1. Segmented Linearization of Power for EES Batteries

At any given time, the operating power of the battery $P(t)$ satisfies the following equation:

$$P_{c,t} = P_t^{ch} + P_t^{dis} \tag{17}$$

However, it is impossible for one battery to charge and discharge simultaneously at any given time, and one of P_t^{ch} or P_t^{dis} must be zero. The dynamic behavior of the battery is simulated using the aforementioned DP equivalent circuit model, and the relationship between the battery SoH and internal resistance is calculated. The charge–discharge cycles of the battery will cause dynamic changes in its SoH and internal resistance, resulting in dynamic changes in the operational efficiency during different periods. To simplify the model, the charging and discharging power of the battery are segmented and linearized separately. If the charging power is divided into M_1 segments, it satisfies:

$$P_t^{ch} = \sum_{m=1}^{M_1} P_{cm,t} \tag{18}$$

$$P_{cm}^{\min} \omega_{c,m,t} \le P_{cm,t} \le P_{cm}^{\max} \omega_{c,m,t}, m = 1, 2, \ldots, M_1 \tag{19}$$

where P_{cm}^{max} and P_{cm}^{min} are the maximum and minimum of the charging power for the segment, respectively, and $\omega_{c,m,t}$ is a 0–1 state variable that characterizes the charging state at time t, where a value of 1 indicates that the charging power is within the mth segment.

$$\sum_{m=1}^{M_1} \omega_{c,m,t} = 1 \tag{20}$$

The above equation indicates that the battery charging power can only be within one power segment at any given moment. Similarly, for the discharging power, it is divided into M_2 segments, which satisfies:

$$P_t^{dis} = \sum_{j=1}^{M_2} P'_{cj,t} \tag{21}$$

$$P_{cj,t}^{\min\prime} \pi_{c,j,t} \le P'_{cj,t} \le P_{cj,t}^{\max\prime} \pi_{c,j,t}, j = 1, 2, \ldots, M_2 \tag{22}$$

$$\sum_{j=1}^{M_2} \pi_{c,j,t} = 1 \tag{23}$$

where $P_{cj,t}^{max\prime}$ and $P_{cj,t}^{min\prime}$ are the maximum and minimum of the discharging power for the j-th segment of the battery, respectively, and $\pi_{c,j,t}$ is a 0–1 state variable that characterizes the discharging power at t, where a value of 1 indicates that the discharging power is within the j-th segment.

3.3.2. Storage Capacity of EES Batteries

After the time Δt, the incremental capacity of the battery is as follows:

$$\Delta E_{c,t} = [\sum_{m=1}^{M_1} P_{cm,t}\eta_{cm}^{ch} + \frac{1}{\eta_{cj}^{dis}}\sum_{j=1}^{M_2} P'_{cj,t}]\Delta t \tag{24}$$

$$\Delta E_{c,t} = E_{c,t-1} - E_{c,t} \tag{25}$$

$$E_c^{\min} \le E_{c,t} \le E_c^{\max} \tag{26}$$

where η_{cj}^{ch} and η_{cj}^{dis} refer to the charging and discharging efficiencies of the m-th segment, respectively, and E_c^{min} and E_c^{max} are the minimal and maximal battery capacity, respectively.

4. Shared Energy Storage Operation Model

In this section, we investigate the optimal strategy for the joint operation of RE units containing multiple wind turbines and SES, considering the dynamic degradation characteristics.

4.1. Objective Function

The objective function is to maximize profit, which comprises the revenue of the day-ahead electricity market and real-time electricity market, and the total cost of SES.

$$\max \sum_{t\in\phi T} (R_t^{DA} + R_t^{BA} - C_t^{sum}) \tag{27}$$

where R_t^{DA} denotes the day-ahead market revenue at time t, R_t^{BA} denotes the real-time market revenue at time t, and C_t^{sum} denotes the total cost of SES at time t.

The day-ahead energy market (DEM) revenue R_t^{DA} and real-time energy market (REM) revenue R_t^{BA} can be expressed as follows:

$$R_t^{DA} = \lambda_t^{DA} P_t^{DA} \tag{28}$$

$$R_t^{BA} = \lambda_t^{down} P_t^{down} - \lambda_t^{up} P_t^{up} \tag{29}$$

$$\lambda_t^{down} = \phi^{down}\lambda_t^{DA}, \lambda_t^{up} = \phi^{up}\lambda_t^{DA} \tag{30}$$

where λ_t^{DA} is the DEM price at time t; P_t^{DA} is the total power in the DEM at time t; P_t^{down} and P_t^{up} represent the positive and negative power imbalance at time t respectively; λ_t^{down} and λ_t^{up} are the settlement prices for the positive and negative imbalances of electricity quantities in the balancing market, respectively; and ϕ^{down} and ϕ^{up} are the penalty factors corresponding to positive and negative imbalances of electricity quantities, respectively.

The total cost of SES C_t^{sum} is expressed as Equation (33), and C_t^{sum} includes the investment cost of SES and its degradation cost, as follows:

$$C_t^{at} = \frac{C_t^{inv} L_{loss,t}}{24 \times (1 - 40\%)} \tag{31}$$

$$C_t^{inv} = \frac{\gamma(1+\gamma)^y}{(1+\gamma)^y - 1} \times \frac{c_P^{SES} P_{\max}^{SES} + c_E^{SES} E_{SES}}{T \times 365} \tag{32}$$

$$C_t^{sum} = C_t^{inv} + C_t^{at} \tag{33}$$

where T is all the dispatch cycle number of SES within one day, and $L_{loss,t}$ is the lifespan degradation rate of EES batteries during period t. Typically, when the health status of a lithium-ion battery drops below 80%, the battery's utilization rate cannot meet the ES requirements and it should be recycled. C_t^{inv} is the SES investment cost, γ refers to the annual percentage rate of funds, y is the lifespan of the SES device, c_P^{SES} and c_E^{SES} are the unit cost prices of shared energy per unit power and unit capacity, respectively, P_{max}^{SES} is the maximum power of the SES, and E_{SES} is the capacity of SES.

The above utilizes the concept of unitized cost, which converts ES replacement cost into cost per unit charge–discharge capacity, in order to obtain the ES degradation cost at each moment.

4.2. Constraints

In this paper, the wind turbine units and the collaborative entity of the SES are selected to participate in the day-ahead energy DEM. Therefore, the total power in the DEM is equal to the sum of the day-ahead power outputs from the wind turbines and the energy storage unit. Similarly, when they participate in the REM, the total power in the REM is equal to the sum of the real-time power outputs from the wind turbines and the energy storage unit, as follows:

$$P_t^{DA} = P_{wind,t}^{DA} + P_{SES,t}^{DA} \tag{34}$$

$$P_\delta^{BA} = P_{wind,\delta}^{BA} + P_{SES,\delta}^{BA} \tag{35}$$

where $P_{wind,t}^{DA}$ is the wind power of the DEM at time t, $P_{SES,t}^{DA}$ is the ES power of the DEM at time t, P_δ^{BA} is the total power in the REM at time t, $P_{wind,\delta}^{BA}$ is the wind power of the REM at time δ, and $P_{SES,\delta}^{BA}$ is the ES power of the REM at time δ. The participation of the energy storage unit in the DEM is determined by both its charging power and discharging power. It is the difference between the discharging power and the charging power. Since the energy storage unit can only be in either a charging or discharging state at a given time t, when it is in the discharging state, it generates positive revenue from participating in the DEM. On the other hand, when it is in the charging state, it incurs negative revenue from participating in the DEM. Therefore, the day-ahead power of the energy storage unit participating in the market is the difference between the discharging power and the charging power. The same principle applies to the power of the energy storage unit participating in REM.

$$P_{SES,t}^{DA} = P_{dis,t}^{DA} - P_{ch,t}^{DA} \tag{36}$$

$$P_{SES,\delta}^{BA} = P_{dis,\delta}^{BA} - P_{ch,\delta}^{BA} \tag{37}$$

where $P_{ch,t}^{DA}$ is charging power of the DEM at time t, $P_{dis,t}^{DA}$ is the ES discharging power of the DEM at time t, $P_{ch,t}^{BA}$ is the ES charging power of the REM at time t, and $P_{dis,t}^{BA}$ is the ES discharging power of the REM at time t. All four of these variables take non-negative values.

Constraints on the system are as follows:

(1) the constraints of wind power output are

$$0 \le P_{wind,t}^{DA} \le P_{sum,t}^{DA} \tag{38}$$

$$0 \le P_{wind,\delta}^{BA} \le P_{sum,t}^{BA} \tag{39}$$

where $P_{sum,t}^{DA}$ represents the day-ahead forecasted total power for multiple wind turbines at time t, and $P_{sum,t}^{BA}$ represents the real-time forecasted total power for multiple wind turbines at time t.

(2) Energy storage capacity and power constraints: Equation (40) represents the constraint on the ES capacity. Equation (41) represents the minimal and maximal of the charging and discharging powers. Equation (42) restricts the device from charging and discharging energy simultaneously. Equation (43) denotes the energy balance constraint of the ES; it means that the charging-and-discharging capacity during the 24 h regulation process must maintain balance with the initial energy level.

$$0 \le E_{SES,t}^{DA} \le E_{SES}, 0 \le E_{SES,\delta}^{BA} \le E_{SES} \tag{40}$$

$$\begin{cases} 0 \le P_{ch,t}^{DA} \le \mu_t^{ch} P_{\max}^{SES} \\ 0 \le P_{dis,t}^{DA} \le \mu_t^{dis} P_{\max}^{SES} \end{cases}, \begin{cases} 0 \le P_{ch,\delta}^{BA} \le \mu_t^{ch} P_{\max}^{SES} \\ 0 \le P_{dis,\delta}^{BA} \le \mu_t^{dis} P_{\max}^{SES} \end{cases} \tag{41}$$

$$\mu_t^{char} + \mu_t^{dis} \le 1 \tag{42}$$

$$E_{SES,0}^{DA} = E_{SES,T}^{DA}, E_{SES,0}^{BA} = E_{SES,T}^{BA} \tag{43}$$

where $E_{SES,t}^{DA}$ and $E_{SES,t}^{BA}$ represent the day-ahead and REM storage capacities at different times, P_{max}^{SES} represents the maximum operational power of the SES, μ_t^{ch} and μ_t^{dis} are 0–1 variables that represent the operation status of the ES at time t, and $E_{SES,T}^{DA}$ and $E_{SES,T}^{BA}$ represent the DEM and REM storage capacities at the last time t of the day.

Additionally, the energy iteration relationship of the ES unit in the DEM and REM is shown in Equations (44) and (45):

$$E_{SES,t+1}^{DA} = E_{SES,t}^{DA} + P_{ch,t}^{DA} \cdot \eta_t^{SES} - P_{dis,t}^{DA} / \eta_t^{SES}, E_{SES,0}^{DA} = 60\% E_{SES} \tag{44}$$

$$E_{SES,\delta+1}^{BA} = E_{SES,\delta}^{BA} + (P_{ch,\delta}^{BA} \cdot \eta_t^{SES} - P_{dis,\delta}^{BA} / \eta_t^{SES}) \Delta t \, , \delta \in [t, t+1] \, , E_{SES,0}^{BA} = 60\% E_{SES} \tag{45}$$

where η_t^{SES} represents the working efficiency of the ES at time t.

Taking into account the dynamic degradation characteristics of EES devices and using SoH as a medium, the changes in the performance parameters of ES are incorporated into the above constraints to reflect the influence of the degradation of ES life on the operation and benefits. The analysis in Section 3 reveals a nonlinear dependence between ES device parameters and SoH. To facilitate the optimization calculation, this nonlinear relationship is first linearized.

By using the idea of piecewise model linearization, the linear relationship between battery internal resistance Z_t and SoH can be fitted as follows:

$$Z_t = \alpha SOH_t + \beta \tag{46}$$

Substituting Equation (46) into the expression for ES charging and discharging powers yields.

$$P_{t,\max}^{SES} = \frac{Z_{start}}{\alpha SOH_t + \beta} \cdot P_{0,\max}^{SES} \tag{47}$$

Similarly, the expression for different segments of ES capacity can be uniformly linearized.

$$E_{SES,t} = aSOH_t + b \tag{48}$$

We can substitute the ES parameter expressions obtained from Equations (47) and (48) into the constraints for ES power and capacity and update them on an hourly basis to account for the dynamic degradation characteristics of the ES device.

(3) Power balance constraints:

$$P_{wind,\delta}^{BA} + g_{SES,t} - d_{SES,t} - P_{wind,t}^{DA} = P_t^{down} - P_t^{up} \tag{49}$$

$$0 \le P_t^{up} \le M_3(1 - z_t) \tag{50}$$

$$0 \le P_t^{down} \le M_4 z_t \tag{51}$$

where $g_{SES,t}$ and $d_{SES,t}$ represent the charging and discharging quantities respectively, of the ES system, z_t is a binary variable indicating the power imbalance status, and M_3 and M_4 are sufficiently large positive numbers.

Equations (27)–(51) are used to establish the coupling relationship between the DEM and REM of the alliance which is composed of REBs and SES.

5. Cost Allocation Mechanism of Shared Energy Storage

To ensure equitable distribution of investment costs for SES, this paper introduces the concept of a "revenue increase rate" as a measure to quantify the demand level of a REB for SES. This metric evaluates the number of occupied ES resources by the REB and the potential revenue that can be obtained. The analysis in this paper considers the market revenue of a REB, including electricity value and system flexibility, in both day-ahead and real-time balancing markets, and compares them with the benefits obtained when the REB participates individually in the market. Finally, the costs of the SES are allocated to each REB based on comprehensive revenue-increase-rate metrics for REB.

5.1. Electricity Value in the Day-Ahead Market

Before allocating the SES costs, it is essential to calculate the revenue obtained by each alliance member from selling electricity in the day-ahead market. The calculation method of this revenue is obtained by multiplying the declared power with the day-ahead market clearance price. To better solve the cost allocation problem, this paper uses the Vickrey–Clarke–Groves (VCG) mechanism, which is a widely used incentive-compatible mechanism for allocating social welfare [36]. In addition, this mechanism can help define the substitute value of SES for other electricity users. As multiple renewable energy base–energy storage systems jointly quoting can only obtain the alliance's overall quotation curve, this paper analyzes the demand for SES by different REBs through the substitute value method to obtain individual quotation curves for each entity. This method indirectly obtains the individual quotation curves of each entity by comparing the changes in the alliance's overall quotation curve, thereby better solving the cost allocation problem, as in Equation (52).

$$R_{DA,i,t}^{\mathrm{WPP}} = \sum_{t \in \Gamma} \lambda_t^{DA} \cdot (P_{DA,t}^{C*} - P_{DA,-i,t}^{C*}), \forall i, j, t \tag{52}$$

where $R_{DA,i,t}^{WPP}$ represents the revenue obtained by a certain REB in the DEM, $P_{DA,t}^{C*}$ represents the optimal day-ahead declared power obtained by the optimization model, and $P_{DA,-i,t}^{C*}$ represents the optimal declared power corresponding to removing a specific REB.

5.2. Flexibility Value in the Real-Time Balancing Market

The revenue earned by the alliance members' flexibility during real-time operations is known as the flexibility value in the REM, which is obtained by multiplying the respective imbalanced electricity quantity with the corresponding settlement price. When comparing the individual deviation direction with the system's overall deviation direction, if they are opposite, this indicates that the member has alleviated the extent of system deviation,

reduced the system's demand for flexibility, and increased overall revenue. Then, the member's revenue is positive. If the directions are the same, it indicates that the member has intensified the degree of system deviation, further increased the system's demand for flexibility, and decreased overall revenue, and the member's revenue is negative. Similar to measuring the energy value of each member in the DEM, we can extract the flexibility value of a member in the real-time market and represent the revenue of REB members in the real-time balancing market through the deviation that appears in the alliance as a whole, as shown in Equation (53):

$$R_{BA,i,t}^{WPP} = \sum_{t\in\Gamma}\sum_{s\in\Omega}\delta_s(\lambda_{s,t}^{+}(P_{s,t}^{C+*} - P_{s,-i,t}^{C+*}) + \lambda_{s,t}^{-}(P_{s,t}^{C-*} - P_{s,-i,t}^{C-*})), \forall s, i, t \tag{53}$$

where δ_s is the possibility of the scenario, $R_{BA,i,t}^{WPP}$ refers to the revenue obtained by the REB in the real-time balancing market, $P_{s,t}^{C+*}$ and $P_{s,t}^{C-*}$ represent the most effective methods for making bids of positive and negative imbalance power of the alliance, respectively, obtained by solving the above optimization model, and $P_{s,-i,t}^{C+*}$ and $P_{s,-i,t}^{C-*}$ represent the positive and negative imbalance power of the alliance, respectively, corresponding to removing a specific wind power merchant.

Similarly, by measuring the revenue obtained by a REB's individual participation in the market from both the day-ahead and real-time dimensions and comparing them with the revenue obtained after forming the alliance, the revenue increment of each REB in the alliance can be obtained, as shown in Equation (54).

$$\Delta R_{i,t}^{WPP} = R_{DA,i,t}^{WPP} + R_{BA,i,t}^{WPP} - R_{i,t,D}^{WPP}, \forall i, t \tag{54}$$

where $\Delta R_{i,t}^{WPP}$ represents the revenue increase in a certain REB in the alliance, and $R_{i,t,D}^{WPP}$ represents the revenue obtained by this REB's individual participation in the market.

Therefore, the revenue increase rate of each REB in the alliance's joint bidding is the ratio of the total revenue increase in this member in the DEM and REM and the total revenue increase in all members in the alliance, as shown in Equation (55).

$$\tau_i^{\mathrm{WPP}} = \frac{\sum_{t\in\Gamma} T_{i,t}^{WPP}}{\sum_{i\in M}\sum_{t\in\Gamma} T_{i,t}^{WPP}}, \forall i, t \tag{55}$$

The main revenue improvement rate characterizes the proportion of the revenue that alliance members can obtain in the DEM and REM from two dimensions: the value of electricity energy and the value of flexibility. The coupling connection between the DEM and REM is established by the concept of imbalance power. Through the determination of penalty prices, a REB can be guided to overproduce or underproduce a certain amount of power in the DEM. SES can exert a controlling function over smoothing the power imbalance that arises as a result, thus achieving the goal of maximizing overall revenue. On this basis, the investment and depreciation costs of SES can be allocated according to the aforementioned revenue improvement rate, as shown in Equation (56).

$$C_i^{WPP} = C_{SES} \cdot \tau_i^{WPP}, C_{SES} = C^{inv} + C^{at} \tag{56}$$

where C_i^{WPP} represents the SES cost that must be allocated to a certain REB, and C_{SES} represents the overall cost of SES.

6. Case Study

6.1. Data Description

In this case study, the alliance consists of 10 wind turbines and 1 shared energy storage, and the operational parameters of the SES are shown in Table 1. To model the wind power output uncertainty, this paper adjusted the real electricity generated by a wind power

plant in a certain northwest region proportionally as the wind power forecast value, and used Monte Carlo sampling to generate multiple wind power output scenarios for each sub-wind-power plant based on the statistical error of the forecast value. Then, this paper used the scenario reduction method to limit the number of scenarios to 10. The market prices were obtained from publicly available data of the PJM electricity market, and the price penalty factors φ^{down} and φ^{up} in REM were taken as 0.8 and 1.2, respectively.

Table 1. Model parameters.

Parameter	Value	Parameter	Value
T_{ref}	20 °C	μ_{ref}	0.5
a_0	0.0693	a_1	1.04
a_2	4.14×10^{-10}/s	a_3	1.40×10^5
a_4	−0.501	a_5	-1.23×10^5
γ_{cell}	0.0575	v_{cell}	121
E_{SES}	100 MW·h	P_{max}^{SES}	30 MW
SOH_0	100%	c_P^{SES}	300 USD/kW
c_E^{SES}	1200 USD/kWh	γ	8%

6.2. Results and Discussion

Based on the existing REB, the reasonable allocation of EES battery capacity and power is critical to SES system planning. If the ES capacity allocated to wind turbines in the REB is too small, it will be difficult to effectively absorb wind power. If the ES capacity is too large, the investment and operation costs will be too high, which could significantly affect the financial advantages of SES. This paper studies the effect of SES capacity allocation on alliance revenue. Figure 3 demonstrates that alliance members experience an increase in market revenue as the energy storage capacity rises, reaching a peak at a certain point when the capacity is relatively low. However, surpassing the optimal energy storage capacity linked to maximum profit leads to a subsequent decline in the members' profitability. This decline can be attributed to excessive energy storage capacity, which introduces redundancy in energy storage resources. The resulting high investment and operational costs associated with this surplus capacity contribute to diminished profits for alliance members. In this case study, for most wind turbines, the ES capacity ratio corresponding to the maximum revenue is mostly between 14% and 21%.

Additionally, Figure 4 shows a significant increase in revenue for wind turbines 7–10, indicating that these four wind turbines need to bear a high SES investment cost. To balance the economic profits of the alliance and ES investment costs, the most suitable SES capacity ratio is within the 17–20% interval, which means that the SES capacity allocation for the REB is most suitable within the range of 90–110 MW. This paper chooses 100 MW as the optimal SES capacity configuration for the REB, and studies the optimized operation and cost allocation of the 100 MW.

The scheduling and operation status of SES with or without considering the cost of dynamic degradation of ES are presented in Figure 5.

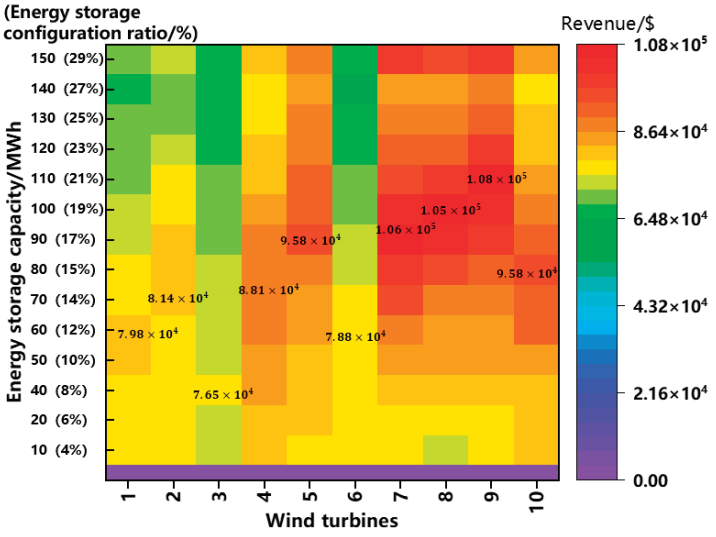

Figure 3. Revenue of alliance members.

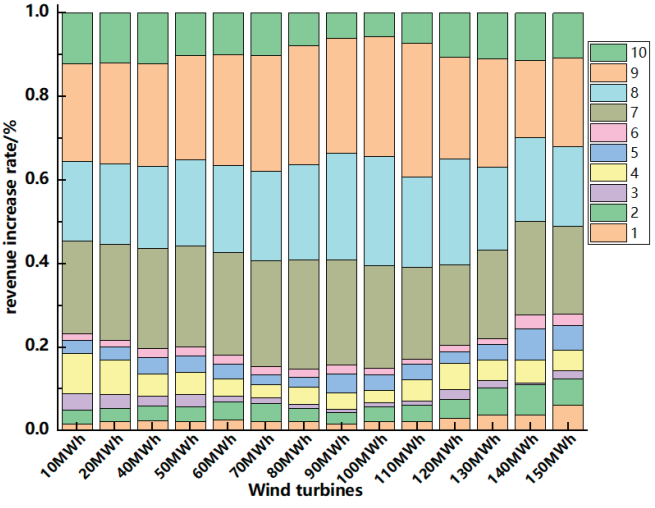

Figure 4. The revenue increase rate of alliance members.

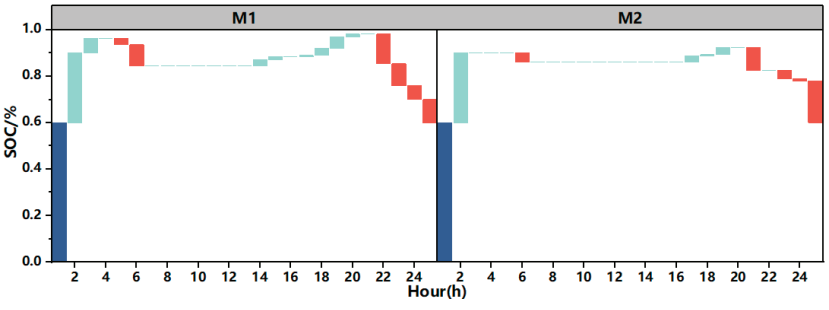

Figure 5. The SOC of energy storage.

In Figure 5, M1 represents the SoC of SES when dynamic attenuation characteristics are not taken into consideration, and M2 represents the SoC of SES when dynamic attenuation characteristics are taken into consideration. And dark blue represents the initial SoC of the ES, green represents an increase in the value of the SoC, and red represents a decrease in SoC. By comparing the SOC of SES with and without considering the dynamic attenuation, it can be observed that when there is a significant difference between the real-time output of the wind turbine and the previously declared power, the SOC of SES changes extensively. This indicates that the REM power of the ES is also substantial, and the storage device can adjust the overall clear power through its charging-and-discharging behavior to maintain the power balance. Consequently, the storage device can minimize the effects of unpredictability in wind power output on system operation, improving the overall alliance revenue. Moreover, compared to the scenario without considering dynamic attenuation, when dynamic attenuation is considered, the SOC change frequency and amplitude of SES are more conservative. This results in a reduced number of charging-and-discharging cycles and a reduced frequency of deep charging or discharging, leading to a smoother change in energy capacity. This prolongs the service life of SES. When dynamic attenuation is not considered, the ES device tends to increase the revenue of various entities in the energy market through frequent charging-and-discharging behavior to maximize overall revenue. However, when dynamic attenuation is considered, the utilization rate of the storage device is significantly reduced to achieve higher total alliance revenue, leading to a lower clear power in the real-time balance market and a lowered frequency of charging-and-discharging behavior.

By analyzing the cross-sections of different stages of SES, it is shown in Figure 6 that when the ES capacity drops below 20%, the optimal scheduling requirement under the initial state has deviated. This will reduce its ability to improve the anti-peak properties of wind power and reduce the imbalance settlement cost of wind power. This further indicates the necessity of considering the dynamic degradation of ES to avoid excessive use of SES.

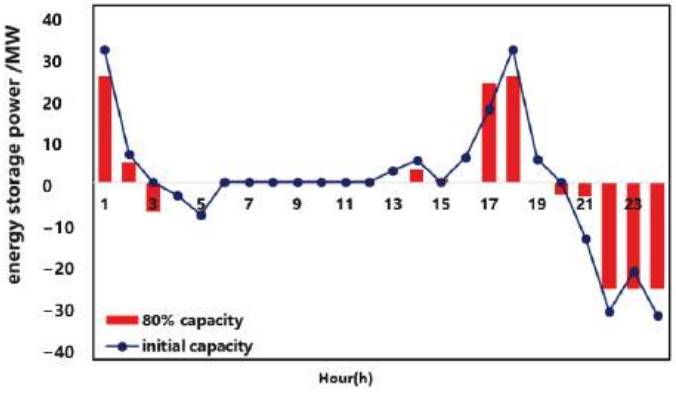

Figure 6. Operation of energy storage before and after degradation.

If fixed decay cost for payment of SES is applied without considering its dynamic characteristic changes, and if ES state parameters are not updated during its usage, and if the charging and discharging costs remain constant and do not change with the changes in charging and discharging capacities, then the health status of the ES cannot be adequately represented, and the overuse of ES cannot be avoided in the sharing mode. This paper proposes that updating the characteristic parameters of ES in a timely manner according to its operating conditions and accounting for the decay cost of ES during different usage stages based on charging and discharging quantities can more reasonably improve the system benefits on the basis of reducing the loss of ES life.

Based on the revenue obtained by wind turbines and SES forming alliances and wind turbines participating in the market individually, the revenue increase brought by forming alliances can be derived. The results are shown in Table 2. Comparing the final revenue situation, it can be seen that after multiple wind turbines share ES, their revenue has increased, but the increase proportion is different, mainly due to the different prediction accuracies of each wind turbine. Wind turbine 9 achieved a 28.61% increase in revenue compared to participating in the market individually, while wind turbine 3, which has the least revenue increase, has also achieved 1.01 times the revenue when participating in the market individually after constructing SES. It is evident that the model proposed in this paper, which involves multiple wind turbines jointly sharing ES to participate in market operation, can take into account the interests of all parties and improve the overall revenue.

Table 2. Revenue increase rate of each wind turbine.

Wind Turbine Number	1	2	3	4	5
Revenue increase rate	2.24%	3.47%	1.00%	2.99%	3.81%
Wind turbine number	6	7	8	9	10
Revenue increase rate	1.51%	24.44%	26.22%	28.61%	5.72%

Comparing the different profits of wind power with the same installed capacity in Figure 7, it can be observed that the distinct profitability of wind power producers with the same capacity are due to different prediction errors. The larger the deviation between the real and reported power data of a wind turbine, the higher the corresponding imbalance costs it incurs, which results in lower actual profits of the RE station than expected. Meanwhile, the profit of a single wind turbine, when forming alliances with other wind turbines and ES, may not increase significantly even if its profitability is high, mainly because the wind turbine itself is already highly matched with the load, and the complementary effects between multiple wind turbines and the regulating function of ES do not significantly reduce their output deviation.

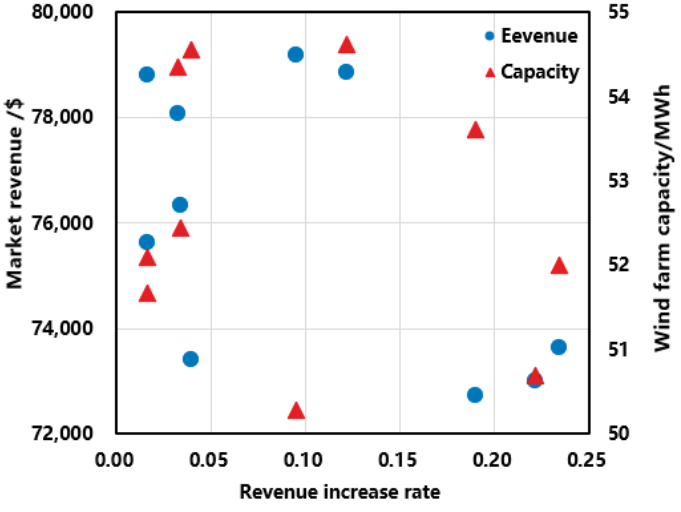

Figure 7. Revenue increase rate of each wind farm.

According to the proportion of revenue improvement from each wind turbine to the total revenue increase, the investment and degradation costs of SES are allocated, and the higher the revenue increase rate of a wind turbine, the more SES cost it needs to bear.

This can ensure enthusiasm for cooperation of all alliance members and the stability of the alliance.

As shown in Figure 8, by comparing the day-ahead and real-time revenues of ten wind farms, it can be seen that the capacity and prediction error of wind turbines both affect their share of investment in SES. In an RE field, wind turbines with larger errors between actual capacity and output and reported values need to bear higher initial investment costs of SES.

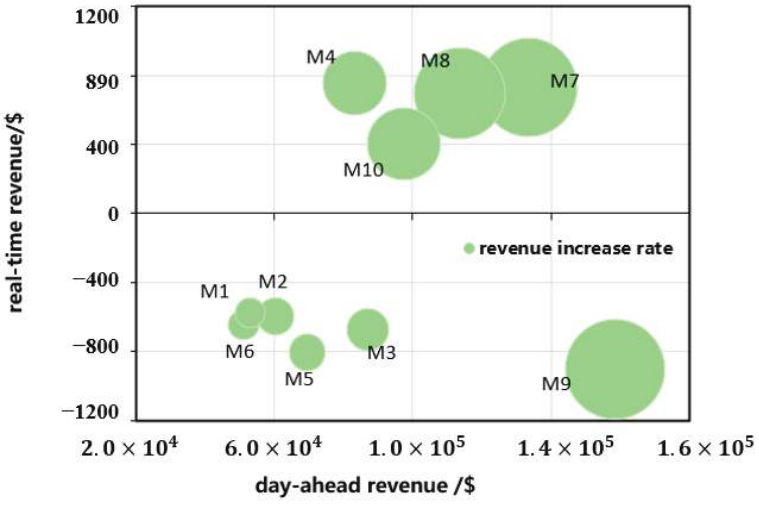

Figure 8. Revenue increase rate of different market members.

The day-ahead revenues of wind farm 3 and wind farm 4 are basically the same, but the investment expense of ES required varies greatly. This is mainly because wind farm 3 has better matching with the load, which can better meet the load demand in each period with its own output characteristics, and therefore has less demand for peak-shaving and filling of ES and flexibility value, resulting in a smaller proportion of corresponding shared investment. The real-time revenue of wind farm 4 and wind farm 7 is basically the same, but the cost of SES is different, indicating that wind turbines with different capacities still need to bear a larger proportion of initial investment costs of ES even if their prediction accuracy is similar.

The impact of wind turbine output prediction accuracy on the cost allocation of an SES alliance is analyzed below, and the results are presented in Figure 9.

As seen in Figures 8 and 9, it can be observed that wind turbines 7, 8, 9, and 10 have higher improvement rates in revenue and higher SES costs. As prediction accuracy improves, the SES cost of each wind turbine unit, especially those with higher revenue increase rates, decreases to varying degrees. This is because the improvement in prediction accuracy reduces the deviation between the pre-bid power and real-time output of each unit, leading to decreased demand for ES capacity and subsequently lowering the SES investment cost. Moreover, the improvement in prediction accuracy reduces the frequency and power of charging and discharging, resulting in a lower degradation cost due to the ES cycle. Therefore, each member of the alliance will also see a reduction in their corresponding SES costs. Additionally, due to the different prediction accuracy of each unit, their demand for ES when participating in the spot market is also different, leading to varying changes in the cost sharing. For turbine 9, which has the highest improvement rate in revenue, when its prediction accuracy improves by 5%, the shared cost can be reduced by about 6%, which is conducive to incentivizing alliance members to actively participate in the spot market and enhancing their market competitiveness.

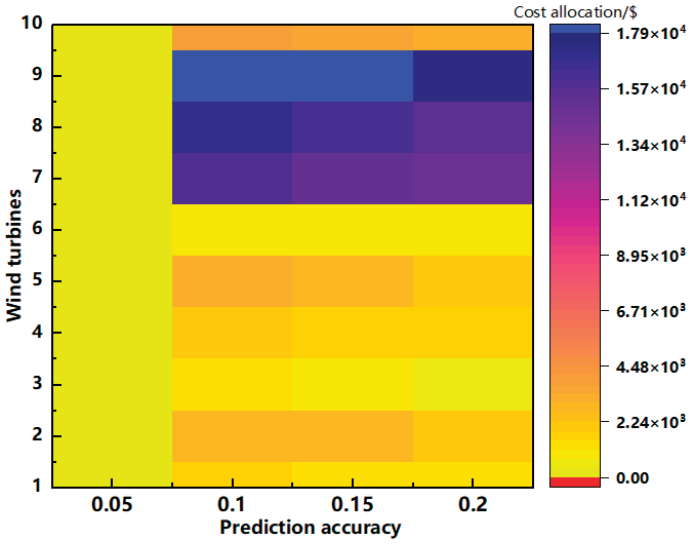

Figure 9. The allocation of ES costs for alliance members under different prediction accuracies.

As shown in Figure 10, the capacity demand of SES in each wind turbine unit in the REB also changes when the electricity price penalty coefficient in the REM of the alliance changes. Specifically, when the overgeneration price penalty coefficient ϕ^{down} decreases or the undergeneration price penalty coefficient ϕ^{up} increases, the optimal SES allocation capacity in the REB will gradually increase. This is because the change in the electricity price penalty coefficient will increase the capacity demand of SES of each wind turbine unit, which will increase the investment expense of SES, and the charging and discharging powers will also increase, resulting in more frequent charging-and-discharging behaviors, and the decay cost will also increase, leading to a continuous increase in the SES cost borne by each unit. However, since the capacity demand for ES of each turbine is different when the electricity price penalty coefficient changes, the increment of their ES allocation cost is also different.

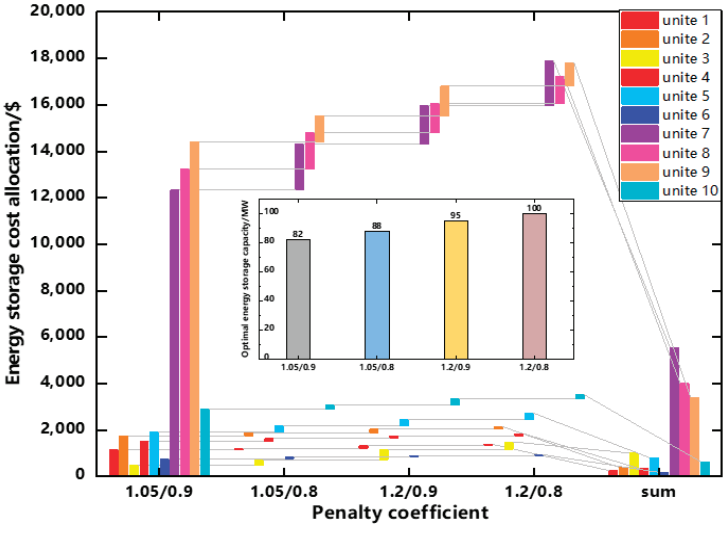

Figure 10. The allocation of ES costs for alliance members under different penalty coefficients.

The output prediction accuracy of each unit is set as shown in Table 3. Combined with Table 3 and Figure 10, for unit 7, 8, and 9, when the electricity price penalty coefficient changes, their increment of ES allocation cost is relatively large. This is mainly because their output prediction accuracy is low, and the day-ahead forecast error is large, which will face higher imbalance penalty fees in the REM. To improve their economic benefits, they will increase the demand for SES to compensate for the fluctuation between their awarded electricity volume and real-time power output, thus reducing the imbalance settlement cost.

Table 3. Prediction accuracy of wind turbine.

Wind Turbine	**1**	**2**	**3**	**4**	**5**
Prediction accuracy	15%	10.5%	6%	20%	13%
Wind turbine	6	7	8	9	10
Prediction accuracy	15%	5%	8%	8.3%	17%

For units with higher prediction accuracy, when the electricity price penalty coefficient changes, their increment of ES allocation cost increases more conservatively. When ϕ^{down} decreases from 0.9 to 0.8, the ES allocation cost for unit 9 increases by USD 1095, which is about 10 times the increment of the ES allocation cost for unit 4. In addition, for wind turbine units with similar installed capacity, such as units 3, 5, and 10, their increments of ES allocation cost are different due to different prediction accuracies. Obviously, for unit 10 with higher prediction accuracy, the increment in ES demand is smaller, and the ES allocation cost increases more conservatively. For unit 3 with lower prediction accuracy, its increment of ES allocation cost is 1.11 times higher than that of unit 10. In fact, according to the cost allocation mechanism proposed in this article, wind power producers must make a trade-off between implementing higher-cost yet more effective prediction technologies and bearing increased shared energy storage investment costs to maximize their own utility.

7. Conclusions

This paper provides a detailed modeling of the degradation of shared energy storage lifespan, and analyzes the impact of dynamic degradation characteristics on the operational strategies and capacity allocation schemes of shared energy storage in renewable energy bases. It establishes an optimization model for the optimal operation of shared energy storage in renewable energy bases, taking into account the dynamic degradation characteristics. Furthermore, a cost allocation mechanism is designed to address the diversity in shared energy storage demands. The following results have been confirmed:

(1) The most suitable capacity ratio for SES in a REB is in the range of 17% to 20%, which can balance the economic benefits of alliances and ES investment costs well. When wind turbines form an alliance with SES, their profits increase compared to when they participate in the market alone. Considering the dynamic decay of ES, the utilization rate of ES is considerably reduced to increase the overall profits of the alliance, and the charging-and-discharging frequency and quantity in the REM are also reduced.

(2) The capacity and prediction errors of wind turbines will affect their share of SES costs. When the prediction accuracy is similar, wind turbines with larger installed capacities need to bear a higher proportion of ES costs, and as the prediction accuracy improves, the SES costs borne by each wind turbine decrease to varying degrees.

(3) The penalty factor of the REM price in the alliance also affects the optimal SES capacity configuration and the SES costs of each wind turbine in the REB. When the penalty factor changes, the capacity demand for SES in each wind turbine in the REB increases, and the SES costs increase. Moreover, wind turbines with lower output prediction accuracy and similar installed capacity have larger increases in SES costs.

In conclusion, the SES optimization model for RE stations, taking into account dynamic decay of EES, is more objective and reasonable. The calculation of profits for different

units in the REB has guidance significance for designing SES cost allocation mechanisms. The proposed model is also applicable to photovoltaic power stations. However, there are still some limitations in this paper that can be improved in the future. On the one hand, this paper does not consider network constraints and power flow constraints. In-depth research can be conducted on the capacity configuration of energy storage in renewable energy bases, taking into account power supply security, reliability, and power quality. On the other hand, this study primarily focuses on multiple renewable energy bases and a single shared energy storage system. Future research can investigate the capacity allocation problem for multiple shared energy storage stations.

Author Contributions: Conceptualization and investigation, C.S.; conceptualization and formal analysis, B.Z.; resources and methodology, B.W.; data curation and software, W.L.; writing—original draft preparation, Y.Y.; supervision, formal analysis and writing—review & editing, Z.W. All authors have read and agreed to the published version of the manuscript.

Funding: This research was funded by the State Grid Gansu Electric Power Company Science and Technology Project "Research on Energy Storage Participation in Marketization Trading Mechanism Based on New Power Systems" (Grant number: 52272222000H).

Data Availability Statement: Datasets are available upon reasonable request.

Acknowledgments: The authors are grateful to the editor and anonymous reviewers for their work.

Conflicts of Interest: The authors declare no conflict of interest.

References

1. Wu, Z.; Zhou, M.; Zhang, Z.; Zhao, H.; Wang, J.; Xu, J.; Li, G. An incentive profit-sharing mechanism for welfare transfer in balancing market integration. *Renew. Sustain. Energy Rev.* **2022**, *168*, 112762. [CrossRef]
2. IRENA. *Global Energy Transformation: A Roadmap to 2050*, 2019th ed.; International Renewable Energy Agency: Abu Dhabi, United Arab Emirates, 2019.
3. Wu, Z.; Chen, L.; Wang, J.; Zhou, M.; Li, G.; Xia, Q. Incentivizing the Spatiotemporal Flexibility of Data Centers Toward Power System Coordination. *IEEE Trans. Netw. Sci. Eng.* **2023**, *10*, 1766–1778. [CrossRef]
4. Wu, Z.; Wang, J.; Zhong, H.; Gao, F.; Pu, T.; Tan, C.-W.; Chen, X.; Li, G.; Zhao, H.; Zhou, M.; et al. Sharing Economy in Local Energy Markets. *J. Mod. Power Syst. Clean Energy* **2022**, *11*, 714–726. [CrossRef]
5. Chen, Y.; Yang, Y.; Xu, X. Towards transactive energy: An analysis of information-related practical issues. *Energy Convers. Econ.* **2022**, *3*, 112–121. [CrossRef]
6. Malka, L.; Daci, A.; Kuriqi, A.; Bartocci, P.; Rrapaj, E. Energy Storage Benefits Assessment Using Multiple-Choice Criteria: The Case of Drini River Cascade, Albania. *Energies* **2022**, *15*, 4032. [CrossRef]
7. Wu, Z.; Wang, J.; Zhou, M.; Xia, Q.; Tan, C.-W.; Li, G. Incentivizing Frequency Provision of Power-to-Hydrogen toward Grid Resiliency Enhancement. *IEEE Trans. Ind. Inform.* **2022**, 1–10. [CrossRef]
8. Liu, D.; Cao, J.; Liu, M. Joint Optimization of Energy Storage Sharing and Demand Response in Microgrid Considering Multiple Uncertainties. *Energies* **2022**, *15*, 3067. [CrossRef]
9. Yao, M.; Molzahn, D.K.; Mathieu, J.L. An Optimal Power-Flow Approach to Improve Power System Voltage Stability Using Demand Response. *IEEE Trans. Control Netw. Syst.* **2019**, *6*, 1015–1025. [CrossRef]
10. Chen, L.; Wang, J.; Wu, Z.; Li, G.; Zhou, M.; Li, P.; Zhang, Y. Communication Reliability-Restricted Energy Sharing Strategy in Active Distribution Networks. *Appl. Energy* **2021**, *282*, 116238. [CrossRef]
11. Atawi, I.E.; Al-Shetwi, A.Q.; Magableh, A.M.; Albalawi, O.H. Recent Advances in Hybrid Energy Storage System Integrated Renewable Power Generation: Configuration, Control, Applications, and Future Directions. *Batteries* **2023**, *9*, 29. [CrossRef]
12. Parag, Y.; Sovacool, B.K. Electricity market design for the prosumer era. *Nat. Energy* **2016**, *1*, 16032. [CrossRef]
13. Sousa, T.; Soares, T.; Pinson, P.; Moret, F.; Baroche, T.; Sorin, E. Peer-to-peer and community-based markets: A comprehensive review. *Renew. Sustain. Energy Rev.* **2019**, *104*, 367–378. [CrossRef]
14. Zhu, K.; Victoria, M.; Andresen, G.B.; Greiner, M. Impact of climatic, technical and economic uncertainties on the optimal design of a coupled fossil-free electricity, heating and cooling system in Europe. *Appl. Energy* **2020**, *262*, 114500. [CrossRef]
15. Zhang, C.; Wu, J.; Long, C.; Cheng, M. Review of existing peer-to-peer energy trading projects. *Energy Procedia* **2017**, *105*, 2563–2568. [CrossRef]
16. Chomać-Pierzecka, E.; Sobczak, A.; Soboń, D. Wind Energy Market in Poland in the Background of the Baltic Sea Bordering Countries in the Era of the COVID-19 Pandemic. *Energies* **2022**, *15*, 2470. [CrossRef]
17. Jiang, Y.; Zheng, C. Two-stage Operation Optimization for Grid-connected Wind Farm Cluster with Shared Energy Storage. *Power Syst. Technol.* **2022**, *46*, 3426–3439.

18. Scarabaggio, P.; Carli, R.; Dotoli, M. Noncooperative Equilibrium-Seeking in Distributed Energy Systems Under AC Power Flow Nonlinear Constraints. *IEEE Trans. Control Netw. Syst.* **2022**, *9*, 1731–1742. [CrossRef]
19. Lai, S.; Qiu, J.; Tao, Y. Credit-Based Pricing and Planning Strategies for Hydrogen and Electricity Energy Storage Sharing. *IEEE Trans. Sustain. Energy* **2022**, *13*, 67–80. [CrossRef]
20. Awnalisa, W.; Soongeol, K. Analysis on impact of shared energy storage in residential community: Individual versus shared energy storage. *Appl. Energy* **2021**, *282*, 116172.
21. Karunakaran, V.; Uma, G. Optimal power flow control of hybrid renewable energy system with energy storage: A WOANN strategy. *J. Renew. Sustain. Energy* **2019**, *11*, 015501.
22. Nicola, M.; Paolo, S.; Raffaele, C.; Dotoli, M. Control frameworks for transactive energy storage services in energy communities. *Control Eng. Pract.* **2023**, *130*, 105364.
23. Niu, J.; Tian, Z.; Lu, Y.; Zhao, H. Flexible dispatch of a building energy system using building thermal storage and battery energy storage. *Appl. Energy* **2019**, *243*, 274–287. [CrossRef]
24. Zafar, R.; Ravishankar, J.; Fletcher, J.E.; Pota, H.R. Multi-Timescale Model Predictive Control of Battery Energy Storage System Using Conic Relaxation in Smart Distribution Grids. *IEEE Trans. Power Syst.* **2018**, *33*, 7152–7161. [CrossRef]
25. Wu, J.; Lu, Z.; Qiao, Y.; Yang, H. Wind-Storage Power Station Operation Optimization Considering Dynamic Efficiency Characteristics of Energy Storage Charging and Discharging. *Autom. Electr. Power Syst.* **2018**, *42*, 41–47+101.
26. Sakti, A.; Gallagher, K.G.; Sepulveda, N.; Uckun, C.; Vergara, C.; de Sisternes, F.J.; Dees, D.W.; Botterud, A. Enhanced representations of lithium-ion batteries in power systems models and their effect on the valuation of energy arbitrage applications. *J. Power Sources* **2017**, *342*, 279–291. [CrossRef]
27. Musallam, M.; Johnson, C.M. An Efficient Implementation of the Rainflow Counting Algorithm for Life Consumption Estimation. *IEEE Trans. Reliab.* **2012**, *61*, 978–986. [CrossRef]
28. You, H.W.; Bae, J.I.; Cho, S.J.; Lee, J.M.; Kim, S.-H. Analysis of equivalent circuit models in lithium-ion batteries. *AIP Adv.* **2018**, *8*, 125101. [CrossRef]
29. Roscher, M.A.; Assfalg, J.; Bohlen, O.S. Detection of Utilizable Capacity Deterioration in Battery Systems. *IEEE Trans. Veh. Technol.* **2011**, *60*, 98–103. [CrossRef]
30. Xu, B.; Oudalov, A.; Ulbig, A.; Andersson, G.; Kirschen, D.S. Modeling of Lithium-Ion Battery Degradation for Cell Life Assessment. *IEEE Trans. Smart Grid* **2018**, *9*, 1131–1140. [CrossRef]
31. Förstl, M.; Azuatalam, D.; Chapman, A.; Verbič, G.; Jossen, A.; Hesse, H. Assessment of residential battery storage systems and operation strategies considering battery aging. *Int. J. Energy Res.* **2020**, *44*, 718–731. [CrossRef]
32. Bašić, M.; Vukadinović, D.; Višnjić, V.; Rakić, I. Dynamic Equivalent Circuit Models of Lead-Acid Batteries—A Performance Comparison. *IFAC-PapersOnLine* **2022**, *55*, 189–194. [CrossRef]
33. Lin, C.; Tang, A.; Wang, W. A Review of SOH Estimation Methods in Lithium-ion Batteries for Electric Vehicle Applications. *Energy Procedia* **2015**, *75*, 1920–1925. [CrossRef]
34. USABC. *Electric Vehicle Battery Test Procedures Manual*; Revision 2; Idaho National Engineering Laboratory: Idaho Falls, ID, USA, 1996.
35. Groenewald, J.; Grandjean, T.; Marco, J. Accelerated energy capacity measurement of lithium-ion cells to support future circular economy strategies for electric vehicles. *Renew. Sustain. Energy Rev.* **2017**, *69*, 98–111. [CrossRef]
36. Sessa, P.G.; Walton, N.; Kamgarpour, M. Exploring the Vickrey-Clarke-Groves Mechanism for Electricity Markets. *IFAC-PapersOnLine* **2017**, *50*, 189–194. [CrossRef]

energies

MDPI

Article

Research on Low-Frequency Stability under Emergency Power Supply Scheme of Photovoltaic and Battery Access Railway Traction Power Supply System

Ying Wang [1,2], Yueyang Xin [1,*], Ziyun Xie [1], Xiuqing Mu [1] and Xiaoqiang Chen [1,2]

[1] School of Automation and Electrical Engineering, Lanzhou Jiaotong University, Lanzhou 730070, China; wangying01@lzjtu.edu.cn (Y.W.)
[2] Key Laboratory of Opt-Electronic Technology and Intelligent Control Ministry of Education, Lanzhou 730070, China
* Correspondence: xyylzjtdx@163.com

Abstract: Photovoltaics and batteries can be connected to a traction power supply system through a railway power conditioner (RPC) to switch between different control strategies. This can address power quality issues or provide emergency traction for locomotives that unexpectedly lose power and even break through traditional energy barriers in the railway field, achieving a low-carbon power supply for railway energy, and a mutual backup with substations. However, methods to coordinate the control strategies of PV and the battery locomotive traction have not been clearly revealed, nor has the actual stability of the system. In this study, to address the above issues, an emergency power supply scheme is proposed for the first time that utilizes a dual-mode RPC inverter combined with a coordinated control strategy for the PV and battery, achieving the traction of locomotives. In addition, a one-dimensional impedance model was established for the PV system, battery system, locomotive (CRH3), and RPC projected onto the dq coordinate system, and the critical amplitude margin (CAM) was defined to quantitatively analyze the sensitivity and laws of different parameters concerning the low-frequency stability of the system. At the same time, impedance ratios and passive criteria were used to reveal the stability mechanism, and parameter adjustment criteria and design suggestions were put forward. Finally, the feasibility of the emergency power supply scheme of the "PV–battery locomotive network" coupling system and the correctness of the low-frequency stability study were verified using the Starsim semi-physical experiment platform.

Keywords: emergency power supply; PV–battery locomotive network; railway power conditioner; low-frequency stability; critical amplitude margin; verification and testing

Citation: Wang, Y.; Xin, Y.; Xie, Z.; Mu, X.; Chen, X. Research on Low-Frequency Stability under Emergency Power Supply Scheme of Photovoltaic and Battery Access Railway Traction Power Supply System. *Energies* **2023**, *16*, 4814. https://doi.org/10.3390/en16124814

Academic Editors: Luis Hernández-Callejo, Jesús Armando Aguilar Jiménez and Carlos Meza Benavides

Received: 16 May 2023
Revised: 18 June 2023
Accepted: 19 June 2023
Published: 20 June 2023

1. Introduction

The "2022 Climate Services Status" report released by the World Meteorological Organization (WMO), a specialized agency of the United Nations, states that the clean energy power supply must be doubled by 2030 to limit the global temperature rise. Railway transportation is a significant contributor to energy consumption and carbon emissions in the transportation sector due to its massive electricity usage. With the depletion of fossil fuels and the consequences of global warming, there is mounting pressure on the railway industry to take action and reduce its carbon emissions. To achieve the green transformation of railways, progress has been made internationally in the adoption of new energy sources for railways: JR-East has installed 453 kW solar panels at Tokyo Station, serving locomotives on the Tokaido line 3 [1]; the subway operator in Santiago, Chile, built two solar photovoltaic power stations in 2017, supplying 60% of the subway's electricity and achieving a renewable energy utilization rate of 76% [2]; 100% of the primary energy used by the Dutch railway is provided by wind [3]; a 2.2 MW rooftop photovoltaic system has been built at Wuhan Railway Station in China; a 10 MW solar power generation device has been installed on the roof of Hangzhou East Station [4]; the total installed capacity of

the photovoltaic system of the Xiong'an high-speed railway in China is 6 MW [5]. The photovoltaic (PV) resources along China's AC-electrified railways are abundant, and their high proportion of utilization can promote China's achievement of the "dual carbon" goal and increase the national independent contribution under the global energy conservation and emission reduction goal [6].

Currently, access methods of PV and battery devices are roughly divided into two categories: one is to access the battery device from the side of the locomotive to recover braking energy and control the voltage fluctuation of the traction network [7], and the other is to access the traction network side. For example, China's electrified railway mainly considers access to PV and battery devices from the high-voltage side (110 kV) and the traction side (27.5 kV). There are two types of PV and battery inverters: one is a three-phase inverter combined with a three-phase/two-phase transformer, and the other is a back-to-back single-phase inverter [8]. The high-voltage side access method is suitable for small-capacity PV and battery devices, and the large capacity required for three-phase inverters leads to higher costs. At present, the railway power conditioners (RPCs) that utilize single-phase inverters to connect multiple source devices from the traction side have received frequent attention due to their excellent comprehensive performance [9]. The authors of [10–14] studied the unbalanced power compensation and harmonic control of the traction power supply systems with different RPC topologies. In [15], the train braking energy was recycled and reused through a RPC in conjunction with battery devices. In [16], a coordinated control scheme based on a RPC for PV and battery access to a traction power supply system was proposed, utilizing new energy to provide additional active power. Most of the above studies considered using PV or battery compensation power to reduce the consumption of fossil fuels but electricity is still mainly provided by thermal power generation. In [17], an overview of an emergency traction scheme for locomotive and substation coordination based on battery devices was presented and this paper aims to solve the problem of sudden accidents such as substation failures leading to locomotive power loss. In this state, the locomotive is completely powered by the battery. However, the research on the combined application of PV and battery for emergency traction in locomotives is not yet widely explored, and more research is needed to explore its potential and feasibility, if the PV power is connected to the battery for charging and collaborates with the battery to traction the locomotive, almost all of the electrical energy comes from renewable energy. However, to design the emergency power supply scheme for PV and battery systems and identify whether the collaborative integration of PV and battery systems can further change the railway energy supply system to achieve the long-term stable full-power traction of locomotives, the above-mentioned problems are worth deep research and solving. Due to the wide coverage of Chinese railways and superior energy storage conditions, as well as the long routes and abundant solar resources along such lines, solar power for AC-electrified railways has broad application prospects and extensive benefits. Therefore, this article takes the AC power supply system of Chinese railways with a rated voltage of 27.5 kV as an example and proposes the use of RPC access to PV and battery devices to achieve the emergency or long-term traction of locomotives, thus, expanding the function of RPCs and promoting the consumption of PV resources. In addition, due to differences in operational modes and design parameters between DC railways and AC railways, this article does not explore issues related to DC railways.

However, it is also important to determine whether the system remains stable when using the PV and battery locomotive traction and to reveal the main factors and laws that affect the stable operation of the system; all of these issues need to be addressed prior to the implementation of PV and battery traction locomotives in practice. At present, there are multiple frequency-scale instability issues in the traction power supply system of railways, such as low-frequency oscillation (LFO), harmonic resonance, and harmonic instability. Among them, LFO has been commonly reported in the electric railway domain around the world, thus, attracting widespread research attention [18,19]. The first reported occurrence of the LFO phenomenon dates back to 1996 in Norway when a rotating converter was

adopted in a traction substation [20]. Since then, in Germany, Sweden, and Norway, rotating converters have been used to interface the traction network, transforming three-phase utility power into a single phase for the catenary network [21]. The main cause of LFO has been attributed to the electromechanical characteristics of rotating converters [22]. However, for other electric railway systems [23,24], the mechanism of LFO remains unclear. Recently, from 2008 to 2016, there has been an increasing frequency of LFOs observed in Chinese railways [25,26]. Many studies have revealed that the occurrence of LFO in China is caused by the introduction of more converters and impedance mismatch [27–29]. Concurrently, locomotives have a LC resonant onboard filter that may oscillate, in addition, such a filter combined with the line can be triggered in oscillation by electric arcs, which is quite a commonplace phenomenon caused by the sliding contact mechanism [30]. In PV and battery locomotive traction, more converters may be introduced, which may further induce LFO. Research on the low-frequency stability of multi-source connected traction power supply systems is not yet complete. In [31], the integration of PV power into the traction network through a RPC was considered and an impedance model of a "PV-locomotive-traction network" was established. It was found that unreasonable parameter settings during the integration of the PV systems did indeed induce LFO; at the same time, the parallel connection of the PV modules led to multiple increases in the converters, which can also lead to LFO in the system. However, the instability mechanism of the system and methods to improve the system stability were not specifically revealed. The variation in the source impedance caused by the parallel connection of the subsystem modules and the parameter adjustment of the converter controller may lead to artificial active enhancement or the weakening of the low-frequency stability of the system. Therefore, to further improve the system stability, it is necessary to specifically reveal the sensitivity and law of the influence of controller parameters on the system's stability.

Regarding the above issues, this article proposes an emergency power supply scheme based on RPC access to PV and battery devices in Section 2.1. Through coordinated control strategies, PV and batteries can be used independently for the day and night emergency traction of locomotives. They may achieve "low-carbon" locomotive operation and also serve as a backup power source for the long-term traction of locomotives. On this basis, an impedance model of the "PV–battery locomotive network" coupling system under this scheme is established on the RPC DC bus side in Section 2.2. Then, the critical amplitude margin is defined for the first time based on the impedance ratio criterion; the influence of parameters on the low-frequency stability of the system is quantitatively evaluated and passive evidence is introduced to reveal the mechanism of the influence of the parallel number of PV and battery modules on the stability. Furthermore, parameter adjustment criteria and main circuit impedance reshaping governance are proposed to prevent LFO in Section 2.3. Finally, the feasibility of the emergency power supply scheme and the correctness of the stability study are verified through testing on the Starsim platform in Section 3.

2. Materials and Methods

2.1. Proposal of Emergency Power Supply Scheme

2.1.1. System Topology

The topology of the "PV–battery locomotive network" system is shown in Figure 1, which includes a traction network, a high-speed locomotive, a railway power conditioner, and a new energy power supply system composed of PV and a battery.

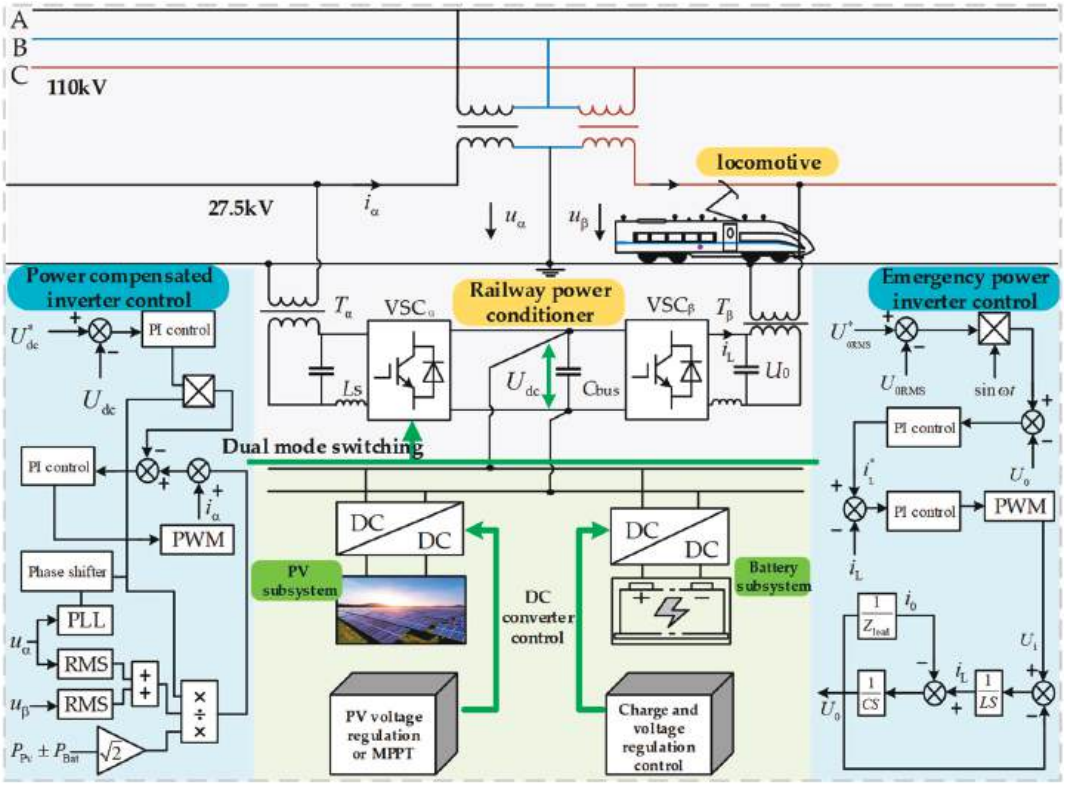

Figure 1. System topology and control block diagram.

The three-phase electricity from the grid is converted from the traction substation to a 27.5 kV single-phase AC current, which is sent to the α and β power supply arms. The PV and battery are integrated into a 2 kV DC bus via their respective DC/DC converters, and the RPC-side single-phase inverter and LC-type filtering circuit are used to convert the power into 1.5 kV single-phase AC power through step-up transformers T_α and T_β, which is then sent to the α and β power supply arms. The U_{dc} is the DC voltage on the input side of the RPC; U_0 is the single-phase AC voltage on the output side of the filtering circuit; U_i is the unfiltered voltage of the RPC; C_{bus} is the capacitor on the DC side of the RPC; VSC_α and VSC_β are single-phase inverters in RPC; i_α, u_α, and u_β are the corresponding voltage and current of the supply arm; RMS means root-mean-square extraction; P_{PV} and P_{Bat}, respectively, represent the output power of the PV and battery; PLL stands for phase-locked loop; U_{0RMS} is the root-mean-square value of U_0; i_L is the output current of the RPC inverter; i_0 is the output current after filtering; and $\sin\omega t$ is the reference sine wave and Z_{load} is the equivalent load in Section 2.2.2. DC converters in PV systems mainly include voltage regulation control and maximum power point tracking control (MPPT), while in battery systems they mainly include charging and voltage regulation control. Under the emergency power supply scheme, the PV and battery systems provide the locomotive's traction but it is still necessary to consider the overall plan for the connection of the PV and battery systems to the traction power supply system to formulate the control strategy.

The RPC converter is a dual-mode single-phase inverter. Its control strategy is shown in Figure 1. When it is applied to power compensation, the voltage U_0 is controlled to track the phase frequency of the traction network voltages u_α and u_β, and the output signal is compared with the harmonic and negative sequence reference signal, followed

by the PWM input signal from the PI controller. At this time, the PV and battery are used as auxiliary power supplies, and the traction net is used as the main power source to control the single-phase inverter to support the voltage amplitude and frequency of both the DC and AC sides of the RPC. In the emergency power supply scheme, the PV and battery provide the DC-side voltage, the U_{dc} amplitude, and the AC-side U_0 frequency support through a DC converter, and the inverter independently outputs the sinusoidal AC power. At this time, the PV and battery serve as the main power supply. The DC converter coordinates with the RPC inverter according to the actual working conditions to achieve traction network voltage management and locomotive traction under different power supply schemes.

2.1.2. Division of Multiple Working Modes

The sum of the power inputs and outputs of the PV, battery, and RPC ports will affect the DC bus voltage U_{dc}, as shown in Figure 1. It is necessary to balance the power of each port through the division of the working modes. The flowchart for the system's power control is shown in Figure 2.

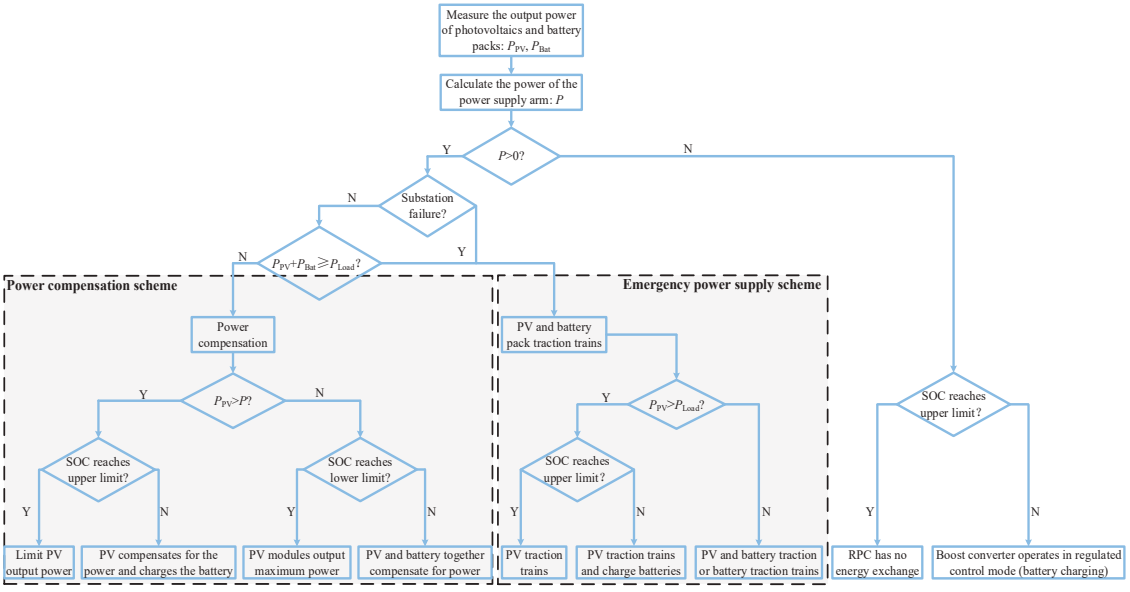

Figure 2. Flowchart for the traction power supply system's power control.

In the above figure, P_{PV} is the output power of the PV system, P_{Bat} is the output power of the battery system, P_{Load} is the maximum operating power of locomotives, and P is the power of the power supply arm calculated by measuring the voltage and current of the power supply arm. Based on the positive, negative, and zero values of P, the locomotive's operating conditions can be distinguished, which are namely, traction, braking, and no-load. In cases where $P \leq 0$, if there is remaining capacity in the battery, it can be used to absorb the energy generated by the braking of the locomotive, as well as the energy provided by the PV system; In cases where $P > 0$ but the total power generated from the PV and battery systems is still lower than P_{load}, the RPC system will operate under the power compensation scheme. However, if the traction substation experiences a fault or the output power generated from the PV and battery systems goes beyond P_{load}, the RPC system will automatically switch to the emergency power supply scheme in order to utilize the PV and battery systems for the locomotive traction. Furthermore, the state-of-charge (SOC)

threshold value is considered to prevent over-charging and over-discharging from affecting the battery life.

This article focuses on the study of using PV and battery systems for emergency locomotive traction. For different working conditions, such as different levels of irradiance and state-of-charge (SOC), the proposed emergency power supply scheme includes different working modes as follows:

Mode One: When the PV power generation is much greater than the sum of the maximum operating power of the load and the lithium battery charging power, i.e., $P_{PV} \gg P_{Load} + P_{Bat}$, and the SOC is less than 90%, the PV system can be used to provide the locomotive's traction and simultaneously charge the battery. When $P_{PV} \gg P_{Load} + P_{Bat}$ but the SOC is above 95%, in order to prevent the battery from over-charging, the PV system will be responsible for the locomotive's traction while the battery will be on standby.

Mode Two: When the PV power generation is slightly greater than the maximum operating power of the load but there is no additional power to charge the battery, that is, $P_{Load} < P_{PV} \leq P_{Load} + P_{Bat}$, and the SOC is less than 90%, the PV system will only supply power to the locomotive, and the battery will be on standby.

Mode Three: When the PV power generation is less than the maximum operating power of the load, that is, $P_{PV} < P_{Load} < P_{PV} + P_{Bat}$, and the battery's SOC is higher than 5%, the PV and battery will work in voltage control mode to jointly provide the locomotive's traction.

Mode Four: When the PV power generation approaches zero, that is, $P_{PV} < P_{Load} < P_{PV} + P_{Bat}$, and the battery's SOC is higher than 5%, the PV system will be on standby, and the battery will provide the locomotive's traction.

The system topologies under the above four modes are different, meaning that it will be time-consuming and complex to analyze the system stability from the RPC AC side by using the impedance method. However, the operating conditions of the PV and battery combined locomotive traction under mode three are relatively common. Meanwhile, when carrying out RPC DC bus segmentation modeling, since the control method of each mode's DC converter is similar to mode three, the parallel connection or split of the DC converter output impedance is equivalent to the switching of modes, and the impedance resolution of the other modes becomes a high-proportion intersection or a subset of mode three, which is convenient to quickly reveal the factors and regularity affecting the stability under multiple working modes. The next section builds a mathematical model for the "PV–battery locomotive network" coupling system using the specific control method of mode three.

2.2. Impedance Modeling of Proposed Emergency Power Supply Scheme

2.2.1. PV and Battery Power Generation Systems

Due to how the topology and control of PV and battery systems are similar, this section will describe and establish the impedance model of the power generation system simultaneously. As shown in Figure 3, in the Boost circuit, u_{PV} is the output voltage of the PV side; i_{PV} is the output current of the PV side; i_{LPV} is the inductor current of the PV side; u_{Bus} and i_{Bus} are the DC bus voltage and current; L_{PV} is the energy storage inductor of the PV side; C_{PV} is the support capacitor of the PV side; C_{Bus1} is the DC-side capacitor of the RPC; d_{PV} is the duty cycle of the Boost converter's switching tube, $d^*_{PV} = 1 - d_{PV}$; and u^*_{Bus} and i^*_{LPV} are the reference signals for their corresponding variables. In the DC/DC circuit, u_{Bat} is the output voltage of the lithium battery side, i_{Bat} is the output current of the lithium battery, L_{Bat} is the energy storage inductor, C_{Bus2} is the DC-side capacitor of the RPC, d_{Bat} is the duty cycle of the T_1 switching tube, and the T_2 switching tube is complementary to the T_1 switching tube. In addition, u^*_{Bus} and i^*_{Bat} are the reference signals for their corresponding variables.

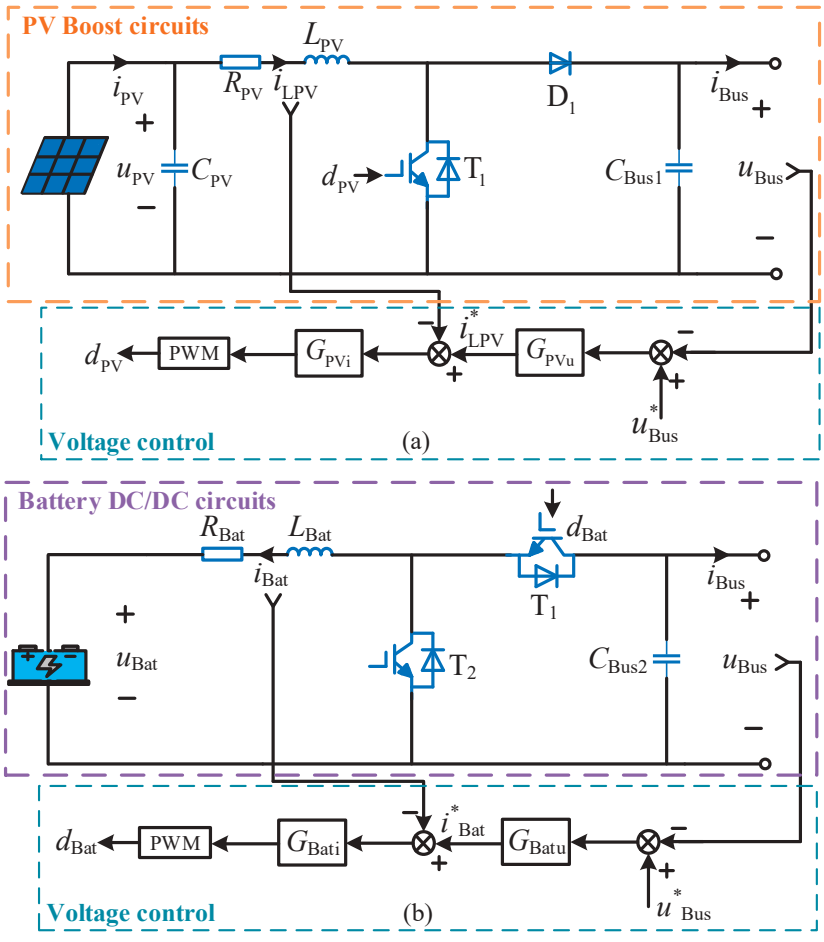

Figure 3. Topology and control of DC converters under mode three. (**a**) PV boost converter; (**b**) battery DC/DC converter.

The state equations for the PV and battery systems are given by Equations (1) and (2), respectively.

$$\begin{cases} L_{PV}\frac{di_{LPV}}{dt} + R_{PV}\cdot i_{LPV} = u_{PV} - d^*_{PV}\cdot u_{Bus} \\ C_{Bus1}\frac{du_{Bus}}{dt} = d^*_{PV}\cdot i_{LPV} - i_{Bus} \\ i_{PV} = i_{LPV} + C_{PV}\frac{du_{PV}}{dt} \end{cases} \tag{1}$$

$$\begin{cases} L_{Bat}\frac{di_{Bat}}{dt} + R_{Bat}\cdot i_{Bat} = u_{Bat} - d_{Bat}u_{Bus} \\ C_{Bus2}\frac{du_{Bus}}{dt} = d_{Bat}i_{Bat} - i_{Bus} \end{cases} \tag{2}$$

With small signal linearizing Equations (1) and (2), we obtain Equations (3) and (4):

$$\begin{cases} (sL_{PV} + R_{PV})\cdot\Delta i_{LPV} = -D^*_{PV}\cdot\Delta u_{Bus} + U_{Bus}\cdot\Delta d_{PV} + \Delta u_{pv} \\ sC_{Bus1}\cdot\Delta u_{Bus} = D^*_{PV}\cdot\Delta i_{LPV} - I_{LPV}\cdot\Delta d_{PV} - \Delta i_{Bus} \\ \Delta i_{PV} = \Delta i_{LPV} + sC_{PV}\cdot\Delta u_{PV} \end{cases} \tag{3}$$

$$\begin{cases} (sL_{\mathrm{Bat}} + R_{\mathrm{Bat}})\Delta i_{\mathrm{Bat}} = -D_{\mathrm{Bat}} \cdot \Delta u_{\mathrm{Bus}} - U_{\mathrm{Bus}} \cdot \Delta d_{\mathrm{Bat}} + \Delta u_{\mathrm{Bat}} \\ sC_{\mathrm{Bus2}}\Delta u_{\mathrm{Bus}} = D_{\mathrm{Bat}} \cdot \Delta i_{\mathrm{Bat}} + I_{\mathrm{Bat}} \cdot \Delta d_{\mathrm{Bat}} - \Delta i_{\mathrm{Bus}} \end{cases} \tag{4}$$

According to the superposition theorem, the transfer functions between each variable of the PV and battery systems can be obtained from Equations (3) and (4), and the specific expressions are shown in Appendix A, where Equation (A1) includes the transfer function expansion of the PV system, and Equation (A2) includes the transfer function expansion of the battery system. Then, based on the control strategies of the PV and battery systems, draw the closed-loop block diagrams of the small signal transfer functions as shown in Figure 4.

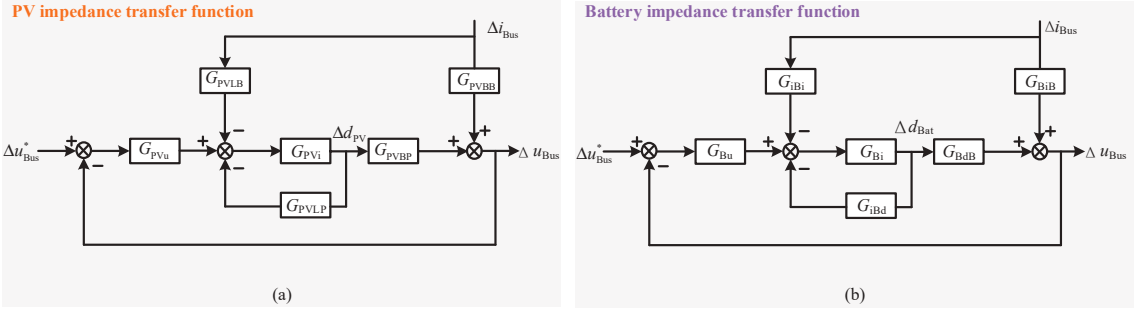

Figure 4. Small-signal closed-loop control block diagram. (**a**) PV transfer function; (**b**) battery transfer function.

Using the Mason's formula, the output impedances of the PV and battery systems are, respectively:

$$Z_{\mathrm{PV}}(\mathrm{s}) = \frac{\Delta u_{\mathrm{Bus}}}{\Delta i_{\mathrm{Bus}}} = \frac{G_{\mathrm{PVBB}} + G_{\mathrm{PVBB}}G_{\mathrm{PVi}}G_{\mathrm{PVLP}} - G_{\mathrm{PVLB}}G_{\mathrm{PVi}}G_{\mathrm{PVBP}}}{1 + G_{\mathrm{PVi}}G_{\mathrm{PVLP}} + G_{\mathrm{PVu}}G_{\mathrm{PVi}}G_{\mathrm{PVBP}}} \tag{5}$$

$$Z_{\mathrm{Bat}}(\mathrm{s}) = \frac{\Delta u_{\mathrm{Bus}}}{\Delta i_{\mathrm{Bus}}} = \frac{G_{\mathrm{BiB}} + G_{\mathrm{BiB}}G_{\mathrm{Bi}}G_{\mathrm{iBd}} - G_{\mathrm{iBi}}G_{\mathrm{BdB}}G_{\mathrm{Bi}}}{1 + G_{\mathrm{Bi}}G_{\mathrm{iBd}} + G_{\mathrm{Bu}}G_{\mathrm{Bi}}G_{\mathrm{BdB}}} \tag{6}$$

2.2.2. Locomotive Network and Railway Power Conditioner

In the study of the low-frequency stability of locomotive network coupling systems, two-level locomotives are often considered. The China railway high-speed 3 (CRH3) locomotive with four power units is the research object of this paper. In [32], the impedance expression of a single power unit is presented. After converting the impedance of the China Railway High-speed 3 (CRH3) locomotive to the RPC AC side, the expression is:

$$Z_{\mathrm{CRH3}}(\mathrm{s}) = \frac{{k_{\mathrm{a}}}^2{k_{\mathrm{b}}}^2 U_{\mathrm{s2}}}{4I_{\mathrm{s2}}} = \frac{{k_{\mathrm{a}}}^2{k_{\mathrm{b}}}^2\left[1 + G_{\mathrm{K}}G_{\mathrm{PWM}}G_{\mathrm{Ln}}(G_{\mathrm{CRH3up}}G_{\mathrm{CRH3ui}}G_{\mathrm{switch}}G_{\mathrm{circuit}} + G_{\mathrm{CRH3ui}})\right]}{4G_{\mathrm{Ln}}(1 - G_{\mathrm{delay}}G_{\mathrm{PWM}})} \tag{7}$$

where the transformation ratio of the onboard transformer is k_{a} and the transformation ratio of the RPC-side step-up transformer is k_{b}.

At present, the equivalent circuit model is commonly used in low-frequency stability analysis of traction networks [31] and its expression corresponds to the RPC AC side:

$$Z_s(s) = k_b^2 \begin{bmatrix} R_s + sL_s & -\omega_0 L_s \\ \omega_0 L_s & R_s + sL_s \end{bmatrix} \tag{8}$$

The equivalent impedance of the locomotive network converted to the RPC AC side is recorded as Z_{load} (s), where Z_{load} $(s) = Z_{\mathrm{s}}$ $(s) + Z_{\mathrm{CRH3}}$ (s).

RPC impedance modeling is conducted on the DC port of the inverter, that is, the input impedance of the RPC is studied. Considering that the back-to-back inverter in the RPC has a symmetrical structure and the impedance calculation and modeling method are similar, the β power supply arm is selected as the research object. For the emergency power supply scheme, the specific control method and topology of the inverter are shown in Figure 5.

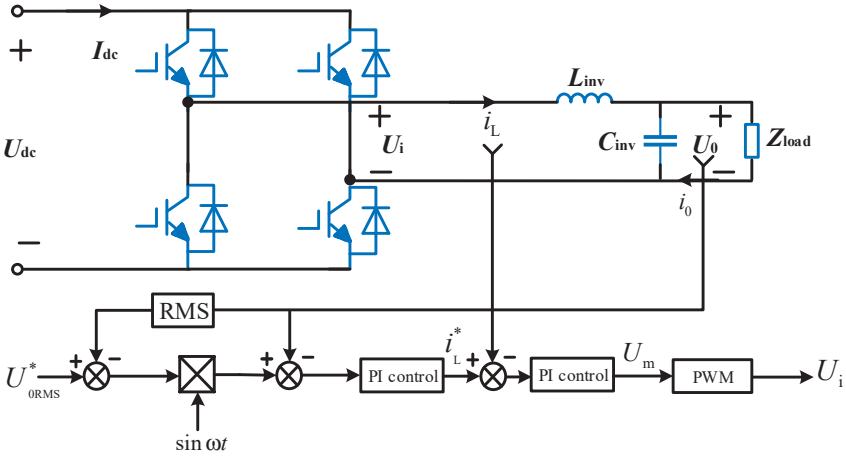

Figure 5. RPC inverter main circuit topology and control.

In the above figure, Z_{load} is the equivalent impedance of the locomotive network converted to the RPC AC side; U_m is the amplitude of the modulated wave signal; and sinωt is the sine wave frequency reference signal. Linearization is performed on the DC side and the variables are decomposed into a closed-loop impedance model in the dq coordinate system. According to the main circuit, the state equation under dq decoupling can be derived by:

$$\begin{cases} L_{inv}\frac{di_{Ld}}{dt} = U_{id} - U_{0d} + \omega L_{inv} I_{Lq} \\ L_{inv}\frac{di_{Lq}}{dt} = U_{iq} - U_{0q} - \omega L_{inv} I_{Ld} \\ C_{inv}\frac{du_{0d}}{dt} = I_{Ld} - I_{0d} + \omega C_{inv} U_{0q} \\ C_{inv}\frac{du_{0q}}{dt} = I_{Lq} - I_{0q} - \omega C_{inv} U_{0d} \\ U_{0d} = Z_{load} \cdot I_{0d} \\ U_{0q} = Z_{load} \cdot I_{0q} \end{cases} \tag{9}$$

Based on the basic derivation process of SPWM, the relationship between the output voltage U_i before filtering and the modulation wave U_m can be obtained using the switch average period method:

$$\begin{cases} U_{id} = 0.5 U_{dc} U_{md} / U_{tri} \\ U_{iq} = 0.5 U_{dc} U_{mq} / U_{tri} \end{cases} \tag{10}$$

In Equation (10), U_{tri} is the amplitude of the triangular carrier wave, and the remaining symbols are the system variables under dq decoupling. In the dual-loop control strategy, the response speed of the inner loop is much faster than that of the outer loop. This article assumes that the response of the current inner loop is approximately the same within the average time of a single switching cycle. Due to the PI controller used in the voltage outer loop, the input–output relationship of the controller is:

$$\begin{cases} (k_{invp} + k_{invi}/s) \cdot (U^*_{vd} - U_{0d}) = U_{md} \\ (k_{invp} + k_{invi}/s) \cdot (U^*_{vq} - U_{0q}) = U_{mq} \end{cases} \tag{11}$$

where U^*_{vd} and U^*_{vq} are the product of the effective value of the voltage outer-loop output and the reference sine signal; k_{invp} and k_{invi} are proportional integral parameters of the voltage outer-loop PI controller.

According to the input power and output power of the RPC that are equal:

$$U_{dc}I_{dc} = 1.5(U_{0d}I_{0d} + U_{0q}I_{0q}) \tag{12}$$

After processing the small signal in Equation (12), the following is obtained:

$$\begin{bmatrix} I_{dc} \\ U_{dc} \end{bmatrix}^T \begin{bmatrix} \Delta u_{dc} \\ \Delta i_{dc} \end{bmatrix} = 1.5\left(\begin{bmatrix} U_{0d} \\ U_{0q} \end{bmatrix}^T \begin{bmatrix} \Delta i_{0d} \\ \Delta i_{0q} \end{bmatrix} + \begin{bmatrix} I_{0d} \\ I_{0q} \end{bmatrix}^T \begin{bmatrix} \Delta u_{0d} \\ \Delta u_{0q} \end{bmatrix} \right) \tag{13}$$

Equations (9) to (11) can be substituted into Equation (13) to obtain the input admittance on the DC side of the β arm inverter:

$$Y_{inv} = \frac{\Delta i_{dc}}{\Delta u_{dc}} = \frac{3}{2U_{dc}}\left(\begin{bmatrix} U_{0d} \\ U_{0q} \end{bmatrix}^T (G_{Zload} + G_{Zload}^T) \begin{bmatrix} \frac{\Delta u_{0d}}{\Delta u_{dc}} \\ \frac{\Delta u_{0q}}{\Delta u_{dc}} \end{bmatrix} \right) - \frac{I_{dc}}{U_{dc}} \tag{14}$$

As output impedance is the reciprocal of admittance, it can be inferred that $Z_{inv} = 1/Y_{inv}$ and the variables in Equation (14) are as follows:

$$\begin{cases} \begin{bmatrix} \frac{\Delta u_{0d}}{\Delta u_{dc}} \\ \frac{\Delta u_{0q}}{\Delta u_{dc}} \end{bmatrix} = 0.5[G_{Linv}(G_{Cinv} + G_{Zload}) + E - 0.5U_{dc}G_{PI}]^{-1} \begin{bmatrix} U_{md} \\ U_{mq} \end{bmatrix} \\ G_{PI} = \begin{bmatrix} s & -\omega \\ \omega & s \end{bmatrix}^{-1} \begin{bmatrix} -(sK_{invp} + K_{invi}) & \omega K_{invp} \\ -\omega K_{invp} & -(sK_{invp} + K_{invi}) \end{bmatrix} \\ G_{Linv} = \begin{bmatrix} sL_{inv} & -\omega L_{inv} \\ \omega L_{inv} & sL_{inv} \end{bmatrix} \\ G_{Cinv} = \begin{bmatrix} sC_{inv} & -\omega C_{inv} \\ \omega C_{inv} & sC_{inv} \end{bmatrix} \\ G_{Zload} = \begin{bmatrix} Z_{load} & 0 \\ 0 & Z_{load} \end{bmatrix}^{-1} \end{cases} \tag{15}$$

2.2.3. Verification of Established Impedance Model

To verify the established one-dimensional impedance model, the disturbance injection method was used for the simulation measurements [33]. By injecting disturbance signals with specific frequencies during the steady-state state of the system and using the Fourier transform to process these signals, the impedances of the three ports of the "PV–battery locomotive network" can be simultaneously measured at specific frequencies, and it should be noted that the impedances of the three ports of the "PV-battery locomotive network" refer to the output impedances Z_{PV} towards the PV boost circuit port, Z_{Bat} towards the battery DC/DC circuit port, and Z_{inv} towards the inverter DC port. We will validate whether the theoretical deduced values of these impedances in the frequency domain match the simulation results.

Validation results are shown in Figure 6, the first row shows the corresponding impedance function's Bode plot, and the second row is the corresponding phase plot, with the blue curves representing the theoretical values of the model and the red circles representing the actual measured values. It can be seen that the modeling of the PV and battery system's output impedance and RPC's input impedance is consistent with the simulation test results.

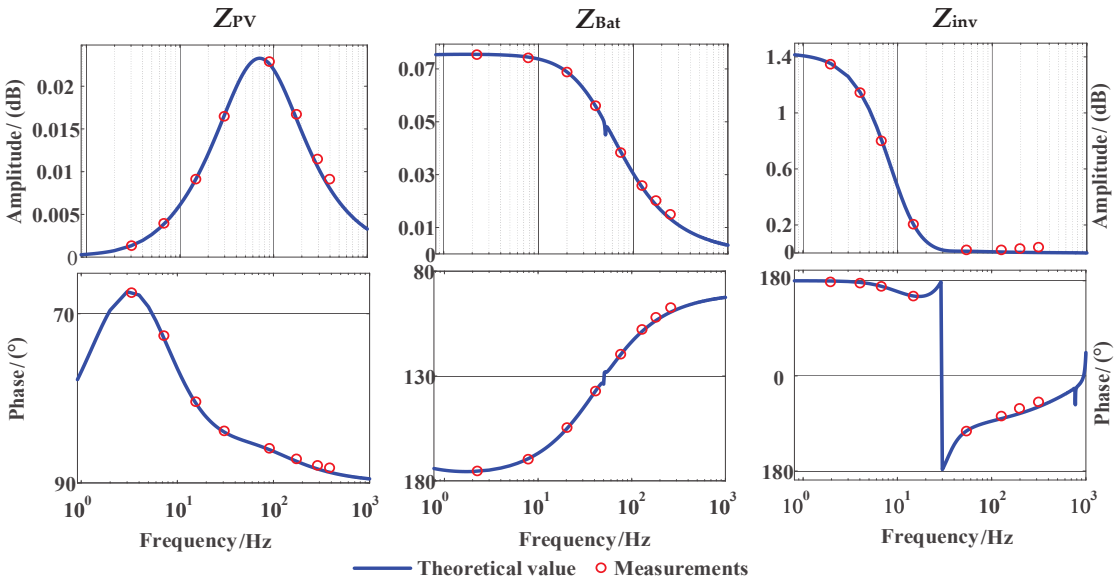

Figure 6. Three-port impedance verification.

2.3. Low-Frequency Stability Analysis of Proposed Emergency Power Supply System

2.3.1. Stability Judgment Based on Generalized Nyquist Criterion

According to the mathematical model established earlier, the impedance equivalent circuit of the PV and battery locomotive traction is shown in Figure 7a, where Z_0 is equal to the parallel value of Z_{PV} and Z_{Bat}, and Z_g is the impedance of the traditional locomotive network system source side. Due to the PI controller parameters of the converters in PV and battery systems that affect the output impedance of the system, Z_0, $Z_{PV,}$ and Z_{Bat} are different from Z_g because the value of Z_g depends on factors such as the material of the transmission line, its length, and the capacity of transformers, which are difficult to adjust in practical operation. In comparison, the values of Z_0, $Z_{PV,}$ and Z_{Bat} are related to the parameters of the PI controller, and adjusting the control parameters of the PI controller is less costly as well as more simple and fast. The introduction of a controllable equivalent impedance may exacerbate the LFO of the system or prevent system instability caused by impedance mismatch; this characteristic makes it particularly important to explore the impact of the control parameters and number of PV and battery parallel connections on the system's low-frequency stability. This section uses stability judgment methods based on impedance ratio criteria to conduct the research [27,28].

Firstly, it must be ensured that there are no RHP poles for Z_0, Z_{PV}, Z_{Bat}, and Y_{inv} and that each subsystem can operate independently and stably in the simulation. Under different traction modes, applying the one-dimensional impedance model established earlier, the Nyquisit curve based on the impedance ratio of Z_0/Z_{inv}, Z_{PV}/Z_{inv}, and Z_{Bat}/Z_{inv} can be obtained. Taking Z_0/Z_{inv} as an example, the expression for the system's impedance ratio can be represented by a transfer function of $G(s) = Z_0/Z_{inv}$. The stability of the system can be measured by plotting the Nyquist curve of $G(s)$ and determining whether it encircles $(-1, j0)$. Additionally, the variations in parameter values based on the impedance model discussed earlier can affect Z_0, thus, modifying the Nyquist curve of $G(s)$. Therefore, the parameters of each variable may have some effect on the stability of the system. Meanwhile, due to the lack of a clear concept of the stability margin in the impedance ratio criterion for MIMO equivalent systems, and to showcase the analysis process concisely and clearly, the critical amplitude margin (CAM) is defined to quantitatively analyze the system stability in order to reveal sensitive parameters and their influence laws. If CAM ≥ 0, the system is

stable; if CAM < 0, the system is unstable. The Nyquist plot of the impedance ratio transfer function for this system may change due to the effect of different parameters, leading to two different scenarios, as shown in Figure 7b.

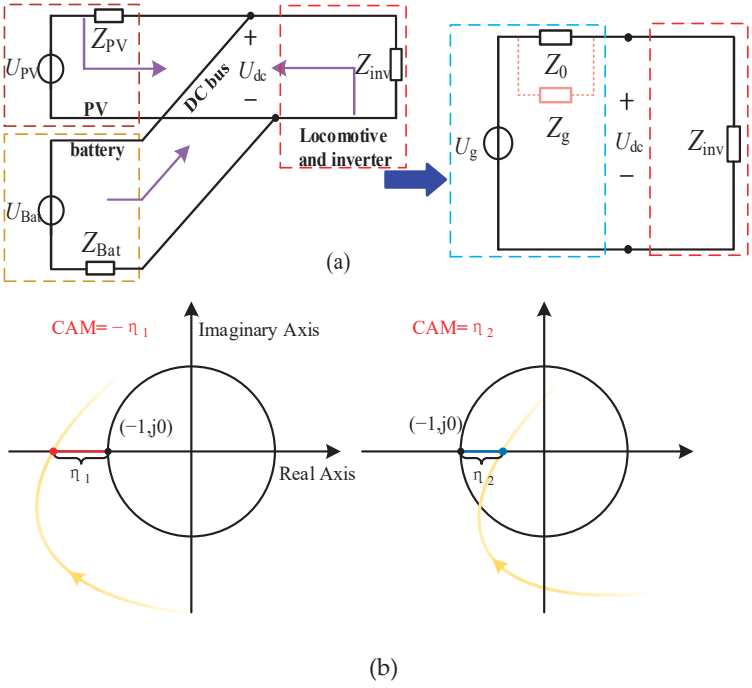

Figure 7. (**a**) System impedance equivalent circuit; (**b**) CAM value scenario diagram.

Scenario 1: When the curve surrounds (−1, j0), the distance from the intersection point of the real axis of the curve to (−1, j0) is expressed as η_1, CAM = $-\eta_1$;

Scenario 2: When the curve does not surround (−1, j0), the corresponding distance is expressed as η_2, CAM = η_2.

In summary, changes in system variables can affect the Nyquist curve of $G(s)$, thus, impacting the stability of the system. Such an impact can be translated into changes in CAM values to quantify the effect of a particular variable on the stability of the system. To further reveal the main controller parameters that affect the system stability, this article defines the sensitivity of the parameters as:

$$\varepsilon = \frac{\mathrm{CAM_n}}{(k_s - k_y)/k_y} \times 100\% \tag{16}$$

where k_y is a certain original parameter in Table 1, k_s is the value of the critical instability parameter with the smallest change from k_y, $(k_s - k_y)/k_y$ is the multiple of the minimum change in the original parameters when the system is in critical instability, and CAMn is the critical amplitude margin corresponding to the original parameter k_y under different operating conditions. The introduction of CAMn is aimed at correcting the sensitivity under different traction conditions (PV traction, battery traction, PV, and battery co-traction). This expression can be simply understood as the sensitivity to the electrical instability of the nearest value of the original parameter.

Table 1. Original simulation system parameters.

Subsystem	Parameter	Description	Value
Traction net	R_s	Grid-side equivalent resistance	0.2 Ω
	L_s	Grid-side equivalent inductance	6 mH
	e_s	Traction net voltage RMS	27.5 kV
	ω_0	Net-side angle frequency	314 rad·s^{-1}
Railway power conditioner	L_{inv}	Filter inductance	0.04 mH
	C_{inv}	Filter capacitors	6 mF
	C_{bus}	DC-side capacitance	300 mF
	u^*_{bus}	DC-side voltage reference value	2000 V
	ω	Reference angle frequency	314 rad·s^{-1}
	k_{invp}	Voltage-loop proportional gain	40
	k_{invi}	Voltage-loop integral gain	20
	k_b	Step-up transformer ratio	1500/27,500
PV subsystem	R_{PV}	PV-side resistance	1 mΩ
	L_{PV}	PV-side energy storage inductance	0.3 mH
	C_{PV}	PV-side support capacitor	2.2 mF
	k_{PVup}	Voltage-loop scaling factor	4
	k_{PVui}	Voltage-loop integration factor	20
	k_{PVip}	Current-loop scaling factor	0.4
	k_{PVii}	Current-loop integration factor	5
Battery subsystem	R_{Bat}	Energy-storage-side resistance	1 mΩ
	L_{Bat}	Energy storage inductance	1 mH
	k_{Bup}	Voltage-loop scaling factor	15
	k_{Bui}	Voltage-loop integration factor	2
	k_{Bip}	Current-loop scaling factor	0.02
	k_{Bii}	Current-loop integration factor	1
CRH3	k_a	On-board transformer ratio	27,500/1500
	L_n	leakage inductance of transformer	2 mH
	L_{CRH3}	DC-side filter inductance	0.84 mH
	C_{CRH3}	DC-side filter capacitors	3 mF
	C_d	DC side supports the capacitor	6 mF
	k_{PWM}	PWM equivalent gain	1
	k_{CRH3up}	Voltage-loop scaling factor	0.1
	k_{CRH3ui}	Voltage-loop integration factor	10
	k_{CRH3ip}	Current-loop scaling factor	1

2.3.2. Influence of DC Converter and RPC Parameters on the Low-Frequency Stability of the Proposed System

Based on the method proposed in Section 2.3.1, Figure 8a shows the electrical sensitivity bar chart of the control parameters of the DC converter and RPC inverter under three different traction modes when the ratio between the PV module, battery module, and CRH3 locomotive is 1:1:1. Due to the sensitivity of the inner-loop control parameters of the system under this scheme being less than 1%, the Nyquist curve hardly changes with the changes in the parameters, and the corresponding test shows that the system remains

stable even after a large number of changes in the inner-loop control parameters; therefore, it is not included in the research object. The bar chart shows that the proportional gain of the outer ring is more sensitive to the system stability and the combined traction of the PV and battery will reduce the parameter sensitivity.

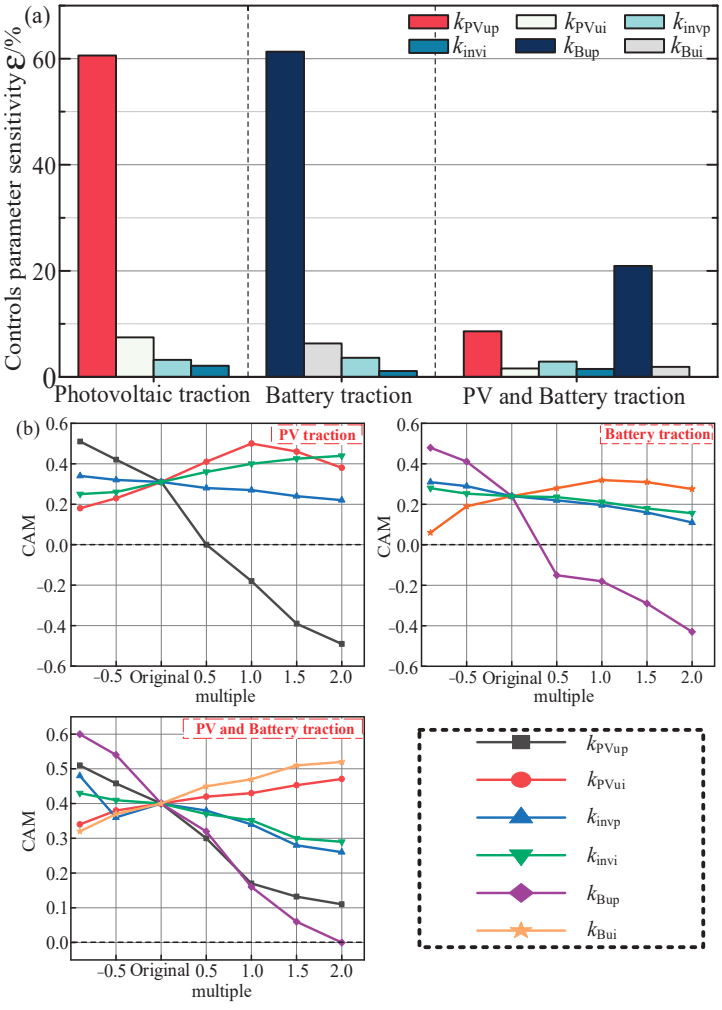

Figure 8. (**a**) Parameter sensitivity of the RPC and DC converters; (**b**) CAM change law of the control parameters.

The corresponding parameter influence law is shown in Figure 8b. Within the range of −0.9 to 2 times the original parameter value, the proportional gain of the outer ring of each converter exhibits monotonic, identical laws under different operating conditions, and the sensitivity (i.e., slope) is relatively high. However, the sensitivity of the integral gain of the outer ring is low, and the impact of the integral gain on the stability of the system exhibits diversification and non-monotonic characteristics under different traction conditions. Therefore, the outer-loop proportional gain of the system can be more easily used to control or prevent system impedance mismatch instability. The specific parameter adjustment criterion and case verification are expounded in Section 2.3.3.

In addition, LFO in locomotive network systems always occurs when the Nyquist curve of the impedance ratio (Z_g/Z_{CRH3}) passes through $(-1, j0)$. To investigate whether the occurrence of LFO under the topology and control scheme proposed in this paper is consistent with the theoretical analysis of locomotive network systems when the locomotive is separately tractioned by the PV or battery, the impedance ratio expression for the PV traction locomotive is Z_{PV}/Z_{inv}, and the expression for battery traction locomotive is Z_{Bat}/Z_{inv}, where Z_{PV}, Z_{Bat}, and Z_{inv} come from Equations (5), (6), and (14), and these impedance ratio expressions are used to plot Nyquist curves under different traction conditions. Then adjust the high sensitivity parameters k_{PVup} and k_{Bup} so that the Nyquist curve just surrounds $(-1, j0)$, thereby obtaining the Nyquist curve shown in Figure 9 and the test waveform shown in Figure 10. The results show that when the Nyquist curve of the impedance ratio for the system described in this paper precisely intersects the $(-1, j0)$ point, LFO at around 9.6 Hz also occurs. The principle and testing results are consistent under other parameters in Figure 8 but due to the large number of parameters, they are not listed in detail.

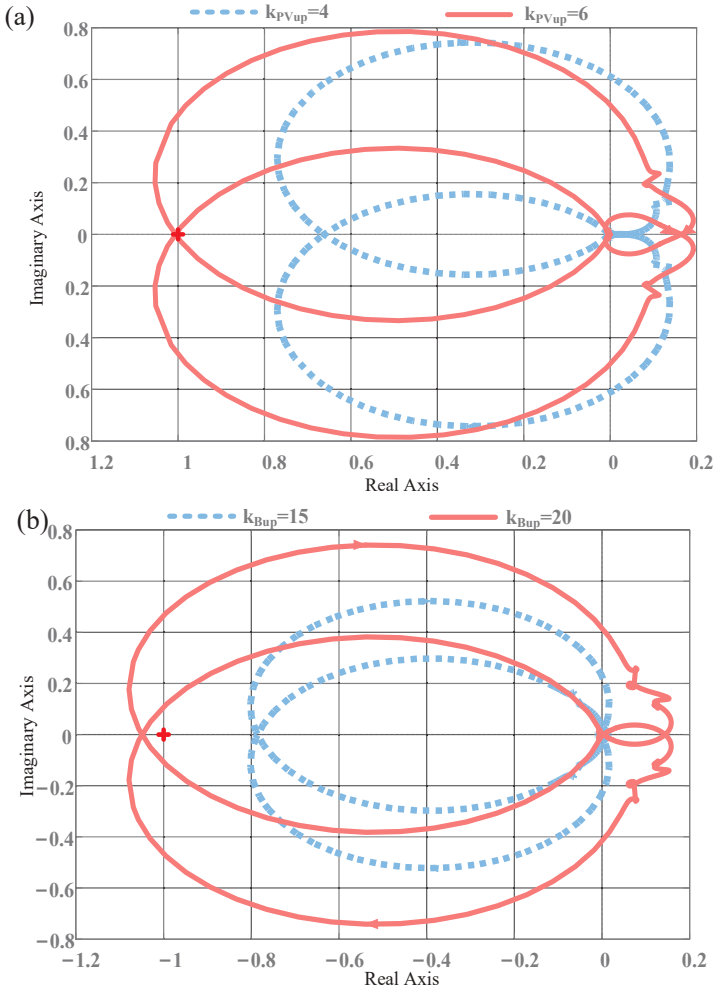

Figure 9. Nyquist curve before and after changes in high-sensitivity parameters: (**a**) working conditions of PV locomotive traction; (**b**) working conditions of battery locomotive traction.

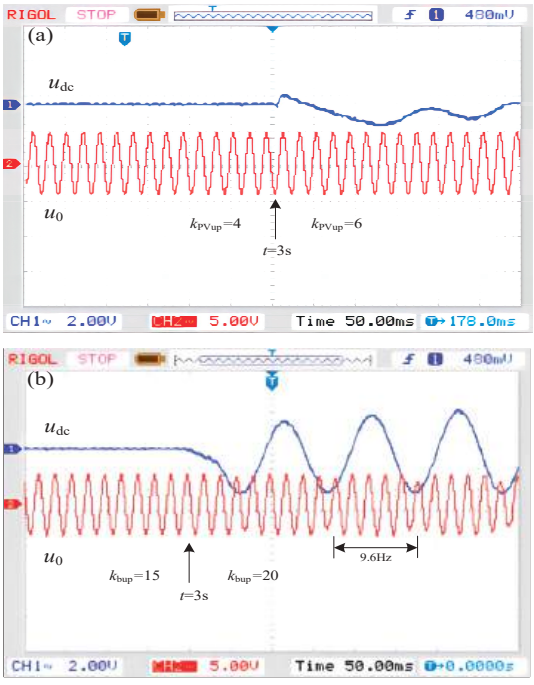

Figure 10. (**a**) Experimental waveform of the critical instability of photovoltaic locomotive traction; (**b**) experimental waveform of the critical instability of battery pack locomotive traction.

2.3.3. Parameter Adjustment Criterion and Case

Usually, an increase in the transformer capacity and the addition of other types of equipment such as static synchronous reactive power compensators on the source side are considered in locomotive network systems to address LFO caused by impedance mismatch. Such problems also exist in systems under emergency power supply schemes. However, when using PV and battery locomotive traction, based on the stability law of the control parameters revealed in Section 2.3.2, the goal can be achieved by adjusting the converter parameters accordingly. The specific parameter adjustment criteria are as follows: Firstly, if the system experiences instability, consider lowering the PV boost converter k_{PVup}, battery DC/DC converter k_{Bup}, and RPC single-phase inverter k_{invp}. Secondly, consider slightly lowering the k_{invi} during PV and battery co-traction or battery traction, and slightly increasing the k_{invi} during PV traction. It is worth noting that the RPC outer-loop proportional gain seriously affects the control accuracy (i.e., voltage amplitude); therefore, prioritize adjusting the proportional gain of the PV and battery DC converters unless faced with a situation that has special requirements. Taking the ratio of PV modules to battery modules as 1:1 as an example, the following explains the methods of parameter adjustment and governance in three cases. The Nyquist curve of Case 1 is shown in Figure 11a. When using the PV and battery locomotive co-traction, the battery system's energy storage inductance deteriorates from 1 mH to 1.23 mH, and the curve surrounds $(-1, j0)$; at this time, the adjustment k_{Bup} is reduced from 15 to 5, and the Nyquist criterion shows that the system will return to stability. The theoretical curve of Case 2 is shown in Figure 11b. When the k_{PVup} of the PV locomotive traction deteriorates, it causes a critical oscillation in the system. The k_{Bup} is adjusted and connected to the battery system; at this time, the PV and battery combined locomotive traction are stable. The test validation waveforms of the parameter adjustment criteria and related conclusions described in this section will be presented in Section 3.2.1.

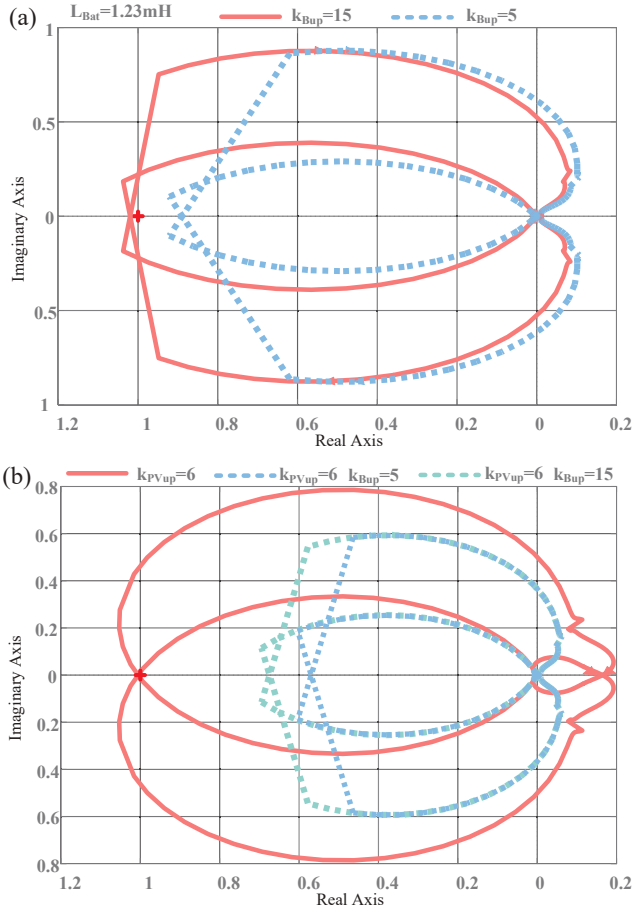

Figure 11. (**a**) Nyquist curve for Case 1; (**b**) Nyquist curve for Case 2.

2.3.4. The Influence of Mixed Proportional Parallel Numbers of PV and Battery Modules on System Stability

The number of PV and battery hybrid proportional parallel connections will also change the source-side impedance model to weaken or improve the stability of the system. Therefore, the original parameters were substituted into the hybrid parallel connection system. Based on the generalized Nyquist criterion, the bar chart shown in Figure 12a was obtained. The results show that the system operated stably under different PV and battery module proportions. To reveal its stability mechanism, the number of PV and battery modules were introduced as system variables, and because all the modules are connected in parallel, thus, expanding the impedance ratio expression Z_0/Z_{inv} in Section 2.3.1, we achieve the following formula:

$$L_{hui} = \left(\frac{\frac{Z_{pv} Z_{Bat}}{n_{pv} n_{bat}}}{\frac{Z_{pv}}{n_{pv}} + \frac{Z_{bat}}{n_{bat}}} \right) / Z_{inv} \tag{17}$$

where n_{pv} represents the number of PV modules, and n_{bat} represents the number of battery modules.

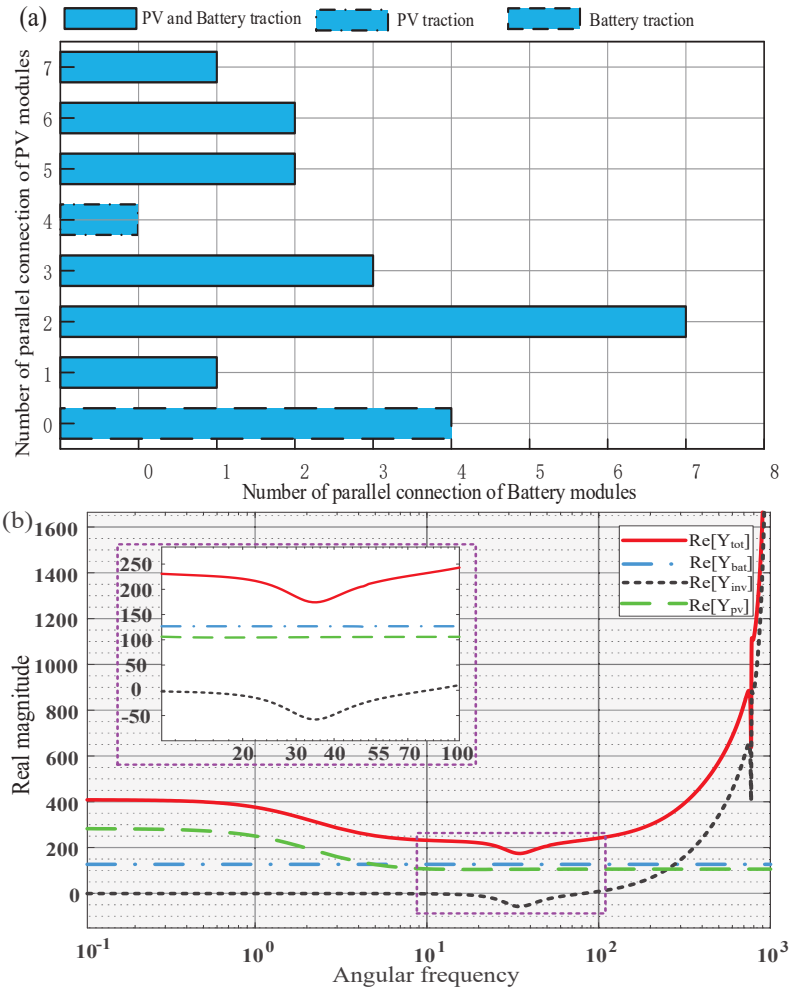

Figure 12. (**a**) The proportion of stable system operation when the PV and battery modules were connected in parallel; (**b**) analysis results of the passive criterion when the ratio of modules was 1:1.

If $n_{pv} = n_{bat} = n$, the expression is rewritten as $L_{hui} = (Z_0/Z_{inv})/n$, which is equivalent to proportionally reducing the Nyquist function curve (L_{hui}) by n times. Systems that do not originally include (−1, j0) will be more stable. In the previous work, it was proven and verified that the system was stable when the PV traction module ratio was 1:0, the battery traction module ratio was 0:1, and the PV and battery co-traction module ratio was 1:1 under the original parameters; therefore, the stability of the system with the PV and battery module ratios of 4:0, 0:4, and 3:3 in Figure 12a is explained. However, it is complex and difficult to give an answer for the stability mechanism of non 1:1, 1:0 systems using the impedance ratio criterion, since it changes a variable to directly judge the stability of the overall system. Therefore, this paper introduces a passive criterion applicable to the stability analysis of variables, subsystems, and overall systems. The judgment criterion is as follows: if the sum of the real parts of the total admittance of all parallel systems in the bus is guaranteed to be constantly greater than 0, all subsystems can operate stably at the same time. This passive criterion was proposed and verified by Riccobono A. in 2012 [34] but compared to the impedance ratio criterion, it is less used. Based on the "PV–battery

locomotive network" coupling system, this article additionally provides the proof process of the passive criterion from the perspective of dissipative system stability, as shown in Appendix B. The criterion combines Equations (5), (6), and (14) and Figure 7a, resulting in the following expression:

$$\begin{aligned} \mathrm{Re}[Y_{\mathrm{tot}}(s)] &= \mathrm{Re}\left[n_{\mathrm{pv}}Y_{\mathrm{PV}}(s) + n_{\mathrm{bat}}Y_{\mathrm{Bat}}(s) + Y_{\mathrm{inv}}(s)\right] \geq 0 \\ &= \mathrm{Re}\left[\frac{n_{\mathrm{pv}}}{Z_{\mathrm{PV}}(s)} + \frac{n_{\mathrm{bat}}}{Z_{\mathrm{Bat}}(s)} + \frac{1}{Z_{\mathrm{inv}}(s)}\right] \geq 0 \end{aligned} \tag{18}$$

Applying Equation (18), the function curve is plotted under the original parameters when the locomotive traction has a PV and battery module ratio of 1:1, as shown in Figure 12b. At this time, the real parts of the admittance of the PV and battery modules are both greater than 0 in the entire frequency band. If the subsystem is paralleled in any proportion, it will increase the distance between $\mathrm{Re}[Y_{\mathrm{tot}}(s)]$ and the horizontal axis, and the system will obtain an additional stability margin to maintain stability. This reveals the reason why the system always maintains stability after the PV and battery module mixing ratio is paralleled. Based on the above analysis, the problem of LFO in PV and battery locomotive co-traction under specific working conditions can also be solved by using the law of the influence of the number of module parallel connections on stability to reshape the system impedance from the main circuit structure through the passive criterion. In Section 3.2.2 Case 1, we designed experiments and demonstrated the validity of the theoretical analysis.

Increasing the number of PV battery parallel connections in a targeted manner can address instability caused by multiple locomotives running together or unreasonable RPC parameter settings but it is difficult to use this method to solve instability caused by the deterioration of the system. The instability process of this phenomenon can be revealed using passive criteria, as shown in Figure 13, which shows the criterion curve after the 1:1 parameters of the PV and battery modules deteriorate. Increasing n_{pv} and n_{bat} will cause $\mathrm{Re}[Y_{\mathrm{PV}}(s)]$, $\mathrm{Re}[Y_{\mathrm{bat}}(s)]$, and $\mathrm{Re}[Y_{\mathrm{tot}}(s)]$ to extend towards negative infinity, thereby exacerbating the system instability, and this was validated in Section 3.2.2 Case 2.

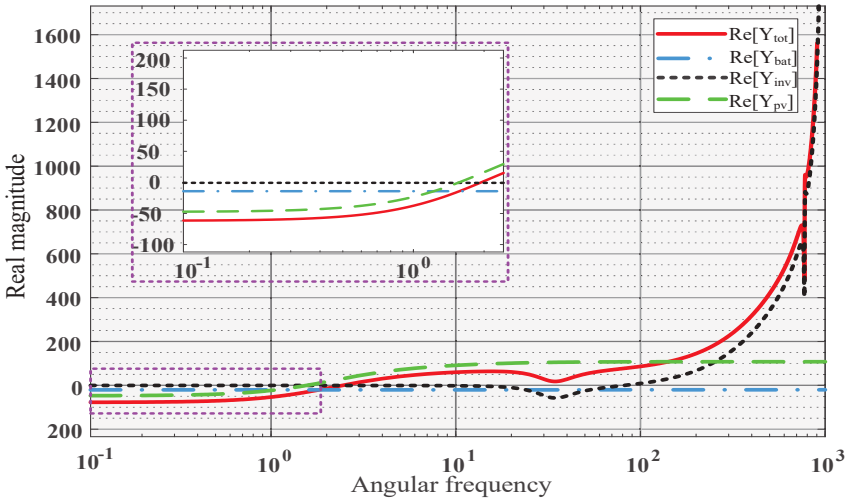

Figure 13. Passive criterion analysis results after deterioration of the system parameters.

Based on the research in this section, it is recommended to ensure that the real part of the admittance of the PV and battery subsystem is always greater than 0 during the design.

2.3.5. Passive Criterion Is Used to Reveal the Influence Law of Parameters on Stability

As shown in Section 2.3.4, the passive criterion based on the DC bus has clear boundary conditions and judgment criteria, which makes it easier to explore the law of the influence of parameters on the stability of the system, in comparison with the Nyquist criterion. This is reflected in the bivariate function curve, which directly shows the influence of a parameter of the system on its stability. This means that the law of stability near the original parameter will no longer be experimentally searched as before, and the three-dimensional plotting of the function can immediately reveal the influence of arbitrary values of a parameter on the stability of the original system. In order to verify the above analysis, passive criteria are used to reveal the stability influence laws of k_{PVup} and k_{Bup}, which have been verified before. By taking k_{PVup} and k_{Bup} as variables, we can obtain functions similar to Equation (19) but because the expressions are verbose, they are presented in the form of graphs, as shown in Figures 14 and 15, where the z axis is $\mathrm{Re}[Y_{\mathrm{tot}}(s)]$.

$$\mathrm{Re}[Y_{\mathrm{tot}}(s)] = F(k, \omega) \tag{19}$$

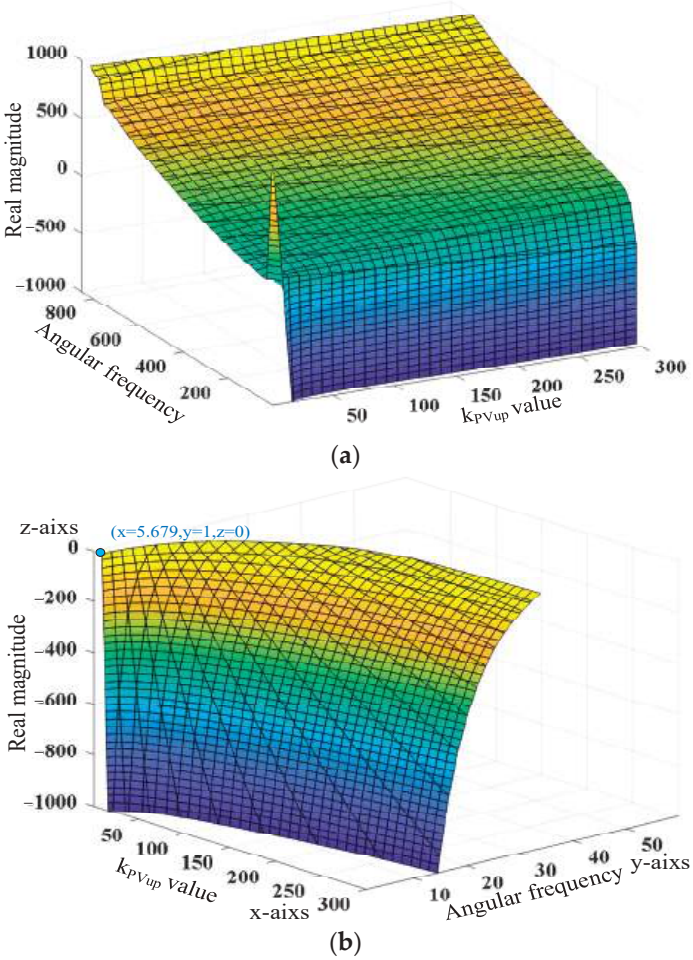

Figure 14. The influence of k_{PVup} on the system stability: (**a**) global diagram; (**b**) local diagram of the system instability.

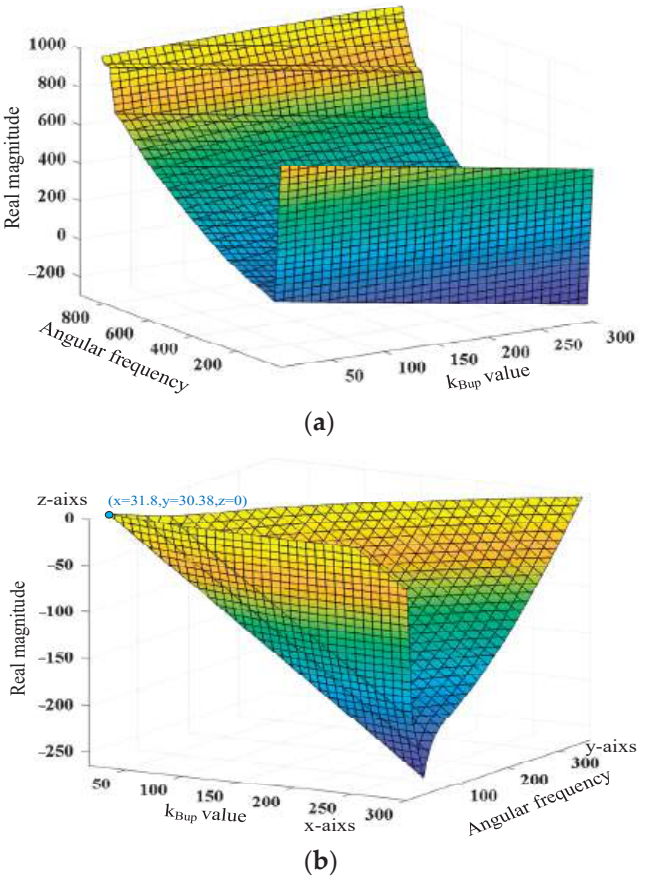

Figure 15. The influence of k_{Bup} on the system stability: (**a**) global diagram; (**b**) local diagram of the system instability.

Figures 14a and 15a show that with the increase in k_{PVup} and k_{Bup}, the surface gradually extends to the negative plane; in other words, the system gradually becomes unstable, which is consistent with the results obtained using Nyquist's criterion and in the semi-physical simulation, however, we are more concerned about the LFO phenomenon that often occurs in actual railway systems, that is, the critical instability of the system. Accordingly, the local amplification when the corresponding parameter is unstable is shown in Figures 14b and 15b, and the values of the LFO parameters given by the criterion are k_{PVup} = 5.679 or k_{Bup} = 31.8, which are obviously lower than the values given by the generalized Nyquist criterion, as shown in Figure 10b. The system ran stably in the simulation experiment under these parameters. It is also necessary to continue to increase the parameter values to cause LFO. This is caused by the large conservatism of the passive criterion. Assuming that the law revealed by the criterion is used to control the LFO, if the stability of a parameter affecting the law is not monotonic and there are lots of extreme points, this situation may lead to a counterproductive parameter adjustment. Here, the law revealed by the criterion is more suitable when parametric influences are monotonic over a large scale. However, in the system design, the conservativeness of the criterion is favorable, and it will leave a certain stability margin.

In addition, by applying passive criteria to the AC bus, the designed virtual impedance compensator successfully suppresses LFO [17] but the specific proof process in the AC system and its conservative improvement are the next research foci concerning this criterion.

3. Results and Discussion

3.1. Emergency Power Supply Scheme Testing

To verify the feasibility of the proposed emergency power supply scheme and the accuracy of the stability analysis, a simulation model of the PV and battery power generation systems, RPC, and CRH3 locomotive, as shown in Figure 1, was built based on Starsim. Figure 16 shows Shanghai Yuankuan Energy's Starsim HIL real-time simulation software 5.0 and HIL real-time simulator (Modeling Tech, Shanghai, China). This system can perform small-step real-time testing on power electronic models based on state equations, switch averaging, and modeling of large and small resistors. In this paper, the model was verified using a real-time test system (MT 6020) with a 5 μs step size and 20 kHz sampling frequency.

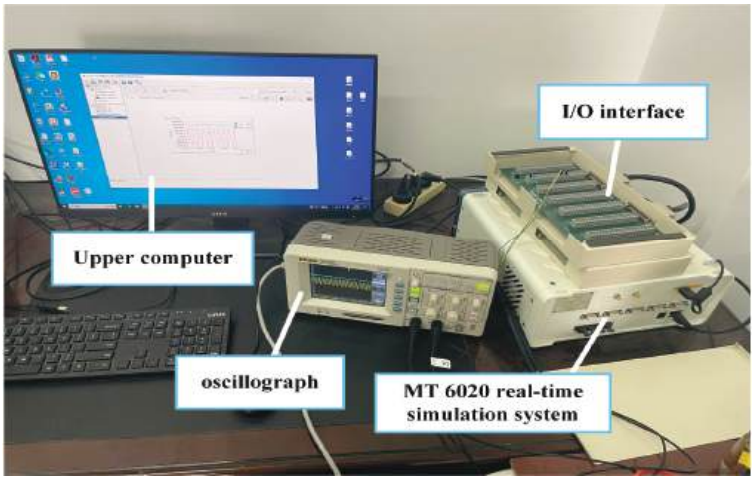

Figure 16. Hardware-in-the-loop real-time testing platform.

Here are the model parameters in the above-mentioned testing system, as shown in Table 1. In this paper, the parameters in Table 1 are referred to as the original parameters. Unless otherwise specified, analysis or testing will default to using the original parameters.

3.1.1. Emergency Traction Test based on Locomotive Power Failure

The upper computer calculation display is shown in Figure 17a, where P_{RPC} is the output power of the PV and battery, P_{net} is the output power of the substation, and P_{CRH3} is the absorbed power of one locomotive. At 1 s, the traction network unexpectedly lost power to the locomotive; after a short response time, the RPC identified the operation status of the PV and battery devices and switched to the corresponding mode to achieve the emergency power supply for the locomotive. At 2 s, the power supply to the substation was restored; to ensure passenger safety, the RPC delayed the power outage. Finally, at 2.5 s, the RPC exited the power supply or returned to the power compensation scheme. During this power outage process, the locomotive remained running, as shown in Figure 17b. If emergency-response-type locomotive traction is started in actual engineering, it can provide on-site measured data support and technical guidance for future new energy self-sufficient traction. For example, the working conditions of delayed power outages are equivalent to the actual test of changing to the substation supply when the new energy self-sufficient traction encounters an accident.

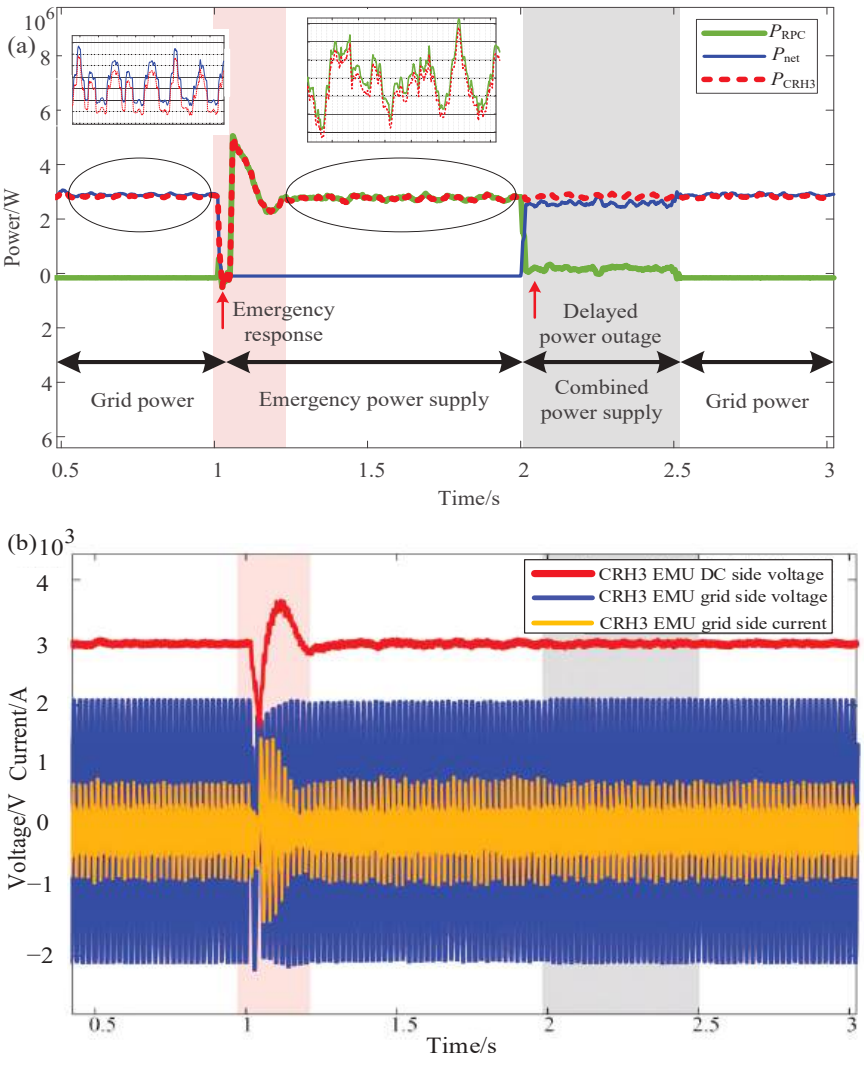

Figure 17. Emergency response traction power supply: (**a**) system energy flow; (**b**) locomotive voltage and current.

3.1.2. Coordinated Traction Test

The test setup of the operating power P_{load} of the high-speed locomotive is set to 3.6 MW, and the light intensity will continue to rise, as shown in Figure 18 obtained from the upper computer. Among the modes, mode four to mode one correspond to battery traction, PV and battery co-traction, PV traction, and PV locomotive traction and battery charging. By switching operation modes under different working conditions, the locomotive traction power can be stabilized while charging the battery. Under this scheme, the renewable energy continuous closed-loop power supply allows the locomotive to remain "low-carbon" for a long time, and a substation can be used for backup power in case of accidents.

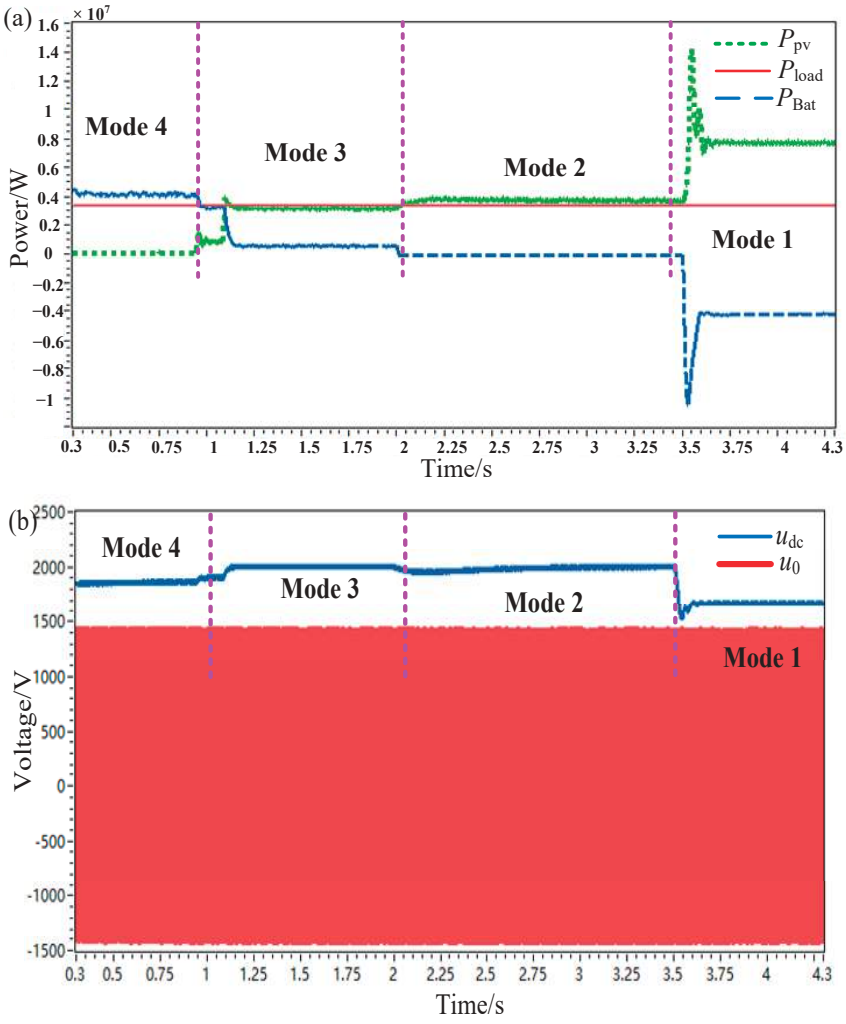

Figure 18. Energy self-sufficient traction power supply: (**a**) multi-mode power flow conditions; (**b**) voltage waveform on both sides of the RPC.

3.2. Verification of Low-Frequency Stability Analysis

The main purpose of this section is to verify the results of the low-frequency stability analysis in Section 2.3 to ensure the correctness of the analysis. The following subsections will present corresponding test results in the order of the analysis in Section 2.3.

3.2.1. Verification of Parameter Adjustment Criterion

1. **Case 1:** Adjusting control parameters to address instability caused by deteriorating circuit parameters. Under the original parameters, the PV and battery stably provided co-traction for the locomotive, which is verified in Figure 18. However, at this time, the parameters of the energy storage inductor L_{bat} deteriorated. The waveform of the traction-network-side voltage U_{ac} and current I_{ac} is shown in Figure 19b. The system experienced a low-frequency constant-amplitude oscillation of 5.7 Hz after 2 s, and after k_{Bup} decreased after 2 s, the system was stabilized and restored. This case

demonstrates that numerically adjustable control parameters can govern LFO caused by the deterioration of topology circuit parameters.

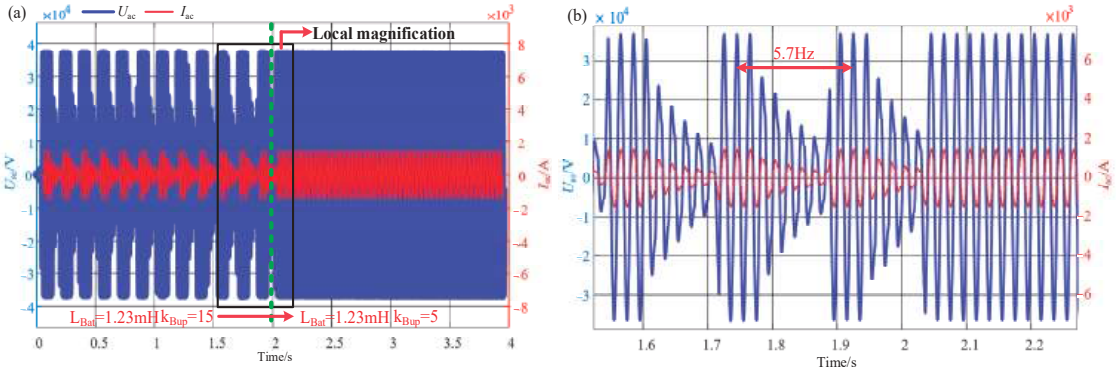

Figure 19. Waveform for parameter adjustment after the deterioration of the main circuit parameters: (**a**) global diagram; (**b**) local diagram.

2. **Case 2:** Connecting a parameter-adjusted other-source subsystem to address single-source traction instability. Due to the unreasonable setting of k_{PVup} during the PV locomotive traction, the system became unstable. Finally, a parameter-adjusted battery system was connected to control the constant-amplitude oscillation. The experimental waveform is shown in Figure 20, where u_{dc} and u_0 are the output voltages of the RPC DC and AC sides, respectively. By comparing and observing the oscilloscope, it was found that a lower value of k_{Bup} made the bus voltage fluctuation smaller and smoother when the battery system was connected. The reason for the successful governance of the parameter adjustment, in this case, is reflected in the addition of the circuit topology of the battery subsystem and the parameter setting under the parameter adjustment criteria, which improved the impedance matching relationship. At the same time, the relatively lower electrical sensitivity under the combined traction of the PV and battery provided the control parameters with a wider range of choices in the stable domain.

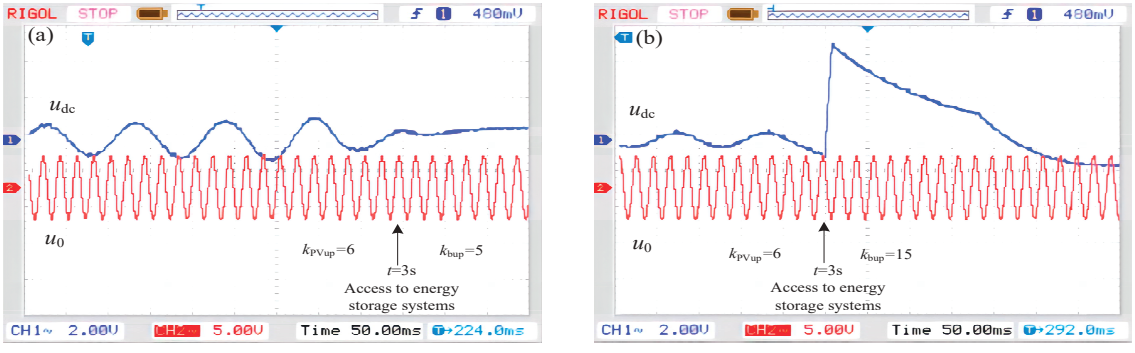

Figure 20. When the PV locomotive traction is unstable, it can be corrected by connecting a parameter-adjusted battery subsystem: (**a**) experimental waveform after the battery was connected when k_{Bup} = 5; (**b**) experimental waveform after the battery was connected when k_{Bup} = 15.

3. **Case 3:** Adjusting the control parameters to govern LFO caused by multi-locomotive operation (heavy load). The impedance ratio criterion mechanism shows that the smaller the load-side impedance, the more unstable the system will be. Therefore,

many studies on locomotive network systems have found that multi-locomotive operation or mixed operation is an important factor inducing LFO. The problem of heavy loads reducing the stability of traction power supply systems also exists in the study of PV and battery locomotive traction but the parameter-adjustable "artificially controllable traction network impedance" has a certain adaptability. The CRH3 high-speed locomotive was used as the research object, and the simulation waveform is shown in Figure 21, which includes the locomotive DC-side voltage U_{CRH3dc}, locomotive-network-side voltage U_{CRH3ac}, and locomotive-network-side current I_{CRH3ac}. After 2.5 s, the addition of three high-speed locomotives caused a 4Hz low-frequency constant-amplitude oscillation among the high-speed locomotives. According to the parameter adjustment criteria, k_{PVup} and k_{Bup} were decreased after 2.5 s, and then the locomotives were stabilized.

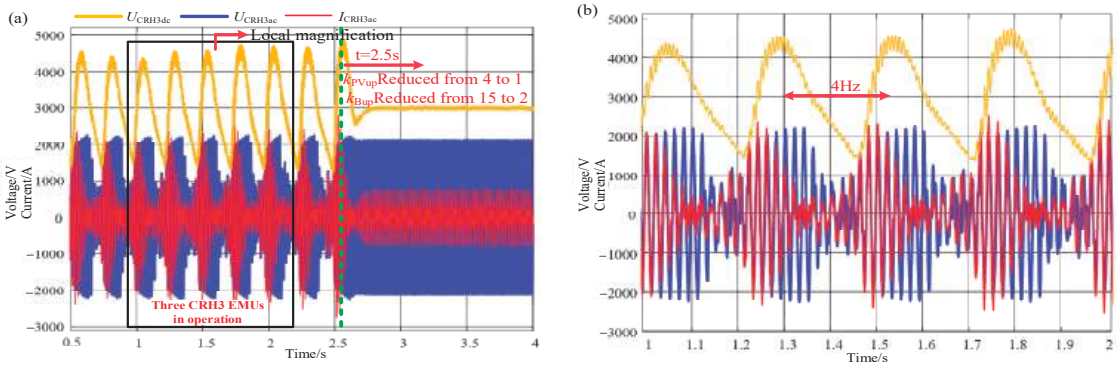

Figure 21. Adjustment of the parameters to control system instability caused by multi-locomotive parallel connection: (**a**) global diagram; (**b**) local diagram.

3.2.2. The Impact of Parallel Connections of PV and Battery Modules

1. **Case 1:** Worsening RPC parameters and overloading lead to LFO and then an increase in the number of parallel connections of the PV and battery modules. According to the passive criterion, overloading and deteriorating RPC parameters will cause $\mathrm{Re}[Y_{\mathrm{inv}}(s)]$ to extend towards the negative plane until the system experiences critical instability. According to the impedance ratio criterion, overloading is equivalent to proportionally amplifying the Nyquist curve until it envelops $(-1, \mathrm{j}0)$. Under this operating condition, it will cause low-frequency divergent oscillations, as shown in Figure 22a, where U_{dc} and U_0 are the voltages on both the RPC DC and AC sides, respectively. Increasing the number of parallel PV battery modules and reshaping the impedance to provide an additional stability margin can compensate for this, as shown in Figure 22b. In this case, the system can regain stability after 1.6 s.
2. **Case 2:** Increasing the number of parallel modules after the module parameters deteriorate. As shown in Figure 23, multiple increases in the number of module parallel connections after the PV and energy storage inductance parameters and control parameters deteriorate will actually exacerbate the system instability.

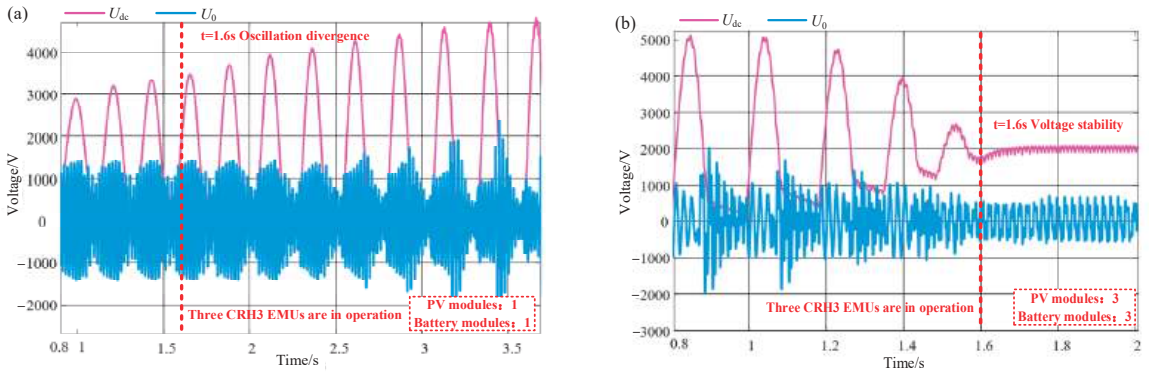

Figure 22. (**a**) Overloading and worsening RPC parameters lead to system instability: (**b**) the ratio of PV and battery module parallel connections can multiply and increase to reshape the system impedance.

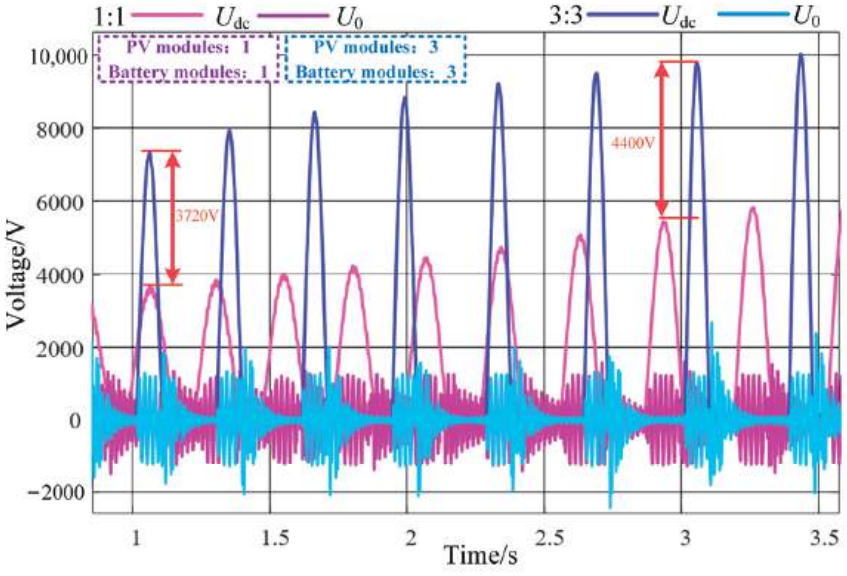

Figure 23. Deterioration of the system parameters leads to instability and multiple increases in the ratio of modules will aggravate the voltage oscillation.

4. Discussion

This paper mainly proposes an emergency power supply scheme to solve the problem of interruption in train power supply caused by unexpected faults in traction substations. The solution coordinates with the PV and battery systems to achieve emergency traction of locomotives, thereby expanding the functions of the railway power conditioner (RPC). Meanwhile, this paper proves through theoretical modeling and verification tests that the PV and battery traction locomotive additionally have the problem of low-frequency oscillation. To curb low-frequency oscillation occurring during the emergency power supply, this paper quantitatively analyzes the influence law of PI control parameters and topological structures on the low-frequency stability of the system, proposes a design method for the impedance real part greater than 0 of the PV and battery systems module, and provides parameter adjustment criteria to suppress or even prevent low-frequency oscillations.

Most studies on the integration of PV and battery into electrified railways focus on RPC grid compensation of traction power and harmonic governance. However, it is necessary to make RPC multifunctional, and few of the literature studies the coordinated control scheme of PV and battery for emergency train traction. If the majority of current RPC research's control strategies, such as the ones described in references [16,31], are used to independently traction the locomotive, the lack of phase information obtained by the phase-locked loop will cause the frequency and current of the traction network to be incorrect, forcing the locomotive to stop running. Therefore, this paper proposes the use of a dual-mode RPC with an independent power supply function, which can not only compensate for the power of the traction power supply system but also provide emergency traction for the locomotive.

Meanwhile, current research of the literature applies various criteria to analyze the low-frequency stability of a system. However, many research methods and processes in the literature are rather similar, in that they require graph redrawing every time a variable is modified to display the corresponding result [18,27,28]. This process is not intuitive enough and does not facilitate a thorough investigation of the impact of parameters on the stability and sensitivity of the system, simultaneously considering that there is little research on the low-frequency stability of the PV–battery locomotive network coupling system. Therefore, this paper defines CAM to quantify system stability and provides a method to calculate the sensitivity ε of parameters, which can weigh the importance of different parameters under different working conditions and explore the main influencing parameters and their influence laws. This paper also proposes the use of a passive criterion to reveal the influence mechanism of the number of PV and battery modules in parallel on system stability. Moreover, it finds that it has great potential for exploring parameter influence laws, it can intuitively give the law that a variable affects system stability within any value range through functions or three-dimensional drawings, however, the passive criterion still needs some improvement to achieve analysis accuracy similar to that of the Nyquist criterion.

Furthermore, PV and battery co-traction locomotives are environmentally friendly, because almost all of the electricity comes from renewable energy sources. Based on the research results of this article, further optimization and improvements in the power supply scheme of emergency traction locomotives, and exploring the impact of more variables on the low-frequency stability of the system, such as different types of locomotives running together under different working conditions, and conducting comprehensive research on the simultaneous impact of multiple parameters on the system, all have a profound significance and great value. Meanwhile, issues such as whether the emergency power supply scheme proposed in this article be used for long-term traction locomotives persist. How to configure the capacity of the PV and battery, whether the PV resources can be recycled by the power grid while the supply arm is idle and the locomotive is running, etc., are also the focus of future research. Compared to the traditional AC-electrified railway, the fact that the output of both PV and energy storage is DC suggests that there may be broader application prospects for PV and battery traction locomotives in DC railways and urban rail transit systems, and how to further explore its specific scheme and system stability are yet to be discussed.

5. Conclusions

This work demonstrates that it is feasible to independently drive locomotives using PV and battery equipment under different working conditions during the day and night, and it established a one-dimensional impedance model for a PV–battery locomotive network system from the DC side. At the same time, this study suggests that low-frequency stability analysis of the system of the PV–battery locomotive network may be very important. On this basis, the stability of the system was studied using the generalized Nyquist criterion and a passive criterion. The critical amplitude margin (CAM) and the sensitivity of the controller parameters were proposed to quantitatively evaluate the influence law of the

source-side DC converter control parameters and RPC control parameters on this system stability under different emergency traction modes, and corresponding parameter tuning criteria and design suggestions were provided to improve the stability of the system. Finally, the findings were verified through time-domain simulation models and semi-physical testing. The main research conclusions are as follows:

(1) Proposal of a coordinated control strategy, achieving locomotives emergency traction by using PV and battery, thus, increasing the function of the RPC.
(2) When the locomotive is co-tractioned by the PV and battery, the sensitivity of the control parameters is reduced compared to when the locomotive is powered by a single source. Moreover, the parameter selection in the stable region is more extensive, and the control accuracy is higher. In addition, the influence of the proportional gain parameters of the outer loop of the PV and battery DC converters on the system stability is consistent under different traction conditions. Compared to the RPC control parameters and the integral gain sensitivity of the outer loop of the PV and battery DC converter controller, it is more reasonable to improve the system stability by adjusting the proportional gain of the PV and battery DC converters. Priority should be given to reducing the proportional coefficient k_{PVup} and k_{Bup} to improve the stability of the system.
(3) The numerical value of the connection ratio between the PV modules and battery modules has a significant impact on the low-frequency stability of the system. If the output admittance of the PV and battery modules is less than 0, increasing the number of parallel connections will weaken the system stability; if it is greater than 0, the stability margin will be increased to a certain extent. By utilizing this feature, the impedance can be reshaped during system design and operation.

Author Contributions: Conceptualization, Y.W.; methodology, Y.X.; software, Z.X.; validation, Y.W. and Y.X.; formal analysis, X.M.; data curation, X.C.; writing—original draft preparation, Y.X.; writing—review and editing, Y.W.; visualization, X.C. All authors have read and agreed to the published version of the manuscript.

Funding: This research was funded by National Natural Science Foundation of China (52067013); the Natural Science Key Foundation of Science and Technology Department of Gansu Province (22JR5RA318, 21JR7RA280, 22JR5RA353).

Data Availability Statement: Data are available on request from the authors. The data that support the findings of this study are available from the corresponding author upon reasonable request.

Conflicts of Interest: The authors declare no conflict of interest.

Appendix A

$$\begin{cases} G_{\mathrm{PVBB}} = \frac{\Delta u_{\mathrm{Bus}}}{\Delta i_{\mathrm{Bus}}} = \frac{s^2 L_{\mathrm{PV}} C_{\mathrm{PV}} + s R_{\mathrm{PV}} C_{\mathrm{PV}} + 1}{s^3 L_{\mathrm{PV}} C_{\mathrm{PV}} C_{\mathrm{Bus1}} + s^2 R_{\mathrm{PV}} C_{\mathrm{PV}} C_{\mathrm{Bus1}} + s\left(C_{\mathrm{Bus1}} + C_{\mathrm{PV}} D_{\mathrm{PV}}^{*2}\right)} \\ G_{\mathrm{PVBP}} = \frac{\Delta u_{\mathrm{Bus}}}{\Delta d_{\mathrm{PV}}} = \frac{-s^2 R_{\mathrm{PV}} C_{\mathrm{PV}} C_{\mathrm{Bus1}} + s\left(C_{\mathrm{PV}} D_{\mathrm{PV}}^{*} U_{\mathrm{Bus1}} - R_{\mathrm{PV}} L_{\mathrm{PV}} C_{\mathrm{PV}}\right) - I_{\mathrm{LPV}}}{s^3 L_{\mathrm{PV}} C_{\mathrm{PV}} C_{\mathrm{Bus1}} + s^2 R_{\mathrm{PV}} C_{\mathrm{PV}} C_{\mathrm{Bus1}} + s\left(C_{\mathrm{Bus1}} + C_{\mathrm{PV}} D_{\mathrm{PV}}^{*2}\right)} \\ G_{\mathrm{PVLB}} = \frac{\Delta i_{\mathrm{LPV}}}{\Delta i_{\mathrm{Bus}}} = \frac{s C_{\mathrm{PV}} D_{\mathrm{PV}}^{*}}{s^3 L_{\mathrm{PV}} C_{\mathrm{PV}} C_{\mathrm{Bus1}} + s^2 R_{\mathrm{PV}} C_{\mathrm{PV}} C_{\mathrm{Bus1}} + s\left(C_{\mathrm{Bus1}} + C_{\mathrm{PV}} D_{\mathrm{PV}}^{*2}\right)} \\ G_{\mathrm{PVLP}} = \frac{\Delta i_{\mathrm{LPV}}}{\Delta d_{\mathrm{PV}}} = \frac{s^2 C_{\mathrm{PV}} C_{\mathrm{Bus1}} U_{\mathrm{Bus}} + s L_{\mathrm{PV}} C_{\mathrm{PV}} D_{\mathrm{PV}}^{*}}{s^3 L_{\mathrm{PV}} C_{\mathrm{PV}} C_{\mathrm{Bus1}} + s^2 R_{\mathrm{PV}} C_{\mathrm{PV}} C_{\mathrm{Bus1}} + s\left(C_{\mathrm{Bus1}} + C_{\mathrm{PV}} D_{\mathrm{PV}}^{*2}\right)} \\ G_{\mathrm{PVu}} = k_{\mathrm{PVup}} + \frac{k_{\mathrm{PVui}}}{s} \\ G_{\mathrm{PVi}} = k_{\mathrm{PVip}} + \frac{k_{\mathrm{PVii}}}{s} \end{cases} \tag{A1}$$

$$\begin{cases} G_{\mathrm{BiB}} = \frac{\Delta u_{\mathrm{Bus}}}{\Delta i_{\mathrm{Bus}}} = \frac{sL_{\mathrm{Bat}}+R_{\mathrm{Bat}}}{s^2L_{\mathrm{Bat}}C_{\mathrm{Bus2}}+sR_{\mathrm{Bat}}C_{\mathrm{Bus2}}+D_{\mathrm{Bat}}^2} \\ G_{\mathrm{BdB}} = \frac{\Delta u_{\mathrm{Bus}}}{\Delta d_{\mathrm{Bat}}} = \frac{(sL_{\mathrm{Bat}}+R_{\mathrm{Bat}})I_{\mathrm{Bat}}-D_{\mathrm{Bat}}U_{\mathrm{Bus}}}{s^2L_{\mathrm{Bat}}C_{\mathrm{Bus2}}+sR_{\mathrm{Bat}}C_{\mathrm{Bus2}}+D_{\mathrm{Bat}}^2} \\ G_{\mathrm{iBi}} = \frac{\Delta i_{\mathrm{Bat}}}{\Delta i_{\mathrm{Bus}}} = \frac{D_{\mathrm{Bat}}}{s^2L_{\mathrm{Bat}}C_{\mathrm{Bus2}}+sR_{\mathrm{Bat}}C_{\mathrm{Bus2}}+D_{\mathrm{Bat}}^2} \\ G_{\mathrm{iBd}} = \frac{\Delta i_{\mathrm{Bat}}}{\Delta d_{\mathrm{Bat}}} = \frac{sU_{\mathrm{Bus}}C_{\mathrm{Bus2}}+D_{\mathrm{Bat}}L_{\mathrm{Bat}}}{s^2L_{\mathrm{Bat}}C_{\mathrm{Bus2}}+sR_{\mathrm{Bat}}C_{\mathrm{Bus2}}+D_{\mathrm{Bat}}^2} \\ G_{\mathrm{Bu}} = k_{\mathrm{Bup}} + \frac{k_{\mathrm{Bui}}}{s} \\ G_{\mathrm{Bi}} = k_{\mathrm{Bip}} + \frac{k_{\mathrm{Bii}}}{s} \end{cases} \quad \text{(A2)}$$

Appendix B

The passive criterion is additionally proven from the perspective of the dissipative system:

Based on the DC bus, the equivalent impedance circuit of "PV-Battery-locomotive network" is obtained by using Thevenin's and Norton theorems, as shown in Figure A1, where $u(t) = U_{\mathrm{dc}}$.

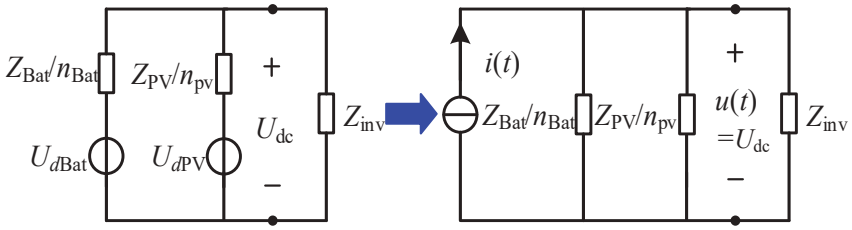

Figure A1. "PV-Battery-locomotive network" equivalent impedance circuit.

The energy function is listed using the output current and voltage, as shown in the following equation.

$$\rho(t) = \int_{-\infty}^{+\infty} u(t)i(t)dt \quad \text{(A3)}$$

When the above equation is always greater than zero, the system is a dissipative system and remains stable at all times. According to Passerval's theorem, the conversion to the frequency domain yields:

$$\begin{aligned} &\int_{-\infty}^{+\infty} u(t)i(t)dt = \frac{1}{2\pi}\int_0^{+\infty} (u^*(\omega)i(\omega) + u(\omega)i^*(\omega))d\omega \\ &= \frac{1}{2\pi}\int_0^{+\infty} (u(\omega))^2(Y_{\mathrm{tot}}(\omega) + Y_{\mathrm{tot}}{}^*(\omega))d\omega \end{aligned} \quad \text{(A4)}$$

Among them, * represents conjugation, Y_{tot} represents the sum of the admittance realities of the optical storage network, and ensuring that the above equation is greater than 0 is ensuring that the admittance Y_{tot} real part is greater than 0.

References

1. JR East Group. *CSR Report 2017: Aiming for a Sustainable Society*; JR East Group: Shibuya City, Japan, 2017.
2. Metro de Santiago. *Sustainability Report 2017*; Metro de Santiago: Santiago, Chile, 2018.
3. Zhong, J.; Bollen, M.; Rönnberg, S. Towards a 100% renewable energy electricity generation system in Sweden. *Renew. Energy* **2021**, *171*, 812–824. [CrossRef]
4. Zhou, X. A Study on Potential for Using New Energy and Renewable Energy Sources in Railways. *Int. J. Energy Power Eng.* **2019**, *8*, 45. [CrossRef]
5. Zhang, G.; Xue, H.; Wang, Y. Systematic study and innovation practice of new concept for the construction of Xiongan station. *China Railw.* **2021**, 50–56. [CrossRef]

6. Wang, J.; Yang, X.; Kumari, S. Investigating the Spatial Spillover Effect of Transportation Infrastructure on Green Total Factor Productivity. *Energies* **2023**, *16*, 2733. [CrossRef]
7. Chen, J.; Wang, Y.; Chen, X. An on board energy storage solution considering voltage fluctuations and harmonic control of traction networks under mountain area conditions. *J. Railw. Sci. Eng.* **2021**, *18*, 1582–1594.
8. Chen, W.; Wang, X.; Li, Q. Review on the development status of pv power station accessing to traction power supply system for rail transit. *Power Syst. Technol.* **2019**, *43*, 3663–3670.
9. Tanta, M.; Pinto, J.G.; Monteiro, V.; Martins, A.P.; Carvalho, A.S.; Afonso, J.L. Topologies and Operation Modes of Rail Power Conditioners in AC Traction Grids: Review and Comprehensive Comparison. *Energies* **2020**, *13*, 2151. [CrossRef]
10. Guo, Y.; Chen, X.; Wang, Y. Negative sequence optimization compensation strategy for energy storage type railway power conditioner considering grid voltage imbalance. *High Volt. Eng.* **2023**, *49*, 772–780.
11. Tanta, M.; Cunha, J.; Barros, L.A.M.; Monteiro, V.; Pinto, J.G.O.; Martins, A.P.; Afonso, J.L. Experimental Validation of a Reduced-Scale Rail Power Conditioner Based on Modular Multilevel Converter for AC Railway Power Grids. *Energies* **2021**, *14*, 484. [CrossRef]
12. Zhang, D.; Zhang, Z.; Wang, W.; Yang, Y. Negative Sequence Current Optimizing Control Based on Railway Static Power Conditioner in V/v Traction Power Supply System. *IEEE Trans. Power Electron.* **2015**, *31*, 200–212. [CrossRef]
13. Li, T.; Shi, Y. Power Quality Management Strategy for High-Speed Railway Traction Power Supply System Based on MMC-RPC. *Energies* **2022**, *15*, 5205. [CrossRef]
14. Barros, L.A.M.; Martins, A.P.; Pinto, J.G. Balancing the Active Power of a Railway Traction Power Substation with an sp-RPC. *Energies* **2023**, *16*, 3074. [CrossRef]
15. Lu, Q.; Gao, Z.; He, B.; Che, C.; Wang, C. Centralized-Decentralized Control for Regenerative Braking Energy Utilization and Power Quality Improvement in Modified AC-Fed Railways. *Energies* **2020**, *13*, 2582. [CrossRef]
16. Chen, W.; Wang, X.; Han, Y. Research on coordinated control method of pv and battery access traction power supply system based on RPC. In Proceedings of the 2020 IEEE Sustainable Power and Energy Conference (iSPEC), Chengdu, China, 23–25 November 2020.
17. Hu, H.; GE, Y.; Huang, Y. A novel "source-network-train-storage" integrated power supply system for electric railways. In Proceedings of the CSEE 2022, Lisbon, Portugal, 10–12 April 2022; Volume 42, pp. 4374–4391.
18. Liao, Y.; Liu, Z.; Zhang, H.; Wen, B. Low-Frequency Stability Analysis of Single-Phase System with *dq*-Frame Impedance Approach—Part II: Stability and Frequency Analysis. *IEEE Trans. Ind. Appl.* **2018**, *54*, 5012–5024. [CrossRef]
19. Hu, H.; Zhou, Y.; Li, X.; Lei, K. Low-Frequency Oscillation in Electric Railway Depot: A Comprehensive Review. *IEEE Trans. Power Electron.* **2020**, *36*, 295–314. [CrossRef]
20. Carlos, S.B. Direct Generation of Low Frequency Single Phase AC for the Railway in Norway and Sweden. Ph.D. Thesis, Royal Institute of Technology, Stockholm, Sweden, 2009.
21. Danielsen, S.; Molinas, M.; Toftevaag, T.; Fosso, O.B. Constant power load characteristic's influence on the low-frequency interaction between advanced electrical rail vehicle and railway traction power supply with rotary converters. In Proceedings of the 9th International Scientific Conference "Modern Electric Traction", Gdansk, Poland, 24–26 September 2009; pp. 1–6.
22. Danielsen, S. Electric Traction Power System Stability. Ph.D. Thesis, Norwegian University of Science and Technology, Trondheim, Norway, 2010.
23. Song, Y.; Liu, Z.; Ronnquist, A.; Navik, P.; Liu, Z. Contact wire irregularity stochastics and effect on high-speed railway pantograph-catenary interactions. *IEEE Trans. Instrum. Meas.* **2020**, *69*, 8196–8206. [CrossRef]
24. Song, Y.; Wang, Z.; Liu, Z.; Wang, R. A spatial coupling model to study dynamic performance of pantograph-catenary with vehicle-track excitation. *Mech. Syst. Signal Process.* **2020**, *151*, 107336. [CrossRef]
25. Frugier, D.; Ladoux, P. Voltage disturbances on 25 kV–50 Hz railway lines Modelling method and analysis. In Proceedings of the SPEEDAM 2010, Pisa, Italy, 14–16 June 2010; pp. 1080–1085. [CrossRef]
26. Jiang, X.; Hu, H.; He, Z.; Tao, H.; Qian, Q. Study on low-frequency voltage fluctuation of traction power supply system introduced by multiple modern trains. *Electr. Power Syst. Res.* **2017**, *146*, 246–257. [CrossRef]
27. Mu, X.; Wang, Y.; Chen, S. Stability research on high-speed railway vehicle network electric coupling system based on improved sum-norm criterion. *Trans. China Electrotech. Soc.* **2019**, *34*, 3253–3264.
28. Xia, W.; Wang, H.; Meng, X. Electrical stability research on vehicle-grid coupling system of high-speed railways for mixed passenger and freight traffic. *Power Syst. Technol.* **2021**, *45*, 4837–4848.
29. Zhang, X.; Wang, L.; Dunford, W.; Chen, J.; Liu, Z. Integrated Full-Frequency Impedance Modeling and Stability Analysis of the Train-Network Power Supply System for High-Speed Railways. *Energies* **2018**, *11*, 1714. [CrossRef]
30. Fan, F.; Wank, A.; Seferi, Y.; Stewart, B.G. Pantograph Arc Location Estimation Using Resonant Frequencies in DC Railway Power Systems. *IEEE Trans. Transp. Electrif.* **2021**, *7*, 3083–3095. [CrossRef]
31. Zhao, X.; Xie, Z.; Wang, Y. Low frequency stability analysis of photovoltaic connected traction power supply system based on extended forbidden region-based criterion. *High Volt. Eng.* **2023**, 1–12. [CrossRef]
32. Zhou, Y. *Research on Low Frequency Oscillation Suppression of Emu Based on On-Board Energy Storage and Virtual Synchronous Machine Technology*; Beijing Jiaotong University: Beijing, China, 2021.

33. Pedra, J.; Sainz, L.; Monjo, L. Three-Port Small Signal Admittance-Based Model of VSCs for Studies of Multi-Terminal HVDC Hybrid AC/DC Transmission Grids. *IEEE Trans. Power Syst.* **2020**, *36*, 732–743. [CrossRef]
34. Riccobono, A.; Santi, E. A novel Passivity-Based Stability Criterion (PBSC) for switching converter DC distribution systems. In Proceedings of the 2012 Twenty-Seventh Annual IEEE Applied Power Electronics Conference and Exposition, Orlando, FL, USA, 5–9 February 2012; pp. 2560–2567. [CrossRef]

electronics

MDPI

Article

Harmonic Distortion and Hosting Capacity in Electrical Distribution Systems with High Photovoltaic Penetration: The Impact of Electric Vehicles

Miguel Dávila-Sacoto [1], L. G. González [2], Luis Hernández-Callejo [1,*], Óscar Duque-Perez [3], Ángel L. Zorita-Lamadrid [3], Víctor Alonso-Gómez [4] and J. L. Espinoza [2]

[1] Department of Agricultural and Forestry Engineering, University of Valladolid, Duques de Soria University Campus, 42004 Soria, Spain; miguelalberto.davila@estudiantes.uva.es
[2] Department of Electrical Engineering, University of Cuenca, Central Campus, Cuenca 010104, Ecuador; luis.gonzalez@ucuenca.edu.ec (L.G.G.); juan.espinoza@ucuenca.edu.ec (J.L.E.)
[3] Department of Electrical Engineering, School of Industrial Engineering, University of Valladolid, 47011 Valladolid, Spain; oscar.duque@eii.uva.es (Ó.D.-P.); zorita@eii.uva.es (Á.L.Z.-L.)
[4] Department of Physics, University of Valladolid, Duques de Soria University Campus, 42004 Soria, Spain; victor.alonso.gomez@uva.es
* Correspondence: luis.hernandez.callejo@uva.es

Abstract: Electric vehicles and the charging stations and their operation require a thorough examination to evaluate the effects on the electrical network. This becomes particularly challenging in the case of high photovoltaic penetration, due to the variability of the solar resource and vehicle connection patterns, which cater to individual user preferences. The current study investigates the impact of harmonics generated by charging stations and electric vehicles on different photovoltaic penetration scenarios within an electrical distribution system. DC and AC charging stations are analyzed. The findings reveal a third harmonic magnitude increase exceeding 300% compared to other cases. Furthermore, this study demonstrates the effects of current and voltage variations on end-users and substation transformers. The impact of harmonics on the hosting capacity of the network is also analyzed, resulting in a 37.5% reduction in the number of vehicles.

Keywords: electric vehicle; charging stations; photovoltaic generation; distribution system; harmonics

Citation: Dávila-Sacoto, M.; González, L.G.; Hernández-Callejo, L.; Duque-Perez, Ó.; Zorita-Lamadrid, Á.L.; Alonso-Gómez, V.; Espinoza, J.L. Harmonic Distortion and Hosting Capacity in Electrical Distribution Systems with High Photovoltaic Penetration: The Impact of Electric Vehicles. *Electronics* **2023**, *12*, 2415. https://doi.org/10.3390/electronics12112415

Academic Editors: Jesús Armando Aguilar Jiménez and Carlos Meza Benavides

Received: 3 May 2023
Revised: 22 May 2023
Accepted: 24 May 2023
Published: 26 May 2023

1. Introduction

Over the past 5 years, there has been significant growth in the adoption of electric vehicles (EVs). However, integrating EVs into electrical distribution systems involves a thorough examination of their impact on the electrical network. The connection of EVs to the power grid may cause an elevation in voltage and current harmonic distortion, as well as a decrease in the lifespan of distribution transformers due to elevated temperatures [1]. In addition, harmonic distortion can also arise from the inverters of grid-connected photovoltaic (PV) systems, with some harmonics reaching high levels [2]. The integration of EVs with a high penetration of PV systems can create challenges for electrical distribution grids. Additionally, a large quantity of electric vehicles may result in power quality issues, such as service interruptions, fluctuations in voltage and current, and harmonic distortion [3]. Hence, it is crucial to carefully plan the integration of electric vehicles into PV-dependent systems to prevent any undesirable disruptions to the distribution system.

Several studies have investigated the influence of EVs on electrical distribution systems, analyzing both EV penetration and PV systems [3–7]. However, there are only a few case studies that investigate the integration of these technologies in electrical grids with a high concentration of PV systems. It has been demonstrated that the presence of EVs in the electrical grid has an impact on total harmonic distortion (THD). In [8], the effect of level two fast chargers on the grid was investigated. As the penetration of EVs on a

feeder rises, the degree of harmonic distortion also rises, as observed. Furthermore, the study investigated the impact of the electric vehicle supply equipment (EVSE)'s location on the feeder. The outcomes indicated that the highest THD value was at the end of the feeder, and the voltage at the user's terminals decreased when the EVSE was located further from the feeder's origin. These findings have significant implications for the deployment of EV charging infrastructure in the power grid, as careful EVSE placement can mitigate the negative effects of EVs on harmonic distortion. Moreover, these findings emphasize the necessity for additional research on the influence of EVs on the electrical grid and the development of strategies to guarantee the dependable and effective integration of electric vehicles into the grid.

It has also been observed that the individual harmonic distortion caused by EVs limits the capacity of the electrical grid. In a study conducted by the authors in [9], a sensitivity analysis of models with uncertainty in medium voltage networks was assessed. The results showed that individual harmonics cause a decrease in the hosting capacity due to the probability of exceeding technical limits by approximately 67%. These findings underscore the need for careful consideration of the impact of EVs on the electrical grid and the potential limitations that may arise. It is essential to ensure the reliability and efficiency of the electrical grid as EV adoption continues to increase. Further research on the impact of EVs on the electrical grid's hosting capacity and the development of strategies to mitigate the negative effects of harmonic distortion will be crucial in facilitating the integration of EVs into the electrical grid.

This study focuses on investigating the harmonic effects of EV charging stations in an electrical distribution grid with high PV penetration, considering both peak and valley demand. To determine the actual harmonic values, the power quality of fast-charging stations employing direct current (DC) and slow-charging stations using alternating current (AC) for KIA- and BYD-brand vehicles was measured. Subsequently, the system was simulated utilizing OpenDSS, and validation was carried out using the IEEE European low-voltage test feeder case.

The current study is an extension of the article titled "Harmonic Impact of Electric Vehicles in Electrical Distribution Systems with High Photovoltaic Penetration", presented at the V Ibero-American Congress of Smart Cities.

This article's key contributions include (a) a comprehensive analysis and assessment of the impact and distinct levels of harmonics on the behavior of distribution systems with high PV penetration and EV loads, proposing that a high penetration of photovoltaic generators and EVs has a direct relationship with amplified harmonics and (b) indicating that THD effects on voltage values at loads are significant and must be considered.

2. Methodology

The electrical parameters for this study were acquired by measuring two EV brands and charging stations under real charging conditions. Furthermore, the charging stations and electric vehicles were modeled as both storage components and sources of harmonic generation. The specific modeling of EVs as storage components was deemed necessary due to the standard model available in OpenDSS, which permits the configuration of various efficiency parameters, including state of charge or discharge and power control. However, as there is no specific model designed for EVs, MATLAB must be employed to control their operations. In contrast, the standard OpenDSS model was deemed sufficient for modeling PV systems, enabling the incorporation of a wide range of parameters, including irradiance, efficiency, and temperature effects. Lastly, a standard electrical IEEE standard case study was utilized to conduct the simulations.

2.1. Charging Stations and Electric Vehicles

Tests were carried out at the University of Cuenca's laboratory [10], using a Fluke 435 II power quality analyzer, to gather real data on current harmonics. The measurements were conducted on a BYD T3 and Kia Soul EVs, as well as on a 7.2 kW AeroVironment

RS 25 AC electric vehicle supply equipment (EVSE) (sourced from California, USA) and a 50 kW Circontrol Raption 50 model (sourced from Barcelona, Spain) fast DC EVSE (refer to Figure 1).

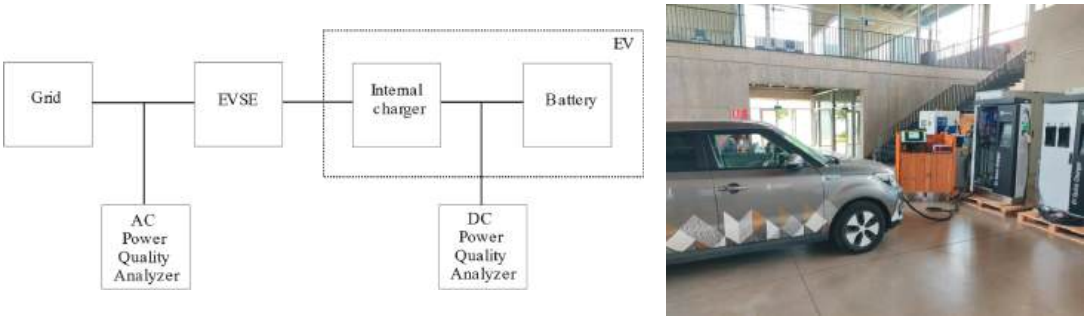

(**a**) (**b**)

Figure 1. Measurement equipment: (**a**) connection diagram; (**b**) EV and EVSE.

The laboratory measurements of voltage harmonics, encompassing both magnitude and angle, yielded the results that are shown in Table 1. Additionally, the values obtained from prior studies available in the literature involving other models of EVs have also been included. Table 1 shows the results of the laboratory measurements up to the eleventh harmonic for the parameters (param) in magnitude and phase angle of voltage. It presents the harmonics generated by an electric vehicle charger (EV charger), a Nissan Leaf vehicle, a BYD-brand vehicle with an alternating current charging station (BYD AC) and direct current (BYD DC), as well as a Kia-brand vehicle, likewise with an alternating current charging station (Kia AC) and a direct current one (Kia DC).

Table 1. Harmonics magnitude and angles obtained from measurements and other studies.

No.	Param	EV Charger [6]	Nissan Leaf [5]	BYD AC	Kia AC	BYD DC	Kia DC
1	Mag.	100	100	100	100	100	100
	Angle	−55	−26	136	143	8.6	28.6
3	Mag.	9.20	25.00	9.91	6.31	2.40	6.22
	Angle	120.00	−94.00	98.00	102.00	6.50	32.00
5	Mag.	62.20	17.00	8.47	1.15	1.73	14.55
	Angle	255.00	−96.00	120.00	131.00	7.20	36.00
7	Mag.	41.80	14.20	8.11	0.83	2.14	5.61
	Angle	−28.00	−72.00	146.00	153.00	6.80	31.00
9	Mag.	1.48	9.69	7.30	0.49	1.13	4.34
	Angle	−3.00	−68.00	152.00	161.00	5.70	34.00
11	Mag.	7.08	5.04	6.92	0.64	2.45	5.06
	Angle	−2.00	−49.00	168.00	182.00	5.60	35.00
Charge Efficiency		-	-	92.90%	89.80%	94.60%	91.70%

Additionally, measurements were carried out to evaluate the efficiency of both the charging station and the internal converter of the vehicle. The performance of an EVSE was assessed using instrumentation to ensure accurate measurements. An AC power quality analyzer Fluke 435 II was utilized at the input of the station to monitor critical electrical parameters, such as the current, voltage, and harmonics in both magnitude and angle.

Furthermore, a Hioki PW3337 DC (sourced from Nagano, Japan) power quality analyzer was connected to the internal charger circuit and the EV battery to obtain the charging efficiency. The charging processes of EVs were tested from a state of charge (SOC) of 10% to 95% to ensure a comprehensive analysis of charging performance. The experiment was conducted in the University of Cuenca's laboratory. The efficiency of EVSEs was examined in both AC and DC charging modes, with the highest efficiency observed during DC charging at 94.6%, while the lowest efficiency was recorded during AC charging at 89.8%.

2.2. Simulation Characteristics

OpenDSS was utilized for simulation purposes, wherein EVs were represented as storage elements and were dispersed across different phases of the system, while also acting as a source of harmonics. The simulation process involved the use of two distinct models, one for the EV and another for the PV. The EV was accurately modeled as a battery with a charge controller, customizable efficiency settings, and a current source to generate harmonic waves. The model employed consists of a battery storage element connected to each load bus of the system. It utilizes a two-phase model, with each phase operating at 230 VAC and a power factor of 1. The specific spectrum and load curve for the model can be found in the study's repository, specifically in the Input_data/circuit/autos folder. Similarly, the PV system was designed to operate with a DC-to-AC converter, which served as the control signal for a harmonic current source. Standard values were employed for efficiency, temperature, and irradiation to ensure consistency throughout the simulation process (see Figure 2). The PV system in OpenDSS is defined as a PVSystem element, connected to the system buses according to each scenario. It is configured as a single-phase system operating at 230 VAC and an operating temperature of 25 °C. Additionally, the irradiation, efficiency, harmonic spectrum, and power–temperature adjustment curve are defined in the repository files, specifically in the Input_data/circuit/fotovoltaico folder.

(**a**) (**b**)

Figure 2. Simulation models. (**a**) Electric Vehicle. (**b**) PV generator.

The models employed for the EV and PV generator incorporate series and parallel impedances, specifically series RL and parallel RL. To accurately align with the power profile, OpenDSS computes the values of conductance (G), susceptance (jB), and impedance (R+jX) for both the vehicle's power consumption and the generator's power generation requirements according to its power delivery requirements. Regarding the harmonic spectrum, the harmonic values obtained from Table 1 are applied to EVs, whereas default values from OpenDSS are utilized for PV generators. Furthermore, the efficiencies (% efficiency) indicated in Table 1 are incorporated into the EV model, and ideal idling losses are assumed.

This approach enables the accurate modeling and analysis of harmonics impact of EVs and PV systems. A critical consideration during the simulation process was the connection time of EVs, which could significantly impact the results of the analysis. To precisely reflect the behavior of EV connections, a multimodal probability distribution function (PDF) was employed. Such a PDF accounts for multiple modes or peaks that demonstrate the connection of electric vehicles at various times of the day. For residential EVSEs, it is worth noting that, while the connection can be established at any point during the day, the maximum modes transpire at 08:00 and 18:00. These timeframes coincide with when users typically return home with their EVs and proceed to connect them for charging

purposes [11]. The function used was designed with modes at 02:00, 08:00, and 19:00, and standard deviations of 2 h, to generate a realistic representation of EV connection behaviors (see Figure 3). In the simulation, EVs maintain a charging regimen lasting between 6 and 8 h, reaching a SOC ranging from 80% to 100%. This encompasses up to 55 distinct charging behaviors, depending on the specific scenario being analyzed. The OpenDSS file utilized to describe the charging duration, as well as the connection and disconnection times, can be downloaded from the repository associated with this study. It is located within the Input_data/circuit/autos folder.

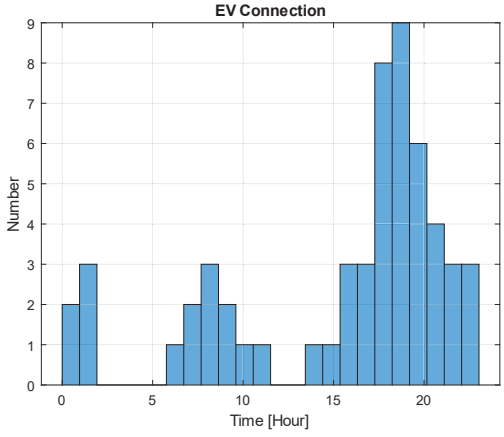

Figure 3. Electric vehicle connection probability distribution function used in simulation.

To automate the simulation process in OpenDSS, MATLAB was employed as a tool for controlling the timing of both customer load profiles and EV connections. The integration of MATLAB with OpenDSS allowed for a streamlined and efficient simulation process, which ultimately facilitated the accurate analysis of the performance of EVSEs.

2.3. Application Scenarios

To evaluate the impact of harmonics, a simulation was conducted utilizing the IEEE European low-voltage test feeder model. Three scenarios were analyzed based on the PV generation location: (1) 14 distributed PV systems with a capacity of 5 kW each and 14 EVSEs with a capacity of 7.2 kW each; (2) a central PV system with a capacity of 70 kW and 14 EVSEs with a capacity of 7.2 kW each, as illustrated in Figure 4; and (3) PV and EV distributed across all loads. The harmonic spectrum from Table 1 was assigned randomly to each scenario, while for the PV generators, the harmonic spectrum from [12] was employed. A clear sky irradiance profile was applied to the PV systems. The study examined the following scenarios:

- The initial test case solely examines residential loads within the system, devoid of EVs or PVs (Case 1).
- EVs connected without PV generation and without harmonic effects (Case 2).
- EVs connected with distributed PV generation and without harmonic effects (Case 3).
- EVs connected with single PV generation and without harmonic effects (Case 4).
- EVs and PV generation distributed across the loads without harmonic effects (Case 5).
- EVs connected without distributed PV generation and with harmonic effects (Case 6).
- EVs connected with distributed PV generation and with harmonic effects (Case 7).
- EVs connected with single PV generation and with harmonic effects (Case 8).
- EVs and PV generation distributed across the loads with harmonic effects (Case 9).

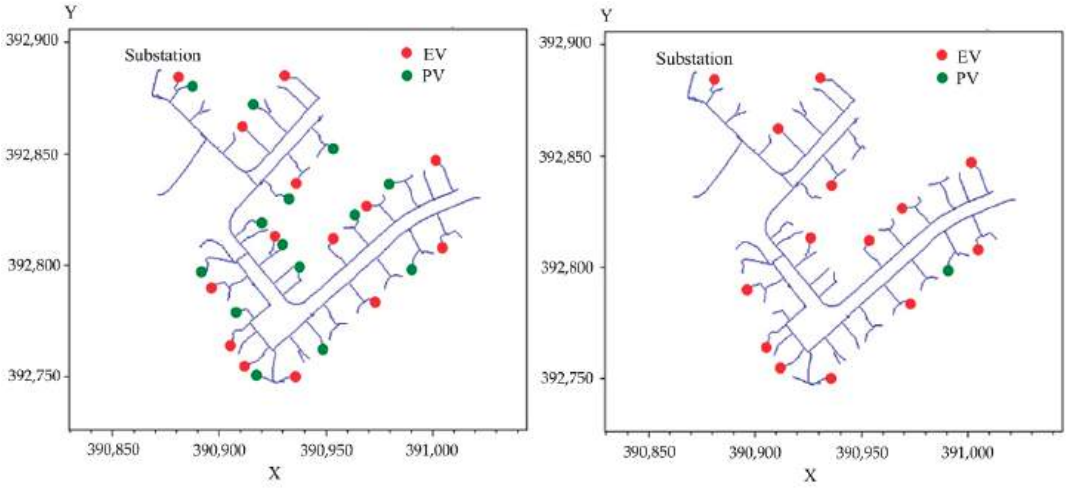

Figure 4. Test cases analyzed: (**a**) distributed EV and distributed PV systems; (**b**) distributed EV and single PV system.

The analysis focused on observing the impact on the substation response, the maximum total harmonic distortion (THD), and the voltage and current at the client terminals.

3. Results

During the simulation, the power rating of the transformer in the substation, as well as the highest and lowest voltages recorded across the loads, were taken into account. Moreover, the maximum THD in the loads was also considered.

3.1. Power of the Substation Transformer

Initially, the power of the substation transformer was analyzed for the scenarios outlined in Section 2.3. Figure 5 illustrates that the power of the substation transformer fluctuates as EVs are introduced into the network and the impact of harmonics caused by the EVs is taken into consideration. Case 2 without harmonics exhibits the lowest power value, whereas the highest power value among all scenarios is observed when harmonics are introduced into the network. The high current resulting from harmonics saturates the system's conductors, which diminishes the effect of power injection by the PV generation. Additionally, the situation deteriorates when there is only one PV generation in the distribution system. Likewise, an analysis of the network's performance in Cases 5 and 9, which include distributed PV and EV systems, reveals a distinct impact of harmonic distortions. Specifically, the presence of harmonics causes a reduction in the current output of the PV systems.

The power with harmonics is internally calculated by OpenDSS through multiple simultaneous simulations. First, the power of the fundamental component is computed, followed by repeated simulations for each of the harmonic components configured in the spectrum file. Consequently, OpenDSS provides separate power results for each harmonic, and in MATLAB, the contribution of each harmonic is summed. Equation (1) illustrates the outcome of this calculation.

$$P = \sum_{n=1}^{m} \frac{V_n I_n}{2} \cos(\theta_n - \varphi_n) \quad (1)$$

where:

P is the active power;

n is the harmonic;
V_n is the voltage of nth harmonic;
I_n is the current of nth harmonic;
θ_n is the voltage angle of nth harmonic;
φ_n is the current angle of nth harmonic.

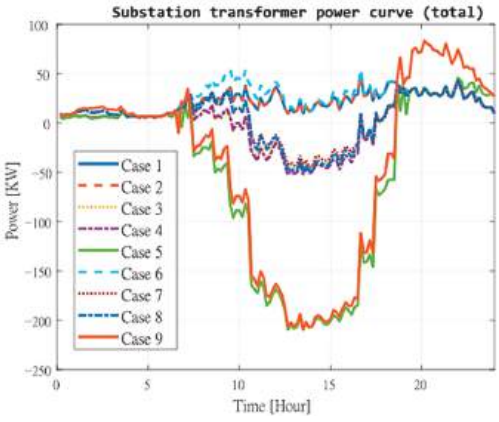

Figure 5. Substation transformer power curve for each case.

3.2. Load Voltages

This study examined the behavior of maximum and minimum voltages across the loads (customers) in the network to ensure that they meet the limit values prescribed by the ANSI C84.1-2006 standard for each simulation scenario. A base RMS voltage of 240 VAC was assumed for the network, and the standard limits of 0.9 pu and 1.05 pu were used, which correspond to 216 VAC and 252 VAC, respectively. The simulations showed that Cases 5 and 9 had lower RMS voltage values than case 8, which had the highest voltage at the customer terminal connected to the PV generator. It was observed that high voltage values coincided across different simulation cases (see Figure 6). Notably, minimum voltage values were found to be within the standard limits across all simulation scenarios.

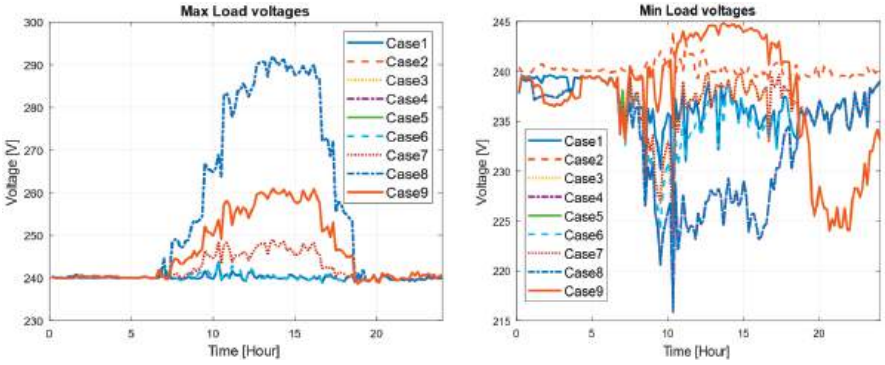

Figure 6. Voltages at customer bars. (**a**) Maximum values on all customers by selected case. (**b**) Minimum values on all customers by selected case.

Table 2 displays the highest and lowest power values of the substation transformer, along with the voltage and current at the customer's terminals. It is evident that in Case 2 with harmonics, the transformer requires the most power, both in terms of maximum and

minimum power during the 24 h period. With regard to voltage, scenarios with harmonics do not seem to have a significant impact. However, the current remains at a high level during the minimum of Case 2 with harmonics.

Table 2. Power, current, and voltage obtained from the analyzed scenarios.

Case		Transformer Power (kW)	Load Voltage (V)
(1) Base	Max	48.95	243.67
	Min	4.81	225.50
(2) Only EVs	Max	48.95	243.99
	Min	4.81	238.89
(3) EV and distributed PV	Max	43.29	249.01
	Min	−47.06	223.07
(4) EV and single PV	Max	43.29	291.93
	Min	−52.75	215.76
(5) Distributed EV and distributed PV	Max	45.76	260.91
	Min	−209.20	224.01
(6) Case 2 plus harmonics	Max	54.48	244.02
	Min	5.79	221.02
(7) Case 3 plus harmonics	Max	43.29	249.02
	Min	−44.94	223.23
(8) Case 4 plus harmonics	Max	43.29	291.97
	Min	−50.28	215.95
(9) Case 5 plus harmonics	Max	83.81	260.94
	Min	−209.20	224.04

3.3. Load Harmonics

Through a comprehensive analysis of the system's response to specific injected harmonics throughout a 24 h duration in each case, notable observations were made. The findings revealed that the third harmonic held a dominant presence, aligning with the measurements conducted in controlled laboratory settings. The obtained results exhibit distinct harmonic profiles for Case 6 and Case 7, showcasing interesting trends in the magnitudes of various harmonics. In Case 6, the analysis unveiled a maximum value of 2.5% for the third harmonic, indicating its prominent influence on the system. On the other hand, the seventh harmonic exhibited the lowest magnitude, with a minimum value of 0.3%. Case 7 demonstrated a similar pattern, with the third harmonic maintaining its position as the most significant harmonic in terms of magnitude, while the seventh harmonic retained its status as the least influential. Moreover, it is worth noting that the minimum values of the fifth harmonic displayed a noticeable increase of approximately 30% compared to the other harmonics. This observation suggests a distinct behavior and potential sources of harmonics within the system, warranting further investigation into the underlying causes and implications of this phenomenon.

These findings shed light on the harmonic characteristics of the system under investigation, highlighting the prevalence of the third harmonic and the varying magnitudes across different harmonics. This analysis provides valuable insights into the harmonic composition and distribution within the network, aiding in the identification of potential sources and facilitating the development of appropriate mitigation strategies.

The behavior in Case 8 was comparable; however, the minimums of the third, fifth, and seventh harmonics (H3, H5, and H7) increased by up to 60% in comparison to previous cases. Finally, Case 9 demonstrated the most significant harmonic behavior, with the

dominance continuing in the third harmonic and its peaks reaching a magnitude of 4.5%. Moreover, the increase in the minimum values was substantial, reaching up to 300% compared to other cases (refer to Figure 7a). The analysis of the maximum THD behavior in loads, as depicted in Figure 7b, revealed that Cases 6 and 7 exhibited higher harmonic levels compared to other cases. Conversely, during the connections of EVs, Case 9 displayed a lower THD value.

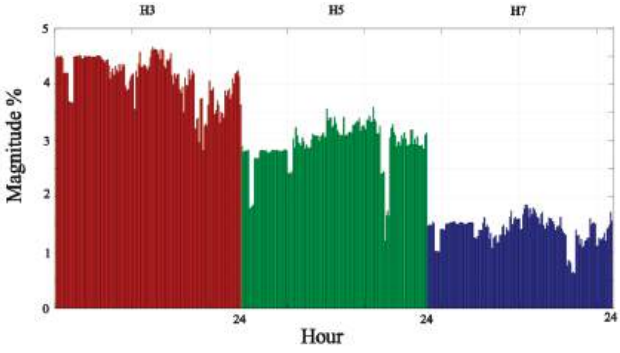

(**a**)

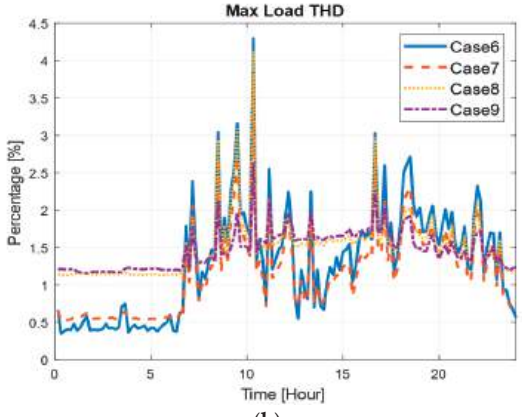

(**b**)

Figure 7. Harmonic behavior. (**a**) Case 9; (**b**) THD.

3.4. Hosting Capacity Limited by Harmonics

One crucial parameter in an electric distribution network with distributed generators and loads such as electric vehicles is the determination of hosting capacity. Traditionally, the analysis of this parameter relies on the limits of power supply quality and the thermal limits of network components. However, there is a limited number of studies addressing hosting capacity specifically considering harmonics.

Within the scope of this study, a hosting capacity analysis was undertaken to assess the influence of harmonic values recorded at customers' premises on the power distribution network. The analysis focused on a specific scenario, namely, Case 9, which encompasses a diverse distribution of both PV system EVs across the network's loads. By examining this particular case, this study aimed to examine the potential repercussions of harmonics on the network's overall performance and functionality. A base case was established with 55 EVs, each with a nominal power rating of 7.2 kW and an average energy consumption of 50.4 kWh, and 55 PV systems, each with a nominal power rating of 5 kW. Through MATLAB simulations, the number of EVs in the system was increased in multiples of their nominal power ratings while ensuring that the maximum THD and individual harmonic distortions

remained in compliance with the IEEE 519-2022 standard (see Table 3). The results indicate that while the system can accommodate the connection of up to 104 EVs, the limitation on the third harmonic restricts the number of vehicles that can be connected to 65. The analysis also considered the probability function of connecting vehicles at different times.

Table 3. Maximum Load Total Harmonic Distortion.

EVs Connected	Max THD (%)	Max Harmonic (%)				
		3th	5th	7th	9th	11th
55	2.64	1.61	1.66	0.71	1.18	0.71
65	5.44	4.73	3.51	1.93	1.48	0.77
104	8.08	7.05	4.95	3.33	1.65	0.82

4. Conclusions and Future Work

This study aimed to investigate the impact of harmonics produced by EV charging stations on an electric distribution network with a high level of photovoltaic generation. Two distinct scenarios were examined, one with distributed photovoltaic power generation and the other with centralized generation. The results indicate that the scenario with single photovoltaic generation and EVs distributed throughout the system had the poorest performance. Overvoltages were observed at the terminals of nearby users, while undervoltages were observed at nodes further away from the system. When the harmonic analysis was added, it was found that undervoltages improved in this case. However, overvoltages were still observed at the terminals, and it was also observed that THD was higher at all nodes in the system. These findings highlight the importance of considering multiple factors when evaluating the performance of an electrical system with distributed electric vehicles and photovoltaic generation. The analysis of both voltage and harmonic distortion is crucial in identifying potential issues and developing strategies to address them. Further research is necessary to investigate the interaction between electric vehicles, photovoltaic generation, and other components of the electrical grid, such as energy storage systems, and to develop more comprehensive approaches for evaluating the performance of these systems. This research reveals that harmonics resulted in considerable variations in the voltage, current, and power of the substation transformer, with the magnitude of the third harmonic exceeding 300% compared to other cases. This study also collected information on the magnitude and angle values of harmonics for EVs and charging stations by directly measuring them at the battery terminals, enabling a comprehensive analysis of the entire energy conversion system of both the station and the EV. Upon reviewing the hosting capacity of Case 9, considering harmonics, it was observed that the high values obtained from the third harmonic decrease the total number of electric vehicles that the network can accommodate by 37.5% in comparison with a grid without PV and harmonics. Expanding the harmonic analysis with a greater number of electric vehicle brands is required, and it is also important to examine the effect of charging station efficiency. Additionally, it is necessary to conduct an analysis involving a wider variety of load types to verify their interaction with EVs, such as heat pumps, motors, and thermal generators, among others.

Author Contributions: Conceptualization and methodology, M.D.-S. and L.G.G.; investigation, M.D.-S. and L.H.-C.; writing—review, and editing, M.D.-S., Ó.D.-P., V.A.-G. and Á.L.Z.-L.; supervision and project administration, Á.L.Z.-L., V.A.-G. and J.L.E. All authors have read and agreed to the published version of the manuscript.

Funding: This research received no external funding.

Data Availability Statement: The data and simulation files used in this study are available at https://github.com/davilamds/harmonicsEVPV_2 (accessed on 15 May 2023).

Acknowledgments: The authors thank Universidad de Cuenca and Universidad de Valladolid, who, through a cooperation framework agreement and the specific agreement to regulate their collaboration in research in the field of electrical microgrids and renewable energies, made this work possible. The authors thank Universidad de Cuenca for easing access to the facilities of the Microgrid Laboratory of the Centro Científico Tecnológico y de Investigación Balzay (CCTI-B), for allowing the use of its equipment, and for authorizing its staff the provision of technical support necessary to carry out the experiments described in this article.

Conflicts of Interest: The authors declare no conflict of interest.

References

1. Alame, D.; Azzouz, M.; Kar, N. Assessing and mitigating impacts of electric vehicle harmonic currents on distribution systems. *Energies* **2020**, *13*, 3257. [CrossRef]
2. Phannil, N.; Jettanasen, C.; Ngaopitakkul, A. Power quality analysis of grid connected solar power inverter. In Proceedings of the 2017 IEEE 3rd International Future Energy Electronics Conference and ECCE Asia (IFEEC 2017—ECCE Asia), Kaohsiung, Taiwan, 3–7 June 2017; pp. 1508–1513. [CrossRef]
3. Wang, X.; He, H.; Sun, F.; Sun, X.; Tang, H. Comparative Study on Different Energy Management Strategies for Plug-In Hybrid Electric Vehicles. *Energies* **2013**, *6*, 5656–5675. [CrossRef]
4. Gusai, A. Harmonic Analysis in PV Connected Power System. *Int. J. Eng. Res.* **2020**, *V9*, 474–477. [CrossRef]
5. Aljanad, A.; Mohamed, A. Harmonic Impact of Plug-In Hybrid Electric Vehicle on Electric Distribution System. *Model. Simul. Eng.* **2016**, *2016*, 5968943. [CrossRef]
6. Masoum, M.A.S.; Moses, P.S.; Deilami, S. Load management in smart grids considering harmonic distortion and transformer derating. In Proceedings of the 2010 Innovative Smart Grid Technologies (ISGT), Gaithersburg, MD, USA, 19–21 January 2010; pp. 1–7. [CrossRef]
7. Staats, P.T.; Grady, W.M.; Arapostathis, A.; Thallam, R.S. A statistical method for predicting the net harmonic currents generated by a concentration of electric vehicle battery chargers. *IEEE Trans. Power Deliv.* **1997**, *12*, 1258–1264. [CrossRef]
8. Zarbil, M.S.; Vahedi, A. Power Quality of Electric Vehicle Charging Stations and Optimal Placement in the Distribution Network. *J. Oper. Autom. Power Eng.* **2023**, *11*, 193–202. [CrossRef]
9. Nakhodchi, N.; Bollen, M.H.J. Impact of modelling of MV network and remote loads on estimated harmonic hosting capacity for an EV fast charging station. *Int. J. Electr. Power Energy Syst.* **2023**, *147*, 108847. [CrossRef]
10. Espinoza, J.L.; Gonzalez, L.G.; Sempertegui, R. Micro grid laboratory as a tool for research on non-conventional energy sources in Ecuador. In Proceedings of the 2017 IEEE International Autumn Meeting on Power, Electronics and Computing (ROPEC), Ixtapa, Mexico, 8–10 November 2017; Volume 2018, pp. 1–7. [CrossRef]
11. Richardson, P.; Moran, M.; Taylor, J.; Maitra, A.; Keane, A. Impact of electric vehicle charging on residential distribution networks: An Irish demonstration initiative. In Proceedings of the 22nd International Conference and Exhibition on Electricity Distribution (CIRED 2013), Stockholm, Sweden, 10–13 June 2013; pp. 10–13. [CrossRef]
12. Pereira, J.L.M.; Leal, A.F.R.; de Almeida, G.O.; Tostes, M.E.d.L. Harmonic Effects Due to the High Penetration of Photovoltaic Generation into a Distribution System. *Energies* **2021**, *14*, 4021. [CrossRef]

energies

MDPI

Article

Balancing Electricity Supply and Demand in a Carbon-Neutral Northern Europe

Lisa Göransson

Department of Space, Earth and Environment, Chalmers University of Technology, 412 96 Göteborg, Sweden; lisa.goransson@chalmers.se

Abstract: This work investigates how to balance the electricity supply and demand in a carbon-neutral northern Europe. Applying a cost-minimizing electricity system model including options to invest in eleven different flexibility measures, and cost-efficient combinations of strategies to manage variations were identified. The results of the model were post-processed using a novel method to map the net load before and after flexibility measures were applied to reveal the contribution of each flexibility measure. The net load was mapped in the space spanned by the amplitude, duration and number of occurrences. The mapping shows that, depending on cost structure, flexibility measures contribute to reduce the net load in three different ways; (1) by reducing variations with a long duration but low amplitude, (2) by reducing variations with a high amplitude but short duration and low occurrence or (3) by reducing variations with a high amplitude, short duration and high occurrence. It was found that cost-efficient variation management was achieved by combining wind and solar power and by combining strategies (1–3) to manage the variations. The cost-efficient combination of strategies depends on electricity system context where electricity trade, flexible hydrogen and heat production (1) manage the majority of the variations in regions with good conditions for wind power while stationary batteries (3) were the main contributors in regions with good conditions for solar power.

Keywords: flexibility measures; variation management; VRE; electricity system modeling; wind power integration; solar power integration; sector coupling

Citation: Göransson, L. Balancing Electricity Supply and Demand in a Carbon-Neutral Northern Europe. *Energies* **2023**, *16*, 3548. https://doi.org/10.3390/en16083548

Academic Editors: Luis Hernández-Callejo, Jesús Armando Aguilar Jiménez and Carlos Meza Benavides

Received: 13 March 2023
Revised: 16 April 2023
Accepted: 18 April 2023
Published: 19 April 2023

1. Introduction

The aim of this work is to visualize how variations in a future northern European electricity system can be cost-efficiently managed. The work first examines climate neutral energy systems with extensive electrification of the industry, transport and heating sectors. Outlooks for Nordic [1], northern European [2,3] and European [4] electricity systems have been presented in recent years. The common features of these outlooks are a substantial increase in electricity demand which, to a large extent, is supplied by wind and solar power. Given the varying generation of wind and solar power, the ability of the electricity system to manage these variations have become a question of high priority [5].

There exists a wide range of technologies and strategies to provide flexibility, ranging from shifting the electricity demand for heat pumps in time in single-family dwellings by exploiting the thermal inertia of buildings, to using large-scale underground storage of hydrogen produced for industrial applications. Lund and Lindgren [6] have compiled a comprehensive overview of the different approaches for increasing energy system flexibility. Flexibility measures serve two main purposes: to assure the reliability or increase the cost efficiency of a given electricity system. This work concerns the latter subset, i.e., flexibility measures with the purpose to manage variability such that the social cost of electricity is reduced. This subset is referred to as variation management strategies (VMSs) [7,8]. The potential of flexibility measures to reduce the social cost of meeting the demand for electricity is well documented. Previous work investigating the impact of flexibility measures on the operation of a given electricity system reported reduced costs because

of reduced curtailment [7,9] and because of reduced operation of peak generation units in favor of varying renewable electricity (VRE) and base load generation [10]. Studies on the impact of flexibility measures on the cost-optimal system composition reported reduced costs as investments in varying renewable electricity generation capacity replace investments in more expensive electricity generation options [8,11]. Johansson et al. [8] investigated the impact of a range of variation management strategies on the cost-optimal system composition of electricity systems with different preconditions for VRE. It was found that different strategies influenced the operation of the electricity system and investment in electricity generation capacity in different ways. In addition, it was found that the cost-optimal investments in variation management strategies depends on the preconditions for VRE generation. These findings indicate that there are different types of variability which need to be matched with the most cost-efficient strategies for each type. It is reasonable to assume that all types of variations are present in all electricity systems, albeit to different degrees, and what we look for is a balanced combination of strategies adequate for the given electricity system.

Few outlooks for the northern European electricity system address in detail how variations in the electricity system can be met cost efficiently. Pursiheimo and Kiviluoma [3] analyzed electrification scenarios for northern Europe with a focus on Finland. They applied the model of Backbone [12], an investment model with a high time resolution and consequentially with the ability to balance options to cost-efficiently manage variations. Variation management was addressed by illustrating the dispatch of one winter week and one summer week for the Finnish electricity system. The illustrations of the dispatch of electricity systems provided a detailed understanding of how the demand for electricity was met every hour, including how variations were managed when plotted for a limited time span such as a couple of weeks. However, to give an overview of how variations are managed more generally across one or several years, other options for visualization are needed. Several efforts have been made to measure and graphically represent flexibility provision in the electricity system. IEA [13] proposed a flexibility assessment tool (FAST) to estimate if there is sufficient flexibility in a given electricity system to accommodate additional wind and solar power, accounting for flexibility on the demand and supply side as well as the storage and interconnection capacity. Yasuda and Carlini [14] introduced flexibility charts which map the capacity for flexible generation and interconnections relative to the peak capacity of a given electricity system. The tools by IEA and Yasuda et al. rely on statistics which are easy to access to give a first idea of the ability of a given electricity system to manage variations. Using time series from actual or modelled electricity system operations, the contribution of each flexibility supplier can be assessed in more detail. Heggarty and Bourmaud [15] introduce two graphical tools, the flexibility solution modulation stacks and the flexibility solution contribution distribution, to visualize the contribution of flexibility suppliers on annual, weekly and daily timescales.

This paper adds to the previous outlooks for future northern European electricity systems by focusing on how variations in the electricity system are managed using a novel approach of visualizing the net load variability and the contribution of different strategies to reduce this net load. A cost-efficient combination of strategies to manage the net load was derived using a cost-minimizing electricity system model with high temporal resolution representing 11 strategies to manage variations on the demand side and the generation side, as well as pure storage technologies. The contribution of each strategy was visualized using a novel graphical representation in the space spanned by the amplitude, duration and the number of occurrences of the net load variations. Based on the results, the functionality of different strategies to manage variations can be generalized and connected to a functionality-based framework for strategies to manage variations which facilitate the choice of a strategy for a given electricity system context.

2. Method

To find cost-efficient strategies to meet the demand for electricity, heat and hydrogen in a carbon-neutral northern Europe, the cost-minimizing electricity system model ENODE was applied. Given a time-resolved demand for electricity, heat and hydrogen, together with costs and technical limitations of generation and storage technologies, ENODE generates investments in and operations of technologies for generating and storing electricity, heat and hydrogen. From these results, net loads (i.e., electricity demand which cannot be moved in time, reduced by wind and solar power generation) for each region with and without accounting for strategies to manage variations were produced to visualize the role of each strategy in a carbon-neutral northern Europe.

2.1. Electricity System Investment Model

In this work, cost-efficient deployment of variation management strategies was identified using the cost-minimizing electricity system investment model ENODE. The objective of the ENODE model is to minimize the cost of investments and operation while meeting a given demand for electricity, heat and electricity-based hydrogen. The ENODE model was first presented in [16] and further developed in [8,17] to include more options to manage variations and to better represent the heat sector. The model has a high temporal resolution and a detailed technology description, while the temporal scope is limited to 1–2 years. As such, the model results provide a good understanding of the interplay between electricity generation technologies and variation management strategies on the timescale of hours to seasons. In this work, the model was run with a 3 h time resolution for two years (with investment costs represented as annualized costs) representing the year 2050 in terms of technology costs and carbon emission limitation, i.e., only technologies without net carbon dioxide emissions were included as investment options. Existing hydropower was assumed to remain in place together with the new nuclear power in Finland and the nuclear power under construction in the UK.

In this work, the ENODE model was applied to northern Europe subdivided into 14 regions as given by the map in Appendix A Figure A1. The demand for electricity, heat and hydrogen must be met in each region at every timestep. Electricity could be traded between regions. The existing transmission grid was assumed to remain in place and additional investments in transmission capacity of up to 5 GW per connection was allowed.

On the supply side, nine technology options were included including thermal base load generation such as nuclear power, biomass-based combined heat and power and bio-blended coal with carbon capture and storage as well as thermal peak generation in terms of biogas open-cycle and combined-cycle gas turbines. A total list of the technologies together with their cost properties are given in Appendix B. On- and offshore wind power and solar PV were represented using time-resolved wind and solar power production potential for the investigated regions. The power production potential was derived using [18] which relies on ECMWF ERA5 [19] and the Global Wind Atlas [20] for the historical years 1991–1992. These two years were chosen since they represent one year with a lower hydropower inflow in the Nordic countries (1991) and one year with a higher hydropower inflow in the Nordic countries (1992). The potential for wind and solar PV investments per region together with their respective full load hours are given in Appendix B. The electricity demand corresponding to temperature variations in the historical years 1991–1992 was also derived using [18].

This work investigated a future northern European electricity system assuming a carbon-neutral energy system which was targeted to be attained by the European Union by around 2050 [4]. By 2050, it is expected that we will have already experienced a significant increase in temperature due to global warming [9]. Thus, in this work, we assumed an increase in global mean temperature of 2 degrees. In northern Europe, a warmer climate is expected to mainly impact the energy system through altered hydropower inflow, reduced demand for heating and increased number of incidents induced by extreme weather [21]. In this work, we accounted for the two former factors based on [22] which showed an

increased annual average hydropower production distributed more evenly across the year in the Nordic countries together with reduced demand for district heating and electricity for heating purposes in the wintertime.

In this work, an electrification of the transport sector and the industry sector was assumed together with a shift from natural gas for heating purposes to individual heat pumps in Germany, the Netherlands, Poland and the UK. The electricity demand for the heating of single-family dwellings was calculated according to Nyholm [23], accounting for energy efficiency improvements. In addition, there was a heat demand corresponding to the demand for district heating in the investigated regions [24]. The heat demand could be met by heat-only boilers, but also combined heat and power plants (CHP), heat pumps and electric boilers. The inclusion of thermal energy storage enabled a temporal decoupling between heat production and electricity production/consumption and facilitated an adapted heat production which offered flexibility to the electricity system.

The electrification of industry includes electrification of steel, cement and ammonia. The total production of steel, cement and ammonia in the investigated regions was assumed to remain at today's levels. In cement production, we assumed plasma burners were used for high temperature heating with a continuous demand for electricity over time. There was an exogenous demand for electricity-based hydrogen (i.e., hydrogen produced from electricity) corresponding to the electricity demand from the steel industry and the ammonia industry. The hydrogen demand was a simplified representation of an electrification of industry and was distributed evenly across all hours of the year, assuming a continuous operation of industrial processes. By overinvesting in the electrolyzer capacity and hydrogen storage, an adapted hydrogen production, which offers flexibility to the electricity system, can be achieved.

A full electrification of the road transport was assumed. The majority of vehicles were assumed to charge as they are parked. However, 30% of the cars charged flexibly over time and could also discharge back to the grid. Vehicle charging was implemented as described by Taljegard [25]. It should be noted that flexible cars were also constrained to meet the demand for transportation as defined by the vehicle movement data collected by Kullingsjö and Karlsson [26].

Furthermore, the model included the option to invest in stationary batteries to manage variations as well as fuel cells to regenerate electricity stored as hydrogen. Thus, the strategies to manage the variations included in this work encompassed supply side, demand-side, and pure storage options. Table 1 list the strategies to manage variations included in this work together with the technologies they involve.

Table 1. Strategies to manage variations included in this work together with the technologies involved and their key properties. CCGT = Combined Cycle Gas turbine, CHP = Combined Heat and Power Plant.

Strategy	Technology	Investment Cost [kEUR/MW(h)]	Efficiency [%]	Fixed O&M Costs [kEUR/MW(h), year]	Lifetime [year]
Charging or discharging of electric vehicles		-	-	-	-
Charging or discharging Li-Ion batteries	Charge/discharge	80	1	1	25
	Storage capacity	70			25
Charging or discharging hydrogen storage system	Fuel cell	500	50	55	10
	Electrolyzer	390	79	18	20
	Hydrogen storage	10	100	-	40
Adapted hydrogen production	Electrolyzer	390	79	18	20
	Hydrogen storage	11	100	-	50
Adapted heat production	Heat pump	1000	300	8	25
	Tank storage	3	80	-	25
Opportunistic heat production	Electric boiler	50	100	-	20
Opportunistic biogas open-cycle electricity production	Gas turbine	450	42	17	30
Adapted biogas combined-cycle electricity production	CCGT	900	61	15	30
Adapted biomass combined heat and power production	CHP	3260	30	105	40
	Tank storage	3	80	-	25
Adapted biomass electricity production	Steam turbine	1980	35	52	40
Adapted nuclear power production	Steam turbine	3980	33	123	60

2.2. Visualizing the Net Load

The method to visualize the net load suggested in this work is based on the proposition that variability can be defined by its amplitude, duration and number of occurrences. Here, we refer to number of occurrences as how often variations with a certain amplitude and duration takes place. According to time series analyses, any time series in a linear system can be described in two dimensions: amplitude and frequency. Weather systems, wind speeds and thus the net load in electricity systems supplied to a large extent by wind power, are composed of a combination of linear and non-linear phenomena. For this reason, we find it practical to subdivide the frequency into duration and number of occurrences and we will refer to the three-dimensional space spanned by the amplitude, duration and number of occurrences as the variation space.

Algorithm 1 describes how to map the net load of any electricity system into the variation space in six steps. The resulting plot illustrates to which extent the net load variations to be managed are variations with a high amplitude, long duration, high occurrence or any combination of these. We refer to the map of the net load in the variation space as the variation profile of the electricity system. An overview of the variation profile is a first step in identifying cost-efficient strategies to manage the net load variations.

To understand the role of different strategies to manage variations in an existing electricity system, or a future system proposed by electricity system models, the remaining net load after the strategy is applied is calculated and plotted. By comparing the original

variability profile and the variability profile after a strategy has been applied, it is possible to identify to which extent the strategy reduces variations with a high amplitude, long duration or high number of occurrences.

Algorithm 1. Creating the Variability Profile.

1: Calculate the net load $n_t \in N$ as the total electricity demand fixed in time and reduced by non-dispatchable generation for every timestep $t \in T$.

2: Define a list L:= (min N:max N, s) where the step length s is small enough to give a high resolution of the amplitude in the plots. Here, we use s = 0.1 GW.
Make a vector $c_{l,t}$ which counts up as long as the net load n is above amplitude $l \in L$ (or as long as net load n is below amplitude l for negative net loads).

3:
For $l \in L$:
  For $n_t \in N$:
    if $l > 0$ **and** $n_t < l$:
      $c_{l,t} = c_{l,t-1} + 1$
    else if $l < 0$ **and** $n_t > l$:
      $c_{l,t} = c_{l,t-1} + 1$
  $n_t = n_{t+1}$
$l = l + s$

4: Find the end of each variation interval and obtain the duration $d_{l,t}$.
For $l \in L$:
  For $n_t \in N$:
    if $l > 0$ **and** $n_{t-1} > l$ and $n_t < l$:
      $d_{l,t} = c_{l,t}$
    else if $l < 0$ **and** $n_{t-1} < l$ and $n_t > l$:
      $d_{l,t} = c_{l,t}$
  $n_t = n_{t+1}$
$l = l + s$

5: Count the number of occurrences $o_{l,d}$ for a certain combination of duration and amplitude.
For $d \in T$:
  $o_{l,d} = \sum_t d_{l,t}$
  $d = d + 1$

6: Plot occurrences of variations with amplitude l on the x-axis, duration d on the y-axis and occurrences o on the z-axis.

3. Results

Figure 1 shows the annual electricity demand for the investigated regions. The historic electricity demand (grey) represents the electricity demand prior to electrification. The direct electricity demand from the transport (yellow) and industry sectors (green) and the electricity for hydrogen production (blue) are a consequence of the assumptions and input data presented in the Section 2. The electricity demand for heating (orange) corresponds to electricity for individual heat pumps replacing natural gas, which is given exogenously, but also electricity demand for district heating, which can be met by combined heat and power plants and heat-only boilers as well as heat pumps and electric boilers. The total electricity demand for heating was thus a result of the optimization. For the case investigated, the increase in electricity demand from electrification corresponded to an increase in the annual electricity demand of around 80% in northern Europe. As illustrated in Figure 1, the electricity demand following the electrification of the transport sector was particularly high in the regions with a high population density such as southern Germany (DE_S), southern Poland (PO_S) and southern UK (UK_S). The electricity for hydrogen production was located in regions with an extensive industrial sector (Sweden, Germany, Poland, the BENELUX region and the UK).

Figure 2 shows the annual electricity production in the investigated regions calculated by the electricity system model presented in the Section 2. Applying the costs presented in the Appendix, it was found to be cost-efficient to meet 2/3 of the annual electricity demand in northern Europe with wind power (blue). As illustrated in Figure 2, there were two

major clusters of offshore wind power in northern Europe: one off the coast of northern Germany, the Netherlands and Denmark and one off the coast of the UK. With very good conditions for wind power but a limited electricity-intensive industry, Denmark was the single largest exporter of electricity (DK exports 90 TWh/year). The opposite was true for southern Germany which imported 165 TWh/year for the investigated years. Solar PV energy supplied 1/5 of the electricity demand in northern Europe and was mainly located in the southmost regions (southern Germany and southern Poland) from which other regions imported solar power. The southern UK also had large solar PV investments to complement wind power since import capacity from continental Europe was limited. The model was limited to northern Europe and trade outside the modeled scope was omitted. In reality, there is significant transmission capacity between northern Europe and continental Europe and the results for regions on the border with central Europe (southern Germany and southern Poland) should be viewed with this simplification in mind.

Figure 3 shows the installed capacity of energy storage for the investigated regions. The total energy storage capacity in northern Europe corresponded to 11 TWh. The volume of energy storage capacity reflected the investment cost of energy storage capacity. Tank heat storages were the cheapest energy storage option but were only relevant in regions with district heating (district heating is very limited in Norway and the UK). Hydrogen storage was the second cheapest option for energy storage, and was relevant to regions with a demand for hydrogen. Batteries were significantly more expensive and battery investments were mainly located in regions with substantial electricity supplies from solar PV energy. To investigate the role of energy storage in the different regions and how electricity demand and supply was balanced every hour, four regions with different conditions for wind and solar power and different access to flexibility measures were further investigated.

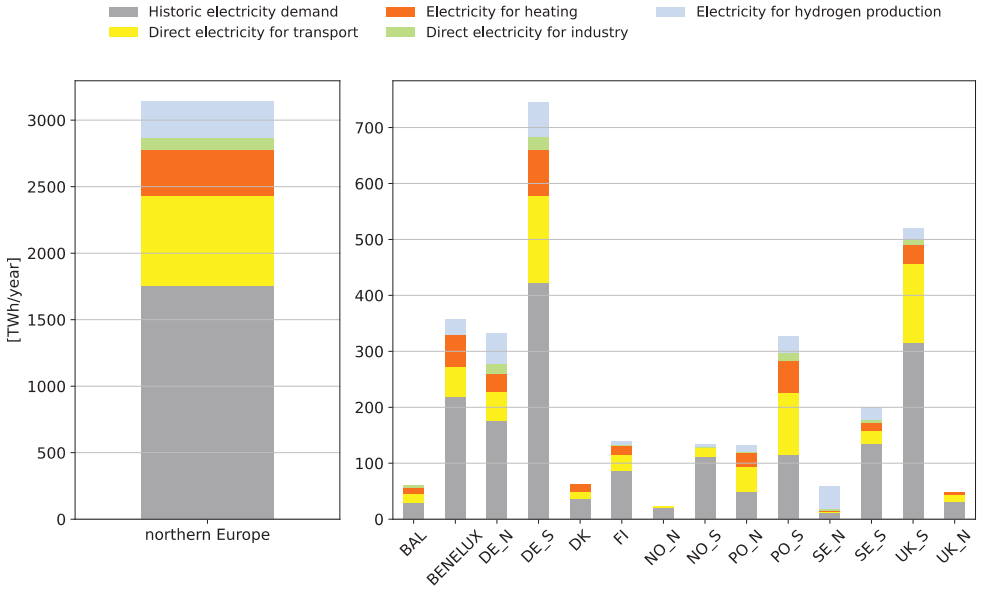

Figure 1. Annual electricity demand for northern Europe as a whole (**left**), together with electricity demand by region investigated in this work (**right**), subdivided into electricity demand of today (grey), electricity demand for heat pumps in district heating systems (orange), for new individual heat pumps replacing natural gas (yellow), for hydrogen production (blue), for light vehicles (light green) and for trucks and buses (dark green).

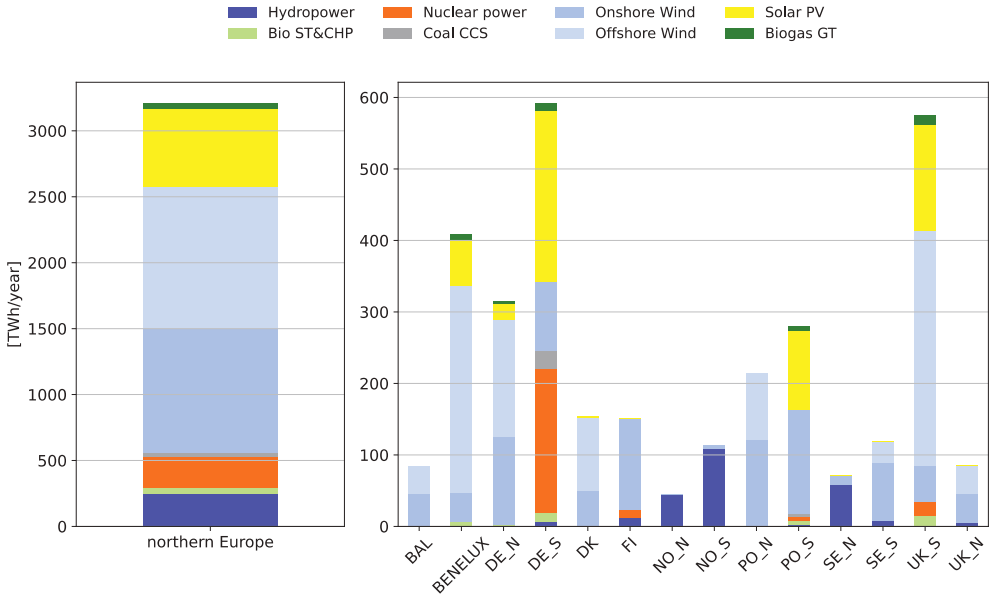

Figure 2. Annual electricity production in northern Europe (**left**) and by region (**right**). ST&CHP = steam turbine and combined heat and power, CCS = carbon capture and storage, GT = gas turbine (open cycle and combined cycle).

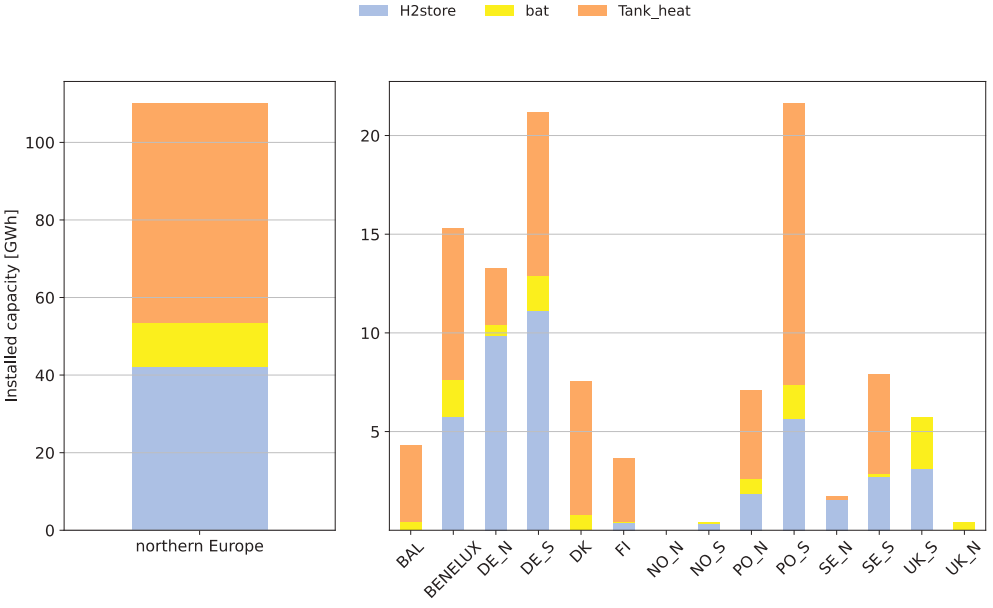

Figure 3. Installed energy storage capacity for northern Europe (**left**) and by investigated region (**right**), subdivided into underground lined-rock cavern hydrogen storage (blue), stationary lithium-ion batteries (yellow) and hot water tank storage in district heating systems (orange).

Figures 4a, 5a, 6a and 7a show the variation profile for DE_S, DK, UK_S and SE_S as defined in the Section 2. These four regions represent four different types of regions

observed in the model of northern Europe; regions with extensive solar PV capacity (DE_S and PO_S), regions with extensive wind power for domestic use and export (DK, BAL, PO_N and UK_N), regions with a combination of wind and solar power (UK_S, BENELUX and DE_N) and regions with access to hydropower (SE_S, SE_N, FI, NO_N and NO_S). The color scale was limited at 50 occurrences, implying that the number of occurrences may be higher in the deep red fields. The y-axis was limited at 168 h (one week). Some variations with a longer duration occurred and plots with a y-axis of 300 h for all regions are shown in Appendix C (Figures A2–A15).

As Figures 4a, 5a, 6a and 7a show, net load variations were very different between the investigated regions. Net load variations in Denmark (Figure 5a), with a supply side dominated by wind power, had a low amplitude and number of occurrences but long duration. This was contrasted by net load variations of southern Germany (Figure 4a) with a high amplitude and high number of occurrences but few variations with a long duration. The pattern of the variations in solar power dominated Germany and represented the nature of solar PV energy with a high occurrence in positive net load at a duration of 12–15 h corresponding to night, high number of occurrences in positive net load with high amplitude and a duration of a few hours corresponding to afternoon peaks and high number of occurrences of negative net load with a duration of 2–10 h and varying amplitude corresponding to daytime solar PV production. Variations with a longer duration reoccurred with 24 h intervals and corresponded to cloudy days. The variation profile of southern UK (UK_S) was a combination of the variation profile of southern Germany and Denmark, with the typical pattern of solar PV variations, but with lower amplitudes and lower number of occurrences than those in southern Germany due to a lower total installed capacity, but there were also positive and negative variations with a longer duration which are characteristic of wind power. The variation profile of southern Sweden (SE_S) resembles the one of Denmark, indicating a wind-dominated net load. However, the net load was oriented towards positive amplitudes corresponding to a need for additional generation capacity to complement the wind power to meet the load.

Figures 4–7 illustrate how strategies to manage variations reduced the net load variability in the four example regions. The 11 strategies in Table 1 were aggregated into six groups of strategies to facilitate an overview. Here, the category Thermal includes all thermal electricity generation options except open-cycle gas turbines (adapted biogas combined-cycle electricity production, adapted biomass combined heat and power production, adapted biomass electricity production, adapted nuclear power production). Based on the electricity generation supplied by different sources (see Figure 2), nuclear power dominated this group of strategies. Batteries included stationary batteries and charging of electric vehicles since previous work showed that these strategies act on the same timescales in the electricity system [2]. This implies that we added a load, which was fixed to 70% and flexible to 30% according to assumptions, together with the charging and discharging of stationary batteries. Finally, here, Heat includes both heat production with heat pumps and electric boilers connected to the district heating system (adapted heat production and opportunistic heat production in Table 1). However, this group mainly represents variation management by heat pumps since electric boilers played a very minor role in all investigated regions.

Figure 4b–g shows the net load reduction by six different strategies for southern Germany. Electricity was imported to solar PV-dominated southern Germany, reducing the positive nighttime net load. The positive net load was further reduced by base load generation (Figure 4d). At the same time, base load generation increased the negative net load with long durations. Due to the limited flexibility of nuclear power, production was not only added when needed but also during hours of low net load. The negative net load with a long duration caused by base load generation was reduced by adapted production of hydrogen and heat (Figure 4f–g). However, in the solar PV-dominated southern Germany, the strategy with the largest impact on the net load was batteries (Figure 4e). Stationary batteries matched the charging of electric vehicles (in this work, 70% of the vehicle charging

was fixed in time) to the solar PV generation and thereby reduced the net load variations. Batteries have a relatively low cost of charging and discharging power and high efficiency which makes them well suited for the solar PV variations with a high amplitude and high number of occurrences. In general, it can be observed that investments in stationary batteries were particularly substantial in regions with a large demand for electricity for transport (cf. Figures 1 and 3) and that solar PV generation was high in the same regions (Figure 2). The net load variations with a low amplitude, duration and a low number of occurrences which remained in Figure 4f was supplied by biogas open-cycle gas turbines.

Figure 5b–g shows the gradual net load reduction by the six strategies to manage the variations in Denmark. Denmark has some of the best conditions for offshore wind power in northern Europe and together with its central location between the Nordic countries and continental Europe it becomes an ideal exporter of electricity. The majority of this electricity was exported to northern Germany and onwards to load centers in southern Germany. The extensive export results in a strong reduction of the wind-dominated net load variations (Figure 5b). Trade with Germany also introduced solar variations in Denmark, as seen in Figure 5b. These variations were efficiently reduced by batteries. The remaining net load variations had a low amplitude but sometimes had a long duration. In Denmark, these variations were primarily reduced by heat pumps in the district heating system (Figure 5g).

Figure 6b–f shows the net load reduction by strategies to manage variations in the southern UK. The system composition here was a combination of wind and solar power, as illustrated in Figure 2, and the net load had both variations with a long duration and variations with a high amplitude and a high number of occurrences. It is important to note that by combining wind and solar power in the electricity mix, net load variations were, to some extent, already reduced from the start. In particular, solar PV production reduced the duration of low wind events and wind power reduced the positive nighttime net load of solar power. These complementary effects can be visualized by comparing the net loads in Figure 6a to those in Figures 4a and 5a. Trade, primarily with northern UK, further reduced net load variations with a 20–24 h duration. However, it was by combining wind and solar power together with the use of batteries for variations with a high amplitude and high number of occurrences that the majority of the variations in this region were managed. Some variations with a low duration and low number of occurrences were managed by adapted production of hydrogen. The net load which remained in Figure 5f was managed by biogas open-cycle gas turbines.

Figure 7b–f illustrates how the net load was reduced by five different strategies to manage variations in southern Sweden. Figure 7b shows the net load reduced by trade (except for northern Sweden). As the figure shows, trade shifted the net load to the left, indicating that southern Sweden imported electricity. However, since the electricity was mainly imported from Denmark, which is wind-dominated like southern Sweden, the variability of the net load curve was similar after accounting for trade. Some solar variations with a high number of occurrences and high amplitude but short duration were introduced with the trade. Figure 7c shows the net load reduced by trade and hydropower, including trade with northern Sweden. Even though electricity demand in northern Sweden increased substantially, hydropower from the north was exported to southern Sweden during low wind events since the demand in the north was predominantly composed of electricity for hydrogen production which was avoided during low wind events. As the figure shows, the positive net load was drastically reduced by hydropower and hydropower managed positive net loads of any duration. Batteries and the charging of electric vehicles reduced the amplitude of the remaining negative net load (Figure 4e). The remaining net load had a low amplitude and any duration which was managed by adapted production of hydrogen (Figure 4f) and heat (Figure 4g). With the high cost of electricity consumption capacity (electrolyzer and heat pump) but low cost of energy storage (underground hydrogen storage and storage of hot water), variations with a low amplitude but long duration matched the cost structure of these strategies. It is important to note that adding electricity consumption adapted to the net load, i.e., adapted production of heat and hydrogen, does

not only imply that "excess" electricity was consumed. These flexible electricity demands stimulated investments in wind power production without increasing consumption during low wind events. Since there was also some wind power production during low wind events, adapted consumption of hydrogen and heat reduced the net load during these events. The little remaining net load visible in Figure 7f was met by open-cycle gas turbines.

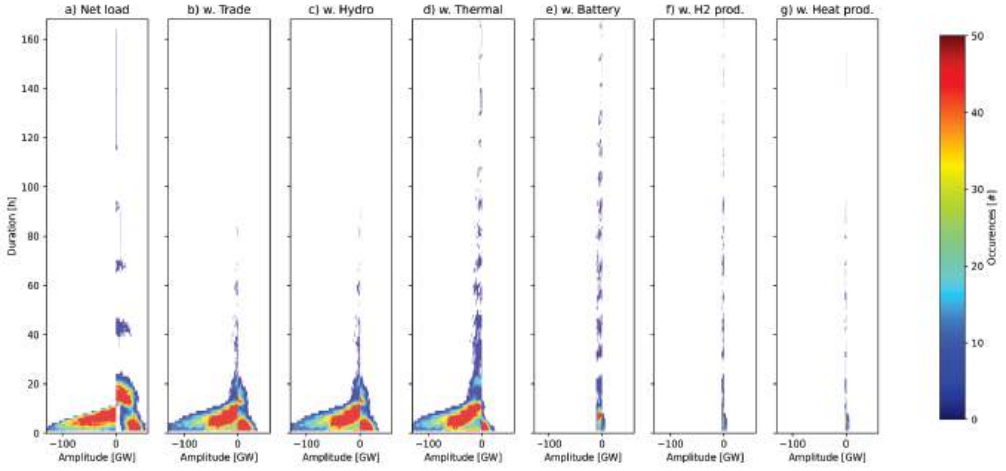

Figure 4. Net load of southern Germany (DE_S) (**a**) reduced by (**b**) trade, (**c**) trade and hydropower, (**d**) trade, hydropower and base load, (**e**) trade, hydropower, base load and batteries, (**f**) trade, hydropower, base load, batteries and adapted hydrogen production and (**g**) trade, hydropower, base load, batteries, adapted hydrogen production and adapted heat production. The color scale indicates number of (#) occurrences and was limited to 50 occurrences, implying that the number of occurrences may be higher in the deep red fields. The y-axis was limited at 168 h (one week).

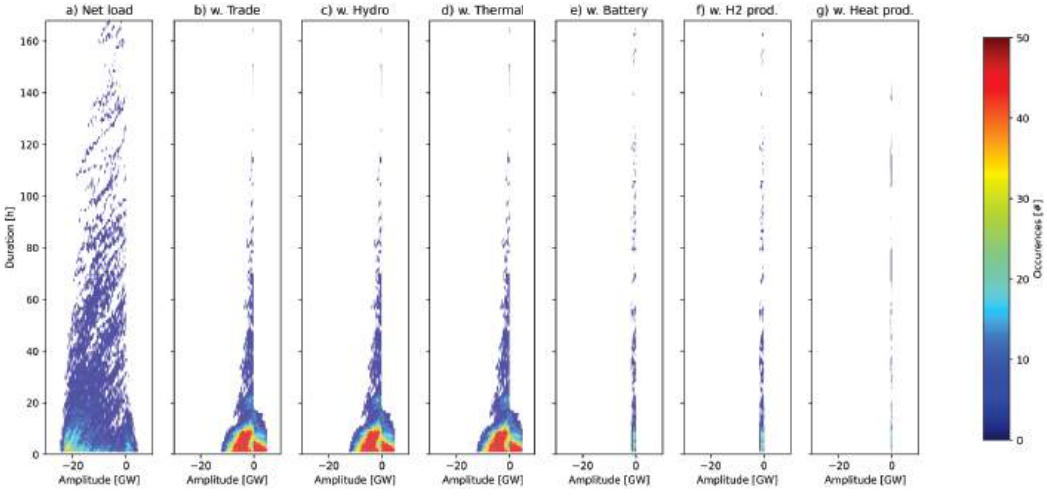

Figure 5. Net load of Denmark (DK_T) (**a**) reduced by (**b**) trade, (**c**) trade and hydropower, (**d**) trade, hydropower and base load, (**e**) trade, hydropower, base load and batteries, (**f**) trade, hydropower, base load, batteries and adapted hydrogen production and (**g**) trade, hydropower, base load, batteries, adapted hydrogen production and adapted heat production. The color scale indicates number of (#) occurrences and was limited to 50 occurrences, implying that the number of occurrences may be higher in the deep red fields. The y-axis was limited at 168 h (one week).

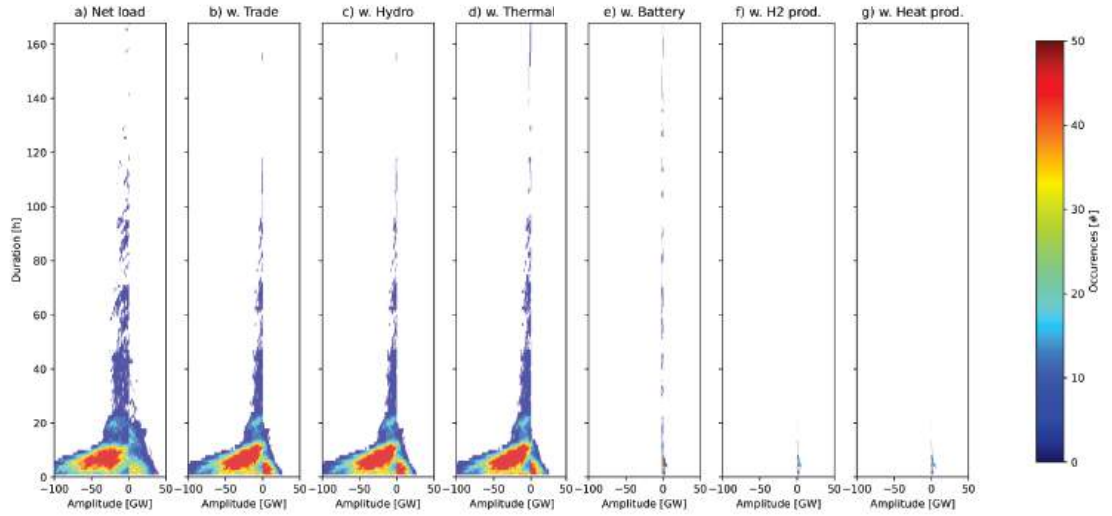

Figure 6. Net load in southern UK (UK_S) (**a**) reduced by (**b**) trade, (**c**) trade and hydropower, (**d**) trade, hydropower and base load, (**e**) trade, hydropower, base load and batteries, (**f**) trade, hydropower, base load, batteries and adapted hydrogen production and (**g**) trade, hydropower, base load, batteries, adapted hydrogen production and adapted heat production. The color scale indicates number of (#) occurrences and was limited to 50 occurrences, implying that the number of occurrences may be higher in the deep red fields. The y-axis was limited at 168 h (one week).

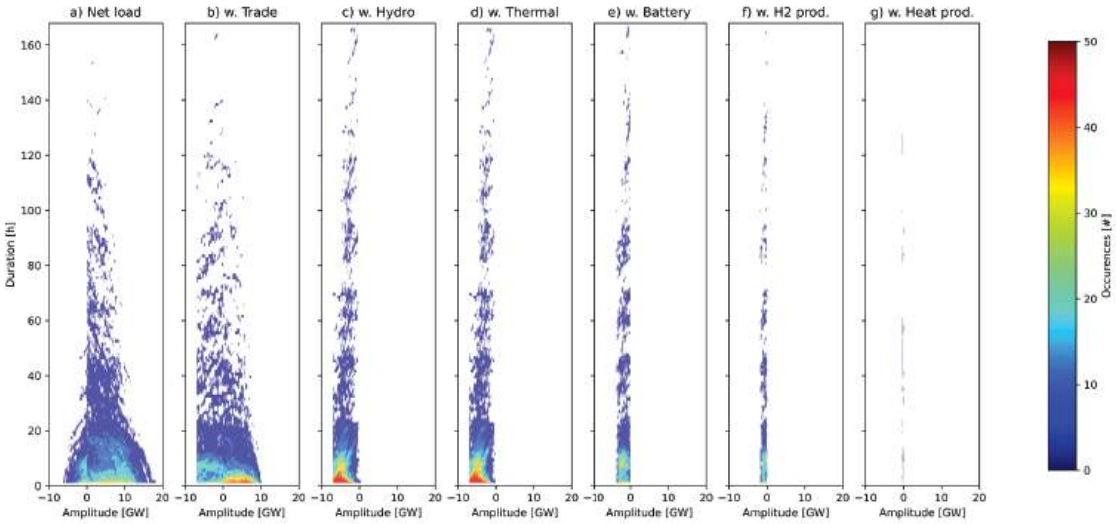

Figure 7. Net load in southern Sweden (SE_S) (**a**) reduced by (**b**) trade, (**c**) trade and hydropower, (**d**) trade, hydropower and base load, (**e**) trade, hydropower, base load and batteries, (**f**) trade, hydropower, base load, batteries and adapted hydrogen production and (**g**) trade, hydropower, base load, batteries, adapted hydrogen production and adapted heat production. The color scale indicates number of (#) occurrences and was limited to 50 occurrences, implying that the number of occurrences may be higher in the deep red fields. The y-axis was limited at 168 h (one week).

4. Categorizing the Cost-Efficient Contribution of Variation Management Strategies

The results confirm that different variation management strategies contributed with different functionalities in the electricity system. At the same time, the contribution from each strategy, in terms of reduction in net load amplitude and number of occurrences on different timescales, was qualitatively similar in the four investigated regions. However, the size of the investments in different strategies and their quantitative contribution was different in the different system contexts.

As the objective of the model applied in this work was to minimize the total cost of the electricity system, the investments in, and operation of, the variation management strategies as given in this work was cost efficient given the available options. That is, the functionality provided was motivated by the cost structure and technical limitations of each strategy. High reductions in the amplitude of recurring variations were cost-efficiently supplied by strategies with a low cost of charging and/or discharging power, such as batteries. To manage variations over longer timescales, a low cost of energy storage is required. In the examples given in this work, the cost of hydrogen storage represents the cost of storing hydrogen in large-scale underground caverns, which is low compared to energy storage in batteries. The cost of storing heat in tank storages is even lower. The cost of storing fuel for thermal generation was omitted in the model, which allows combined-cycle gas turbines and combined heat and power plants to manage the variations with a long duration. Variations with a low number of occurrences were managed most efficiently using strategies with a low investment cost, such as open-cycle gas turbines. With a low number of occurrences a high running cost is acceptable.

The roles identified by these measures can form the basis for a functionality-based categorization of strategies to manage variations. Whereas previous categorizations of strategies to manage variations were based on the technical properties of the strategies, a categorization supporting the understanding of the functionality of the strategies to manage variations in the electricity system should rely on the cost structure. Based on the above reasoning and the work by [7,8], the following categories are proposed:

- Peaking strategies, which manage variations with a low number of occurrences. Similar to peak production plants, peaking variation management strategies have low investment costs in terms of charging, discharging and storage capacity. However, the low investment cost is typically accompanied by a high operational cost, i.e., a high cost of electricity discharged or low value of electricity charged.
- Shifting strategies, which reduce recurring variability on shorter timescales. These strategies are associated with a low cost of charging and discharging capacity and a low cost of operation, since variability on shorter timescales have high amplitude and high number of occurrences. However, a low cost of charging and discharging capacity is typically associated with a high cost or a limited capacity to store energy. Thus, these strategies are mainly applied for shifting loads or production during shorter time intervals.
- Complementing strategies, which manage recurring variations on longer timescales. These strategies are associated with a low cost of energy storage. However, since the amplitude of variations on longer timescales is lower, a higher cost associated with the charging and discharging power is acceptable. A low to medium cost of operation is required from these strategies since the variations being managed have a long duration and medium recurrence. This category could be further subdivided to differentiate between complementing strategies managing variations on weekly and seasonal timescales.

A categorization based on the cost structure has the advantage that the category reveals the functionality of the strategy. This categorization thus facilitates the choice of variation management strategies for different system services and contexts.

5. Discussion and Limitations

In this work, net load variations were plotted in the space spanned by amplitude, duration and number of occurrences (i.e., the variation space) to better understand how different strategies to manage variations complement each other. For this analysis, the cost-efficient combination of a large set of strategies provided by the electricity system investment model was required. However, plotting a gradually reduced net load in the variation space can also be useful to understand how variations are managed in an existing system, using electricity production data.

Applying the method proposed to map the contribution of flexibility measures to reduce the net load, functionality-based categories of variation management strategies can be identified. The vast majority of previous categorizations have focused on the technical properties of the flexibility measures. For example, Fuchs and Lunz [27] and Zhao and Wu [28] subdivided electricity storage systems into electrical, mechanical, chemical and thermal storage units, while Sauer [29] differentiated between electricity-to-electricity storage, electricity-to-anything storage and anything-to-electricity storage systems. Palizban and Kauhaniemi [30] have mapped energy storage systems with respect to those applications for which they are suitable and unsuitable for, using a color-coded matrix. Other categorizations have focused on the motive for the investment, such as single-use/double-use [31] which distinguished between investments that are actively made and are dedicated to provide flexibility in the electricity system (single-use) and those cases in which assets that are already integrated in the electricity system for other purposes are used (double-use). While all these categorizations support the understanding of flexibility measures, measures with the same functionality in the electricity system are distributed between the categories in the above-mentioned frameworks. A previous work by the author [7] proposed instead a functionality-based framework, organizing variation management strategies according to the service they provide in the electricity system. This work further developed this framework.

The strategies applied in the regions modeled in this work are cost efficient from an energy-only perspective. However, without the perfect foresight of the modelled world, flexibility markets may be needed to stimulate investments prior to large electricity price variations. In the design of flexibility markets, a market for each of the above-mentioned categories would assure competition between strategies providing the same function to the electricity system and stimulate investments in a balanced set of strategies. The size of the different markets should be defined by the electricity system context, i.e., the need for the different functionalities based on the variability profile of the present and future electricity systems.

This work investigates strategies to manage variations on the timescale of hours to a couple of years. Variations within the hour as well as variations with very a low number of occurrences (e.g., once every ten or thirty years) is outside the scope of this work. Meng and Zafar [32] provided an overview on how variations on very short timescales, to recover the frequency after faults, can be managed in electricity systems with a high share of wind and solar power. They concluded that batteries with grid-forming converters, with the ability to provide active power very rapidly, are able to replace synchronous generators while maintaining the ability to recover the frequency after a fault. However, if synchronous generators can be replaced completely remains to be investigated. Ullmark [33] showed that if batteries are allowed to meet the demand for variations within the hour, these variations can be managed at a low cost (<1% of total system cost).

Ruhnau and Qvist [34] investigate the impact of variations in the German electricity system over a 30-year period and found that there were low wind events with a long duration (60 days with short periods of interruption) which occurred very rarely. As shown in this work, the choice of strategy for a certain type of variation depends on the cost structure. Variations with a long duration and low number of occurrences are cost-efficiently managed by strategies with a low cost of storage and low investment cost. A cost-efficient strategy to manage the variations identified by [34] would thus be biogas

gas-turbines with a sufficiently large storage of biogas. Sufficient biogas turbine capacity is likely to already be available to the electricity system to manage variations with a shorter duration occurring on a yearly basis. The fuel costs during the 60-day period would be significant but, since these events occur very rarely, this fuel cost would have a low impact on the total system cost and the overall electricity system composition.

6. Conclusions

In this work, a novel tool to map variations in electricity systems was applied to visualize how variations can be cost-efficiently managed in a future northern Europe. The results show that cost-efficient variation management depends on the system context. More specifically, it depends on the nature of the variations present in the electricity system as well as the context-specific prerequisites for variation management, such as extensive demand for hydrogen from industry, availability of district heating grids or access to hydropower. In particular, the access to strategies suitable to manage variations with a long duration varied between the investigated regions. As a consequence, the dominant strategy to manage variations with a long duration varied between, for example, Denmark, where adapted heat production has an important role, and southern Sweden, which relies more on hydropower and adapted hydrogen production to manage these variations.

Electricity systems with good conditions for solar power and extensive electricity demand for transportation were subject to variations with a high amplitude and high number of occurrences which can be cost-efficiently managed using batteries with a low cost of charging and discharging power and low losses per cycle. Examples of such regions in northern Europe were southern Germany and southern Poland, with inland locations and high population densities. In these regions, there may also be potential for some base load generation.

Electricity systems with good conditions for wind power, such as Demark, the Netherlands and northern Germany, managed variations through trade, including import of solar PV energy and adapted production of hydrogen and/or heat. Extensive industrial hydrogen demand or district heating systems facilitated the integration of wind power since wind variations have long durations and hydrogen and heat can be stored at a relatively low cost.

In regions with good conditions for wind power but limited trade, such as the UK, it was cost efficient to combine wind power capacity with solar PV capacity to reduce the duration of low wind events. It was often cost efficient to combine hydropower with batteries, where the former managed the positive net loads with short and long durations but the latter managed variations with a high amplitude including negative net load. In general, cost-efficient variation management was achieved by combining wind and solar power, and with strategies to manage variations with different cost structures.

Funding: This research was funded by MISTRA, grant number 2019-0026, and the Swedish Energy Agency, grant number 49341-1.

Data Availability Statement: The key data applied in this work are provided in the manuscript, in the appendix or is referenced. The data can be made available on request.

Acknowledgments: The author would like to thank Viktor Walter and Filip Johnsson for valuable discussions, as well as Tom Brown and Juha Kiviluoma for feedback on early work.

Conflicts of Interest: The author declares no conflict of interest.

Appendix A

Figure A1. Northern Europe subdivided into 14 regions as applied in this work.

Appendix B

Table A1 shows the investment costs together with the operation and maintenance costs (O&M) for electricity and heat generation applied in this work. The costs are based on IEA [35] and the Danish Energy Agency [36], except for nuclear power and wind power with low specific power (SP). The investment costs for nuclear power were estimated after dialogues with experts. It corresponds to the average investment cost in the case where several units are invested in and is lower compared to levels given for Europe by the IEA. The cost to manage waste (today 4 EUR/MWh in Sweden) was expressed as a small addition to the variable cost (0.5 EUR/MWh) to manage fuel waste and a larger fixed cost to manage the plant at the time of decommissioning (corresponding to 3.5 EUR/MWh after 60 years with 90% utilization) were allocated to fixed O&M. Nuclear energy was assumed to be able to vary its output between 70–100% of rated power. The majority of wind turbines today have a specific power around 300 W/m^2. However, turbines with a lower specific power (generator capacity over swept rotor area) are advantageous for sites with lower average wind speeds and offshore locations. Hodel and Göransson [37] assessed cost-efficient turbine designs in different system contexts using a cost model to assess the cost of a range of wind turbine designs. Investment costs for onshore wind turbines with a specific power of 100 W/m^2 and tower height of 150 m and for offshore wind turbines with 200 W/m^2 and 150 m tower height were based on their work.

Table A2 shows the cost and properties of the energy storage options. These costs were based on the Danish Energy Agency [36]. The cost of transmission capacity was assumed to 2k EUR/MW and km, where the distance is taken as the distance between a point in each region with extensive grid capacity. The calculations applied annual investment costs

which were derived using a 5% interest rate and technical lifetimes as given in Table A1. Table A3 shows the fuel costs applied in this work.

Table A1. Costs and properties of electricity and heat generation units. CHP = Combined Heat and Power, CCS = Carbon Capture and Storage, CCGT = Combined Cycle Gas Turbine, OCGT = Open Cycle Gas Turbine.

Technology	Investment Cost [MEUR/MW(h)]	Variable O&M Cost [EUR/MWh]	Fixed O&M Cost [kEUR/MW, year]	Technical Lifetime [year]	Efficiency [%]
Biomass steam	2.0	2.1	52	40	35
Biomass CHP	3.3	2.1	105	40	30
Coal w. CCS [1]	3.5	2.1	107	40	40
Biogas CCGT	0.90	0.8	17	30	61
Biogas OCGT	0.45	0.4	15	30	42
Nuclear power	4.0	7.1	123	60	33
Solar PV power	0.3	0.5	7	40	100
Onshore wind power (100 W/m^2 150 m)	1.65	1.1	13	30	100
Onshore wind power (300 W/m^2 100 m)	1.0	1.1	13	30	100
Offshore wind power (200 W/m^2 150 m)	1.75	1.1	36	30	100
Heat pump	0.9	2.2	2	25	3
Electric boiler	0.1	1	1	20	1

[1] Coal was assumed to be mixed with biomass in order to compensate for emissions which are not captured.

Table A2. Costs and properties of storage technologies. Investment costs for batteries (power), electrolysis and fuel cells are given in MEUR/MW while costs for batteries (energy) hydrogen storage and heat storage are given in MEUR/MWh.

Technology	Investment Cost [MEUR/MW(h)]	Efficiency (ch/disch) [%]	Fixed O&M Cost [kEUR/MW(h), year]	Technical Lifetime [year]
Battery, Li-ion (energy)	0.08	96/96	-	25
Battery, Li-ion (power)	0.07	100	0.5	25
Electrolysis	0.4	70	18	20
Fuel cell	0.5	50	55	10
Hydrogen storage	0.011	100	-	40
Heat storage	0.003	100 [1]	0.009	25

[1] Heat storages have a continuous loss corresponding to 0.023% per unit of time and energy stored.

Table A3. Cost of fuel applied in the calculations.

Fuel	Fuel Cost [EUR/MWhth]
Biomass	40
Biogas	77
Uranium	1.65
Coal w. biomass blend	7.5

On- and offshore wind power and solar PV power were represented using time-resolved wind and solar power production potential for the investigated regions derived using [18] which rely on ECMWF ERA5 [19] and the Global Wind Atlas [20] for the historical years 1991–1992. These two years were chosen since they represent one year with a lower hydropower inflow in the Nordic countries (1991) and one year with a higher hydropower inflow in the Nordic countries (1992). The potential for wind and solar PV investments per region together with their respective full load hours are given in Tables A4 and A5. Electricity demand corresponding to temperature variations in the historical years 1991–1992 was also derived using [18]. After the removal of unsuitable and protected areas, the potentials for onshore wind power, offshore wind power and solar power were derived applying an assumed factor of social acceptability. For offshore wind power and solar PV power, 33% and 5% of the share of the remaining land was assumed to be available in all regions, respectively. For onshore wind power, 8% of the remaining land was assumed to be available except for Norway (1%), Sweden, the UK and Ireland (4%) where acceptance for wind power investments has proven to be low. The potential area for wind power was subdivided into five wind classes for each region representing different wind conditions. Wind turbine technologies were chosen to match the conditions of their respective area, with wind turbines with 100 SP (Specific Power, i.e., generator capacity relative to swept rotor area in W/m^2) and 150 m hub height for onshore sites with low average wind speeds (i.e., wind class 1–3), 300 SP and 100 m hub height for areas with high average wind speeds (i.e., wind class 4–5) and 200 SP and 150 m hub height for offshore wind turbines.

Table A4. Potential for electricity production (GW) for the five classes of onshore wind power (WON1-WON5), the five classes of offshore wind power (WOFF1–WOFF5) and solar PV parks (PV) for the regions considered in this work. SP = Specific Power, i.e., generator capacity relative to swept rotor area in W/m^2.

Region	WON1 100SP	WON2 100SP	WON3 100SP	WON4 300SP	WON5 300SP	WOFF1 200SP	WOFF2 200SP	WOFF3 200SP	WOFF4 200SP	WOFF5 200SP	PV
SE_N	0.7	5.1	5.3	3.4	2.1	0.0	0.0	1.7	16.3	2.8	86.3
SE_S	0.2	1.5	7.0	8.2	0.9	0.0	0.0	0.1	22.9	47.7	44.1
DE_N	0.0	0.0	2.9	18.7	9.6	0.0	0.0	0.0	0.0	29.4	161.4
DE_S	1.0	5.1	6.7	10.1	0.6	0.0	0.0	0.0	0.0	0.0	180.2
BAL	0.0	0.0	7.3	34.9	0.5	0.0	0.0	0.0	10.5	41.9	193.5
PO_S	0.1	0.9	8.4	27.3	0.1	0.0	0.0	0.0	0.0	0.0	256.3
NO_N	0.1	0.3	0.5	1.8	2.0	0.1	0.7	1.3	4.9	7.9	194.5
DK_T	0.0	0.0	0.0	1.1	10.8	0.0	0.0	0.0	0.1	77.4	53.2
BENELUX	0.0	0.0	0.4	6.2	4.2	0.0	0.0	0.0	0.0	83.5	51.3
FI	0.0	7.1	26.1	7.7	0.9	0.0	0.0	1.4	27.3	31.6	43.7
NO1	0.4	0.6	0.6	1.1	1.0	0.0	0.0	0.1	2.2	18.3	125.0
PO3	0.0	0.1	4.2	27.4	0.4	0.0	0.0	0.0	1.0	17.5	160.2
UK1	0.0	0.0	0.1	5.4	12.2	0.0	0.0	0.0	0.8	134.5	181.6
UK2	0.0	0.0	0.2	2.9	9.5	0.0	0.0	0.0	0.3	46.7	85.6

Table A5. Full load hours before curtailment for the five classes of onshore wind power (WON1-WON5), the five classes of offshore wind power (WOFF1–WOFF2) and solar PV parks (PV) for the regions considered in this work. SP = Specific Power, i.e., generator capacity relative to swept rotor area in W/m^2.

Region	WON1 100SP	WON2 100SP	WON3 100SP	WON4 300SP	WON5 300SP	WOFF4 200SP	WOFF5 200SP	PV
SE_N	4127	5062	-	-	4244	-	-	1006
SE_S	4162	5178	5823	3451	4131	5159	5348	1233
DE_N	-	4932	5734	3556	4265	5338	5577	1263
DE_S	3313	4560	5190	3417	3987	-	-	1320
BAL	-	5387	5799	3407	4076	5256	-	-
PO_S	3762	4808	5644	3364	4006	-	-	1288
NO_N	3614	-	-	-	4393	-	-	-
DK_T	-	-	-	3823	4270	-	5555	1299
BENELUX	-	5020	5475	3483	4106	-	5198	1267
FI	4607	5470	5852	-	4340	-	-	998
NO1	3319	-	-	3429	4251	-	4869	1156
PO3	-	5424	5838	3490	4086	5215	5390	1271
UK1	0	0	5303	0	4254	5026	5237	1237
UK2	0	4933	5345	3624	4558	0	5501	1087

Appendix C

Appendix C.1 Solar PV Dominated Regions (DE_S, PO_S)

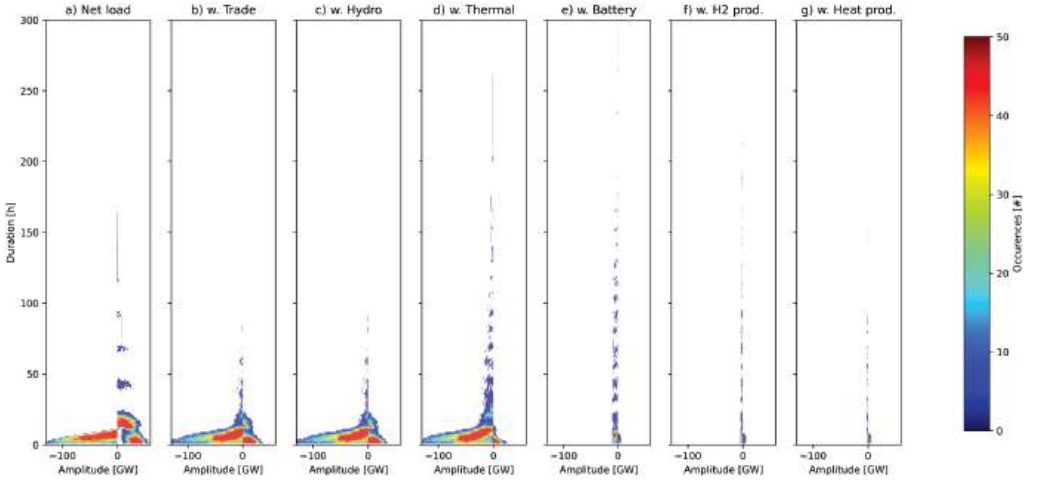

Figure A2. Net load in southern Germany (DE_S) (**a**) reduced by (**b**) trade, (**c**) trade and hydropower, (**d**) trade, hydropower and base load, (**e**) trade, hydropower, base load and batteries, (**f**) trade, hydropower, base load, batteries and adapted hydrogen production and (**g**) trade, hydropower, base load, batteries, adapted hydrogen production and adapted heat production. The color scale indicates number of (#) occurrences and was limited to 50 occurrences, implying that the number of occurrences may be higher in the deep red fields.

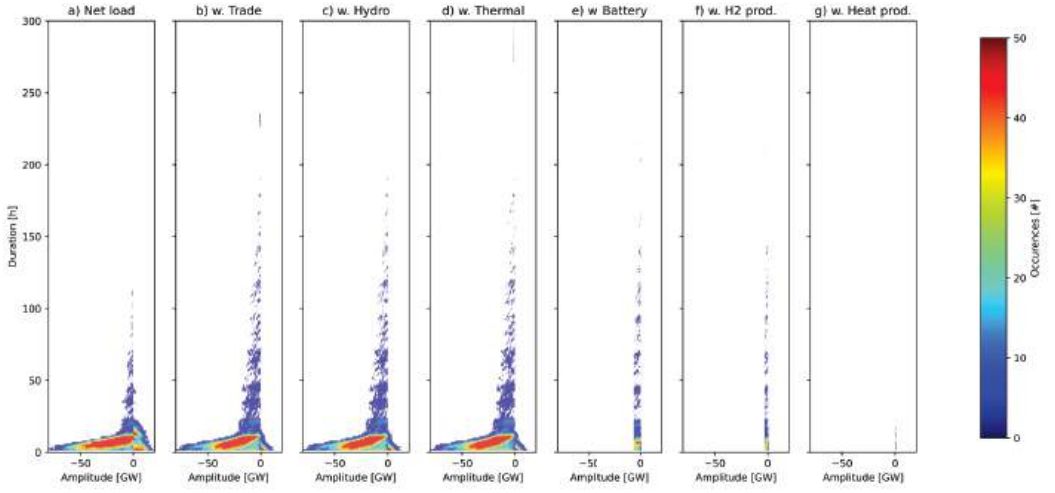

Figure A3. Net load in southern Poland (PO_S) (**a**) reduced by (**b**) trade, (**c**) trade and hydropower, (**d**) trade, hydropower and base load, (**e**) trade, hydropower, base load and batteries, (**f**) trade, hydropower, base load, batteries and adapted hydrogen production and (**g**) trade, hydropower, base load, batteries, adapted hydrogen production and adapted heat production. The color scale indicates number of (#) occurrences and was limited to 50 occurrences, implying that the number of occurrences may be higher in the deep red fields.

Appendix C.2 Wind Dominated Exporting Regions (DK_T, BAL, PO3, UK_N)

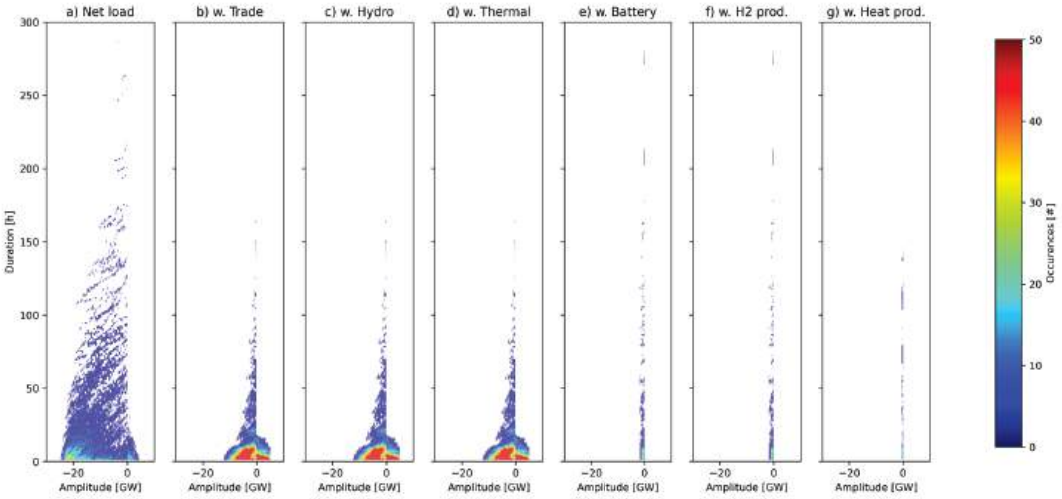

Figure A4. Net load in Denmark (DK_T) (**a**) reduced by (**b**) trade, (**c**) trade and hydropower, (**d**) trade, hydropower and base load, (**e**) trade, hydropower, base load and batteries, (**f**) trade, hydropower, base load, batteries and adapted hydrogen production and (**g**) trade, hydropower, base load, batteries, adapted hydrogen production and adapted heat production. The color scale indicates number of (#) occurrences and was limited to 50 occurrences, implying that the number of occurrences may be higher in the deep red fields.

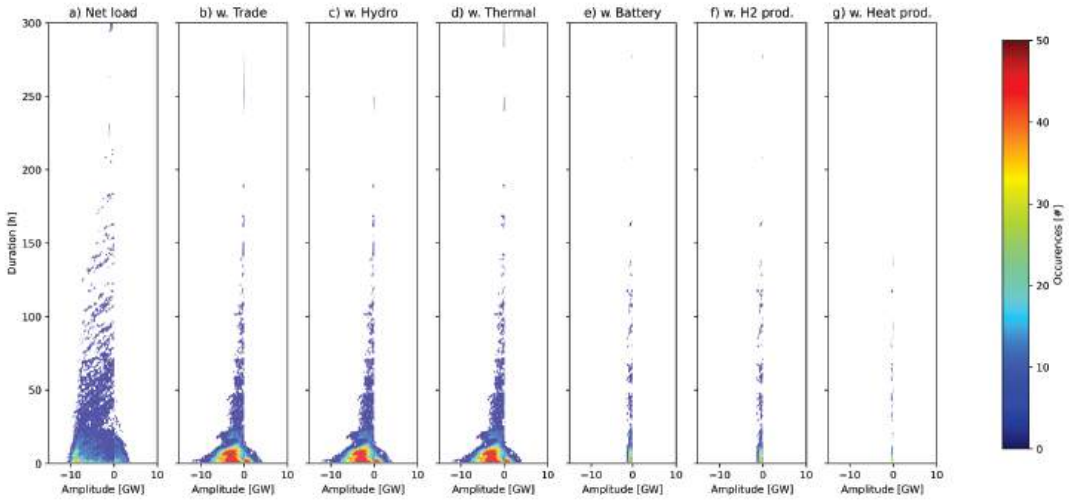

Figure A5. Net load in Estonia, Latvia and Lithuania (BAL) (**a**) reduced by (**b**) trade, (**c**) trade and hydropower, (**d**) trade, hydropower and base load, (**e**) trade, hydropower, base load and batteries, (**f**) trade, hydropower, base load, batteries and adapted hydrogen production and (**g**) trade, hydropower, base load, batteries, adapted hydrogen production and adapted heat production. The color scale indicates number of (#) occurrences and was limited to 50 occurrences, implying that the number of occurrences may be higher in the deep red fields.

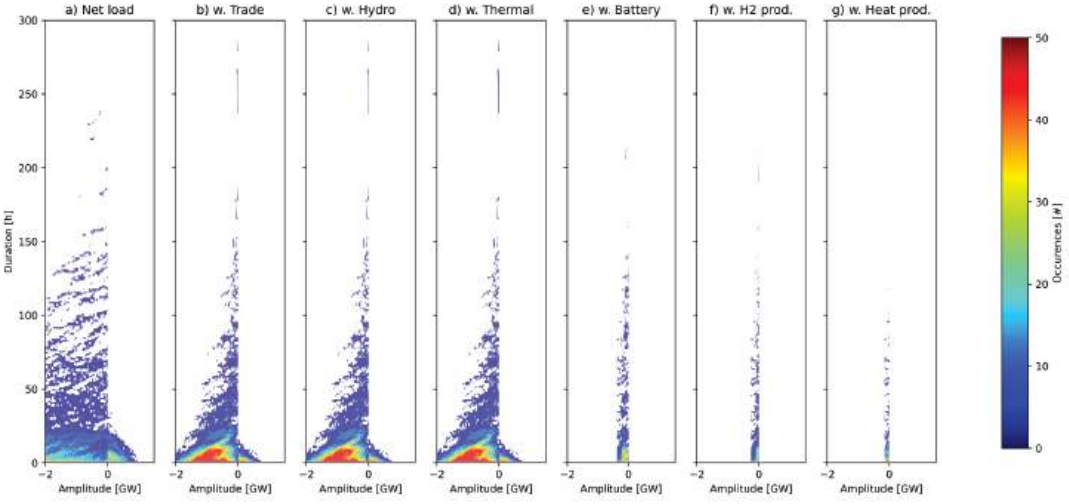

Figure A6. Net load in northern Poland (PO_N) (**a**) reduced by (**b**) trade, (**c**) trade and hydropower, (**d**) trade, hydropower and base load, (**e**) trade, hydropower, base load and batteries, (**f**) trade, hydropower, base load, batteries and adapted hydrogen production and (**g**) trade, hydropower, base load, batteries, adapted hydrogen production and adapted heat production. The color scale indicates number of (#) occurrences and was limited to 50 occurrences, implying that the number of occurrences may be higher in the deep red fields.

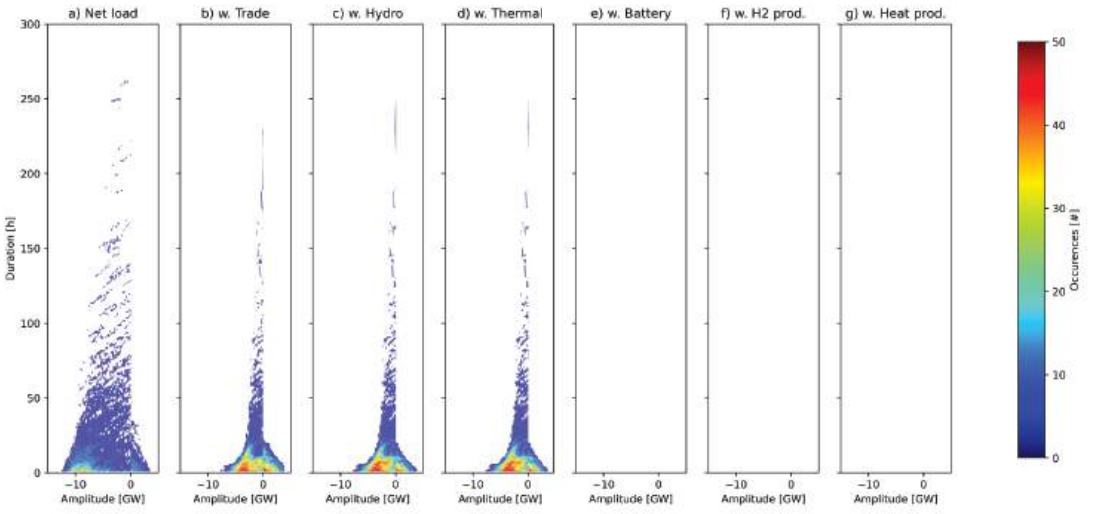

Figure A7. Net load in northern UK (UK_N) (**a**) reduced by (**b**) trade, (**c**) trade and hydropower, (**d**) trade, hydropower and base load, (**e**) trade, hydropower, base load and batteries, (**f**) trade, hydropower, base load, batteries and adapted hydrogen production and (**g**) trade, hydropower, base load, batteries, adapted hydrogen production and adapted heat production. The color scale indicates number of (#) occurrences and was limited to 50 occurrences, implying that the number of occurrences may be higher in the deep red fields.

Appendix C.3 Regions with Wind and Solar Power (UK_S, DE_N, BENELUX)

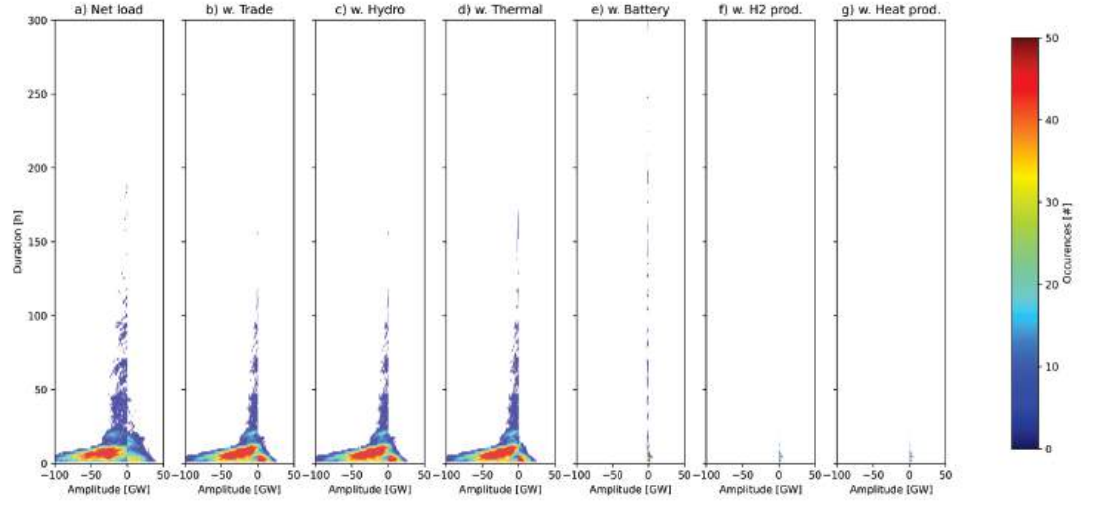

Figure A8. Net load in southern UK (UK_S) (**a**) reduced by (**b**) trade, (**c**) trade and hydropower, (**d**) trade, hydropower and base load, (**e**) trade, hydropower, base load and batteries, (**f**) trade, hydropower, base load, batteries and adapted hydrogen production and (**g**) trade, hydropower, base load, batteries, adapted hydrogen production and adapted heat production. The color scale indicates number of (#) occurrences and was limited to 50 occurrences, implying that the number of occurrences may be higher in the deep red fields.

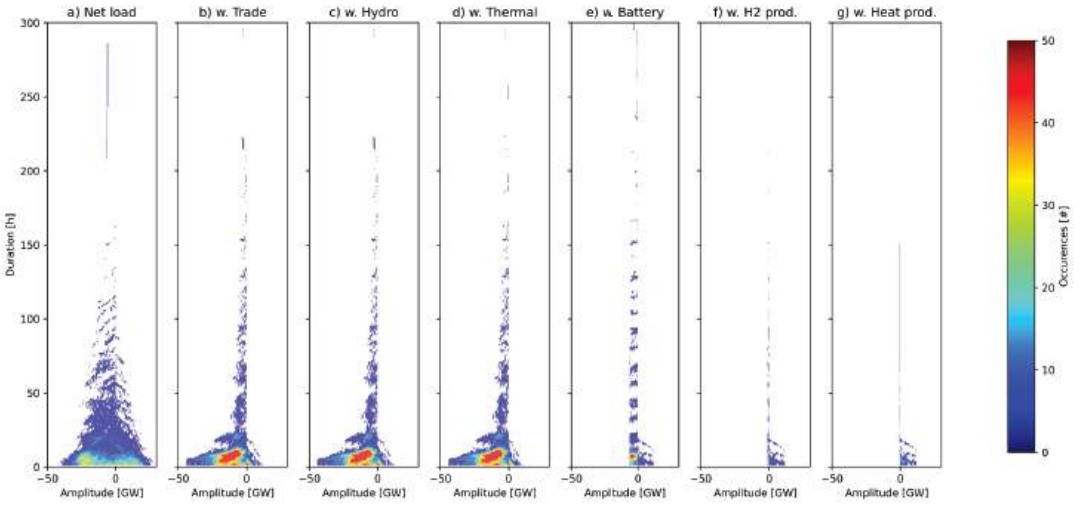

Figure A9. Net load in northern Germany (DE_N) (**a**) reduced by (**b**) trade, (**c**) trade and hydropower, (**d**) trade, hydropower and base load, (**e**) trade, hydropower, base load and batteries, (**f**) trade, hydropower, base load, batteries and adapted hydrogen production and (**g**) trade, hydropower, base load, batteries, adapted hydrogen production and adapted heat production. The color scale indicates number of (#) occurrences and was limited to 50 occurrences, implying that the number of occurrences may be higher in the deep red fields.

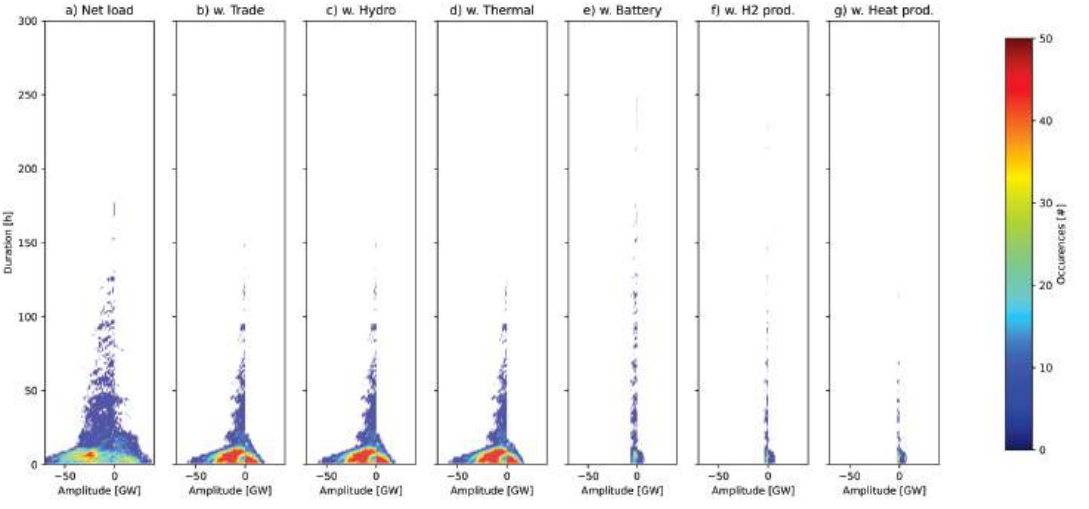

Figure A10. Net load in Belgium, the Netherlands and Luxemburg (BENELUX) (**a**) reduced by (**b**) trade, (**c**) trade and hydropower, (**d**) trade, hydropower and base load, (**e**) trade, hydropower, base load and batteries, (**f**) trade, hydropower, base load, batteries and adapted hydrogen production and (**g**) trade, hydropower, base load, batteries, adapted hydrogen production and adapted heat production. The color scale indicates number of (#) occurrences and was limited to 50 occurrences, implying that the number of occurrences may be higher in the deep red fields.

Appendix C.4 Regions with Access to Hydropower (SE_S, FI, NO1, SE_N, NO_N)

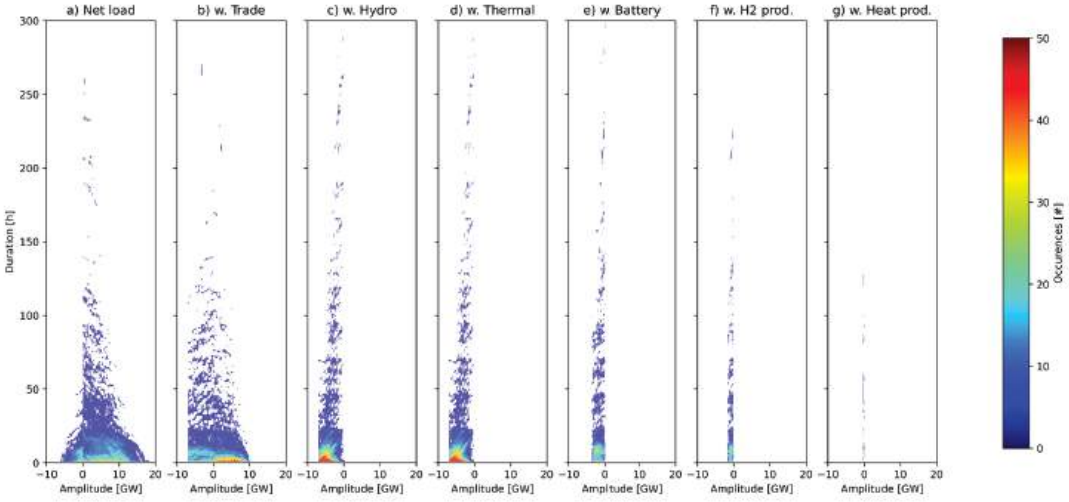

Figure A11. Net load in southern Sweden (SE_S) (**a**) reduced by (**b**) trade, (**c**) trade and hydropower, (**d**) trade, hydropower and base load, (**e**) trade, hydropower, base load and batteries, (**f**) trade, hydropower, base load, batteries and adapted hydrogen production and (**g**) trade, hydropower, base load, batteries, adapted hydrogen production and adapted heat production. The color scale indicates number of (#) occurrences and was limited to 50 occurrences, implying that the number of occurrences may be higher in the deep red fields.

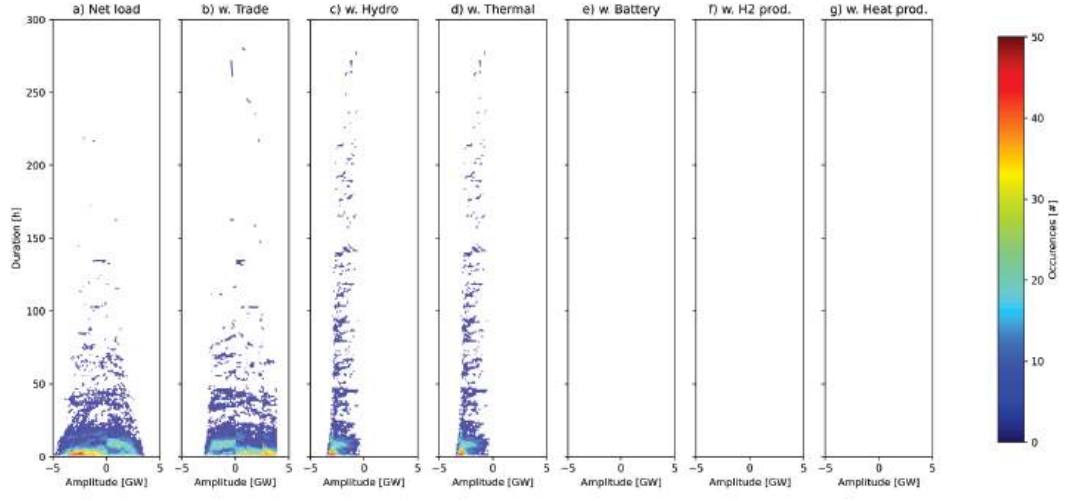

Figure A12. Net load in northern Sweden (SE_N) (**a**) reduced by (**b**) trade, (**c**) trade and hydropower, (**d**) trade, hydropower and base load, (**e**) trade, hydropower, base load and batteries, (**f**) trade, hydropower, base load, batteries and adapted hydrogen production and (**g**) trade, hydropower, base load, batteries, adapted hydrogen production and adapted heat production. The color scale indicates number of (#) occurrences and was limited to 50 occurrences, implying that the number of occurrences may be higher in the deep red fields.

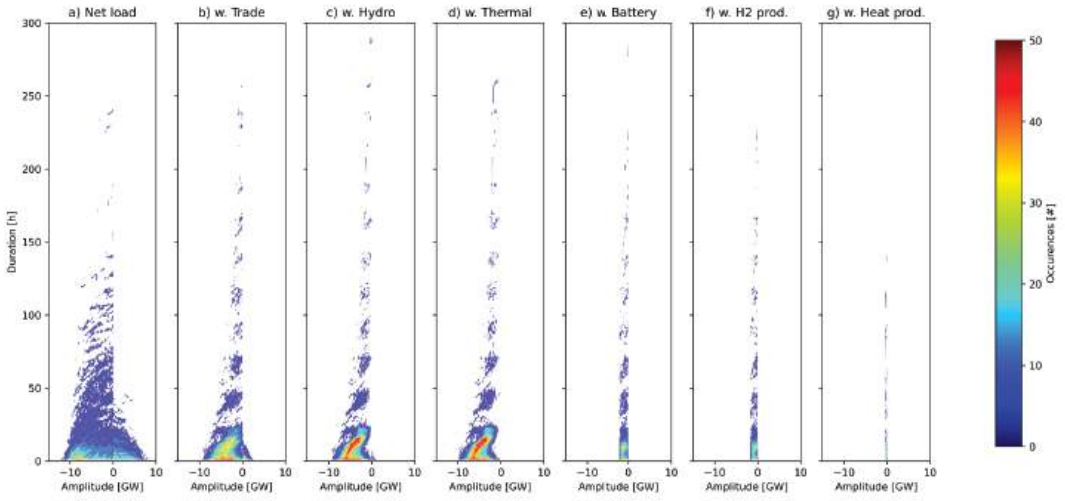

Figure A13. Net load in Finland (FI) (**a**) reduced by (**b**) trade, (**c**) trade and hydropower, (**d**) trade, hydropower and base load, (**e**) trade, hydropower, base load and batteries, (**f**) trade, hydropower, base load, batteries and adapted hydrogen production and (**g**) trade, hydropower, base load, batteries, adapted hydrogen production and adapted heat production. The color scale indicates number of (#) occurrences and was limited to 50 occurrences, implying that the number of occurrences may be higher in the deep red fields.

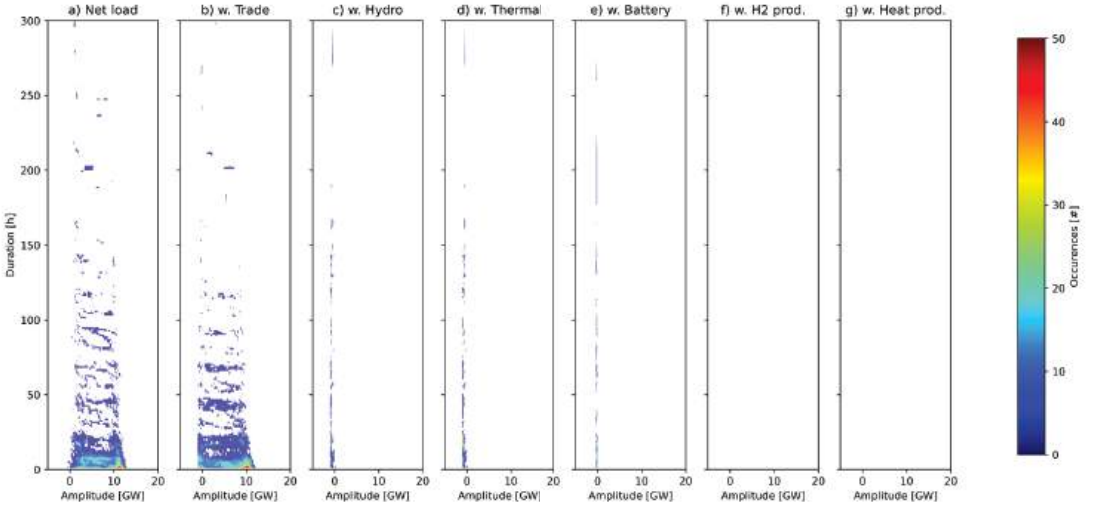

Figure A14. Net load in southern Norway (NO_S) (**a**) reduced by (**b**) trade, (**c**) trade and hydropower, (**d**) trade, hydropower and base load, (**e**) trade, hydropower, base load and batteries, (**f**) trade, hydropower, base load, batteries and adapted hydrogen production and (**g**) trade, hydropower, base load, batteries, adapted hydrogen production and adapted heat production. The color scale indicates number of (#) occurrences and was limited to 50 occurrences, implying that the number of occurrences may be higher in the deep red fields.

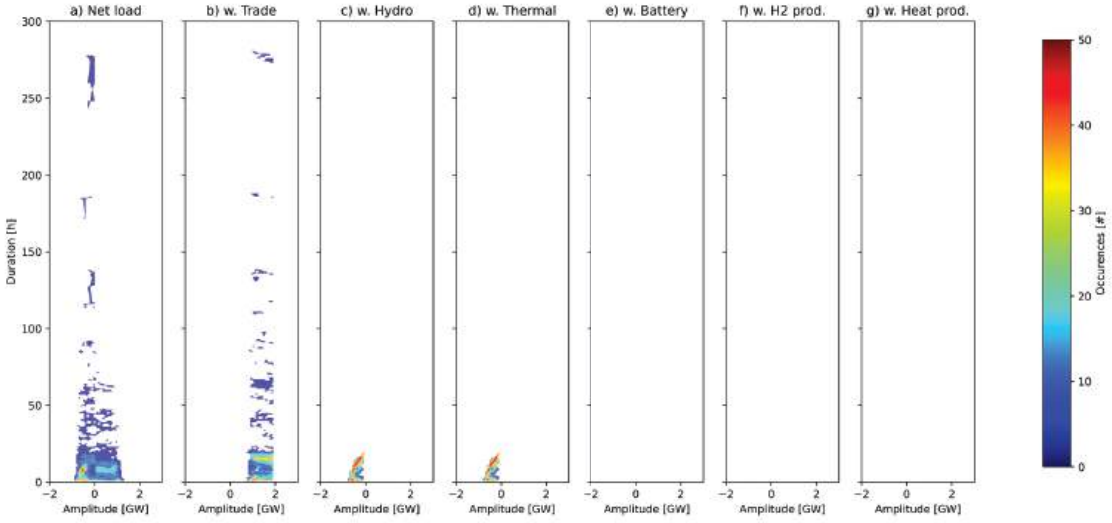

Figure A15. Net load in northern Norway (NO_N) (**a**) reduced by (**b**) trade, (**c**) trade and hydropower, (**d**) trade, hydropower and base load, (**e**) trade, hydropower, base load and batteries, (**f**) trade, hydropower, base load, batteries and adapted hydrogen production and (**g**) trade, hydropower, base load, batteries, adapted hydrogen production and adapted heat production. The color scale indicates number of (#) occurrences and was limited to 50 occurrences, implying that the number of occurrences may be higher in the deep red fields.

References

1. Wråke, M.; Karlsson, K.; Kofoed-Wiuff, A.; Folsland Bolkesjø, T.; Lindroos, T.J.; Hagberg, M.; Bosack Simonsen, M.; Unger, T.; Tennbakk, B.; Ogner Jåstad, E.; et al. *Nordic Clean Energy Scenarios*; Nordic Energy Research: Oslo, Norway, 2021.
2. Göransson, L.; Lehtveer, M.; Nyholm, E.; Taljegard, M.; Walter, V. The Benefit of Collaboration in the North European Electricity System Transition-System and Sector Perspectives. *Energies* **2019**, *12*, 24. [CrossRef]
3. Pursiheimo, E.; Kiviluoma, J. Chapter 12—Analyzing electrification scenarios for the northern European energy system. In *Electrification*; Aalto, P., Ed.; Academic Press: Cambridge, MA, USA, 2021; pp. 271–288.
4. European Commission. *A Clean Planet for All—A European Adapted Long-Term Vision for a Prosperous, Modern, Competitive and Climate Neutral Economy*; European Commission: Brussels, Belgium, 2018.
5. IEA. *Status of Power System Transformation*; International Energy Agency: Paris, France, 2018.
6. Lund, P.D.; Lindgren, J.; Mikkola, J.; Salpakari, J. Review of energy system flexibility measures to enable high levels of variable renewable electricity. *Renew. Sustain. Energy Rev.* **2015**, *45*, 785–807. [CrossRef]
7. Göransson, L.; Johnsson, F. A comparison of variation management strategies for wind power integration in different electricity system contexts. *Wind. Energy* **2018**, *21*, 837–854. [CrossRef]
8. Johansson, V.; Göransson, L. Impacts of variation management on cost-optimal investments in wind power and solar photovoltaics. *Renew. Energy Focus* **2020**, *32*, 10–22. [CrossRef]
9. Denholm, P.; Mai, T. Timescales of energy storage needed for reducing renewable energy curtailment. *Renew. Energy* **2019**, *130*, 388–399. [CrossRef]
10. Nyamdash, B.; Denny, E.; O'Malley, M. The viability of balancing wind generation with large scale energy storage. *Energy Policy* **2010**, *38*, 7200–7208. [CrossRef]
11. Kiviluoma, J.; Rinne, E.; Helistö, N. Comparison of flexibility options to improve the value of variable power generation. *Int. J. Sustain. Energy* **2018**, *37*, 761–781. [CrossRef]
12. Helistö, N.; Kiviluoma, J.; Ikäheimo, J.; Rasku, T.; Rinne, E.; O'Dwyer, C.; Li, R.; Flynn, D. Backbone—An Adaptable Energy Systems Modelling Framework. *Energies* **2019**, *12*, 3388. [CrossRef]
13. IEA. *Harnessing Variable Renewables—A Guide to the Balancing Challenge*; International Energy Agency: Paris, France, 2011.
14. Yasuda, Y.; Carlini, E.M.; Estanqueiro, A.; Eriksen, P.B.; Flynn, D.; Herre, L.F.; Hodge, B.-M.; Holttinen, H.; Koivisto, M.J.; Gómez-Lózaro, E.; et al. Flexibility chart 2.0: An accessible visual tool to evaluate flexibility resources in power systems. *Renew. Sustain. Energy Rev.* **2023**, *174*, 113116. [CrossRef]
15. Heggarty, T.; Bourmaud, J.-Y.; Girard, R.; Kariniotakis, G. Quantifying power system flexibility provision. *Appl. Energy* **2020**, *279*, 115852. [CrossRef]

16. Göransson, L.; Goop, J.; Odenberger, M.; Johnsson, F. Impact of thermal plant cycling on the cost-optimal composition of a regional electricity generation system. *Appl. Energy* **2017**, *197*, 230–240. [CrossRef]
17. Holmér, P.; Ullmark, J.; Göransson, L.; Walter, V.; Johnsson, F. Impacts of thermal energy storage on the management of variable demand and production in electricity and district heating systems: A Swedish case study. *Int. J. Sustain. Energy* **2020**, *39*, 446–464. [CrossRef]
18. Mattsson, N.; Verendel, V.; Hedenus, F.; Reichenberg, L. An autopilot for energy models—Automatic generation of renewable supply curves, hourly capacity factors and hourly synthetic electricity demand for arbitrary world regions. *Energy Strategy Rev.* **2021**, *33*, 100606. [CrossRef]
19. ECMWF. *ERA-Interim u- and v-Components of Horizontal Wind, Surface Solar Radiation Downward, Skin Temperature*; ECMWF: Reading, UK, 2010.
20. DTU. *Global Wind Atlas*; DTU Wind and Energy Systems Group, Ed.; DTU: Lyngby, Denmark, 2018.
21. Gode, J. *Klimatförändringarnas Inverkan På Energisystemet*; Energiforsk: Stockholm, Sweden, 2021.
22. Scharff, R. *Klimatförändringarnas Inverkan På Vatten- Kraftens Produktions- Och Reglerförmåga*; Energiforsk: Stockholm, Sweden, 2023.
23. Nyholm, E. The Role of Swedish Single-Family Dwellings in the Electricity System—The Importance and Impacts of Solar Photovoltaics, Demand Response, and Energy Storage. In *Energy and Environment*; Chalmers University of Technology: Gotheburg, Sweden, 2016.
24. Werner, S. *ECOHEATCOOL Work Package 1*; Euroheat and Power: Brussels, Belgium, 2005.
25. Taljegard, M. Electrification of Road Transport-Implications for the Electricity System; Chalmers: Gothenburg, Sweden. In *Space, Earth and Environment*; Chalmers University of Technology: Gotheburg, Sweden, 2019.
26. Kullingsjö, L.-H.; Karlsson, S. The Swedish Car Movement Data Project. In Proceedings of the European Electric Vehicle Congress, Brussels, Belgium, 19–22 November 2012.
27. Fuchs, G.; Lunz, B.; Leuthold, M.; Sauer, D.U. Overview of Nonelectrochemical Storage Technologies. In *Electrochemical Energy Storage for Renewable Sources and Grid Balancing*; Elsevier: Amsterdam, The Netherlands, 2015; pp. 89–102.
28. Zhao, H.; Wu, Q.; Hu, S.; Xu, H.; Rasmussen, C.N. Review of energy storage system for wind power integration support. *Appl. Energy* **2015**, *137*, 545–553. [CrossRef]
29. Sauer, D.U. Classification of storage systems. In *Electrochemical Energy Storage for Renewable Sources and Grid Balancing*; Elsevier: Amsterdam, The Netherlands, 2015; pp. 13–21.
30. Palizban, O.; Kauhaniemi, K. Energy storage systems in modern grids—Matrix of technologies and applications. *J. Energy Storage* **2016**, *6*, 248–259. [CrossRef]
31. Magnor, D.; Lunz, B.; Sauer, D.U. 'Double Use' of storage systems. In *Electrochemical Energy Storage for Renewable Sources and Grid Balancing*; Elsevier: Amsterdam, The Netherlands, 2015; pp. 453–463.
32. Meng, L.; Zafar, J.; Khadem, S.K.; Collinson, A.; Murchie, K.C.; Coffele, F.; Burt, G.M. Fast Frequency Response from Energy Storage Systems—A Review of Grid Standards, Projects and Technical Issues. *IEEE Trans. Smart Grid* **2020**, *11*, 1566–1581. [CrossRef]
33. Ullmark, J.; Göransson, L.; Chen, P.; Bongiorno, M.; Johnsson, F. Inclusion of frequency control constraints in energy system investment modeling. *Renew. Energy* **2021**, *173*, 249–262. [CrossRef]
34. Ruhnau, O.; Qvist, S. Storage requirements in a 100% renewable electricity system: Extreme events and inter-annual variability. *Environ. Res. Lett.* **2022**, *17*, 044018. [CrossRef]
35. IEA. *Global Energy and Climate Model Documentation 2022*; International Energy Agency: Paris, France, 2022.
36. ENS. *Technology Data—Energy Plants for Electricity and District Heating Generation*; Danish Energy Agency and Energinet: København, Danish, 2016.
37. Hodel, H.; Göransson, L.; Chen, P.; Carlsson, O. Cost Efficient Design of Wind Turbines from An Electricity System's Perspective. 2023, *submitted for publication*.

solar

MDPI

Article

Sheet Metal Design Approach for 3D Shaped Facade Elements with Integrated Solar Thermal Functionality

Peter Scholz [1,*], Dieter Weise [1], Linda Schmidt [2], Martin Dembski [2], Alexander Stahr [2], Martin Dix [1], Florin Duminica [3], Sebastien Le Craz [3] and Jiri Koziorek [4]

[1] Department of Sheet Metal Forming, Fraunhofer Institute for Machine Tools and Forming Technology, 09126 Chemnitz, Germany
[2] Hochschule für Technik, Wirtschaft und Kultur Leipzig HTWK, 04277 Leipzig, Germany
[3] Department Advanced Surface and Smart Solutions, CRM Group, 4000 Liege, Belgium
[4] Department of Cybernetics and Biomedical Engineering, VSB—Technical University of Ostrava, 70800 Ostrava, Czech Republic
* Correspondence: peter.scholz@iwu.fraunhofer.de

Abstract: This paper provides an overview of the development of a 3D formed and metal-based facade element that combines a custom design and solar thermal functionality. To achieve this, a novel simplified solar thermal collector structure was developed using formed sheet metal half-shells with an integrated channel structure on the inside and a special absorber coating on the outside. The sheet metal half-shells were manufactured by highly innovative incremental sheet forming (ISF), which allows seamless integration into existing facades. As a part of this paper, the initial test results on thermal efficiency and the energy accumulation of the new collector type are presented.

Keywords: absorbance coating; facade elements; sheet metal design; solar thermal collector

Citation: Scholz, P.; Weise, D.; Schmidt, L.; Dembski, M.; Stahr, A.; Dix, M.; Duminica, F.; Le Craz, S.; Koziorek, J. Sheet Metal Design Approach for 3D Shaped Facade Elements with Integrated Solar Thermal Functionality. *Solar* **2023**, *3*, 213–228. https://doi.org/10.3390/solar3020014

Academic Editors: Luis Hernández-Callejo and Jürgen Heinz Werner

Received: 13 January 2023
Revised: 3 April 2023
Accepted: 6 April 2023
Published: 13 April 2023

1. Introduction

The reduction of harmful greenhouse gases is one of the biggest challenges of our time. The use of unlimited available solar thermal power as renewable energy can help to support efforts to reduce CO_2 emissions worldwide. More than 40% of the total energy consumption in Europe can be allocated to heating, hot water, and illumination [1]. This corresponds to almost 20% of the total CO_2 emissions. Especially in the building industry, reducing CO_2 emissions is one of the main drivers. By using modern building envelopes, the required energy for heating and cooling can be minimized [2]. The major goal is the realization of affordable zero-energy buildings. One effective way of achieving these objectives is the use of solar thermal energy. The solar radiation at our latitudes is perfectly suited for thermal use.

In central Europe, solar radiation produces, on a 1 m^2 area, 1000 kWh/year to 1100 kWh/year [3], which is equivalent to 100 L of fuel oil or 100 m^3 of natural gas. For this reason, the building sector has a strongly growing interest in facade-integrated solar thermal absorbers, which shall be presented in this paper.

A broad range of solar thermal collectors have been available on the market for decades worldwide. These products are credible and generally made to a high technical standard, especially in Europe with a homogeneous market. However, there is a shortage in the field of solar thermal products that are suited for building envelope integration to create high-quality architecture [4,5]. Functional and constructive aspects, together with aesthetics, have to be considered. State-of-the-art solar thermal collectors are not flexible in shape and size due to the hydraulic fluid circuits fixed to solar absorbers. Architectural requests for design freedom require the hydraulic system concept to be redesigned, which is generally difficult and expensive for conventional means of production. Conventional production methods for absorbers limit the flexibility in collector design [6] and such a lack

of flexibility significantly reduces the potential application of solar thermal systems [7]. The production of solar collectors in sheet metal half-shell design by means of hydroforming was investigated in the European Union (EU) project with the acronym "BIONICOL" [8] and in "Industrielle Gemeinschaftsforschung" (IGF) project No. 339 ZN [9]. However, curved surfaces cannot be obtained with the shown technologies and the channel structures can only be manufactured on both sides, which has a disadvantageous effect on the design freedom of the facade. The integration of flat-plate solar thermal collectors is only possible for opaque envelopes (roofs and facades) so far [10]. The structure of evacuated tubes allows mounting on transparent envelopes as sun shading, but this kind of application is rare. The application potential of incremental sheet forming (ISF) in solar absorbers was demonstrated in [11] by the production of absorber lamellae using incremental forming technology.

The thickness of solar collectors affects their integration, especially for facades. Thick solar thermal collectors are difficult to implement as functional elements or as sun shading. The appearance of solar collectors is affected by the glass (glazed collector) and absorber surface treatment. State-of-art collectors apply highly transparent, low-iron glass for glazing and black or dark-blue spectrally selective coatings with high absorptance (0.95) and low emittance (0.05). Solar collectors integrated into facades are more conspicuous than collectors installed on rooftops. Many studies and surveys have shown that architects prefer a large variety of absorber colors [12], and they even regard the possibility of a custom color choice as essential. Manufacturers can meet the demand for a variety of absorber colors by means of solar paint coatings, but such collectors show considerably reduced thermal performance compared with quality selective coatings in the usual solar collectors commercially available in Europe [13].

This paper presents a new design of a solar thermal collector. The focus of this paper is fabrication with ISF, concepts for integration into facade systems, possible design arrangements, and the development of the absorber coating. Furthermore, initial results on the thermal efficiency and performance of the new collector type are presented and evaluated.

2. Materials and Methods

2.1. Principal Collector Design

Figure 1 shows the layout of the developed collector design, which consists of two layers of cold-rolled deep-drawing steel DC06 (t = 0.8 mm) joined together in a fluid-tight manner by laser welding.

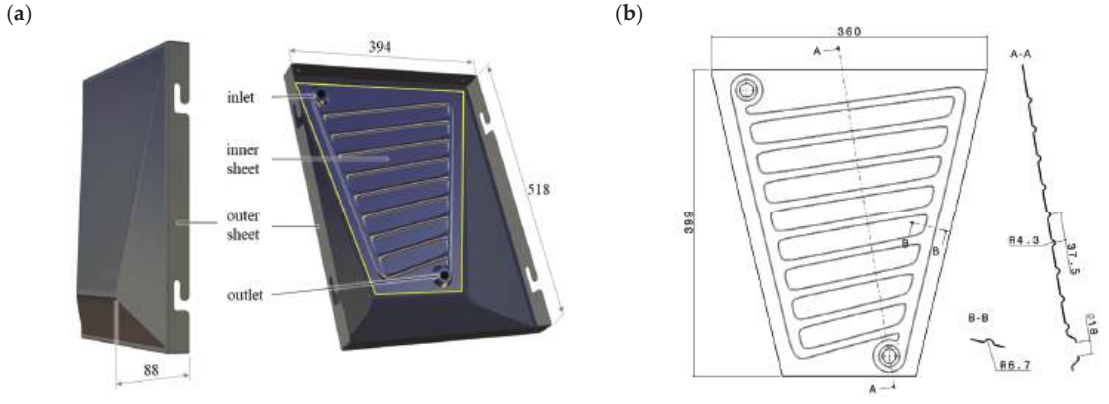

Figure 1. Principal collector design: (**a**) CAD model of the assembled collector and (**b**) drawing of the inner sheet with the channel structure.

The three-dimensional shaped outer sheet is designed as a closed cassette with integrated notches for hooking into the façade's substructure. To integrate the solar thermal functionality, the flat inner sheet has a two-dimensional channel structure and is attached to the outer sheet. The use of this simple geometry for the inner sheet ensures a good fit between the two components, which is essential for the joining process. The channel structure chosen was a harp structure, which has also been used in commercially available flat plate collectors. With this structure, the area to be cooled can be efficiently passed through with low pressure loss at the same time. For hydraulic connection, parallel planar surfaces were proposed in the inlet and outlet areas for the easy integration of conventional fittings.

The representative design of the geometry of the exterior sheet was determined by the results of the solar gain analysis, the architectural design boundaries, and the constraints of the forming process, which are described in the following sections.

2.2. Architectural Aspects and Facade Integration

2.2.1. Necessity of Research into Solar Thermal Facade Elements in Architecture

Endeavoring to be part of the solution, the publicly funded research project "FutureFacade" strives to do its part for climate protection in the construction industry by utilizing the inextricable connection to resource and energy efficiency. The integration of solar thermal energy into facades holds great potential for generating solar yields that have, so far, remained largely untapped. Although a study by the Leibniz Institute for Ecological and Regional Development (IÖR) shows that a total of 12,000 km^2 of facade area in Germany can be used for solar energy, no architecturally sophisticated solar thermal facade elements exist yet [14,15]. The combination of solar thermal energy with inner-city building surfaces can be used for domestic hot water, heating support, and cooling. Regarding unforeseeable developments in the cost of all fuels, solar thermal energy offers a sustainable and cost-effective alternative.

2.2.2. Architectural Innovation

While conventional collectors are visually recognizable by the glass and the dark-blue absorber surface, more complex appearances can be created using mono-material panels made of metal. Hence, through innovating solar modules, a novel structure was created in this project. Linking architectural aspiration and sustainability was paramount. The functional integration, which was not visible on the outside, was achieved by two combined sheet metal panels invisibly welded together.

2.2.3. Design Criteria for the Collector Geometry based on Solar Thermal Aspects

Optimizing the geometry of the outer panel was most important in order to adapt the modules as efficiently as possible to the irradiation conditions using site-specific weather data while also taking into account the manufacturing constraints (e.g., maximum wall angle and minimal radius). The adjustment of the module geometry and, thus, the solar-active area and the irradiation angle was regulated by a digital parametric design tool. This allowed the yields to be controlled and optimized, which is a pioneering development in sustainable building construction.

The solar gain analysis showed that the chosen shape could provide 792 kWh/m^2 per year for a southern orientation using the Chemnitz, Germany, region as an example (Figure 2). Different rectangular-based shapes were tested throughout the project. The analysis showed that flat collectors had the lowest potential for solar gain. Plenty of design studies have been conducted. Round, triangular, rectangular, and hexagonal formats were also tested as irregular freeform shapes. In the end, the final polygonal shape lent itself best to the chosen forming technique and the solar gains that were to be achieved. The rectangular base allowed standardized substructures to be used. The rather simple basic shape contained a lot of freedom in the arrangement and variation of the geometry as a pattern, ensuring that design freedom could be kept (Figure 3). Compared with the chosen

polygonal shape, there would be a loss of 165 kWh/m^2 per year. Round double-curved shapes had the best solar-gain effect (809 kWh/m^2 per year), but were excluded due to the manufacturing technique after some forming tests, as there was a large spring-back effect after forming. Therefore, the polygonal shape was optimal from all tested design studies (Figure 2).

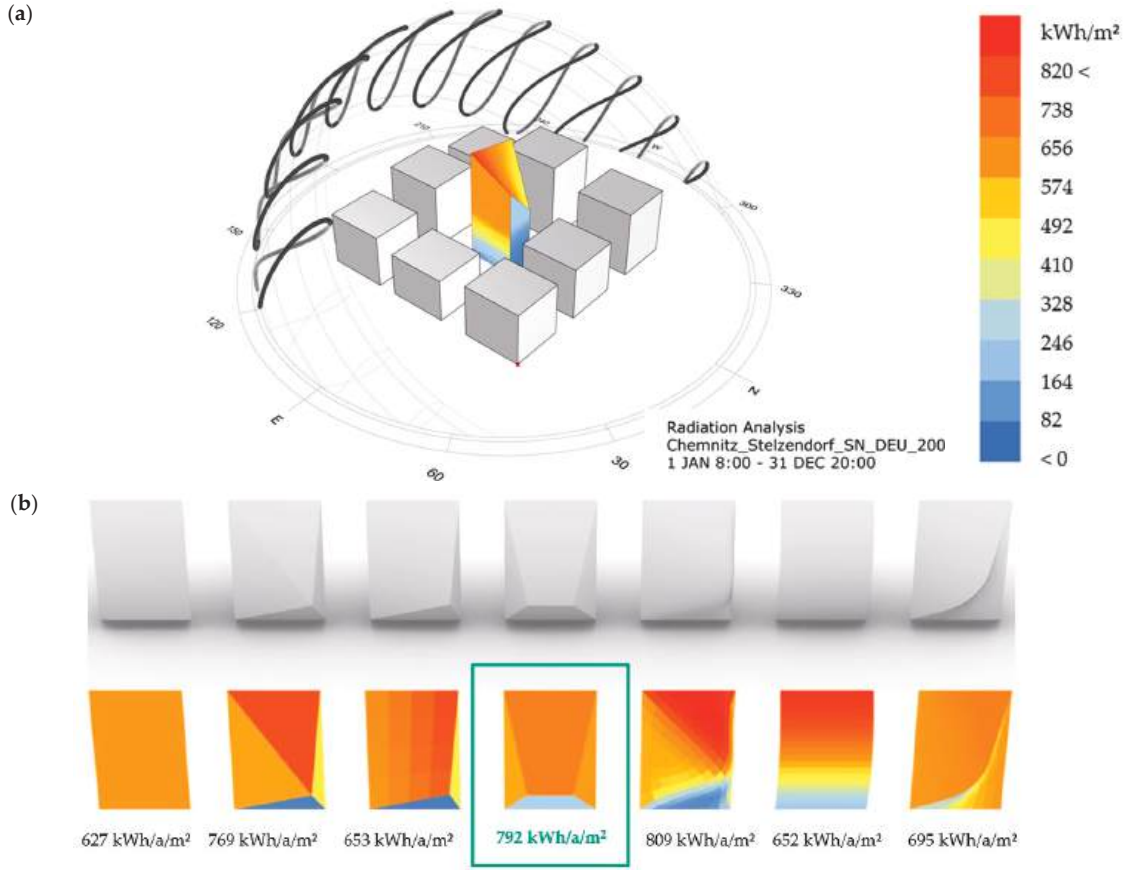

Figure 2. Solar gain analysis (**a**) of different shapes (**b**) with a rectangular base performed with the energy-simulation engine EnergyPlus™ in combination with the Grasshopper plugin Ladybug for Rhinoceros® 3D.

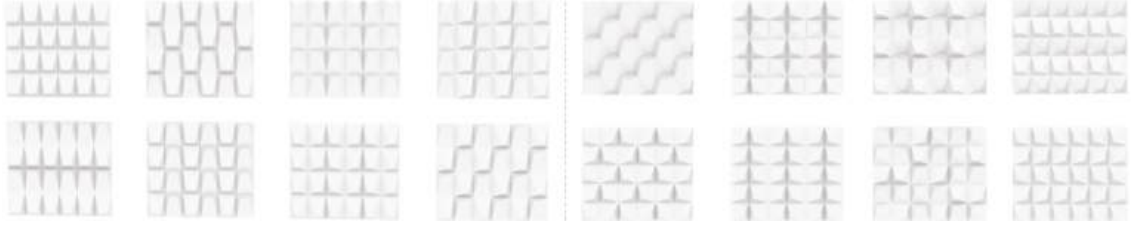

Figure 3. Variations and patterns of polygonal panels.

2.2.4. Facade Construction and Hydraulic System

The facade panel was designed as a simple standardized cassette and could thus be hooked into the bolt suspension. (Figure 4b). Owing to the standardized system used, it was possible to use facade (under-) constructions from various manufacturers. (Figure 4a). By using a standardized substructure, the effort required for assembly and maintenance can be decreased and the economic efficiency can be increased.

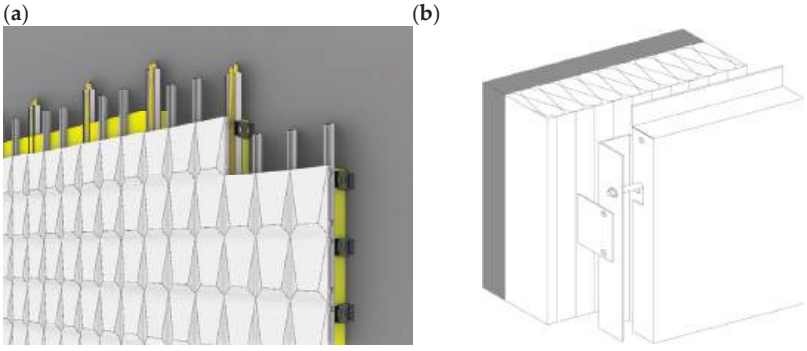

Figure 4. Visualization of facade construction (**a**) and under-construction detail (**b**).

The facade panel was a mono-material system. There was an outer panel and an inner panel welded together. The inner panel represented the channel structure, which was designed as a common harp shape. (Figure 5a) With regard to the most energy-efficient design of the fluid channels within the facade elements, computational fluid dynamics (CFD) simulations were carried out to achieve optimized performance for the facade element.

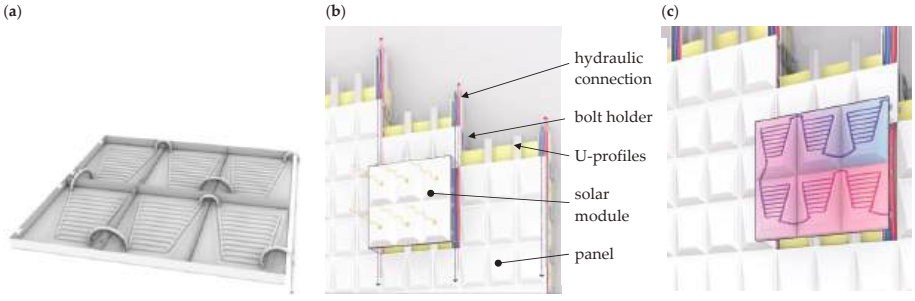

Figure 5. Schematic illustration of the addition of the panels (**a**), schematic illustration of facade construction (**b**), and schematic illustration of panel function (**c**).

To build a facade system that can operate as a power plant, the panels were connected in series and formed one module when connected in a mirrored position. (Figure 5c). One module at a time was then connected to the vertical cable routing. (Figure 5b). A pump ensured the circulation of the fluid in the facade. A heat exchanger provided the energy to the heating units, so the facade system became its own sustainable power plant to harvest renewable heat.

2.2.5. Architectural Results

The designed panel holds the potential to create new appearances for urban spaces and positively influence the use of renewable energy. (Figure 6) The panel can be used for new construction and existing projects. It can be used on large-scale installations in rural areas, as well as on urban facades, and thus has multiple applications. Therefore,

the project is a huge step in Mono-Material Design, facade design, architecture, and the building industry and renewable energies in general.

Figure 6. Visualization of a sample façade.

2.3. Demonstrator Manufacturing

2.3.1. Forming

For the manufacturing of the solar collector sheets, incremental sheet metal forming (ISF) in combination with subsequently performed bending operations (only for the outer sheet) was used. With ISF, the final part of the geometry is successively formed by the CNC-controlled movement of a forming stylus over a counter die (Figure 7a). In comparison with conventional forming methods (e.g., deep drawing), this reduces tool costs and the time required to achieve the first finished part.

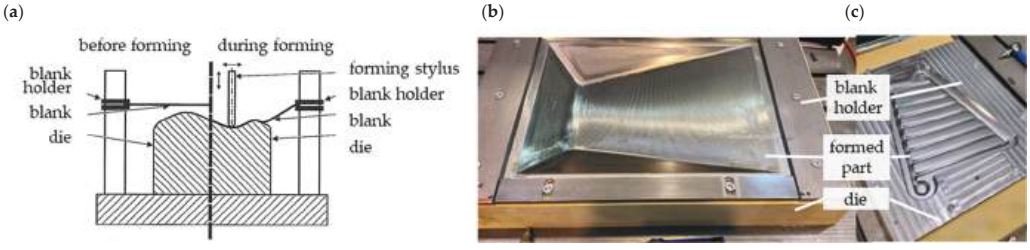

Figure 7. Incremental sheet forming: (**a**) process principle, (**b**) clamped outer sheet after forming, and (**c**) clamped inner sheet after forming.

For the forming of the test components, a polyurethane counter-die (material: obomodulan® 1600 sand) was used, in which the cut-to-size sheets were clamped by means of a blank holder (Figure 7b,c). As a lubricant, Raziol CLF 125F was used for all forming trials.

To avoid wrinkling during forming, the outer sheet was formed in two steps. In the first step, a stylus diameter of 100 mm with a z-increment of 0.2 mm was used. In the second step, the final shape was formed with a stylus diameter of 6 mm and an increment of 0.2 mm. For both steps, a z-constant tool path in helix design was chosen, with a total forming time of approx. 2 h. After unclamping, the edges of the outer sheet were folded and mechanically joined at the corners to create the closed cassette design shown in Figure 1.

The shape of the inner sheet could be formed in one step with a forming stylus diameter of 6 mm, a z-increment of 0.2 mm, and a forming time of approx. 45 min, also by using a z-constant tool path in helix design. With these parameters, the inner and outer sheets could be successfully formed without failures. For both geometries, the global shape deviation was approx. 1 mm compared with the original CAD geometry which is within the common tolerances for facade panels.

2.3.2. Joining

A welding Nd:YAG laser of 3 kW mounted on a robot was used for the assembly of the inner and outer formed sheets. The experimental set-up is presented in Figure 8a. Specific tools were used to optimize the contact between the welded surfaces and to prevent gaps from forming between the steel sheets; otherwise, the upper sheet could be pierced by the laser beam. The first tool (Figure 8b) was developed to allow the welding of the outer contour of deformed panels, and the second one (Figure 8c) was designed for the welding of lines between the channels, allowing the passage of fluid through the drawn network and avoiding the swelling of the panels. Finally, the fluid connectors were fixed using manual tungsten inert gas (TIG) welding (Figure 8d).

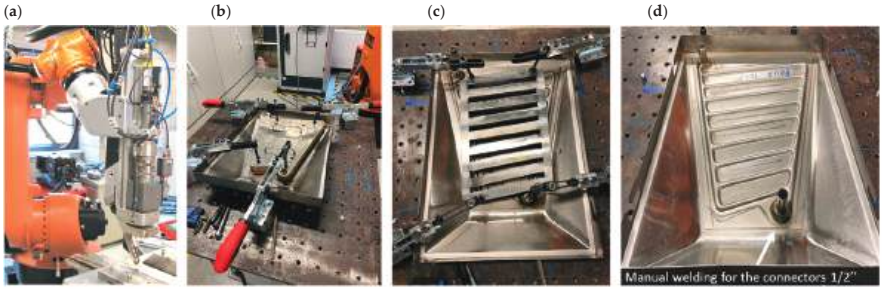

Figure 8. Laser welding setup: (**a**) laser head mounted on a robot, (**b**) clamped tool for outer contour, (**c**) clamped tool for inner channels; (**d**) TIG welding for fluid connectors.

Laser welding requires a compromise between the thermal load and the welding speed in order to limit damage to the outer sheet's steel surface. The laser beam must cross the top sheet and penetrate the bottom one without crossing it. Figure 9a shows a cross-section micrograph of the welding of two steel sheets. The focal spot is in the range of 0.8 mm to 1 mm for the following welding parameters: laser head speed of 3 m/min, steel sheet thickness of 0.8 mm, and laser power of 1.4 kW. Various parameters, such as the accuracy of the robot trajectory, the variation in the steel thickness generated by the incremental forming, as well as the distance between the steel sheets, can influence the welding beam penetration, leading to marks on the back side of the panel. Figure 9b (left) shows the impact of the welding beam on the back side of the panel. However, additional surface treatment, such as sandblasting, can remove the oxides generated by the laser beam overheating and can also considerably decrease the thermal stress near the welding lines. Figure 9b (right) shows the same surface as Figure 9b (left) after sandblasting.

A potential optimization requires an increase in the thickness of the back metal sheet to decrease the thermal effect and to increase the welding process parameters. However, for this project, the choice to simplify the assembly system drove the use of the same material and same thickness for both the inner and outer shaped steel sheets.

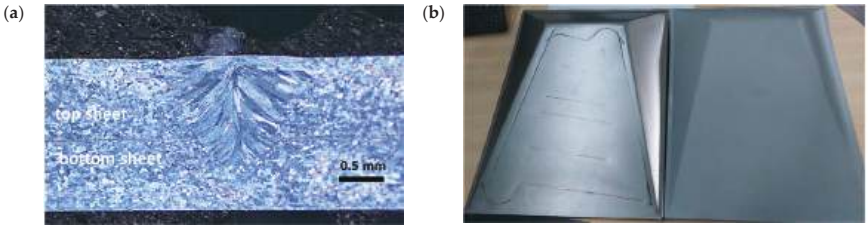

Figure 9. (**a**) Cross-section micrograph of the welding of two steel sheets and (**b**) welding lines on the front side of the panel: as initially welded (left) and after sand-basting (right).

2.3.3. Strategies and Concepts for Absorbing Coatings

The design of a non-glazed solar absorber for practical application requires the development of a robust coating applied by low-cost techniques. This coating must exhibit high absorption efficiency in the ultraviolet and visible regions of the solar radiation spectrum. Therefore, the reflectance should be minimized in these regions of the solar spectrum. Additionally, the loss of heat to the surroundings via convection or conduction should be reduced as much as possible. Thus, there are conflicting requirements for strong absorption in the solar spectrum, with minimum emission in the infrared range. The use of deep-drawing steel DC06 as a substrate requires additional corrosion protection. The outer formed steel sheet was protected by an 80 µm-thick aluminum coating deposited by the twin arc-wire thermal spray technique. The role of this additional coating is to prevent steel corrosion in case of surface scratches during the manipulation of the panels. Thermally sprayed aluminum, in combination with organic and ceramic coatings, is a common method used for corrosion protection for bridges, ships, and oil and gas installations. These systems are supposed to provide a long lifetime (>20 years) and, with that, be both cost-effective and environmentally friendly [16]. The sand-blasting used to remove the welding defects on the outer steel formed surface is a convenient surface treatment for the thermal spray arc-wire coating of aluminum. The twin arc-wire system was the PERFECT Spray from SMS Group, Düsseldorf, Germany. The typical conditions for arc spraying were arc parameters of 28 V and 90 A, and a wire speed of 2 m/min. The diameter of the aluminum wire was 1.6 mm. The coating was sprayed uniformly over all of the surface of the outer formed steel sheet.

A black absorbing coating was applied to the outer formed steel sheet by spraying, followed by curing at 300 °C. The benefits of such surfaces are their comparative simplicity to produce and the potential for cost-effectiveness. This novel coating chemistry combines high solar-absorbing performance, high thermal resistance to withstand excessive heat from the metal surface, and good resistance to UV and humid conditions to ensure a long service life. The coating thickness can be controlled in the range of a few micrometers to several tens of microns by using several steps of spraying and drying. The reflectance spectrum of the coating deposited as a solar absorber is presented in Figure 10. The solar absorptance in the UV-VIS-NIR spectra is 95% and can slightly change depending on the surface roughness and the coating thickness. The emissivity of the coating was relatively high, as the solar absorbance was low in the NIR region of the spectrum, leading to the solar absorber exhibiting non-selective behavior.

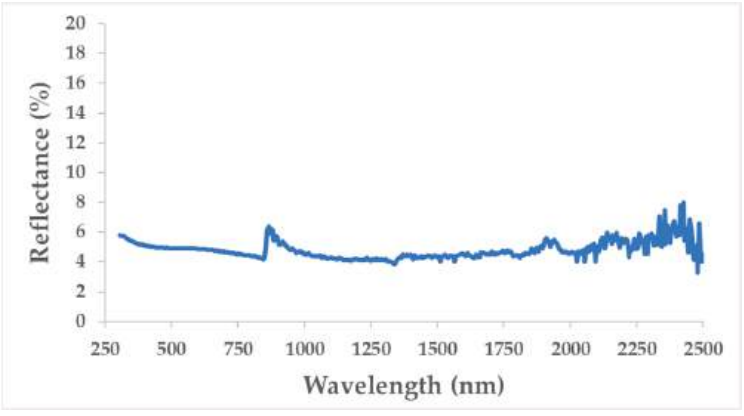

Figure 10. Reflectance spectrum of the silica–carbon sol-gel coating applied as the solar absorber.

2.4. Collector Testing Setup

A solar thermal collector integrating incremental formed panels coated with sol-gel absorbing layers was manufactured for thermal testing. The collector contained eight

panels to generate a surface of 1.6 m^2, comparable to solar thermal collectors available on the market. Figure 11a shows a view of the rear side of the solar collector as manufactured, while Figure 11b shows the same view with insulation. The insulation material installed on the back of the solar panels was PIR foam boards laminated with aluminum foil, 4 cm thick, from IKO Enertherm (thermal conductivity 0.022 W/m·K). The flexible pipes were insulated with polyethylene slotted-pipe lagging (inner diameter 15 mm, wall thickness 13 mm, and thermal conductivity 0.036 W/m·K). Leakage tests were performed to confirm the quality of the welding and the connections of the flexible fluid pipes.

(**a**) (**b**)

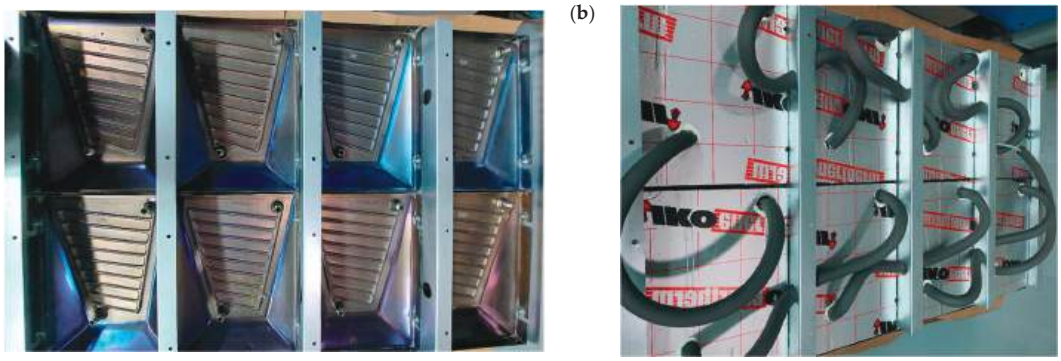

Figure 11. Pictures of the solar collector as manufactured without insulation (**a**) and with rear insulation (**b**).

3. Collector Characterization

A schematic diagram of the experimental set-up is presented in Figure 12. This system provides the fluid to the thermal panels via insulated pipes equipped with measurement probes and a circulator. The probes are placed directly at the inlet and outlet of the panel in order to minimize the losses and errors of measurements related to the pipes. The flow rate is adjusted via a manual valve in series on the sample supply circuit. The temperatures are measured at the inlet and outlet of the panel via thermocouples. In order to achieve very good stability for the inlet temperature, the measuring system has a large buffer tank and an internal temperature regulation system. This system is cooled via an external water cooling unit (chiller). The storage tank is equipped with a water-mixing unit to guarantee the homogeneity of the temperature. The heat output of the panel is determined by considering the characteristics of the fluid, the temperature variation, and the flow rate. The thermal conversion efficiencies of the panel are determined by controlling the flux density of the radiation source and knowing the active surface of the panel.

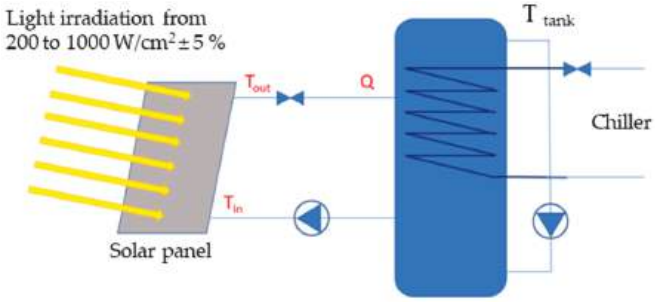

Figure 12. Schematic diagram of experimental test for thermal characterization.

The thermal performance tests were carried out in collaboration with ELIOSYS SA, Liege, Belgium. The investigated heat transfer fluid was water without glycol. As the thermal characteristics of the thermal solar collector were multifactorial, we decided to fix certain parameters. The sample inlet temperature was fixed at room temperature to avoid losses between the pipes and the environment. The measurement of the ambient temperature was carried out in a ventilated enclosure and by obscuring solar irradiance. The measurement time was at least 15 min in steady state. The irradiance measurement was carried out during all tests using a calibrated pyranometer and the thermal environment was controlled by a pyrgeometer. The stability of the irradiation was 0.1% for the duration of the test. Figure 13a shows the experimental setup. Knowing the characteristics of the heat transfer fluid, temperature variations, and flow rate, it was possible to determine the heat output of the system. By controlling the stability of the surface power of the radiation source and knowing the active surface of the sample, it was possible to calculate the thermal conversion efficiencies of the sample. The source of the irradiation was a continuous solar simulator capable of creating irradiation of 200 W/m^2 to 1100 W/m^2 with a maximum variation of less than 1% over 1 h. The spectrum of this simulator was classified B for the wavelength from 800 nm to 900 nm and A for all other wavelengths according to IEC 60904-9 [17].

(**a**)

(**b**)

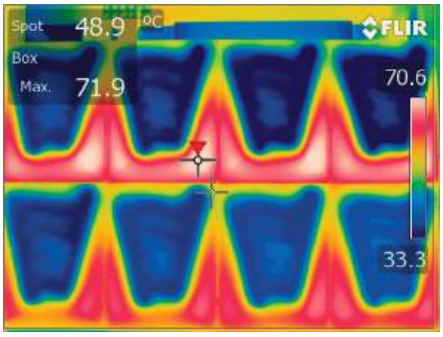

Figure 13. Experimental setup, including the solar collector and irradiance lamps (**a**) and infrared camera image of the solar collector in operation (**b**).

Figure 13b shows an example of thermal imaging, helping to visualize the interconnection of panels. The first panel (top right) was cooler than the last panel in the chain (bottom right). The irradiation power was fixed at 1000 W/m^2 and the water temperature input was fixed at 30 °C +/− 0.2 °C in the panel located at the top-right and exits at the temperature given at the bottom-right. Outside the cooled areas of the panels, a significant increase in temperature was detected, contributed by thermal conduction to the increase in fluid temperature.

3.1. Thermal Power

The thermal power of the collector was determined for various irradiance values (Figure 14a). For a typical irradiance of 1000 W/m^2 and a cooling water flow of 3.7 L/min, the total output power of the collector was 745 W/m^2. This graph also shows that the thermal conversion was better at low irradiance than at high irradiance. This phenomenon was slight and mainly originated from first- and second-order thermal losses, which increased with the temperature difference between the collector and the environment. The tilt angle of the collector significantly influenced the thermal power, as presented in Figure 14b). Indeed, the installation of the collector in a vertical orientation decreased the output power to around 17% compared with the horizontal orientation.

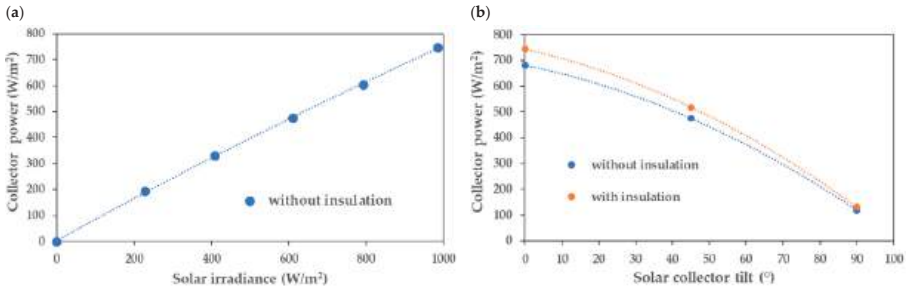

Figure 14. Variation in the thermal power of the collector versus the irradiance for a constant water flow rate of 3.7 L/min (**a**) and variation in the thermal power versus the irradiance angle (**b**).

3.2. Thermal Efficiency

The European standard EN 12975 [18] defines the efficiency η of a thermal collector on the basis of four parameters according to Equations (1) and (2):

$$\eta = \eta_0 \left(\frac{a_1 \cdot \Delta T}{E_0} \right) - \left(\frac{a_2 \cdot \Delta T^2}{E_0} \right) \quad (1)$$

$$\Delta T = T_{water\ out} - T_{water\ in} \quad (2)$$

where:

η—collector efficiency;
η_0—optical efficiency;
a_1 and a_2—heat loss coefficients;
E_0—solar radiation;
ΔT—Temperature difference of the solar fluid between the inlet and outlet of the collector.

The overall efficiency η is, therefore, not a single value, but a characteristic curve. The optical efficiency η_0 represents the maximum efficiency of the thermal collector when the temperature of the fluid is at ambient temperature (no thermal losses). Measured under standardized test conditions (AM1.5 spectrum, solar irradiation E_0 = 1000 W/m^2, perpendicular to the sensor), the efficiency of a thermal collector depends on the properties of the glazing and/or the selectivity of the absorber. Figure 15 shows the variation in the collector efficiency as a function of the flow rate of the cooling fluid. The thermal insulation of the collector slightly influenced its efficiency. On the characteristic curve, the stagnation temperature of the collector was defined as the temperature difference at which the solar gains could not compensate for the thermal losses.

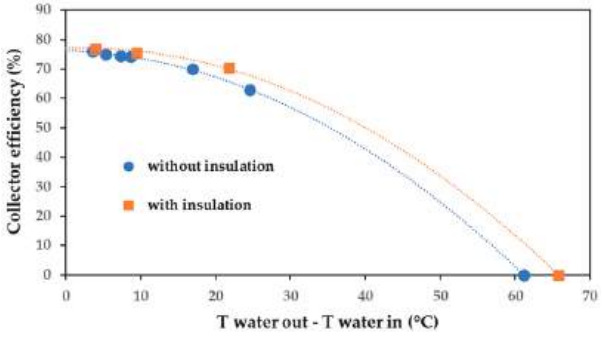

Figure 15. Collector efficiency with and without back insulation for E_0 = 1000 W/m^2.

4. Economic Analysis

An economic feasibility study was carried out to estimate the manufacturing costs of the new type of collector. To show the influence of the forming technology used on the total manufacturing costs, ISF was compared with a conventional deep drawing for quantities n of 1 and 1000 pieces.

The starting point for the cost calculation was the scaled collector geometry shown in Figure 1 and the consideration of the process chain described in Figure 16.

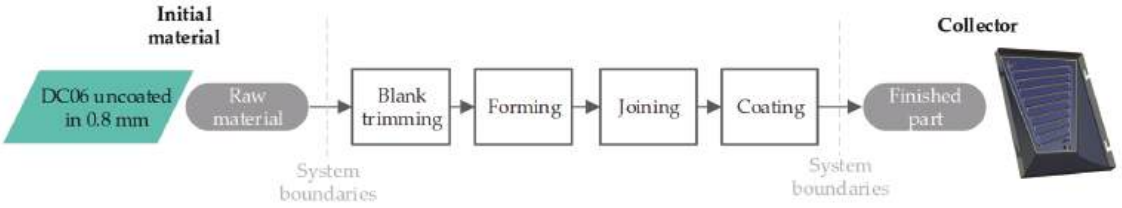

Figure 16. Simplified process chain for the manufacture of the collector.

In this simplified representation of the manufacturing process, the steps of the single-part production of the inner and outer sheets are summarized in the first three superordinate processes of blank trimming, forming, and trimming.

In addition to the main forming costs, the one-time costs for the formation of simulation (deep drawing), as well as the path generation (ISF), are included in the forming process step. All trimming and joining operations were performed using a laser. The coating process itself was divided into the sub-processes of corrosion protection and solar coating.

The assumed boundary conditions and the determined costs for each (sub-)process step are given in Table 1.

Table 1. Boundary conditions and detailed cost distribution by process step for collector-manufacturing depending on the formation technology and quantity *n*.

Process	Sub Process	ISF		Deep Drawing	
		$n = 1$	$n = 1000$	$n = 1$	$n = 1000$
Raw material (inner + outer sheet)	-	≈16 €		≈16 €	
Forming (inner + outer sheet)	Simulation (one-time)	-		≈800 €	
	Tool-path generation (one time)	≈200 €		-	
	Tooling costs (one time)	≈1500 €		≈20,000 €	
	Manufacturing time per collector	≈2.9 h		≈0.09 h	
	Forming cost per collector	≈292 €		≈22 €	
	Total forming cost per collector	≈2192 €	≈294 €	≈21,622 €	≈43 €
Trimming (inner + outer sheet)	Jig costs (one-time)	≈250 €		≈250 €	
	Laser trimming cost per collector	≈4.20 €		≈4.20 €	
	Total trimming cost per collector	≈254 €	≈5 €	≈254 €	≈5 €
Joining	Total joining cost per collector	≈270 €	≈25 €	≈270 €	≈25 €
Coating	Costs of corrosion protection (Al-Zn)	≈245 €	≈20 €	≈245 €	≈20 €
	Costs of solar coating (sol-gel)	≈37 €	≈17 €	≈37 €	≈17 €
	Total coating cost per collector	≈282 €	≈37 €	≈282 €	≈37 €
Total manufacturing costs per collector		≈3014 €	≈376 €	22,444 €	126 €

The results of the process chain analysis show that the formation and associated tooling investment costs were the drivers for all process variants investigated. As expected, for small quantities, ISF can take advantage of its universal forming stylus and low overall tooling costs. With total manufacturing costs per collector of approx. 3014 € for a quantity of one, the costs of ISF were 87% lower compared with the use of conventional deep-drawing technology. In contrast, deep drawing has advantages for larger quantities due to the significantly short process times. When considering a number of 1000 pieces, the unit price per collector of 126 € for the deep drawing variant was 33% lower than that of the ISF variant. For large quantities, conventional forming is clearly preferable. In the case of prototypes or small quantities, however, ISF is an interesting alternative. In this specific case, the break-even would be at 73 collectors. From this point on, the manufacturing costs for deep drawing are lower than those for ISF.

In view of the large-scale production capability of the collector type presented, the graphical representation of the cost distribution in Table 2 shows that, in addition to formation, coating and joining account for the largest shares in terms of total costs. In the deep drawing scenario at a quantity of n = 1000, the share of formation is approx. 34%, followed by coating (≈29%) and joining (≈20%).

Table 2. Overview of the estimated manufacturing costs per collector depending on the forming technology and quantity *n*.

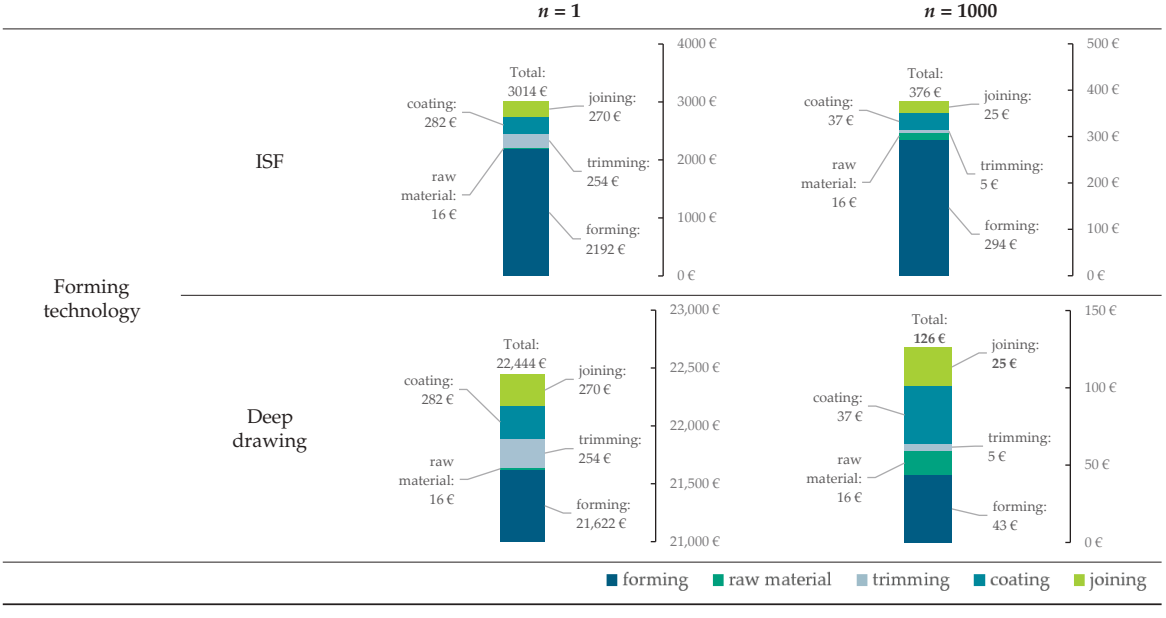

If the costs are related to the collector area, the costs for the new collector type were approx. 625 €/m^2 under the assumptions made. In combination with the degree of design freedom made possible for the first time, the type of collector presented represents an interesting addition and extension to existing systems.

5. Discussion

As shown above, there is good potential for all-sheet metal solar collectors, as the thermal performance and cost were comparable to those of modern flat plate collectors, with the added benefit of three-dimensional design freedom for seamless integration into facade systems.

It was demonstrated that the manufacture of complex collector geometry with the chosen parameters without cracks was possible by ISF. However, as expected, the cost analysis showed that the area of application for this manufacturing technology was only limited to small quantities (e.g., prototypes or individualized elements) due to the long manufacturing time. For large quantities with recurring geometries, it would make more economic sense to use conventional forming technologies with high output rates. The high quantities amortize the initial investment costs in the forming tools and enable low marketable unit costs.

Laser welding was proven to be an efficient method for the assembly of an all-sheet metal collector, despite the 3D complex shape. However, the increase in the metal thickness could considerably improve the welding robustness influenced by sheet formation.

The use of sol-gel painting spray was an efficient and low-cost way to deposit the solar-absorbing layer on a complex-shaped surface. The high solar absorptance and high emissivity of the solar layer could generate a high thermal efficiency of the solar collector at a low temperature. The overheating effect of the present thermal panels was significantly reduced, as the maximum heating temperature was under 100 °C. Indeed, the overheating effect observed in the case of fluid stagnation (e.g., power cut, failure of the primary pump, or when the heat demand is low) for conventional glazed thermal panels using selective absorbing layers generates a high increase in the fluid temperature (>150 °C), leading to premature component degradation. The large surface available for the implementation of these new solar facades, combined with their high efficiency at low temperature, can generate an economical approach to saving energy. However, the coating design could be improved to decrease the surface emissivity and, consequently, to increase the efficiency at higher temperatures; however, this can be achieved only by using complementary antireflective coatings.

6. Conclusions

This project has shown that, within the research project "FutureFacade", new potential for renewable energies in cities can be created. Solar thermal-active facades are particularly suitable for large buildings with large facade areas, as these are the first places where it becomes economically viable.

The approach of using standardized facade substructures was proven successful. However, this project still has a lot of development potential. With regard to the manufacturing process, it is advisable to switch to the more economical manufacturing process for subsequent projects. This would also make the production of smaller facades and quantities more economical. The material could also be changed to aluminum instead of steel in order to minimize the weight of the facade construction. Changes in material and forming technology also allow new design freedom in the geometry of further developed facade panels, which can be further extended by adapting the coating. In terms of appearance, it would be desirable to be able to create more variance in color with the same or similar efficiency. In terms of efficiency, it would also be advisable to further develop the channel structure professionally with the help of meaningful CFD simulations. When considering the efficiency, its ratio with the absorber surface must always be taken into account. With regard to the panel size, adjustments could be made in the future. As long as the absorber surface area is 2 m^2, the collector remains comparable to conventional absorbers.

All in all, the "FutureFacade" approach has brought many new insights and provides new stimuli for further research on solar thermal facades.

Author Contributions: Conceptualization, P.S.; collector design, P.S., D.W., L.S. and M.D. (Martin Dembski); architectural aspects, L.S., M.D. (Martin Dembski) and A.S.; facade construction and integration, L.S. and M.D. (Martin Dembski); incremental forming tests, P.S. and D.W.; joining and coating experiments, F.D. and S.L.C.; collector characterization, F.D. and S.L.C.; economic analysis, P.S. and F.D; resources, J.K., M.D. (Martin Dix) and A.S.; writing—review and editing, P.S., D.W., L.S., M.D. (Martin Dembski), A.S., J.K. and M.D. (Martin Dix). All authors have read and agreed to the published version of the manuscript.

Funding: This research is supported by the Federal Ministry for Economic Affairs and Climate Action (BMWK) on the basis of a decision by the German Bundestag. This article is based on the project "Future Facade—Combination of individualised design and solar heat functionality by application of a new forming technology for metal based facade elements" coordinated by the German Federation of Industrial Research Associations (AiF) via Forschungsvereinigung Stahlanwendung e.V. (FOSTA) under Grant No. 269 EBR.

Institutional Review Board Statement: Not applicable.

Informed Consent Statement: Not applicable.

Data Availability Statement: Not applicable.

Acknowledgments: This paper was completed in association with the European Union's Horizon 2020 research and innovation program under grant agreement N°856670. The authors would like to acknowledge ELIOSYS SA, Liege, Belgium for their help in the thermal collector's characterization.

Conflicts of Interest: The authors declare no conflict of interest. The funders had no role in the design of the study; in the collection, analyses, or interpretation of data; in the writing of the manuscript; or in the decision to publish the results.

References

1. Bundesregierung. CO_2-Gebäudesanierung. Available online: https://www.bundesregierung.de/breg-de/aktuelles/co2-kohlenstoffdioxid-oder-kohlendioxid-gebaeudesanierung-614754 (accessed on 29 November 2022).
2. International Energy Agency. Technology Roadmap—Energy Efficient Building Envelopes. Available online: https://www.iea.org/reports/technology-roadmap-energy-efficient-building-envelopes (accessed on 29 November 2022).
3. Rynska, E. Review of PV Solar Energy Development 2011–2021 in Central European Countries. *Energies* **2022**, *15*, 8307. [CrossRef]
4. Kaufmann, D. Multifunktionales energieeffizientes Dach- und Fassaden-Solarelement—DAFASOL: Teilvorhaben: Entwicklung des Bauelementes und Anpassung an Einsatzfälle im Stahlbau: Sachbericht: Laufzeit des Vorhabens: 01.12.2014–30.11.2017. Available online: https://www.tib.eu/de/suchen?tx_tibsearch_search%5Baction%5D=download&tx_tibsearch_search%5Bcontroller%5D=Download&tx_tibsearch_search%5Bdocid%5D=TIBKAT%3A1017755027&cHash=ef067e89bb2d1593251944ea0064ceb0#download-mark (accessed on 29 November 2022).
5. Munari-Probst, M.; Roecker, C.; Schueler, A. Architectural integration of solar thermal collectors: Results of a European survey. In Proceedings of the ISES 2005 Solar World Congress, Orlando, FL, USA, 6–12 August 2005.
6. Munari-Probst, M.; Cristina, M.; Roecker, C. *Architectural Integration and Design of Solar Thermal Systems*, 2nd ed.; EPFL Press: Lausanne, France, 2011.
7. Buker, M.S.; Riffat, S.B. Building integrated solar thermal collectors—A review. *Renew. Sustain. Energy Rev.* **2015**, *51*, 327–346. [CrossRef]
8. Hermann, M.; Karin, L.; Hillerns, F. BIONICOL—Entwicklung eines bionischen Solarkollektors mit Aluminium-Rollbond-Absorber. In Proceedings of the 20. Symposium Thermische Solarenergie, Bad Staffelstein, Germany, 5–7 May 2010; pp. 74–79.
9. Tekkaya, E.; Rainer, S. Entwicklung von Solarabsorbern in Stahlbauweise auf Basis partiell plattierter Hybridhalbzeuge. In *Forschung für die Praxis P820*; Verl. und Vertriebsges. mbH: Düsseldorf, Germany, 2015.
10. Maurer, C.; Cappel, C.; Kuhn, T.E. Progress in building integrated solar thermal systems. *Sol. Energy* **2017**, *154*, 158–186. [CrossRef]
11. Schreiber, R.G.; Schaeffer, L. Manufacture of absorber fins for solar collector using incremental sheet forming. *J. Mater. Res. Technol.* **2019**, *8*, 1132–1140. [CrossRef]
12. Weiss, W.; Stadler, I. Facade integration—A new promising opportunity for thermal solar collectors. In *Proceedings of the Industry Workshop of the IEA Solar Heating and Cooling Programme*; Task 26; International Energy Agency: Delft, The Netherlands, 2001.
13. Matuška, T.; Sourek, B. Aspects of solar collector integration into building facade. In Proceedings of the 6th EuroSun, Glasgow, UK, 27–30 June 2006.
14. Behnisch, M.; Münzinger, M.; Poglitsch, H. Die vertikale Stadt als solare Energiequelle? Theoretische Flächenpotenziale für bauwerksintegrierte Photovoltaik und Abschätzung der solaren Einstrahlung. *Transform. Cities* **2020**, *4*, 58–62.
15. Behnisch, M.; Münzinger, M.; Poglitsch, H.; Willenborg, B.; Kolbe, T.H. Anwendungsszenarien von Geomassendaten zur Modellierung von Grünvolumen und Solarflächenpotenzial. In *IÖR Schriften Band 78*; Rhombos Verlag: Berlin, Germany, 2020; pp. 251–261.
16. Knudsen, O.Ø. *Coatings Systems for Long Lifetime: Thermally Sprayed Duplex Systems*; Final Report; SINTEF Rapport: Trondheim, Norway, 2010.

17. *IEC 60904-9:2020*; Photovoltaic Devices—Part 9: Classification of Solar Simulator Characteristics, 3rd ed. IEC Central Office: Geneva, Switzerland, 2020.
18. *DIN EN 12975:2022-06*; Solar Collectors—General Requirements. Beuth Verlag GmbH: Berlin, Germany, 2022. [CrossRef]

energies

MDPI

Article

Thermal-Hydraulic-Mechanical (THM) Modelling of Short-Term Gas Storage in a Depleted Gas Reservoir—A Case Study from South Germany †

Muhammad Zain-Ul-Abedin * and Andreas Henk *

Institute of Applied Geosciences, Technical University of Darmstadt, 64287 Darmstadt, Germany
* Correspondence: abedin@geo.tu-darmstadt.de (M.Z.-U.A.); henk@geo.tu-darmstadt.de (A.H.); Tel.: +49-6151-1622-347 (M.Z.-U.-A.); +49-6151-1622-344 (A.H.)
† This paper is an extended version of my PhD thesis with title "Coupled Thermal-Hydraulic-Mechanical (THM) Modelling of Underground Gas Storage—A Case from the Molasse Basin, South Germany" submitted in 2022 Technical university of Darmstadt, Darmstadt, Germany, March 2022; p. 103.

Abstract: This study addresses the use of former gas storage facilities as short-term storage for renewable energy through power-to-gas (PtG) technology in Germany. Three test cases with coupled thermal-hydromechanical (THM) modelling were conducted to evaluate short-term injection and production schedules. The operating rates were controlled by the upper and lower limits of the wellbore pressure. The maximum difference in pore pressure and effective stress was 0.6 MPa in all cases. Fault reactivation analysis was performed on the THM models to estimate fault stability. The critical pore pressure for safe reservoir operation was determined to be 1.25 times the original pore pressure, corresponding to a WBHP value of 20.25 MPa. The upper limit of the gas injection rate for safe storage operation was estimated to be between 100,000 and 150,000 m^3/day. The thermal stresses were found to be negligible for short-term cases. The storage capacity of PtG technology was reported to be up to 1,322,400 kWh/d of renewable electricity, which can contribute to Germany becoming a greenhouse gas neutral country by 2050. The workflows and results of the study are applicable to all gas storage in a porous medium, including methane, CO_2, and hydrogen.

Keywords: THM modelling; short term underground gas storage; dynamic modelling; "battery" for power-to-gas

Citation: Zain-Ul-Abedin, M.; Henk, A. Thermal-Hydraulic-Mechanical (THM) Modelling of Short-Term Gas Storage in a Depleted Gas Reservoir—A Case Study from South Germany. *Energies* **2023**, *16*, 3389. https://doi.org/10.3390/en16083389

Academic Editors: Luis Hernández-Callejo, Jesús Armando Aguilar Jiménez and Carlos Meza Benavides

Received: 27 February 2023
Revised: 5 April 2023
Accepted: 10 April 2023
Published: 12 April 2023

1. Introduction

High energy demand has intensified research into the "underground gas storage" (UGS) discipline [1]. As a result, both long-term (seasonal) and short-term (weekly) gas storage projects have gained the attention of UGS researchers [1]. An idea in this context is to store methane produced by "power-to-gas (PtG)" technology from excessive electricity produced by renewable sources, such as solar and wind. The stored gas can then be reused for power generation whenever needed. Thus, UGS is used as a kind of "battery" for surplus green energy.

Short-term storage cycles may cause some geomechanical issues in the porous reservoir. The pore fluid pressure in the reservoir fluctuates due to intensive gas injection and withdrawal phases. These fluctuations in fluid pressure change the effective stresses in the reservoir and may also change the in-situ stress state outside the reservoir area [2]. These changes have implications for geomechanical phenomena related to fault stability, caprock integrity, and surface deformation. Numerical modelling, e.g., 3D geomechanical modelling, provides a platform to integrate lithological and mechanical heterogeneities and investigate stress state changes during injection-production cycles of high frequency.

This study concentrates on a geomechanical assessment of a former gas field in the Bavarian Molasse Basin east of Munich (Germany) for which a hypothetical transformation into an UGS site is investigated. Various scenarios with variable short-term (weekly)

schedules to test cases for gas storage and withdrawal are considered to evaluate stresses (e.g., effective stress) and deformation due to pressure changes with high-frequency injection/production cycles. German data for excess electricity from renewable energy sources (such as solar and wind) throughout the calendar year 2017 are also considered in two cases to address the issue of irregular schedules in gas supply (via PtG) and energy demand.

The modelling results provide information about the stress state within and around the reservoir because of the production and injection of each selected time step, and they are compared with the stress states at the depletion and replenishment stages. The production history of the reservoir (porous media) is categorically useful to determine stress paths within and around the reservoir and wellbore periphery, as well as caprock integrity. Further, the modelling results provide information about ground surface subsidence during peak depletion and replenishment time steps, which can be useful to minimize geomechanical risks to any gas storage facility, not only for methane or CO_2 but also for hydrogen. Finally, fault reactivation analyses are also incorporated to obtain a safe gas injection rate for safe storage capacity.

The most popular gas storage method is underground gas storage among others, such as liquefied natural gas (LNG), storage tanks, and pipeline storage [3,4]. Two important issues are associated with UGS. First, it relies on gas imports due to increased demand for power generation (gas-to-power) and other domestic usages. Second, any damage to infrastructure could lead to higher gas prices or disruption of supply, with unpredictable, costly consequences for customers [1]. To address these challenges, various research has suggested using depleted gas/oil porous reservoirs or aquifers as UGS, with which significant volumes can be strategically stored [1,5].

One of the main advantages of depleted gas reservoirs is that they allow convenient and cost-effective gas storage, as they have suitable permeability properties and pore connections [6,7]. Some vital data, such as geological and geophysical characteristics, petrophysical properties, storage capacity, pressure, and the production history of depleted gas reservoirs, have been thoroughly studied and well recorded during the development phase of the reservoir field, enabling numerical modelling to simulate the injection-production process of underground gas reservoirs [3,6,8].

Water encroachment occurs in the porous reservoir vertically and laterally during the development phase of the gas reservoir. This water invasion causes fewer porous spaces in the reservoir, and different fluid distribution areas are formed in the longitudinal and traverse planes of the reservoir. During the injection and production operations of gas storage, the gas-water interface moves downward when gas is injected and moves upward when gas is produced [9]. Furthermore, as the foreign gas is injected into the reservoir, which has a different temperature than the reservoir's actual temperature, these thermal changes in the reservoir also cause some thermal stress changes in the reservoir, which is not the case in the reservoir exploitation phase. Therefore, it is necessary to conduct a systematic modelling study of the changes in the thermal-hydraulic-mechanical properties of UGS due to repeated water intrusion and multiphase seepage rules during high-speed injection production operations. The state-of-the-art thermal-hydro-mechanical (THM) modelling provides a platform to analyse and investigate all these issues related to porous UGS systems discussed above. THM models are typically derived from a wide range of geological, geophysical, and engineering data, including field measurements, core tests, well logs, drilling, and production data. After calibration, these THM models can be used for ground surface subsidence, thermal stress changes, maximum safe storage capacity, and maximum threshold pressure, avoiding fault reactivation and maintaining caprock integrity [10–12].

This modelling case study is a THM assessment of a former depleted gas reservoir field from the Molasse Basin in South Germany and has been presented in [10]. This dynamic modelling study addresses the following issues related to short-term and long-term operations of UGS: (1) the storage capacity of the reservoir; (2) thermal analysis with changing temperatures of the reservoir due to the injection of gas; (3) potential fault

reactivation analysis; and (4) stress path changes due to changes in pore pressure because of short-term production/injection cycles. These types of THM models, particularly short-term scheduled models, have implications for PtG technology in which simulations help us to understand that excess power from renewable resources can be stored in underground gas storage reservoirs and vice versa.

2. Methodology

2.1. Hydraulic Model

The flow simulation accounts for multiphase fluid flow in porous media. A hydraulic model is usually conducted by reservoir simulation, i.e., a form of numerical modelling in which physical phenomena are quantified and interpreted throughout the history of a reservoir and beyond, with the ability to extend this model to future performances. Reservoir simulation is a proven and effective method for dealing with uncertainties during exploration and production [13]. It is also helpful to determine the amount of gas that can be stored in each underground gas (CO_2, hydrogen, or methane) storage reservoir [13]. The physical phenomenon behind (fluid flow) reservoir simulations are based mainly Darcy's law and mass material balance [10].

The composition of the fluid can be treated in different ways in reservoir simulations. Black oil simulators assume oil and gas phases to be one component through space and time. The properties of this component can change with pressure and temperature, while the composition does not change [13]. Thereby, the behaviour of the multiphase system can be described by complex PVT (pressure, volume, temperature) and SCAL (special core analysis) relations [13].

As a general solution method, the reservoir is divided into several cells with provided petrophysical properties, such as porosity and permeability. Then, the wells are placed within cells, and production rates are provided with different time steps. Last, the equations are solved to determine the pressure, temperature, and saturation for each cell. Each cell is solved simultaneously; therefore, the number of cells in the reservoir simulation is directly related to the time required to solve a time step [13].

2.2. Thermal Model

The thermal-flow-stress simulation model considers the proportional heat transfer in porous media when considering the multi-fluid flow concept in a THM simulation. The thermal flow model is usually performed by numerical modelling, in which the thermal hydraulic aspects are quantified together with the geomechanical simulation and interpreted throughout the history of a reservoir and storage operations in underground gas storage facilities. The main governing law in the thermal modelling is Fourier's law, also known as the law of heat conduction. The law states that the rate of heat transfer through a material is proportional to the negative temperature gradient and to the area at right angles to that gradient through which the heat flows. The governing equation of Fourier's law describes that the local heat flux density (q_h) is equal to the product of the thermal conductivity (k_t) and the negative local temperature gradient ($-\nabla T$) [14]:

$$q_h = -k_t \nabla T, \tag{1}$$

where q_h is in (W/m^2), k_t is in (W/m. K), and ∇T is in (K/m). Fourier's law can also be used in uni-dimensional form in any direction, i, j, k; for that reason, the equation becomes:

$$q_h = -k_t \frac{dT}{d(i,j,k)}\,, \tag{2}$$

2.3. Coupled Thermal-Hydraulic-Mechanical (THM) Modelling

The coupling of a reservoir simulator with a geomechanics module is an integral component for analysing hydrocarbon reservoirs in petroleum, underground gas storage, and the geothermal industry. A conventional geomechanical simulator provides surface

subsidence, which is often estimated using a simple mechanical formula without knowing the full geomechanical response. The only geomechanical parameter considered may be the pore compressibility, which is not sufficient to reproduce the changes in pore volume caused by complex pressure and temperature variations [15,16]. For some problems, such as primary production and linear elastic responses of reservoirs, subsidence calculated by a reservoir simulator alone can produce results comparable to coupled solutions [16,17].

In a coupled simulator, flow can be strongly influenced by the stress and strain distributions that lead to changes in porosity and permeability, but effective stress changes are ignored in conventional simulation methods. Such approaches cannot provide adequate predictions when considering a stress-sensitive reservoir (e.g., underground gas storage reservoir) [15,18]. There are two main components of coupling: volume coupling and fluid flow coupling according to [15,17].

In volume coupling, the changes in pore volume occur in response to variations in stress, pressure, and temperature. For convergence, the calculated pore volume changes should be the same in both the fluid flow model and the geomechanical model. The pore volume changes of the geomechanical model are usually more accurate than those of the fluid flow model because they are calculated by volumetric strain via a more realistic complex material constitutive model. This method is well suited to shear and plastic deformation, which involve large changes in pore volume or porosity. These problems are common in unconsolidated heavy oils and oil sands, North Sea chalk, Californian diatomite, and possibly some other materials [15,17].

In case of fluid flow coupling, the changes in permeability and relative permeability are related to the changes in stress, shear stress, and compaction. Material parameters, such as permeability, relative permeability, compressibility, and others, change when conditions encounter a shear fracture. This fact is important in some reservoirs where the rock compressibility does not play a significant role in volumetric behaviour, such as gas reservoirs where volume coupling is not important. Another example is cold water/fluid injection, which leads to a thermally-induced decrease in horizontal stress until the injection pressure increases the minimum horizontal stress [19].

To achieve the stress states of the reservoir and surrounding formations throughout history, as well as during future gas storage operations, the fluid flow and the geomechanical simulation must be coupled. The pore pressure controls the effective stresses and, hence, deformation, in turn changing rock porosity and permeability, which again affect fluid flow.

2.3.1. Effective Stress and Poroelasticity

The effective stress for incompressible rock and the concept of one-dimensional consolidation are the fundamentals of poroelasticity formulated by Terzaghi in 1923 [17]. Successively, using the basic principles of continuum mechanics and applying the concept of the coupling of stress and pore pressure in a porous medium, Biot developed a comprehensive three-dimensional theory of consolidation [17,20]. Biot's theory and the papers that he published are more aligned towards geomechanics than flow models, due to which they are rarely compatible with the coupling of geomechanics and flow models. By introducing the so-called Skempton pore pressure parameters (A and B), Skempton in 1954 procured a relationship between the total stress and the pore pressure under undrained initial loading [17,21]. Later, however, the relationships among pore pressure, stress, and volume and the concept of compressibility in a porous medium were better clarified by Geerstma in 1957 [17,22]. Later, Van der Knaap (1959) extended Geerstma's work to nonlinear elastic geomaterials only for dense and uncemented sands [17,23]. By applying Biot's theory, Geerstma in 1966 examined subsidence problems in oil fields and published prototype geomechanical modelling, which is probably the first-ever coupled analysis of fluid flow [17,20]. Nur and Byerlee (1971) demonstrated that the effective stress law proposed by Biot is far more general and precise than that proposed by Terzaghi [17,24]. Nevertheless, there are certain limitations (one-dimensional analysis, neglect of the compressibility of

fluids and rocks, etc.) that Terzaghi recognized in the assumptions that he made in the 1920s to solve problems of applied rock mechanics in clay consolidation [17]. Later in the 1970s, there were further developments on coupled flow stress issues; e.g., fluid compressibility was introduced into the classical soil mechanical consolidation theory of Ghaboussi and Wilson [17,25]. Rice and Cleary (1976) showed how poroelasticity problems could be solved using pore pressure and stress as primary variables, instead of the displacements used by Biot [17,26].

2.3.2. Simulation Concept and Governing Equations

The numerical modelling of an underground gas reservoir can contribute to the understanding of the interaction mechanisms between the injected gas and the deformation of the reservoir. The injection of cold foreign gas into the reservoir leads to thermal and mechanical disequilibrium in the reservoir by altering the transport properties, including porosity and permeability. A three-dimensional THM coupling model of a reservoir is created by incorporating the mechanical equilibrium equation, the fluid flow or seepage equation (Darcy equation), the heat transfer equation (Fourier equation) of the formation's rock matrix, and the THM stress equation. These equations are based on the porosity, permeability, thermal diffusivity, and other physical and mechanical parameters of the sandstone formation [27].

The mechanical equilibrium equation can be expressed as follows [27]:

$$S_{i,j,j} + f_i = 0, \tag{3}$$

where, $S_{i,j,j}$ is the total stress tensor (N/m^2), and f_i is the body force (N/m^3). The equation of the continuity of the fluid flow in the rock can be written as [27]:

$$\frac{\partial \rho_l}{\partial t} + \frac{\partial(\rho_l r v_r)}{r\partial r} + \frac{\partial(\rho_l v_\theta)}{r\partial \theta} + \frac{\partial(\rho_l w)}{\partial_z} = 0, \tag{4}$$

In this equation v_r, v_θ, and w are the Darcy velocities (m/s) along the radial, hoop, and well-depth directions, respectively, in the porous reservoir. The relationship between stress and porosity/permeability changes in porous rock can be described with the following equations [27,28],

$$\phi = \phi_r + (\phi_0 - \phi_r) exp(e.S_M), \tag{5}$$

$$k = k_0\, exp(c.(\frac{\phi}{\phi_0} - 1)), \tag{6}$$

In the above equations, S_M denotes mean effective stress; ϕ_0 and k_0 are the porosity and permeability at zero stress, respectively; ϕ_r represents the residual porosity at high stress; and the exponents e and c are determined experimentally.

The heat transfer process and the total energy conservation can be express by rewriting the Fourier equation [29]:

$$(\rho c)_t \frac{\partial T}{\partial t} - \frac{1}{r}\frac{\partial}{\partial r}(k_t r \frac{\partial T}{\partial t}) - \frac{1}{r^2}\frac{\partial}{\partial \theta}(k_t \frac{\partial T}{\partial \theta}) - \frac{\partial}{\partial z}(k_t \frac{\partial T}{\partial z}) - q_t r = 0, \tag{7}$$

$$(\rho c)_t = (1-\phi)c_s\rho_s + \phi c_f \rho_f, \tag{8}$$

$$k_{total} = \phi k_f + (1-\phi)k_s, \tag{9}$$

In the above equations, the total heat capacity of the solid and fluid phases is denoted by $(pc)_t$ in units (J/(m^3.°C)); k_{total} is the total thermal conductivity (J/(m.s.°C)); q_t is the intensity of the internal heat source (J/(m^3.s)); c_s and c_f are the specific heat capacities of the formation and the fluid, respectively (J/kg.K); ρ_s and ρ_f are the density of the formation

and the fluid (Kg/m^3), respectively; and k_s and k_f are the thermal conductivity of the formation and the fluid (W/(m·K)), respectively [29].

Finally, the governing equation involving all important thermal-hydro-mechanical parameters is as follows [30]:

$$2\alpha\frac{(1-2\nu)}{1+\nu}\nabla^2 p + 6\beta K_B\frac{(1-2\nu)}{1+\nu}\nabla^2 T - \nabla.f - 3\frac{(1-\nu)}{1+\nu}\nabla^2 S_{m(total)} = 0, \quad (10)$$

where $S_{m(total)}$ is the mean total stress (MPa), ν is the Poisson's ratio of the rock mass, α is the Biot coefficient, β is the coefficient of linear thermal expansion (1/°C), and K_B is the bulk modulus of the rock (MPa). The term $(2\alpha\frac{(1-2\nu)}{1+\nu}\nabla^2 p)$ describes the effect of poroelastic stress; $(6\beta K_B\frac{(1-2\nu)}{1+\nu}\nabla^2 T)$ represents thermalelastic stress; and the term $(\nabla.f - 3\frac{(1-\nu)}{1+\nu}\nabla^2 S_{m(total)})$ shows the body force [30].

2.4. ECLIPSE™_VISAGE™ THM Modelling

The THM modelling is performed using two commercial software packages, referred to here as the ECLIPSE™-VISAGE™ coupling. ECLIPSE™ is a conventional reservoir simulator used as the flow simulator for the multiphase flow processes. In the following study, the ECLIPSE™ 100 finite difference black oil simulator is used for the flow calculations. VISAGE™ is one of the most advanced and comprehensive stress analysis simulators commercially available. It is designed for applications in which nonlinear mechanics play a greater role, for example, in disciplines such as rock mechanics and geomechanics. It is flexible and can also be used in many other scientific disciplines, e.g., fluid mechanics, heat transfer, materials science, etc. The system provides high computational power and sophisticated modelling for many analytical situations, which currently include mining, civil engineering, reservoir engineering, and geothermal energy.

The advanced and comprehensive finite element code (VISAGE™) has been coupled with the ECLIPSE™ reservoir simulator to include geomechanical processes in this modelling study. Fluid flow is first calculated in ECLIPSE™, and the results are then transferred from ECLIPSE™ to VISAGE™ via the ECL2VIS interface for specified time steps. Updates of porosity and permeability can be calculated via constitutive relations, e.g., Kozeny–Carman.

The coupled THM models are based on three fundamental laws, namely Hooke's law of elasticity, Fourier's law of heat conduction, and Darcy's law of fluid flow in porous media. The governing equations are discussed above.

One-way coupling is usually sufficient for THM modelling of gas reservoirs, as gas compressibility dominates the bulk rock compressibility, and the mass balance is mainly controlled by gas pressure rather than by the stresses of solid rock [31]. The THM-coupled model presented in this paper is a one-way coupled model. With this approach, pressure data are transferred from the reservoir simulator (fluid flow simulator) ECLIPSE™ to the mechanical finite element simulator (geomechanical simulator) VISAGE™ at regular and/or critical times. The fluid pressure drives the geomechanics, but mechanically induced changes in porosity and permeability are not fed back into the dynamic reservoir simulation. It is therefore assumed that permeability and porosity are the same for each time step in the modelling and are not influenced by changes in stresses or ageing effects of the reservoir. This type of approach is feasible in this case study due to the high permeability of up to 80 mD, which is characteristic of the reservoir.

3. Case Study

The presented modelling study is a working example of how to set up and populate a 3D coupled thermal-hydraulic-mechanical model of an underground gas storage site. The case study reservoir is a depleted gas reservoir located about 65 km east of Munich in the Central Molasse Basin. It is an anticlinal structural trap bounded by a normal fault. The reservoir formation is mainly Early Cenozoic Chattian sand, with 85-m thick, three gas-

bearing layers, found at a depth of 1770 m (1200 m below sea level). The initial gas-water contact is at 1239 m below sea level (BSL). The reservoir has produced 528 million m^3 of gas over 18 years from 1958 till 1976; replenishment started in 1978 and has continued to the present, and the reservoir has not been in operation to date [10]. The modelling study uses pore pressure development during the production history and subsequent shut-in phase to calibrate the dynamic reservoir fluid model.

The 3D MEM model is built using a hydraulic model (green area in Figure 1), which comprises a high-resolution reservoir section and regions of lower resolution away from the reservoir section, called the sideburden, overburden, and underburden sections. Topography is extracted from the elevation maps of the ground level to include the top surface of the model. The horizons bounding the reservoir are used to make overburden layers and underburden layers. The basal unit of the model comprises crystalline basement rocks at a depth of about 5 km. However, as none of the wells has reached this depth, this information is inferred from regional geological knowledge. The final 3D THM model consists of 12 horizons and 11 lithostratigraphic units with dimensions of about $30 \times 24 \times 5$ km^3 in the X, Y, and Z directions, respectively. The grid of the THM with the reservoir model embedded is shown in Figure 1. The higher resolution in the area of interest (reservoir) and the lower resolution outside make up a grid that creates balance between simulation precision and computational demand. The initial pore pressures and elastic properties are upscaled and interpolated from the 1D MEM's. The calculated and calibrated log-derived properties, including pore pressure, Young's modulus, Poisson's ratio, and density, are upscaled from the well locations to the entire model domain. The Kriging interpolation method is used to populate the 3D geomechanical model. The precision is of course decreasing away from the wells, but the model fits well with overall trends.

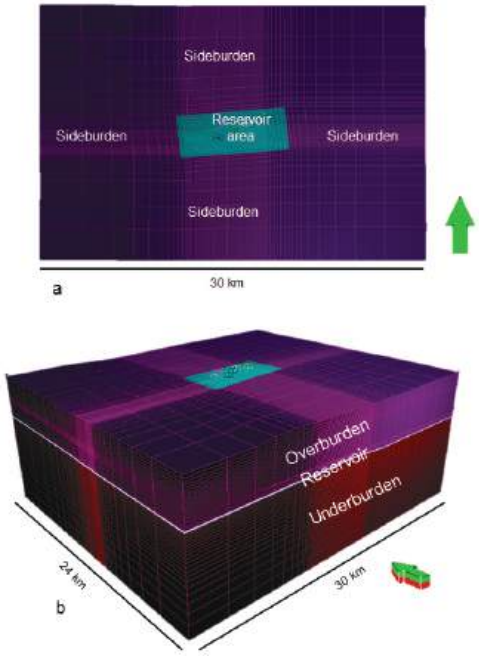

Figure 1. Reservoir model proper embedded in 3D geomechanical model with reservoir, overburden, underburden, and sideburden zones: (**a**) is the top view, and (**b**) is the oblique view, the arrows represent north direction [10].

Further details regarding the model setup, population of the model from 1D MEMs, history match, etc., are explained in our previous publication [10]. The starting point of the

further modelling study in the following sections is the state after the replenishment phase, achieved by a history match of the production and pressure data from the production and subsequent shut-in phases, respectively.

4. Modelling

4.1. Modelling Scenarios

The following section describes the dynamic fluid flow models setup for future scenario testing cases designed for short-term (weekly) gas storage operations. The pressure profile of different future testing scenarios can be coupled with and incorporated into the THM model. The concept for these scenario tests is to evaluate geomechanical stresses on the reservoir due to pressure changes with intensive injection/production cycles. There are various models with different short-term cases that have been considered. German data for excess electricity throughout 2017 have also been considered in one case to address the issues of renewable energy aspects. This case implies that the excess of power energy (electricity) in Germany can be stored in underground gas storage with the power-to-gas (PtG) concept, and then the stored gas can be reused for power generation (gas-to-power) when needed. All the cases are summarized in Table 1. The starting pressure point of these future scenario testing cases is the end point pressure of the replenishment phase, i.e., ~15.8 MPa.

Table 1. All modelling scenarios with input parameters. WBHP is well bottom hole pressure, WGIR is well gas injection rate, and WGPR is well gas production rate.

Modelling Scenarios	Subdivisions		Input Parameters			
			WBHP upper limit (MPa)	WBHP lower limit (MPa)	WGIR (m^3/day)	WGPR (m^3/day)
Short-term (weekly) cases	Case A (with water-cut 5 m^3/day)	With three wells (two vertical wells, one horizontal well)	18.8	13.8	100,000	100,000
	Case B (without limited water-cut)	With three wells (two vertical wells and one horizontal well)	18.8	13.8	100,000	100,000
Real-world cases	Case C (with water-cut 5 m^3/day)	With one well	18.8	13.8	100,000	100,000
	Case D (without limited water-cut)	With one well	18.8	13.8	100,000	100,000

Short-term scenario cases represent weekly storage operations. The scenario scheme has been designed to compensate for the excess power produced in a season and to store power-to-gas energy into same underground gas storage. A short-term cycle consists of phases of one week of injection, one week of shut in, two weeks of production, and one week of shut (1wkInj-1wkShut-2wkProd-1wkShut) for one year. During the injection week, gas is injected into the reservoir, which builds up field pressure (but again limited by 18.8 MPa, the upper limit of WBHP); then, one week of shut in maintains the pressure, followed by a two-week production phase to withdraw gas, which drops the field pressure (lower limit constraint to 13.8 MPa), and again a shut in phase to maintain the well bore pressure.

4.2. Case A

There are three wells considered for this scenario: two wells are vertical wells (X2 and X6), and one is a horizontal well (H1). All the wells have been considered to have the same short-term weekly schedule as discussed above. This case comprises the same schedule as discussed above, but the well water production rate (WWPR) is limited to 5 m^3/day to take into consideration the economic aspects of operating the gas storage. The commercial storage industry limits the water production rates to minimize operating costs and enhance economic returns. Therefore, this aspect has also been considered in this case study. The gas rate for injection and production both is 100,000 m^3/day. Bottom hole pressure is constrained by an upper limit of 18.8 MPa and a lower limit of 13.8 MPa in cases of injection and production, respectively. The water cut-off is again 5 m^3/day in the production phase to limit the production of water from each well.

The FPR profile for this case is shown in Figure 2. The progressive oscillation cycles of FPR are injection (upward) and production (downward) phases. The overall upward trend of FPR from its initial pressure of ~15.39 MPa represents the buildup pressure with each passing schedule cycle.

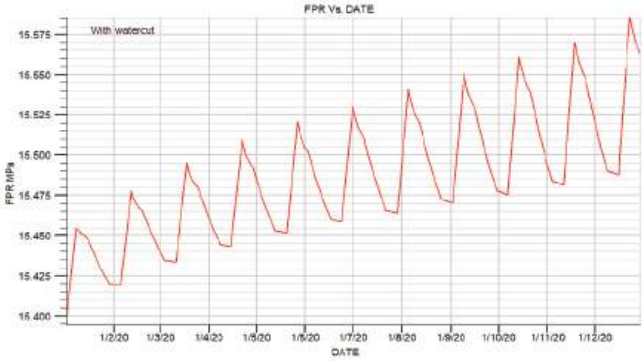

Figure 2. Field pressure (FPR) profiles of all three wells (X2, X6, and H1) with schedule 1wkInj-1wkShut-2wkProd-1wkShut for one year.

The upward trend of FPR throughout the schedule year is due to the well water production rate (WWPR) (Figure 3d), and as a result, the field pressure is not stabilized in such a short time span. To maintain material balance in this scenario, the injection rate should be lowered to the actual production rates of each cycle.

The comparison of the properties of all three wells is summarized in Figure 3. The WBHP of X6 reaches the maximum limit of 18.8 MPa at the end of each injection cycle and drops back to ~15 MPa at the end of the production phase. The WBHP of X2 also shows similar behaviour but at a lower pressure; e.g., it varies between 16 MPa and 17 MPa at the end of each injection phase and drops back to the same level of ~15 MPa. The WBHP behaviour of H1 is however different from that of both X2 and X6. It reaches a maximum value of 16 MPa at the peak injection time and drops to the lowest level of ~14 MPa (Figure 3a). The WGPR behaviour of all three wells is similar with respect to linear increases with each increasing cycle. However, the rates are completely different for each well. The WGPR of well X2 ranges within ~10,000–11,000 m^3/day during the initial cycles but reaches up to 18,000 m^3/day at the end of the schedule. Contrarily, the WGPR of well X6 ranges within ~5000–6000 m^3/day during the initial cycles but reaches up to ~9000 m^3/day at the last cycle. An entirely different behaviour of WGPR is exhibited by well H1, showing ~50 m^3/day during the initial cycles but reaching up to ~1100 m^3/day at the end of the schedule year (Figure 3b).

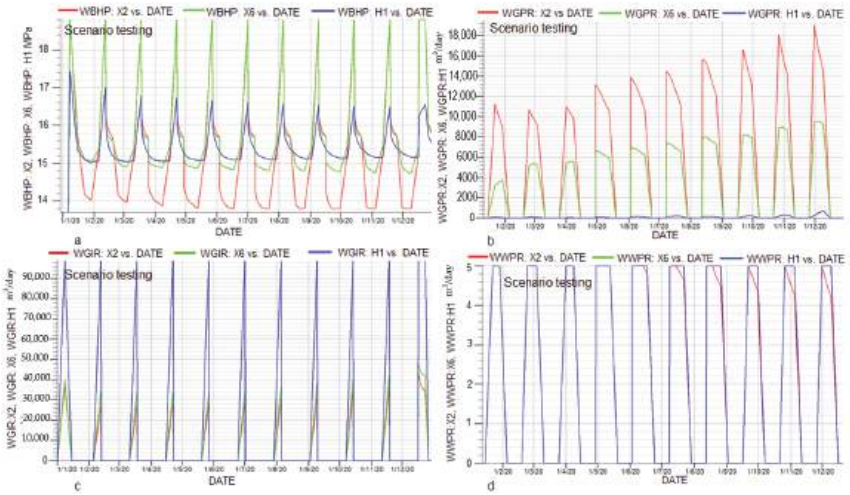

Figure 3. Well properties comparison of the three-well case scenario with the short-term schedule 1wkInj-1wkShut-2wkProd-1wkShut for one year. X2 and X6 are vertical wells, and H1 is the horizontal well: (**a**) well bottom hole pressure (WBHP) of all wells; (**b**) production gas rates (WGPRs) for all three wells; (**c**) injection gas rates (WGIRs) for all three wells and; (**d**) well water production rate (WWPR) for all the wells.

The WGIR profile of each well is completely different from the profile of the WGPR; the WGIR of well H1 shows the highest WGIR rates among other vertical wells (X2 and X6). The WGIR of H1 reaches to the maximum rate of 100,000 m^3/day. The WGIR of well X2 and X6 reach a maximum of 40,000 m^3/day and 50,000 m^3/day, respectively (Figure 3c).

The comparison shows that the horizontal well allows more gas injection and less gas production than the vertical wells and vice versa.

Results

The modelling results of this case are presented in the form of pore pressure and effective stress changes of the top layer of the reservoir. Two-time steps have been selected for the analyses of changes in pore pressure and effective stresses acting on the reservoir. Time step t1 (16 December 2020) represents the lowest pressure during the production phase of the schedule cycle, and t2 (23 December 2020) indicates the maximum injection pressure. The fluctuations in pore pressure and effective stress on the reservoir during t1 and t2 are the main results of this model.

Figure 4 shows the locations of three wells, which are denoted by H1, X2, and X6. The pore pressures at t1 and t2 for the well H1 are ~15.0 MPa and ~15.3 MPa, respectively, whereas the effective stress values are ~29.3 MPa at t1 and about 29.0 MPa at t2. There is a difference of about ~0.3 MPa for both pore pressure and effective stress from t1 to t2.

The vertical wells X2 and X6 are close to each other; therefore, the differences in the change in pore pressure and effective stress at these well locations are negligible. The values of pore pressure at both well locations at t1 and t2 are about 15.4 MPa and ~15.7 MPa, respectively. The effective stresses at t1 and t2 are ~28.5 and ~28.2 MPa, respectively, at both well locations. There is an increase in pore pressure of ~0.3 MPa from t1 to t2 and a decrease in effective stress of about 0.3 MPa.

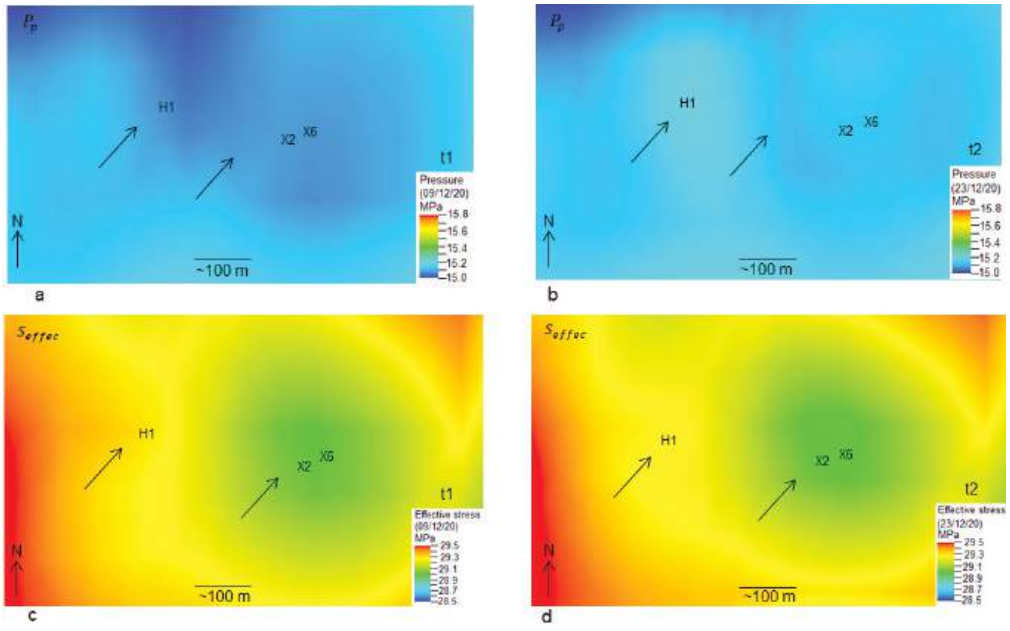

Figure 4. Pore pressure (P_p) and effective stress (S_{effec}) changes from t1 (16 December 2020) to t2 (23 December 2020) in the short-term case with three wells (X2, X6, and H1) with a water cut-off rate of 5 m^3/day. The arrows show the location of maximum observed fluctuations in P_p and S_{effec} from t1 to t2. The color scale is in MPa. (**a**) is pore pressure at time t1; (**b**) is pore pressure at time t2; (**c**) is effective stress at time t1; (**d**) is effective stress at time t2.

4.3. Case B

Three wells are considered for this scenario, two of which are vertical wells (X2 and X6), and one is a horizontal well (H1). All wells are assumed to have the same short-term weekly schedule as described above. WGIR and WGPR both have same value of 100,000 m^3/day; however, they are constrained by the upper limit of BHP of 18.8 MPa and the lower limit of BHP of 13.8 MPa in the cases of injection and production, respectively.

The FPR profile for this case is shown in Figure 5. The progressive oscillation cycles of the FPR are injection (upward) and production (downward) phases. The general trend of the FPR remains within the limits of ~15.85 MPa and ~15.375 MPa during the injection and production phases, respectively.

The comparison of the properties of all three wells is summarized in Figure 6. The WBHP of X6 reaches the maximum limit of 18.8 MPa at the end of each injection cycle and falls back to ~13.8 MPa at the end of the production phase. The WBHP of X2 also shows almost similar behaviour. However, the WBHP behaviour of H1 is different from both X2 and X6. It reaches a maximum value of 17.4 MPa at peak injection time and drops to the lowest level of ~13.8 MPa (Figure 6a). The WGPR behaviour of all three wells is similar in terms of linear increase with each increasing cycle. However, the rates are completely different for each well. The WGPR of well X2 is ~12,000–16,000 m^3/day during the initial cycles but reaches up to 24,000 m^3/day at the end of the schedule. In contrast, the WGPR of well X6 varies between 14,000 and 15,000 m^3/day during the initial cycles and reaches up to 22,000 m^3/day at the end of the last schedule cycle. The WGPR of well H1 is entirely different from the other two wells because it shows ~400–500 m^3/day during the initial cycles but reaches up to ~70,000 m^3/day at the end of the schedule year (Figure 6b).

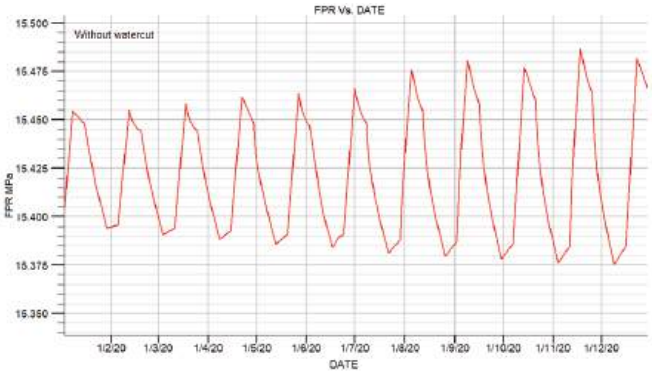

Figure 5. Field pressure (FPR) profile of all three wells (X2, X6, and H1) with schedule 1wkInj-1wkShut-2wkProd-1wkShut for 1 year.

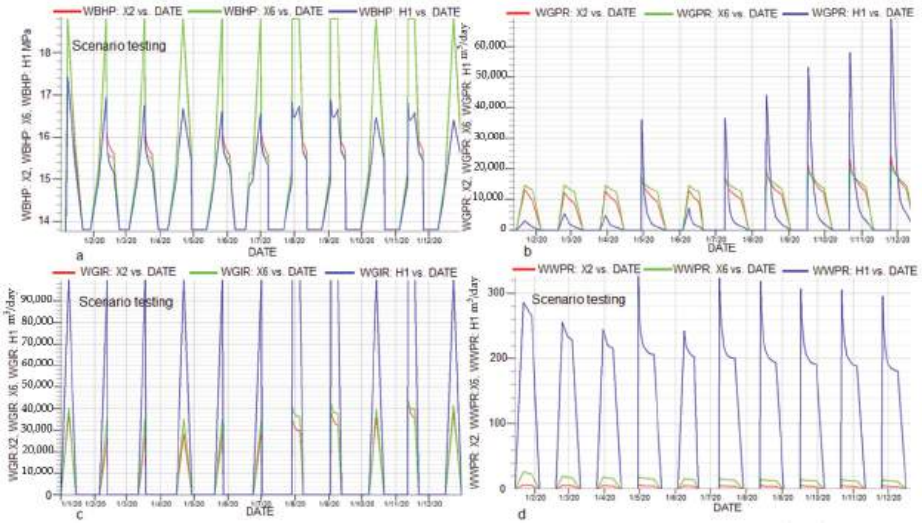

Figure 6. Well properties comparison of the three-well case scenario with short-term schedule 1wkInj-1wkShut-2wkProd-1wkShut 1 year. X2 and X6 are vertical wells, and H1 is the horizontal well: (**a**) well bottom hole pressure (WBHP) of all wells; (**b**) production gas rate (WGPR) for all three wells; (**c**) injection gas rate (WGIR) for all three wells and; (**d**) well water production rate (WWPR) for all the wells.

The WGIR profile of each well is completely different from the WGPR profile; the WGIR of well H1 shows the highest WGIR among the other vertical wells (X2 and X6). The WGIR of well H1 reaches the maximum value of 100,000 m^3/day. The WGIRs of wells X2 and X6 reach maximum values of 44,000 m^3/day and 45,000 m^3/day, respectively (Figure 6c). The comparison shows that the horizontal wells allow for higher WGIR and WGPR than the vertical wells under the same WBHP conditions.

The WWPR of well X2 allows a maximum rate of 5 m^3/day throughout schedule year, and the WWPR of well X6 also remain constant over the schedule year with a rate of 10 m^3/day, while the WWPR of well H1 remains higher, within the range of 250 m^3/day to 310 m^3/day (Figure 6d).

4.3.1. Results

The modelling results of this case are presented in the form of pore pressure and effective stress changes of the top layer of the reservoir. Two time steps with the greatest fluctuations in pore pressure have been selected. Time step t1 (9 December 2020) corresponds to the lowest pore pressure point, and t2 (23 December 2020) corresponds to the highest pore pressure point of the schedule cycle. The fluctuation in pore pressure and the effective stress on the reservoir during time t1 and t2 are the main results of this model.

Figure 7 shows the locations of three wells, which are denoted by H1, X2, and X6. These three wells are the operating wells for this scenario. The main changes in pore pressure, along with the effective stress, occur around these wells. The pore pressures at t1 and t2 for well H1 are ~15.5 MPa and ~15.4 MPa, respectively, whereas the effective stress values are ~29.1 MPa at t1 and about ~28.7 MPa at t2. There is a difference of about ~0.4 MPa for both pore pressure and effective stress at t1 and t2.

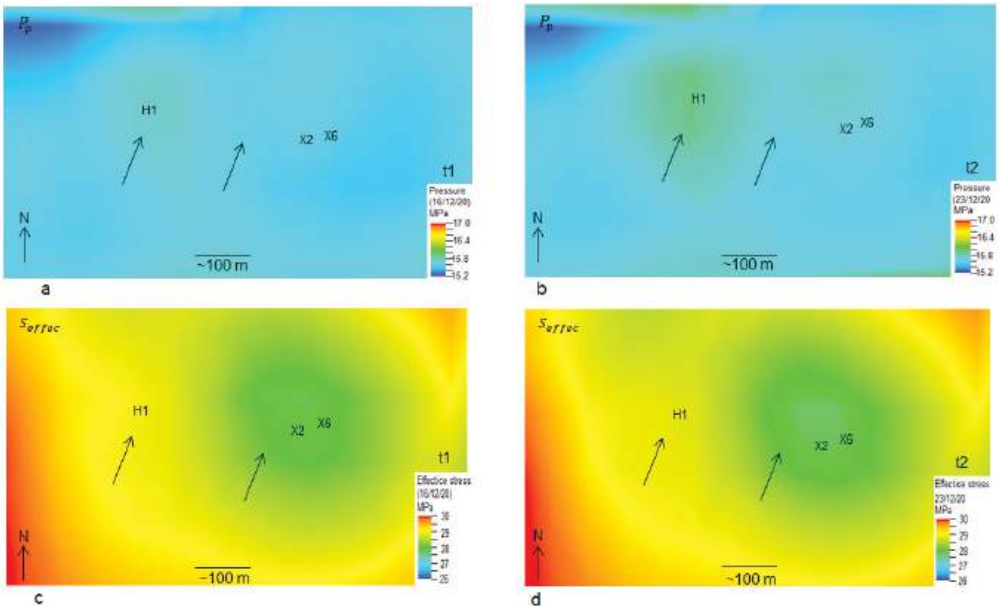

Figure 7. Pore pressure (P_p) and effective stress (S_{effec}) changes from t1 (9 December 2020) to t2 (23 December 2020) in the short-term case with three wells (X2, X6, and H1) without a water cut-off rate of 5 m^3/day. The arrows show the location of maximum observed changes in P_p and S_{effec} from t1 to t2. The color scale is in MPa. (**a**) is pore pressure at time t1; (**b**) is pore pressure at time t2; (**c**) is effective stress at time t1; (**d**) is effective stress at time t2.

4.3.2. Real World Cases

The excess of electricity produced [32,33] in Germany could be stored in underground gas storage by converting the power energy into gas (Power-to-Gas). PtG is a process of generation of a gas with high energy density through the electrolysis of water. The first intermediate product is power-to-hydrogen, which can be converted into synthetic methane gas power-to-methane in a subsequent methanation process that requires injection of CO_2. In this way, the same seasonal underground gas storage can also be used as a battery for excess energy in a calendar year. Figure 8 shows Germany's data on excess electricity produced in calendar year 2017. It can be seen from the data that, during the summertime (from March till August), electricity produced from renewable sources, such as wind and solar, increases enormously. The combined wind energy (onshore and offshore) shows high variation during the first and fourth quarters of the year, meaning this high variation of

electricity production from renewable sources can be stored (power-to-gas) and reused (gas-to-power) in cases of excesses and shortages of electricity, respectively.

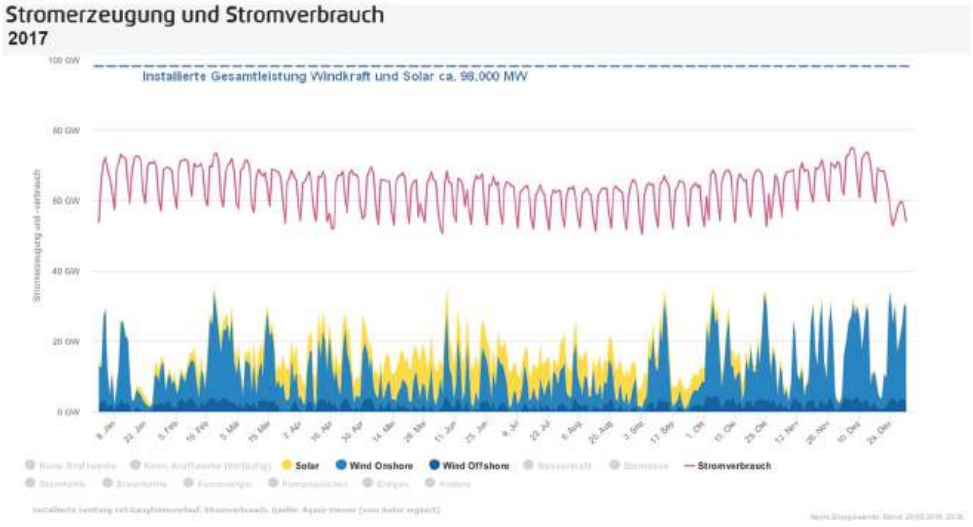

Figure 8. Data show the consumption of total electricity in Germany, along with electricity produced from renewable energy sources (such as wind, either offshore or onshore, and solar) in calendar year 2017 [32,33].

These scenarios have been performed on well X6. The schedule is based on the data shown in Figure 8. The baseline of 10 GW is the shut-in period. Greater than the 10-GW baseline is considered to have an excess of electricity that can be used as injection periods for power-to-gas storage, and less than the limit of 10 GW is a shortage of electricity. These periods have been considered for the production of gas for gas-to-power conversion. These data [32,33] on excess electricity from Germany have been used to conduct two short-term real world case schedule cases: one with limited water cut-off and one without limited water cut-off.

4.4. Case C

This scenario has been performed on vertical well X6. The schedule timeline of one year has been adopted from Figure 8. The well water production rate (WWPR) is restricted to 5 m^3/day (Figure 9c). The FPR eventually increases in this case to up to 15.72 MPa with slight variations during the gas production cycles. Gas injection succeeds to maintain the pressure, and it increases from ~15.39 MPa and reaches approximately ~15.72 MPa at the end of the one-year period (Figure 9a). The variability in WBHP is directly proportional to the gas production cycles. As shown in Figure 9a, as the gas production increases, the well bottom-hole pressure decreases even as the gas injection continues. The maximum WBHP reaches a value of 18.8 MPa, the minimum WBHP reaches a value of 14.4 MPa, and these maximum and minimum pressure values represent injection and production cycles (Figure 9b). The well gas injection rate (WGIR) varies during the year, having a minimum injection rate of approximately 32,000 m^3/day and a maximum rate of about 66,000 m^3/day. In contrast, the well gas production rate (WGPR) has minimum and maximum values of 4300 m^3/day and 19,000 m^3/day, respectively (Figure 9d). The lower WGPR compared to the WGIR is due to the limited WWPR, which does not allow the well to produce at a higher WGPR.

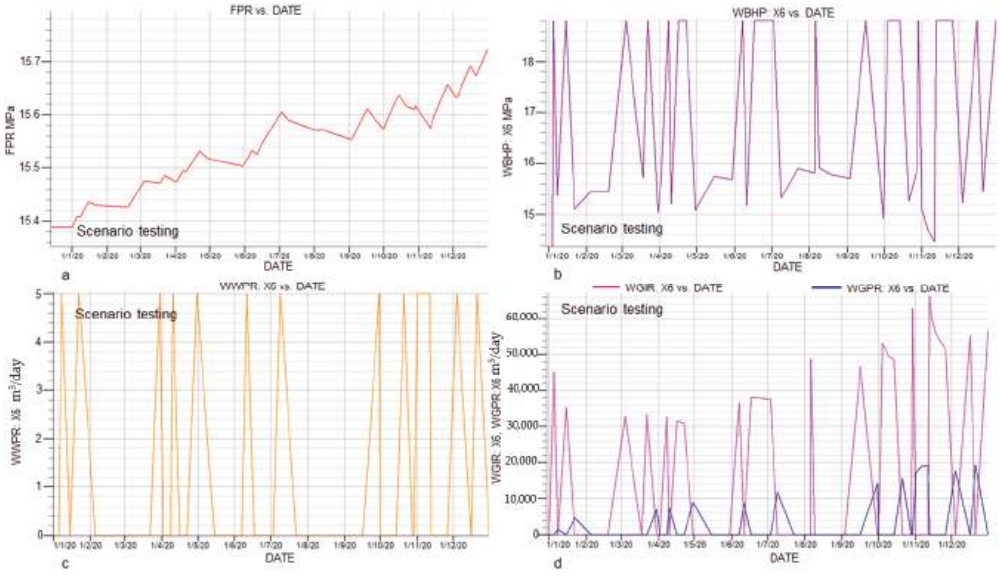

Figure 9. The fluctuation in electricity produced in Germany from renewable sources in 2017 is modelled into a future scenario testing case with limited water cut-off (5 m^3/day). The excess of energy can be stored in UGS and can be used when needed. This schedule is helpful to understand in which month of the year energy can be stored as gas in UGS and in which month of the year this energy can be utilized when shortage occurs: (**a**) field pressure (FPR) profile for these cycles; (**b**) well bottom hole pressure (WBHP) of well X6; (**c**) well water production rate (WWPR) for well X6; and (**d**) well gas injection rate (WGIR) and well gas production rate (WGPR) for well X6.

Results

The modelling results of this case are presented in the form of the pore pressure and effective stress changes in the top layer of the reservoir. Two time steps have been selected for the conclusion of the results for this model. Time step t1 is the starting point of the schedule case, i.e., 1 January 2020, and t2 is the end schedule point (31 December 2020). The pore pressure at the well X6 location is about 15.2 MPa at t1 and increases to about 15.8 MPa at t2; simultaneously, the effective stresses at well X6 is about 28.6 MPa, and it decreases to about 28.0 MPa at time steps t1 and t2 (Figure 10). There is an increase of 0.6 MPa in pore pressure and decrease of 0.6 MPa in effective stress at the top surface of the reservoir layer near well X6 from t1 to t2.

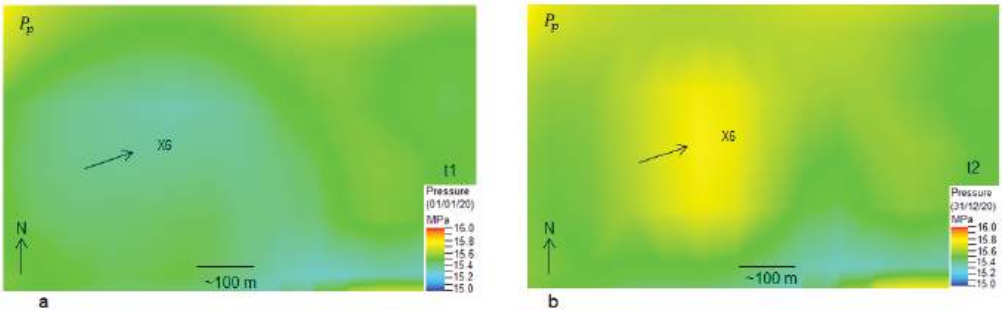

Figure 10. *Cont.*

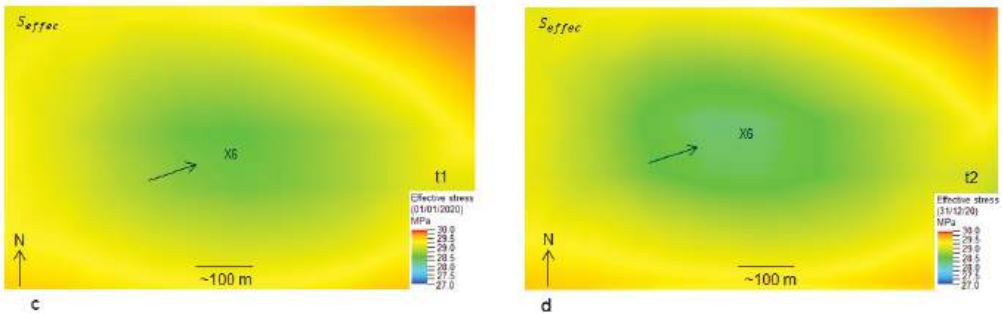

Figure 10. Pore pressure (P_p) and effective stress (S_{effec}) changes from t1 (1 January 2020) to t2 (31 December 2020) in the short-term case with one well (X6) with a water cut-off rate of 5 m^3/day and a random schedule. The arrows show the location of the maximum observed fluctuation in P_p and S_{effec} from t1 to t2. The color scale is in MPa. (**a**) is pore pressure at time t1; (**b**) is pore pressure at time t2; (**c**) is effective stress at time t1; (**d**) is effective stress at time t2.

4.5. Case D

This scenario has been performed on vertical well X6. The schedule timeline of one year has been adopted from Figure 8. There was no water cut-off rate limit set in this scenario; hence, the maximum water production rate (WWPR) increases up to 43 m^3/day and remains less than 20 m^3/day throughout the production and injection period of one year, respectively (Figure 11c). The FPR is sustained in this case by gas injection and increases to up to a maximum value of 15.62 MPa with slight variation during the gas production cycles in the one-year period (Figure 11a). The alteration in WBHP is directly proportional to the gas production cycles without a water cut-off limit. As shown in Figure 11b, the WBHP reaches a maximum value of 18.8 MPa and a minimum value of approximately 13.8 MPa. The well gas injection rate (WGIR) varies during the year, having a minimum injection rate of approximately 32,000 m^3/day and a maximum rate of about 60,000 m^3/day, whereas the well gas production rate (WGPR) has minimum and maximum values of 16,000 m^3/day and 40,000 m^3/day, respectively (Figure 11d).

Results

The modelling results of this case are presented in the form of pore pressure and effective stress changes of the top layer of the reservoir. Two time steps have been selected for the conclusion of the results for this model. Time step t1 is the starting point of the schedule case, i.e., 1 January 20, and t2 is the end schedule point (31 December 2020). The pore pressure at the well X6 location is about 15.1 MPa at t1 and increases to about 15.7 MPa at t2, whereas the effective stress at well X6 is about 28.7 MPa, and it decreases to about 28.1 MPa at time steps t1 and t2. There is an increase of 0.6 MPa in pore pressure and a decrease of 0.6 MPa in effective stress at the top layer of the reservoir around well X6 from t1 to t2 (Figure 12).

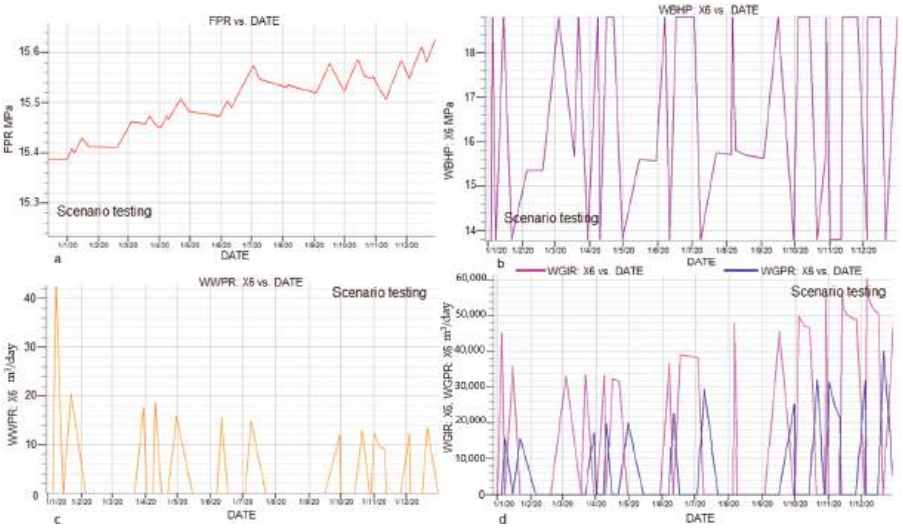

Figure 11. The fluctuation of electricity produced in German from renewable sources in 2017 is modelled into a future scenario testing case without limited water cut-off. The excess of energy can be stored in UGS reservoirs and can be used when needed. This schedule is helpful to understand which month of the year's energy can be stored as gas in UGS and in which month of the year this energy can be utilized when shortages occur: (**a**) field pressure (FPR) profile for these cycles; (**b**) well bottom hole pressure (WBHP) of well X6; (**c**) well water production rate (WWPR) for well X6; and (**d**) injection (WGIR) and production (WGPR) gas rates for well X6.

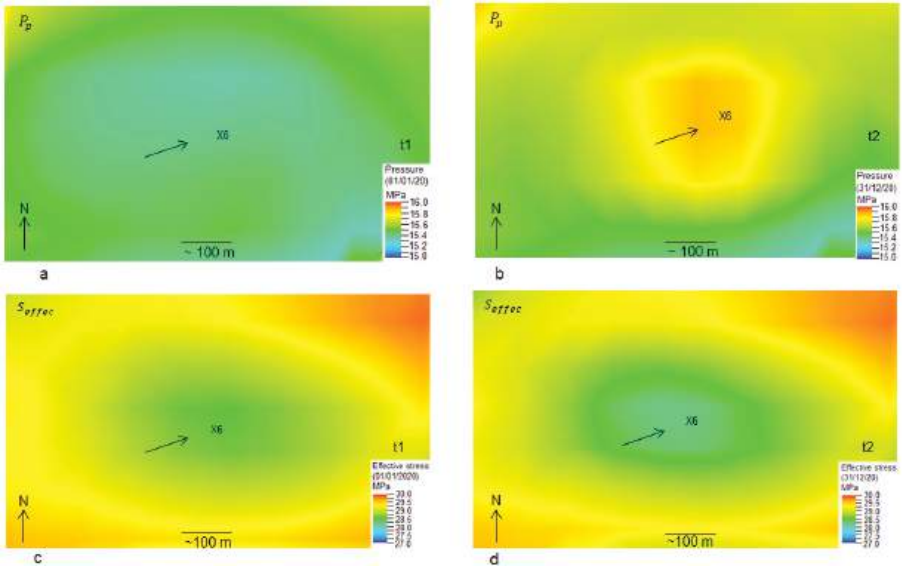

Figure 12. Pore pressure (P_p) and effective stress (S_{effec}) changes from t1 (1 January 2020) to t2 (31 December 2020) in short-term case with one well (X6) without a water cut-off rate of 5 m^3/day with a random schedule. The arrows show the location of the maximum observed fluctuation in P_p and S_{effec} from t1 to t2. The color scale is in MPa. (**a**) is pore pressure at time t1; (**b**) is pore pressure at time t2; (**c**) is effective stress at time t1; (**d**) is effective stress at time t2.

The summary of all the results is compiled in Table 2 to have better understanding of pore pressure and effective stress changes of all future testing cases with time (t1 to t2).

Table 2. Summary of results for all future test scenarios. The sign + in the pore pressure changes indicates a positive change or an increase in pore pressure from time step t1 to t2, while the sign—in the changes in effective stresses denotes a decrease in magnitudes of effective stresses for time step t1 to t2. These two quantities are inversely proportional to each other and are expressed in MPa and KPa for a better understanding of the changes.

Modelling Scenarios	**Subdivisions**		**Results**	
			Pore pressure changes ΔP_p	Effective stress changes ΔS_{effec}
Short-term (weekly) cases	Case A	With three wells (two vertical wells, one horizontal well)	+0.3 MPa +300 KPa	−0.3 MPa −300 KPa
	Case B	With three wells (two vertical wells, one horizontal well)	+0.4 MPa +400 KPa	−0.4 MPa −400 KPa
Real-world cases	Case C	With one well	+0.6 MPa +600 KPa	−0.6 MPa −600 KPa
	Case D	With one well	+0.6 MPa +600 KPa	−0.6 MPa −600 KPa

5. Thermal Analysis

The same dynamic model has been used for thermal analyses. Since long-term injection would impact the thermal changes in the reservoir significantly, a long-term seasonal case is used to analyse the temperature changes within the reservoir if a foreign gas is injected into it. Therefore, six months of gas injection and six months of gas withdrawal are considered in this modelling case. The initial reservoir temperature is ~45 °C, and the foreign gas temperature is 25 °C. Two cycles have been considered to analyse the temperature changes during these injection/production operations. Gas is injected into the reservoir for the first half year and produced in the second half of the year. Two wells, X2 and X6, are considered to analyse the temperature changes around the well bore vicinity. The bottom hole pressure (WBHP) for both wells is set to an upper limit of 18.8 MPa and a lower limit of 13.8 MPa in case of the injection and production phases, respectively. These pressure limits are set in place to avoid fault reactivation or fracture-inducing phenomena during the injection phase, as well as to avoid sand production or contraction of the reservoir during the production phase. The WGIR and WGPR are set to 100,000 m^3/day for both wells.

Thermal stresses are the stresses that occur due to the change in temperature in the system, i.e., original temperature minus final temperature. If foreign gas is injected into the underground gas reservoir, the temperature in the reservoir changes, which causes thermal-related stress changes in the reservoir. The relationship of temperature changes and thermal stress is expressed by the following equation [34]:

$$S_t = E * \alpha_t (T_f - T_0) = E * \alpha_t (\Delta T), \quad (11)$$

In the above equation, S_t is thermal stress, E is the Young's modulus, α_t is the thermal coefficient, T_f is the final temperature of the reservoir, T_0 is the original temperature of the reservoir, and ΔT is the temperature difference in the reservoir. Less ΔT causes less thermal stress in the reservoir and vice versa.

The following section describes the results, i.e., temperature changes with injection of colder foreign gas (25 °C) into the reservoir (i.e., about 45 °C) through space and time with seasonal cyclic injection/production phases. The top view of the reservoir surface is

shown in the figure at different time steps (Figure 13). Two injection/production cycles with four-time steps have been selected to show thermal changes in the reservoir with injection and production phases. Time step t1 (1 January 2020) is the pre-operational history temperature of the reservoir at wells X2 and X6 (Figure 13a). Time step t2 (1 July 2020) represents the end of the injection time of colder foreign gas (25 °C), which is injected for the first half of 2020 (Figure 13b). Time step t3 (1 January 2021) is the end of the production period of the cycle (Figure 13c), and t4 (1 July 2021) is again the end of injection phase of the second cycle (Figure 13d).

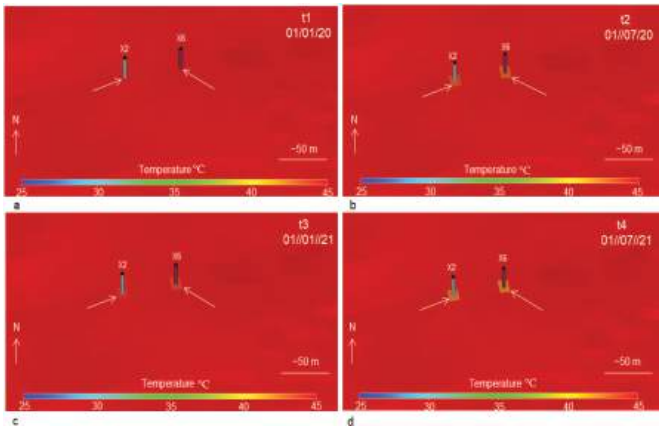

Figure 13. Temperature changes around wells X2 and X6 by injecting colder foreign gas at different time steps (t1, t2, t3, and t4). Time steps t1, t2, t3, and t4 correspond to 1 January 2020, 1 July 2020, 1 January 2021, and 1 July 2021, respectively. The arrows show the exact location of significant temperature differences during injection/production phases. The colour scale is in °C, whereas the arrows with N indicate a northward direction. (**a**) is temperature at time t1; (**b**) is temperature at time t2; (**c**) is temperature at time t3; (**d**) is temperature at time t4.

The reservoir temperature is 45 °C at time step t1, which is the pre-operational temperature. The temperature decreases to about 43 °C at well X6 and 42.5 °C at well X2 at time step t2 after constant injection of colder gas (25 °C), with a well gas injection rate (WGIR) of 100,000 m^3/day for six months. The temperature increases to about 43.5 °C and ~43 °C at wells X6 and X2, respectively, at time step t3. There is only about a 0.5 °C increase in temperature from t2 to t3. Temperatures at well X6 and X2 decrease to about 41.5 °C and 42 °C, respectively, again in the second cycle of injection at t4. Thermal changes are minor and occur only at the vicinity and around the well locations. The thermal effects on the stress are not significant in the reservoir even after injection of 100,000 m^3/day of colder gas for about a half year. This outcome shows that the thermal changes in the short-term cases are negligible for analysing the geomechanical stresses on the reservoir in storage operations.

6. Potential Fault Reactivation Analyses

6.1. Model Setup

Fault reactivation is the possibility of failure in geomechanical assessment of the reservoir, which can risk operational safety, cause micro seismicity within and around reservoirs, and provide a leakage path for gas to escape. Fault reactivation occurs when the shear stress acting on the fault planes exceeds the shear strength of the fault. The

Mohr–Coulomb failure criterion relationship of pore pressure and the principal stresses of this case study reservoir (lies in normal stress regime) are expressed by this equation [35]:

$$P_p = \frac{1}{\alpha}[\frac{1}{2}(S_v + S_{hmin}) + \frac{1}{2}(S_v - S_{hmin})\cos 2\theta - \frac{1}{2}(S_v - S_{hmin})\frac{\sin 2\theta}{\mu}], \quad (12)$$

where α is the Biot coefficient (assumed 1), S_v is the vertical and maximum principal stress, S_{hmin} is the minimum horizontal stress, θ is the angle between the dip line of the fault and the S_{hmin} direction, P_p is the critical pore pressure, and μ is the coefficient of friction.

These analyses include the calculation of the critical pore pressure with the aim of observing possible differences in pore pressure required for fault reactivation. The pore pressure derived from the history matching scenario is multiplied by a fixed factor controlled by gas rates until fault reactivation occurs. The upper limit of the BHP is removed to obtain a higher pore pressure. The factors used for this operation are 1.15, 1.25, and 1.5 (Figure 14). It is then possible to evaluate pressure changes in the reservoir required to reactivate the fault, as well as the safe storage capacity of the reservoir.

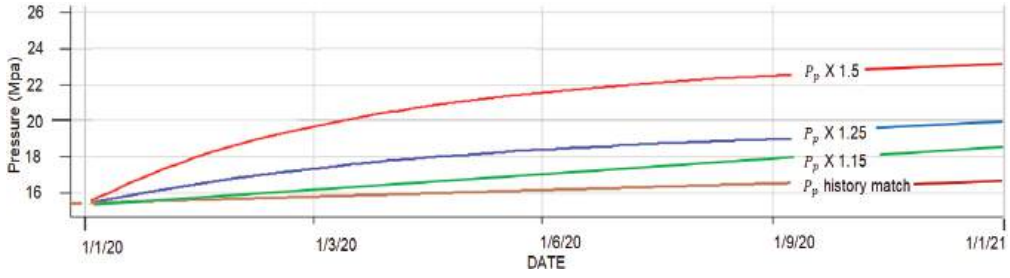

Figure 14. Pressure profiles for the history matching scenario and scenarios multiplied by fixed factors (P_p, P_p X 1.15, P_p X 1.25, and P_p X 1.5) controlled by gas injection rates until fault reactivation occurs.

Figure 14 shows different pressure profiles based on distinct gas injection scenarios. The P_p (history match pressure) curve exhibits a maximum value of ~16.2 MPa with gas injected at a rate of 100,000 m^3/day for one year, whereas to reach a pressure value 1.15 times the actual history match pressure case, 175,000 m^3/day of gas are injected for 1 year. The pressure increased up to 18.6 MPa. In case P_p X 1.25, 240,000 m^3/day is injected to reach a pressure of about 20.25 MPa. Similarly, in case of P_p X 1.5, a gas volume of 560,000 m^3/day is injected (for one year), which increases the pressure up to 24.3 MPa.

6.2. Results

The results of this section are based on the model setup explained in the above section. The methodology follows the different cases in which the initial reservoir pore pressure is multiplied by a factor of 1, 1.15, 1.25, and 1.5, corresponding to pore pressure values of ~16.2 MPa, ~18.6 MPa, ~20.25 MPa and ~24.3 MPa, respectively. The results display the oblique view of the topmost layer of the reservoir (Figure 15). The Mohr circles correspond to the well X6 location near the main fault (Figure 15). Two time steps have been considered for all the cases: t1 (1 January 2020) is the starting time step, and t2 (1 January 2021) is the end time step of the schedule year.

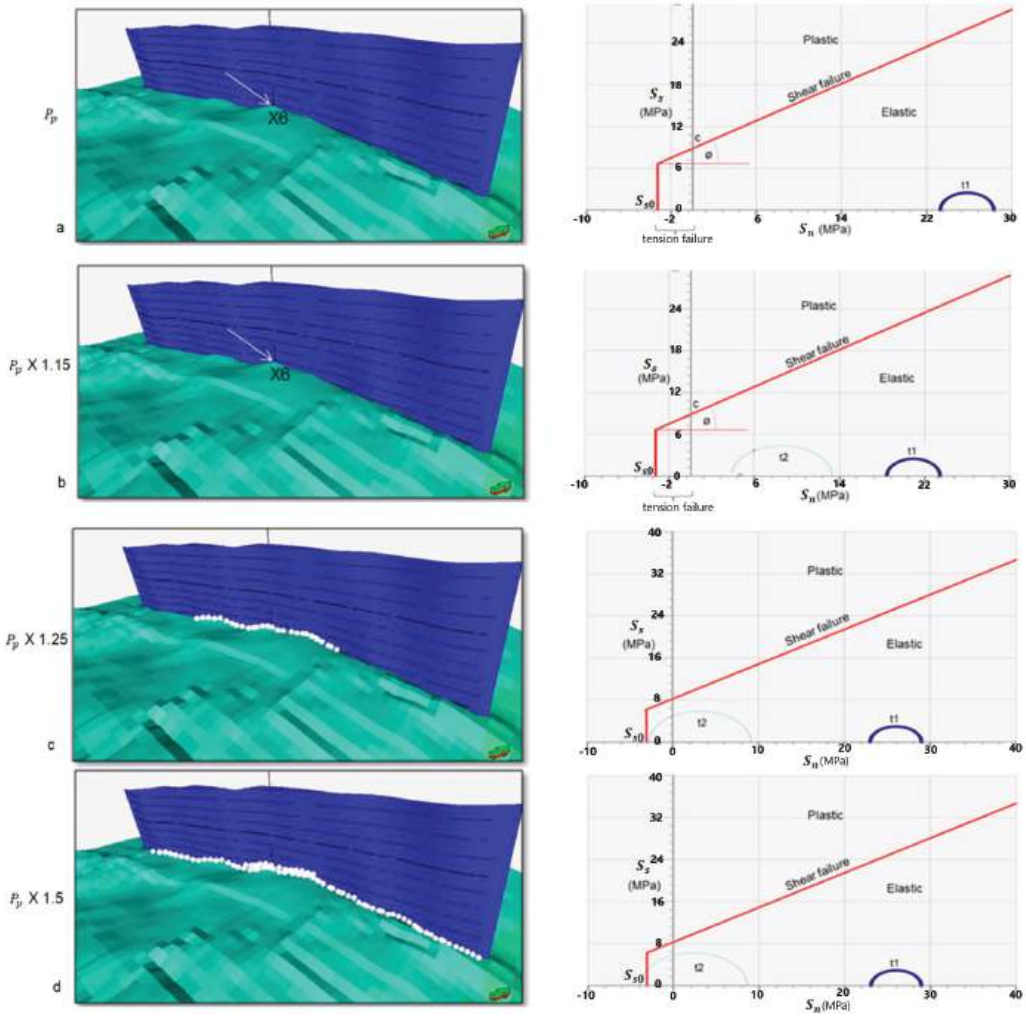

Figure 15. The computation of fault reactivation for initial pore pressure multiplied by a factor of 1 (**a**), 1.15 (**b**), 1.25 (**c**), and 1.5 (**d**) is shown on the left side. White boxes show the cells with stress states exceeding the failure criterion (arrows show northward direction). On the right side of the figure are the shear stress S_s vs. normal stress S_n diagrams, showing the Mohr–Coulomb failure criterion at the well X6 location (which is nearest the main fault of the reservoir). Time steps t1 and t2 correspond to the starting (1 January 2020) and final (1 January 2021) time steps of the tested cases, respectively. The increase in pore pressure leads to a decrease in effective stresses, causing the corresponding Mohr circle to shift to the left. If the failure line is finally touched, plastic straining and—in case of a fault zone—fault reactivation occur.

Fault reactivation is observed already at P_p X 1.25 (~20.25 MPa) (Figure 15b), at which the corresponding Mohr circle has just touched the tensile failure line. The amount of failure in the cells becomes more prominent as pore pressure increases to greater than the pore pressure factor of 1.25 (i.e., P_p X 1.5), and it causes the corresponding Mohr circles to move further left (Figure 15c,d). The increase in pore pressure causes decreases in effective stress, causing the Mohr circles to move to the tensile failure line. Thereafter, the material enters the plastic regime; therefore, in case of failure, fault reactivation occurs.

6.3. Safe Injection Rate for Safe Storage Capacity

The pore pressures for fault reactivation for the different scenarios calculated in the numerical modelling analysis provide an estimate of the pressure at different injection rates. The injection rate (in terms of volume rate) to achieve a perfect history match (16.2 MPa) is about 100,000 m^3/day, and fault reactivation is already observed at P_p times 1.25, i.e., about 20.25 MPa at an injection rate of 240,000 m^3/day. With the determination of the critical pore pressure, it is also possible to derive an upper limit for the injection rate to be selected for injection processes. By considering the highest safety margin, the injection rate between 100,000 m^3/day and 150,000 m^3/day would be the considered safe injection rate for safe storage for the case study reservoir. A gas injection rate greater than this threshold value can have a significant impact on the risk management and operational setup of underground gas storage.

6.4. Storage Capacity of Power-to-Gas and Gas-to-Power

Regarding the storage capacity of power-to-gas technologies, the case study reservoir can store 881,600 kWh/d up to maximum of 1,322,400 kWh/d of power from renewable or other resources with respect to the conversion of a natural gas volume of 100,000 m^3/day to a maximum of 150,000 m^3/day, respectively. Power-to-gas and gas-to-power convertible units are summarized in Table 3.

Table 3. Power-to-gas and gas-to-power convertible units.

m^3 Natural Gas	kWh Power
1	8.816
0.113	1

7. Discussions

7.1. Hydraulic Model

The results of the hydraulic model show variations in gas saturation at different phases during short-term injection-production cycles. Figure 16 shows that the injection-production cycle increases the gas saturation during the later cycles, as more gas is produced with increasing cycles until convergence is reached. This outcome indicates the adoption of high-speed multicycle injection-production in UGS with time. This characteristic of UGS indicates the increase in gas-containing pore space with time and explains encroachment of gas flow continuously into the ground water zone for production in the pore throat development area, as the injection-production cycle increases. Meanwhile, under the wetting function, the water film is concentrated in the small pore space compared to the larger pore space; the storage space occupied by the formation of water and dead gas zones is released by the gas execution. Further analysis of the data shows notable findings on the correlation between the time and the amplitude of the gas saturation increase, as shown in Figure 16.

During injection and production cycles, gas saturation increases from ~35% to ~50% from the first cycle to the sixth cycle. Therefore, it appears that, during multi-cycle injection and production in the pre-UGS gas zone, the pore gas storage space in reservoirs with low permeability generally increases sharply, as evident from the correlation between low permeability and high initial water saturation (according to [6]). Moreover, the higher the relative quantity of liquid phase that is continuously transported and dried during high velocity development, the greater the increase in gas saturation.

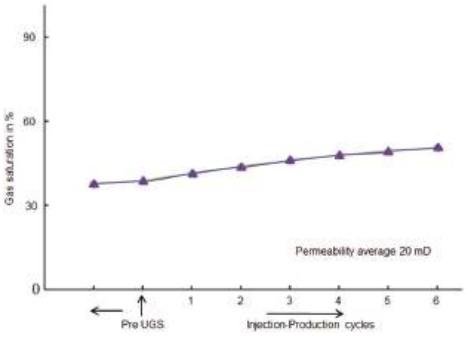

Figure 16. Gas saturation (%) during injection-production cycles.

The gas injection production capacity tends to improve in the UGS gas zone when gas production is increased during the injection production cycle. Further investigation of the UGS gas zone shows that the degree of gas production also increases with the injection-production cycle, but the degree of gas production varies according to the different physical properties and connectivity of the pore spaces [6]. Strong seepage is observed in reservoirs with high permeability, and the gas production and degree of gas recovery are also high under the same injection-production conditions [6].

The gas saturation first decreases in the pre UGS phase and then increases significantly during multi-cycle injection and production, showing the decrease in gas saturation and gas storage space when the gas-drive water zone (gas-water zone, where gas saturation is more dominant) is converted into gas storage. Due to the intrusion of lateral and bottom water, part of the gas storage space is occupied by water during the slow exploitation phase, and a capillary trap for the gas-containing space is also created. Further data show that higher permeability causes water to penetrate, leading to an even greater reduction in gas saturation. During the multi-cycle injection and production phase in UGS, there is no water encroachment, or the part where water encroachment occurs is displaced in the initial gas injection phase of gas storage into the gas-drive water zone. In contrast, under the influence of high velocity injection and production cycle extraction, residual water is produced that is like that in the gas zone before UGS [6]. The experimental analysis shows that the gas-drive water zone is the main expansion zone of the UGS, as the storage space and storage capacity are greatly increased in this gas-drive water zone [6].

The variation of gas saturation in the gas-drive water zone shows the same trends compared to both the trend in the single core experiment and the trends of average gas saturation in the parallel multicore experiment. However, in the multicore parallel experiment, the reduction in gas saturation caused by water encroachment is relatively small [6]. The distinctive feature of reservoir heterogeneity, a formation with high permeability, has a great impact on the water body as it promotes water intrusion, while formations with medium and low permeability are less affected by water intrusion. During high velocity injection and production, the gas preferentially percolates into the high permeability formation, resulting in gas saturation recovery in the high permeability reservoir.

The gas permeability of the reservoir may also decrease due to clay minerals in the reservoir, which may expand when they encounter water, thereby occupying the pore space. For this reason, gas production and gas content are relatively low in the first injection and production cycle. Meanwhile, the gas recovery level and gas production level are low due to lower vertical permeability [6]. Furthermore, gas production and injection increase with increasing permeability.

The transition of the reservoir characteristic of the gas-water transition may indicate that water intrusion is caused not only by exploitation of the gas field but also by the gas storage cycle in the operational phase. In general, the gas saturation decreases both in operational zones of the reservoir and in the gas-water zone. However, the effects of

physical properties and heterogeneity, wettability, and capillary pressure of the reservoir make the production mechanism of multicycle injection complex. The relationship between gas and water in the gas-water transition zone tends to be rational, and the gas saturation tends to plateau during multicycle injection production [6]. Alternatively, residual gas and trapped gas are effectively reduced due to the back-and-forth movement of gas and water through the gas-containing spaces, but the changes in gas saturation are small throughout the reservoirs. Conversely, in high-speed injection and production, water is still continuously transported into the pore throat for production, but in gas storage, the main discharge concerns water in the large pore throat because it is difficult to displace water in the micropores. For this reason, gas saturation tends to plateau in the gas-water transition zone. Due to the reduction in water intrusion energy, gas saturation increases slightly in the subsequent phases of injection and production operations.

These results show that low gas saturation and poor recovery are observed in the gas-water transition zone of UGS and that effective exploitation of the gas-water transition zone is affected by reservoir heterogeneity [6]. Therefore, the effective utilization of the gas-containing pore space under the high-speed injection and production conditions of gas storage is significantly different from the utilization of the gas reservoir. For that reason, the optimal design of UGS capacity and calculation of gas storage parameters should be founded on the effective utilization of the gas-containing pore space, as well as on the effective pore space of the reservoir structure in different zones [6].

7.2. THM Coupled Modelling

The geomechanical approach presented in this paper allows for characterization, from a geomechanical point of view, of the target reservoir in a very understandable way. The coupled simulation of one-way flow and geomechanics (VISAGE^{TM}) focuses on understanding the variation in effective stresses due to pressure changes associated with gas injection into the subsurface reservoir. In other words, the focus is on the pore pressure changes during operation. The VISAGE^{TM} model is created directly from the geological model and can therefore be considered more accurate in terms of geometry compared to another finite element model, such as an ANSYS^{TM} model. The material properties in the VISAGE^{TM} model are scaled up from borehole logs, and their population contains information about the original vertical and horizontal variations. The VISAGE^{TM} simulator treats faults as 3D cells with different material parameters in relation to the surrounding rock. The output of the VISAGE^{TM} model is continuous through space, and the presence of faults can be detected by an abrupt change in depth at the point of displacement, even if the horizon is technically not present at that point. Therefore, VISAGE^{TM} is used for ECLIPSE^{TM}-VISAGE^{TM} coupling to build a coupled THM model to achieve the desired geomechanical results.

THM coupled modelling involves coupling of static geomechanical model with dynamic fluid (hydraulic) modelling. The geomechanical stresses of the reservoir change in space and time when coupled with pore pressure, either from reservoir history or from future testing scenarios. In general, these dynamic models are based on the concept of effective stress to characterize the effects of pore pressure changes on reservoir and caprock integrity, as well as fault stability. Simplified geomechanical models rely mainly on the concept of effective stress to distinguish the effects of pore fluid changes on reservoir integrity and fault stability. Terzaghi [36] proposed this effective stress concept for soil systems. The result of the increase in pore fluid pressure is equal to the decreased effective stress on the rock mass, and conversely, this concept implies that the effective stress experienced by the rock framework is due to the changes in fluid pressure, with the absolute magnitudes of the principal in situ stresses themselves remaining unaltered.

From a classical point of view from Terzaghi [36], changes in vertical stress can be predicted as the effective vertical stress increases and decreases during withdrawal and injection, while the reservoir stress path effect can clearly distinguish the changes in the effective minimum horizontal stresses. As a result of the increased fluid pressure, the Mohr

circle drifts to the left, in turn reducing the diameter of the circle, implying that the fault is under a lower differential stress. The theoretical viewpoint consolidates only the concept of effective stress, and the assumption can be made that the stress path during compression is parallel to the failure envelope rather than towards it [2]. A steeper stress path during the injection process is the result of a small Poisson's ratio, a large Biot coefficient, a large shear modulus, and a shallower reservoir, further causing drift away from the failure envelope.

At the case study reservoir, reactivation of the fault with increasing fluid pressure would not be possible if the stress path could be assumed to be exactly linear to higher fluid pressures. The magnitude of the stress path in the reservoir is an absolute criterion to ensure that the faults are not tapered by pressurization or depressurization. Furthermore, this linear extrapolation of the stress path is obviously only suitable for moderate fluid pressure levels. During pressurization of the system, there are some points at which the horizontal stress becomes the maximum principal stress instead of the vertical stress. This outcome shows that, in the absence of stress path effects, the stress path changes and moves towards the failure criterion.

One of the main aspects of the THM modelling results is the deformation within and outside of the reservoir formation because of injection and withdrawal of fluid/gas in reservoirs. Pressurization and depressurization cause deformations in both the reservoir and the overburden, which are part of the effective results of geomechanical modelling. During overpressure or underpressure, the elastic or non-elastic expansion or contraction of the rock mass causes such deformations. The reactivation of faults and the integrity of the rock may be affected by deformations within the reservoir. In addition, deformations associated with reservoir depletion can also pose a serious problem in terms of casing collapse and can become a major obstacle to subsequent drilling [37].

The main risks related to pressurization and depressurization of a field during injection and withdrawal periods, respectively, are fault reactivation and associated permeable leakages. During gas injection and production phases, reactivation of the fault and associated permeable pathways is one of the main risks associated with pressurization and depressurization. The classical fault model would predict that, as the fault approaches shear reactivation, there will be an increase in fluid pressure that would reduce the effective normal stress on the fault. However, the stability of the fault is significantly affected by the progression of reservoir stresses through the effects on horizontal stress magnitudes. As discussed in the above section, the simulation results of the THM model predict decreases in effective stresses but increases in pore pressure in various short-term storage cases. If this difference in effective stresses and consequently in pore pressures is very small, no significant stress perturbations would occur. However, if this difference is large, i.e., if the pore pressure in the reservoir is large, then there is a high probability of fault reactivation with increasing pore pressure, as described in the above regarding the various fault reactivation cases. Fault reactivation occurs in the reservoir already at 1.25 times the initial pore pressure of the reservoir, indicating that the Mohr circle reaches the failure line at this pressure.

Distinguishing deformations above and at the surface of the reservoir is also important for surface monitoring and for potential reactivation of faults in the reservoir section. These deformations (either elastic or sometimes plastic) occur due to contraction and expansion of the rock mass during over-pressuring and under-pressuring phases. Over- and under-pressuring of reservoirs are directly related to large amounts of gas injection and production rates, respectively. For this reason, the upper (18.8 MPa) and lower (13.8 MPa) limits of bottom hole pressure (BHP) are considered, which do not allow the pressure to rise or drop below the designated pressure limits. The deformation caused by this over-pressuring and under-pressuring of reservoirs could initiate fault reactivation and may affect caprock integrity. The significant drop in reservoir pressure due to rapid depletion may damage the casing and induce drilling complications for newly planned wells in the reservoir [37].

This study does not include a sensitivity analysis to determine the stress field or displacement of the ground surface when elastic properties vary. Due to the poor correlation

between the mechanical properties of the rock and the porosity in the individual wells, there can be considerable variation in the construction of the static geomechanical model, which can affect the distribution of the mechanical properties, rather than the magnitudes. In contrast, the successive calibration of the sonic logs and the mechanical tests themselves appear to have close correlations, demonstrating their accuracy. However, it is possible that the actual values for Poisson's ratio and Young's modulus may differ slightly from those used in the modelling. There are several studies have already been performed on these parameter studies and the effects of parameter variation on geomechanical stresses and ground surface displacement [38]. Chen (2012) modelled the pressurization of a reservoir at 600 m of depth by 1 MPa using Young's modulus and Poisson's ratio values close to our case study reservoir. This modelling study suggests reducing the stiffness of the reservoir; i.e., reducing the value of Young's modulus from 5 GPa to 3 GPa, the vertical displacement increases from 0.08 to 0.12 mm [38]. Similarly, a reduction in the Poisson ratio from 0.3 to 0.2 results in an increase in the ground surface displacement from 0.11 to 0.13 mm [38]. It should be borne in mind that the sensitivity of these parameters is highly dependent on several different factors, including the depth and size of the reservoir, the stress field, and the properties attributed to the surrounding formations [38]. However, the work presented by Chen gives a rough idea of the types of variations that might be expected from such modelling.

8. Conclusions

THM modelling provide important results for short term gas storage, e.g., conversion of the former gas field to a storage site with short-term (weekly) injection-production schedules. There have been three cases tested for future scenarios with short-term operations. German surplus energy data from renewable energy sources (such as wind and solar energy) from 2017 have also been incorporated into these future testing cases to implement PtG technology on former gas reservoirs to meet Germany's future energy demand. The operating volumes in these cases are controlled by the upper (18.8 MPa) and lower limits (13.8 MPa) of well bottom hole pressure (WBHP). The results of the coupled THM modelling of these cases show that the maximum difference in pore pressure and subsequently effective stress is observed to be 0.6 MPa among all tested cases.

Fault reactivation analyses are performed on the THM models, which evaluate various gas injection scenarios without any upper limit of WBHP. The quantified stresses are then examined against Mohr–Coulomb failure criterion to estimate fault stability. This goal is achieved by including faults with specific properties in the 3D geomechanical model. The stress state of the 3D cells with fault properties exceeding the shear failure line is observed against different gas injection volumes. Fault reactivation occurred at the gas injection rate of 240,000 m^3/day, yielding a value of critical pore pressure. This critical pore pressure was observed to be 1.25 times the original pore pressure, which is equivalent to the WBHP value of 20.25 MPa. With the determination of pore pressure, it is also possible to estimate an upper limit of the gas injection rate for safe storage operation, which in this case study is observed to be in the range between 100,000 and 150,000 m^3/day.

In this study, the critical pore pressure is calculated at the well location, whereas the reference location for further studies can be anywhere in the reservoir, and the high permeability of the reservoir can reduce possible differences in the reference sites. Analysis of the case study numerical modelling results shows that a 4-MPa increase in pore pressure would be sufficient to trigger fault failure.

Thermal stresses depend merely upon the thermal-dynamic processes in the system. Therefore, one case (seasonal) has been tested for thermal stress analysis using the same THM model. The original reservoir temperature is 45 °C, and the injected gas temperature is set at 25 °C. The thermal changes are small (0.5 °C) and occur only near and around the wellbore. The thermal effects on stress are not significant in the reservoir, even after injecting 100,000 m^3/day of colder gas for about half a year. This outcome suggests that the thermal changes in the short-term cases are negligible to be considered in the analysis

of geomechanical stresses in the reservoir during storage operations. This finding is due to the low operating volumes and short time cycles for injection production (weekly schedule) in short-term cases.

In terms of storage capacity of PtG technologies, the case study storage can store up to maximum of 1,322,400 kWh/d of electricity from renewable or other resources, converting the maximum gas volume of 150,000 m^3/day. This amount of energy storage can at least contribute to Germany becoming a greenhouse gas neutral country (GHGND) in 2050, corresponding to an energy demand of 1600 TWh of electricity.

The entire workflow outlined and tested in this study is not site specific but generally applicable to any gas storage in a porous medium including methane, CO_2, and hydrogen.

Perspectives

The modelling schemes described in this study provide a thermal-hydraulic-geomechanical assessment consistent with the observational data presently available. This THM modelling study can be used to assess borehole stability, which can be achieved by analysing the hydraulic and mechanical limits of the borehole walls. Another application of the model can be a fully coupled model, in which geomechanical and hydraulic models are coupled in such a way that both can receive and process the required parameters simultaneously (explained in the last paragraph). This modelling study can also serve as a benchmark for the use of UGS as a seasonal battery for PtG technologies. In this way, the excess energy can be stored as gas in the UGS and later converted back into electricity when needed.

The rock properties of the reservoir have an important influence on the estimated amount of subsidence. For future modelling, it would be useful to conduct detailed rock mechanics experiments with representative samples from the deposits in the region. It is important to have as much reliable data as possible on vertical elevation changes in the region to test different hypotheses related to subsidence. Such data could come from repeated surveys of existing first-order contour lines, GPS, or InSAR observations. In addition, sensitivity analyses or parameter studies to determine the stress field or displacement of the ground surface as elastic properties vary would be useful to understand the reservoir behaviour in response to changes in, for example, Young's modulus or Poisson's ratio.

THM modelling in this study uses a one-way coupling simulation approach. The coupling between dynamic fluid flow and geomechanical simulation can improved by adopting two-way or even fully coupled simulations. Such a simulation means that not only the pore pressure is passed from the fluid flow model to the geomechanical model, but also properties from the geomechanical model, such as porosity, permeability, and rock compressibility, are passed back to the fluid flow model to obtain continuously updated accurate modelling results. Two-way and fully coupled simulation approaches would also be useful to analyse ageing effects in reservoirs due to long- and short-term storage operations.

Author Contributions: Conceptualization, M.Z.-U.-A. and A.H.; methodology, M.Z.-U.-A.; software, M.Z.-U.-A.; validation, M.Z.-U.-A. and A.H.; formal analysis, M.Z.-U.-A.; investigation, M.Z.-U.-A.; resources, M.Z.-U.-A.; data curation, M.Z.-U.-A.; writing—original draft preparation, M.Z.-U.-A.; writing—review and editing, A.H.; visualization, M.Z.-U.-A.; supervision, A.H.; project administration, A.H.; funding acquisition, A.H. All authors have read and agreed to the published version of the manuscript.

Funding: This research was funded by BMBF (Federal Ministry of Education and Research), grant number 03G0869.

Data Availability Statement: Data available in a publicly accessible repository. The data presented in this study are openly available in [TUprints, Darmstadt] at [DOI: 10.26083/tuprints-00022537, CC-BY-SA 4.0 International.

Acknowledgments: The authors thank Uniper SE for providing data for this research. We acknowledge the German Federal Ministry of Education and Research (BMBF) for providing financial support for the SUBI research project. In addition, we acknowledge support from the Deutsche Forschungsgemeinschaft (DFG, German Research Foundation) and the Open Access Publishing Fund of the Technical University of Darmstadt.

Conflicts of Interest: The authors declare no conflict of interest.

References

1. Teatin, P.; Castelletto, N.; Ferronato, M.; Gambolati, G.; Janna, C.; Cairo, E.; Marzorati, D.; Colombo, D.; Ferretti, A.; Bagliani, A.; et al. Geomechanical response to seasonal gas storage in depleted reservoirs: A case study in the Po River basin, Italy. *J. Geophys. Res. AGU J.* **2011**, *116*, 21. [CrossRef]
2. Tenthorey, E.; Vidal-Gilbert, S.; Backe, G.; Puspitasari, R.; Pallikathekathil, Z.; Maney, B.; Dewhurst, D. Modelling the geomechanics of gas reservoir: A case study from the Iona gas field, Australia. *Int. J. Greenh. Gas Control* **2013**, *13*, 138–148. [CrossRef]
3. Aminian, K.; Brannon, A.; Ameri, S. Gas storage in a depleted gas/condensate reservoir in the appalachian basin. In Proceedings of the SPE Eastern Regional Meeting, Canton, OH, USA, 11–13 October 2006.
4. Juez-Larre, J.; Remmelts, G.; Breunese, J.; Van Gessel, S.Q.; Leeuwenburgh, O. Using underground gas storage to replace the swing capacity of the giant natural gas field of Groningen in the Netherlands. A reservoir performance feasibility study. *J. Pet. Sci. Eng.* **2016**, *145*, 34–53. [CrossRef]
5. Industry, D.O.T.A. *Meeting the Energy Challenge: A White Paper on Energy*; Her Majesty's Stationary Off.: Norwich, UK, 2007.
6. Zhang, J.; Fang, F.; Lin, W.; Gao, S. Research on Injection-Production Capability and Seepage Characteristics of Multi-Cycle Operation of Underground Gas Storage in Gas Field—Case Study of the Wen 23 Gas Storage. *Energies* **2020**, *13*, 17. [CrossRef]
7. Kuncir, M.; Chang, J.; Mansdorfer, J.; Dougherty, E. Analysis and optimal design of gas storage reservoirs. In Proceedings of the SPE Eastern Regional Meeting, Pittsburgh, PA, USA, 6–10 September 2003; pp. 1066–1076.
8. Mazarei, M.; Davarpanah, A.; Ebadati, A.; Mirshekari, B. The feasibility analysis of underground gas storage during an integration of improved condensate recovery processes. *J. Pet. Explor. Prod. Technol.* **2019**, *9*, 397–408. [CrossRef]
9. Dharmananda, K.; Kingsbury, N.; Singh, H. Underground gas storage: Issues beneath the surface. In Proceedings of the SPE Asia Pacific Oil and Gas Conference and Exhibition, Perth, Australia, 18–20 October 2004; pp. 10–17.
10. Abedin, M.Z.; Henk, A. Building 1D and 3D Mechanical Earth Models for Underground Gas Storage—A Case Study from the Molasse Basin, Southern Germany. *Energies* **2020**, *13*, 21.
11. Khaksar, A.; White, A.; Rahman, K.; Burgdorff KOllarves, R.; Dunmore, S. Geomechanical Evaluation for Short Term Gas Storage in Depleted Reservoirs. In Proceedings of the 46th US Rock Mechanics/Geomechanics Symposium, Chicago, IL, USA, 24–27 June 2012.
12. Bachmann, G.H.; Müller, M.; Weggen, K. Evolution of the Molasse Basin (Germany, Switzerland). *Tectonophysics* **1987**, *137*, 77–92. [CrossRef]
13. Dake, L.P. *Fundamentals of Reservoir Engineering*; Elsevier Scientific Pub. Co.: Amsterdam, The Netherlands, 1978.
14. Dai, W.J.; Gan, Y.X.; Hanaor, D. Effective Thermal Conductivity of Submicron Powders: A Numerical Study. *Appl. Mech. Mater.* **2015**, *846*, 500–505. [CrossRef]
15. Settari, A.; Mourits, F. A Coupled Reservoir and Geomechanical Modeling System. *SPE J.* **1998**, *SPE 50939*, 219–226. [CrossRef]
16. Tortike, W.; Farouq, A.S. Reservoir Simulation Integrated with Geomechanics. *J. Can. Pet. Technol.* **1993**, *5*, 28–37. [CrossRef]
17. Jalali, M.R.; Dusseault, M.B. Coupling Geomechanics and Transport in Naturally Fractured Reservoirs. *Int. J. Min. Geol. Eng. (IJMGE)* **2012**, *46*, 105–131.
18. Mainguy, M.; Longuemare, P. Coupling Fluid Flow and Rock Mechanics: Formulation of the Partial Coupling between Reservoir and Geomechanical Simulators. *Oil Gas Sci. Technol.* **2002**, *57*, 355–367. [CrossRef]
19. Perkins, T.K.; Gonzalez, J.A. The Effect of Thermoelastic Stresses on Injection Well Fracturing. *Soc. Pet. Eng.* **1985**, *25*, 78–88. [CrossRef]
20. Geertsma, J. Problems of Rock Mechanics in Petroleum Production Engineering. *First Congr. Int. Soc. Rock Mech.* **1966**, *1*, 585–594.
21. Skempton, A. The Pore Pressure Coefficients A and B. *Geotechnique* **1954**, *4*, 143–147. [CrossRef]
22. Geertsma, J. The Effect of Pressure Decline on Volumetric Changes of Porous Rocks. *Trans. AIME* **1957**, *201*, 331–340. [CrossRef]
23. Van der Knaap, W. Nonlinear Behavior of Elastic Porous Media. *Trans. AIME* **1959**, *216*, 179–187. [CrossRef]
24. Nur, A.; Byerlee, J. An Exact Effective Stress Law for Elastic Deformation of Rock with Fluid. *J. Geophys. Res.* **1971**, *76*, 6414–6418. [CrossRef]
25. Ghaboussi, J.; Wilson, E. Flow of Compressible Fluid in Porous Elastic Media. *Int. J. Numer. Methods Eng.* **1973**, *5*, 419–442. [CrossRef]
26. Rice, J.; Cleary, M. Some Basic Stress-Diffusion Solutions for Fluid Saturated Elastic Porous Media with Compressible Constituents. *Rev. Geophys. Space Phys.* **1976**, *14*, 227–241. [CrossRef]
27. Huan, X.; Xu, G.; Zhang, Y.; Sun, F.; Xue, S. Study on Thermo-Hydro-Mechanical Coupling and the Stability of a Geothermal Wellbore Structure. *Energies* **2021**, *14*, 649. [CrossRef]

28. Rutqvist, J.; Wu, Y.; Tsang, C.F.; Bodvarsson, G. A modeling approach for analysis of coupled multiphase fluid flow, heat transfer, and deformation in fractured porous rock. *Int. J. Rock Mech.* **2002**, *39*, 429–442. [CrossRef]
29. Pang, M.; Xu, G.; Sun, F.; Xue, S.; Wang, Y. Formation Damage and Wellbore Stability of Soft Mudstone Subjected to Thermal–Hydraulic–Mechanical Loading. *J. Eng. Sci. Technol.* **2019**, *12*, 95–102. [CrossRef]
30. Hu, L.; Winterfeld, P.H.; Fakcharoenphol, P.; Wu, Y.S. A novel fully-coupled flow and geomechanics model in enhanced geothermal reservoirs. *J. Pet. Sci. Eng.* **2013**, *107*, 1–11. [CrossRef]
31. Tran, D.; Nghiem, L.; Buchanan, L. *Improved Iterative Coupling of Geomechanics with Reservoir Simulation*; Society of Petroleum Engineers: Houston, TX, USA, 2005.
32. Frey, C. Ministerin Hendricks: Wir Haben im Gegenteil Sogar Gigantische Stromüber-Schüsse. 2018. Available online: https://eike-klima-energie.eu/2018/01/07/ministerin-hendricks-wir-haben-im-gegenteil-sogar-gigantische-stromueberschuesse/?print=pdf (accessed on 1 June 2020).
33. Burger, B. Fraunhofer ISE Fraunhofer ISE, Freiburg. 2018. Available online: https://www.ise.fraunhofer.de/content/dam/ise/de/documents/publications/studies/daten-zu-erneuerbaren-energien/Stromerzeugung_2017.pdf (accessed on 1 June 2020).
34. Carter, G.F.; Paul, D.E. *Materials Science & Engineering, Materials Park Ohio*; ASM International: Novelty, OH, USA, 1991.
35. Fjaer, E.; Holt, R.M.; Horsrud, P.; Raaen, A.M.; Risnes, R. *Petroleum Related Rock Mechanics*; Elsevier Science: Oxford, UK, 2008; p. 514.
36. Terzaghi, K. *Theoretical Soil Mechanics*; Chapman and Hall Limited: London, UK, 1948.
37. Zoback, M. *Reservoir Geomechanics*; Cambridge University Press: Cambridge, UK, 2007; p. 449.
38. Chen, Z.R. Poroelastic model for induced stresses and deformations in hydrocarbon and geothermal reservoirs. *J. Pet. Sci. Eng.* **2012**, *80*, 41–52. [CrossRef]

energies

MDPI

Article

Exploring the Impact of Regional Integrated Energy Systems Performance by Energy Storage Devices Based on a Bi-Level Dynamic Optimization Model

Baohong Jin *, Zhichao Liu and Yichuan Liao

College of Civil Engineering, Hunan University, Changsha 410082, China
* Correspondence: jinbh@hnu.edu.cn; Tel.: +86-18829344979

Abstract: In the context of energy transformation, the importance of energy storage devices in regional integrated energy systems (RIESs) is becoming increasingly prominent. To explore the impact of energy storage devices on the design and operation of RIESs, this paper first establishes a bi-level dynamic optimization model with the total system cost as the optimization objective. The optimization model is used to optimize the design of three RIESs with different energy storage devices, including System 1 without an energy storage device, System 2 with a thermal energy storage (TES) device, and System 3 with TES and electrical energy storage (EES) devices. According to the design and operation results, the impact of energy storage devices on the operational performance of RIESs is analyzed. The results show that under the design conditions, energy storage devices can significantly increase the capacity of the combined heating and power units and absorption chillers in System 2 and System 3 and reduce the capacity of the ground source heat pumps and gas boilers; the impact of the TES device on System 3 is more significant. Affected by systems' configuration, the operating cost, carbon tax, and total cost of System 2 are reduced by 2.9%, 5.5%, and 1.5% compared with System 1, respectively. The EES device can more significantly reduce the operating cost of System 3, with a reduced rate of 5.7% compared with that in System 1. However, the higher equipment cost makes the total cost reduction rate of System 3 less than that of System 1, which is 1.75%. Similar to the design conditions, under the operation conditions, the TES device can effectively reduce the carbon tax, operating cost, and total cost of System 2, while System 3 with an EES device can significantly reduce its operating cost regardless of whether the energy price changes or not. To some extent, this study systematically elucidated the impact of TES and EES devices on the optimal design and operation performance of RIESs and provided a certain reference for the configuration of energy storage devices.

Keywords: regional integrated energy system; energy storage device; Bi-level dynamic optimization model; optimal design; operational analysis

Citation: Jin, B.; Liu, Z.; Liao, Y. Exploring the Impact of Regional Integrated Energy Systems Performance by Energy Storage Devices Based on a Bi-Level Dynamic Optimization Model. *Energies* **2023**, *16*, 2629. https://doi.org/10.3390/en16062629

Academic Editors: Luis Hernández-Callejo, Jesús Armando Aguilar Jiménez and Carlos Meza Benavides

Received: 10 February 2023
Revised: 2 March 2023
Accepted: 8 March 2023
Published: 10 March 2023

1. Introduction

In recent years, the sustainable development of energy has received extensive attention. Regional integrated energy systems (RIESs) are expected to become an important way to improve the energy structure and achieve sustainable energy development [1]. However, the intermittency and volatility of renewable energy have brought certain challenges to the stable operation of RIESs [2,3]. With the rapid development of energy storage technology, the development of RIESs with hybrid energy storage has become the main way to solve the volatility of renewable energy and alleviate the contradiction between supply and demand [4,5].

To explore the performance of the integrated energy system with hybrid energy storage, the studies shown in Table 1 have conducted in-depth research on RIESs from aspects of system structure, operation strategy, and optimization model. Different from the

traditional energy system, the RIES involves the deep coupling of multiple heterogeneous energy sources. The modeling idea of the Energy Hub (EH) proposed by Geidl et al. [6] was used to describe the relationship between energy conversion and conservation. However, this modeling idea is not conducive to the RIES's extension and matrix representation in the model. To improve the model portability, an EH modeling method based on graph theory was proposed [7]. Based on this modeling idea, Ma et al. [8] adopted the static equipment model to establish the coupling system optimization model with the total system cost as the optimization objective. User-side energy saving and load management are also one of the main ways to reduce the total cost of RIESs [9–11]. To make full use of the flexibility of loads, Liu et al. [12] established a coupling system optimization model considering the comprehensive demand response. At the same time, this model is also used to explore the impact of energy storage devices on the design and operation of a RIES [13]. The static system optimization model cannot reflect the off-design characteristics of the equipment. To address the issue, a dynamic system optimization model, considering the off-design characteristics of the equipment, was established [14]. On this basis, Mansouri et al. [15] established a dynamic multi-objective optimization model and used it to optimize the design of a RIES with power-gas (P-G) technology. The results showed that the gas storage device could effectively improve the utilization of renewable energy. Unfortunately, none of the above optimization models realizes the decoupling of design and operation.

To achieve the decoupling of design and operation, Mago et al. proposed the following electric load (FEL), following thermal load (FTL), and following hybrid electric-heating load (FHL) strategies according to the role of the combined heating and power (CHP) unit in RIESs [16,17]. Based on the above strategies, Kang et al. [18] explored the operational performance of a RIES under different loads. Wang et al. [19] investigated the impact of energy storage characteristics on the system optimization results based on the system optimization model with the total system cost as the optimization objective. To take the economic, energy-saving, and environmental performance of systems into account, a weighted multi-objective optimization model was established for the optimal design of RIESs [20]. Based on the weighted multi-objective optimization model, Zeng et al. [21,22] used the static and dynamic equipment models to optimize the coupling systems of CCHP and ground source heat pump(GSHP), respectively. However, the value of weight is often subjective. Thus, a multi-objective optimization model with the optimization objectives of cost-saving rate, primary energy saving rate, and CO_2 emission reduction rate was proposed for the optimal design of a RIES [23]. Zhai et al. [24,25] used this model to explore the impact of building types on the operational performance of RIESs. Different types of building loads have certain complementary characteristics. For this reason, Li et al. [26] explored the impact of loads' complementary characteristics on optimization results and operational performance of a RIES. The research showed that the complementary characteristics of loads could reduce the capacity of energy storage devices to a certain extent. In addition, the equipment model and operation strategy also have a certain impact on the optimization results of RIESs. Therefore, Deng et al. [27] established a dynamic multi-objective optimization model based on the dynamic equipment model. Han et al. [28] used a dynamic multi-objective optimization model to optimize the design of a RIES with hybrid, compressed air energy storage. To improve the operational performance of RIESs, an improved FEL strategy was used in the optimal design of a RIES [29]. Compared with the traditional FEL strategy, the improved operation strategy could effectively reduce the energy consumption, operating cost, and CO_2 emission of the RIES. At the same time, the adaptive operation strategy, based on user load, was proposed successively to improve the operational performance of RIESs [30]. However, the relatively fixed operation strategy could not realize the flexible scheduling of RIESs. Hence, Luo et al. [31] adopted the decision tree method to formulate the operation strategy of RIESs. Nonetheless, machine learning greatly relies on building historical load data. To avoid this problem and achieve the flexible scheduling of RIESs, a bi-level optimization model was proposed where the upper-level optimization model is used to determine the optimal configuration of systems, and the lower-level optimization

model is used to realize the flexible scheduling of systems [32]. Based on the bi-level optimization model, Luo et al. [33] optimized the standalone renewable energy system with the total system cost as the optimization objective. Energy storage devices can improve the penetration rate of renewable energy. Li et al. [34] used the bi-level optimization model to optimize the design of an electricity-hydrogen RIES. Ma et al. [35] used this model to explore the impact of shared energy storage on the renewable energy utilization rate and operating cost of RIESs. Although the bi-level optimization model has been widely used in the optimization design and operation analysis of the integrated energy system with energy storage devices, few studies have systematically explored the effects of different energy storage devices on the optimal design and operational performance of the system by the bi-level dynamic optimization model.

Table 1. Literature review of the integrated energy system with energy storage.

Ref.	Renewable Energy	Energy Storage Device	Operation Strategy	Equipment Model	System Optimization Model
[8]	Solar and wind energy	EES, TES	/	Static model	Coupled single objective optimization
[13]	Wind energy	EES, TES	/	Static model	Coupled single objective optimization
[14]	Solar and wind energy	EES, TES, Fuel cell	/	Dynamic model	Coupled single objective optimization
[15]	Wind energy	EES, HES	/	Dynamic model	Coupled multi-objective optimization
[18]	Geothermal energy	/	FEL FTL	Static model	Weak decoupling single objective optimization
[21]	Geothermal energy	TES	FEL FTL	Static model	Weak decoupling weighted multi-objective optimization
[22]	Geothermal energy	TES	FEL FTL	Dynamic model	Weak decoupling weighted multi-objective optimization
[24]	Solar energy	TES	FEL FTL	Static model	Weakly decoupled multi-objective optimization
[25]	Solar energy Geothermal energy	EES TES	FEL FTL FHL	Static model	Weakly decoupled multi-objective optimization
[27]	Geothermal energy	TES	FEL FTL	Dynamic model	Weakly decoupled multi-objective optimization
[30]	Solar, wind and geothermal energy	EES TES	FSF	Dynamic model	Weakly decoupled multi-objective optimization
[31]	Solar energy	EES TES	Dynamic strategy	Dynamic model	Weakly decoupled multi-objective optimization
[34]	Solar, wind and geothermal energy	EES, hydrogen storage	FOF	Static model	Bi-level optimization model
[35]	Solar and wind energy	SES	FOF	Static model	Bi-level optimization model

Different energy storage devices can realize the time-series transfer of different energies. To explore the impact of energy storage devices on the design and operation of RIESs, this paper optimizes three RIESs with different energy storage devices and compares their operational performance according to a public building load in Changsha. The main contributions of this paper are as follows: (1) A bi-level dynamic optimization model is established based on the dynamic equipment model; (2) Three RIESs with different energy storage devices are optimally designed; (3) According to the optimization results, the operational performance of three RIESs with different energy storage devices is compared. The remainder of this study is organized as follows: Part II is the introduction and equipment modeling of RIESs with different energy storage devices; Part III is the establishment of the bi-level system optimization model; Part IV presents the impact of different energy storage

devices on the optimal design and operational performance of the integrated energy system based on the case results; and the conclusions of this work are drawn in Part V.

2. Modeling of RIESs

2.1. Basic structure of RIESs

RIESs can not only realize efficient energy conversion but also gratify the cooling, heating, and electricity needs of users simultaneously. In the RIES shown in Figure 1, the input energy mainly comes from grid electricity, municipal gas, and regional renewable energy (such as solar and geothermal energy). Energy conversion equipment is used to realize the conversion of input energy to output energy, mainly including the transformer, photovoltaic (PV) arrays, CHP unit, gas boiler, GSHP, and absorption chiller (ABC). Therefore, the power, heating, and cooling hubs are introduced in the modeling idea of EH to realize the collection and distribution of different energies and ensure the balance of the supply and demand for energy. In addition, to explore the influence of energy storage devices on the optimal design and operational performance of RIESs, three RIESs with different energy storage devices are considered, and their energy storage configurations are shown in Table 2.

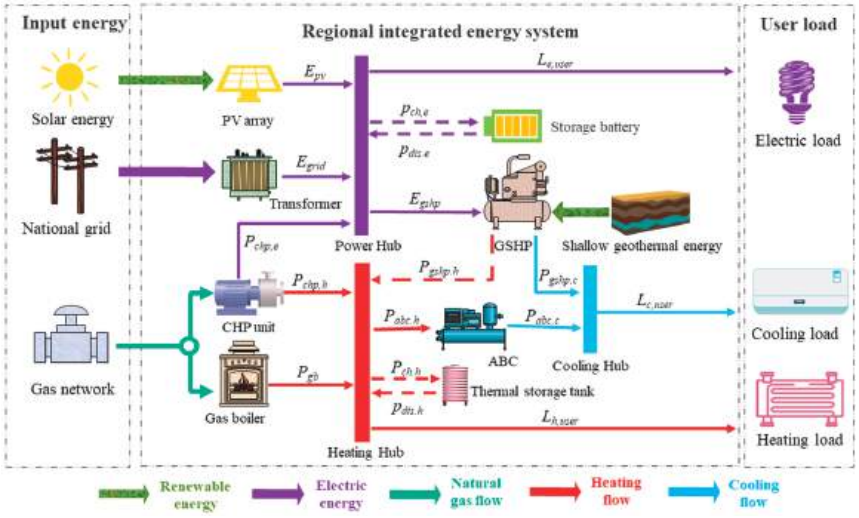

Figure 1. The basic structure of RIESs.

Table 2. Three RIESs with different energy storage devices.

System Name	TES Device	EES Device
System 1	×	×
System 2	✓	×
System 3	✓	✓

2.2. Equipment Mathematical Model

2.2.1. Energy Conversion Device

The equipment model is the basis of system design and operation optimization. In the RIES shown in Figure 1, the PV arrays are one of the effective ways to utilize solar energy, and its power generation is usually affected by the ambient temperature, solar irradiation intensity, and power generation efficiency. Compared with PV arrays, the CHP unit can not only generate electricity, but also the waste heat can be used to meet the cooling and heating needs of buildings. Other than that, the rest of the building's cooling and heating loads are met by the GSHP and gas boiler. When constructing mathematical models for the CHP

unit and cooling and heating equipment, relevant studies generally adopt the black-box model based on energy efficiency. The model is usually divided into two types: the static equipment model and the dynamic equipment model. The static model assumes that the operating efficiency of the equipment is constant. The dynamic equipment model considers the influence of equipment partial load rate on its efficiency. To accurately describe the operation performance of the equipment, the dynamic equipment model will be established in this paper, and the specific expressions for different equipment dynamic models are shown in Table 3.

Table 3. Equipment dynamic model.

Items	Mathematical Models	Ref.
PV	$P_{pv}(t) = A_{pv} \cdot \eta_{pv} \cdot I(t) \cdot (1 - 0.005 \times (t_a(t) - 25))$, $\eta_{pv} = 0.165$.	[36]
CHP unit	$P_{chp,e} = F_{chp} \cdot \eta_{chp.e}$, $P_{chp,h} = F_{chp} \cdot \left(1 - \eta_{chp,e} - \eta_{loss}\right)$ $\eta_{chp,e} = \begin{cases} 0 & PLR_{chp} < 0.2 \\ a_0 + a_1 \cdot PLR_{chp} + a_2 \cdot PLR_{chp}^2 & PLR_{chp} \geq 0.2 \end{cases}$ $PLR_{chp} = E_{chp}/E_{chp,r}$, $a_0 = 0.1$, $a_1 = 0.4$, $a_2 = -0.2$.	[37]
GB	$P_{gb} = G_{gb} * \eta_{gb}$, $PLR = P_{gb}^{out}/P_{gb,r}^{out}$, $PLF = \eta_{gb}/\eta_{gb,r}$, $\eta_{gb,r} = 0.9$, $PLF_{gb} = -0.046 PLR_{gb} + 1.046$, $0.1 \leq PLR_{gb} \leq 1$.	[38]
GSHP	$P_{gshp} = E_{gshp} * COP_{gshp}$, $PLR_{gshp} = P_{gshp}/P_{gshp,r}$, $PLF_{gshp} = COP_{gshp}/COP_{gshp,r}$, $COP_{gshp,r} = 4.5$, $PLF_{gshp} = PLR_{gshp}/\left(-0.2137 PLR_{gshp}^2 + 1.119 PLR_{gshp} + 0.1007\right)$, $0.1 \leq PLR_{gshp} \leq 1$.	[38]
ABC	$P_{abc,c} = P_{abc,h} * \eta_{abc}$, $PLR_{abc} = P_{abc}/P_{abc,r}$, $PLF = \eta_{abc}/\eta_{abc,r}$, $\eta_{abc,r} = 0.9$, $PLF_{abc} = PLR_{abc}/\left(0.75 PLR_{abc}^2 + 0.0195 PLR_{abc} + 0.213\right)$, $0.2 \leq PLR_{abc} \leq 1$.	[39]

2.2.2. Energy Storage Devices

On the basis of System 1, this paper investigates the impact of energy storage devices on the optimization and operation of RIESs by sequentially configuring TES and EES devices in System 2 and System 3. Different from the energy conversion equipment, the source-load duality of energy storage devices allows it to achieve the time-series transfer of energy to meet the supply-demand balance of RIESs. Therefore, the mathematical model of energy storage devices can be expressed by the charging and discharging state and power, and its specific expression is shown as follows [40]:

$$S_k(t+1) = S_k(t) + \left(P_{ch,k}(t)\eta_{ch,k} - \frac{P_{dis,k}(t)}{\eta_{dis,k}}\right)\Delta t \quad (1)$$

where $S_k(t+1)$ and $S_k(t)$ are the energies stored in energy storage device k at time $t+1$ and t, respectively; $\eta_{ch,k}$ and $\eta_{dis,k}$ are the charging and discharging efficiency of energy storage device k; and $P_{ch,k}(t)$ and $P_{dis,k}(t)$ are the charging and discharging powers of energy storage device k at time t.

3. Bi-Level Optimization Model

Energy storage devices not only affect the optimal design of RIESs but also affect their operational performance. To explore the impact of energy storage devices on the optimal design and operation of RIESs, a bi-level dynamic optimization model is established in this paper. In this model, the upper-level optimized configuration model takes the system's total

cost as the optimization objective to determine the equipment capacity of RIESs. The lower-level optimal scheduling model takes the operating cost as the optimization objective to determine the reasonable scheduling scheme. To facilitate the understanding of the solution process of this model, the optimization process is drawn in Figure 2. Firstly, based on the outdoor design parameters, the design and operating loads of the building are calculated by Energy Plus. Secondly, the constraints of the upper-level and lower-level optimization models are established according to the design loads and the EH model. Among them, the main constraints of the upper-level optimized configuration model include the maximum equipment capacity and the design load in winter. And the constraints of the lower-level scheduling model include energy conservation and equipment operating power. Finally, the design load, outdoor parameters, and economic parameters are imported into the bi-level optimization model for solving to obtain the equipment capacity of three RIESs. With the equipment capacity known, this paper uses the lower-level scheduling model to optimize the operation of three RIESs and analyzes the impact of energy storage devices on their operational performance.

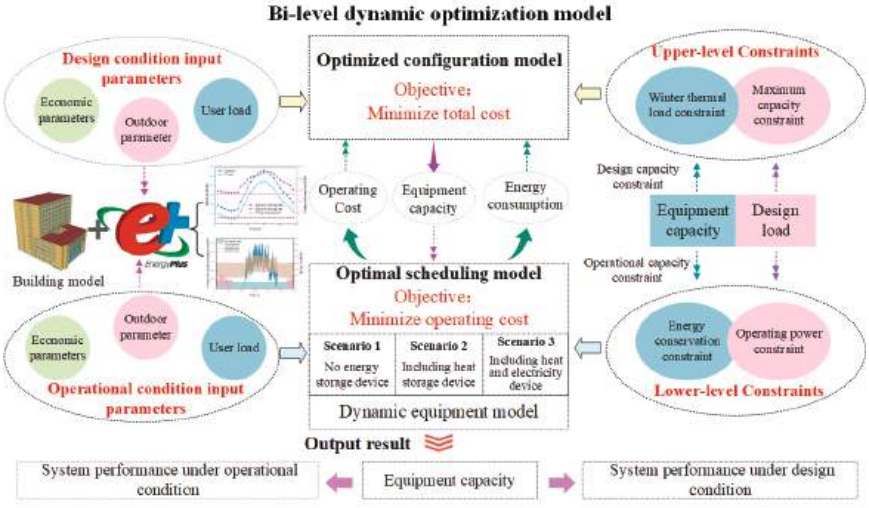

Figure 2. Flow chart of system optimization configuration and operation analysis.

3.1. Upper-Level Optimal Configuration Model

3.1.1. Optimization Objective

To determine the equipment capacity of the three RIESs, this paper optimizes them with the minimum total cost as the optimization objective. In this study, the total cost mainly includes the system equipment cost, operating cost, and carbon tax. The specific calculation expressions are shown below:

$$\min C_{total} = C_{equ} + C_{tax} + C_{op} \tag{2}$$

where C_{total} is the total cost; C_{equ} is the equipment cost; C_{tax} is the carbon tax; and C_{op} is the operating cost, the values can be obtained from the lower-level scheduling model.

The system equipment cost mainly includes the initial investment and equipment maintenance cost. The initial investment in equipment depends on its capacity and the initial unit investment. The initial unit investment in the RIESs, showed Figure 1, is listed in Table 4. Under the condition that the initial unit investment of equipment is known,

the initial investment of RIESs on the design day can be determined by the following formula [41].

$$C_{inv} = \sum_{k=1}^{k} \left(\frac{i(1+i)^n}{(1+i)^n - 1} \cdot Cap_k \cdot C_k \right) / 365 \tag{3}$$

where i is the annual interest rate, which is 0.08 in this paper; n is the planning period, which is 20 years; Cap_k is the design capacity of the equipment k; and C_k is the initial unit investment in the equipment k. As the initial investment in the system's equipment is known, the maintenance cost of the system's equipment can be estimated at 2% of its initial investment [42].

Table 4. The initial unit investment in equipment Reproduced from [43,44].

Equipment Name	Unit Price	Equipment Name	Unit Price
PV	2315 (CNY/m^2)	CHP unit	6812 (CNY/kW)
Boiler	790 (CNY/kW)	GSHP	2782 (CNY/kW)
ABC	1436 (CNY/kW)	TES device	358 (CNY/kW)
EES device	1794 (CNY/kW)		

In the context of peak carbon dioxide emissions and carbon neutrality, carbon tax compensation has become an effective means to limit greenhouse gas emissions. In the RIESs shown in Figure 1, CO_2 emissions mainly come from grid power and gas, so the carbon tax cost can be calculated by the following formula.

$$C_{tax} = \vartheta_{tax} \sum_{t=1}^{24} \left(P_{grid}(t) \cdot \lambda_{CO_2,grid} + P_{gas}(t) \cdot \lambda_{CO_2,gas} \right) \tag{4}$$

where ϑ_{tax} is the carbon tax price; $\lambda_{CO_2,grid}$ and $\lambda_{CO_2,gas}$ are the equivalent CO_2 emissions of coal power and gas, which are 0.968 kg/kWh and 0.220 kg/kWh, respectively [45]; and $P_{grid}(t)$ and $P_{gas}(t)$ are the consumption of grid power and gas at time t, which can be obtained from the lower-level scheduling model.

3.1.2. Optimization Variables and Constraints

In the upper-level optimization model, the optimization variable is the capacity of the candidate equipment. Considering the equipment installation conditions and building loads, its optimization variables must satisfy the following constraints.

$$0 \le Cap_k \le Cap_k^{max} \tag{5}$$

where Cap_k^{max} is the maximum design capacity of equipment k, whose value is usually the maximum value of the corresponding load.

In addition, this study uses the design-daily load in summer as the design parameter. To gratify the load demand in winter, the maximum heat production capacity of the system must be greater than the maximal heating load.

$$P_{gshp,h}^{max} + P_{chp,h}^{max} + P_{gb,h}^{max} \ge L_{user,h}^{max} \tag{6}$$

where $P_{gshp,h}^{max}$ is the maximum heat production of the GSHP; $P_{chp,h}^{max}$ is the maximum heat production of the CHP unit; $P_{gb,h}^{max}$ is the maximum heat production of the gas boiler; and $L_{user,h}^{max}$ is the maximum heating load in winter.

3.2. Lower-Level Optimal Scheduling Model

3.2.1. Optimization Objective

To achieve flexible scheduling, the minimum operating cost is used as the optimization objective to optimize the operation of three RIESs. The operating cost mainly comes from the electricity and gas costs, whose values can be determined by the following formula:

$$\min C_{op} = \sum_{t=1}^{24} \left(P_{grid}(t) \cdot \vartheta_{grid}(t) + P_{gas}(t) \cdot \vartheta_{gas} \right) \tag{7}$$

where ϑ_{grid} is the time-of-use (TOU) electricity price; and ϑ_{gas} is the gas price.

3.2.2. Optimization Variables and Constraints

In the lower-level optimization model, the main optimization variable is the operating power of the equipment. The operating power should not only gratify the capacity constraints of the upper-level equipment but also meet the supply-demand balance constraints of the EH.

1. Equipment operating power constraints

(1) Energy conversion equipment

The operating power of the energy conversion equipment is both restricted by the capacity of the upper-level equipment and affected by the start-up and shutdown of the equipment. Therefore, the operating power is a semi-continuous variable whose range is shown in the following formula:

$$\begin{cases} 0 & PLR_k < PLR_k^{min} \\ P_k^{min} \le P_k \le P_k^{max} & PLR_k \ge PLR_k^{min} \end{cases} \tag{8}$$

where PLR_k is the part-load ratio of equipment k; PLR_k^{min} is the minimum part-load ratio for the start-up of equipment k; and P_k^{min} and P_k^{max} are the minimum and maximum output power of equipment k in the operating state.

(2) Energy storage equipment

Different from energy conversion equipment, energy storage devices should not only gratify the charging and discharging power constraints but also the charging and discharging state constraints, which are specifically expressed as follows:

$$0 \le P_{ch,k}(t) \le u_k \cdot \gamma_{ch,k}^{max} \cdot S_k \tag{9}$$

$$0 \le P_{dis,k}(t) \le (1 - u_k) \cdot \gamma_{dis,k}^{max} \cdot S_k \tag{10}$$

$$\alpha_k^{min} \cdot S_k \le S_k(t) \le \alpha_k^{max} \cdot S_k \tag{11}$$

where u_k is a variable of 0 or 1, which is introduced to ensure that the charging process and discharging process will not happen simultaneously; $\gamma_{ch,k}^{max}$ and $\gamma_{dis,k}^{max}$ are the maximum charging and discharging ratios of energy storage device k; α_k^{min} and α_k^{max} are the minimum and the maximum energy storage ratios of energy storage device k, respectively; and S_k is the capacity of energy storage device k.

2. Energy balance constraint

During the operation of RIESs, the EH is only used for energy collection and distribution. Therefore, the three energy hubs must maintain a balance between supply and demand, with the balance constraint shown below.

$$P_{grid}(t) + P_{chp,e}(t) + P_{pv}(t) + P_{dis,ees}(t) = L_{user,e}(t) + P_{gshp,e}(t) + P_{ch,ees}(t) \tag{12}$$

$$P_{gshp,c}(t) + P_{abc,c}(t) = L_{user,c}(t) \tag{13}$$

$$P_{chp,h}(t) + P_{gb}(t) + P_{dis.tes}(t) = L_{user,h}(t) + P_{abc,h}(t) + P_{ch.tes}(t) \quad (14)$$

where $P_{gshp,e}$ is the electricity consumption of GSHP; $P_{gshp,c}$ is the cooling power of GSHP; $P_{abc,c}$ is the cooling power of ABC; $P_{abc,h}$ is the heat consumption of ABC; and P_{gb} is the heat production of the gas boiler.

3.3. Model Solving

The solution methods of the bi-level optimization model usually include classical mathematical programming theory and the combination of intelligent optimization algorithms and classical mathematical programming theory [46,47]. In this study, the lower-level scheduling model takes into account the off-design characteristics of the equipment, which makes the lower-level scheduling model non-convex and nonlinear, and thus makes it difficult for classical mathematical programming theory to solve the bi-level dynamic optimization model. Therefore, this study will adopt the method of combining an intelligent optimization algorithm and classical mathematical programming theory to solve it, in which the upper-level optimization model is solved by a genetic algorithm. However, the calculation of the upper-level optimization objective often depends on the solution of the lower-level model. To realize the fast and accurate solution of the lower-level optimization model, this paper performs piecewise linearization on the performance curve of the equipment and calls Gurobi's non-convex solver to solve it to obtain the minimum operating cost and operating energy consumption. The lower-level optimization model transfers the optimization results to the upper-level optimization model to calculate the total cost of the system, while the upper-level optimization model transfers the optimized equipment capacity to the lower optimization model to constrain its scheduling. After repeated iterations, the optimal configuration and scheduling schemes of three RIESs can be obtained. Figure 3 shows the flow chart of the bi-level dynamic optimization model.

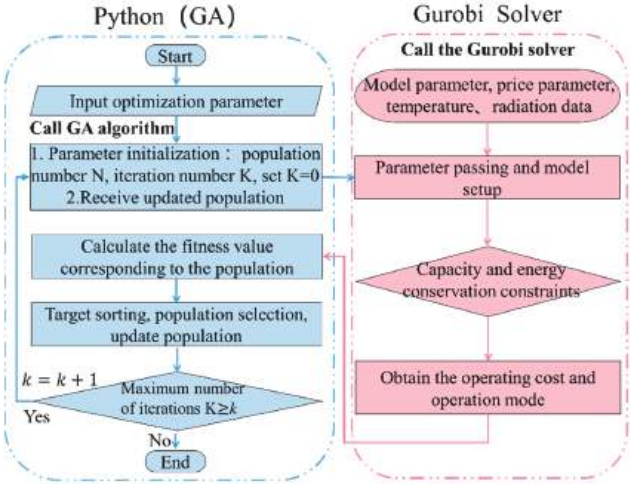

Figure 3. Solution flow chart of the bi-level optimization model.

4. Case Study

This paper takes a public building in Changsha as an example to explore the impact of energy storage equipment on the optimal design and operation results of RIESs. The building consists of two parts, the main building and the podium building, of which the main building has twelve floors, and the podium building has five floors, covering a total area of 2500 m^2. Considering the energy-saving requirements of the building, its envelope adopts the standard building envelope structure in hot-summer and cold-winter climates.

4.1. System Design Parameters

In the process of the optimization of RIESs, outdoor meteorological parameters and design load are the basis of system optimization design. Therefore, through relevant literature, this paper determines the outdoor design temperature of air conditioning in Changsha and the average water temperature of the Xiangjiang River, whose values are shown in Table 5. Unlike the heat load in winter, the cooling load calculation in summer is usually transient. For this reason, this paper corrects the outdoor design temperature of air conditioning in summer, and the hourly outdoor design temperatures and solar radiation intensities obtained from the correction are shown in Figure 4a. Based on the above design parameters, this paper uses Energy Plus to calculate the design load of the building, and the result is shown in Figure 4b. On summer design days, the heating load is mainly domestic hot water load, while the winter heating load includes air conditioning heating load and domestic hot water load. When the design load is known, this paper determines the equipment capacity optimization range, shown in Table 6, according to the design load and equipment installation requirements.

Table 5. Air conditioning outdoor design temperature and groundwater temperature Reproduced from [48,49].

Design Conditions	Design Dry-Bulb Temperature	Groundwater Temperature
Summer	36 °C	17 °C
Winter	−1 °C	11 °C

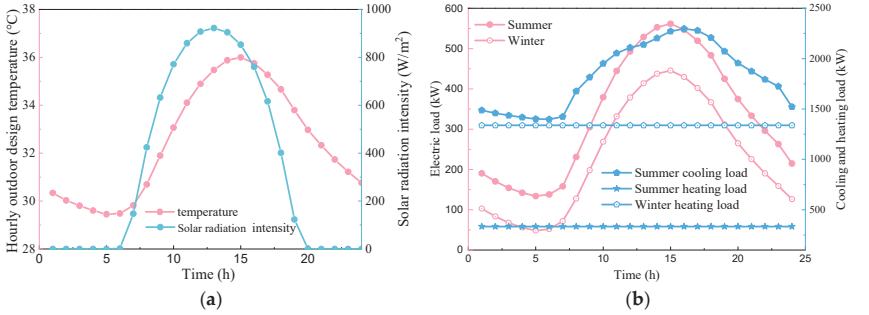

Figure 4. Outdoor parameters and building load under design conditions: (**a**) Hourly outdoor design temperature and solar radiation intensity in summer; (**b**) Cooling, heating, and electric load on the design day.

Table 6. Optimization range of equipment capacity.

Equipment Name	Symbol	Unit	Limitations
CHP unit	Cap_{chp}	kW	[0,2000]
Boiler	Cap_{gb}	kW	[0,1000]
GSHP	Cap_{gshp}	kW	[0,2300]
TES device	Cap_{tes}	kW·h	[0,1000]
EES device	Cap_{ees}	kW·h	[0,1000]
PV	A_{pv}	m^2	[0,1500]

In addition, the energy price and carbon tax price are also indispensable input parameters for calculating the optimization objectives. For this reason, this paper determines the energy and carbon tax prices shown in Table 7 according to relevant literature.

Table 7. Energy price and carbon tax Reproduced from [50–52].

Item	Unit Price (CNY/kWh)	Time Period	Description
Gas	0.3275	–	–
Electricity	1.224	20:00–23:00	Peak hours
	0.911	9:00–12:00, 16:00–20:00	High hours
	0.68	8:00–9:00, 12:00–16:00	Flat hours
	0.306	0:00–8:00, 23:00–24:00	Valley hours
Carbon tax	0.3 (CNY/kgCO_2)	–	–

4.2. System Optimization Results and Analysis

4.2.1. Optimization Results

Based on the above inputs, this paper takes the total cost as the optimization objective and adopts the bi-level dynamic optimization model to optimize the design of three RIESs. The equipment capacity obtained by optimization is shown in Table 8. Compared with System 1, the TES device can significantly increase the capacity of the CHP unit and ABC in System 2 and reduce the capacity of the GSHP and boiler. Identically to the TES device, the EES device can also increase the capacity of the CHP unit and ABC in System 3. However, the EES device has less impact on the capacity of energy conversion equipment than the TES device.

Table 8. System equipment capacity.

System Name	Cap_{chp} (kW)	Cap_{gb} (kW)	Cap_{gshp} (kW)	Cap_{abc} (kW)	Cap_{tes} (kW · h)	Cap_{ees} (kW · h)	A_{pv} (m^2)
System 1	1122	205	1780	520	0	0	1500
System 2	1265	0	1682	618	961	0	1500
System 3	1272	0	1678	622	947	926	1500

The difference in equipment capacity affects the equipment cost and operational performance of RIESs. Figure 5 shows the equipment costs, carbon taxes, operating costs, and total costs of the three systems under the design conditions. The difference in equipment capacity makes the equipment cost of System 2 and System 3 larger than that of System 1, with increasing rates of 5.7% and 17.8%, respectively. In comparison to the TES device, the EES device will significantly increase the equipment cost of System 3. Different from the equipment cost, the carbon tax, operating cost, and total cost of System 2 and System 3 are all less than that of System 1. Compared with System 1, the carbon tax, operating cost, and total cost of System 2 decreased by 5.5%, 2.9%, and 1.5%, respectively.The EES device can significantly reduce the operating cost of System 3, with a reduction of 5.7% compared with System 1. However, affected by the equipment cost, the total cost reduction rate of System 3 compared with System 1 is only 1.75%. It can be seen that under the design conditions, the TES and EES devices can reduce the operating cost, carbon tax, and total cost of the RIES to different degrees. However, the EES device has less impact on the carbon tax and total cost of RIESs.

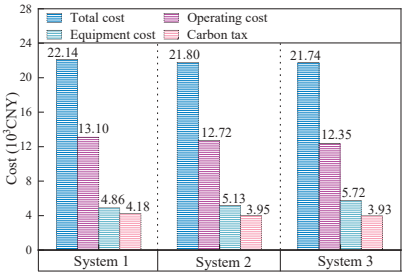

Figure 5. Cost differences between the three systems.

4.2.2. Analysis of Results

The energy utilization cost directly affects the operational performance of RIESs. To analyze the influence of energy storage devices on the operating cost, this paper first calculates the electric load supply-demand relationship and the part-load ratio of the CHP unit in System 1 under design operating conditions. As seen from Figure 6, during the low tariff hours, the grid power consumption is larger than gas-fired generation, and the CHP unit is at the minimum part-load ratio. However, the CHP unit is operating at full load during other hours. This shows that the electricity cost from the grid is less than the utilization cost of gas during the low tariff hours, while during other hours, the electricity cost from the grid is greater than the utilization cost of gas.

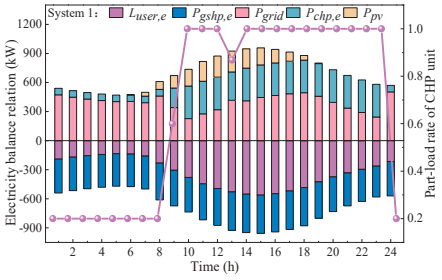

Figure 6. Electric load supply−demand relationship and part-load rate of CHP unit in System 1.

On the premise that the difference in energy utilization cost is known, this paper compares the scheduling process of System 1 and System 2 under the design conditions, as displayed in Figure 7. Figure 7a depicts the cooling load supply-demand relationship of the two systems. First, during the low tariff hours, the cooling load of the two systems is gratified by the GSHP. During other hours, the cooling load is met by the GSHP and ABC. However, the difference in equipment capacity makes the cooling power of the GSHP in System 2 less than that in System 1. Secondly, as seen in Figure 8, the operating efficiency of the GSHP in System 2 is greater than in System 1. The electric load of System 2 is less than System 1 due to the higher operating efficiency and lower cooling power. As shown in Figure 7b, the heating load of System 1 is gratified by the CHP unit and the gas boiler, while the heating load of System 2 is gratified by the CHP unit under the action of the TES device. This ensures the efficient use of gas while avoiding the use of the gas boiler in System 2. When combined with the relationship between supply-demand of electric load shown in Figure 7c, the larger capacity of the CHP unit can effectively reduce the power purchased from the grid during other hours for System 2. Based on the above analysis, the TES device can improve the overall energy efficiency of System 2 and reduce the electric load. Moreover, it increases the power generation of the CHP unit and reduces the grid power consumption, especially during other hours. Therefore, the carbon tax and operating costs of System 2 are less than System 1.

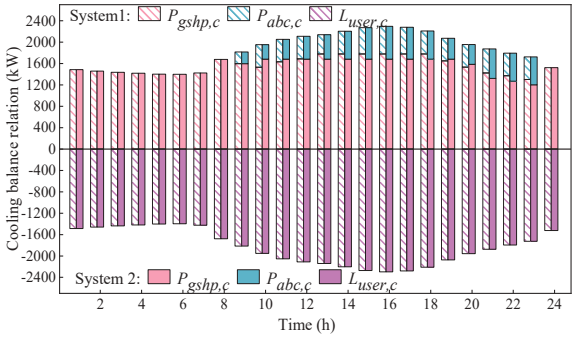

(**a**)

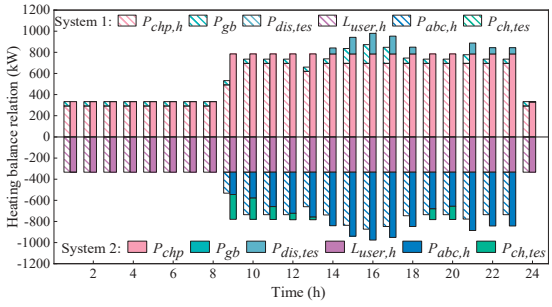

(**b**)

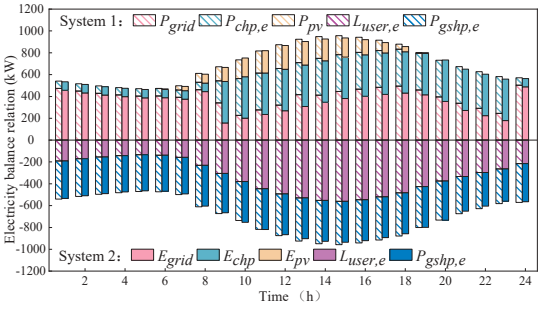

(**c**)

Figure 7. Scheduling process of System 1 and System 2 in design conditions: (**a**) Cooling load; (**b**) Heating load; (**c**) Electric load.

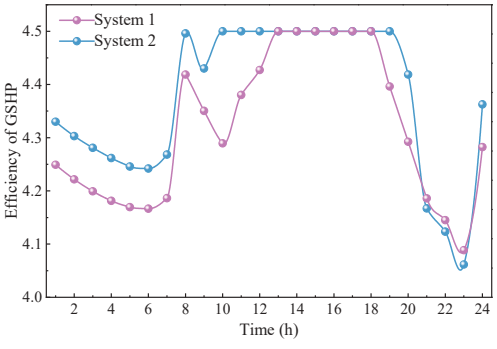

Figure 8. The efficiency of GSHP in System 1 and System 2.

To analyze the difference between the impact of the TES and EES devices on RIESs, this paper compares the electric load supply-demand relationship in System 2 and System 3 under the design conditions, as illustrated in Figure 9. First, the smaller capacity of the GSHP makes the electric load of System 3 less than that of System 2, while the larger CHP unit increases the power generation of the CHP unit in System 3. However, the carbon tax of System 3 is slightly less than that of System 2 due to the slight capacity difference between the GSHP and CHP units between System 2 and System 3. Secondly, the EES device can increase the grid power consumption during flat and valley hours and reduce the grid power consumption during high and peak hours. The difference in grid power consumption during different hours makes the operating cost of System 3 less than that of System 2.

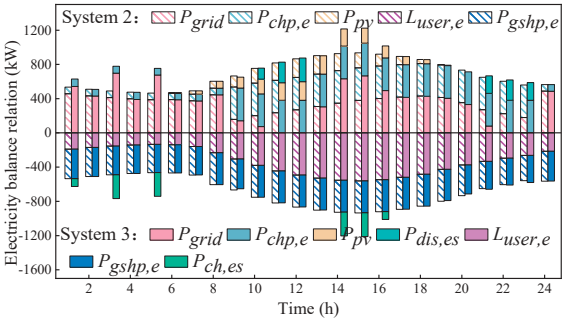

Figure 9. Electricity scheduling process of system 2 and system 3.

4.3. System Operation Result and Analysis

4.3.1. Calculation of Operating Load

The purpose of optimization design is to improve the operational performance of RIESs. To compare the operational performance of the three systems, the annual operating load was calculated by Energy Plus based on the typical annual outdoor meteorological parameters shown in Figure 10a, as shown in Figure 10b. In Changsha, which is hot in summer and cold in winter, the cooling load of the building is much greater than the heating load. Under summer operating conditions, the system cooling load is the building cooling load, and the heating load is the domestic hot water load. However, under winter operating conditions, the system heating load includes the building heating load and domestic hot water load. In addition, since the design parameters are determined by the method of non-guarantee days, the operating load may be greater than the design load most of the time. However, to ensure the feasibility of operation optimization, this study only considers days when the operating load is less than or equal to the design load.

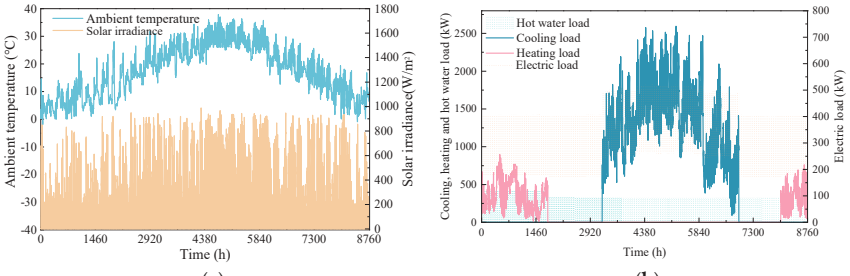

Figure 10. Outdoor parameters and building load under the operating conditions: (**a**) Annual outdoor meteorological parameters; (**b**) Building load under operating conditions.

4.3.2. Operation Results

Based on the above operating loads, the carbon taxes, operating costs, and total costs of the three systems are calculated under winter and summer operating conditions, and the results are shown in Table 9. Under the summer operating conditions, the carbon tax, operating cost, and total costs of System 2 and System 3 are less than those of System 1. Compared with the carbon tax, operating cost, and total cost of System 1, the corresponding costs in System 2 are reduced by 3.2%, 1.5%, and 0.3%, respectively. Different from System 2, since the carbon tax of System 3 is larger than that of System 2, the carbon tax reduction rate of System 3 compared with System 1 is smaller, only 2.7%. However, the EES device can significantly reduce the operating cost of System 3, which results in a 6.2% reduction in the operating cost of System 3 compared to System 1. Affected by the difference in building loads between winter and summer, the carbon taxes, operating costs, and total costs of the three systems under winter operating conditions are less than those under summer operating conditions. Under winter operating conditions, the carbon tax, operating cost, and total cost reduction rates of System 2 compared with System 1 are greater, whose values are 5.5%, 7.3%, and 2.8%, respectively. Similar to the summer operating conditions, System 3 can significantly reduce operating costs compared to System 2 but can also increase its carbon tax. Therefore, under operating conditions, compared with System 1, the TES device can significantly reduce the carbon tax, operating cost, and total cost of System 2, while the EES device can reduce the operating cost of System 3 even more significantly.

Table 9. Costs of three systems under winter and summer operating conditions.

Operating Condition	Summer			Winter		
	C_{tax} (CNY)	C_{op} (CNY)	C_{total} (CNY)	C_{tax} (CNY)	C_{op} (CNY)	C_{total} (CNY)
System 1	526,636	1,582,405	2,672,662	301,465	774,952	1,581,733
System 2	509,527	1,558,375	2,663,411	285,012	718,724	1,537,640
System 3	512,367	1,484,274	2,660,567	294,405	688,785	1,578,434

4.3.3. Operation Result Analysis

According to the analysis of the design condition results, the performance difference of RIESs is mainly affected by energy consumption and the consumption of different types of energy. To analyze the energy consumption of the three systems, this paper compares the average operation efficiency of the GSHPs and CHP units under the operating conditions, as shown in Figure 11. Firstly, under winter and summer operating conditions, the average operation efficiency of the GSHP in System 1, System 2, and System 3 increases sequentially due to the influence of energy storage devices. However, there is little difference between the average operation efficiency of the GSHP in System 2 and System 3. Secondly, the average operation efficiency of the CHP unit in System 2 is greater than in System 1 and System 3, especially in winter operating conditions. This shows that the TES device can significantly improve the operation efficiency of the GSHP and the CHP unit. In addition, the average operation efficiency of the CHP unit in System 3 is greater than that in System 1 under summer operating conditions, while under winter operating conditions, the average operating efficiency of the CHP unit in System 3 is approximately the same as that in System 1. The higher the average operation efficiency of the GSHP and the CHP units, the lower the energy consumption. Therefore, under the operating conditions, the energy consumption of System 2 and System 3 is less than that of System 1.

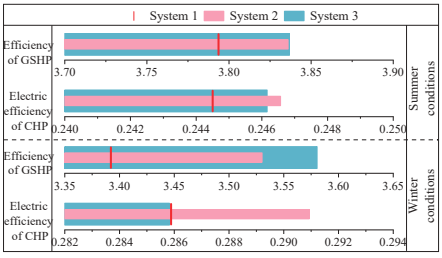

Figure 11. The average efficiency of GSHPs and CHP units under two operating conditions.

In the RIESs, carbon tax not only depends on the energy consumption of systems but is also affected by the ratio of different energy consumptions. To this end, different power consumption ratios of the three systems under winter and summer operating conditions are counted in this paper, and the results are shown in Figure 12. Under summer and winter operating conditions, the ratio of grid power consumption in System 1 is greater than that of System 2 and System 3; hence the carbon tax of System 2 and System 3 is less than that of System 1. Although there is a slight difference in the ratio of grid power consumption between System 2 and System 3 under summer operating conditions, the average operation efficiency of the CHP unit in System 3 is lower than that in System 2. Therefore, under summer operating conditions, the carbon tax of System 3 is slightly larger than System 2. Different from the summer operating conditions, the grid power consumption ratio of System 2 is significantly smaller than for System 3 under the winter operating conditions. As a result, the carbon taxes of System 2 and System 3 are greater than that of System 1, especially System 2.

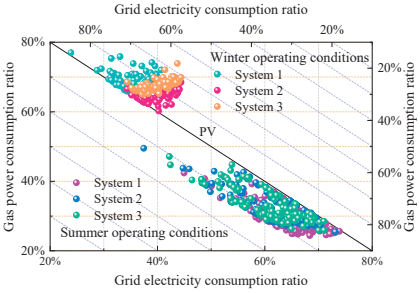

Figure 12. Different power consumption ratios under two operating conditions.

The system's operating cost is closely related to the TOU power price. To analyze the operating cost difference between the three systems, this paper draws the power consumption ratio of the three systems under TOU price hours, as shown in Figure 13. Under the summer operating conditions, the grid power consumption ratios of System 2 and System 3 during high and peak hours are less than that of System 1, especially for System 3, which accounts for only 22.12% during high and peak hours. Similar to the summer operating conditions, the power consumption ratios of System 2 and System 3 during high and peak hours are less than that of System 1 under winter operating conditions. However, under winter operating conditions, the difference in the grid power consumption ratio between System 1 and System 2 is greater than that between System 2 and System 3 during high and peak hours. Therefore, under winter and summer operating conditions, the operating costs of System 2 and System 3 are greater than that of System 1, and the operating cost of System 3 is the lowest, especially under winter operating conditions.

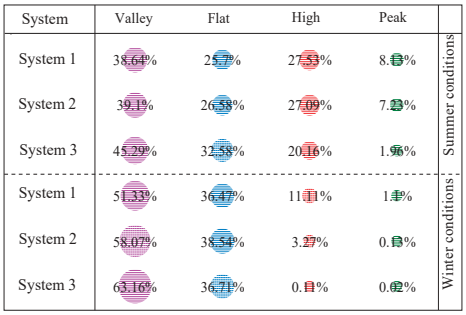

Figure 13. The ratio of grid power consumption under the TOU power price.

The above analysis shows that the carbon taxes and operating costs of System 2 and System 3 are less than those of System 1 under winter and summer operating conditions due to the impact of the average efficiency of the equipment, the ratio of different energy consumptions, and the grid power consumption ratio under the TOU power price. The smaller carbon tax and operating cost make the total cost of Systems 2 and System 3 less than that of System 1. However, affected by the equipment cost, the total cost reduction rate difference between System 2 and System 3 compared with System 1 is not so obvious. In addition, under winter operating conditions, the total cost of System 3 is greater than that of System 2 due to the lower operating cost difference between System 2 and System 3.

4.4. Uncertainty Analysis of Energy Price

In the actual operation process, the price of grid power and gas directly affected the operation result of the system. To explore the impact of energy price uncertainty on system operation results, this study increases or decreases the energy prices to ±30% in a 10% step, based on the energy prices in the design conditions. The three systems are optimized for operation according to different energy prices. Based on optimization results, the cost reduction rates of System 2 and System 3 compared with System 1 are calculated, as shown in Figure 14. In the case of changes in energy prices, the reduction rates of the carbon tax, operating cost, and total cost of System 2 compared with System 1 are greater than zero. Different from System 2, the operating cost reduction rate of System 3 compared with System 1 is larger, while the carbon tax and total cost reduction rates are lower. Even under partial energy prices, the carbon tax and total cost of System 3 are greater than they are for System 1. Under different energy prices, the TES device can effectively reduce the operating cost, carbon tax, and total cost of the RIES, while the EES device can significantly reduce the system operating cost.

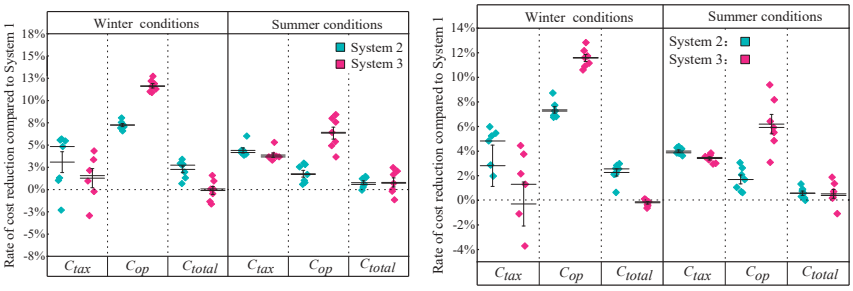

Figure 14. Cost reduction rates of system 2 and system 3 compared with system 1 under changes in electricity and gas prices: (**a**) Affected by changes in electricity prices; (**b**) Affected by changes in gas prices.

5. Conclusions

The purpose of this study is to explore the impact of energy storage devices on the optimal design and operation of RIESs. For this purpose, a bi-level dynamic optimization model was first established based on the dynamic equipment model. Then, the bi-level dynamic optimization model was used to optimize the design of RIESs with different energy storage devices, and the optimization results are System 1, System 2, and System 3, respectively. According to the optimization results, the impact of energy storage devices on system performance is compared and analyzed. The main conclusions of this study include the following three points:

1. Compared with System 1 without energy storage devices, energy storage devices can increase the capacity of CHP units and ABCs in System 2 and System 3 and reduce the capacity of GSHPs and gas boilers, especially the TES device. Affected by the equipment capacity, the equipment cost increase rates of System 2 and System 3 compared with System 1 are 5.7% and 17.8%, respectively. This shows that the EES device will significantly increase the equipment cost of System 3.
2. The difference in equipment capacity affects not only the equipment cost but also the operation performance of the system. Under the design conditions, higher equipment operation efficiency and lower grid power consumption make the operation cost, carbon tax, and total cost of System 2 lower than that of System 1, with reductions of 2.9%, 5.5%, and 1.5%, respectively. Under the influence of TOU electricity price, the EES device can significantly reduce the operating cost of System 3, which is 5.7% lower than that of System 1.
3. Under the operating conditions, the operating cost, carbon tax, and total cost of System 2 and System 3 remain lower than that of System 1, even if the energy price changes. Therefore, in the design of future RIESs, energy storage devices, especially TES devices, can be used to improve the energy efficiency of RIESs and reduce the operation cost and total cost.

Author Contributions: Conceptualization, B.J.; methodology, B.J.; software, B.J. and Z.L.; validation, B.J. and Z.L.; formal analysis, B.J. and Z.L.; investigation, B.J.; data curation, B.J. and Z.L.; writing—original draft preparation, B.J. and Z.L.; writing—review and editing, B.J. and Y.L.; visualization, B.J.; supervision, B.J.; project administration, B.J. All authors have read and agreed to the published version of the manuscript.

Funding: This research received no external funding.

Institutional Review Board Statement: Not applicable.

Informed Consent Statement: Not applicable.

Data Availability Statement: Not applicable.

Conflicts of Interest: The authors declare no conflict of interest.

Nomenclature

Nomenclature

Abbreviation

A	Area
ABC	Absorption chiller
Cap	Capacity
CCHP	Combined cooling heating and power
CHP	Combined heating and power
COP	Coefficient of performance

Greek symbols

η	Charging and discharging efficiency
ϑ	Energy price/ carbon tax price
α	Energy storage ratios
λ	Carbon dioxide emissions factor
γ	Charging and discharging ratios

Subscript

a	Ambient

EES	Electrical energy storage	abc	Absorption chiller
EH	Energy hub	c	Cooling
FEL	Following electric load	ch	Charge
FHL	Following hybrid electric-heating load	chp	Combined heating and power
FOF	Following objective function	CO_2	carbon dioxide
FSF	Following system flexibility	dis	Discharge
FTL	Following thermal load	e	Electricity
GA	Genetic algorithm	equ	Equipment
GB	Gas boiler	ees	Electrical energy storage
GSHP	Ground source heat pump	gas	Natural gas
HES	Hydrogen energy storage	gb	Gas boiler
L	Load	gshp	Ground source heat pump
P	Power	grid	Grid power
P-G	Power-gas	h	Heating
PLF	Part-load ratio	inv	Initial investment
PLR	Part-load factor	k	Device type
PV	Photovoltaic	op	Operating
RIES	Regional integrated energy system	pv	Photovoltaic
S	Energy storage device status	r	Rated
SES	Share energy storage	tes	Thermal energy storage
t	Temperature/Time	**Superscript**	
TES	Thermal energy storage	max	Maximum
TOU	Time-of-use	min	Minimum

References

1. Zhang, Q.; Ren, Z.; Ma, R.; Tang, M.; He, Z. Research on Double-Layer Optimized Configuration of Multi-Energy Storage in Regional Integrated Energy System with Connected Distributed Wind Power. *Energies* **2019**, *12*, 3964. [CrossRef]
2. Al-Najjar, H.M.T.; Mahdi, J.M.; Bokov, D.O.; Khedher, N.B.; Alshammari, N.K.; Opulencia, M.J.C.; Fagiry, M.A.; Yaïci, W.; Talebizadehsardari, P. Improving the Melting Duration of a PV/PCM System Integrated with Different Metal Foam Configurations for Thermal Energy Management. *Nanomaterials* **2022**, *12*, 423. [CrossRef] [PubMed]
3. Guo, J.; Liu, Z.; Wu, X.; Wu, D.; Zhang, S.; Yang, X.; Ge, H.; Zhang, P. Two-Layer Co-Optimization Method for a Distributed Energy System Combining Multiple Energy Storages. *Appl. Energy* **2022**, *322*, 119486. [CrossRef]
4. Wei, W.; Guo, Y.; Hou, K.; Yuan, K.; Song, Y.; Jia, H.; Sun, C. Distributed Thermal Energy Storage Configuration of an Urban Electric and Heat Integrated Energy System Considering Medium Temperature Characteristics. *Energies* **2021**, *14*, 2924. [CrossRef]
5. Ben Khedher, N.; Bantan, R.A.; Kolsi, L.; Omri, M. Performance Investigation of a Vertically Configured LHTES via the Combination of Nano-Enhanced PCM and Fins: Experimental and Numerical Approaches. *Int. Commun. Heat Mass Transf.* **2022**, *137*, 106246. [CrossRef]
6. Geidl, M.; Koeppel, G.; Favre-Perrod, P.; Klockl, B. Energy Hubs for the Future. *IEEE Power Energy Mag.* **2007**, *5*, 24–30. [CrossRef]
7. Ma, T.; Wu, J.; Hao, L.; Li, D. Energy Flow Matrix Modeling and Optimal Operation Analysis of Multi Energy Systems Based on Graph Theory. *Appl. Therm. Eng.* **2019**, *146*, 648–663. [CrossRef]
8. Ma, T.; Wu, J.; Hao, L.; Lee, W.J.; Yan, H.; Li, D. The Optimal Structure Planning and Energy Management Strategies of Smart Multi Energy Systems. *Energy* **2018**, *160*, 122–141. [CrossRef]
9. Ben Salah, S.; Ben Hamida, M.B. Alternate PCM with Air Cavities in LED Heat Sink for Transient Thermal Management. *Int. J. Numer. Methods Heat Fluid Flow* **2019**, *29*, 4377–4393. [CrossRef]
10. Ben Hamida, M.B.; Hajlaoui, K.; Almeshaal, M.A. A 3D Numerical Analysis Using Phase Change Material for Cooling Circular Light Emitting Diode. *Case Stud. Therm. Eng.* **2023**, *43*, 102792. [CrossRef]
11. Waseem, M.; Lin, Z.; Liu, S.; Sajjad, I.A.; Aziz, T. Optimal GWCSO-Based Home Appliances Scheduling for Demand Response Considering End-Users Comfort. *Electr. Power Syst. Res.* **2020**, *187*, 106477. [CrossRef]
12. Liu, C.; Li, Y.; Wang, Q.; Wang, X.; Chen, C.; Lin, Z.; Yang, L. Optimal Configuration of Park-Level Integrated Energy System Considering Integrated Demand Response and Construction Time Sequence. *Energy Rep.* **2022**, *8*, 1174–1180. [CrossRef]
13. Ding, Y.; Xu, Q.; Yang, B. Optimal Configuration of Hybrid Energy Storage in Integrated Energy System. *Energy Rep.* **2020**, *6*, 739–744. [CrossRef]
14. Deng, Z.G.; Yang, J.H.; Dong, C.L.; Xiang, M.Q.; Qin, Y.; Sun, Y.S. Research on Economic Dispatch of Integrated Energy System Based on Improved Krill Swarm Algorithm. *Energy Rep.* **2022**, *8*, 77–86. [CrossRef]
15. Mansouri, S.A.; Nematbakhsh, E.; Ahmarinejad, A.; Jordehi, A.R.; Javadi, M.S.; Matin, S.A.A. A Multi-Objective Dynamic Framework for Design of Energy Hub by Considering Energy Storage System, Power-to-Gas Technology and Integrated Demand Response Program. *J. Energy Storage* **2022**, *50*, 104206. [CrossRef]
16. Mago, P.; Chamra, L. Analysis and optimization of CCHP systems based on energy, economical, and environmental considerations. *Energy Build.* **2009**, *41*, 1099–1106. [CrossRef]

17. Mago, P.J.; Chamra, L.M.; Ramsay, J. Micro-combined cooling, heating and power systems hybrid electric-thermal load following operation. *Appl. Therm. Eng.* **2010**, *30*, 800–806. [CrossRef]
18. Kang, S.; Li, H.; Liu, L.; Zeng, R.; Zhang, G. Evaluation of a Novel Coupling System for Various Load Conditions under Different Operating Strategies. *Energy Convers Manag* **2016**, *109*, 40–50. [CrossRef]
19. Wang, Y.; Zhang, Y.; Xue, L.; Liu, C.; Song, F.; Sun, Y.; Liu, Y.; Che, B. Research on Planning Optimization of Integrated Energy System Based on the Differential Features of Hybrid Energy Storage System. *J. Energy Storage* **2022**, *55*, 105368. [CrossRef]
20. Duan, Z.; Yan, Y.; Yan, X.; Liao, Q.; Zhang, W.; Liang, Y.; Xia, T. An MILP Method for Design of Distributed Energy Resource System Considering Stochastic Energy Supply and Demand. *Energies* **2018**, *11*, 22. [CrossRef]
21. Zeng, R.; Li, H.; Jiang, R.; Liu, L.; Zhang, G. A Novel Multi-Objective Optimization Method for CCHP-GSHP Coupling Systems. *Energy Build.* **2016**, *112*, 149–158. [CrossRef]
22. Zeng, R.; Zhang, X.; Deng, Y.; Li, H.; Zhang, G. An Off-Design Model to Optimize CCHP-GSHP System Considering Carbon Tax. *Energy Convers. Manag.* **2019**, *189*, 105–117. [CrossRef]
23. Yang, G.; Zhai, X. Optimization and Performance Analysis of Solar Hybrid CCHP Systems under Different Operation Strategies. *Appl. Therm. Eng.* **2018**, *133*, 327–340. [CrossRef]
24. Yang, G.; Zhai, X.Q. Optimal Design and Performance Analysis of Solar Hybrid CCHP System Considering Influence of Building Type and Climate Condition. *Energy* **2019**, *174*, 647–663. [CrossRef]
25. Ren, F.; Wei, Z.; Zhai, X. Multi-Objective Optimization and Evaluation of Hybrid CCHP Systems for Different Building Types. *Energy* **2021**, *215*, 119096. [CrossRef]
26. Li, Y.; Tian, R.; Wei, M. Operation Strategy for Interactive CCHP System Based on Energy Complementary Characteristics of Diverse Operation Strategies. *Appl. Energy* **2022**, *310*, 118415. [CrossRef]
27. Deng, Y.; Zeng, R.; Liu, Y. A Novel Off-Design Model to Optimize Combined Cooling, Heating and Power System with Hybrid Chillers for Different Operation Strategies. *Energy* **2022**, *239*, 122085. [CrossRef]
28. Han, Z.; Ma, F.; Wu, D.; Zhang, H.; Dong, F.; Li, P.; Xiao, L. Collaborative Optimization Method and Operation Performances for a Novel Integrated Energy System Containing Adiabatic Compressed Air Energy Storage and Organic Rankine Cycle. *J. Energy Storage* **2021**, *41*, 102942. [CrossRef]
29. Ghersi, D.E.; Amoura, M.; Loubar, K.; Desideri, U.; Tazerout, M. Multi-Objective Optimization of CCHP System with Hybrid Chiller under New Electric Load Following Operation Strategy. *Energy* **2021**, *219*, 119574. [CrossRef]
30. Zhou, Y.; Wang, J.; Dong, F.; Qin, Y.; Ma, Z.; Ma, Y.; Li, J. Novel Flexibility Evaluation of Hybrid Combined Cooling, Heating and Power System with an Improved Operation Strategy. *Appl. Energy* **2021**, *300*, 117358. [CrossRef]
31. Luo, X.; Xia, J.; Liu, Y. Extraction of Dynamic Operation Strategy for Standalone Solar-Based Multi-Energy Systems: A Method Based on Decision Tree Algorithm. *Sustain. Cities Soc.* **2021**, *70*, 102917. [CrossRef]
32. Lu, S.; Li, Y.; Xia, H. Study on the Configuration and Operation Optimization of CCHP Coupling Multiple Energy System. *Energy Convers. Manag.* **2018**, *177*, 773–791. [CrossRef]
33. Luo, X.; Zhu, Y.; Liu, J.; Liu, Y. Design and Analysis of a Combined Desalination and Standalone CCHP (Combined Cooling Heating and Power) System Integrating Solar Energy Based on a Bi-Level Optimization Model. *Sustain. Cities Soc.* **2018**, *43*, 166–175. [CrossRef]
34. Li, K.; Wei, X.; Yan, Y.; Zhang, C. Bi-Level Optimization Design Strategy for Compressed Air Energy Storage of a Combined Cooling, Heating, and Power System. *J. Energy Storage* **2020**, *31*, 101642. [CrossRef]
35. Ma, M.; Huang, H.; Song, X.; Peña-Mora, F.; Zhang, Z.; Chen, J. Optimal Sizing and Operations of Shared Energy Storage Systems in Distribution Networks: A Bi-Level Programming Approach. *Appl. Energy* **2022**, *307*, 118170. [CrossRef]
36. Song, Z.; Liu, T.; Lin, Q. Multi-Objective Optimization of a Solar Hybrid CCHP System Based on Different Operation Modes. *Energy* **2020**, *206*, 118125. [CrossRef]
37. Guan, T.; Lin, H.; Sun, Q.; Wennersten, R. Optimal Configuration and Operation of Multi-Energy Complementary Distributed Energy Systems. *Energy Procedia* **2018**, *152*, 77–82. [CrossRef]
38. Biglia, A.; Caredda, F.V.; Fabrizio, E.; Filippi, M.; Mandas, N. Technical-Economic Feasibility of CHP Systems in Large Hospitals through the Energy Hub Method: The Case of Cagliari AOB. *Energy Build.* **2017**, *147*, 101–112. [CrossRef]
39. Jian, W.; Yuan, R. *Design and Optimization on Building Distributed Energy System*; Tong Ji University Press: Shanghai, China, 2016; pp. 37–56.
40. Waseem, M.; Lin, Z.; Liu, S.; Zhang, Z.; Aziz, T.; Khan, D. Fuzzy Compromised Solution-Based Novel Home Appliances Scheduling and Demand Response with Optimal Dispatch of Distributed Energy Resources. *Appl. Energy* **2021**, *290*, 116761. [CrossRef]
41. Liu, Y.; Wang, Y.; Luo, X. Design and Operation Optimization of Distributed Solar Energy System Based on Dynamic Operation Strategy. *Energies* **2021**, *14*, 69. [CrossRef]
42. Ma, W.; Fang, S.; Liu, G. Hybrid Optimization Method and Seasonal Operation Strategy for Distributed Energy System Integrating CCHP, Photovoltaic and Ground Source Heat Pump. *Energy* **2017**, *141*, 1439–1455. [CrossRef]
43. Luo, Z.; Yang, S.; Xie, N.; Xie, W.; Liu, J.; Souley Agbodjan, Y.; Liu, Z. Multi-Objective Capacity Optimization of a Distributed Energy System Considering Economy, Environment and Energy. *Energy Convers. Manag.* **2019**, *200*, 112081. [CrossRef]
44. Ren, F.; Wang, J.; Zhu, S.; Chen, Y. Multi-Objective Optimization of Combined Cooling, Heating and Power System Integrated with Solar and Geothermal Energies. *Energy Convers. Manag.* **2019**, *197*, 111866. [CrossRef]

45. Zhang, T.; Wang, M.; Wang, P.; Liang, J. Optimal Design of a Combined Cooling, Heating, and Power System and Its Ability to Adapt to Uncertainty. *Energies* **2020**, *13*, 3588. [CrossRef]
46. Guo, S.; Song, G.; Li, M.; Zhao, X.; He, Y.; Kurban, A.; Ji, W.; Wang, J. Multi-Objective Bi-Level Quantity Regulation Scheduling Method for Electric-Thermal Integrated Energy System Considering Thermal and Hydraulic Transient Characteristics. *Energy Convers. Manag.* **2022**, *253*, 115147. [CrossRef]
47. Ju, L.; Yin, Z.; Yang, S.; Zhou, Q.; Lu, X.; Tan, Z. Bi-Level Electricity–Carbon Collaborative Transaction Optimal Model for the Rural Electricity Retailers Integrating Distributed Energy Resources by Virtual Power Plant. *Energy Rep.* **2022**, *8*, 9871–9888. [CrossRef]
48. Air Conditioning Outdoor Design Parameters, Energy Plus Is Available Online. 2022. Available online: https://energyplus.net/weather-location/asia_wmo_region_2/CHN/CHN_Hunan.Changde.576620_CSWD (accessed on 15 June 2022).
49. Zou, X. Study on Optimization and Control Strategies of Solar-Assisted Ground-Coupled Heat Pump Domestic Hot Water System. Master's Thesis, Hunan University, Changsha, China, 2016.
50. Changsha ENN Gas Co., Ltd. Natural Gas Price. 2022. Available online: http://www.cs95158.cn/contents/68/1594.html (accessed on 15 June 2022).
51. Zou, B.; Peng, J.; Li, S.; Li, Y.; Yan, J.; Yang, H. Comparative Study of the Dynamic Programming-Based and Rule-Based Operation Strategies for Grid-Connected PV-Battery Systems of Office Buildings. *Appl. Energy* **2022**, *305*, 117875. [CrossRef]
52. Chen, Y.; Xu, J.; Wang, J.; Lund, P.D.; Wang, D. Configuration Optimization and Selection of a Photovoltaic-Gas Integrated Energy System Considering Renewable Energy Penetration in Power Grid. *Energy Convers. Manag.* **2022**, *254*, 115260. [CrossRef]

energies

MDPI

Review

Maximizing the Integration of a Battery Energy Storage System–Photovoltaic Distributed Generation for Power System Harmonic Reduction: An Overview

Adedayo Owosuhi [1,*], Yskandar Hamam [1,2] and Josiah Munda [1]

[1] Department of Electrical Engineering, French South African Institute of Technology (F'SATI), Tshwane University of Technology, Pretoria 0001, South Africa
[2] École Supérieure d'Ingénieurs en Électrotechnique et Électronique, Cité Descartes, 2 Boulevard Blaise Pascal, Noisy-le-Grand, 93160 Paris, France
* Correspondence: owosuhiadedayo@gmail.com; Tel.: +2348032381702

Abstract: The highly variable power generated from a battery energy storage system (BESS)–photovoltaic distributed generation (PVDG) causes harmonic distortions in distribution systems (DSs) due to the intermittent nature of solar energy and high voltage rises or falls in the BESS. Harmonic distortions are major concerns in the DS, especially when the sizes and locations of these resources are sub-optimal. As a result, many studies are being performed on the optimal allocation of BESS/PVDG systems in distribution network systems. In this regard, this paper seeks to review the existing planning models, optimization methods and renewable energy resources that uncertainty models have employed in solving BESS/PVDGs allocation problems in terms of obtaining optimal solutions/allocations and curtailing the harmonic contents of the DSs. However, studies on optimal allocation planning of BESS/PVDGs have achieved minimum cost but were not able to meet the standard harmonic level of the DSs. The results identified GA, PSO and AIS as some of the most used methodologies while LP, MILP and different configurations of NLP were used in the model formulations of BESS/PVDGs problems. The results also revealed DC-link voltage and switching and grid voltage harmonics as the notable causes and sources of harmonic distortions in BESS/PVDG systems. The current allocation models presented in the recent literature for the planning of BESS/PVDGs do not include the variables necessary for curtailing the harmonic contents in their planning formulations. This paper, therefore, recommends an improved and all-encompassing planning model with an efficient intelligent search algorithm capable of obtaining a global optimum solution and curtailing harmonic distortions from the BESS/PVDG-connected DSs.

Keywords: photovoltaic distributed generation; battery energy storage system; distribution network system; optimization methodologies; harmonic distortions

Citation: Owosuhi, A.; Hamam, Y.; Munda, J. Maximizing the Integration of a Battery Energy Storage System–Photovoltaic Distributed Generation for Power System Harmonic Reduction: An Overview. *Energies* **2023**, *16*, 2549. https://doi.org/10.3390/en16062549

Academic Editors: Branislav Hredzak, Luis Hernández-Callejo, Jesús Armando Aguilar Jiménez and Carlos Meza Benavides

Received: 20 December 2022
Revised: 17 February 2023
Accepted: 24 February 2023
Published: 8 March 2023

1. Introduction

The rapid expansion in socioeconomics has led to increasing global energy demand and usage. To balance the resulting widening energy deficiency, renewable energy distributed generation (REDG) is considered as an effective approach to solve the rising energy demand and other power system issues that are technical, economic and environmental in nature [1–3]. REDGs are generation technologies integrated at distribution networks near load users to satisfy immediate power demand, defer network upgrade, enhance power quality and reliability, diversify energy resources, and to reduce power losses, distribution and transmission loading, distribution and transmission costs and on-peak operating costs [4].

The battery energy storage system–photovoltaic DG (BESS/PVDG) is a viable renewable option because the resources are inexhaustible, complementary, economically

profitable, environmentally friendly and bi-directional [5–8]. However, the power generated from BESS/PVDG depends on charge and discharge schedules of BESS, which is associated with high voltage rise or fall, and temperature and irradiation of solar energy that is intermittent in nature [6,9–11]. Hence, a substantial number of research studies have unanimously agreed/concurred that harmonics occur in the distribution system when BESS/PVDG units are absorbed due to the intermittent and variable nature of PVDG output power and the high variability of voltage and frequency of BESS schedules. In essence, current harmonics occur as a result of sudden disparity between the aggregate output power of BESS/PVDGs and other generations and the total power demand at an instant in a distribution system. The high rises and falls of the voltage and frequency from battery charge/discharge schedules may result in voltage harmonics [11].

The harmonic distortions are a troubling power quality issue for BESS/PVDG power generation, and they have significant consequences on the DNs. The extent of current harmonics is determined by the active output power from BESS/PVDGs. Thus, the magnitudes of current harmonics are enormous at utility-scale BESS/PVDGs penetration levels. The intermittency of PVDG units and the high voltage rise or fall from BESS/PVDG raise concerns on distribution system harmonic distortions, which have negative effects on power quality, stability and reliability of distribution systems [6,12,13]. The high harmonic contents in the power system lead to increased losses in system elements such as transformers and generating plants; economic costs such as productivity, energy and device/equipment losses; and fire hazards due to overheating of system elements [7,14,15]. The issues mentioned make the integration of a large-scale BESS/PVDG into the distribution systems difficult [6,15,16]. Meanwhile, the locations and sizes of BESS/PVDG units could either improve or impair the magnitudes current and voltage harmonic levels of the networks [17–19]. The mentioned issues make the solution of BESS/PVDG allocation problems formulated using simple mathematical models unrealistic. A realistic model, therefore, requires a dynamic model representation of the network, the use of multi-period planning horizon as well as all the necessary constraints. The problem then becomes a multi-objective one with a maximisation of renewable active and reactive powers into the DNs and a minimisation of the total cost subject to the capacity, investment, technical, stability and harmonic constraints throughout the planning horizon.

Several studies have been performed to proffer optimal solutions for the planning allocation of BESS/PVDG in distribution systems [11,13,16,20–23]. The studies on optimal planning of REDG allocation warrant detailed investigations on the prospects of BESS/PVDGs for generating power, the impact on the DNs, and the effects on the inadequate availability and rising cost of energy, the global economy and environment. Various researchers have reviewed some aspects of the BESS/PVDG allocation planning (BESS/PVDGs-AP) problem. Many solution algorithms, planning models, and emerging technologies deployed in BESS/PVDG-AP have been presented [24–28]. Zahraee et al. [24] presented an analysis of some artificial intelligence optimum plans used in the optimization and sizing of hybrid renewable energy systems. The main contribution of this work is the extensive penetration of renewable energy features for economic performance of the systems. The authors in [25] dealt with the review of some solutions that were used to improve the ability of the distribution system to cope with variable renewable energy source unpredictability such as energy storage technologies, PV and wind energy systems. This study concluded that battery energy storage and pump hydro energy storage are the most used technologies to improve the impact of the variable renewable power on distribution systems. A review presented by Hannan et al. [26] on the planning of BESS and renewable energy hybrid DGs discussed the optimal sizing objectives, various optimization models, the BESS system constraints together with their advantages and weaknesses. A detailed discussion of the BESS applications and shortage of optimal BESS sizing models could be identified as the strong point of this study. In [27], a review of the latest research developments and challenges on optimal planning of a BESS-PVDG connected distribution system was presented. The authors suggested key parameters in the process of optimal

planning for a PV–battery system such as economic and technical data, objective functions, energy management schemes, design constraints, optimization algorithms, and electricity pricing regimes.

In view of the contribution of the existing review works on the BESS/PVDGs-AP problem, this study is distinct in these ways:

- Based on the authors' awareness, no literature has presented the evaluation of harmonic components of BESS/PVDGs during integration into distribution networks/systems.
- Unlike the existing reviews, this review presents an overview of harmonic distortions in battery energy storage–photovoltaic hybrid distributed generation systems.
- This study provides a methodology for curtailing harmonic distortions from the BESS/PVDGs-connected distribution systems.
- Moreover, a substantial and diverse number of optimization/solution algorithms deployed in solving the BESS/PVDGs allocation problem is surveyed, comparing all their characteristics to assist the researchers to utilize them successfully and in a cost-effective way.

Despite numerous reviews and studies on BESS/PVDGs, some aspects have not been adequately captured for investigation, review and research. These themes, bulleted above, are comprehensively treated in this paper.

The remaining parts of this paper are organized as follows: Section 2 presents the overview of harmonic components in the BESS/PVDG connected distribution networks. Section 3 details a review of various optimization models and techniques published in the existing research works and some promising algorithms that are recently introduced and used for solving BESS/PVDG allocation optimization problems. The methodological approach for curtailing the harmonic distortions in a BESS/PVDG connected distribution system is presented in Section 4. The characteristics of all the models and techniques are compared, and their shortcomings are discussed under Results and Discussion in Section 5, to assist the researchers in choosing and applying them successfully and in a cost-effective way. Section 6 is the concluding part of the paper, and the recommendations for future research directions are also presented here.

2. Overview of Harmonic Components in BESS/PVDG Systems

Power system harmonic distortion is a major issue for power utilities throughout the world. In recent times, statistical analysis reports have revealed that power system harmonics has become a very troubling power quality issue in BESS/PVDG systems. These harmonics have resonating impacts in generating other power quality problems in large-scale BESS/PVDG [7,15,29–31]. The sources of harmonics produced in BESS/PVDGs are broadly classified into DC-link voltage harmonics, switching harmonics and grid voltage harmonics [7,32].

2.1. DC-Link Voltage Harmonics

The DC-link voltage ripples have become a major source of harmonics produced by BESS/PVDGs [32]. The DC-link voltage harmonics are generated by PVDGs due to solar irradiation intermittency and the high rises or falls of BESS voltage. Du et al. [32] illustrated this phenomenon with the experimental setup simulated in MATLAB Simulink. The experimental results in Figure 1 show that the harmonic distortion increases as DC-link voltage increases. However, these harmonics are usually taken as constant in the analyses and designs of BESS/PVDG inverters. They are not always so in the practical sense. This accounts for the odd harmonic frequencies discovered in the spectrum of BESS/PVDG inverter's output current [33]. In addition, Mansor et al. [34] investigated harmonic generation in three-phase BESS/PVDG inverters and found that the second-order harmonics in the DC link produced the third-order harmonic discovered on the AC side of the inverter. [34]. Many methods have been proposed by the researchers to eliminate the current harmonics generated by the DC-link voltage ripple [35–39]. Some of the proposed methods reduced the dynamic performance of the system, and many lack

quality information on the connection between the output current harmonics and DC-link voltage ripples [32].

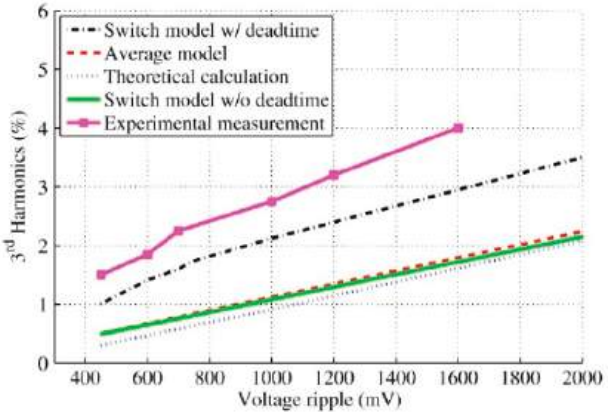

Figure 1. Impact of BESS/PVDG DC-link voltage ripples on harmonics [32].

2.2. Switching Harmonics

Switching harmonics is one other cause of current harmonics in BESS/PVDG inverter output. It occurs due to a mismatch in thee generation of switching pulses. The switching harmonics in PWM inverters always double their switching frequency [40,41]. Switching harmonics are very difficult to control and require an appropriate control strategy and optimized BESS/PVDG units; otherwise, system instabilities, harmonic generation and power losses ensue [32,42,43]. Various researchers have presented different methods to control or eliminate the switching harmonics of BESS/PVDG inverters [40,44,45].

Other research works maintained that the effects of quantization and resolution on control systems' measuring instruments are another potent source of harmonics in BESS/PVDG systems [44,46]. Also listed are the inadequacies of the current controllers of inverters in reducing harmonic contents and the positioning of sensors and locations of BESS and PVDG units in the distribution networks [47–49]. The outer voltage control loop of a two-series control algorithm and the PLL system could be another cause of reference current harmonics. In addition, output current harmonics could emerge from the dead time for switching pulse of the BESS/PVDG inverters [32,43].

2.3. Grid Voltage Harmonics

The BESS/PVDG inverter output current is produced due to the variation between the inverter's AC output voltage and the distribution network voltage. The output current harmonics are generated from the grid voltage when the grid voltage waveform includes harmonic components. The field measurements and research literature revealed that the grid voltages consistently have harmonics in varying degrees at different locations of the network [7,31,42,43]. For example, Figure 2a,b show the measured individual voltage harmonics up to the 31st order for one PVDG inverter at phase B of the grid and the combination of one PVDG and one BESS inverter for harmonics up to order 25 at phase B [31]. Grid voltage harmonics are usually low orders and are very difficult to annihilate by the filters. Numerous methods have been presented to control current harmonics generated from the grid voltage harmonics [50–53]. Du et al. [43] stated that the current harmonics sourced from grid background voltage do not depend on the magnitude of inverter output power. The grid voltage harmonics only reflect the magnitude of output current harmonics [43].

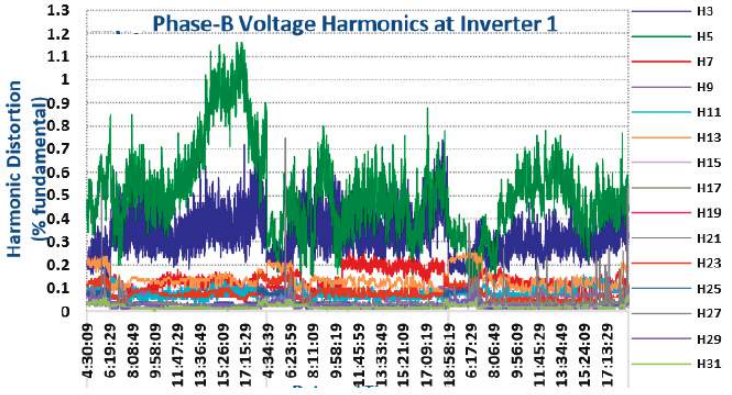

(**a**)

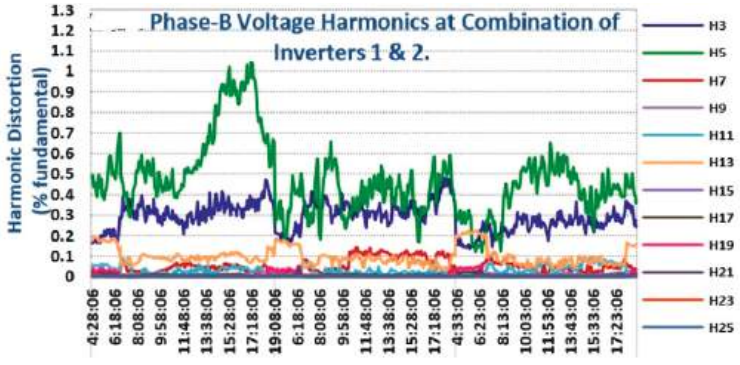

(**b**)

Figure 2. Individual voltage harmonics of phase B at (**a**) PVDG, (**b**) BESS outputs [31].

2.4. Harmonic Standards for Large-Scale BESS/PVDGs

Power quality is a power system requirement stipulated in all the international standards governing the grid connection of BESS/PVDG systems. Table 1 shows the IEEE 1547 and IEC 61727 standards as related to the requirements for current harmonics of the grid-connected BESS/PVDG systems [42,54,55]. The total harmonic distortion (THD) of generated current should not exceed 5% limit.

Table 1. Current harmonics limits by IEEE 1547 and IEC 61727 standards [54].

Harmonics Orders (I_H)	Corresponding to Fundamental (%)
A. Odd Harmonics	
3, 5, 7, 9	Less than 4%
11, 13, 15	Less than 2%
17, 19, 21	Less than 1.5%
23, 25, 27, 29, 31, 33	Less than 0.6%
>33	Less than 0.3%
B. Even Harmonics (All)	Less than 25% of various Odd harmonics
Total Harmonic Distortion (THD)	Less than 5%

During the conversion processes, the total harmonics produced by a BESS/PVDG system are in high quantity, despite that the inverters are parallel connected and multileveled [48,54]. This is a big issue when such inverter outputs are delivered into the distribution network. The current magnitude of many high-power inverters together with their harmonic contents can release large quantities of harmonics into a distribution system. This is because the magnitudes of current harmonics is proportional to the active output power of the BESS/PVDG system [7,31]. The loss of power in BESS/PVDG is mostly due to harmonics produced during the BESS/PVDG power conversions. In this sense, the proper location of BESS/PVDG units in the DN will result in network harmonic reduction due to harmonic cancellation effects. Power losses as a result of harmonics is seen as a very challenging issue worldwide due to technical damage and economic losses it causes. The economic losses related to harmonics have been geometrically growing at a high rate in recent years because of the high penetration of large-scale BESS/PVDGs into the distribution system. Consequently, re-evaluating the existing optimization models and algorithms used in the planning allocation of BESS/PVDGs to determine their effectiveness in curtailing the harmonics produced by the BESS/PVDGs is important, while taking cognizance of the huge amount of technical damage and economic losses occasioned by the harmonics.

3. Framework for Optimizing BESS/PVDGs into Distribution Networks

BESS/PVDG optimization is the methodological approach for obtaining optimal locations, sizes and times of BESS and PVDG units and installing them in a distribution network under network operating, investment and BESS/PVDG capacity constraints. The sizing and placement of BESS/PVDG units is a highly constrained, complex, nonlinear, mixed-integer and multi-objective optimization problem whose global optimum solution is very hard to find. The optimization of hybrid BESS/PVDGs involves considering contradicting objective functions such as maximising BESS/PVDG capacity and minimising power quality index; complex decision variables such as DG type, size, location and time; constraints such as network harmonic limits, DG voltage limit and power flow constraint; and the required conditions for modelling the uncertainties, especially the intermittency of the constituent distributed units (inaccurate mathematical model) [4,6,56]. Figure 1 provides the framework for optimizing BESS/PVDG into the distribution networks.

3.1. Optimization Objectives

The BESS/PVDG optimization objective functions can be either a single objective or multi-objective. The common single-objective functions used in the recent research works are minimisation of costs, energy losses, power losses, copper losses, emissions, voltage deviations, total harmonic distortions level (voltage and current); maximisation of benefits, profits, revenue of distribution system, DG capacity, reliability metric; enhancement of voltage profile, voltage stability; etc. The formulation of single-objective optimization problem can be from the perspectives of distribution system operator (DSO), the distribution energy resources developer, etc. [2,4,6,57]. A multi-objective function optimization problem requires the addition or combination of many single objectives that are conflicting and from which a single solution obtained may not be able to solve all the different objectives. The multi-objective function optimization involves simultaneous minimisation or maximisation of decision variables to obtain a single-objective formulation.

3.2. Decision Variables for BESS/PVDG Optimization

The decision variables are the unknown design variables that are determined during BESS/PVDG optimization procedures. The BESS/PVDG decision variables are formed from one or an amalgamation of size, location, number of DG, DG type, generated power of DG, installation year, real power and reactive power of DG or storage device, bus voltage angle and bus voltage magnitude [2,4,6]. The bus voltage angle and magnitude are the variables used for the decisions on the stability and power quality of the network.

3.3. Constraints for BESS/PVDG Optimization

Constraints are used in DG optimization problems to impose restrictions on some decision variables during the optimization of the objective function. Some of the commonly applied constraints in the formulation of DG allocation problems are as grouped [2,4,57].

3.3.1. Investment Constraints

They are constraints enforced on investment variables. Investment constraints can take on continuous, discrete or binary values. For example, the inequality constraints imposed on budget limit, divestment and investment options.

3.3.2. Safety Constraints

These are constraints to guarantee network and people's safety. Examples are the inequality constraints imposed for right of way in the installation of DG units, etc.

3.3.3. Technical Constraints

These are the power generation, network power flow and reliability constraints. These guarantee constant and continuous generation, transmission and distribution of power to the consumers. Some of the technical constraints are:

- The equality constraints for power balance that are imposed on active and reactive power of each network bus.
- The inequality constraints imposed on generations from DG units. e.g., DG penetration limits, discrete sizes of DG units, DG capacity limits, DG unit's constant power factor, maximum number of DGs, etc.
- The inequality constraints imposed on transmission lines and other network equipment/elements, e.g., transmission supply limits, transformer or line-overloading limits, dedicated buses for DG installations, transformer or line capacity limit, etc.
- The inequality constraints imposed on the transmission of power to the consumers, e.g., short-circuit constraints, maximum SAIDI, and radiality constraints.

3.3.4. Network Stability Constraints

Network stability constraints are imposed on the system to ensure power system stability. They are the constraints imposed on voltage drop, bus voltage magnitude, voltage angle, etc. The network stability constraints are formulated based on two network variables—voltage magnitude and voltage angle.

- The voltage magnitude constraints are imposed in the networks to ensure voltage stability. Inappropriate voltage magnitude could lead to voltage instabilities in power systems and cause damage to customers' devices, equipment and apparatuses.

$$V_{i(min)} \leq V_i \leq V_{i(max)} \text{ OR } \Delta V_{i(min)} \leq \Delta V_i \leq \Delta V_{i(max)}; i = 1, 2, \ldots n. \quad (1)$$

The inequality constraint presented in (1) is imposed on all the network buses to enforce voltage stability of the network.

- The phase angle constraints are imposed on the network based on some stability conditions to ensure dynamic stability such as small signal stability of the network. Voltage angle limits are crucial to dynamic stability, as the voltage magnitude is related to voltage stability of the network. Failure to maintain appropriate voltage angle limits can cause enormous dynamic instabilities that can result in total power outage and other serious economic losses. However, almost all the works on distributed generation allocation expansion planning do not utilize voltage angle constraints in the formulation models.

$$\theta_{min} \leq \mid \angle V_i - \angle V_j \mid \leq \theta_{max}; \text{OR } \theta_{min} \leq \theta_{ij} \leq \theta_{max} \quad (2)$$

This constraint (2) is imposed on all the network buses to enforce some stability criteria.

3.3.5. Power Quality Constraints

These power quality constraints are imposed to ensure the quality of power integrated into the distribution system. Different power quality indices such as total harmonic distortion (THD), total demand distortion (TDD), displacement power factor (DPF), oscillation power factor (OsPF) and transmission efficiency power factor (TEPF) could be used for power quality evaluation. A single power quality index that represents these indices could be formulated to evaluate the power quality of the distribution systems.

- The inequality constraints include voltage rise limits, voltage and current total harmonic distortion (THD) bounds, voltage sag bounds, etc.
- The harmonic constraints can be formulated based on the most important distribution network' constraints such as the voltage magnitude limits and voltage angle constraints.

The voltage magnitude constraints of the system can be reformulated and extended to impose constraints on the voltage harmonics of the distribution system during the integration of BESS/PVDG systems.

$$THD_v = \frac{\sqrt{\sum_{h=2}^{\infty} V_h^2}}{V_1} \tag{3}$$

$$V_{h(\min)} \leq V_h \leq V_{h(\max)} \; ; \; h = 1, \ldots N \tag{4}$$

Similarly, the phase angle constraints could be formulated considering some parameters and assumptions that relate phase angle to active power (current) and can be extended to distribution networks if current harmonics are expected to be curtailed.

$$THD_I = \frac{\sqrt{\sum_{h=2}^{\infty} I_h^2}}{I_1} \tag{5}$$

$$\theta_{h(\min)} \leq \theta_h \leq \theta_{h(\max)} \; ; \; h = 1, \ldots N \tag{6}$$

3.4. Modelling the Uncertainty of BESS/PVDGs

Modelling the uncertainties of BESS/PVDG units, including BESS and solar PV units, and the uncertainties of loads are very important to obtaining accurate solutions for a BESS/PVDG optimal allocation problem. The uncertain parameters that can be modelled in the planning of an electric power system for accounting the uncertainties in the distribution system are also presented in Figure 3. However, several previous research works place the uncertainties of these resources into consideration in their formulation models. Some of the uncertainties that are being considered and modelled in BESS/PVDG optimization studies include uncertainties of solar irradiance, wind speed, PV modules, wind and solar DG units, uncertainties of fuel, generated power, electricity market price, uncertainty of BESS and uncertainty of loads [1,4,14].

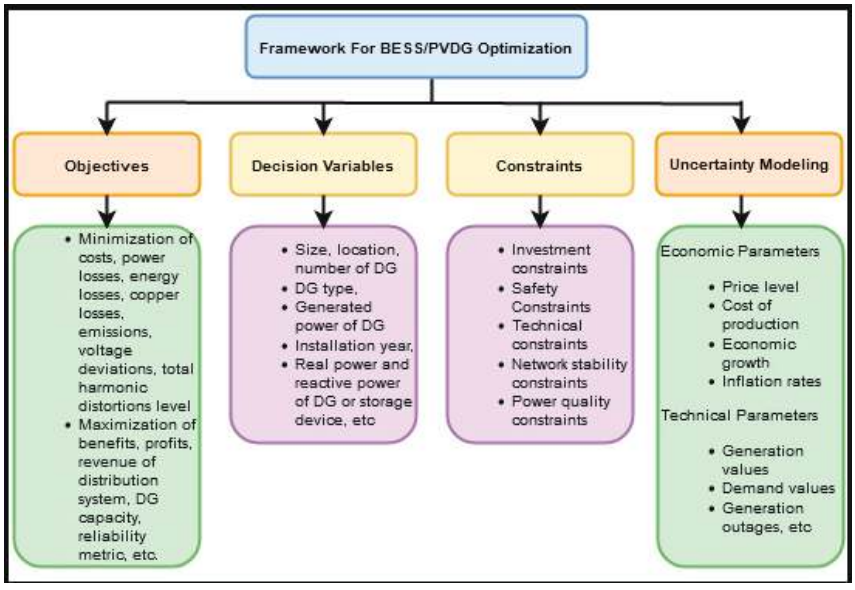

Figure 3. Framework for optimizing BESS/PVDG into distribution networks.

4. Optimization Models and Methods for BESS/PVDGs Allocation

The design and planning of battery energy storage system–photovoltaic distributed generation system is a research area that has continued to generate a lot of interest from many researchers, hence the large number of literature studies on the topic. The planning problem mentioned above concerns the hybrid energy systems that have optimal patterns and whose optimal sizes, placement/location and type of generation components/units can be assigned with minimum costs over the lifetime of the technologies. Therefore, the planning by the minimum net present value (NPV) of cost is called the optimal planning or optimal allocation of all probable hybrid technologies that are in optimal transition [11,24,56,58].

There are several methods for obtaining an optimal planning solution and many real-time, commercially available software applications for energy systems integration. In addition, various researchers have applied different optimal techniques to solve BESS/PVDG allocation problems. Different optimization methods, such as conventional methods, population-based intelligence search methods, some promising heuristic intelligence search approaches and commercial software applications, have been applied by the researchers to optimize hybrid BESS/PV distributed generation systems.

4.1. Conventional Optimization Methods

Conventional optimization methods are analytical and numerical techniques that usually present numerical equations to resolve optimal allocation problems. The methods involve computations, mathematical and theoretical analysis. The accuracy of these methods greatly depends on the efficacy of the model formulated. The advantages of these methods are the ease of implementation and short computation time to obtain convergence for the problem. However, under a complex problem, the accuracy of the solution may not be satisfactory because of the hypotheses used in simplifying the problem. Some of the conventional methods are discussed as [2,57–59].

4.1.1. Sensitivity Analysis Methods

Sensitivity-analysis-based methods use sensitivity indices used to optimally allocate DG units. In these methods, the original nonlinear equations are linearized about their starting operating points to lower the numbers of feasible solutions in the search space. The

advantages of sensitivity analysis methods are reduced computation time, which is critical for large practical systems, and good ability to assess the uncertainties of renewable energy resources. Anuradha et al. [60] present a loss-voltage sensitivity index for optimizing the renewable DG size, BESS capacities and power dispatch in distribution networks. The objective is to simultaneously evaluate both minimum effects of network losses and voltage variations for optimizing the DG size [60]. A hybrid of loss sensitivity analysis methods and novel voltage stability index is applied by Murty and Kumar [61] to find optimal sizes and locations of active and reactive power DGs. The objective is to minimise copper losses and enhance network voltage profile. In Saini and Gidwani [62], a comprehensive assessment of battery energy storage system installation and the placement of photovoltaic (PV) units in a radial distribution network is performed utilizing different load models. The objective is to minimise annual energy losses, control overvoltage and reverse power flow problems in a distribution network. Nevertheless, the solutions obtained from the sensitivity analysis methods solely found optimal placements of distributed generators, but the levels of optimality of such solutions are not known [4,58].

4.1.2. Linear Programming

Linear programming (LP) is a method that uses a mathematical model with linear mathematical relationships for optimizing the objective function(s). LP is used in power system optimization problems to obtain optimal sizes of DG units, because it provides precise solutions [2,56,57]. In Altintas et al. [63], the authors proposed a two-objective LP algorithm to incorporate solar and wind renewable DGs as well as BESS into distribution system expansion planning. The objective minimises the total cost of investment and carbon emissions. This algorithm performed a sensitivity analysis test on the effect of investment costs with respect to wind and solar DGs and BESS. Alturki et al. [64] presented an LP method to obtain optimal hosting capacity of a distribution grid with the objective to maximise the PVDG power using some fundamental variables and to minimise total cost using some uncertain criteria. The results revealed that the computation time for the proposed LP algorithm was very small, especially for large-scale problems. However, the network harmonic level and stability were not considered for evaluation in these works.

4.1.3. Mixed-Integer Linear Programming

The mixed-integer linear programming (MILP) method uses a mathematical model with linear objective function and linear constraints in which, at the minimum, one design variable must be an integer. The implementation of MILP is difficult in large-scale problems because it uses too much computation time. In Santos et al. [1], MILP is applied to determine the optimal locations, sizes and timing of smart-grid technologies for minimising the net present value of the total cost and for maximising the renewable DG integration. In Mishra et al. [65], a chance-constrained stochastic MILP algorithm is modelled to determine optimal investment decisions of DGs considering operational uncertainties, while an evolutionary vertical sequencing protocol algorithm is used to further optimize the objective function that minimises the total cost of investment and operation. Santos et al. [66] proposed an improved model aimed at optimizing the system operation in a coordinated way, where distributed renewable energy sources (DRES), energy storage systems (ESS) and distribution network system reconfiguration (DNSR) are considered along with the uncertainty of the resources. The objective function was modelled to incentivize the uptake of DRES by considering the cost of emissions to decarbonize the power system. In Ajeigbe et al. [67,68], the authors applied the MILP algorithm to maximise the optimal allocation of solar, wind and biomass DGs into the distribution system by minimising the NPV of total cost and by confining the small signal stability of the networks to a required level. All the works reviewed here modelled uncertainties of renewable energy resources and evaluated voltage stability of the network but were not able to evaluate the impact of BESS/RERDG powers on the harmonic contents of the networks. Likewise, their results did not report global optimal solutions to BESS/PVDG optimal allocation problems.

LP and MILP suffer from a lack of flexibility. They normally require pre-conditions such as convexity, linearity and continuity of objective functions, which are difficult to meet in practice [2,57].

4.1.4. Nonlinear Programming

Nonlinear programming (NLP) is a mathematical programming method that uses nonlinear objective function and solely continuous variables and constraints. The NLP computation involves the differentials of objective functions and constraints. In solving nonlinear problems, a search path is selected iteratively by defining the starting partial differentials of the problem equation. This approach could be based on first-order or higher-order methods such as the reduced gradient method [69,70] and other search methods [71,72], Newton Raphson method [73] and successive quadratic programming [74,75] which are used for solving DG allocation planning problems.

4.1.5. Mixed-Integer Nonlinear Programming

Mixed-integer nonlinear programming (MINLP) utilizes a mathematical model with nonlinear objective functions and constraints and both continuous and discrete variables. MINLP algorithms have been applied in power systems to determine the optimal sizes and locations of DGs and BESSs. Some of the disadvantages of MINLP are long computation time and a very large number of decision variables [2,56,57]. Salyani et al. [76] applied MINLP in the mathematical modelling for the simultaneous optimal allocation planning of high- and medium-voltage substations, robust medium-voltage feeder routing and renewable DG units. The authors used adaptive GA to find optimal locations and sizes while the uncertainties of renewable DGs, fuel prices, electricity and demand were evaluated. A mixed-integer nonlinear programming-model-based methodology is presented in Valencia et al. [11] for the optimal location, selection, and operation of BESSs and renewable distributed generators (DGs) in medium–low-voltage distribution systems.

4.1.6. Fuzzy Logic

The fuzzy logic (FL) method was developed in 1979 to solve power system problems. The FL method is based on the concept of a classical set, such as the identification of a membership function that is associated with each member as indicated by a binary number 0 and 1 [77]. The membership function dictates the resemblance level of a member in a fuzzy subset. Some of the common membership functions are the triangular, trapezoidal, piecewise-linear and Gaussian functions [2,57,59]. In Injeti and Kumar [78], FL is applied to DG allocation problems, with minimisation of power losses and improvement in voltage profiles as the objective function. Sharma et al. [79] proposed a FL controller in determining the optimal sizes and locations of DGs in order to minimise power losses and to enhance loadability and voltage profiles of distribution networks. However, the results from these works did not report the optimality of their solutions, the evaluation of network stability or harmonic contents.

The works discussed thus far on FL have not considered the impact of DGs and BESS on the oscillatory modes and harmonic contents of the distribution networks. To achieve practical solutions, dynamic networks must be simulated for the evaluation of distribution system stability and harmonic contents.

4.2. Intelligence Search Methods for BESS/PV Distributed Generations

Artificial intelligence (AI) is the application of human intelligence to perform tasks in machines [59]. AI is applied in the intelligence search methods (ISM) used in power systems for optimal sizing and placement of DGs. Intelligence search methods are heuristics algorithms that fasten up the processes of obtaining near-optimal solutions for complex and large DG problems. The advantages of intelligence search methods over other conventional methods is the simplicity of implementation and robustness. However, the accuracy and

precision of ISMs are not reliable. They usually take much computation effort [2,56,57,80]. Some of intelligence search methods are presented below.

4.2.1. Genetic Algorithm

Genetic algorithm (GA) is an intelligence search algorithm that was introduced earlier to solve optimization problems. GA is developed from natural selection and genetics principles such as selection, mutation, inheritance and crossover [56,57]. In GA, a set of selection rules is specified to allow a population to achieve a maximum state of fitness. Then, the elements in a population are integrated into chromosomes to enable the potential elements to achieve a better state. The first population of elements evolved through the evolution of generations. The principle of mutation is applied to modify the chosen element to evolve into a new population. The algorithm repeats this procedures until an acceptable solution or the highest number of iterations is attained. [4,6,56]. Genetic algorithms utilize continuous and discrete variables for implementation and work better at obtaining global optimums of various functions. GAs can effectively solve poorly defined and complex problems. GA is the most used optimization method to find optimal locations and sizes of DGs in the literature [22,81,82]. In Liu et al. [22], the authors presented a mixed-integer GA to obtain optimal sizes and locations of hybrid battery energy storage and renewable energy DGs units with objective aiming to minimise system total cost, end-user satisfaction loss caused by demand side management, and tie-line power fluctuation. The methodology in Liu et al. effectively determined the solution of the multi-objective optimization problem compared to others validated with it. However, neither uncertainties of the renewable energy sources nor the voltage variability of the BESS were modelled. In addition, the requirements for the evaluation of network stability and harmonic contents were not included in the proposed methodology. Moreover, genetic algorithms have the disadvantage of evaluating the repeated fitness functions that are time intensive for large and complex problems. The various configurations of GA that are proposed to improve the performance of the GA method in the DG allocation problems are quantum GA (QGA) [83], adaptive genetic algorithm (AGA) [84], etc.

4.2.2. Simulated Annealing

Simulated annealing (SA) uses an iterative procedure for solving combinatory optimization problems. SA employs the process of crystallization at a discrete search space of a physical system [57]. The SA algorithm depends on the cooling criterion and uses initial temperature (T), final temperature (T_{min}) and cooling rate (β) variables. SA algorithms are extensively proposed in the literature to allocate DG units at lower computational time. Simulated annealing algorithms perform effectively in solving reliability-criteria-based optimization problems [2,57]. The advantages of SA algorithms are robustness, simplicity of implementation, and capability to provide feasible solutions to combinatorial problems. Nevertheless, SA algorithms have large computation times without upper limits, terminate at local minimums and lack details on the level of variation between a local minimum and global minimum [56,85]. In Koziel et al. [86], the authors presented a feasibility-preserving SA algorithm to obtain DN reconfiguration with the objective to minimise power loss and improve voltage profile. This study concluded that the proposed algorithm was more efficient than some published population-based intelligence search methods with respect to computational cost and solution repeatability. However, the optimality of the solution was not reported, and the harmonic contents and dynamic stability of the networks were not evaluated in the proposed work.

4.2.3. Particle Swarm Optimization

Particle swarm optimization (PSO) methods are developed based on the social adaptation of flocking bird and schooling fish. In PSO, single intersection of all dimensions produces a particle, and these particles move randomly in a complex search space. The system is then adjusted using a number of solutions that are randomly selected. During each

iteration, the particles use their fitness level to assess their positions. Then, the contiguous particles update their previous "best" position to upgrade the final solution [2,57,87]. The advantages of PSO are robustness, simple implementation and running simultaneous computations in less computation time. PSO algorithms use a couple of parameters to modify and converge faster. PSO can also be effectively used to solve DG allocation problems with inaccurate mathematical models. However, the initial design parameter are difficult to define with PSO. During complex DG allocation problems, PSO may converge prematurely and terminate at the local minimum [6,56]. In Prabpal et al. [88], the PSO technique was applied to obtain optimal sizes and locations of multiple BESS and PVDG units with the objective to minimise total cost, minimise the impact of large-scale penetration of BESS, improve voltage profile and increase the stability of the power system. The results showed that PSO and GA methods equally performed better in achieving fewer numbers of iterations and quality of solutions. Shahzad et al. [23], Jamian et al. [89], Rathore et al. [90] and Zeinalzadeh et al. [91] proposed multi-objective PSO methods for determining optimal locations and sizes of BESSs/PVDGs to minimise power losses and improve voltage profiles. However, the uncertainties of the intermittent DGs and BESSs were not modelled, and the impact of their variable output power on the dynamic stabilities and harmonic contents of the distribution networks was not considered. Only the uncertainties related to BESS/PVDG market scenarios were evaluated in Rathore et al. [90].

4.3. Promising Intelligence Search Methods

Promising intelligence search methods are the additional optimization algorithms developed to effectively solve distributed generation optimization problems. Some of these methods are as stated [2,57,59].

4.3.1. Artificial Bee Colony Algorithm

The artificial bee colony (ABC) algorithm was developed from the searching behaviour of a swarm of honeybees. Khasanov et al. [16] proposed an application of hybrid teaching-learning and artificial bee colony (TLABC) technique for determining the optimal allocation of PV-based distributed generation and battery energy storage units in a distribution system with the aim of minimising the total power losses. ABC algorithms are applied in Mohandas et al. [92] and Dixit et al. [93] to find optimal DGs locations and sizes with the objective of minimising power losses and of improving voltage stability of the network. In Abu-Mouti and El-Hawary [94], the authors proposed an algorithm of ABC to adjust the control inputs, iteration number and colony size in the DG allocation optimization. El-Zonkoly and Kefayat et al. [95,96] utilized ABC algorithms to solve distribution expansion planning problems and to obtain optimal reinforcement and commitment scheduling for PVDG allocation. Padma Lalitha et al. [97] presented and compared the ABC and PSO algorithms. The authors observed that the ABC algorithm outperformed PSO, having better solutions and convergence. Notwithstanding, the works discussed here do not provide indices to evaluate harmonic contents and dynamic stabilities of the systems.

4.3.2. Ant Colony Algorithm

The ant colony (AC) algorithm is adapted from ants' social behaviours in searching for the shortest route to obtain food. The AC algorithm process begins with random solutions obtained from the ants' random searches in their movements. Ants share information about their movements by leaving chromosome trails behind during their movements. Consequently, a path with trail density becomes the shorter path. This knowledge is utilized in the optimization search to obtain feasible solutions [57]. The advantages of AC algorithms are the ability to discover good solutions and guarantee convergence and the ability to search among a population simultaneously and adapt to changes such as new distances. However, AC optimization algorithms are weak in changing probability distribution, uncertainty of convergence time, sequences of random decisions and theoretical analysis, since they are highly experimental researches. These algorithms are variously used in

the literature for optimal allocation of DGs [6,56]. In Gomez et al. [98], Vlachogiannis et al. [99], Wang and Singh [100] and Amohadi and Fotuhi-Firuzabad [101], the variant of AC and ant colony system (ACS) algorithms were presented. They found optimal sizes of DGs, locations of DGs and re-closers in the radial DNs with an objective to use the composite reliability index. Transient stability and reliability of the distribution systems were evaluated to validate the proposed methods. ACS algorithms were observed to be more satisfactory in many engineering applications. However, these works did not include the installation of renewable DGs and could not access the impacts of integrating BESS/PV-distributed generations on the harmonic distortion and oscillation of the networks.

4.3.3. Artificial Immune System Algorithm

The artificial immune system (AIS) algorithm is adapted from immunology, the importance of the immune system and their values in the natural world [102]. The immune system is an indispensable defence against self-approach to protect human health from pathogens such as viruses and microbes. The procedure differentiates between self-cells and non-self-cells. Thereafter, the immune system effects immune actions to destroy the non-self-cells [103–105]. To apply the AIS optimization process in solving DG allocation problems, the instructions in the search area (objective functions, design variables, constraints, etc.) are encrypted in an antigen population of an AIS algorithm. AIS algorithms are proposed in Aghaebrahimi et al. [106] and Hatata et al. [107] to find the optimal locations and sizes of the DGs, with the objective to minimise the power losses of the DN considering bus voltage limits and line current. Souza et al. [108] proposed an AIS algorithm in expansion planning to allocate DG units into distribution network considering the uncertainty of load demands.

4.4. Probable Hybrid Intelligence Search Methods

Hybrid optimization methods are a useful combination or collaboration of more than one different intelligence search method. These approaches extract the benefits of the component methods to obtain an optimum solution for a specific planning problem. The allocation expansion planning of BESS/PVDGs problems is multi-objective in nature. Hence, applying a hybrid method in their investigation begets an excellent planning objective and a suitable alternative algorithm to solve the problems that involve better understanding of the methods.

A summary of the various optimization techniques that are developed and applied by the researchers for BESS/PVDGs allocation is presented in Table 2.

Table 2. Summary of optimization methods.

Optimization Method	Optimized Factor	Comment
Conventional Method • Sensitivity Analysis [60–62] • Linear Programming (LP) [63,64] • Mixed Integer Linear Programming [65–68] • Nonlinear Programming (NLP) [69–75] • Mixed-Integer Nonlinear Programming (MINLP) [76] • Fuzzy Logic [77–79]	Hybrid renewable energy sources (solar, wind) and battery energy storage, and cost	Using numerical equations that can be applied to optimization problems due to their capability to provide accurate mathematical model formulation
Intelligence Search • Genetic Algorithm [81–84] • Simulated Annealing [85,86] • Particle Swamp [87–91] • Artificial Bee Colony [92–97] • Artificial Immune System [102–108] • Ant Colony [98–101]	Hybrid renewable energy sources (solar, wind) and battery energy storage, and cost	Using the exhibition of intelligence in machines to determine optimal locations and sizes of hybrid DGs in power system
Deterministic Approaches [59–63]	Standalone renewable energy sources (solar, wind) with battery energy storage, and cost	Using mathematical equations for determining particular values when fixed factors are set

Table 2. *Cont.*

Optimization Method	Optimized Factor	Comment
Probabilistic Approaches [63–67,74,75]	• Efficiency of hybrid renewable energy systems, and cost • Uncertain parameters in power system	Using statistical data gathering methods for finding optimized factors
Software Based Methods [109–116] • HOMER • HYBRIDS, etc.	Hybrid solar/wind and or diesel generators with battery energy storage	Using software applications that uses input file with all necessary data

4.5. Commercial Software Applications for Allocation of (BESS/PV) Hybrid DG Systems

Several software applications have been developed and applied for the sizing of hybrid renewable energy systems (HRESs) such as HOMER [109–111], HYBRIDS [112], HYBRID 2 [113], RET Screen [114], TRNSYS [115] and IHOA [116].

Comparatively, HOMER has a significant application in optimal sizing of HRESs because of its capacity to quickly obtain optimal sizes of energy systems. In addition, it is useful in investigating sensitivity analyses of some uncertainty parameters and changing factors related to the HRESs. However, the mentioned software tools are incapacitated to investigate major network system issues related to the integration of distributed HRESs (DHRESs) such as harmonics and small signal and transient stabilities. A list of commercially available software for the planning of HRES is presented in Table 3.

Table 3. Software applications for optimizing BESS/PVDGs.

Name of Software	Optimization Input	Optimized Output
HOMER	• Load command • Resource input • Cost details (capital, O&M, replacement costs • System control	• Optimize unit size(s) • NPV and energy cost
HYBRIDS	• Wind turbine size(s) and type • Solar size(s) • Type and number of battery storage	• NPV and energy cost • Amount of green-house gases
HYBRID 2	• Resources input • Load demand • Cost details (O&M, investment, components costs)	• Optimize unit size(s) • NPV and energy cost • Proportion of green-house gases released. • System payback time
RET SCREEN	• Load command • Solar size(s) • Climate data input • Invention and hydrology data input	• NPV and energy costs • Economic capability • Production rate • Risk analysis • Energy used and saved
IHOGA	• Load command • Resources data input • Components and economic factors	• Improve multi-objective optimization • Cost of energy • Life cycle release
TRYSYS	• Climate data • Ingrained models	• Dynamic simulation of renewable energy resources

5. Results and Discussion

The increasing needs for energy and the resultant environmental issues arising from fossil energy utilization have encouraged the extensive study of renewable energy technologies in place of traditional fossil fuels. Precisely, hybrid distributed generations, which have been described as a collaboration of renewable energies and support systems, are a significant alternative to confront the concerns over sustainability of energy demands and environmental safety. The planning and optimization of hybrid distributed power systems can meet the essential requirements of a geographical location in terms of availability of

potential energy resources, area topography and various kinds of energy demands. Consequently, the optimal allocation of renewable energy sources and storage systems relating to environmentally friendly hybrid distributed systems considerably improves the technical and economic aspects of the power supply system. The addition of storage technologies in the allocation of distributed generations can smoothen output power and reduce REHDG intermittent effects in the network. Including storage devices in the DGs allocation problems provides supporting services to the optimal solutions by eliminating the effects of intermittency in the renewable sources power output. Several allocation methodologies have been proposed to determine the best hybrid renewable energy system with respect to the economy and technology. Determining the optimal allocation of hybrid battery storage and PV-distributed generation systems and other hybrid renewable energy systems is important to increase the technical and economic efficiency of the power distribution system and to encourage the extensive use of environmentally friendly resources.

Various allocation methodologies presented in the recent literature with different optimization algorithms are reviewed here. The GA, PSO, SA and AIS are some of the feasible artificial intelligence algorithms used to investigate the planning and optimization of DG allocation problems. The most important benefit of GAs are the ordered capability to find the global optimal and the ease of achieving a local minimum when used in hybrid system allocation. Another advantage that makes GA suitable for allocation planning studies is code-ability because it is not accessible in other methods such as PSO. For instance, when at most three parameters are to be coded such as in a wind/PV/BESS system, both GA and PSO can perform effectively. However, when more than three elements are involved, only the GA method would be more capable of obtaining optimal solutions. Some other times, PSO has some advantages over GA, although both are very effective in utilizing the same repeatable search approach. Moreover, employing SA in hybrid distributed systems is not as common as GA and PSO methods, but presently, SA is generating more research interest in some approved areas of application. The ACS algorithms have been presented to reduce power losses and to improve power system factors of a radial distributed system. Similar to GA, the AIS optimization algorithm has "collection" and "transformation" operatives which improve the probability of the algorithm to find the global optimum point.

AIS is bound to have a high application in sizing studies because it is similar to GA and can be effective in finding the global optimum in difficult problems. However, GA has greater application than AIS, especially in addressing a large number of parameters. In addition, conventional methods such as LP, MILP and NLP are still being applied in existing studies to detail the features of any physical system into a mathematical model formulation. Often, hybrid optimization methods are applied by combining two or more methods to take beneficial advantage of them in terms of their convergence time during the optimization process. Hybrid methods are characterized due to their dynamic flexibility during the allocation process. Hence, they are the most applied allocation methods.

The intermittent nature of photovoltaic and wind output power and the high voltage rise and fall from BESS cause harmonic distortions which have a negative impact on the power quality, reliability and stability of the distribution networks. The majority of the current works do not include the uncertainties of the renewable and battery storage power sources in their formulation models. They did not combine all the associated investment, technical, safety, DG capacity, network stability, power quality and reliability constraints in the formulation models for the DG allocation problems. In most of these works, the minimum harmonic level and dynamic stability of the network are not constrained but are only assumed, while the constraints for the right of way are neglected for the required buses. All these necessary and associated constraints need to be incorporated to obtain a practical solution from the REHDG allocation models. In essence, future research studies should give adequate consideration to modelling of the impacts of renewable energy intermittencies and the resulting variable output power to culminate in more feasible solutions to BESS/PVDG optimization problems.

In addition, the operations of hybrid DG systems are dynamic. Hence, the planning and design of optimal sizes and placement of RERDGs should be optimized on dynamic networks but not on static ones, as they are mostly performed in the existing planning models. The dynamical issues such as harmonic and system instabilities are very visible while using dynamic networks, since the real power networks are dynamic networks whose load profile periods are estimated hourly during a dynamic planning horizon. Future research needs to focus on the use of dynamic networks to entirely incorporate the intrinsic characteristics of the distribution network such as the harmonic components and dynamic stability of the network.

Moreover, the sizes and locations of battery energy storage, photovoltaic and wind DG units in the distribution network (DN) affect the network harmonic contents by having either positive or negative impacts on the magnitude of the current and voltage harmonics of the networks.

6. Conclusions

This study presents a review of prior research on the optimization methodologies for designing and planning hybrid renewable energy resource distributed generation such as hybrid battery energy storage–photovoltaic DG and other hybrid distributed systems. This paper reviewed more than one hundred papers published by renowned referenced journals on battery energy storage systems and renewable energy resources as well as on robust and efficient optimization methods for solving hybrid DG allocation planning problems. Optimization studies, in the last decade, on DG allocation planning using conventional and intelligence search methods have been analysed, and hybrid optimization algorithms have been presented.

Intelligence search methods have been mostly used in the last decade due to their capacity for shorter computation times, and because they provide better accuracy and have better convergence than the conventional methods. In conclusion, at the beginning, this study investigated a number of research works that have applied optimization methods to solve renewable energy DG allocation problems, including solar, wind and battery energy systems. Many research works use intelligence search methods, most especially GA, PSO and AIS, to solve these allocation problems. Notwithstanding, conventional methods, especially LP and MILP and different configurations of NLP methods are still being used in current studies. In the case of curtailing harmonic distortions of the DNs, which indicate the strength of this study, an optimal planning model is yet to be developed for optimal sizing, placement and timing of renewable DGs and battery energy storage systems. Although, in most cases, the optimal sizing and placement of BESS/REDGs may have attained a minimum cost, the requirements for minimum harmonic levels are yet to be achieved. These requirements are merely presumed in the existing works. Further research is required in this regard to improve the current expansion planning model to obtain optimal allocation of BESS and renewable energy DGs and to constrain the decision variables related to harmonic distortions to a required level. A more comprehensive expansion planning model together with an efficient intelligence search algorithm that has that capability to obtain a global optimum solution is an important approach towards solving optimal BESS/PVDG allocation problems and towards reducing harmonic components of distribution systems during the integration of hybrid battery energy storage systems and photovoltaic DGs.

Author Contributions: The mathematical formulations and programming in this work were developed within the framework of the doctorate of A.O. He is supervised by Y.H. and is co-supervised by J.M. The written manuscript was extensively discussed with the supervisors. All authors have read and agreed to the published version of the manuscript.

Funding: This research received no external funding.

Institutional Review Board Statement: Not applicable.

Informed Consent Statement: Not applicable.

Data Availability Statement: Data sharing is not applicable to this article.

Acknowledgments: The authors would like to acknowledge the research support received from Tshwane University of Technology (TUT), Pretoria, South Africa.

Conflicts of Interest: The authors declare no conflict of interest.

References

1. Santos, S.F.; Fitiwi, D.Z.; Shafie-Khah, M.; Bizuayehu, A.; Catalão, J. Optimal sizing and placement of smart-grid-enabling technologies for maximizing renewable integration. In *Smart Energy Grid Engineering*; Elsevier: Amsterdam, The Netherlands, 2017; pp. 47–81.
2. Ajeigbe, O.A.; Munda, J.L.; Hamam, Y. Towards maximising the integration of renewable energy hybrid distributed generations for small signal stability enhancement: A review. *Int. J. Energy Res.* **2020**, *44*, 2379–2425. [CrossRef]
3. Babatunde, O.M.; Munda, J.L.; Hamam, Y. A comprehensive state-of-the-art survey on hybrid renewable energy system operations and planning. *IEEE Access* **2020**, *8*, 75313–75346. [CrossRef]
4. Jordehi, A.R. Allocation of distributed generation units in electric power systems: A review. *Renew. Sustain. Energy Rev.* **2016**, *56*, 893–905. [CrossRef]
5. Hosenuzzaman, M.; Rahim, N.A.; Selvaraj, J.; Hasanuzzaman, M.; Malek, A.A.; Nahar, A. Global prospects, progress, policies, and environmental impact of solar photovoltaic power generation. *Renew. Sustain. Energy Rev.* **2015**, *41*, 284–297. [CrossRef]
6. Bullich-Massagué, E.; Cifuentes-García, F.-J.; Glenny-Crende, I.; Cheah-Mañé, M.; Aragüés-Peñalba, M.; Díaz-González, F.; Gomis-Bellmunt, O. A review of energy storage technologies for large scale photovoltaic power plants. *Appl. Energy* **2020**, *274*, 115213. [CrossRef]
7. Ajeigbe, O.A.; Chowdhury, S.P.; Olwal, T.O.; Abu-Mahfouz, A.M. Harmonic Control Strategies of Utility-Scale Photovoltaic Inverters. *Int. J. Renew. Energy Res. (IJRER)* **2018**, *8*, 1354–1368.
8. Babatunde, D.E.; Babatunde, O.M.; Emezirinwune, M.U.; Denwigwe, I.H.; Okharedia, T.E.; Omodara, O.J. Feasibility analysis of an off-grid photovoltaic-battery energy system for a farm facility. *Int. J. Electr. Comput. Eng.* **2020**, *10*, 2874–2883. [CrossRef]
9. do Nascimento, Á.D.J.; Rüther, R. Evaluating distributed photovoltaic (PV) generation to foster the adoption of energy storage systems (ESS) in time-of-use frameworks. *Sol. Energy* **2020**, *208*, 917–929. [CrossRef]
10. Lee, M.; Park, J.; Na, S.-I.; Choi, H.S.; Bu, B.-S.; Kim, J. An analysis of battery degradation in the integrated energy storage system with solar photovoltaic generation. *Electronics* **2020**, *9*, 701. [CrossRef]
11. Valencia, A.; Hincapie, R.A.; Gallego, R.A. Optimal location, selection, and operation of battery energy storage systems and renewable distributed generation in medium-low voltage distribution networks. *J. Energy Storage* **2021**, *34*, 102158. [CrossRef]
12. Mirhassani, S.; Ong, H.C.; Chong, W.; Leong, K. Advances and challenges in grid tied photovoltaic systems. *Renew. Sustain. Energy Rev.* **2015**, *49*, 121–131. [CrossRef]
13. Kumar, V.V.; Babulal, C. Application of Fuzzy Logic in Power Quality Assessment of Modern Power Systems. *Microgrid Technol.* **2021**, *1*, 377–403.
14. Manoj Kumar, N.; Ghosh, A.; Chopra, S.S. Power resilience enhancement of a residential electricity user using photovoltaics and a battery energy storage system under uncertainty conditions. *Energies* **2020**, *13*, 4193. [CrossRef]
15. Karimi, M.; Mokhlis, H.; Naidu, K.; Uddin, S.; Bakar, A.A. Photovoltaic penetration issues and impacts in distribution network—A review. *Renew. Sustain. Energy Rev.* **2016**, *53*, 594–605. [CrossRef]
16. Khasanov, M.; Kamel, S.; Ayman, A.; Jurado, F. Optimal planning DG and BES units in distribution system considering uncertainty of power generation and time-varying load. *Turk. J. Electr. Eng. Comput. Sci.* **2021**, *29*, 773–795. [CrossRef]
17. Akagi, S.; Yoshizawa, S.; Ito, M.; Fujimoto, Y.; Miyazaki, T.; Hayashi, Y.; Tawa, K.; Hisada, T.; Yano, T. Multipurpose control and planning method for battery energy storage systems in distribution network with photovoltaic plant. *Int. J. Electr. Power Energy Syst.* **2020**, *116*, 105485. [CrossRef]
18. Duong, M.Q.; Pham, T.D.; Nguyen, T.T.; Doan, A.T.; Tran, H.V. Determination of optimal location and sizing of solar photovoltaic distribution generation units in radial distribution systems. *Energies* **2019**, *12*, 174. [CrossRef]
19. Caballero-Peña, J.; Cadena-Zarate, C.; Parrado-Duque, A.; Osma-Pinto, G. Distributed energy resources on distribution networks: A systematic review of modelling, simulation, metrics, and impacts. *Int. J. Electr. Power Energy Syst.* **2022**, *138*, 107900. [CrossRef]
20. Guo, C.; Luo, F.; Cai, Z.; Dong, Z.Y.; Zhang, R. Integrated planning of internet data centers and battery energy storage systems in smart grids. *Appl. Energy* **2021**, *281*, 116093. [CrossRef]
21. Emad, D.; El-Hameed, M.; El-Fergany, A. Optimal techno-economic design of hybrid PV/wind system comprising battery energy storage: Case study for a remote area. *Energy Convers. Manag.* **2021**, *249*, 114847. [CrossRef]
22. Liu, B.; Zhou, B.; Yang, D.; Li, G.; Cao, J.; Bu, S.; Littler, T. Optimal planning of hybrid renewable energy system considering virtual energy storage of desalination plant based on mixed-integer NSGA-III. *Desalination* **2022**, *521*, 115382. [CrossRef]
23. Shahzad, K.; Amin, A.A. Optimal Planning of Distributed Energy Storage Systems in Active Distribution Networks using Advanced Heuristic Optimization Techniques. *J. Electr. Eng. Technol.* **2021**, *16*, 2447–2462. [CrossRef]
24. Zahraee, S.; Assadi, M.K.; Saidur, R. Application of artificial intelligence methods for hybrid energy system optimization. *Renew. Sustain. Energy Rev.* **2016**, *66*, 617–630. [CrossRef]

25. Groppi, D.; Pfeifer, A.; Garcia, D.A.; Krajačić, G.; Duić, N. A review on energy storage and demand side management solutions in smart energy islands. *Renew. Sustain. Energy Rev.* **2021**, *135*, 110183. [CrossRef]
26. Hannan, M.; Wali, S.; Ker, P.; Abd Rahman, M.; Mansor, M.; Ramachandaramurthy, V.; Muttaqi, K.; Mahlia, T.; Dong, Z. Battery energy-storage system: A review of technologies, optimization objectives, constraints, approaches, and outstanding issues. *J. Energy Storage* **2021**, *42*, 103023. [CrossRef]
27. Khezri, R.; Mahmoudi, A.; Aki, H. Optimal planning of solar photovoltaic and battery storage systems for grid-connected residential sector: Review, challenges and new perspectives. *Renew. Sustain. Energy Rev.* **2022**, *153*, 111763. [CrossRef]
28. Ajeigbe, O.A.; Munda, J.L.; Hamam, Y. Renewable Distributed Generations' Uncertainty Modelling: A Survey. In Proceedings of the 2020 IEEE PES/IAS PowerAfrica, Nairobi, Kenya, 25–28 August 2020; pp. 1–5.
29. Ortega, M.; Hernández, J.; García, O. Measurement and assessment of power quality characteristics for photovoltaic systems: Harmonics, flicker, unbalance, and slow voltage variations. *Electr. Power Syst. Res.* **2013**, *96*, 23–35. [CrossRef]
30. Umamaheswararao, C. Modeling and Simulation of Statcom for Power Quality Improvement. *Inf. Technol. Ind.* **2021**, *9*, 217–229.
31. Chidurala, A.; Saha, T.; Mithulananthan, N. Harmonic characterization of grid connected PV systems & validation with field measurements. In Proceedings of the 2015 IEEE Power & Energy Society General Meeting, Denver, CO, USA, 26–30 July 2015; pp. 1–5.
32. Du, Y.; Lu, D.D.-C.; Chu, G.M.; Xiao, W. Closed-form solution of time-varying model and its applications for output current harmonics in two-stage PV inverter. *IEEE Trans. Sustain. Energy* **2014**, *6*, 142–150. [CrossRef]
33. Reddy, G.R.; Rayaguru, N.; Karthikumar, K.; Chandrasekar, P.; Murthy, P. Enhancement of Power Quality With Fuzzy Based UPQC in Grid Integrated and Battery Assisted PV System. In Proceedings of the 2021 2nd Global Conference for Advancement in Technology (GCAT), Bangalore, India, 1–3 October 2021; pp. 1–8.
34. Mansor, M.A.; Hasan, K.; Othman, M.M.; Noor, S.Z.B.M.; Musirin, I. Construction and performance investigation of three-phase solar PV and battery energy storage system integrated UPQC. *IEEE Access* **2020**, *8*, 103511–103538. [CrossRef]
35. Sanchez-Ruiz, A.; Abad, G.; Echeverria, I.; Torre, I.; Atutxa, I. Continuous phase-shifted selective harmonic elimination and dc-link voltage balance solution for H-bridge multilevel configurations, applied to 5L HNPC. *IEEE Trans. Power Electron.* **2016**, *32*, 2533–2545. [CrossRef]
36. Freddy, T.K.S.; Rahim, N.A.; Hew, W.-P.; Che, H.S. Modulation techniques to reduce leakage current in three-phase transformerless H7 photovoltaic inverter. *IEEE Trans. Ind. Electron.* **2014**, *62*, 322–331. [CrossRef]
37. Vahedi, H.; Shojaei, A.A.; Dessaint, L.-A.; Al-Haddad, K. Reduced DC-link voltage active power filter using modified PUC5 converter. *IEEE Trans. Power Electron.* **2017**, *33*, 943–947. [CrossRef]
38. Deshmukh, S.; Thorat, A.; Korachagaon, I. Modelling and Analysis of PV Standalone System With Energy Management Scheme. In Proceedings of the 2020 IEEE International Conference on Electronics, Computing and Communication Technologies (CONECCT), Bangalore, India, 2–4 July 2020; pp. 1–5.
39. Kumar, M. Modelling and Simulation of Compound PV-BESS Systems. 2018. Available online: https://trepo.tuni.fi/bitstream/handle/123456789/25480/kumar.pdf?sequence=4&isAllowed=y (accessed on 18 December 2022).
40. Rashmi, V.; Khare, M.; Lnct, B. Study of Cascaded H-Bridge Converter Control Strategies and their Impact on Switching Harmonics. *Int. J. Online Sci.* **2018**, *4*, 8. [CrossRef]
41. Ajeigbe, O.; Munda, J.; Hamam, Y. Characterisation of harmonic distortions produced by small domestic back-up generators. In Proceedings of the 2018 IEEE PES/IAS PowerAfrica, Cape Town, South Africa, 26–30 June 2018; pp. 432–437.
42. Shabbir, N.; Kütt, L.; Jarkovoi, M.; Iqbal, M.N.; Rassõlkin, A.; Daniel, K. An overview of measurement standards for power quality. *Agron. Research.* **2021**, *19* (Suppl. S1), 944–960.
43. Du, Y.; Lu, D.D.-C.; James, G.; Cornforth, D.J. Modeling and analysis of current harmonic distortion from grid connected PV inverters under different operating conditions. *Sol. Energy* **2013**, *94*, 182–194. [CrossRef]
44. Sengamalai, U.; Ramasamy, P.; Thentral, T.; Balasubramani, K.; Alagarsamy, M.; Muthusamy, S.; Panchal, H.; Sachithanandam, M.P.; Sadasivuni, K.K. A simplified methodology for mitigating the harmonics and common-mode voltage using multi-level inverters for renewable energy applications. *Energy Sources Part A Recovery Util. Environ. Eff.* **2021**, 1–23. [CrossRef]
45. Rajput, S.; Averbukh, M.; Yahalom, A.; Minav, T. An approval of MPPT based on PV Cell's simplified equivalent circuit during fast-shading conditions. *Electronics* **2019**, *8*, 1060. [CrossRef]
46. Kerekes, T.; Séra, D.; Mathe, L. Three-phase photovoltaic systems: Structures, topologies, and control. In *Renewable Energy Devices and Systems with Simulations in MATLAB® and ANSYS®*; CRC Press: Boca Raton, FL, USA, 2017; pp. 67–90.
47. de Jesus, V.M.R.; Cupertino, A.F.; Xavier, L.S.; Pereira, H.A.; Mendes, V.F. Operation Limits of Grid-Tied Photovoltaic Inverters With Harmonic Current Compensation Based on Capability Curves. *IEEE Trans. Energy Convers.* **2021**, *36*, 2088–2098. [CrossRef]
48. Eroğlu, H.; Cuce, E.; Cuce, P.M.; Gul, F.; Iskenderoğlu, A. Harmonic problems in renewable and sustainable energy systems: A comprehensive review. *Sustain. Energy Technol. Assess.* **2021**, *48*, 101566. [CrossRef]
49. Todeschini, G. Control and derating of a PV inverter for harmonic compensation in a smart distribution system. In Proceedings of the 2017 IEEE Power & Energy Society General Meeting, Chicago, IL, USA, 16–20 July 2017; pp. 1–5.
50. Hrishikesan, V.; Kumar, D.; Kumar, C. Dynamic Voltage Control Using Unified Power Quality Conditioner with Storage. In Proceedings of the 2021 IEEE 15th International Conference on Compatibility, Power Electronics and Power Engineering (CPE-POWERENG), Florence, Italy, 14–16 July 2021; pp. 1–6.

51. Lakshmi, S.; Ganguly, S. Multi-objective planning for the allocation of PV-BESS integrated open UPQC for peak load shaving of radial distribution networks. *J. Energy Storage* **2019**, *22*, 208–218. [CrossRef]
52. Xu, J.; Xie, S.; Qian, Q.; Zhang, B. Adaptive feedforward algorithm without grid impedance estimation for inverters to suppress grid current instabilities and harmonics due to grid impedance and grid voltage distortion. *IEEE Trans. Ind. Electron.* **2017**, *64*, 7574–7586. [CrossRef]
53. Yan, Q.; Wu, X.; Yuan, X.; Geng, Y. An improved grid-voltage feedforward strategy for high-power three-phase grid-connected inverters based on the simplified repetitive predictor. *IEEE Trans. Power Electron.* **2015**, *31*, 3880–3897. [CrossRef]
54. Parvez, M.; Elias, M.; Rahim, N.; Osman, N. Current control techniques for three-phase grid interconnection of renewable power generation systems: A review. *Sol. Energy* **2016**, *135*, 29–42. [CrossRef]
55. Nel, C.; Ajeigbe, O.; Chowdhury, S.D. Taming the total harmonic distortion on the 132kV Arlington Traction Station. In Proceedings of the 2017 IEEE PES PowerAfrica, Accra, Ghana, 27–30 June 2017; pp. 550–554.
56. Zubo, R.H.; Mokryani, G.; Rajamani, H.-S.; Aghaei, J.; Niknam, T.; Pillai, P. Operation and planning of distribution networks with integration of renewable distributed generators considering uncertainties: A review. *Renew. Sustain. Energy Rev.* **2017**, *72*, 1177–1198. [CrossRef]
57. Abdmouleh, Z.; Gastli, A.; Ben-Brahim, L.; Haouari, M.; Al-Emadi, N.A. Review of optimization techniques applied for the integration of distributed generation from renewable energy sources. *Renew. Energy* **2017**, *113*, 266–280. [CrossRef]
58. Shuaibu Hassan, A.; Sun, Y.; Wang, Z. Optimization techniques applied for optimal planning and integration of renewable energy sources based on distributed generation: Recent trends. *Cogent Eng.* **2020**, *7*, 1766394. [CrossRef]
59. Theo, W.L.; Lim, J.S.; Ho, W.S.; Hashim, H.; Lee, C.T. Review of distributed generation (DG) system planning and optimisation techniques: Comparison of numerical and mathematical modelling methods. *Renew. Sustain. Energy Rev.* **2017**, *67*, 531–573. [CrossRef]
60. Anuradha, K.; Jayatunga, U.; Perera, H.R. Loss-Voltage Sensitivity Analysis Based Battery Energy Storage Systems Allocation and Distributed Generation Capacity Upgrade. *J. Energy Storage* **2021**, *36*, 102357. [CrossRef]
61. Murty, V.V.; Kumar, A. Optimal placement of DG in radial distribution systems based on new voltage stability index under load growth. *Int. J. Electr. Power Energy Syst.* **2015**, *69*, 246–256. [CrossRef]
62. Saini, P.; Gidwani, L. An investigation for battery energy storage system installation with renewable energy resources in distribution system by considering residential, commercial and industrial load models. *J. Energy Storage* **2022**, *45*, 103493. [CrossRef]
63. Altıntaş, O.; Okten, B.; Karsu, Ö.; Kocaman, A.S. Bi-objective optimization of a grid-connected decentralized energy system. *Int. J. Energy Res.* **2018**, *42*, 447–465. [CrossRef]
64. Alturki, M.; Khodaei, A.; Paaso, A.; Bahramirad, S. Optimization-based distribution grid hosting capacity calculations. *Appl. Energy* **2018**, *219*, 350–360. [CrossRef]
65. Mishra, S.; Bordin, C.; Tomasgard, A.; Palu, I. A multi-agent system approach for optimal microgrid expansion planning under uncertainty. *Int. J. Electr. Power Energy Syst.* **2019**, *109*, 696–709. [CrossRef]
66. Santos, S.F.; Gough, M.; Fitiwi, D.Z.; Pogeira, J.; Shafie-khah, M.; Catalão, J.P. Dynamic Distribution System Reconfiguration Considering Distributed Renewable Energy Sources and Energy Storage Systems. *IEEE Syst. J.* **2022**, *16*, 3723–3733. [CrossRef]
67. Ajeigbe, O.A.; Munda, J.L.; Hamam, Y. Optimal allocation of renewable energy hybrid distributed generations for small-signal stability enhancement. *Energies* **2019**, *12*, 4777. [CrossRef]
68. Ajeigbe, O.A.; Munda, J.L.; Hamam, Y. Enhancing Small-Signal Stability of Intermittent Hybrid Distributed Generations. In Proceedings of the 2020 5th International Conference on Renewable Energies for Developing Countries (REDEC), Marrakech, Morocco, 29–30 June 2020; pp. 1–6.
69. Wu, F.F.; Gross, G.; Luini, J.F.; Look, P.M. A two-stage approach to solving large-scale optimal power flows. In Proceedings of the IEEE Conference Proceedings Power Industry Computer Applications Conference (PICA-79), Cleveland, OH, USA, 15–19 May 1979; pp. 126–136.
70. Vovos, P.N.; Bialek, J.W. Direct incorporation of fault level constraints in optimal power flow as a tool for network capacity analysis. *IEEE Trans. Power Syst.* **2005**, *20*, 2125–2134. [CrossRef]
71. Pesaran, M.; Mohd Zin, A.A.; Khairuddin, A.; Shariati, O. Optimal sizing and siting of distributed generators by a weighted exhaustive search. *Electr. Power Compon. Syst.* **2014**, *42*, 1131–1142. [CrossRef]
72. Khan, H.; Choudhry, M.A. Implementation of Distributed Generation (IDG) algorithm for performance enhancement of distribution feeder under extreme load growth. *Int. J. Electr. Power Energy Syst.* **2010**, *32*, 985–997. [CrossRef]
73. Van Cutsem, T. A method to compute reactive power margins with respect to voltage collapse. *IEEE Trans. Power Syst.* **1991**, *6*, 145–156. [CrossRef]
74. Sfikas, E.; Katsigiannis, Y.; Georgilakis, P. Simultaneous capacity optimization of distributed generation and storage in medium voltage microgrids. *Int. J. Electr. Power Energy Syst.* **2015**, *67*, 101–113. [CrossRef]
75. Lazzeroni, P.; Repetto, M. Optimal planning of battery systems for power losses reduction in distribution grids. *Electr. Power Syst. Res.* **2019**, *167*, 94–112. [CrossRef]
76. Salyani, P.; Salehi, J.; Gazijahani, F.S. Chance constrained simultaneous optimization of substations, feeders, renewable and non-renewable distributed generations in distribution network. *Electr. Power Syst. Res.* **2018**, *158*, 56–69. [CrossRef]
77. Zadeh, L.A. Information and control. *Fuzzy Sets* **1965**, *8*, 338–353.

78. Injeti, S.K.; Kumar, N.P. Optimal planning of distributed generation for improved voltage stability and loss reduction. *Int. J. Comput. Appl.* **2011**, *15*, 40–46.
79. Sharma, S.K.; Palwalia, D.; Shrivastava, V. Distributed generation integration optimization using fuzzy logic controller. *AIMS Energy* **2019**, *7*, 337–348. [CrossRef]
80. Sharma, A.; Sharma, A.; Chowdary, V.; Srivastava, A.; Joshi, P. Cuckoo search algorithm: A review of recent variants and engineering applications. *Metaheuristic Evol. Comput. Algorithms Appl.* **2021**, *1*, 177–194.
81. Mohamad, F.; Teh, J.; Lai, C.-M. Optimum allocation of battery energy storage systems for power grid enhanced with solar energy. *Energy* **2021**, *223*, 120105. [CrossRef]
82. He, Y.; Guo, S.; Zhou, J.; Ye, J.; Huang, J.; Zheng, K.; Du, X. Multi-objective planning-operation co-optimization of renewable energy system with hybrid energy storages. *Renew. Energy* **2022**, *184*, 776–790. [CrossRef]
83. Liao, G.-C. Solve environmental economic dispatch of Smart MicroGrid containing distributed generation system–Using chaotic quantum genetic algorithm. *Int. J. Electr. Power Energy Syst.* **2012**, *43*, 779–787. [CrossRef]
84. Ma, Y.; Yang, P.; Guo, H.; Wu, J. Power source planning of wind-PV-biogas renewable energy distributed generation system. *Power Syst. Technol.* **2012**, *36*, 9–14.
85. HA, M.P.; Huy, P.D.; Ramachandaramurthy, V.K. A review of the optimal allocation of distributed generation: Objectives, constraints, methods, and algorithms. *Renew. Sustain. Energy Rev.* **2017**, *75*, 293–312.
86. Koziel, S.; Rojas, A.L.; Moskwa, S. Power loss reduction through distribution network reconfiguration using feasibility-preserving simulated annealing. In Proceedings of the 2018 19th International Scientific Conference on Electric Power Engineering (EPE), Brno, Czech Republic, 16–18 May 2018; pp. 1–5.
87. Ashoornezhad, A.; Asadi, Q.; Falaghi, H.; Hajizadeh, A. Optimal Battery Energy Storage Placement in PV-connected Network Considering Uncertainty. In Proceedings of the 2021 11th Smart Grid Conference (SGC), Tabriz, Iran, 7–9 December 2021; pp. 1–5.
88. Prabpal, P.; Kongjeen, Y.; Bhumkittipich, K. Optimal Battery Energy Storage System Based on VAR Control Strategies Using Particle Swarm Optimization for Power Distribution System. *Symmetry* **2021**, *13*, 1692. [CrossRef]
89. Jamian, J.J.; Mustafa, M.W.; Mokhlis, H. Optimal multiple distributed generation output through rank evolutionary particle swarm optimization. *Neurocomputing* **2015**, *152*, 190–198. [CrossRef]
90. Rathore, A.; Patidar, N. Optimal sizing and allocation of renewable based distribution generation with gravity energy storage considering stochastic nature using particle swarm optimization in radial distribution network. *J. Energy Storage* **2021**, *35*, 102282. [CrossRef]
91. Zeinalzadeh, A.; Mohammadi, Y.; Moradi, M.H. Optimal multi objective placement and sizing of multiple DGs and shunt capacitor banks simultaneously considering load uncertainty via MOPSO approach. *Int. J. Electr. Power Energy Syst.* **2015**, *67*, 336–349. [CrossRef]
92. Mohandas, N.; Balamurugan, R.; Lakshminarasimman, L. Optimal location and sizing of real power DG units to improve the voltage stability in the distribution system using ABC algorithm united with chaos. *Int. J. Electr. Power Energy Syst.* **2015**, *66*, 41–52. [CrossRef]
93. Dixit, M.; Kundu, P.; Jariwala, H.R. Integration of distributed generation for assessment of distribution system reliability considering power loss, voltage stability and voltage deviation. *Energy Syst.* **2019**, *10*, 489–515. [CrossRef]
94. Abu-Mouti, F.S.; El-Hawary, M. Optimal distributed generation allocation and sizing in distribution systems via artificial bee colony algorithm. *IEEE Trans. Power Deliv.* **2011**, *26*, 2090–2101. [CrossRef]
95. El-Zonkoly, A.M. Multistage expansion planning for distribution networks including unit commitment. *IET Gener. Transm. Distrib.* **2013**, *7*, 766–778. [CrossRef]
96. Kefayat, M.; Ara, A.L.; Niaki, S.N. A hybrid of ant colony optimization and artificial bee colony algorithm for probabilistic optimal placement and sizing of distributed energy resources. *Energy Convers. Manag.* **2015**, *92*, 149–161. [CrossRef]
97. Padma Lalitha, M.; Veera Reddy, V.; Sivarami Reddy, N. Application of fuzzy and ABC algorithm for DG placement for minimum loss in radial distribution system. *Iran. J. Electr. Electron. Eng.* **2010**, *6*, 248–257.
98. Gomez, J.; Khodr, H.; De Oliveira, P.; Ocque, L.; Yusta, J.; Villasana, R.; Urdaneta, A. Ant colony system algorithm for the planning of primary distribution circuits. *IEEE Trans. Power Syst.* **2004**, *19*, 996–1004. [CrossRef]
99. Vlachogiannis, J.G.; Hatziargyriou, N.D.; Lee, K.Y. Ant colony system-based algorithm for constrained load flow problem. *IEEE Trans. Power Syst.* **2005**, *20*, 1241–1249. [CrossRef]
100. Wang, L.; Singh, C. Reliability-constrained optimum placement of reclosers and distributed generators in distribution networks using an ant colony system algorithm. *IEEE Trans. Syst. Man Cybern. Part C (Appl. Rev.)* **2008**, *38*, 757–764. [CrossRef]
101. Amohadi, M.; Fotuhi-Firuzabad, M. Optimal placement of automatic switching equipment in radial distribution networks based on protective coordination. *J. Electr. Eng. Technol.* **2019**, *14*, 1127–1137. [CrossRef]
102. Prakash, A.; Deshmukh, S. A multi-criteria customer allocation problem in supply chain environment: An artificial immune system with fuzzy logic controller based approach. *Expert Syst. Appl.* **2011**, *38*, 3199–3208. [CrossRef]
103. Aydin, I.; Karakose, M.; Akin, E. A multi-objective artificial immune algorithm for parameter optimization in support vector machine. *Appl. Soft Comput.* **2011**, *11*, 120–129. [CrossRef]
104. Gong, M.; Jiao, L.; Zhang, X. A population-based artificial immune system for numerical optimization. *Neurocomputing* **2008**, *72*, 149–161. [CrossRef]
105. Basu, M. Artificial immune system for dynamic economic dispatch. *Int. J. Electr. Power Energy Syst.* **2011**, *33*, 131–136. [CrossRef]

106. Aghaebrahimi, M.; Amiri, M.; Zahiri, S. An immune-based optimization method for distributed generation placement in order to optimize voltage profile. In Proceedings of the 2009 International Conference on Sustainable Power Generation and Supply, Nanjing, China, 6–7 April 2009; pp. 1–7.
107. Hatata, A.; Osman, G.; Aladl, M. An optimization method for sizing a solar/wind/battery hybrid power system based on the artificial immune system. *Sustain. Energy Technol. Assess.* **2018**, *27*, 83–93. [CrossRef]
108. Souza, B.B.; Carrano, E.G.; Neto, O.M.; Takahashi, R.H. Immune system memetic algorithm for power distribution network design with load evolution uncertainty. *Electr. Power Syst. Res.* **2011**, *81*, 527–537. [CrossRef]
109. Ma, J.; Yuan, X. Techno-economic optimization of hybrid solar system with energy storage for increasing the energy independence in green buildings. *J. Energy Storage* **2023**, *61*, 106642. [CrossRef]
110. Chisale, S.W.; Eliya, S.; Taulo, J. Optimization and design of hybrid power system using HOMER pro and integrated CRITIC-PROMETHEE II approaches. *Green Technol. Sustain.* **2023**, *1*, 100005. [CrossRef]
111. Masih, A.; Verma, H. Optimum sizing and simulation of hybrid renewable energy system for remote area. *Energy Environ.* **2022**, *33*, 933–951. [CrossRef]
112. Masrur, H.; Howlader, H.O.R.; Elsayed Lotfy, M.; Khan, K.R.; Guerrero, J.M.; Senjyu, T. Analysis of techno-economic-environmental suitability of an isolated microgrid system located in a remote island of Bangladesh. *Sustainability* **2020**, *12*, 2880. [CrossRef]
113. Akorede, M.F. Design and performance analysis of off-grid hybrid renewable energy systems. In *Hybrid Technologies for Power Generation*; Elsevier: Amsterdam, The Netherlands, 2022; pp. 35–68.
114. Yakub, A.O.; Same, N.N.; Owolabi, A.B.; Nsafon, B.E.K.; Suh, D.; Huh, J.-S. Optimizing the performance of hybrid renewable energy systems to accelerate a sustainable energy transition in Nigeria: A case study of a rural healthcare centre in Kano. *Energy Strategy Rev.* **2022**, *43*, 100906. [CrossRef]
115. Cao, Y.; Taslimi, M.S.; Dastjerdi, S.M.; Ahmadi, P.; Ashjaee, M. Design, dynamic simulation, and optimal size selection of a hybrid solar/wind and battery-based system for off-grid energy supply. *Renew. Energy* **2022**, *187*, 1082–1099. [CrossRef]
116. Shaheen, A.M.; El-Sehiemy, R.A.; Hasanien, H.M.; Ginidi, A.R. An improved heap optimization algorithm for efficient energy management based optimal power flow model. *Energy* **2022**, *250*, 123795. [CrossRef]

applied sciences

MDPI

Article

Parallel Water Column Technique for Obtaining a Smooth Output Power of the Pump as a Turbine at a Variable Water Flow Rate

Sajjad Hussain [1], Muhammad Humza [2,*], Tanveer Yazdan [3], Ghulam Abbas [3] and Han-Wook Cho [2,*]

[1] Department of Electrical Engineering, Institute of Southern Punjab, Multan 59300, Pakistan
[2] Department of Electrical, Electronics, and Communication Engineering Education, Chungnam National University, Daejeon 34134, Republic of Korea
[3] Department of Electrical Engineering, The University of Lahore, Lahore 54000, Pakistan
* Correspondence: engr.humza7@gmail.com (M.H.); hwcho@cnu.ac.kr (H.-W.C.)

Abstract: Hydro generation is the simplest and oldest method of electricity generation, with a century of successful operation. Using a pump as a turbine (PAT) is an optimal solution for minimizing the cost, particularly in low-head and small-scale hydro plants. Commercially available centrifugal pumps have become a popular solution for small-scale hydro and pumped-hydro facilities owing to their simple geometry, ease of operation, maintenance, and abundant availability in local markets. Variations in the water flow in hydro facilities, such as pumped-hydro and small-scale hydro facilities, are common; however, a PAT is unable to respond to variable flows because it is a fixed-speed device. To overcome this problem, different techniques have been suggested by researchers: (a) a system of parallel PATs; (b) geometrical modifications in the impeller of the PAT; and (c) power electronics-based variable frequency drives. All the aforementioned techniques have limitations, such as low output, high cost, complexity, transportation, and operation and maintenance. In this study, a simple and economical technique is proposed to smooth the output of a PAT on variable/decreasing water flow profiles. In the proposed technique, water columns connected in parallel (PWCs) are used to produce a pressurized water flow, as they have a convergent nozzle at the outlet. The PWC creates more space for water, and this additional mass of water boosts the water flow at the outlet. In this manner, the PWC technique maintains the flow at the inlet of the turbine. A serial integration of five PWCs with the same dimensions was conducted to inject the additional flow into the existing PAT penstock, governing a 37-kW generator. The design flow was maintained at 192.1 L/s without any additional power usage at the inlet of the PAT, and the output was smoothed even at the minimum water flow/head. Pump design and computational fluid dynamics simulations were performed using ANSYS software, whereas generator simulations were performed using MATLAB/Simulink software.

Keywords: energy resources; hydropower generation; small hydro; pump as turbine; PWC technique; smooth output power

Citation: Hussain, S.; Humza, M.; Yazdan, T.; Abbas, G.; Cho, H.-W. Parallel Water Column Technique for Obtaining a Smooth Output Power of the Pump as a Turbine at a Variable Water Flow Rate. *Appl. Sci.* **2023**, *13*, 3232. https://doi.org/10.3390/app13053232

Academic Editor: Luis Hernández-Callejo

Received: 31 January 2023
Revised: 27 February 2023
Accepted: 1 March 2023
Published: 2 March 2023

1. Introduction

Environmental effects, fear of the extinction of conventional energy sources (such as oil, gas, nuclear, and coal), and the high running costs of these costs have compelled planners toward renewable energy sources [1–4]. Among these resources, hydro energy contributes to nearly 16% of the global energy mix [5,6]. However, extensive capital costs, danger to aquatic life, significantly long construction times, and limited locations are the drawbacks of hydro-generation technology. To overcome these drawbacks, new arrangements for hydro facility construction, such as run-of-river, small hydro, and mini, micro, and pico-hydro plants, have been studied [7–9]. These new arrangements of hydro technology have reduced the initial cost, construction time, and environmental effects while increasing the location spectrum for the construction of hydro plants.

In pumped hydro storage (PHS) and small-scale hydro plants, using pumps in reverse (PAT) instead of conventional turbines is preferable to minimize the capital cost [10–12]. However, commercially available pumps are not designed to function in reverse mode, and if this mode is exercised, the pumps prove to be low-efficiency devices. Despite their low efficiency, PATs are used in small-scale hydro-generation and PHS facilities [13]. The use of PATs is abundant for numerous reasons, such as their low cost, bulk availability in local markets, and ease of installation. Furthermore, no specialty is required for operation and maintenance [14]. However, small-scale PHS and hydro-generation plants encounter flow fluctuations for several reasons, including intermittent upstream inflows and the decrement of the head in the upper reservoir of the PHS facility during generation. A PAT is unable to respond to these flow fluctuations owing to its simple geometry, and the output of the plant decreases. The design flow, which is obtained by the design head, determines the maximum efficiency of a PAT. Variations in the flow from its original design flow, for any reason, have an adverse effect on the output [15].

Researchers have adopted various methods to mitigate the adverse effects of flow fluctuations on the output, such as parallel PATs of different capacities, geometrical modifications of a PAT, and power electronics-based variable frequency drives (VFDs). In parallel PATs, when the flow is reduced and a PAT with a large capacity cannot deliver its rated output, it is either manually or automatically turned off. A PAT with a lower capacity is operated to minimize the adverse effects of flow fluctuations. However, the output is reduced by the newly available water flow, and the cost increases owing to paralleling, thereby making the design more complex [13,16]. Regarding the geometrical modifications of PATs, different researchers have suggested certain design modifications of the impeller [13,17–22], which better manage the variable flows. However, these modifications are unable to manage all the flow variations, and the cost is increased. Power electronics-based VFDs can provide any speed profile of variable flow inputs [23,24]. When the flow decreases, which affects the output of the plant, the VFD changes the speed of the generator, and the output of the plant becomes smooth. However, this method is significantly costly because devices with high ratings are required, causing installation, operational, maintenance, and transportation problems.

In this study, a simple technique is proposed to mitigate the adverse effects of flow variations on the output of a plant. This study is novel because a parallel water column (PWC) technique is used to smooth the output of a PAT system while maintaining the water flow at the inlet of the PAT by acting as an auxiliary penstock. With this technique, water columns connected in parallel are used with the existing penstock of a plant to inject additional flow at the inlet of the PAT in the event of a decreasing flow. This additional flow will maintain the smooth rated output of the plant, even at the minimum head. The effectiveness of the PWC technique was confirmed by performing a simulation using ANSYS software for the case study of a variable flow profile. Subsequently, based on the output obtained from the PAT, the electrical output of the generator was analyzed using MATLAB/Simulink software.

2. Materials and Methods

The details of the adverse effects of the flow fluctuations on the output of the PAT are discussed herein, along with the basic concepts of the PWC theory for a better understanding of the proposed PWC technique.

2.1. Effect of Flow Variations on the Output of PAT

The output of any hydro system is solely determined by the water flow, as given below [14,25]:

$$P_{out} = \eta \rho g H Q \quad (1)$$

where P_{out} is the output power, η is the efficiency, ρ is the density of water, g is the gravitational acceleration due to gravity (9.81 m/s^2), H is the head, and Q is the water flow.

The fluctuation of the flow "Q" varies the output of the hydro system. A smooth output can be achieved while maintaining a constant flow, which can be accomplished using the aforementioned techniques. A smooth output makes the system more efficient. The effects of flow fluctuations on the efficiency of PAT are shown in Figure 1, in which five scenarios were considered for the calculations based on a previous study [15]. Notably, the total reduction in flow is 38.4 L/s, which causes a significant decrease of 6.62% in the efficiency of the system. This decrease in plant efficiency is dangerous for the stability of the system.

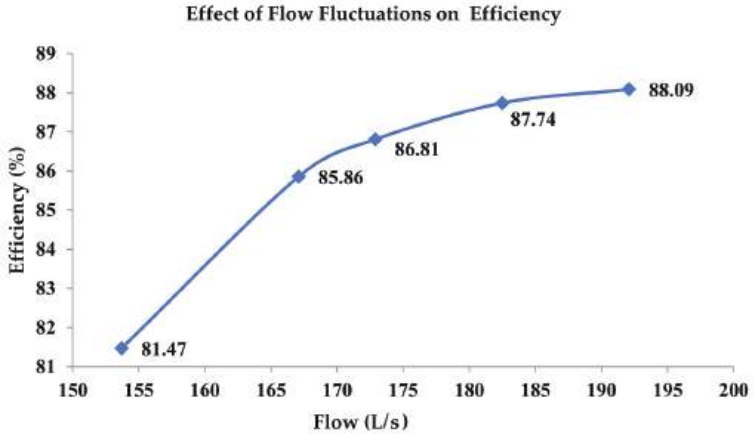

Figure 1. Effect of flow variations on efficiency.

The reduction in flow can be eliminated using the PWC technique. The basics of this newly proposed technique are discussed herein.

2.2. Water Column Theory

The atmospheric pressure (0.1 MPa) is created by a column of air over the surface of the earth. Similarly, water exerts pressure at its bottom, owing to the weight of water acting vertically downward. A water column having a height of 10.3 m creates pressure that is equal to the atmospheric pressure, that is, 101 kPa [26]; pressure is the force acting on an area. Mathematically,

$$P = F/A \tag{2}$$

where P is the pressure, F is the force, and A is the area. In this study, "A" indicates the area of the water discharge. If the area of discharge decreases, then the pressure will increase while the force remains constant, which is the weight of water working vertically downward and is indicated by the following:

$$w = mg \tag{3}$$

where w is the weight of water, m is the mass of water, and g is the gravitational acceleration. Here, "g" is a constant, and the mass of water should be increased to increase the weight. Traditionally, no arrangement can be used for the increment of the mass of water because the penstock is a fixed entity and functions as a singular body. Therefore, flow fluctuations threaten the stability of the system. Therefore, the PWC technique is presented in this study. Increasing the number of PWCs allows more space for a larger mass of water, which increases the force at the same height. In particular, the PWC technique makes the penstock more flexible and can manage increased flows per the requirements.

Alternatively, the pressure is inversely proportional to the area of the discharge area. Therefore, to increase the pressure, the discharge area must be reduced. This reduction was achieved using a nozzle to increase the pressure, which boosted the velocity of the water.

As the PAT is a low-head device, and this study is regarding low heads, only the Q parameter, which indicates the discharge/flow of water, in Equation (1) can increase the output of the PAT system. Mathematically,

$$Q = Av \tag{4}$$

where Q is the water discharge, A is the area of the water discharge, and v is the velocity of the water. According to the continuity equation, the flow in a closed system is always constant. Mathematically,

$$Q_1 = Q_2 \tag{5}$$

where Q_1 is the flow through point 1, and Q_2 is the flow through point 2. Furthermore,

$$A_1 v_1 = A_2 v_2 \Rightarrow v_2 = A_1 v_1 / A_2 \tag{6}$$

The inlet of the PAT is constant since it is a fixed body, and the only option for increasing the value of Q through the PAT while maintaining the same height is by increasing the velocity. The nozzle at the bottom, which has a velocity of "v_2", as indicated in Equation (6), will increase the velocity of water, which will in turn increase the value of 'Q'.

In this manner, as the number of water columns increases, A_1 increases, which increases v_2. The PWC technique injects the additional flow at the inlet of the PAT in the event of a flow decrease with the existing penstock of a plant; the adverse effects of the flow fluctuations are filtered, which smooths the output of the PAT.

2.3. PWC Technique with the Design of Experiment

The PWC follows certain rules to produce an output. To understand the behavior of the PWC, an experiment in which five water columns were connected in parallel was conducted. This experimental design is called a "double-nozzle setup", in which one nozzle makes the main outlet, which injects the additional water into the existing penstock of the PAT, while each water column has a separate nozzle. Computational fluid dynamics (CFD) simulations were performed using ANSYS software R1 2021 [27]. The dimensions of the PWC and specifications of the FLUENT solver are listed in Table 1.

Table 1. Dimension of the water columns and solver settings.

Dimensions/Settings	Values
Head	10 m
Diameter of the outlet nozzle	0.0635 m
Upper diameter of each water column	0.4572 m
Diameter of the nozzle used at the bottom of each water column	0.2286 m
Working fluid	Water (liquid)
Outlet pressure	0 Pascals
Turbulence model	k-ω (SST)
Density of water	1000 kg/m^3
Boundaries	
Inlet	Velocity inlet
Outlet	Pressure outlet
Wall function	Standard

The geometrical dimensions of the PWC were composed in a design modeler, and the settings were changed from solid to fluid, while meshing of the PWC was performed using ANSYS meshing. A tetrahedral mesh was created using a patch-confirming algorithm, and the span angle center was set to fine. Meshing of the PWC is shown in Figure 2, the details

of which are provided in Table 2, including the meshing method, inflation layers, element size, and number of elements per PWC.

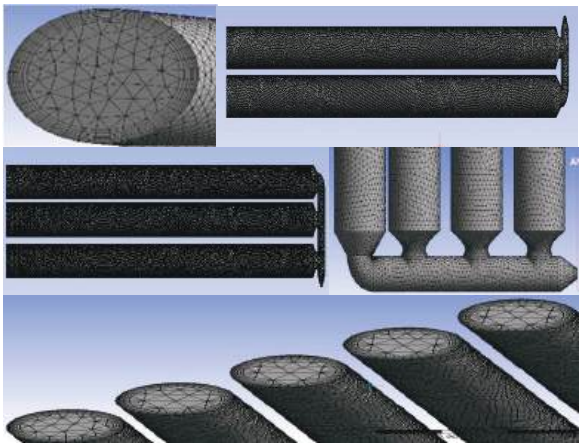

Figure 2. Meshing of PWCs.

Table 2. Mesh report of PWC.

No. of PWC	Element Size	Method of Meshing	Inflation Layers	No. of Elements
1	40	Tetrahedrons	7	274,274
2	40	Tetrahedrons	7	358,456
3	40	Tetrahedrons	7	543,020
4	40	Tetrahedrons	7	736,088
5	40	Tetrahedrons	7	926,713

A mesh independence test was performed for two PWCs to obtain the optimal element size and number of elements. Element sizes of 20, 30, 40, 50, 60, 70, 80, and 90 mm were applied to create 1,477,215, 655,237, 358,456, 237,308, 174,459, 138,933, 100,099, and 77,206 mesh elements, respectively. The optimal element size was 40 mm, which was selected for all the PWC simulation cases. A size of 40 mm yielded 358,456 elements for the two PWCs, as proven by the grid independence test shown in Figure 3.

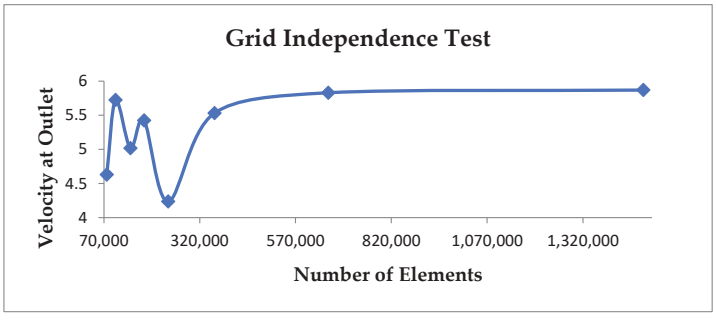

Figure 3. Grid independence test of the two PWCs.

In the experimental design, the dimensions of the PWCs were kept constant, while the number of PWCs was increased individually. The velocity inlet was assigned as the

boundary condition at the inlet of the PWCs, whereas the pressure outlet was assigned at the outlet. The velocity and pressure produced in each case, which were processed in CFD-Post, are illustrated in (a–e) of Figure 4.

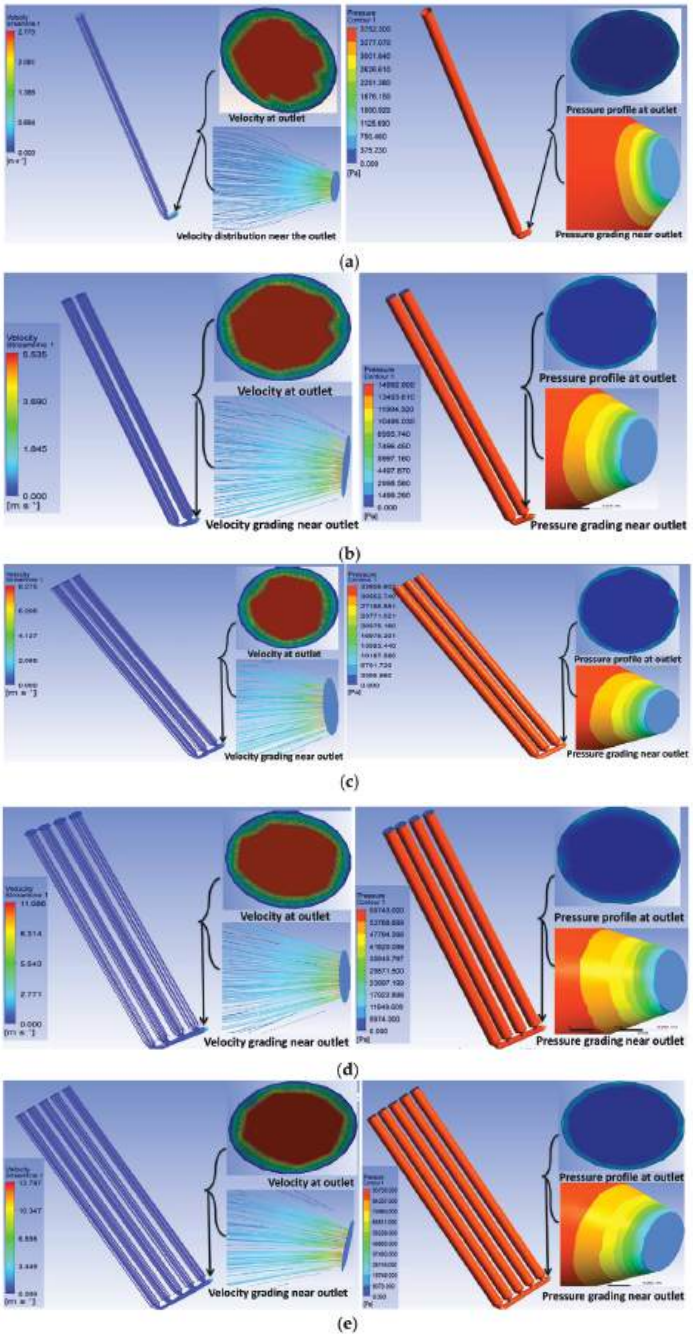

Figure 4. Velocity and pressure produced by (**a**) one water column, (**b**) two water columns, (**c**) three water columns, (**b**) four water columns, and (**e**) five water columns.

Two types of results were obtained from the experimental design study. First, the output behavior of the PWC was determined, and a mathematical model was developed. If the dimensions and output of the water column are known, the optimal number of PWCs can be derived for any flow, velocity, or pressure profile. Second, the optimal number of PWCs was derived for the aforementioned PAT, the water flow of which was variable at its inlet owing to the variations in the head of the upper reservoir during generation.

The results of the flow, outlet velocity, and pressure were calculated in CFD-Post with a function calculator, while the dimensions of the PWC were maintained to be the same; only the number of PWCs was increased individually according to the requirements of the design flow, as shown in Figure 5.

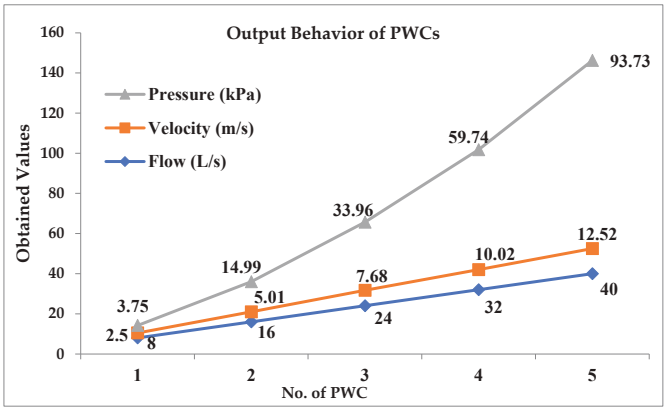

Figure 5. Variations in the pressure, flow, and velocity as the number of PWCs increases.

2.4. Findings from the Design Experiment

The findings obtained from the design experiment are presented (Figure 5) while developing a mathematical model to determine the output of the PWC.

Finding 1: Flow

The flow graph shown in Figure 5 demonstrates that the flow increases linearly as the number of water columns increases. Mathematically,

$$F = F_i \times n \tag{7}$$

where F is the flow of water, F_i is the flow obtained from one water column, and n is the number of PWCs used.

Finding 2: Velocity

The velocity of water also increases linearly as the number of water columns increases, as shown in the velocity graph (Figure 5). The mathematical relationship between the velocity and PWCs is as follows:

$$v = v_i \times n \tag{8}$$

where v is the velocity at the outlet, v_i is the velocity obtained from one water column, and n is the number of PWCs used.

Finding 3: Pressure

The water pressure at the nozzle inlet increases with the square of the number of water columns, which increases the water flow at the nozzle outlet. The pressure graph (Figure 5) describes the mathematical relationship between the PWC and the generated pressure. Mathematically,

$$P = P_i \times n^2 \tag{9}$$

where P is the total generated pressure, P_i is the pressure obtained from one water column, and n is the number of PWCs used in any setup.

3. Optimal Number of PWCs for a Smooth Output of the PAT

Based on Section 2.1, the decrease in the flow of the PAT is 38.4 L/s, for which, according to Equation (7), a total of five PWCs with a flow of 8 L/s each are required to smooth the flow at the inlet of the PAT. The PWC dimensions used for this purpose were the same as those shown in Table 1. Thus, the outlet nozzle of the PWC design becomes an additional inlet of the PAT, injecting the flow into the existing penstock, which is required for a particular stage of operation. Initially, the flow through the turbine was a design flow, and no change was required. As the flow decreases, the output also decreases. One water column is added by the system to acquire the design flow; if the new flow through the turbine meets the design flow, no further water column will be added by the system. However, considering a further deviation from the smooth output, another water column is added to the system to check whether the new scenario provides a smooth output. No changes are required if the new output is smooth. These five PWC were added to the system according to the flowchart shown in Figure 6.

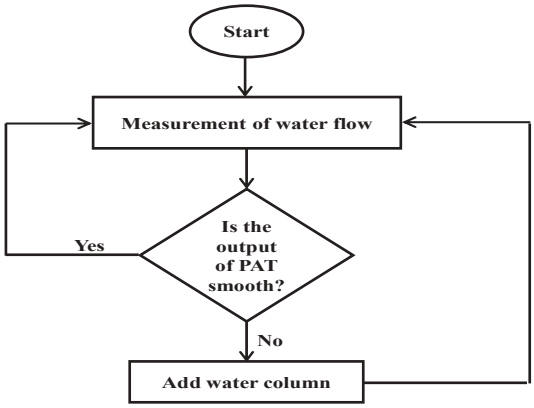

Figure 6. Integration of the PWC to maintain the flow.

The integration of the five PWCs with the existing PAT penstock and the injection of an additional flow at the inlet were conducted in ANSYS, as shown in Figure 7.

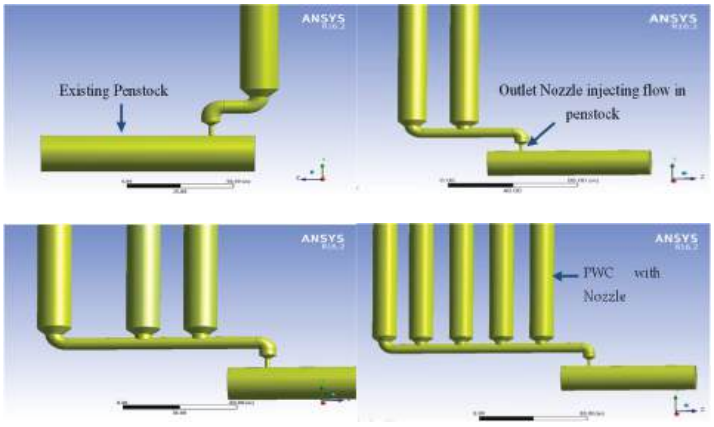

Figure 7. Integration of the PWC with the existing penstock.

As the number of PWCs is increased according to the demand, the flow is maintained at approximately the designed value, as listed in Table 3.

Table 3. Flow profile of PAT before and after the addition of the PWCs.

Flow (L/s)	Reduced Flow (L/s)	PWC Added (8 L/s Each)	Additional Flow (L/s)	New Flow (L/s)
192.1	Nil	No	Nil	192.1
182.2	9.9	1	8	190.2
172.9	19.2	2	16	188.9
167.1	25	3	24	191.7
153.7	38.4	5	40	193.7

4. Torque Calculation and Generator Behavior

The aforementioned flow profile produces torque in the PAT, which is applied as an input to the generator to monitor its output. Simulations were performed using ANSYS and MATLAB software.

4.1. Torque Produced by PAT on Different Flow Values

A pump with a flow of 192.1 L/s was designed using the ANSYS (Vista CPD) tool, consisting of a volute and impeller with six blades, as shown in Figure 8. A flow analysis through PAT was conducted in ANSYS CFX [13,28], in which water was used as the material, and the standard atmospheric pressure was considered to be one atm.

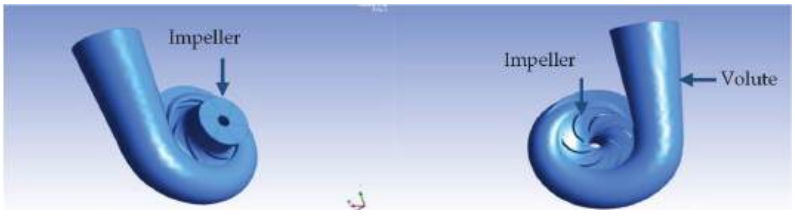

Figure 8. Side views of the pump designed in Vista CPD.

The pump was meshed using TURBO GRID, while the impeller and volute were separately meshed, achieving a good quality mesh, as shown in Figure 9.

Figure 9. Meshing of the impeller and volute.

A detailed mesh report is provided in Table 4, which demonstrates the domains of the analysis, location of the domains, number of nodes, and number of elements.

Table 4. Mesh report of the pump.

Domain	Nodes	Elements	Tetrahedra	Wedges	Hexahedra
R1(Passage)	663,175	627,640	0	0	627,640
S1(B75)	82,927	258,746	165,196	93,550	0
All Domains	746,102	886,386	165,196	93,550	627,640

The mesh independence is checked for the pump and eight different cases with regard to. element numbers, which are obtained by changing the element size and global size factor for the volute and impeller, respectively. Element sizes of 15, 20, 25, 30, 35, 40, 45, and 50 mm were applied for the volute in meshing, yielding 330,438, 281,176, 258,746, 248,172, 240,762, 237,168, 234,902, and 232,452 elements, respectively. In contrast, the global size factor was the main parameter that was manipulated for impeller meshing, achieving a range of eight element numbers. Different global size factors for the impeller were assigned in TURBO GRID; the 0.8, 0.9, 1.0, 1.1, 1.2, 1.3, 1.4, and 1.5 sizes produced 141,792, 203,553, 280,080, 385,118, 501,128, 781,482, and 1,019,900 elements, respectively. The output parameter was the velocity at the outlet, which is demonstrated by the mesh independence test shown in Figure 10; 886,386 elements were selected for the simulations, which were produced by a 25-mm element size and a 1.3 global size factor.

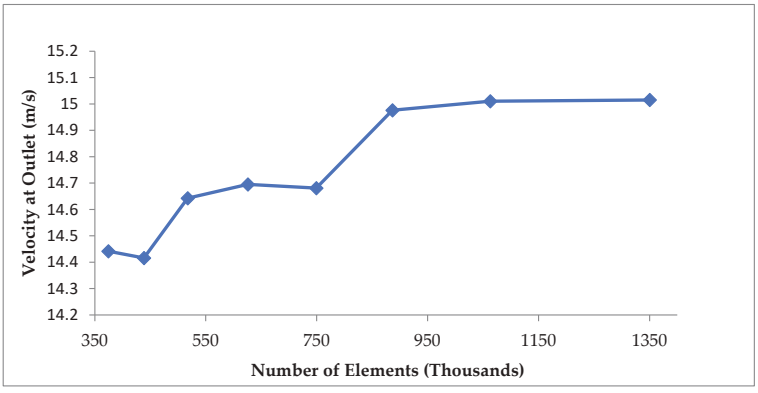

Figure 10. Meshing independency test of the pump.

The steady-state boundary conditions for this simulation were set for the PAT. The stationary (S1) domain is the volute, while the rotating (R1) domain is the impeller of the pump. The inlet was assigned a boundary condition for the mass flow, while the outlet was the pressure, and the standard atmospheric pressure was assigned. The blade and all other boundary walls were assigned a boundary condition (no slip). A frozen-rotor mixing model was adopted for the interface between S1 and R1. The SST turbulence model was applied for the flow analysis, while in the solver control panel, a high resolution was applied as an advection scheme, 1.0×10^{-5} for convergence, first order for numeric turbulence, and SIMPLEC [27,29,30]. Transient or unsteady simulations were also performed after steady simulations. The total time was set to 1 s, the time step to 0.0001 s, and the initial time value to 0 s for the transient case. The transient rotor-stator mixing model was assigned to the interface between S1 and R1. Cartesian velocity components were selected as u = 0 m/s, v = 0 m/s, and z = 0 m/s for the global initialization [31].

Here, the pump functions as a turbine; therefore, the outlet of the pump is the inlet of the PAT, and the direction of the flow of water through the PAT is shown in Figure 11.

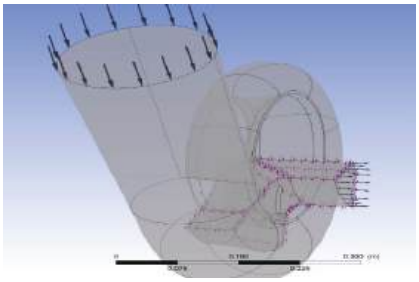

Figure 11. Direction of the flow of water for the PAT.

As indicated in Section 2.1, the torque produced by the variable water flow was calculated using ANSYS CFD-Post, which is a function calculator. A graphical representation of the flow and the produced torque is shown in Figure 12a. When the PWC is integrated, and a new range of flows at the inlet of the PAT is obtained, the model is simulated once again to calculate the new torque produced by the new values of the water flow. A graphical representation of the new flow and torque produced is shown in Figure 12b.

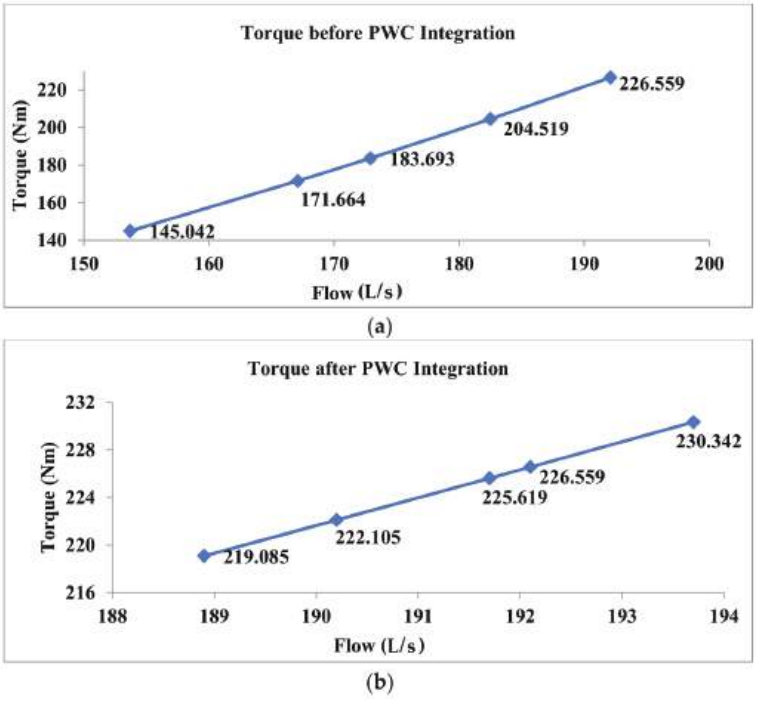

Figure 12. Torque produced by PAT (**a**) before PWC integration and (**b**) after PWC integration.

The torque produced by the PAT at variable and smooth flows is compared in Table 5, along with the deviations given before and after the integration of the PWC. These results clearly demonstrate that the values of the produced torque decrease with decreasing flow. Hence, fluctuations in the flow rate significantly affect the torque of the PAT. When the flow rate is kept constant with the integration of the PWC, the torque of the PAT is smoothed and maximized according to the design flow.

Table 5. Torque of PAT regarding different flow values.

Before PWC Integration			After PWC Integration		
Flow (L/s)	**Torque (Nm)**	**Deviation (%)**	**Flow (L/s)**	**Torque (Nm)**	**Deviation (%)**
192.1	226.559	0	192.1	226.559	0
182.5	204.519	9.73	190.2	222.105	1.97
172.9	183.693	18.92	188.9	219.085	3.3
167.1	171.664	24.23	191.7	225.619	0.41
153.7	145.042	35.98	193.7	230.342	1.64

4.2. Generator Behavior on the Variable and Smooth Torque

Although a smooth torque is obtained, which ultimately smooths the output of the PAT, in most cases, the PAT and generator are directly coupled. However, a Simulink model was developed to observe the behavior of the generator with variable and smooth torques, as shown in Figure 13.

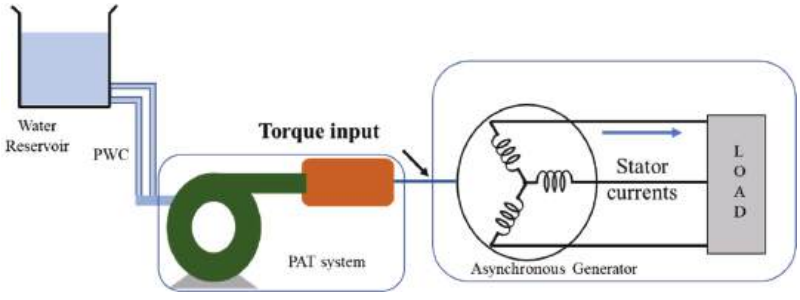

Figure 13. Overall system to observe the behavior of the generator.

A built-in asynchronous machine block rated at 37 kW was selected from the Simulink library to simulate the behavior of the generator. This block can simulate both motors and generators, using (+) and (−) signs with the torque, respectively. The variable and smoothed torques obtained from ANSYS CFX, as shown in Figure 14, were used as the input signals in the Simulink model [32,33]. The model was simulated for 25 s, and each duration of five seconds corresponds to a different torque value.

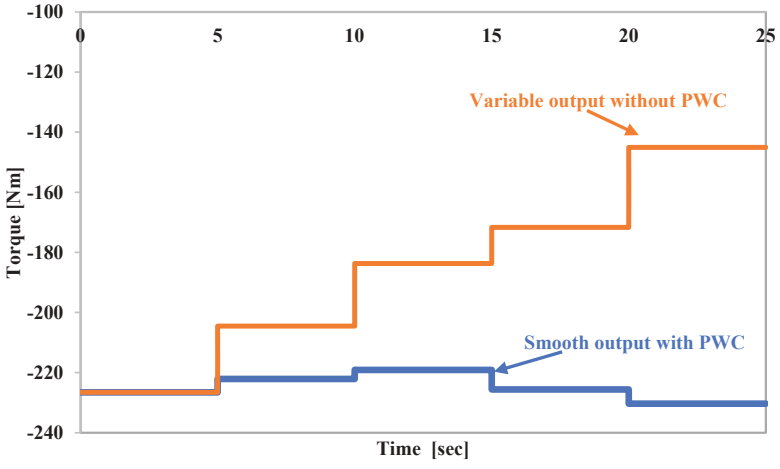

Figure 14. Torque input signal to the generator.

The simulation results of the peak value of the generator current are shown in Figure 15, which demonstrates the variations in the current with respect to the torque obtained from the PAT. In a hydro system, the torque varies with the flow variation. The current depends on the torque value. Therefore, any fluctuation in the flow rate affects the output current of the generator. However, the PWC technique provides a smooth flow, which results in a smooth output.

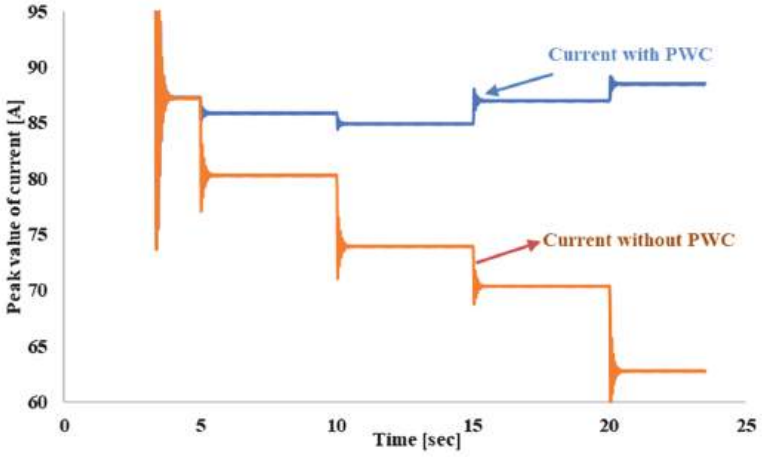

Figure 15. Output current of the generator for both variable and smooth torques.

5. Conclusions

A simple and economical PWC technique was proposed in this study to maintain the design flow at the inlet of a PAT under variable flow conditions. The proposed technique employs the series integration of parallel water columns with the same dimensions using a double-nozzle design. Paralleling the water columns creates more space for water to provide the design flow at the outlet. When water flow is decreased owing to a decrease in the upstream flow or in a PHS facility, the PWC maintains a flow at the inlet of the PAT by acting as an axillary penstock.

The design of the experiment and its findings indicate that, for a given case, the designed flow of 192.1 L/s can create a maximum torque of 226.559 Nm. The reduction in the flow to 153.7 L/s produced a reduced torque of 145.042 Nm. A total reduction of 38.4 L/s in the water flow was compensated for by integrating five PWCs, each having a flow capacity of 8 L/s. After the integration, the new flow and torque values were 193.7 L/s and 230.342 Nm, respectively, which were nearly identical to the designed values with a deviation of only 1.64%. Furthermore, based on the smooth output of the PAT, the generator output was confirmed. Thus, integration of the PWC using a double-nozzle design is an effective technique for maintaining smooth output of the PAT and generator.

Author Contributions: Conceptualization, S.H. and M.H.; methodology, M.H. and T.Y.; software, S.H. and G.A.; formal analysis, M.H., T.Y. and G.A.; writing and draft preparation, S.H., M.H. and T.Y.; review and editing, T.Y. and G.A.; supervision, H.-W.C. and M.H.; funding acquisition, H.-W.C. All authors have read and agreed to the published version of the manuscript.

Funding: This research received no external funding.

Institutional Review Board Statement: Not applicable.

Informed Consent Statement: Not applicable.

Data Availability Statement: Not applicable.

Acknowledgments: This work was supported by the National Research Foundation of Korea (NRF) grant funded by the South Korean government (No. 2022R1I1A3072104).

Conflicts of Interest: The authors declare no conflict of interest.

Nomenclature

A	area of water discharge [m^2]
F	force [N]
g	gravitational acceleration [m/s^2]
H	head height [m]
m	mass of water [kg]
n	number of water columns
P	pressure [Pa]
P_{out}	output power [W]
PAT	pump as turbine
PWC	parallel water columns
Q	flow of water [L/s]
v	velocity of water [m/s]
w	weight of water
η	efficiency [%]
ρ	density of water [kg/m^3]

References

1. Olabi, A.; Abdelkareem, M.A. Renewable energy and climate change. *Renew. Sustain. Energy Rev.* **2022**, *158*, 112111. [CrossRef]
2. Bilgili, F.; Lorente, D.B.; Kuşkaya, S.; Ünlü, F.; Gençoğlu, P.; Rosha, P. The role of hydropower energy in the level of CO2 emissions: An application of continuous wavelet transform. *Renew. Energy* **2021**, *178*, 283–294. [CrossRef]
3. Jurasz, J.; Ciapala, B. Solar–hydro hybrid power station as a way to smooth power output and increase water retention. *Sol. Energy* **2018**, *173*, 675–690. [CrossRef]
4. Wang, Z.; Yen-Ku, K.; Li, Z.; An, N.B.; Abdul-Samad, Z. The transition of renewable energy and ecological sustainability through environmental policy stringency: Estimations from advance panel estimators. *Renew. Energy* **2022**, *188*, 70–80. [CrossRef]
5. International Energy Agency. Available online: https://www.iea.org/reports/renewables-information-overview/supply (accessed on 6 January 2022).
6. International Hydro Power Association (IHA). Available online: https://www.hydropower.org/iha/discover-facts-about-hydropower (accessed on 6 January 2022).
7. Tkac, S. Hydro power plants, an overview of current types and technology. *SSP-J. Civ. Eng.* **2018**, *13*, 115–126.
8. Paish, O. Small hydro power: Technology and current status. *Renew. Sustain. Energy Rev.* **2002**, *6*, 537–556. [CrossRef]
9. Kaunda, C.S.; Kimambo, C.Z.; Nielsen, T.K. Hydropower in the Context of Sustainable Energy Supply: A Review of Technologies and Challenges. *Int. Sch. Res. Not.* **2012**, *2012*, 730631. [CrossRef]
10. Alatorre-Frenk, C. Cost Minimization in Micro-Hydro System Using. PAT. Dissertation, University of Warwickshire, Coventry, UK, 1994.
11. Aggidis, G.A.; Luchinskaya, E.; Rothschild, R.; Howard, D.C. The costs of small-scale hydro power production: Impact on the development of existing potential. *Renew. Energy* **2012**, *35*, 2632–2638. [CrossRef]
12. Hossain, I.M.; Ferdous, S.M.; Salehin, S.; Saleque, A.M.; Jamal, T. Pump-as-turbine (PAT) for small scale power generation: A comparative analysis. In Proceedings of the 2014 3rd International Conference on the Developments in Renewable Energy Technology (ICDRET), Dhaka, Bangladesh, 29–31 May 2014.
13. Binamaa, M.; Sua, W.-T.; Li, X.-B.; Weia, X.-Z.; Anc, S. Investigation on pump as turbine (PAT) technical aspects for micro hydropower schemes: A state-of-the-art review. *Renew. Sustain. Energy Rev.* **2017**, *79*, 148–179. [CrossRef]
14. Morabito, A.; Furtado, G.A. Variable speed regulation for pump as turbine in micro pumped hydro energy storage application. In Proceedings of the 38th IAHR Congress, Panama City, Panama, 1–6 September 2019.
15. Deyou, L.; Hongji, W.; Goaming, X.; Ruxhi, G.; Zhansheng, L. Unsteady simulation and analysis for hump characteristics of a pump turbine model. *Renew. Energy* **2015**, *77*, 32–42. [CrossRef]
16. Nobile, E.; Sari, G.; Schwery, A. Variable Speed Hydro Pumped Storage as Flexible Enabler of Intermittent Renewable Penetration. In Proceedings of the 2018 IEEE Power & Energy Society General Meeting (PESGM), Portland, OR, USA, 5–10 August 2018; pp. 1–5.
17. Elbatran, A.H.; Yakoob, O.B.; Ahmed, Y.M. Operation, performance and economic analysis of low head micro-hydropower turbines for rural and remote areas: A review. *Renew. Sustain. Energy Rev.* **2015**, *43*, 40–50. [CrossRef]
18. Derakhshan, S.; Kasaeian, N. Optimization, Numerical, and Experimental Study of a Propeller Pump as Turbine. *J. Energy Resour. Technol.* **2014**, *136*, 012005. [CrossRef]

19. Yang, S.-S.; Kong, F.-Y.; Jiang, W.-M.; Qu, X.-Y. Effects of impeller trimming influencing pump as turbine. *Comput. Fluids* **2012**, *67*, 72–78. [CrossRef]
20. Yang, S.-S.; Liu, H.-L.; Kong, F.-Y.; Dai, C. Experimental, Numerical, and Theoretical Research on Impeller Diameter Influencing Centrifugal Pump-as-Turbine. *J. Energy Eng.* **2013**, *139*, 299–307. [CrossRef]
21. Yang, S.-S.; Wang, C.; Chen, K.; Yuan, X. Research on Blade Thickness Influencing Pump as Turbine. *Adv. Mechan. Eng.* **2014**, *6*, 190530. [CrossRef]
22. Yang, S.-S.; Kong, F.-Y.; Qu, X.-Y.; Jiang, W.-M. Influence of blade number on the performance and pressure pulsations in a pump used as a turbine. *J. Fluids Eng.* **2012**, *134*, 124503. [CrossRef]
23. Lugauer, F.J.; Kainz, J.; Gehlich, E.; Gaderer, M. Roadmap to Profitability for a Speed-Controlled Micro-Hydro Storage System Using Pumps as Turbines. *Sustainability* **2022**, *14*, 653. [CrossRef]
24. Binama, M.; Kan, K.; Chen, H.-X.; Zheng, Y.; Zhou, D.-Q.; Su, W.-T.; Ge, X.-F.; Ndayizigiye, J. A Numerical Investigation into the PAT Hydrodynamic Response to Impeller Rotational Speed Variation. *Sustainability* **2021**, *13*, 7998. [CrossRef]
25. Hunt, J.D.; Zakeri, B.; Lopes, R.; Barbosa, P.S.F.; Nascimento, A.; de Castro, N.J.; Brandão, R.; Schneider, P.S.; Wada, Y. Existing and new arrangements of pumped-hydro storage plants. *Renew. Sustain. Energy Rev.* **2020**, *129*, 109914. [CrossRef]
26. Bansal, R.K. *A Textbook of Fluid Mechanics and Hydraulic Machines*; Laxmi Publication (P) Ltd.: New Delhi, India, 2010.
27. ANSYS Fluent Tutorial Guide. Release 18.0, January 2017. Available online: www.ansys.com (accessed on 5 December 2021).
28. Zhou, L.; Hang, J.; Bai, L.; Krzemianowski, Z.; El-Emam, M.A.; Yasser, E.; Agarwal, R. Application of entropy production theory for energy losses and other investigation in pumps and turbines: A review. *Appl. Energy* **2022**, *318*, 119211. [CrossRef]
29. Weidong, C.; Lingiun, Y.; Bing, L.; Yining, Z. The influence of impeller eccentricity on centrifugal pump. *Adv. Mech. Eng.* **2017**, *9*, 1–17. [CrossRef]
30. El-Emam, M.; Zhou, L.; Yasser, E.; Bai, L.; Shi, W. Computational Methods of Erosion Wear in Centrifugal Pump: A State-of-the-Art Review. *Arch. Comput. Methods Eng.* **2022**, *29*, 3789–3814. [CrossRef]
31. Wei, Y.; Shi, Y.; Shi, W.; Pan, B. Numerical Analysis and Experimental Study of Unsteady Flow Characteristics in an Ultra-Low Specific Speed Centrifugal Pump. *Sustainability* **2022**, *14*, 16909. [CrossRef]
32. Simulink Getting Started Guide, Release 2015. Available online: www.mathworks.com (accessed on 15 December 2021).
33. Alberizzi, J.C.; Renzi, M.; Nigro, A.; Rossi, M. Study of a Pump-as-Turbine (PAT) speed control for a Water Distribution Network (WDN) in South-Tyrol subjected to high variable water flow rated. *Energy Procedia* **2018**, *148*, 226–233. [CrossRef]

energies

MDPI

Article

Optimal Configuration of Energy Storage Systems in High PV Penetrating Distribution Network

Jinhua Zhang [1], Liding Zhu [1,*], Shengchao Zhao [1], Jie Yan [2] and Lingling Lv [1]

[1] School of Electric Power, North China University of Water Resources and Electric Power, Zhengzhou 450045, China
[2] State Key Laboratory of New Energy Power System, School of New Energy, North China Electric Power University, Beijing 100096, China
* Correspondence: z20211050617@163.com

Abstract: In this paper, a method for rationally allocating energy storage capacity in a high-permeability distribution network is proposed. By constructing a bi-level programming model, the optimal capacity of energy storage connected to the distribution network is allocated by considering the operating cost, load fluctuation, and battery charging and discharging strategy. By constructing four scenarios with energy storage in the distribution network with a photovoltaic permeability of 29%, it was found that the bi-level decision-making model proposed in this paper saves 2346.66 yuan and 2055.05 yuan, respectively, in daily operation cost compared to the scenario without energy storage and the scenario with single-layer energy storage. After accessing IEEE-33 nodes for simulation verification, it was found that the bi-level decision-making model proposed in this paper has a good inhibition effect on voltage fluctuation and load fluctuation after energy storage configuration. In addition, this paper analyzes the energy storage that can be accessed by photovoltaic distribution networks with different permeability and finds that when photovoltaic permeability reaches 45% and corresponding energy storage is configured, the economic and energy storage benefits of the system are the best.

Keywords: high PV penetration; energy storage; optimal configuration; bi-level decision-making models

Citation: Zhang, J.; Zhu, L.; Zhao, S.; Yan, J.; Lv, L. Optimal Configuration of Energy Storage Systems in High PV Penetrating Distribution Network. *Energies* **2023**, *16*, 2168. https://doi.org/10.3390/en16052168

Academic Editors: Luis Hernández-Callejo, Jesús Armando Aguilar Jiménez and Carlos Meza Benavides

Received: 31 January 2023
Revised: 16 February 2023
Accepted: 20 February 2023
Published: 23 February 2023

1. Introduction

In recent years, with global carbon dioxide emissions hitting record highs, China has proposed a "two-carbon" target to tackle environmental problems. Promoting the development of new energy and the transformation of energy structures has become an important part of global development. Due to abundant reserves and easy access, solar energy has been developing rapidly in recent years, and its proportion in the power grid has been increasing year by year [1]. While improving energy utilization, this has brought a lot of trouble to the power distribution network. With the continuous increase in the penetration rate of photovoltaics integrated into the power distribution network, problems such as voltage collapse may occur, which has a serious impact on the safe and stable operation of the system [2].

Studies have shown that a large number of photovoltaics connected to the distribution network will also increase the number of system equipment, which will bring a burden to the system and easily generate harmonic interference. In addition, the retrograde power generated by the grid connection is prone to exceed the limit of the system node voltage, which not only reduces the power quality but also deteriorates the user experience. When high-penetration photovoltaics are connected to the grid, the uncertainty of output cannot be matched with the load of the distribution network in real-time, which will affect the power balance of the system. When the photovoltaic output fluctuates greatly due to the change in environment and climate, the stability of the system will be affected [3]. In addition, the high-penetration photovoltaic grid connection requires a large number of

power electronic equipment to join the distribution network, which leads to the existence of harmonics and affects the power quality [4], and the dispatching flexibility of the distribution network is greatly reduced, which makes it more difficult for the power system to develop a power generation plan. If such problems cannot be properly solved, it will not only seriously threaten the safe and stable operation of the system but also cause a waste of energy and limit the future development of photovoltaic power generation [5].

The authors in [6–8] analyze the influence of photovoltaic systems from the aspects of voltage fluctuation, voltage amplitude, and frequency. From the perspective of stability, Rasoul proposed a new framework to analyze the influence of different photovoltaic permeability on voltage stability [9]. During the study, Zetty found that in a high permeability renewable energy distribution network, load fluctuation is the main factor leading to the voltage fluctuation of the system, and the realization of various fluctuations in the high-light voltage permeability distribution network is important content to achieve the increase of photovoltaic permeability in the distribution network [10]. The introduction of energy storage devices improves the power quality while improving the photovoltaic stable output [11–13]. Through reasonable regulation and control of a BESS, the absorption of new energy on the power generation side can be completed, the permeability of distributed power supply on the transmission side and distribution side can be improved, and the safe, stable, and economic operation of the system can be ensured [14,15]. The authors in [16–18] studied the working principle and characteristic analysis of different types of energy storage devices and different types of BESSs and discussed the practicability of combining BESS energy storage and generation measurement. From the perspective of photovoltaic and load output prediction, Rahman and Zhao verified the feasibility of combining energy storage optimization configuration with the prediction by comparing scenarios with or without prediction [19,20]. In order to meet the photovoltaic energy storage demand in the distribution network, Wang's multiple operation scenarios of energy storage were divided into grid scenarios to obtain the demand relationship of energy storage capacity under different operating conditions and to complete the calculation of energy storage capacity [21].

Access to energy storage equipment requires considerable capital investment in actual project construction and operation and maintenance. Therefore, the demand response for energy storage capacity is important content in optimizing energy storage configuration. In [22], Balouch proposed an optimization goal of matching demand and supply. Based on the analysis of line planning, low-cost scheduling, and demand response, the energy utilization efficiency and comprehensive operating cost of a smart grid were optimized. The authors in [23,24] introduced the improved optimization algorithm to improve the optimization ability so as to determine the optimal scheme of energy storage optimization configuration and realize a higher degree of response between demand and supply by analyzing various indicators of access to the power grid. In [23], Balouch optimized a response scheduling scheme by introducing the GWCSO algorithm. Higher robustness and computational efficiency of the algorithm make the optimization results more advantageous in power cost and peaking ratio. In [24], Mostafa improves the PSO algorithm, improves the accuracy and effectiveness of the algorithm, and optimizes the location and capacity allocation of energy storage in distributed networks. While the optimization objects are complex and diverse when connecting to the power system, the choice and update of the Pareto optimal solution will determine the quality of the final optimization result [25].

In the existing studies, it seems obvious for everyone to apply energy storage in high-permeability photovoltaic distribution networks [26–32]. In the case of low photovoltaic permeability, access to energy storage can indeed improve photovoltaic output and power quality. However, few researchers have analyzed whether energy storage can still meet expectations in the scenario of high photovoltaic permeability, and how to rationally allocate energy storage in a distribution network with high photovoltaic permeability. In this paper, the application of energy storage in a high permeability photovoltaic scenario is analyzed, and the energy storage in a high-light volt distribution network is configured by

establishing a two-layer planning model of the distribution network. The optimal size of energy storage was configured considering the fluctuation of power grid voltage and load, economic benefits and energy storage benefits, and the working condition of energy storage in the scenario of high-light voltage permeability, and the improvement of benefits in all aspects of the distribution network were studied. Finally, the feasibility of the proposed method was verified in the IEEE-33 node system.

The main contributions of this study are summarized below:

- Proposed a method for optimal allocation of energy storage capacity of a distribution network based on a two-layer programming model and verified its feasibility.
- Used the K-means method to complete an analysis of the uncertain photovoltaic output into the deterministic scenario.
- The multi-objective particle swarm optimization algorithm was improved to solve the optimal configuration, and the advantages of the improved algorithm were compared.
- By constructing different scenarios, it was verified that energy storage can still improve the power quality in the distribution network with high-light voltage and permeability.
- Through analysis of the optimal configuration of energy storage in the distribution network with different photovoltaic permeabilities, the optimal economic photovoltaic permeability was concluded.

The rest of this paper is organized as follows: The treatment method for the PV uncertainty and the selection of the PV working curve is introduced in Section 2. In Sections 3 and 4, the bi-level decision-making programming model is constructed and solved to realize the addressing and capacity selection of the energy storage device. At the same time, in the fourth section, the specific content of particle swarm optimization is described. In Section 5, four scenarios are constructed to discuss the benefits generated by energy storage configuration and optimization benefits brought by algorithm improvement. Finally, in Section 6, we summarize the content of the thesis.

2. Analysis of Photovoltaic Output Characteristic

Due to the great influence of light and the environment, photovoltaic power generation is full of uncertainties. For further analysis, we collected the annual daily output data of photovoltaic power stations (annual output of an operational photovoltaic power station in Henan Province from June 2019 to July 2020), as shown in Figure 1. When considering energy storage benefits, excessive uncertainty in output will lead to uncertainty in energy storage benefits. In order to avoid this influence, this paper will process various output curves by clustering the division method, summarizing the photovoltaic output with high uncertainty into six typical output scenarios and analyzing them, and transforming the uncertainty into a deterministic analysis.

2.1. K-Means Cluster Analysis Method

The K-means clustering method is a classical clustering analysis method based on the iterative method which has the advantages of high efficiency and convenience in processing large-scale uncertain data [33]. Through the K-means clustering method, a large number of output data can be refined and extracted, and fewer typical output scenarios can be obtained that can represent the output of photovoltaic power stations.

The K-means algorithm sets an initial cluster center in all scenes and iterates clustering for a large number of scenes based on the optimal distance. The iteration is not finished until the clustering presents a steady-state equilibrium. The iteration results are shown in Figure 2. After the whole process is complete, the center of each cluster scene is set as the partition scene, and the probability of each cluster scene is set as the required partition probability $P_r(s)$.

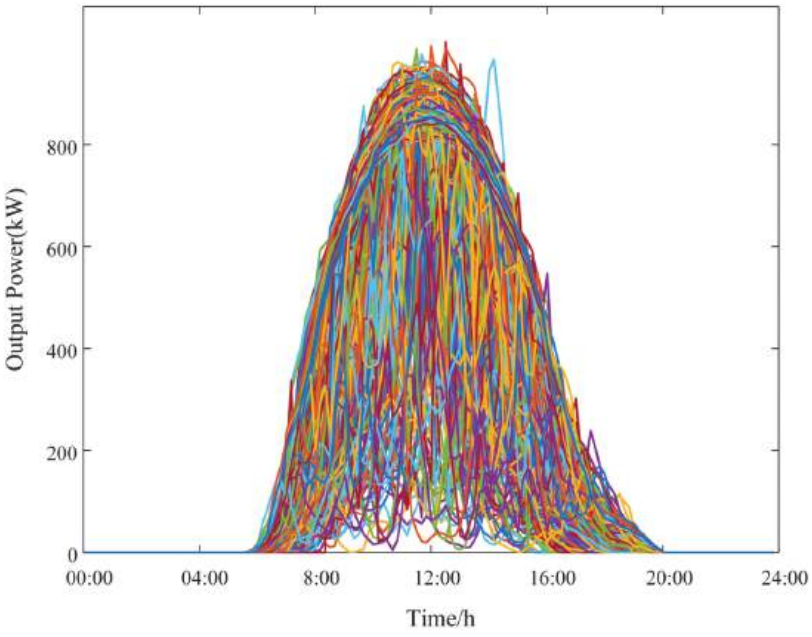

Figure 1. Annual daily output curve of photovoltaic power plants.

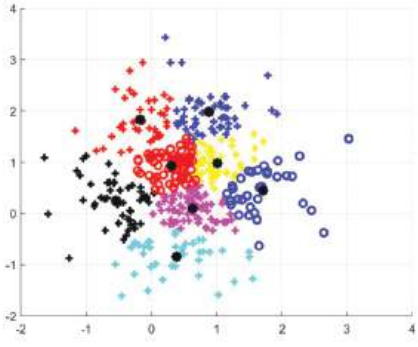

Figure 2. K-means clustering method results.

Set the number of initial scenarios $\xi_s (s = 1, 2 \ldots N)$ to N_s. The number of target scenarios is M_s, and the entire calculation procedure is as follows:

① M_s target scenes with random data are set as the cluster center, and the set of these scenes is $Center = \{\xi_s^{Center}\}$ $(s = 1, 2 \ldots M_s)$.

② Excluding the cluster center set, the other scene set is set as $Member = \{\xi_s^{Center}\}$ $(s = 1, 2 \ldots M_s)$, and the distance from the other scene set to the cluster center scene set is calculated: $\begin{cases} DT_{s,s'} = DT\left(\xi_s^{Center}, \xi_s^{Member}\right) = ||\xi_s^{Center} - \xi_s^{Member}||_2 \\ s = 1, 2 \ldots M_s \ , s' = 1, 2 \ldots N_s - M_s \end{cases}$

③ The other scene sets excluding the cluster center set are divided into the nearest cluster center according to the distance calculated in ②. We obtain the cluster set $Cluster = \{C_i\}, i = 1, 2 \ldots M_s$, where C_i is a set of similar scenarios.

④ Set the same cluster C_i including L_s scenarios. Add the distances from each scenarios to the others: $CT_s = \sum_{\substack{s'=1 \\ s' \neq s}}^{L_s} ||\xi_s - \xi_{s'}||_2$, and scene ξ_k in $CT_s = Min(CT_s)$ is selected as

the clustering center of the next iteration. This is used to calculate the next iteration cluster center set.

⑤ At this point, stable cluster centers and clustering results can be obtained by repeating steps ②–④. The probability number of each type of scenario is the probability number of a single scenario in that type of scenario.

The process of the clustering algorithm to reduce the scene is shown in Figure 3.

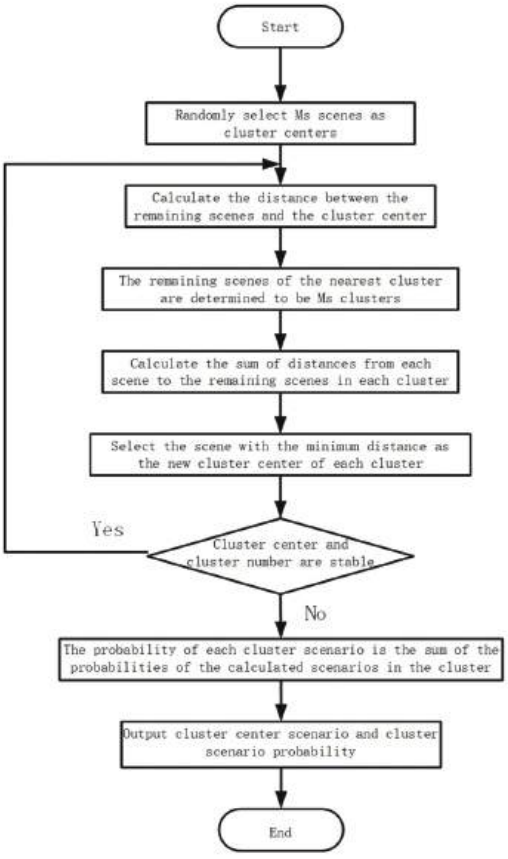

Figure 3. Cluster reduction flowchart.

2.2. Selection of Typical Output Scenarios

After data processing and division by the K-means clustering method, six output scenarios as shown in Figure 4 can be obtained. The occurrence probability and the number of curves of each output scenario are shown in Table 1.

Table 1. Typical scenario probability.

Scenario	Number of Curves	Probability	Scenario	Number of Curves	Probability
1	35	0.0959	4	24	0.0658
2	7	0.0192	5	127	0.3479
3	75	0.2055	6	97	0.2658

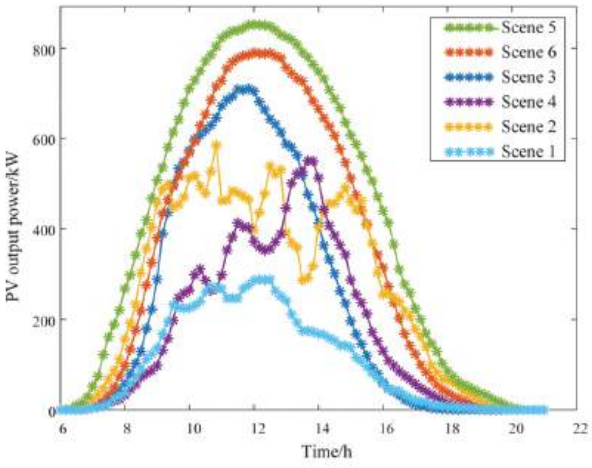

Figure 4. Clustering of typical scenarios.

As can be seen from Figure 4 and Table 1, the photovoltaic output power in Scenario 1 is low, while the output in Scenario 2 has great fluctuation and uncertainty. The intermediate level of output in Scenarios 3 and 4 cannot represent photovoltaic output, and Scenarios 5 and 6 have a high probability and good output curve. In contrast, Scenario 5 with the maximum annual output is selected as the typical photovoltaic output curve, which can better reflect the output characteristics of photovoltaic power generation. In order to facilitate the analysis of the combined effect of photovoltaic and energy storage under different permeability, in this paper, we will only select Scenario 5, which is the most representative and has the highest probability of occurrence at the same time, as the analysis object to study the influence of energy storage access to the power grid during daily operation on voltage fluctuation, operation cost, and other benefits of the distribution network.

3. BESS Bi-Level Decision-Making Model Configuration

Due to the mutual influence between the optimal configuration of the energy storage system and the stable operation of the distribution network, this will bring difficulties to the dispatching of the energy storage devices and will cause the operation stability of the distribution network to decline. Therefore, it is necessary to consider a reasonable location and capacity while taking into account the operation economy of the distribution network. The bi-level decision-making model relies on its own two-level hierarchical structure to optimize the system objectives hierarchically. The upper and lower levels influence each other and seek the overall optimal solution according to the independent objective function and the corresponding constraints [34,35].

3.1. Upper-Level Model Objective Function

In the upper-level optimization, energy storage configuration location, rated power, and installed capacity are considered to reduce the total cost of the energy storage system and distribution network investment and maintenance. The installation location and capacity of the BESS are optimized. After the optimal configuration of energy storage is obtained, the information is transmitted to the lower level to adjust the charge and discharge power of energy storage.

$$\begin{cases} F_{min} = f_{sto} + f_{ope} \\ s.t. g(X) \leq 0 \end{cases} \quad (1)$$

where F_{min} is the minimum daily total cost after the energy storage is connected; f_{ope} is the total cost of distribution network operation investment. f_{sto} is the input costs for energy storage construction. $X = [x_1, x_2, x_3]$, and x_1, x_2, x_3, respectively, represent the BESS input node, power, and capacity.

3.2. Lower Objective Function

In the lower-level optimization, due to the influence of the energy storage installation location and capacity selection on the energy storage life, the lower-level decision-making model fully considers the change of the energy storage charging and discharging power to realize the economical operation mode of the distribution network and achieve the smallest fluctuation range of node voltage and load. The lower optimization objective function is as follows:

$$\begin{cases} min(f_{ope}, f_2, f_3) \\ s.t.h(y) \le 0 \end{cases} \tag{2}$$

where f_2 is the amplitude of the voltage fluctuation of the distribution network node caused by the access to energy storage, f_3 is the amplitude of the load fluctuation of the distribution network, and $y = [y_1, y_1, y_2 \dots y_{24}]$ is the average hourly charging and discharging power of the energy storage system throughout the day.

(1) The voltage fluctuation of distribution network nodes caused by energy storage access can be expressed as:

$$min\ f_2 = \sum_{t=1}^{24} \sum_{k=1}^{N} \left[\frac{u_k(t) - u_{kn}}{\Delta u_{kmax}} \right]^2 \tag{3}$$

where N indicates the number of system nodes, and $u_k(t)$ indicates the voltage value of node k at time t.

(2) The load fluctuation of the distribution network caused by access to energy storage can be expressed as:

$$min\ f_3 = \frac{1}{T} \sum_{t=1}^{T} [P'_{load}(t) - P'_{ave}]^2 \tag{4}$$

where P'_{ave} represents the average load in a period of time when energy storage is connected.

3.3. Constraints

(1) Constraints at the BESS access node

$$1 \le x_1 \le N_{max} \tag{5}$$

where x_1 are nodes invested in energy storage, and N_{max} is the maximum number of nodes expressed as energy storage input.

(2) The constraints of power rating and capacity energy storage devices can be expressed as

$$\begin{cases} P_{ess}^{min} \le P_{essn} \le P_{ess}^{max} \\ E_{ess}^{min} \le E_{essn} \le E_{ess}^{max} \end{cases} \tag{6}$$

where P_{ess}^{max} and P_{ess}^{min} is the maximum and minimum value of the rated output of the energy storage, and E_{ess}^{max} and E_{ess}^{min} are the maximum and minimum values of the energy storage input capacity.

(3) Power balance constraints

$$P_{grid} + P_{gv} = P_{load} + P_{loss} + P_{ess} \tag{7}$$

where P_{grid} is the power value received by the grid, P_{gv} is the PV output power, P_{load} is the output power, P_{loss} is the network loss, and P_{ess} is the BESS input power.

(5) BESS charge and discharge power constraints

$$\begin{cases} 0 \le P_{ess}^{cha}(t) \le P_{essn} \\ -P_{essn} \le P_{ess}^{cha}(t) \le 0 \end{cases} \tag{8}$$

(6) Voltage constraints in distribution network nodes

$$u_k^{min} \le u_k(t) \le u_k^{max} \tag{9}$$

where u_k^{min} and u_k^{max} are the minimum and maximum voltages of node k at time t. Energy storage system *SOC* constraints

$$SOC(t) = \frac{E(t)}{E_{sn}} = SOC_0 + \frac{\sum_{k=1}^{t}\left\{d_1(t)P_{ess}^{cha}(t)n_c\right\}\Delta t + \sum_{k=1}^{t}\left\{d_2(t)P_{ess}^{cha}(t)/n_d\right\}\Delta t}{E_{ssn}} \tag{10}$$

where SOC_0 is the initial state of the energy storage system, including power and capacity. E_{ssn} is the rated capacity of the energy storage battery.

(7) Supplementary constraints

① Due to the limitation of the *SOC* range of the BESS, there will be a large number of infeasible solutions during the recovery of its all-day charging and discharging power. If its charge and discharge power is processed, this will greatly improve the convergence rate in the solution process and reduce the amount of calculation.

$$P'_{ess} = \begin{cases} P_{ess}(t)\ SOC_{min} \le SOC(t) \le SOC_{max} \\ 0\ otherwise \end{cases} \tag{11}$$

where $P'_{ess}(t)$ is the energy storage charge and discharge power value that has been processed at time t. In this way, the infeasible solution is transformed into an effective feasible solution, and the charging and discharging power that is not within the SOC range of the energy storage is changed to 0.

② Using the penalty function method to deal with the constraints that are not within the valid range:

$$F(x, M) = f(x) + M\sum_{i=1}^{r} max(g_i(x), 0) - M\sum_{i=1}^{s} min(h_i(x), 0) + M\sum_{i=1}^{t}|k_i(x)| \tag{12}$$

where M is the penalty coefficient. $g_i(x)$ indicates the negative inequality constraint. $h_i(x)$ indicates the positive inequality constraints. $k_i(x)$ indicates the equality constraint at zero. r, s, t are the number of constraints.

4. Solution of Model

For the bi-level programming model, this paper selects the genetic algorithm (GA) for the optimization of the upper layer and improved multi-objective particle swarm optimization (IMOPSO) for the optimization of the lower level. The calculation process is as follows:

① Input the demand parameters of the distribution network into the system.

② Initialize the decision variables for the upper level (including BESS installation location, power rating, and capacity). Under the constraint, the population and other parameters of the GA algorithm are initialized.

③ Initialize the decision variables of the lower level, including the BESS charge–discharge method. Under its constraints, the IMOPSO algorithm population and other related parameters are initialized to solve the initial fitness of each optimization objective.

④ After the optimization of the lower layer is completed, the TOPSIS multi-attribute decision-making method is used to select the upper Pareto solution set obtained, and

the best scheme is selected and fed back to the upper layer to solve the fitness of the upper layer target.

⑤ The upper-level GA algorithm population is updated, and the third and fourth steps are continuously executed until the upper-level optimization is completed.

⑥ The optimal BESS configuration scheme of the upper layer, the corresponding optimal charge-discharge method of the lower layer, and the optimal Pareto solution set are obtained.

The calculation process is shown in Figure 5. In the following sections, we will give a specific description of the improvement content of the multi-objective particle swarm optimization.

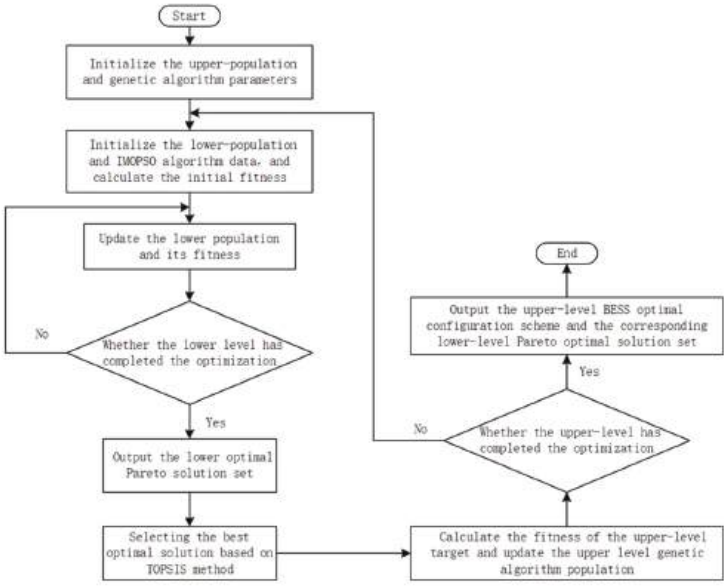

Figure 5. Calculation process.

4.1. Improved PSO Algorithm

The particle swarm optimization (PSO) algorithm is an iterative optimization algorithm. By converting the target into a certain number of particles, the position is updated in each iteration, and the optimal solution is searched through continuous iteration. The updating method is as follows:

$$v_{id}^{k+1} = wv_{id}^{k} + c_1 r_1 \left(p_{id}^{(k)} - x_{id}^{(k)} \right) + c_2 r_2 \left(g_d^{(k)} - x_{id}^{(k)} \right) \tag{13}$$

$$x_{id}^{(k+1)} = x_{id}^{(k)} + v_{id}^{(k+1)} \tag{14}$$

where w represents inertia weight; c_1, c_2 are acceleration coefficients of particle motion respectively. r_1, r_2 are randomly selected in the range of 0 to 1; $P_{id}^{(k)}$ represents the d-dimensional component of the particle numbered i in the optimal position vector at time k; and $g_d^{(k)}$ represents the d-dimensional component of the optimal position of all particles at time k.

In the process of iterative optimization, the traditional muti-objective particle swarm optimization algorithm is prone to fall into local optimal and appear 'Premature conver-

gence'. Therefore, this paper cross-mutates the prescribed bit vectors of particles to prevent them from falling into the local optimum.

$$X_{i,d} = X_{min} + (X_{max} - X_{min})r \tag{15}$$

where X_{min} represents the minimum position variable of the particle; r represents any value between 0 and 1.

Random cross variation is carried out when the probability distribution $P < P_m$ is satisfied. When the fitness of particles tends to be the same or locally optimal, the w will increase. Otherwise, the w will decrease as the particles tend to disperse [36].

$$w = \begin{cases} w_{max} - \frac{(w_{max} - w_{min})(f_i - f_{avg})}{f_{max} - f_{avg}} & f_i \geq f_{avg} \\ w_{max} & f_i \leq f_{avg} \end{cases} \tag{16}$$

where f_i is the fitness value of the particle i, w_{max},w_{min} are the maximum and minimum of w, and f_{max},f_{min},f_{avg} are the average and maximum, minimum, and average fitness of all particles at present, respectively.

In order to make the optimal solution distributed evenly in a certain range, the Pareto solution set should be optimized step by step. In this paper, a dynamic image Pareto solution set updating method is adopted, as is shown in Figure 6. In the initial distribution stage of particles, referring to all particles of the original comparison rule, an image V_{iD} is established with the optimal particle as an optimal Pareto solution set. With the progress of iteration, the average value of particles is obtained between every two images, and the optimal solution is used to make the speed and position of particles updated at this time so that the particle population moves towards the target direction. In the whole process, new particles constantly exchange information with image particles and update data in image particles continuously until the end of iteration:

$$V_{iD}^{t+1} = wv_{iD}^{t+1} + c_1 rand_1\left(p_{iD} - X_{iD}^{t+1}\right) + c_2 rand_2\left(Average\left(pbest_p\right) - x_{iD}^{t}\right) \tag{17}$$

$$x_{iD}^{k+1} = x_{iD}^{k} + v_{iD}^{k+1} \tag{18}$$

where t is the number of iterations; D is the dimension of the decision variable; p_{iD} is the best historical value of single particle i; and $pbest_p$ is the optimal particle of the current Pareto solution set in the image. $Average\left(pbest_p\right)$ is the superior particle of the optimal Pareto solution set in the two images.

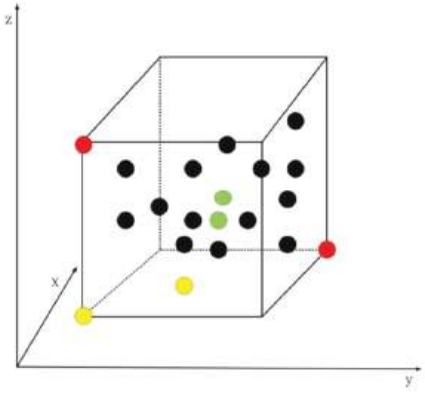

Figure 6. Dynamic image Pareto solution updates schematic.

There are differences in the selection of the optimal solutions between the multi-objective particle swarm optimization and single-objective particle swarm optimization, and the results obtained are complementary dominated Pareto solutions, which cannot be obtained by direct comparison of the particle fitness function. Therefore, in this section, the first 20% Pareto solutions with lower crowding distances and higher priority orders are randomly selected to guide the iterative updating of the particle population.

4.2. Multi-Attribute Decision-Making Based on TOPSIS Method

After solving the lower multi-objective optimization problem, the optimal solution obtained by the IMOPSO algorithm is a set of Pareto solutions, and the selection of the optimal solution is essentially a multi-attribute decision problem. TOPSIS is a method for ordering by similarity to an ideal solution, it selects the optimal solution set and the worst solution set through the established initial decision matrix, then compares the distance between the two solution sets and the evaluation index with the optimal solution set and finally sorts them to evaluate the pros and cons of the scheme. The TOPSIS method has high strict requirements in selecting weights. In this paper, the information entropy method is used to determine the weight of each target value. The information entropy method determines w by the difference of the target value in the Pareto solution, improves the accuracy of the final decision, reduces the difference, and ensures the objectivity of the decision. By using the TOPSIS method, we can determine a set of optimal Pareto solutions to guide us to choose an energy storage configuration scheme.

The optimal solution of the Pareto solution set obtained is selected from $X_1 \sim X_N$ and combined into N alternative schemes. The scheme X_i is selected from N records. It is the composition of some optimal solutions in the Pareto solution set. $g_m(X_i)$ represents the value of the mth attribute of the scheme X_i. Since each attribute is different, it should be unified and changed into the same type. The new attribute value is $G_m(X_i)$, which can be expressed as:

$$G_m(X_i) = \frac{g_m(X_i)}{\sqrt{\frac{1}{N}\sum_{i=1}^{N} g_m^2(X_i)}} \tag{19}$$

$$d(x_i) = \frac{d_+(x_i)}{d_+(x_i) + d_-(x_i)} \tag{20}$$

$$d_+(x_i) = \sqrt{\sum_{m=1}^{n} \left[\lambda_m g'_m(x_i) - \lambda_m g'_{m+}\right]^2} \tag{21}$$

$$d_-(x_i) = \sqrt{\sum_{m=1}^{n} \left[\lambda_m g'_m(x_i) - \lambda_m g'_{m-}\right]^2} \tag{22}$$

where $d(x_i)$ is the relative distance of scheme x_i; $d_+(x_i)$ represents the distance between scheme x_i and the optimal solution. $d_-(x_i)$ represents the distance from solution x_i, the negative worst solution. λ_m indicates the weight value of $g_m(X_i)$, which is randomly set between 0 and 1. g'_{m+} and g'_{m-} indicate the optimal and worst values of all schemes g_m.

5. Analysis and Discussion

5.1. Case Description

In this paper, the proposed scheme is tested on the IEEE-33 node distribution network [37]. In addition, the structure of the system is shown in Figure 7.

In this paper, the rated voltage of the selected distribution network is 12.66 kV, and the total load is 3715 kW + j2300 kvar. The upper and lower limits of the node voltage are specified as not exceeding ±5% of the rated voltage. Node 1 is a balance node, which is connected to the upper-level distribution network for power transmission. Taking into account the actual work and construction of photovoltaic power generation connected to the distribution network, photovoltaic power generation is connected to Node 9, and its installed power generation capacity is 1.077 MW (29% penetration rate).

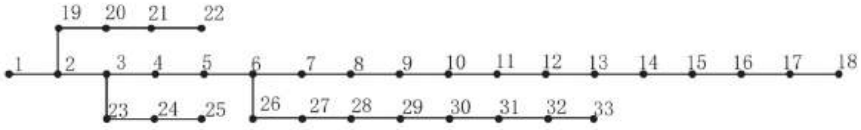

Figure 7. The topology diagram of IEEE-33 bus system.

The typical PV output curve selected by the method in Section 2 is shown in Figure 8. The typical daily load curve in this area is shown in Figure 9.

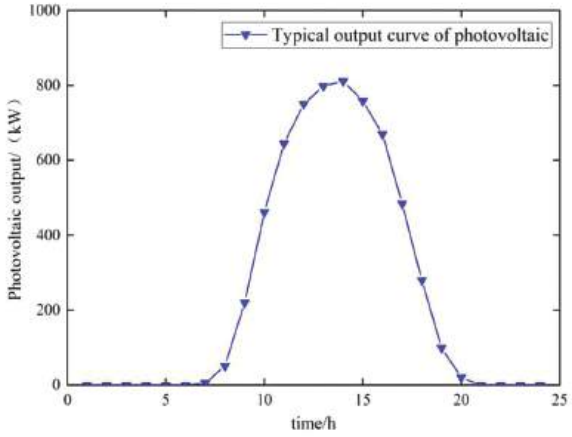

Figure 8. Photovoltaic typical sunrise force curve.

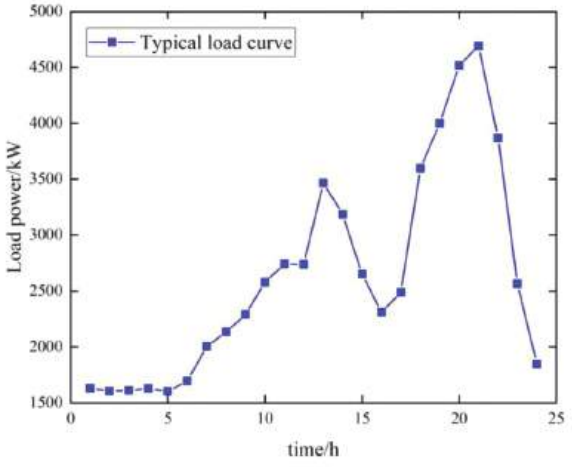

Figure 9. Typical daily characteristic curve of load.

In this paper, the battery is used as the energy storage system for research and introduces the time-of-use pricing strategy proposed in [38]. The specific time-of-use price is shown in Table 2. The energy storage control parameters are shown in Table 3. The specific setting parameters of the energy storage configuration optimization simulation are shown in Table 4.

Table 2. Time-of-use electricity price table.

Type	Period	Electricity Price (yuan/kWh)
Peak time	17:00–22:00	0.9796
Normal time	8:00–17:00 22:00–00:00	0.6570
Trough time	00:00–8:00	0.35

Table 3. Energy storage control parameter table.

Energy Storage Control Parameters	Data
Service life (year)	11
Discount Rate	0.02
Rated power cost (yuan/kW)	1000
Installation cost (yuan/kW)	2500
Operation and maintenance cost (yuan/kW)	0.05
State of charge SOC range	20–90%
Rated power upper limit (MW)	1
Maximum installed capacity (MWh)	5

Table 4. Simulation parameter settings.

Parameter	Data
Power purchase cost of grid	0.35
Expansion cost	1000
Expansion annual profit margin	8%
Load annual growth rate	1.5%
Genetic algorithm population size/number of iterations	60/200
IMOPSO algorithm population size/number of iterations	100/200
Crossover/variation rate	0.1/0.05
Inertia weight range	0.4–0.9
Threshold for difference X	0.1
The size of the Pareto solution set	100

In order to study the actual effect of energy storage configuration, we first analyzed the specific benefits of a photovoltaic distribution network connecting to energy storage configuration and demonstrated that energy storage still has good benefits in the high-light volt distribution network. Then, we compared the photovoltaic distribution network scenarios under different permeability and analyzed and compared the change of photovoltaic permeability with the corresponding change of optimal energy storage configuration scheme. The specific analysis content is introduced in the following section.

5.2. Energy Storage Optimization Scenario Division

Analyze the effectiveness of the method proposed in this paper, set different conditions, divide it into four scenarios, and compare them one by one to verify the feasibility of the method:

Scenario 1: No energy storage.

Scenario 2: With access to energy storage, use the IMOPSO algorithm in this paper to solve the optimization objective of lower-level model in the bi-level decision-making model; introduce the charging and discharging strategy of the energy storage system to simulate and analyze it.

Scenario 3: When solving its single-level model, ignore the charging and discharging management strategy of energy storage in the lower model, and only the energy storage system and distribution network are considered to have the lowest total cost. At the same time, in the time-of-use electricity price model, the energy

storage system is charged and discharged at a constant power regardless of the high or low electricity price.

Scenario 4: The optimal configuration result of energy storage in Scenario 2 is used as the constraint condition of this scenario, and the traditional multi-objective PSO algorithm is used to simulate and analyze the lower model in the optimal configuration model of the energy storage double-level. Node voltage curves and load curves in different scenarios are shown in Figures 10 and 11 below, and Table 5 shows the optimization results of different scenarios.

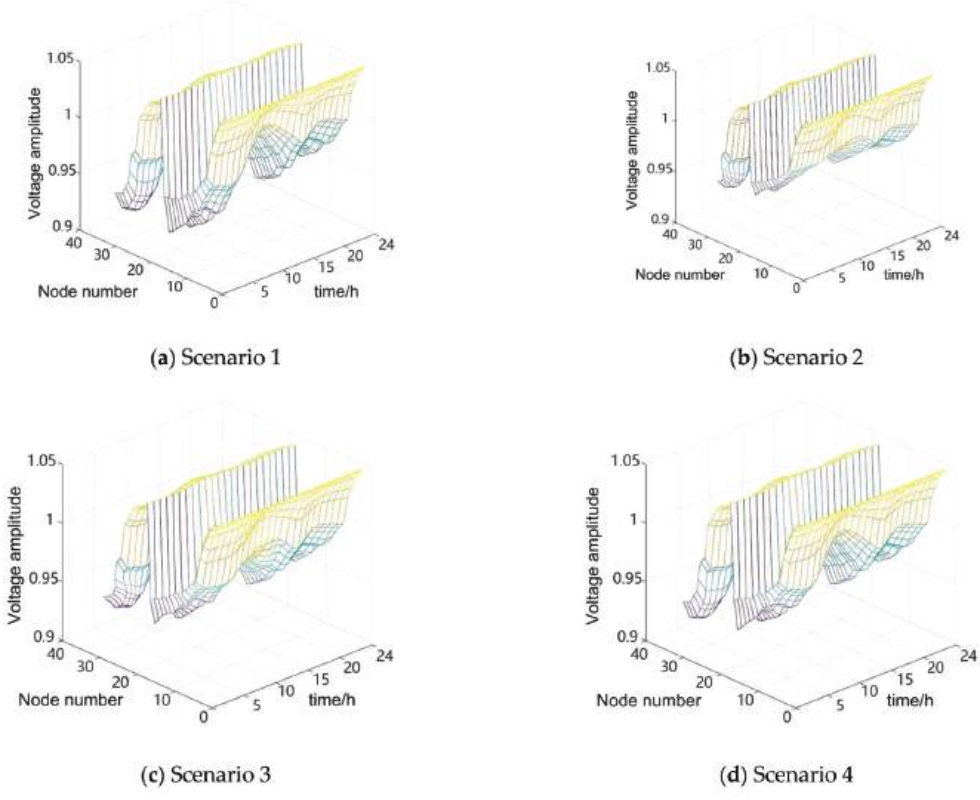

Figure 10. System node voltage curve in different scenarios.

Table 5. Optimization results in different scenarios.

Scenario	Node/Power (kw)/Capacity (kwh)	Cost of Investment	Distribution Network Operating Costs (Yuan)	Voltage Fluctuation Value	Load Variance	Total Cost (Yuan)	Degrees of Savings
1	-	0	16,703.6	70.21	36,5721.76	16,703.6	1.77%
2	14,650,3392	1879.32	14,532.67	63.52	15,3971.12	16,411.99	0%
3	20,273,2733	1497.62	15,717.64	64.98	24,9754.21	17,215.26	4.89%
4	14,650,3392	1879.32	14,767.71	64.85	15,9894.09	16,647.03	1.43%

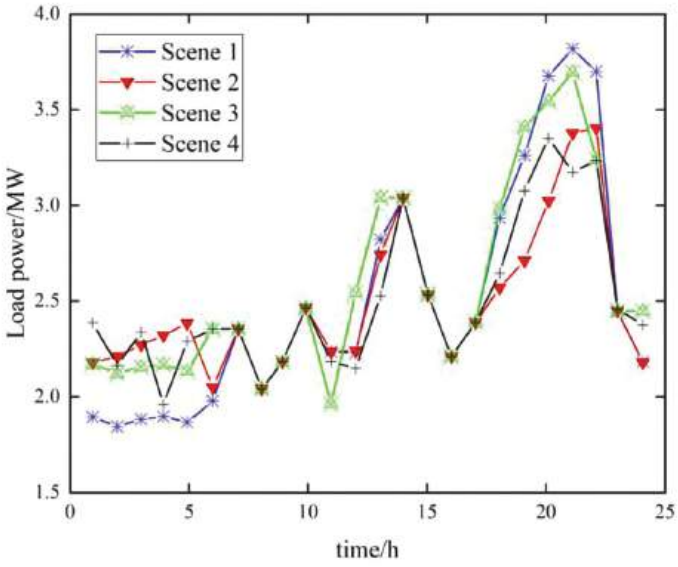

Figure 11. Load curve in different scenarios.

By comparing Scenario 1 and Scenario 2, it can be found that the voltage amplitude curve of the photovoltaic distribution network is smoother after the energy storage is connected, and the voltage fluctuation and load fluctuation are reduced to a large extent, which indicates that the BESS plays a good role in suppressing the node voltage fluctuation and load fluctuation when it is connected to the distribution network. Compared with Scenario 3, the load fluctuation range of Scenario 2 is smaller, and the load smoothing capacity is better. At the same time, the total cost of Scenario 2 is 803.27 yuan lower than that of Scenario 3 economically, which verifies the good characteristics of the model proposed in this paper.

The optimal Pareto solution set distribution of Scenario 2 and Scenario 4 is shown in Figure 12. Scenario 2 adopts the improved IMOPSO algorithm in this paper to solve the inner model, and Scenario 4 adopts the unimproved MOPSO algorithm to solve it. The Pareto solution set in Scene 2 is more evenly distributed than that in Scene 4 due to the introduction of particle cross mutation, adaptive inertia weight, and the Pareto solution set update method of the dynamic image. Moreover, Scene 2 adopts multi-attribute decisions based on the TOPSIS method, resulting in a more diverse solution set.

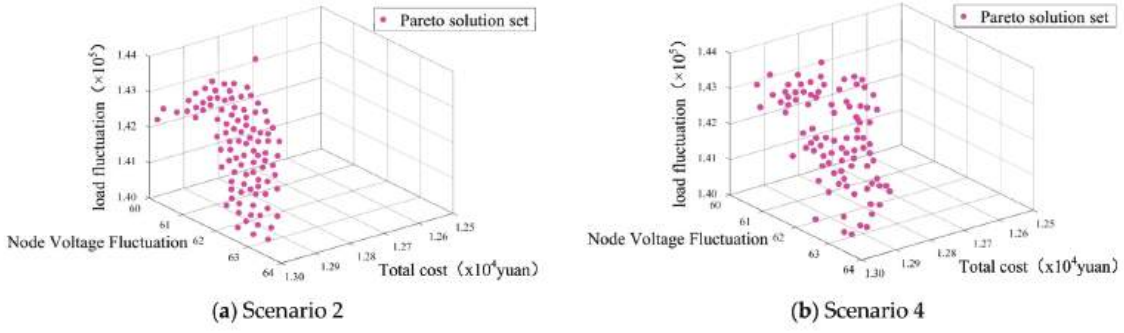

Figure 12. Pareto solution set distribution.

Through the comparison of scenes, it is obvious that the optimization results of the IMOPSO algorithm are obviously better than the MOPSO algorithm, and the search accuracy is higher. In order to compare the performance of the two algorithms, the external solution set and the spacing S are used in this paper to measure the optimization performance of the two algorithms. The S index refers to whether the particles in the Pareto solution set are evenly distributed in space. The mean variance of the particle density distance is used in this paper to characterize the uniformity and global nature of the population particles, as shown in Equation (23).

$$S = \sqrt{\frac{1}{N}\sum_{i=1}^{N}[I(x_i) - \overline{I}]^2} \tag{23}$$

where $\overline{I}$ represents the average of all particles $I(x_i)$ in the Pareto solution set.

According to the different internal environments of the two algorithms, after 20 cycles, the node voltage and load fluctuations in the optimization target are taken as the research object, as shown in Figure 13 and Table 6.

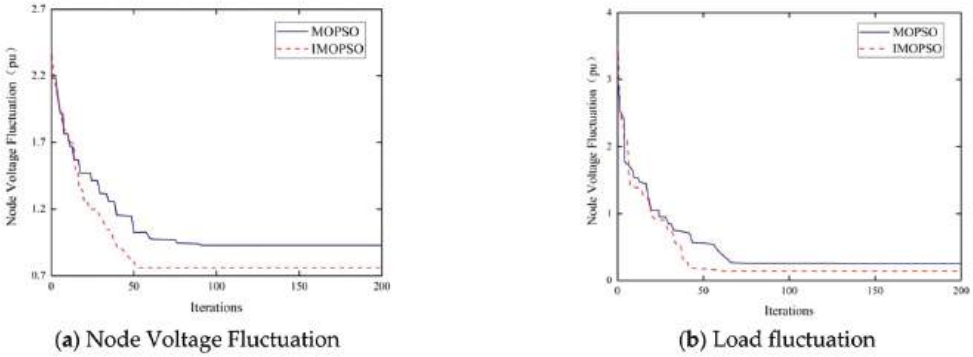

Figure 13. Convergence curves of external solutions for different objectives.

Table 6. Algorithm performance comparison.

Algorithm	External Solution		Distance 'S'
	Node Voltage Fluctuation	Load Fluctuation	
MOPSO	0.8869	0.2103	0.0485
IMOPSO	0.7154	0.1226	0.0317

By combining and comparing the charts, it was concluded that the IMOPSO algorithm proposed in this paper reduces the number of iterations in the node voltage fluctuation and load fluctuation, and the convergence performance is obviously better than the MOPSO algorithm. In addition, the improved algorithm and Pareto solution set update strategy make the solution set distribution more uniform and the type of solution set more diverse, and the improved MOPSO has better robustness and convergence.

5.3. Energy Storage Benefit Analysis under Different Photovoltaic Permeability

In order to verify the effectiveness of the dual-layer multi-objective optimal configuration model of the energy storage system proposed in this paper in the high-light volt permeability distribution network, the upper limit of photovoltaic power generation permeability was set at 60%, and the verification started from 30% permeability. Using the optimal configuration strategy of the BESS, the curve as shown in Figure 14 was obtained.

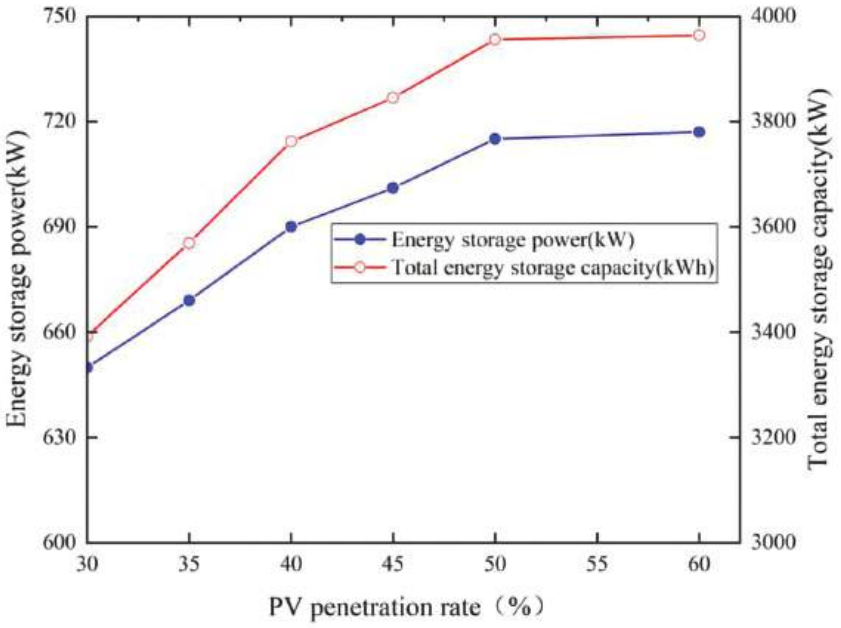

Figure 14. Changes in energy storage capacity and power under different photovoltaic penetration rates.

When the photovoltaic permeability increases from 30% to 60%, the capacity and power of the energy storage system have an obvious rising trend. When the photovoltaic permeability reaches 50%, the growth slows down and tends to remain unchanged. In other words, it is of little significance to increase the capacity of the energy storage system when the permeability reaches a certain level.

Figure 15 below shows the variation trend of energy storage investment and the total cost of distribution network operation under different photovoltaic permeability. It can be clearly seen that the total cost of the system decreases first and then increases when the photovoltaic permeability increases, and the total cost is the minimum when the permeability is 45%. As the cost of photovoltaic power generation decreases with the continuous increase of the permeability but is limited by the load level, the cost of the energy storage system increases with the increase of the capacity. The interaction between the two makes the total cost of the system decrease to the minimum when the photovoltaic permeability is 45%. When the permeability increases again, the system's total cost will keep rising, and the system operation economy will be seriously affected.

Based on the discussion of the above two legends, it is found that the total capacity of the BESS should be controlled in the optimal range according to the actual situation, and the photovoltaic permeability should also be controlled at a certain value so as to ensure the system operation economy while ensuring the safe and stable operation of the system. In order to improve the overall economy of the system, this paper selected 45% photovoltaic permeability to verify and analyze the two-layer programming model of the energy storage system proposed in this paper.

As shown in Figure 16 below, after optimizing the configuration of the energy storage system with 45% photovoltaic permeability, the load curve of the distribution network presents an obvious smoothing trend, and the peak–valley difference decreases. The sufficiency proves that the two-layer optimal configuration model of energy storage can still effectively improve the off-peak load, reduce the peak load of the distribution network,

and increase the scheduling flexibility of the distribution network under the condition of high photovoltaic permeability.

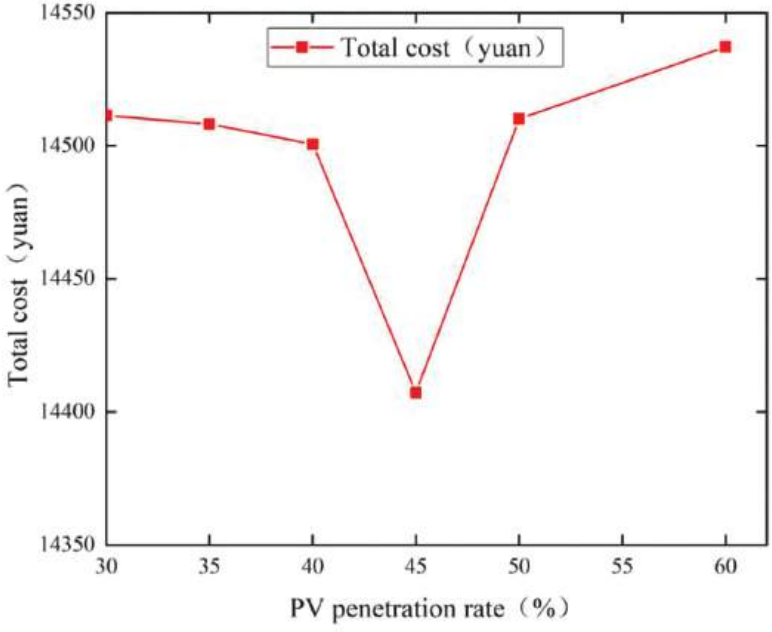

Figure 15. Total cost curve under different PV penetration rates.

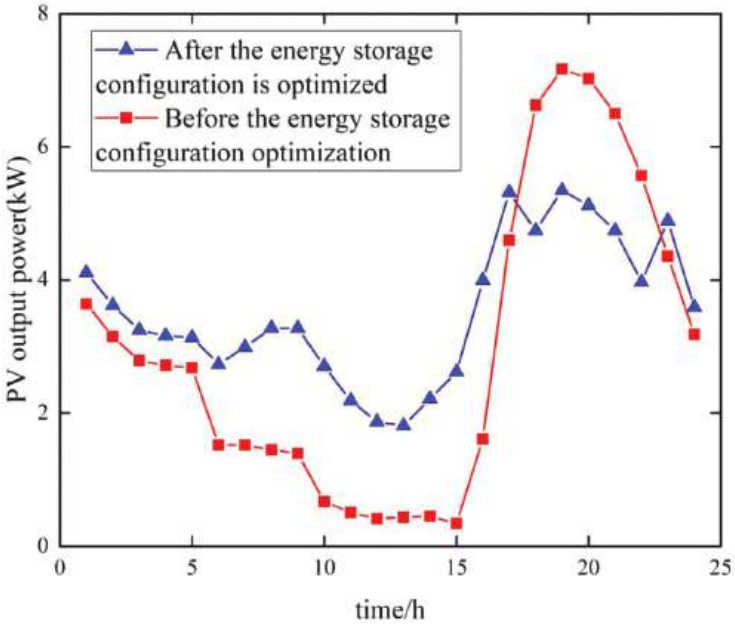

Figure 16. Distribution network load curve before and after energy storage configuration optimization under 45% photovoltaic penetration rate.

6. Conclusions

In order to ensure the power quality and scheduling flexibility of the photovoltaic distribution network with increasing permeability, this paper proposes a joint optimization operation mode of optical storage. Firstly, the PV output model was analyzed, and the scenario planning method was applied. The K-means clustering algorithm was used to divide the output scenarios, and the typical output scenarios were selected for analysis. A BESS two-layer decision model was established, and the improved IMOPSO algorithm was used to solve the two-layer model. The IEEE-33 node example was adopted, and the simulation verification was carried out based on the current feed-in price, selected energy storage parameters, and other parameters. The simulation analysis results are as follows:

① Access to energy storage can effectively smooth the load fluctuation and voltage fluctuation of system nodes in a photovoltaic distribution network. In a distribution network with high-light volt permeability, energy storage can effectively improve the off-peak load of the distribution network and reduce the peak load, thus increasing the scheduling flexibility of the distribution network.

② The bi-level programming model proposed in this paper has a good optimization ability for the rational allocation of energy storage.

③ The improved IMOPSO in this paper has good convergence performance and robustness and has good applicability in application optimization

④ When the optimal energy storage capacity under different photovoltaic permeability is configured, the total cost of the system is optimal when the photovoltaic permeability is 45%, and when the permeability increases again, the total cost of the system will keep rising and seriously affect the operation economy of the system. The analysis of this paper provides a theoretical basis for the optimal configuration of the energy storage system and an important reference for the safe, stable, and economic operation of a high permeability photovoltaic distribution network.

7. Future Work

In this paper, only batteries are considered in the selection of batteries in the energy storage system. However, with a wider application of energy storage, a single energy storage system may not be able to meet the actual demand in the future. In subsequent research, we will combine other types of energy storage for optimization analysis of hybrid energy storage.

At the same time, because of the variety of renewable energy, more and more distributed power is connected to the distribution network. This paper only analyzes access to photovoltaic power generation. In a follow-up study, we will conduct a further study on scenarios with access to various energy sources.

In addition to the voltage fluctuation and load fluctuation considered in this paper, the power system with energy storage access has more indicators to measure security. In a follow-up study, we will also analyze the improvement and influence of energy storage access on various indicators.

Author Contributions: Conceptualization, J.Z. and L.Z.; methodology, S.Z.; software, S.Z. and L.Z.; validation, J.Z., S.Z. and L.Z.; formal analysis, J.Y.; investigation, L.L.; resources, J.Y.; data curation, J.Y.; writing—original draft preparation, L.Z.; writing—review and editing, J.Z.; visualization, L.L.; supervision, J.Y. All authors have read and agreed to the published version of the manuscript.

Funding: This work is supported in part by the National Key Research and Development Program Project (Grant number: 2019YFE0104800), Natural Science Foundation of Henan Province (Grant number: 202300410271) and the Key Project of Science and Technology in Colleges and Universities of Henan Province (Grant number: 162102110130).

Data Availability Statement: The original contributions presented in the study are included in the article; further inquiries can be directed to the corresponding author.

Conflicts of Interest: The authors declare no conflict of interest.

References

1. Yao, M.; Cai, X. An Overview of the Photovoltaic Industry Status and Perspective in China. *IEEE Access* **2019**, *7*, 181051–181060. [CrossRef]
2. Jothibasu, S.; Dubey, A.; Santoso, S. Two-Stage Distribution Circuit Design Framework for High Levels of Photovoltaic Generation. *IEEE Trans. Power Syst.* **2019**, *34*, 5217–5226. [CrossRef]
3. Pan, W.; Mao, M.; Zhou, Y.; Quan, X.; Li, Y. The impact of extreme weather condition on the voltage regulation in distribution systems with high penetration of roof-top photovoltaic. *Energy Rep.* **2021**, *7*, 320–331. [CrossRef]
4. Chidurala, A.; Saha, T.K.; Mithulananthan, N. Harmonic impact of high penetration photovoltaic system on unbalanced distribution networks—Learning from an urban photovoltaic network. *IET Renew. Power Gener.* **2016**, *10*, 485–494. [CrossRef]
5. Karimi, M.; Mokhlis, H.; Naidu, K.; Uddin, S.; Bakar, A. Photovoltaic penetration issues and impacts in distribution network – A review. *Renew. Sustain. Energy Rev.* **2016**, *53*, 594–605. [CrossRef]
6. Gandhi, O.; Rodríguez-Gallegos, C.D.; Zhang, W.; Reindl, T.; Srinivasan, D. Levelised cost of PV integration for distribution networks. *Renew. Sustain. Energy Rev.* **2022**, *169*, 112922. [CrossRef]
7. Dhivya, S.K.; Anurag, S.; Dipti, S.; Reindl, T. Stability implications of bulk power networks with large scale PVs. *Energy* **2019**, *187*, 115927.
8. Maharjan, S.; Dhivya, S.K.; Khambadkone, A.M. Enhancing the voltage stability of distribution network during PV ramping conditions with variable speed drive loads. *Appl. Energy* **2020**, *264*, 114733. [CrossRef]
9. Garmabdari, R.; Moghimi, M.; Yang, F.; Lu, J. Multi-objective energy storage capacity optimisation considering Microgrid generation uncertainties. *Int. J. Electr. Power Energy Syst.* **2020**, *199*, 105908. [CrossRef]
10. Kamaruzzaman, Z.A.; Mohamed, A. Dynamic voltage stability of a distribution system with high penetration of grid-connected photovoltaic type solar generators. *J. Electr. Syst.* **2016**, *12*, 239–248.
11. Xu, Z.; Yuan, B.; Liu, J.; Zheng, K.; Xu, S. Energy storage configuration for smoothing the output volatility of PV power generation. *IOP Conf. Ser. Earth Environ. Sci.* **2019**, *295*, 052045. [CrossRef]
12. Rana, M.M.; Uddin, M.; Sarkar, M.R.; Shafiullah, G.M.; Huadong, M.; Atef, M. A review on hybrid photovoltaic—Battery energy storage system: Current status, challenges, and future directions. *J. Energy Storage* **2022**, *51*, 104597. [CrossRef]
13. Haytham, M.A.A.; Ahmed, S.A.A.; Mohamed, H.A.; Salama, M.M.A. Mitigating voltage-sag and voltage-deviation problems in distribution networks using battery energy storage systems. *Electr. Power Syst. Res.* **2020**, *184*, 106294.
14. Amini, M.; Khorsandi, A.; Vahidi, B.; Hosseinian, S.H.; Malakmahmoudi, A. Optimal sizing of battery energy storage in a microgrid considering capacity degradation and replacement year. *Electr. Power Syst. Res.* **2021**, *195*, 107170. [CrossRef]
15. Hossain, S.J.; Biswas, B.D.; Bhattarai, R.; Ahmed, M.; Abdelrazek, S.; Kamalasadan, S. Operational Value Based Energy Storage Management for Photo-Voltaic(PV) Integrated Active Power DistributionSystems. *IEEE Trans. Ind. Appl.* **2019**, *99*, 5320–5330. [CrossRef]
16. Koohi-Fayegh, S.; Rosen, M.A. A review of energy storage types, applications and recent developments. *J. Energy Storage* **2020**, *2*, 101047. [CrossRef]
17. Chang, L.; Zhuo, J.; Zhao, D.; Li, S.; Chen, J.; Wang, J.; Yao, Q. A review on Flexible and safe operation of renewable energy microgrid using energy storage system. *Proc. CSEE* **2020**, *1*, 1–18+369.
18. Rajamand, S.; Miadreza, S.-K.; Catalão, J.P.S. Energy storage systems implementation and photovoltaic output prediction for cost minimization of a Microgrid. *Electr. Power Syst. Res.* **2022**, *202*, 107596. [CrossRef]
19. Rahman, S.; Saha, S.; Haque, M.E.; Islam, S.N.; Arif, M.T.; Mosadeghy, M.; Oo, A.M.T. A framework to assess voltage stability of power grids with high penetration of solar PV systems. *Int. J. Electr. Power Energy Syst.* **2022**, *139*, 107815. [CrossRef]
20. Zhao, L.; Zhang, T.; Peng, X.; Zhang, X. A novel long-term power forecasting based smart grid hybrid energy storage system optimal sizing method considering uncertainties. *Inf. Sci.* **2022**, *610*, 326–344. [CrossRef]
21. Liang, J.; Lan, F.; Li, J. A grid scenario evaluation method for energy storage capacity demand of photovoltaic-based distribution network. *Autom. Electr. Power Syst.* **2018**, *42*, 40–47+85.
22. Shoaib, B.; Muhammad, A.; Muqeet Hafiz, A.; Muhammad, S.; Harun, J.; Monia, H.; Sattar, M.A.; Habib, H. Optimal Scheduling of Demand Side Load Management of Smart Grid Considering Energy Efficiency. *Front. Energy Res.* **2022**, *10*, 861571.
23. Waseem, M.; Lin, Z.; Liu, S.; Sajjad, I.A.; Aziz, T. Optimal GWCSO-based home appliances scheduling for demand response considering end-users comfort. *Electr. Power Syst. Res.* **2020**, *187*, 106477. [CrossRef]
24. Rezaeimozafar, M.; Eskandari, M.; Hadi Amini, M.; Moradi, M.H.; Siano, P. A Bi-Layer Multi-Objective Techno-Economical Optimization Model for Optimal Integration of Distributed Energy Resources into Smart/Micro Grids. *Energies* **2020**, *13*, 1706. [CrossRef]
25. Waseem, M.; Lin, Z.; Liu, S.; Zhang, Z.; Aziz, T.; Khan, D. Fuzzy compromised solution-based novel home appliances scheduling and demand response with optimal dispatch of distributed energy resources. *Appl. Energy* **2021**, *290*, 116761. [CrossRef]
26. Li, D.; Cai, W. Optimal configuration of photovoltaic energy storage capacity for large power users. *Energy Rep.* **2021**, *7* (Suppl. S7), 468–478. [CrossRef]
27. Yang, P.; Nehorai, A. Joint Optimization of Hybrid Energy Storage and Generation Capacity with Renewable Energy. *IEEE Trans. Smart Grid* **2014**, *5*, 1566–1574. [CrossRef]
28. Wu, J.; Wen, C.; Li, S.; Shi, Q. Capacity optimization allocation of photovoltaic energy storage system based on TOU. *Adv. Technol. Electr. Eng. Energy* **2018**, *37*, 23–30.

29. Lima, D.A.; Feijão, V.R. Stochastic approach for economic viability of photovoltaic systems with battery storage for big electricity consumers in the regulated marketin Brazil. *Electr. Power Syst. Res.* **2022**, *205*, 107744. [CrossRef]
30. Guo, Y.; Xiang, Y. Cost–benefit analysis of photovoltaic-storage investment in integrated energy systems. *Energy Rep.* **2022**, *8* (Suppl. S5), 66–71. [CrossRef]
31. Lu, S.; Wang, X.; Wu, J. Location and Size Planning of Distributed Photovoltaic Generation in Distribution network System Based on K-means Clustering Analysis. *IOP Conf. Ser. Earth Environ. Sci.* **2018**, *108*, 052022. [CrossRef]
32. Home-Ortiz, J.M.; Pourakbari-Kasmaei, M.; Lehtonen, M.; Sanches Mantovani, J.R. Optimal location-allocation of storage devices and renewable-based DG in distribution systems. *Electr. Power Syst. Res.* **2019**, *172*, 11–21. [CrossRef]
33. Wang, W.; Dou, F.; Yu, X.; Liu, G. Scenario analysis of wind power output based on improved k-means algorithm. *IOP Conf. Ser. Earth Environ. Sci.* **2021**, *675*, 012092. [CrossRef]
34. Liang, G.; Sun, B.; Zeng, Y.; Ge, L.; Li, Y.; Wang, Y. An Optimal Allocation Method of Distributed PV and Energy Storage Considering Moderate Curtailment Measure. *Energies* **2022**, *15*, 7690. [CrossRef]
35. Feng, J.; Zhou, H. Bi-Level Optimal Capacity Planning of Load-Side Electric Energy Storage Using an Emission-Considered Carbon Incentive Mechanism. *Energies* **2022**, *15*, 4592. [CrossRef]
36. Feng, H.; Ma, W.; Yin, C.; Cao, D. Trajectory control of electro-hydraulic position servo system using improved PSO-PID controller. *Autom. Constr.* **2021**, *127*, 103722. [CrossRef]
37. Wang, G.; Wan, Z.; Wang, X. Review of two (double) level planning. *Adv. Math.* **2007**, *5*, 513–529.
38. Gong, Z. Study on Two-Stage Optimal Scheduling Strategy and Time-of-Use Price Optimization of Optical Storage System. Master's Thesis, Hefei University of Technology, Hefei, China, 2021.